First-Row Transition Metal Complexes for Electrochemical Carbon Dioxide Activation

Von der Fakultät für Mathematik, Informatik und Naturwissenschaften der RWTH Aachen University zur Erlangung des akademischen Grades eines Doktors der Naturwissenschaften genehmigte Dissertation

vorgelegt von

Niklas Werner Kinzel

M. Sc.

aus

Vechta.

Berichter: Univ.-Prof. Dr. rer. nat. Walter Leitner

Univ.-Prof. Dr. rer. nat. Regina Palkovits

Tag der mündlichen Prüfung: 30. September 2022

La normalité est une route pavée :

On y marche aisément mais les fleurs n'y poussent pas.

– VINCENT VAN GOGH

Eidesstattliche Erklärung/Declaration of Authorship

I, Niklas Werner Kinzel,

declare that this thesis and the work presented in it are my own and have been generated by me as the result of my own original research.

Hiermit erkläre ich an Eides statt/I do solemnly swear that:

1. This work was done wholly or mainly while in candidature for the doctoral degree at this faculty and university;
2. Where any part of this thesis has previously been submitted for a degree or any other qualification at this university or any other institution, this has been clearly stated;
3. Where I have consulted the published work of others or myself, this is always clearly attributed;
4. Where I have quoted from the work of others or myself, the source is always given. This thesis is entirely my own work, with the exception of such quotations;
5. I have acknowledged all major sources of assistance;
6. Where the thesis is based on work done by myself jointly with others, I have made clear exactly what was done by others and what I have contributed myself;
7. Parts of this work have been published before as:

- N. W. Kinzel, C. Werlé, W. Leitner, *Angew. Chem. Int. Ed.* **2021**, *60*, 11628.

  International Edition: Doi.org/10.1002/anie.202006988

  German Edition: Doi.org/10.1002/ange.202006988
- N. W. Kinzel, D. Demirbas, E. Bill, T. Weyhermüller, C. Werlé, N. Kaeffer, W. Leitner, *Inorg. Chem.* **2021**, *60*, 19062.

November 14, 2022

This thesis was prepared at the MAX PLANCK INSTITUTE FOR CHEMICAL ENERGY CONVERSION between April 2018 and March 2022 under the scientific supervision of Prof. Dr. WALTER LEITNER.

Acknowledgment

First and foremost, I would like to thank **Prof. Dr. WALTER LEITNER** for the scientific supervision of this work, for providing an excellent research environment at the MAX PLANCK INSTITUTE FOR CHEMICAL ENERGY CONVERSION, and for his wholehearted support throughout the entire time of my doctoral studies.

Then, I thank **Dr. NICOLAS KAEFFER** for all aspects of his day-to-day supervision in the second half of my work, but particularly for his enormous expertise in electrochemistry that he never got tired of sharing.

I also want to thank **Dr. CHRISTOPHE WERLÉ** for supervising the first half of my doctoral studies, his advice on the synthesis of ligands and complexes, and his commitment to the review's writing process.

Many thanks also go to the analytics department: **ALINA JAKUBOWSKI** for her helpfulness in all respects but specifically in questions concerning GC and HPLC, **JUSTUS WERKMEISTER** for setting up the headspace GC system, and **ANNIKA GUROWSKI** for elemental analysis of my compounds.

Further thanks go to **LUKAS SCHUBERT** and **Dr. THOMAS WEYHERMÜLLER** for conducting NMR measurements. Special thanks are due to the latter and **BERND MIENERT** for recording and refining the various crystal structures.

Gratitude is owed to **Dr. ECKHARD BILL** and **DERYA DEMIRBAS** for recording and interpreting EPR and MÖSSBAUER spectra as well as SQUID measurements.

I am most thankful to my former laboratory assistant **JULIA ZERBE** for her help in the lab, which allowed me to take the time to write the review. Further thanks for his aid with the synthetic work go to my research student **LUKAS FÖBINGER**.

I thank my group members and lab colleagues of the ORGANOMETALLIC ELECTROCATALYSIS group **Dr. MI-YOUNG LEE**, **Dr. AJEET SINGH**, **PHILLIP RECK**, **CHRISTIAN KAHL**, and **PETRA HÖFER** for the pleasant working atmosphere, fruitful discussions, and overall support.

My lab colleague **ALEXANDER SCHMITZ** deserves gratitude for his (more or less) impeccable taste in music and for reminding me of the carnival season, whether wanted or not.

I want to express my sincerest thanks to **KIRA EHMANN** for proofreading every important manuscript I have written during my doctoral studies and for our discussions about the most unimportant details in them.

Thanks to the whole MOLECULAR CATALYSIS group for the enjoyable time together inside and outside the institute.

NIKLAS WESSEL is thanked for designing the piping and instrumentation diagram of the electrolysis setup.

For writing the EXCEL macros used to analyze electrochemical data, I thank **JANIS KRÖGER**.

I want to express my deepest gratitude to my parents, **AFRA** and **WERNER**, for doing everything in their power to grant me access to the best possible education and always motivating me to take the next step.

Lastly, to my sisters **FRANZISKA** and **LOUISA**: Thank you for taking care of all the big and small family matters, which allowed me to focus on this work.

Abstract

In the endeavor to substitute fossil resources for the production of energy and chemicals with renewable carbon feedstocks and energy sources, the electrochemical reduction of carbon dioxide is considered a “dream reaction”. It holds the potential to use CO_2 from industrial waste streams or the atmosphere and recycle the C_1 building block into the chemical value chain by adding electrons. Molecular coordination complexes, particularly those based on 3d transition metals, can be introduced as catalysts to enable the reaction and expand the scope of accessible products. Thus, the alleviation of the global climatic and socio-economic effects of the greenhouse gas CO_2 is combined with producing industrially relevant carbon-containing compounds.

In this context, the present study is dedicated to investigating the role of the 3d metal center and the coordinated auxiliary ligands on the structural and electrochemical properties of the corresponding complexes. The obtained results shall be used to conclude the effect of these components on the traversed catalytic mechanism in the electrochemical activation of CO_2.

A series of mid to late 3d transition metal complexes (from manganese to zinc) was synthesized from the redox-innocent pincer ligand N^2,N^6-bis(diphenylphosphaneyl)-N^2,N^6-diphenylpyridine-2,6-diamine. Metal precursors were chosen in their +II or +I oxidation states and coordinated by chloride or acetonitrile (MeCN) ligands. The application of various analytical techniques allowed the correlation of the observed coordination geometries to the electronic configuration of the metal via crystal field theory. A qualitative increase in electronic density at the metal center could be observed throughout the 3d row.

Cyclic voltammetry (CV) analyses revealed metal-centered redox processes for iron, cobalt, and nickel down to the zero-valent state. While cobalt and nickel undergo several ligand exchange reactions during this pathway, iron is surmised to dimerize or disproportionate.

NMR spectroscopic and CV experiments tracked the ligand exchange between chloride and acetonitrile at the metal center. It was found that a single acetonitrile ligand coordinates cobalt and nickel at the zero-valent state in MeCN, independent from the auxiliary ligand in the starting complex. The π back bonding of MeCN supposedly removes electron density from the metal center, decreasing the potential required to reduce the complex but also its reduction strength.

The stability of the complexes was found to be higher when chloride rather than labile acetonitrile ligands are coordinated and increased from iron to nickel, explainable by shorter and, hence, stronger bonds for the later transition metals.

Electrochemical analyses under CO_2 atmosphere showed the substrate coordination at the oxidation state zero for each of the complexes, yet substantial electron transfer to CO_2 is only proposed for iron and cobalt.

CV under the addition of the LEWIS acid magnesium triflate identified cobalt as promising for the reductive disproportionation of CO_2. A CV-based proton source screening revealed methanol as a suitable BRØNSTED acid for CO_2 reduction with the same metal. Controlled potential electrolysis experiments, however, showed hydrogen as the preferred product with only minor amounts of CO. Likely, the probed complexes disintegrate at the electrode surface under formation of heterogeneous species. The *para* position in the pyridine core of the ligand backbone was identified as a possible weakness of the complex, the protection and further improvement of which will constitute a perspective for this work.

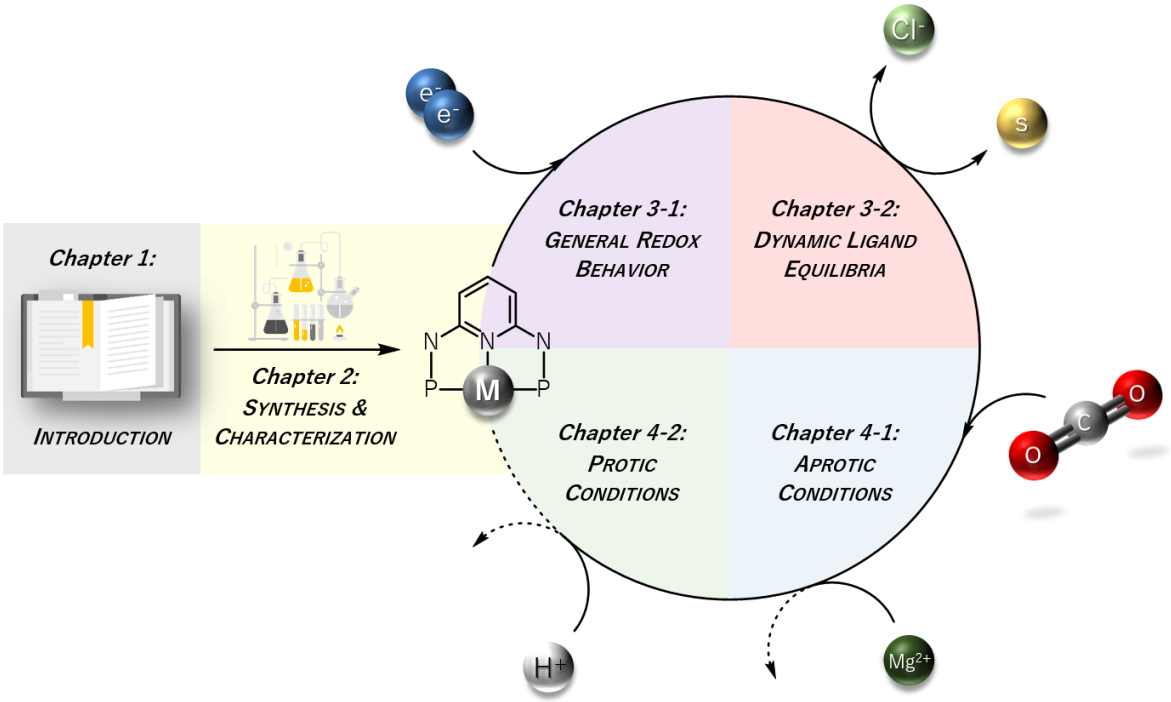

Overall, the present study elucidates how the metal center determines the activity and stability of otherwise redox-innocent systems in electroreduction reactions such as carbon dioxide conversion. The in-depth knowledge of the electrochemical behavior of the cobalt and nickel complexes under inert conditions, in contact with CO_2, and combined with further co-catalysts provides the means to adjust the properties of the complexes for CO_2 activation. These insights will be used to improve the so-far unsatisfactory long-term stability of the complexes under electrocatalytic conditions.

Zusammenfassung

In dem Bestreben, fossile Ressourcen für die Energieerzeugung und die Herstellung von Chemikalien durch erneuerbare Kohlenstoff- und Energiequellen zu ersetzen, gilt die elektrochemische Reduktion von Kohlendioxid als "Traumreaktion". Sie birgt das Potenzial, CO_2 aus industriellen Abgasströmen oder aus der Atmosphäre durch Addition von Elektronen in die chemische Wertschöpfungskette zurückzuführen. Die Einführung molekularer Katalysatoren, insbesondere auf Basis von 3d-Übergangsmetallen, ermöglicht es, die Reaktion ablaufen zu lassen und die Bandbreite der zugänglichen Produkte zu erweitern. Auf diesem Wege wird die Milderung der globalen klimatischen und sozioökonomischen Auswirkungen des Treibhausgases CO_2 mit der Herstellung industriell relevanter kohlenstoffhaltiger Verbindungen kombiniert.

In diesem Zusammenhang widmet sich die vorliegende Arbeit der Untersuchung des Einflusses des 3d-Metallzentrums und der koordinierten Hilfsliganden auf die strukturellen und elektrochemischen Eigenschaften der daraus geformten Metallkomplexe sowie auf den bevorzugt durchlaufenen Katalysemechanismus bei der elektrochemischen Aktivierung von CO_2.

Eine Reihe von mittleren bis späten 3d-Übergangsmetallkomplexen (von Mangan bis Zink) wurde aus dem redox-inerten Pincerliganden N^2,N^6-Bis(diphenylphosphanyl)-N^2,N^6-diphenylpyridin-2,6-diamin synthetisiert. Hierbei stellen Chlorid- und Acetonitril (MeCN)-Metallvorstufen in der Oxidationsstufe +II oder +I den Kern der synthetisierten Komplexverbindungen dar. Die Anwendung komplementärer Analysemethoden ermöglichte die Korrelation der beobachteten Koordinationsgeometrien mit der Elektronenkonfiguration des Metalls unter Anwendung der Kristallfeldtheorie. Eine qualitative Zunahme der Elektronendichte am Metallzentrum konnte in Richtung der späteren Metalle beobachtet werden.

Cyclovoltammetrie (CV)-Analysen zeigten metallzentrierte Redoxprozesse für Eisen, Kobalt und Nickel bis hin zum nullwertigen Zustand. Während Kobalt und Nickel dabei mehrere Ligandenaustauschreaktionen durchlaufen, wird vermutet, dass der Eisenkomplex dimere Strukturen bildet oder disproportioniert.

Der Ligandenaustausch am Metallzentrum wurde für die Chlorid- und Acetonitrilkomplexe von Eisen, Kobalt und Nickel durch NMR- und CV-Experimente analysiert. Die Ergebnisse der Analyse indizieren, dass Kobalt und Nickel, unabhängig vom Hilfsliganden im Ausgangskomplex, im nullwertigen Zustand in MeCN von einem einzigen Acetonitrilmolekül koordiniert werden. Durch die π-Rückbindung von MeCN wird dem Metallzentrum vermutlich Elektronendichte entzogen, wodurch sowohl das erforderliche Potential als Triebkraft für die Reduktion als auch die Reduktionskraft des Komplexes verringert werden.

Es wurde festgestellt, dass die Komplexe stabiler sind, wenn Chlorid- anstatt der labilen Acetonitrilliganden an das Metall koordinieren, und die Stabilität von Eisen zu Nickel zunimmt, was sich auf kürzere Bindungsabstände und damit stärkere Bindungen bei späteren Übergangsmetallen zurückführen lässt.

Die elektrochemische Analyse unter CO_2-Atmosphäre ergab, dass die Koordination von Kohlendioxid bei jedem der Komplexe in der Oxidationsstufe Null stattfindet. Ein substanzieller Elektronentransfer auf das Substrat wird jedoch nur für Eisen und Kobalt postuliert.

Cyclovoltammetrie unter Zugabe der LEWIS-Säure Magnesiumtriflat identifizierte Kobalt als vielversprechend für die reduktive Disproportionierung von CO_2. CV-basierte Tests von Protonenquellen ergaben Methanol als geeignete BRØNSTED-Säure für die CO_2-Reduktion mit demselben Metall. Bei Elektrolyseexperimenten unter konstantem Potential wurden jedoch bevorzugt Wasserstoff und nur geringe Mengen von CO detektiert. Wahrscheinlich zerfallen die untersuchten Komplexe an der Elektrodenoberfläche unter Bildung von heterogenen Spezies. Die *para*-Position im Pyridinkern des Ligandenrückgrats wurde als mögliche Schwachstelle des Komplexes identifiziert, deren Schutz und weitere Verbesserung eine Perspektive für die Zukunft darstellt.

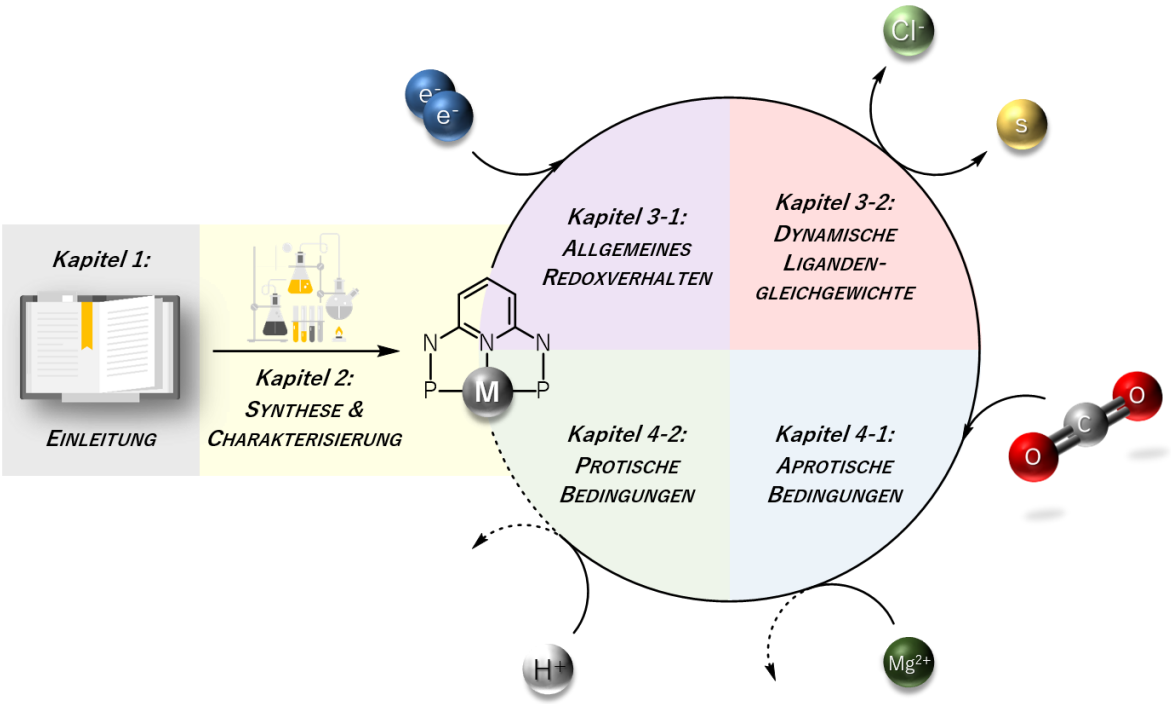

Insgesamt verdeutlicht die vorliegende Studie, wie das Metallzentrum die Aktivität und Stabilität ansonsten redox-inerter Systeme in Elektroreduktionsreaktionen wie der Kohlendioxidumwandlung bestimmt. Das vertiefte Wissen über das elektrochemische Verhalten der Kobalt- und

Nickelkomplexe unter inerten Bedingungen, aber auch im Kontakt mit CO_2 sowie in Kombination mit weiteren Cokatalysatoren bietet die Möglichkeit, die Eigenschaften der Komplexe für die CO_2-Aktivierung anzupassen. Diese Erkenntnisse werden zukünftig dazu genutzt, um die bisher unbefriedigende Langzeitstabilität der Komplexe unter elektrokatalytischen Bedingungen zu verbessern.

Table of Contents

CHAPTER 3: ELECTROCHEMISTRY UNDER INERT CONDITIONS

CHAPTER 4: ELECTROCHEMICAL CARBON DIOXIDE ACTIVATION

Glossary

a	ordinate intercept
A	electrode surface area or hyperfine coupling constant
AL	auxiliary ligand
An	aniline
ap	apical
ax	axial
BA	benzoic acid
bpy	2,2'-bipyridine
C	chemical (step)
c^0	bulk concentration of the analyte
CE	counter electrode
CN	coordination number
COSY	correlation spectroscopy
CPE	controlled potential electrolysis
CTP	catalytic TAFEL plot
CV	cyclic voltammetry
cyclam	1,4,8,11-tetra-azacyclo-tetradecane
d	distance
D	diffusion (kinetic zone)
D_0	diffusion coefficient of the analyte
DBA	dibenzylideneacetone
DBP	2,6-dibromopyridine
DCM	dichloromethane
DFT	density functional theory
DISP	disproportionation
DMF	*N,N*-dimethylformamide

DPPDA	N^2,N^6-diphenylpyridine-2,6-diamine
Dppp	1,3-bis(diphenylphosphino)propane
E	extraordinary (kinetic zone)
E	electron transfer/electrochemical (step)
E	potential
E^0	standard potential
E_0	starting potential
$E_{1/2}$	half-wave potential
EA	elemental analysis
E_{app}	applied potential
E_{cat}	potential of catalyst reduction
e-cat$_{(ox/red)}$	(oxidized/reduced) electrocatalyst
eCO_2r	electrochemical carbon dioxide reduction
E_{dir}	potential of direct CO_2 conversion at the electrode surface
$E_{p,a/c}$	anodic/cathodic peak potential
EPR	electron paramagnetic resonance
Eq	equatorial
eq.	equation
equiv.	equivalent
ΔE_Q	quadrupole splitting
ET_H	electron transfer through the hydride
ET_M	electron transfer through the molecular complex
E_λ	reverse potential
Fc	ferrocene
FE	faradaic efficiency
G	general (kinetic zone)
GC	gas chromatography
HA	BRØNSTED acid

HOMO	highest occupied molecular orbital
HPLC	high-performance liquid chromatography
hs	high spin
HSQC	heteronuclear single quantum coherence
I/*i*	current
$i_{p,a/c}$	anodic/cathodic peak current
IR	infrared
IS	inner-sphere
j^n	normalized current density
$j^n_{p,a/c}$	normalized anodic/cathodic peak current density
K	kinetic (zone)
K	equilibrium constant
$k^{+/-}$	forward (+)/backward (-) rate constant
L	ligand
L	N^2,N^6-bis(diphenylphosphaneyl)-N^2,N^6-diphenylpyridine-2,6-diamine
LA	LEWIS acid
ls	low spin
LUMO	lowest unoccupied molecular orbital
m	*meta*
m	stoichiometry of coordinated ligands
M	molar
M	metal
Mes	mesityl
MFC	mass flow controller
(HR)MS	(high-resolution) mass spectrometry
n	amount or charge of the metal complex
NHE	normal hydrogen electrode

NMR	nuclear magnetic resonance
O	*ortho*
O	ordinary (kinetic zone)
O_h	octahedral
OS	outer-sphere
P	*para*
P	product or pure (kinetic zone)
P&ID	piping and instrumentation diagram
Ph	phenyl
Py	pyridine
Q	transferred charge
RE	reference electrode
RHE	reversible hydrogen electrode
$R_{N/P}$	atom/group bound to the nitrogen/phosphorus atom
S	solvent
S	spin
SBP	square-based pyramidal
SCE	saturated calomel electrode
SHE	standard hydrogen electrode
SOMO	singly occupied molecular orbital
SP	square planar
SQUID	superconducting quantum interference device
t	time
T	temperature
TBA	tetrabutylammonium
TBP	trigonal bipyramidal
T_d	tetrahedral
TFE	2,2,2-trifluoroethanol

THF	tetrahydrofuran
tim	2,3,9,10-tetramethyl-1,4,8,11-tetraazacyclotetradeca-1,3,8,10-tetraene
TMS	tetramethylsilane
TOF	turnover frequency
TOF_0	turnover frequency at zero overpotential
TOF_{max}	maximum turnover frequency
TON	turnover number
TPP	tetraphenyl porphyrin
UV/VIS	ultraviolet/visible
V_x	Volt vs. x (x = Ag → Ag^+/Ag, Fc → Fc^+/Fc, NHE, SCE, SHE)
WE	working electrode
XRD	x-ray diffraction
xs.	excess
Y	yield
z	oxidation state
Δ	orbital energy difference
Γ	line width
δ	chemical shift or isomer shift
η	coordination mode
η	overpotential
θ	tetrahedral bond angle
θ_{ap}	angle between the apical ligand and the basal plane
λ	kinetic parameter for the competition of chemical reaction and diffusion
μ_B	BOHR magneton
μ_{eff}	effective magnetic moment
ν	scan rate
τ	geometry index
X_M	metal electronegativity

Chapter 1: Background & Motivation

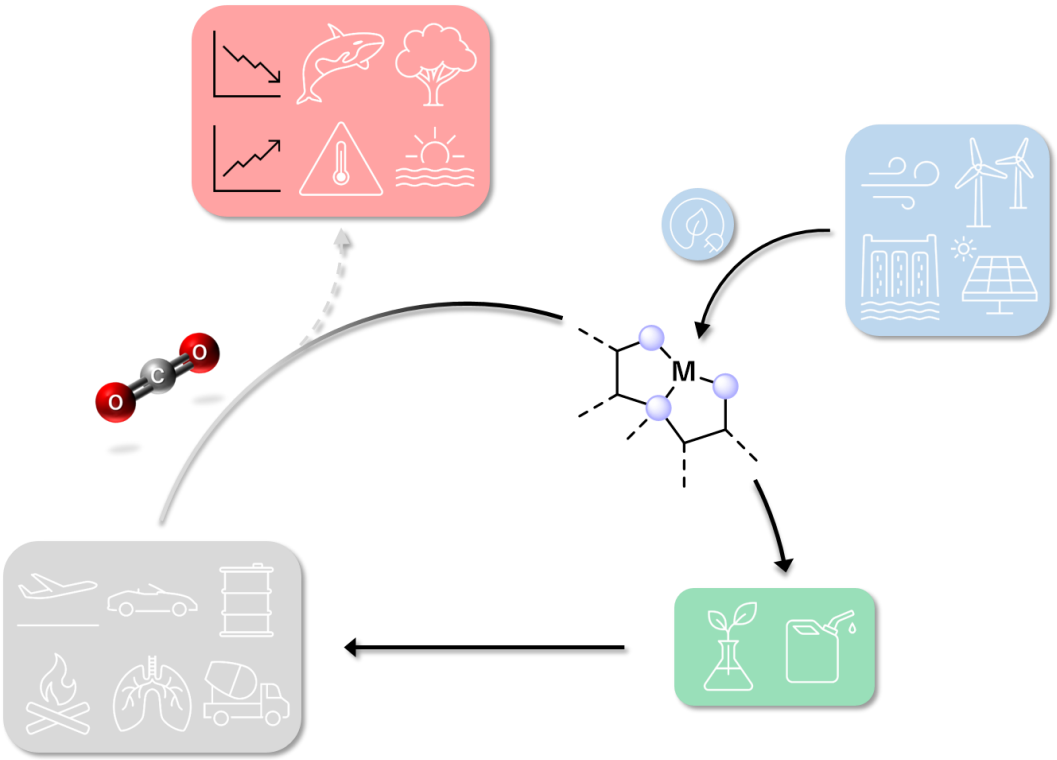

In the following chapter, the general context of this work is introduced by addressing the various facets of carbon dioxide – sources, global impact, and sustainable valorization.

Organometallic electrocatalysis constitutes a promising technique for the direct use of electric energy in the reductive conversion of carbon dioxide and is therefore presented in detail. Focus is set on the role of the catalyst, particularly regarding potential reaction pathways in the endeavor to expand the accessible product scope starting from the C_1 building block.

After giving an overview of the most efficient catalyst systems based on molecular transition metal complexes known to date and the metrics used to evaluate their catalytic properties, the influence of the central metal on the outcome of the reaction is scrutinized.

The present work's approach to addressing this question by tailoring the principles of organometallic catalyst design to electrochemical needs is outlined at the end of the chapter.

Parts of this chapter have been published in:

N. W. Kinzel, C. Werlé, W. Leitner, *Angew. Chem. Int. Ed.* **2021**, *60*, 11628.

1.1 Carbon Dioxide

1.1.1 Impact on Nature, Society, Industry & Science

In the last decades, the involvement of carbon dioxide in vitally important areas of humankind, such as nature, society, industry, and science, has become increasingly visible and, hence, an essential topic for humanity's everyday life. However, the intertwinement of CO_2 and these areas goes far back in time and is not solely limited to humankind.

Already before the existence of human beings on the planet, CO_2 constituted the main (gaseous) intermediate in the earth's carbon cycle.[1] On the one hand, plants in the bio- and hydrosphere performed (and still perform) photosynthesis to convert CO_2 into carbohydrates with the help of solar energy. On the other hand, the oxidation of carbohydrates by combustion[2] or respiration yielded carbon dioxide and closed the cycle (Figure 1.1).[1]

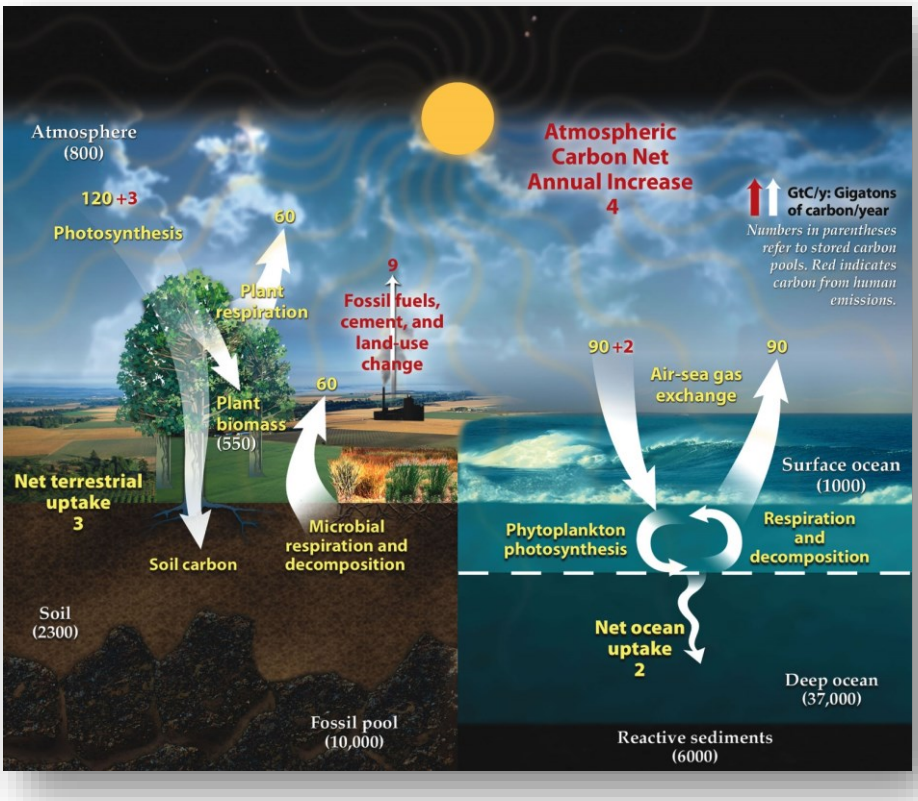

Figure 1.1. Schematic representation of the fast global carbon cycle including natural fluxes (yellow), human contributions (red), and stored carbon (white) in gigatons of carbon per year. Reprinted from ref. [3] with permission.

Simultaneously, the burial of plant material by natural phenomena removed CO_2 from the cycle on the earth's surface and atmosphere. Anaerobic conditions, high pressures, and elevated temperatures over the course of millions of years allowed the subterranean transformation of these

carbohydrates to coal, oil, and natural gas – the so-called "fossil resources".[4] With the beginning of the industrial revolution at the end of the 19th century, humanity began to understand the importance of the enormous energy contained in these various forms of reduced carbon and started to build their entire economy on this energetic foundation. Combustion of fossil fuels shifted the equilibrium between reduced and oxidized carbon – initially located far on the reduced side – more and more to carbon dioxide and, thus, carbon in its highest possible oxidation state +IV.[5] Up to today, society relies on fossil resources to satisfy its needs in terms of energy generation,[6] production of nutrients/fertilizers,[7] transport and aviation,[5c, 8] construction industry,[9] and production of chemical goods[10] eventually resulting in continuous emissions of CO_2 and, hence, increasing concentrations in the atmosphere. The relatively stable percentage of 280 ppm of CO_2 in the air before the industrial revolution[11] increased to more than 400 ppm in 2015 (Figure 1.2), a threshold that environmental scientists claim to mark a point at which nature alone is not capable of regulating the CO_2 balance anymore.[12] In January 2022, the MAUNA LOA OBSERVATORY in HAWAII determined the concentration of carbon dioxide in the atmosphere at ~418 ppm.[13]

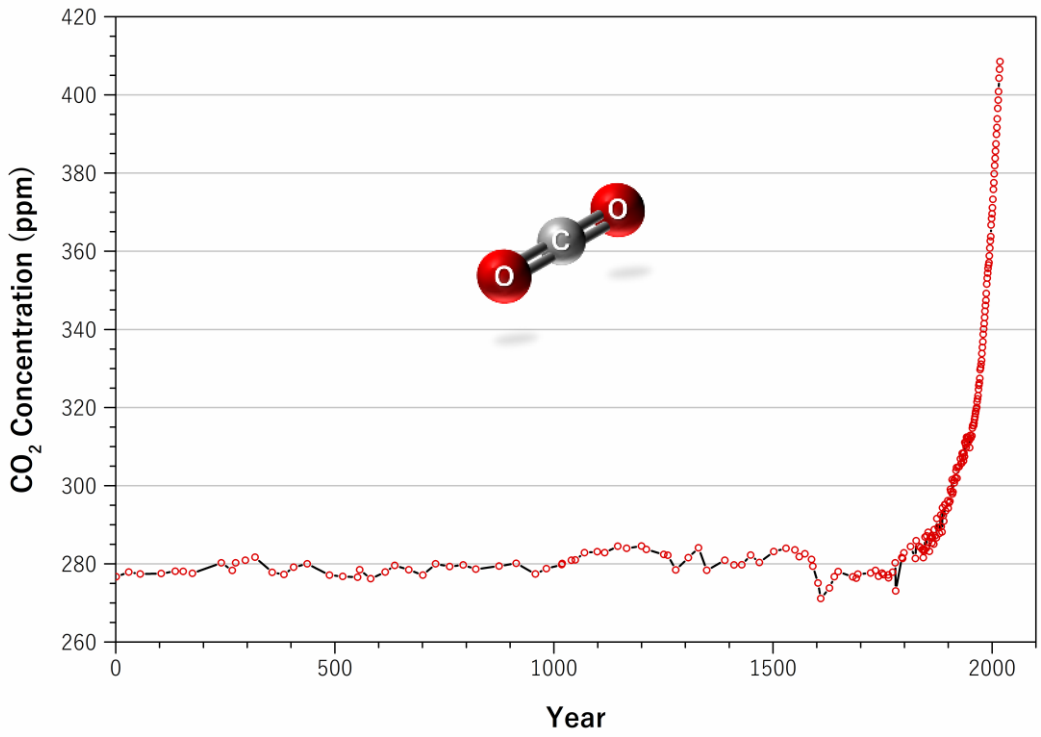

Figure 1.2. Average concentration of CO_2 in the global atmosphere between year one and 2018.[14]

Elevated levels of atmospheric CO_2 severely impact the earth's climate and ecosystem due to the direct correlation of this quantity with extreme phenomena such as global warming, rising sea levels, ocean acidification, and declining biodiversity.[15] Therefore, effective and efficient methods to decrease CO_2 emissions and, eventually, its concentration in the atmosphere are

highly sought. The primary requirement for this approach is a severe paradigm shift of humankind's mindset on political and economic questions: The current "Fossil Age" needs to be converted into a "Sustainable Energy and Chemistry Nexus" that relies on renewable energy sources rather than fossil ones and offers an interchangeable industrial system between chemicals/fuels and "green" energy (Figure 1.3).

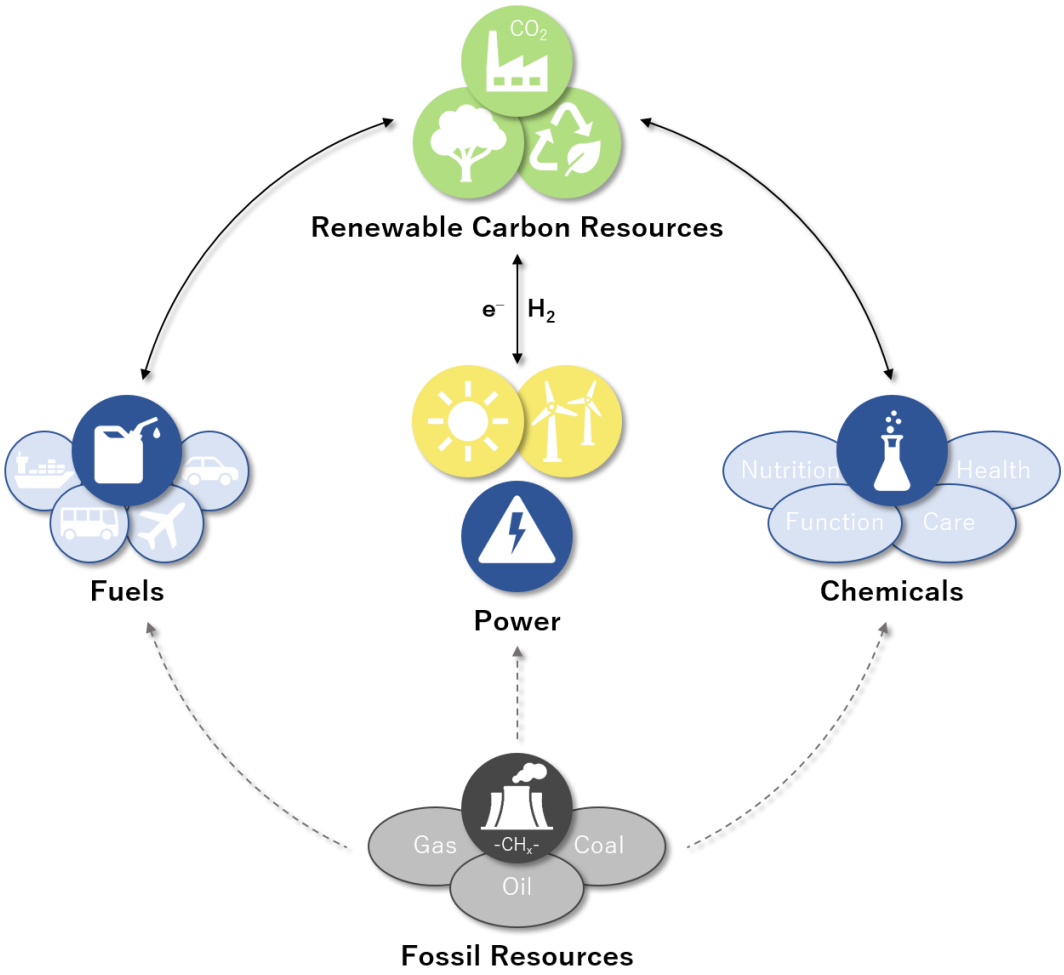

Figure 1.3. From the "Fossil Age" (bottom) to a "Sustainable Energy and Chemistry Nexus" (top).

1.1.2 Sustainable Conversion using Renewable Energies

Although the activation of CO_2 as a pre-requisite for its conversion is challenging from a scientific point of view (*vide infra*), projects summarized under the concept of POWER-TO-X are already pursuing this endeavor.[16] Wind, water, and solar power are employed to provide carbon-free and renewable energy for various chemical, biochemical and electrochemical processes that allow the synthesis of valuable reduced-carbon products. Starting from energy carriers mainly represented by C_1 compounds such as formic acid and methanol, the aim is to expand the product scope toward functional materials, fine chemicals, and even pharmaceuticals.[17] Careful attunement of the underlying reactions may even allow the

synthesis of so far inaccessible compounds utilizing the concepts of Green Chemistry (e.g., atom economy and use of renewable feedstocks).[18]

From this perspective, the conversion of carbon dioxide does not only help to alleviate the environmental effect of the greenhouse gas, but its reduced forms can be used as a recyclable C_1 building block in the chemical industry with the potential to replace oil as the substrate basis in the future. Apart from high-concentration flue gas streams of industrial processes,[19] the carbon reserves under the various forms of CO_2 (i.e., gaseous in the atmosphere, dissolved in the hydrosphere, and chemically bound as carbonates in the terrestrial environment) can be exploited to ensure a sufficient supply with the C_1 substrate.[20]

Regarding solar and wind power as green energy sources for the transformation of CO_2, the preferred technological option for renewable energy can differ depending on the regional climatic situations. Hence, in Europe, wind is most efficiently converted to electric power in northern areas close to the sea, whereas the highest irradiation benefitting solar energy generation can be found in southern countries (Figure 1.4).

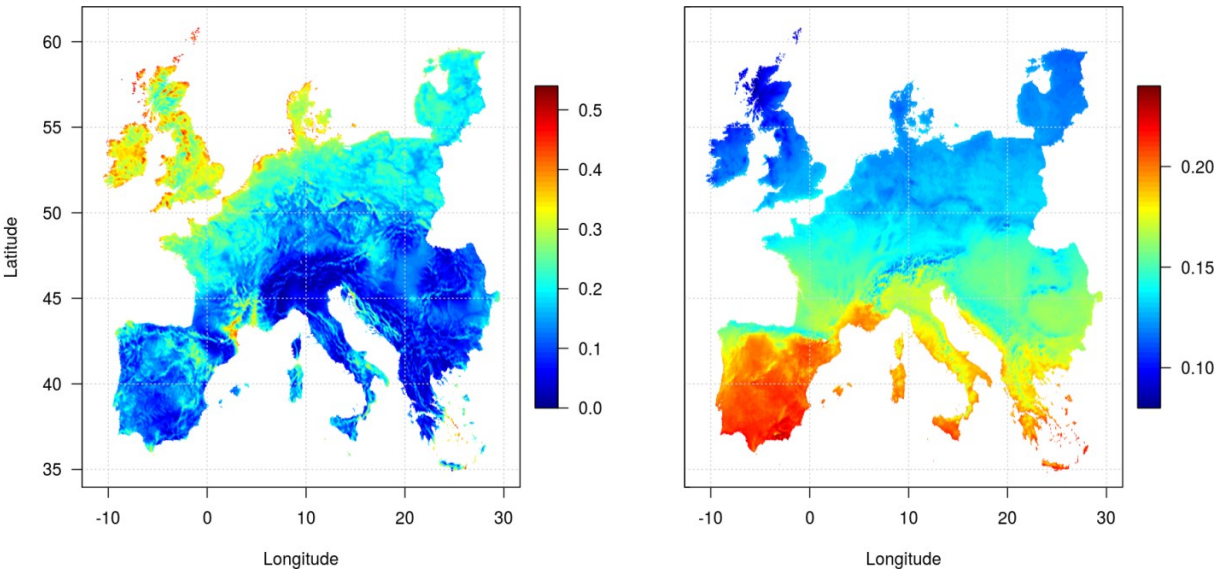

Figure 1.4. Average capacity factors for wind (left) and photovoltaics (right) in Europe (1995–2015). Reprinted from ref. [21] with permission.

Irrespective of the preferred technology, green electricity ("power") generation is intermittent and fluctuating, thus requiring efficient and flexible storage technologies. In this context, direct electricity storage could be substituted by conversion into molecular energy carriers or chemical products as an attractive possibility to balance supply and demand.[22]

The direct formation of chemical bonds from electrons can be provided by electrochemistry, the impact of which is represented (among others) in FARADAY's pioneering work,[23] the KOLBE electrolysis,[24] and the TAFEL rearrangement[25]. Although controlling the many system parameters

in synthetic electrochemistry on a laboratory scale (i.e., cells, electrodes, electrolytes, solvents, and others)[26] can be challenging, processes such as the chloralkali[27] or HALL–HÉROULT[28] electrolysis are producing valuable chemicals (chlorine and aluminum) on a scale of millions of tons per year.

For carbon dioxide, thermochemical routes employing catalytically active transition metal catalysts have proven to be capable of converting the substrate into more valuable chemicals.[15, 29] Industrial implementation of this approach is already pursued in singular cases,[30] but various factors still impair a broader application. In particular, (1) high costs for the capture, purification, storage, and transport of carbon dioxide to the processing sites, (2) the energy requirements for the conversion of CO_2, and (3) the limited diversity of CO_2-based chemicals are reasons for (4) a limited market size and industrial investment as well as an insufficient socio-economical demand.[31]

Electrocatalytic (inter)conversion of electrical power into chemical bonds (of low-concentration substrate streams) can contribute innovative solutions to overcome the obstacles inherent to challenges (1) to (3). Tackling the challenges mentioned above will also solve issue (4), eventually enabling the substitution of conventional synthetic routes by greener methodologies for CO_2 conversion.

From a fundamental level, the thermodynamic stability and kinetic inertness of the CO_2 molecule constitute the central challenges for POWER-TO-X strategies.[29, 32] Its conversion into valuable C_1 chemicals and more sophisticated products requires a combination of reduction (addition of electrons) and bond-forming processes (addition of protons or other reagents, Figure 1.5).

Reduction along the C_1 pathway yields products with high potential production volumes that, if used as a synthon for further transformations (horizontal pathways), grant access to economic and ecologic benefits compared to today's value chains.[33]

Although synthetic methods for the valorization of CO_2 using dihydrogen are increasingly available,[34] electrocatalysis constitutes a promising alternative. Heterogeneous electrode materials and deposits[35] (especially copper in its various modifications[36]), enzymes[37] as well as molecularly defined organic[38] and (immobilized)[39] organometallic species[40] offer a variety of approaches in the reduction of CO_2 by electrons.

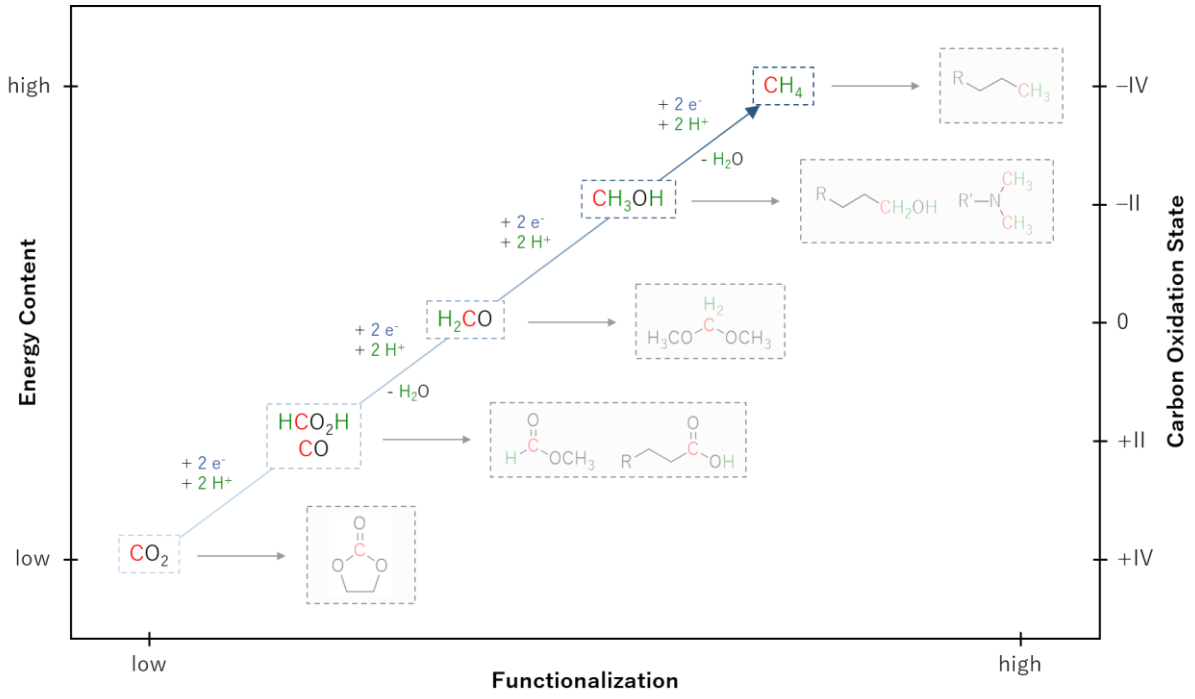

Figure 1.5. Schematic correlation between energy content and carbon oxidation state for CO_2-based C_1 compounds and possible higher molecular products.

These electrochemical methods enable the electron transfer from the electrode material to CO_2 and compensation of the charge balance by protons. This principle eliminates the extra step of electrochemical hydrogen generation via water electrolysis [challenge (2)]. Also, it offers the possibility to operate at lower substrate concentrations [challenge (1)],[41] temperatures, and pressures than those often necessary for CO_2 hydrogenation.

The opportunity brought by molecularly defined transition metal complexes in this field is based on structural simplicity and their ability to grant access to the elementary steps in the molecular mechanisms for "CO_2 activation" by decoupling electron transfer and bond formation. Hence, molecular electrocatalysis can open novel pathways to devise synthetically useful transformations exceeding the C_1 stage, which currently comprises the majority of the accessible products [challenge (3)].

However, a prerequisite for developing new reaction routes is the detailed knowledge of the organometallic electrocatalyst's behavior during CO_2 reduction and the identification of molecular properties that define the mechanistic pathway traversed toward the various accessible products. Correlating the catalyst structure to its activity, selectivity, and stability in the electrochemical activation of CO_2 marks the frame of the present work and is introduced in the following section.

1.2 Organometallic Perspectives on Electrochemical CO_2 Conversion

The capability of molecular transition metal complexes to act as mediators for the electron transfer from the electrode to the CO_2 molecule sets the motivation to gain a deeper understanding in this field. The following sections will thus present the basic ideas of organometallic electroreduction of CO_2 by molecular catalysts. An overview of the state-of-the-art catalyst systems, reaction mechanisms, and benchmarking metrics will be given. Eventually, methods to identify the molecular component(s) responsible for a catalyst's reactivity are discussed.

1.2.1 Thermodynamics, Kinetics & Metrics

The main obstacle in the conventional electrochemical activation of carbon dioxide is to provide the required energy to force the CO_2 molecule from its neutral and linear state into the bent geometry of the reduced radical anion $CO_2^{\bullet-}$.[40a] This thermodynamic obstacle manifests in a standard potential $E^0 = -2.21$ V vs. standard calomel electrode (V_{SCE}) in *N,N*-dimethylformamide (DMF),[42] which corresponds to −2.68 V vs. the ferrocenium/ferrocene couple (V_{Fc}).[43]

Adding multiple electrons and coupling the reduction steps with bond formations to protons (ideally generated by electrochemical water oxidation in the anodic half-cell)[44] circumvents this thermodynamically unfavorable reaction and offers a variety of C_1 products (P) at less negative potentials (Table 1.1).

Table 1.1. Selected CO_2 reduction processes and standard redox potentials E^0 in aqueous solutions.[35]

Cathodic Half-Reaction	E^0 (V_{SHE})
$2\ CO_{2(g)} + 2\ e^- \rightarrow\ C_2O_4^{2-}{}_{(aq)}$	−0.590
$CO_{2(g)} + 2\ H^+ + 2\ e^- \rightarrow\ HCO_2H_{(aq)}$	−0.250
$CO_{2(g)} + 2\ H^+ + 2\ e^- \rightarrow\ CO_{(g)} + H_2O_{(l)}$	−0.106
$CO_{2(g)} + 4\ H^+ + 4\ e^- \rightarrow\ H_2CO_{(aq)} + H_2O_{(l)}$	−0.070
$CO_{2(g)} + 6\ H^+ + 6\ e^- \rightarrow\ CH_3OH_{(aq)} + H_2O_{(l)}$	+0.016
$CO_{2(g)} + 8\ H^+ + 8\ e^- \rightarrow\ CH_{4(g)} + 2\ H_2O_{(l)}$	+0.169

The influences of a variety of kinetic factors (e.g., mass and charge transfer)[45] within the chosen reaction setup yet necessitate an additional driving force to be exerted for conversion that exceeds the thermodynamic standard potential of the reaction. This driving force is defined as the overpotential η [eq. (1.1), E_{app} = applied potential].

$$\eta = E_{app} - E^0 \tag{1.1}$$

Nevertheless, the kinetic nature of the overpotential enables the introduction of (transition metal) electrocatalysts (e-cats), which grant access to new reaction pathways based on the principles of catalysis known in thermochemistry. These reaction pathways are less impeded by kinetic barriers, manifesting in lower overpotential requirements, as illustrated in Figure 1.6.

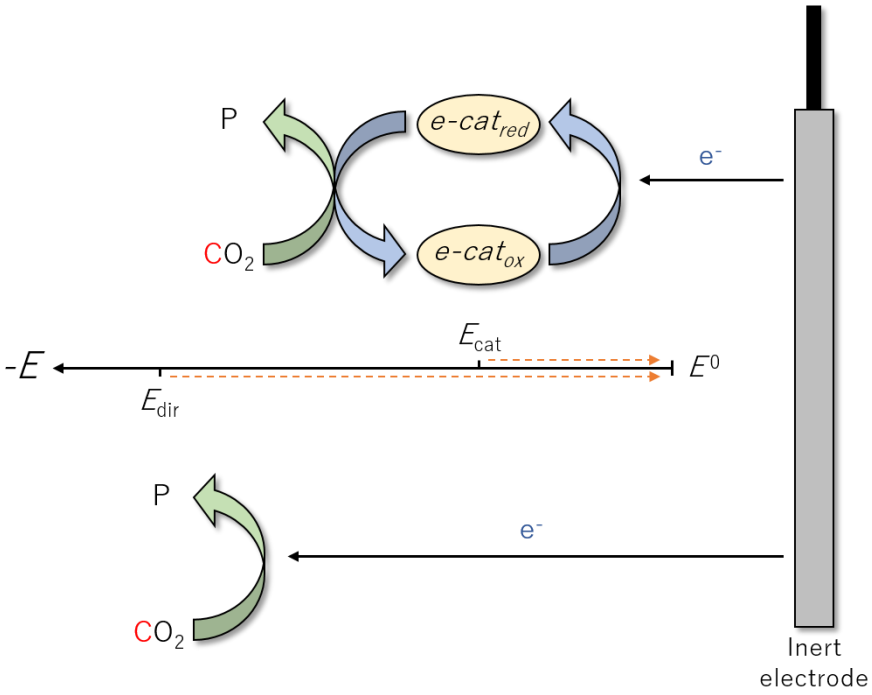

Figure 1.6. Relative positions of defining potentials for the direct (E_{dir}) and the transition metal-catalyzed (E_{cat}) electrochemical conversion of CO_2.

In a typical reaction setup, the first electron transfer from the inert electrode to the oxidized catalyst species e-cat$_{ox}$ (Figure 1.6, top) generates the reduced electrocatalyst e-cat$_{red}$ and primarily depends on interfacial parameters (e.g., electrode composition/conductivity, surface structure, the conductivity of the solution).[45a, 46] The reduced species can transfer the required electron(s) to the CO_2 molecule and initiate the subsequent bond-making and -breaking steps toward the product. Since the principles of organometallic chemistry influence these parts of the mechanism, they will be the focus of this work. In particular, the geometric and electronic properties of the catalytically active coordination complex can be attuned by the choice of metal and ligand. Eventually, this allows optimizing vital catalytic features such as activity, selectivity, energy efficiency, and stability.

Optimizing the balance between catalytic activity (represented by the turnover frequency TOF; Table 1.2, entry 1) toward the desired product and the required driving force (≙ overpotential) to reach said activity is of paramount interest. This balance is displayed by the catalytic TAFEL plot (CTP; Table 1.2, entry 2), which opposes log(TOF) and η (Figure 1.7).

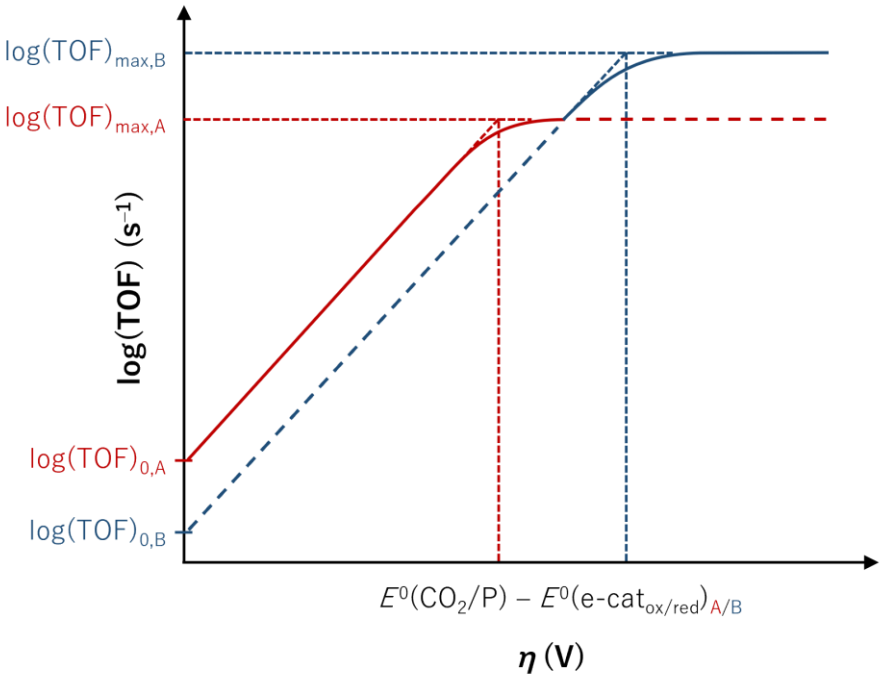

Figure 1.7. Schematic catalytic TAFEL plots for two electrocatalysts, A (red) and B (blue). Adapted with permission from ref. [47]. Copyright 2014 American Chemical Society.

The *y*-intercept yields $\log(TOF)_0$, which can be interpreted as the intrinsic turnover frequency of a catalyst (at $\eta = 0$). At the plateau, the maximum turnover frequency TOF_{max} is reached. The solid line in Figure 1.7 indicates the overpotential region of superior TOF for one of the two catalysts. Catalyst A in red exhibits a larger TOF_0, while catalyst B in blue has a higher TOF_{max}. When the horizontal and the diagonal parts are extrapolated, both lines' intersection allows extraction of the value for E_{cat}.

The most frequently reported metrics describing the different facets of an electrocatalyst are summarized in Table 1.2.

Table 1.2. Metrics commonly used to evaluate catalysts in the electrocatalytic reduction of CO_2.[47b, 48]

Entry	Metric	Definition[a]	Described Properties
1	turnover frequency (TOF)	$\frac{n(\text{P})}{n(\text{e-cat}) \cdot t}$	activity
2	catalytic TAFEL plot (CTP)	log(TOF) vs. η	activity, efficiency
3	turnover number (TON)	$\frac{n(\text{P})}{n(\text{e-cat})}$	activity, stability
4	faradaic efficiency (FE)	$\frac{n_{e^-}(\text{P})}{n_{e^-}(\text{total})}$	selectivity (, stability)

[a] n = amount, t = time.

Besides the turnover number (TON; Table 1.2, entry 3) that allows assessment of the activity and stability of a catalyst system, the faradaic efficiency (FE, entry 4) is a type of selectivity commonly used to evaluate an electrochemical reaction. The FE quantifies the percentage of electrons used to generate a specific product and, hence, also goes by the terms faradaic yield or electron efficiency/yield. This indicator can also identify degradation processes if the number of electrons transferred to the detected products does not equal the total number of electrons.

In summary, various metrics are available to evaluate the different features of catalytic importance comprised within an electrochemical CO_2 reduction (eCO_2r) catalyst. As discussed in the next section, these features depend on the degree of substrate interaction along the mechanistic route.

1.2.2 Mechanistic Pathways

The traversable reaction pathways are classified according to the interaction between the involved species, which gives rise to outer-sphere (OS) and inner-sphere (IS) mechanisms.

In the catalysis of electrochemical reactions, the outer-sphere mechanism, also referred to as "redox catalysis", describes a pathway in which the catalyst system only behaves as an electron carrier ("shuttle" or "relay") from the electrode to carbon dioxide.[49] In this case, the ligand environment is not substantially involved in the reaction due to minimal electronic interaction between both participants.[50] Consequently, the electron needs to bridge a particular spatial dimension, which is comparable to the direct electron transfer from the electrode surface to CO_2 under the formation of the $CO_2^{\bullet-}$ radical anion as described by COSTENTIN et al. (Scheme 1.1).[51]

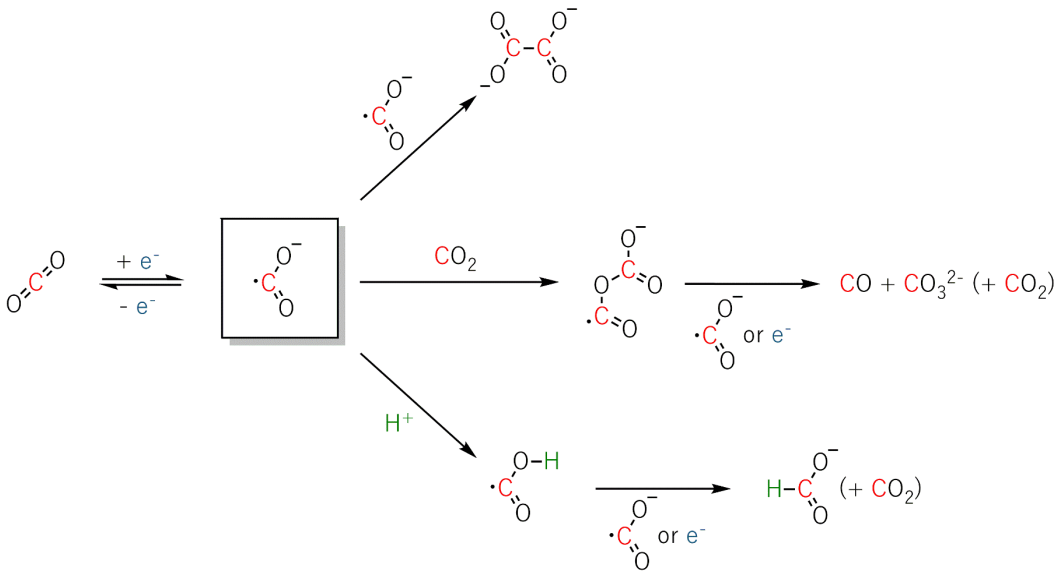

Scheme 1.1. Typical reaction pathways for CO_2 activation initiated by OS one-electron transfer.[51]

The radical anion can either dimerize to an oxalate species (top) or give CO and carbonate by reaction with a second CO_2 molecule due to its amphoteric character (center). In the presence of a proton source such as water, the formate anion is formed (bottom).[51] The outer-sphere mechanism is favored over the direct electron transfer to the substrate at the electrode because the electron shuttle disperses between the substrate molecules and, thus, improves electron distribution. Furthermore, the activation can be accelerated by shifting the equilibrium if the follow-up reactions are thermodynamically favored and rapid (e.g., protonation or radical coupling).[40a]

In contrast to the outer-sphere pathway, the inner-sphere mechanism traverses a chemically bound carbon dioxide adduct at which the electron transfer occurs. Subsequently, the activation barriers for bond formation or breaking must be overcome to yield the desired product. Compared to the OS mechanism, which suffers from the energetic impediment of needing to bend the linear CO_2 molecule (*vide supra*), the IS catalytic conversion of CO_2 takes advantage of substrate coordination to the transition metal.[52]

In the realm of organometallic chemistry, inner-sphere and outer-sphere mechanisms describe bond formation processes and are distinguished according to the coordination of the substrate that is attacked by a reactive group already bound at the metal center. If an electron transferred to a metal-bound CO_2 molecule during an electrocatalytic reaction is considered a reactive group, this would automatically classify the associated mechanism as IS. However, CO_2 reduction can also be achieved by forming an intermediate metal hydride complex formally incorporating electrons and protons in the metal hydride (**M**-H) bond. While the transfer of the hydride as the reducing agent may be preceded by coordination of CO_2, which would categorize the reaction as inner-sphere, this is by no means required.[53] More than this, the hydride transfer to C=O units constitutes the prime example of an outer-sphere reaction in organometallic catalysis, as prominently featured in the NOYORI mechanism for asymmetric hydrogenation of ketones.[54] Formally, these reactions comprise a stepwise or concerted transfer of hydride and proton to the non-coordinated substrate, either through a five- or six-membered transition state. The OS hydride transfer from transition metal centers to CO_2 in molecular thermocatalytic CO_2 hydrogenation is widely inferred to be a direct analogy to this mechanism.[34c]

In the molecularly-catalyzed electrochemical reduction of CO_2, the two disciplines of electro- and organometallic chemistry are brought into contact and essentially distinguish two pathways opened by the reduced catalyst species in Scheme 1.2: (1) electron transfer through the molecular complex (ET_M) or (2) electron transfer through the hydride (ET_H).

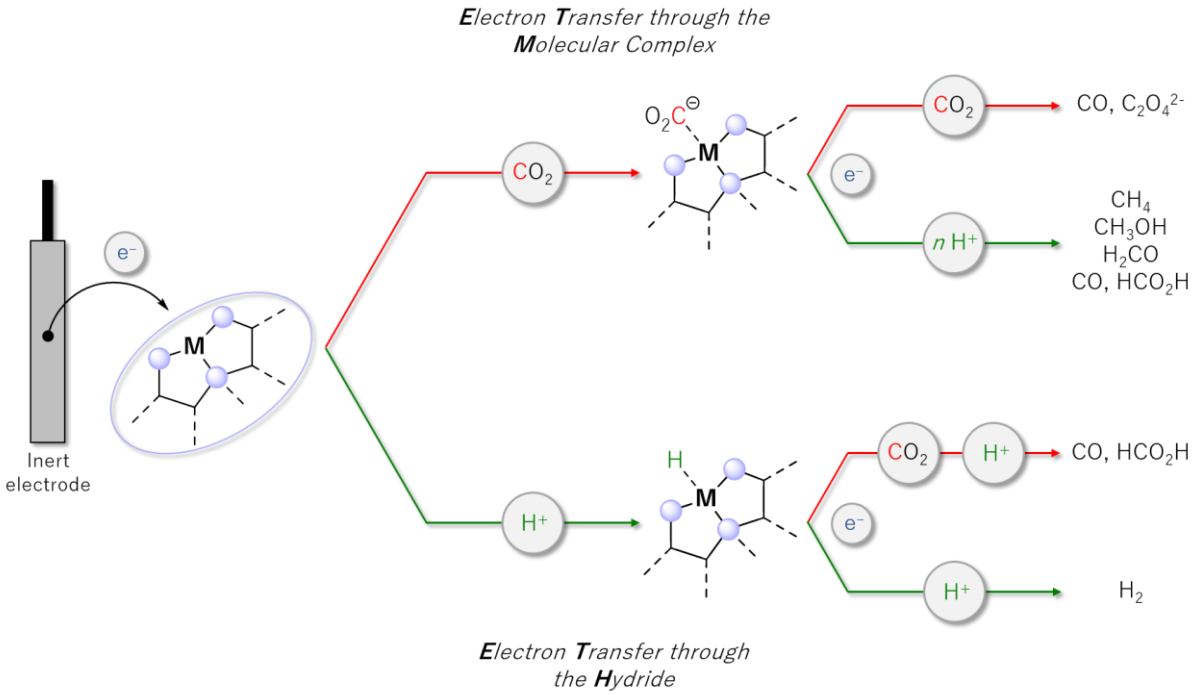

Scheme 1.2. Categorization of the ET_M and ET_H pathways for electron transfer to CO_2 during the transition metal-catalyzed electroconversion of carbon dioxide (**M** = metal).

1.2.2.1 Electron Transfer through the Molecular Complex

The ET_M pathway is primarily characterized by the coordination of CO_2 to the transition metal (Scheme 1.3). Ligand involvement in the electron transfer processes to CO_2 is also possible as long as CO_2 is chemically bound in the coordination sphere of the complex.

Coordination of CO_2 to a metal center was observed in more than ten coordination modes, including up to four metal centers simultaneously in various oxidation states.[17a, 53, 55] In this work, only monometallic cases are discussed, of which the stable side-on η^2-C,O bonding mode in the ARESTA complex[56] is undoubtedly one of the most prominent. Back bonding into the π^* orbital according to the DEWAR-CHATT-DUNCANSON model already leads to a bending of CO_2 which potentially activates the molecule toward the complete electron transfer.[57]

The side-on bonding constitutes the precursor to three different coordination modes of the formal radical anion and, hence, defines a mechanistic junction for the formation of C_1 or C_2 products. Notably, the η^2-C,O complexation is not necessarily an intermediate in the catalytic cycle but rather a transition state on the way to the other binding modes.

When the η^2-C,O mode isomerizes into an η^2-O,O bound CO_2 radical anion (Scheme 1.3, left), dimerization with a second radical leads to covalent C-C-bond formation. Dissociation of the two metal complexes then releases oxalate. In the presence of cations, oxalate can precipitate and shift the reaction equilibrium to the product side.

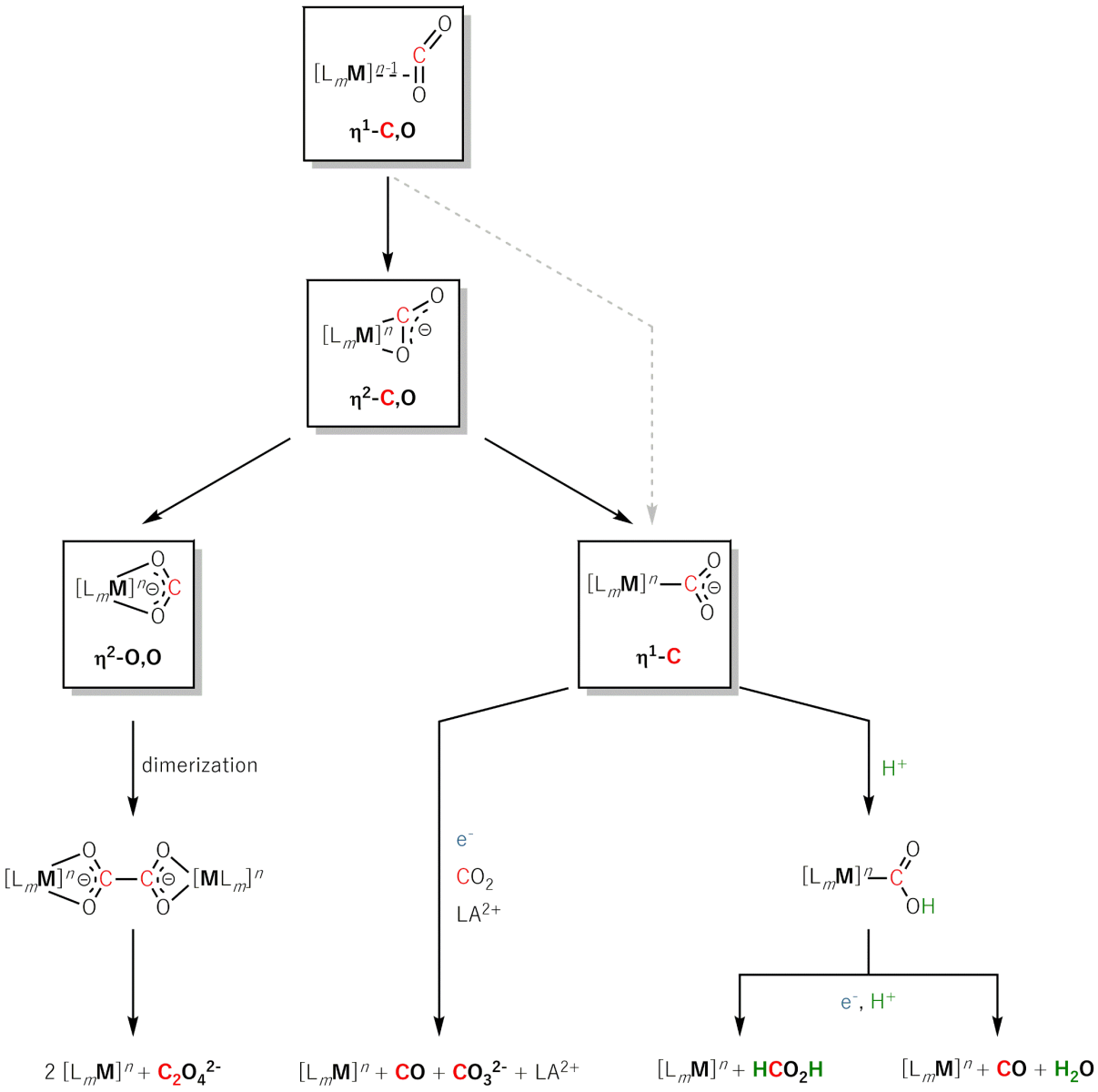

Scheme 1.3. CO_2 coordination modes, reaction pathways, and possible products of the ET_M route (*m* = stoichiometry of coordinated ligands, *n* = charge of the complex, LA = LEWIS acid).

Alternatively to the pathway shown in Scheme 1.3, mechanistic[58] and theoretical investigations[59] on the thermocatalytic transition metal-mediated oxalate formation suggest CO_2^{2-} as the activated species due to its characterization as a local minimum on the potential energy surface of many CO_2 reactions.[59] Furthermore, the reaction traverses a bimetallic intermediate featuring a μ-η^2:η^1 CO_2 sandwich complex from which the CO_2^{2-} unit can directly react with an uncoordinated molecule of CO_2[59-60] rather than involving an electrochemically generated CO_2 radical anion.[61]

The presence of earth-alkaline LEWIS acids (LAs; Scheme 1.3, center) grants access to a different reaction channel. The LA stabilizes the reactive η^1-CO_2^- intermediate species and allows the binding of a second equivalent of CO_2. In the proposed six-membered cyclic transition state, a

formal O^{2-} dianion is transferred from one CO_2 unit to another and ultimately yields the two-electron reduced CO as well as carbonate released as the LA salt. SAMPSON et al. postulated this so-called reductive disproportionation of CO_2 for the mesityl (Mes)-substituted 2,2'-bipyridine (bpy) complex $[Mn(bpy^{Mes})(CO)_3(MeCN)]^+$ in Scheme 1.4.[62]

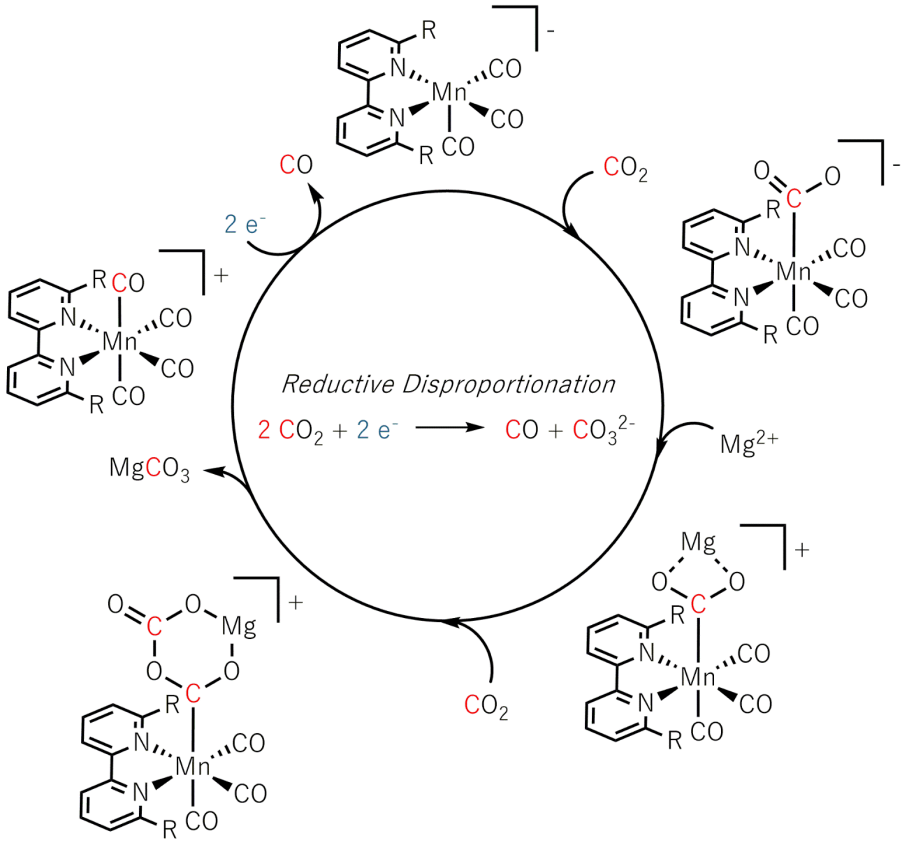

Scheme 1.4. LEWIS acid-assisted electrocatalytic reduction of CO_2 to CO and CO_3^{2-} (R = Mes). Adapted with permission from ref. [62]. Copyright 2016 American Chemical Society.

The η^1-C coordination constitutes the crucial intermediate in most ET_M reactions reported so far. Protonation of the subsequently formed metalla carboxylate intermediate yields a hydroxycarbonyl species that includes a second mechanistic junction (Scheme 1.3, right). From here, proton addition either initiates the release of water and carbon monoxide or the production of formic acid. However, CHEN et al. also reported the conjunction of both routes by isomerization of the hydroxycarbonyl intermediate to the formate species prior to the release of formic acid (Scheme 1.5).[63]

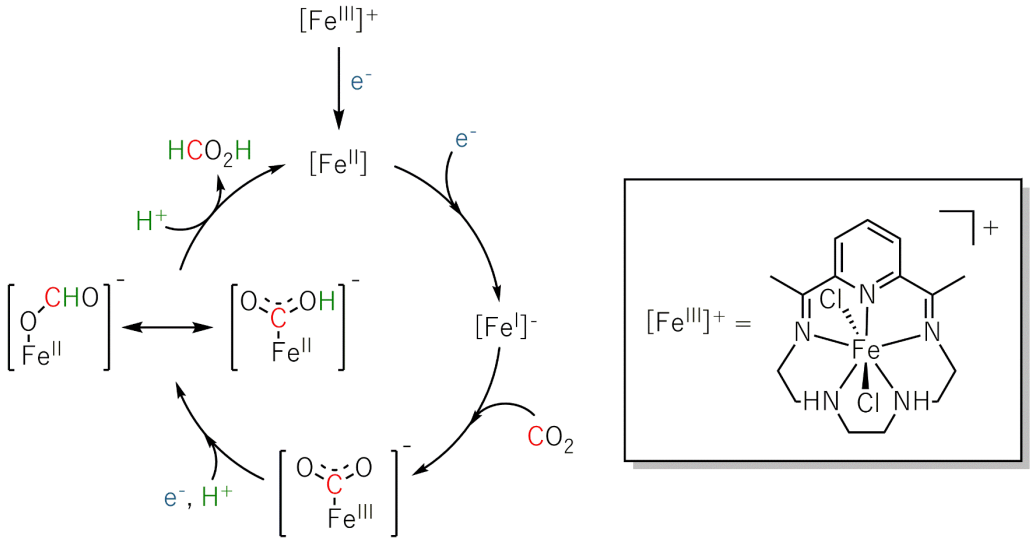

Scheme 1.5. Isomerization during Fe-catalyzed CO_2 electroreduction to HCO_2H proposed by CHEN et al. Adapted with permission from reference [63]. Copyright 2015 American Chemical Society.

CO evolution is generally inferred to be catalyzed via a push-pull mechanism (Scheme 1.6), during which the reduced metal center donates electron density to the carbon atom through the η^1-C coordination. While these electrons occupy the antibonding orbitals of the carbon atom, electron density is withdrawn from the anionic oxygen atom by two equivalents of BRØNSTED acid (HA). In combination, the two factors weaken the C-O bond to an extent to which elimination of water is favored. Further uptake of an electron leads to CO release and catalyst recovery.[40a, 64]

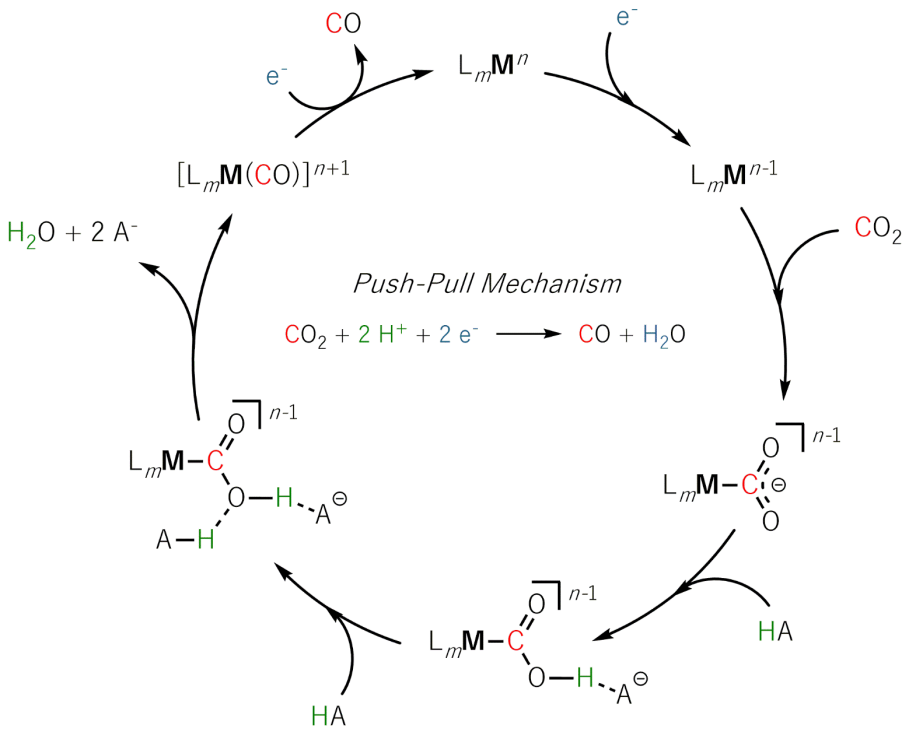

Scheme 1.6. Push-pull mechanism of the BRØNSTED acid-assisted reduction of CO_2 to CO.

The ideal proton source must be acidic enough to catalyze the reaction yet keep the concentration of protons around the electrode low to limit direct proton reduction to molecular hydrogen (*vide infra*). Hence, weak acids such as methanol, 2,2,2-trifluoroethanol (TFE), phenol, or even water are commonly employed.[64a, 65] Since the influence of proton donors is crucial for catalytic performance, the incorporation of carboxylic acid or phenol groups as so-called "proton relays" in the second coordination sphere around the active center constitutes one of the most reported approaches to optimize ligand structures.[66]

In order to abstract the oxygen from the CO_2 molecule two protons and two electrons are required in each case. Nevertheless, the sequence of reduction (electron transfer) and protonation (H^+ transfer) can be altered. Variations in the applied potential or the rate constant of protonation give rise to the "reduction first" and "protonation first" mechanisms described by RIPLINGER et al. in Scheme 1.7.[64a] Generally, "reduction first" occurs at more negative potentials, making it less energy-efficient and the less desired pathway.[64a, 67]

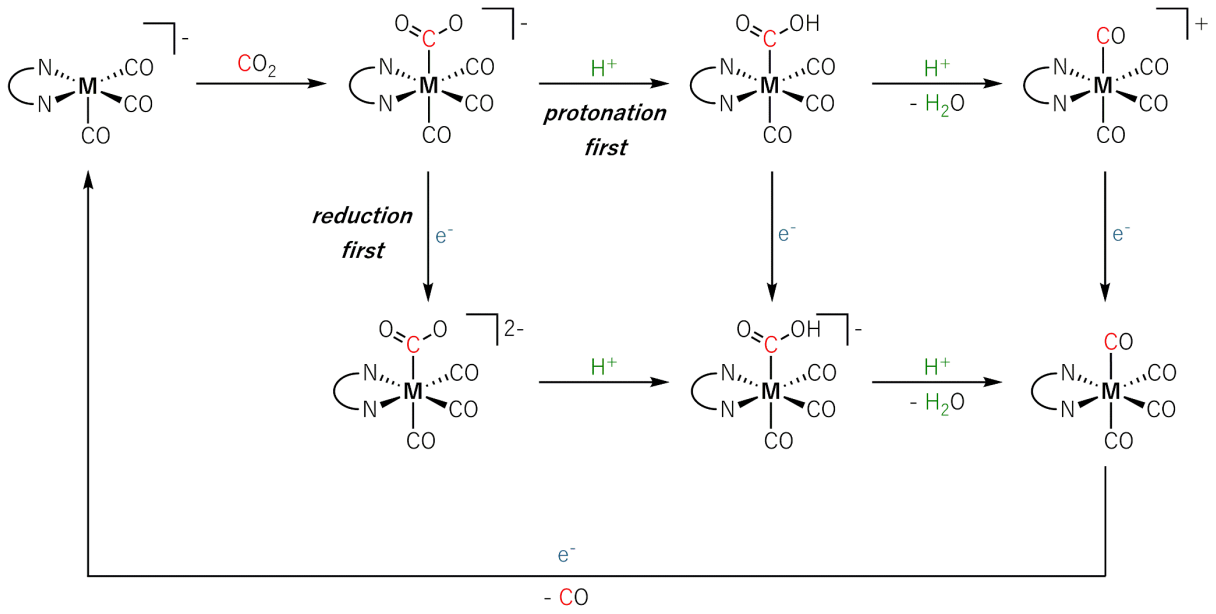

Scheme 1.7. "Protonation first" and "reduction first" mechanisms described by RIPLINGER et al. for **M** = Mn/Re and N∩N = bpy. Adapted with permission from ref. [64a]. Copyright 2015 American Chemical Society.

The expansion of the ET_M scope to ligand-mediated electron transfers is mainly caused by the significant number of transition metal complexes in electrochemical CO_2 reduction relying on molecular architectures comprising so-called "non-innocent" ligands (e.g., polypyridines or imines). Their ability to share an excess of electron density (redox non-innocence) or relay protons (chemical non-innocence) often proves beneficial for catalytic activity.[68] One of the pioneering examples within the former group is the $[Re(bpy)(CO)_3]^+$ CO_2 electroreduction catalyst investigated by the LEHN group.[69] Investigations of the activation mechanism toward the twice-

reduced $[Re(bpy)(CO)_3]^-$ species undertaken by BENSON et al. revealed a formal one-electron reduction of the rhenium center to the zero-valent state and uptake of the second electron into the π* orbital of the bpy unit.[70]

1.2.2.2 Electron Transfer through the Hydride

In the ET_H route, a reactive metal hydride complex initiates the reaction with carbon dioxide. This **M**-H key intermediate is formed by protonating the reduced metal center. Hydride attack at the electrophilic carbon atom of the substrate combines the simultaneous transfer of electrons with the bond formation. The elementary steps occurring after the generation of the metal hydride are similar or even identical to the thermocatalytic hydrogenation of CO_2 into C_1 molecules such as formic acid or methanol (Scheme 1.8). Literature offers many examples of transition metal complexes catalyzing the reaction and studies on the intricate details within their mechanisms of CO_2 conversion.[34b, 71]

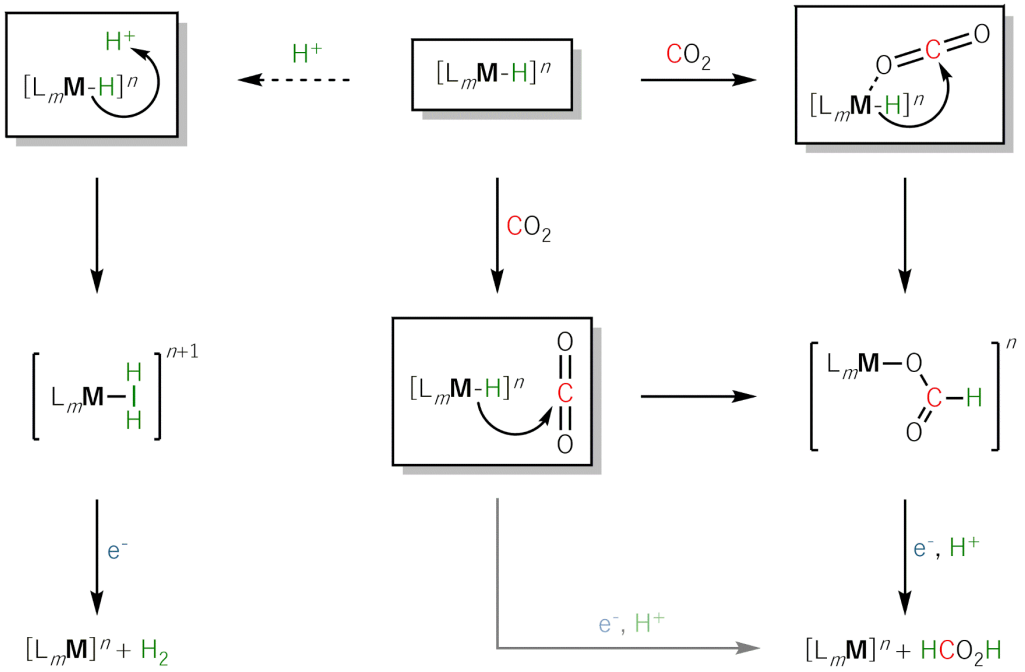

Scheme 1.8. Reaction pathways and possible products of the ET_H route.

In cases of migratory insertion, CO_2 typically coordinates the metal in an end-on η^1-O mode prior to the hydride transfer (Scheme 1.8, top right). Although there is the alternative of a side-on η^2-C,O coordination, this binding mode constitutes a less likely intermediate due to the reduced electrophilicity of the carbon center. The preferred η^1-O coordination is based on a LEWIS acid/base interaction between the electrophilic metal center and the free lone pair of the CO_2 molecule. Nevertheless, the hydride transfer through the direct outer-sphere attack at CO_2 is considered a viable alternative in such systems (Scheme 1.8, center). Irrespective of the exact route, a formate complex can be formed after the hydride transfer in which coordination of the

carboxylate group may occur in a monodentate or bidentate fashion. Protonation of the formate ligand allows dissociation of formic acid and usually occurs at the non-coordinated C=O bond in the monodentate form. Alternatively, initial outer-sphere protonation of the activated CO_2 molecule followed by one-electron reduction also yields formic acid.

When the hydride is protonated, hydrogen evolution – the most critical side reaction in electrochemical CO_2 reduction – occurs. This possibility renders the proton source and potential intramolecular proton relays (*vide supra*) essential parameters for controlling the pH and, eventually, the selectivity of the reaction.

While transition metal hydride intermediates preferentially produce formate, CO can be evolved in singular cases. Investigations conducted by MACHAN et al. identified the isomerization of the metal formate intermediate to the hydroxycarbonyl species of the ET_M pathway as the critical step for this reaction.[72] The mechanism proposed for the $[Ru(bpy^{Mes})(CO)_2Cl_2]$ complex in Scheme 1.9 hence forms the reciprocal counterpart to the isomerization mechanism postulated by CHEN et al. in Scheme 1.5.

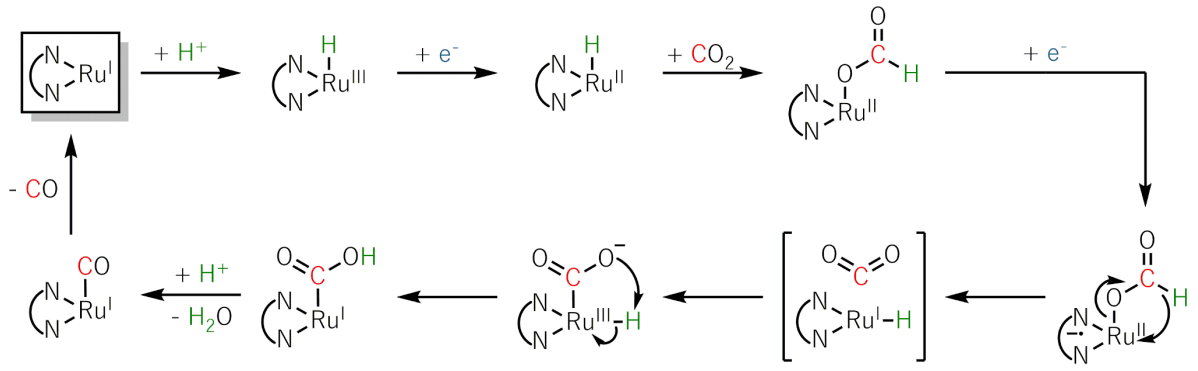

Scheme 1.9. Isomerization mechanism of the ET_H-formed formate species to the hydroxycarbonyl intermediate of the ET_M pathway and CO formation proposed by MACHAN et al. Adapted with permission from ref. [72]. Copyright 2015 American Chemical Society.

1.2.3 State-of-the-Art Catalyst Systems

A manifold of transition metal complexes is known to catalyze the electrochemical reduction of CO_2 via one of the presented reaction routes. The most efficient examples are highlighted in the following section, sorted by their main products.

1.2.3.1 Carbon Monoxide

Figure 1.8 shows a compilation of the most efficient transition metal electrocatalysts and crucial catalytic parameters for their application in the quantitative production of CO from CO_2 by controlled potential electrolysis (CPE).

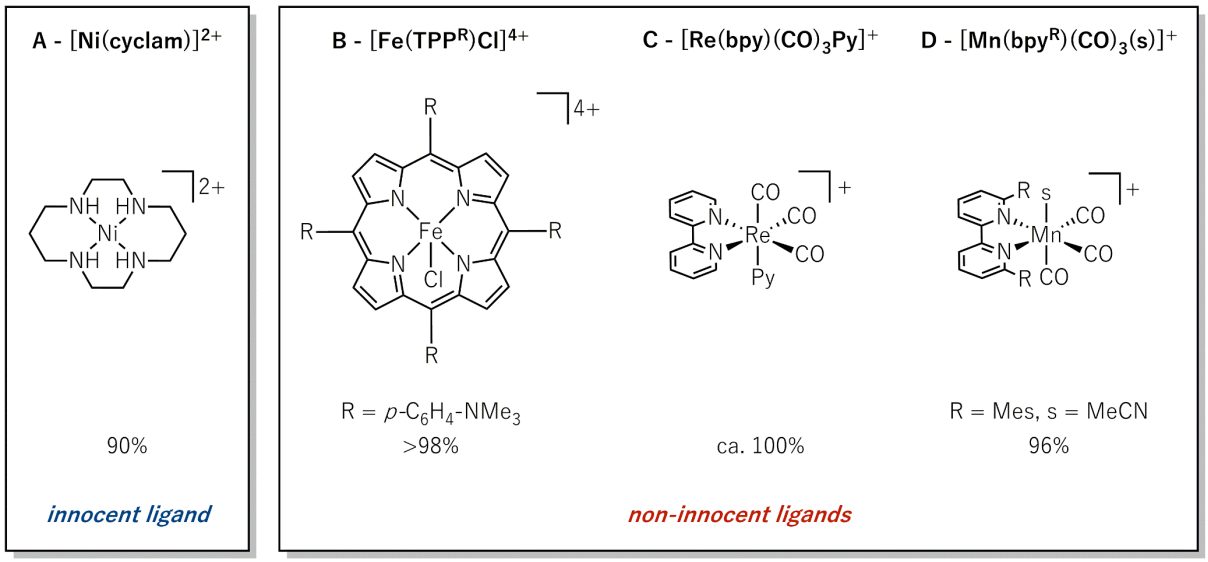

Figure 1.8. Most efficient transition metal complexes and their FEs for the electrocatalytic reduction of CO_2 to CO.[62, 73]

Each catalyst system produces CO selectively in FEs ≥ 90% via the ET_M pathway in the presence of protons. CO was chosen over HCO_2H as the exemplary two-electron product since it constitutes the most frequently reported reaction outcome (for further information on HCO_2H electrocatalysts, cf. section 1.2.3.3).

Nickel-1,4,8,11-tetra-azacyclo-tetradecane (cyclam, Figure 1.8A) is the best example of an efficient transition metal complex comprising a redox-innocent ligand system. In 1984, the group of SAUVAGE reported $[Ni^{II}(cyclam)]^{2+}$ and found almost quantitative selectivity toward CO at $\eta \approx -0.5$ V in H_2O.[74] Although exhibiting a $\log(TOF)_{max}$ lower than those of the reference eCO_2r complexes depicted in Figure 1.9, the $\log(TOF)_0$ of ca. -4.8 s^{-1} is remarkable.

Since then, extensive studies on the reaction mechanism,[75] the role of the electrode,[75a, 76] and possible deactivation pathways[77] have been performed. Ultimately, adjustment of the reaction conditions, as well as the introduction of unsaturated (C=N and C=C) bonds or partial substitution of the coordinating nitrogen atoms by oxygen, enabled the predominant formation of formic acid (FE = 75%)[57a] and oxalate (FE = 98%).[57b, 78]

Iron in particular,[73c, 79] but also cobalt[80] and zinc complexes[81] are active in the electrocatalytic reduction of CO_2 to CO when environed by redox non-innocent porphyrins, especially tetraphenyl porphyrin (TPP) derivatives. The catalytic performance benefits from the two-fold reduction of the TPP ligand, which increases the electron density of the metal center at the catalytically active state via the four coordinated nitrogen atoms. Since more electron density is transferred to the CO_2 carbon atom, the C-O bond is weakened, and catalytic conversion via the push-pull mechanism is accelerated.[73c, 79b-d, 79f-h, 82] The introduction of trimethylammonium

moieties in the *para* position of the phenyl rings (Figure 1.8B) stabilizes the resulting $[Fe(TPP^{NMe_3})Cl]^{4+}$ complex by removing some of the excess electron density. This interplay of electron donation and withdrawal is surmised to be the key to its exceptional catalytic performance in eCO_2r (Figure 1.9).[73c]

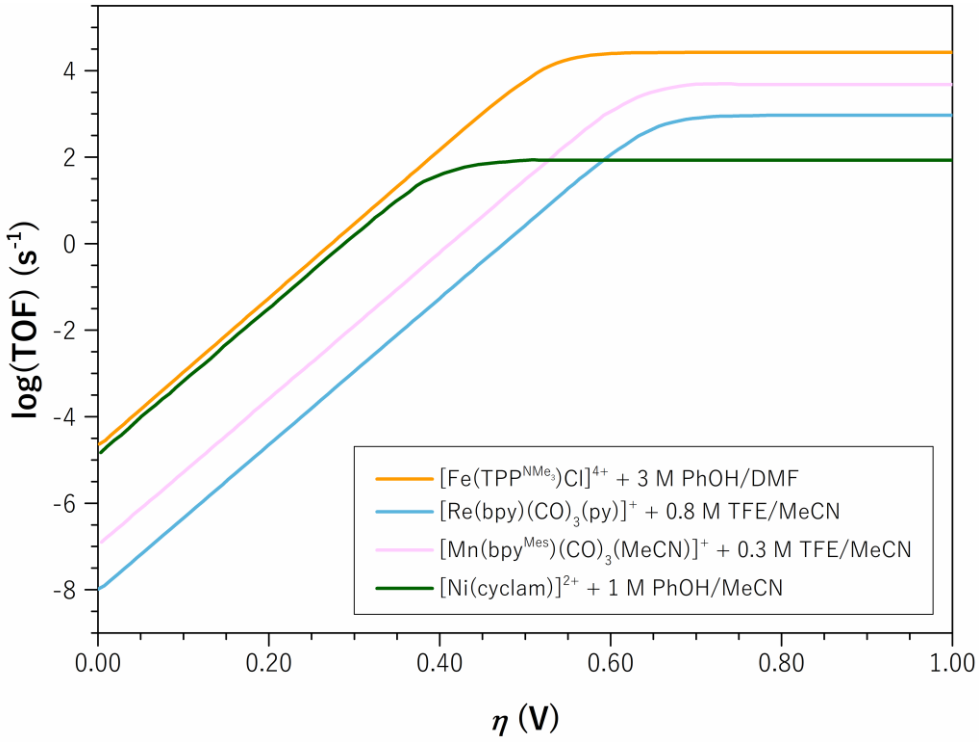

Figure 1.9. Catalytic TAFEL plots for the BRØNSTED acid-assisted electrocatalytic conversion of CO_2 to CO with the complexes in Figure 1.8. The plots were compiled from data in ref. [62, 83].

Bipyridines are easily modifiable structures and constitute one of the most frequently reported ligand systems. Although complexes centered by transition metals of groups 6,[68c, 84] 7,[41, 62, 66a, 67, 69, 85] 8,[72, 86] 9,[87] and 10[87c] are known to convert CO_2 to two-electron products, Mn and Re carbonyl halides are among the most efficient ones (Figure 1.8C and D). Shutting down the dimerization upon reducing the manganese species by introducing bulky mesityl groups allows Mn to outperform Re (Figure 1.9). While bipyridine complexes give CO in almost quantitative faradaic yields from the ET_M route when early transition metals (up to group 7) are coordinated, later metals tend to give formate/formic acid via metal hydride species (*vide infra*). Nevertheless, the attunement of the reaction conditions (i.e., proton source, potential, and solvent) remains a factor to consider when discussing product selectivities.

Beyond the three presented archetypes, other frequently investigated ligand backbones are terpyridines (tpy), phenanthrolines, phthalocyanines as well as various forms of phosphines, pincer structures, and *N*-heterocyclic carbenes.[88] Catalysts based on some of these moieties are even capable of forming products beyond CO and HCO_2H.

1.2.3.2 C_2 and Higher Reduced Compounds

One such example of a catalyst producing C_2 compounds in the electrocatalytic reduction of CO_2 is the dicationic copper dimer **[Cu]**$^{2+}$ described by ANGAMUTHU et al.[61] X-ray diffraction analysis and mass spectrometry confirmed that the dimeric species forms the oxalate-bridged tetramer **[Cu]**$^{4+}$ after single-electron transfer to four CO_2 molecules (Scheme 1.10).

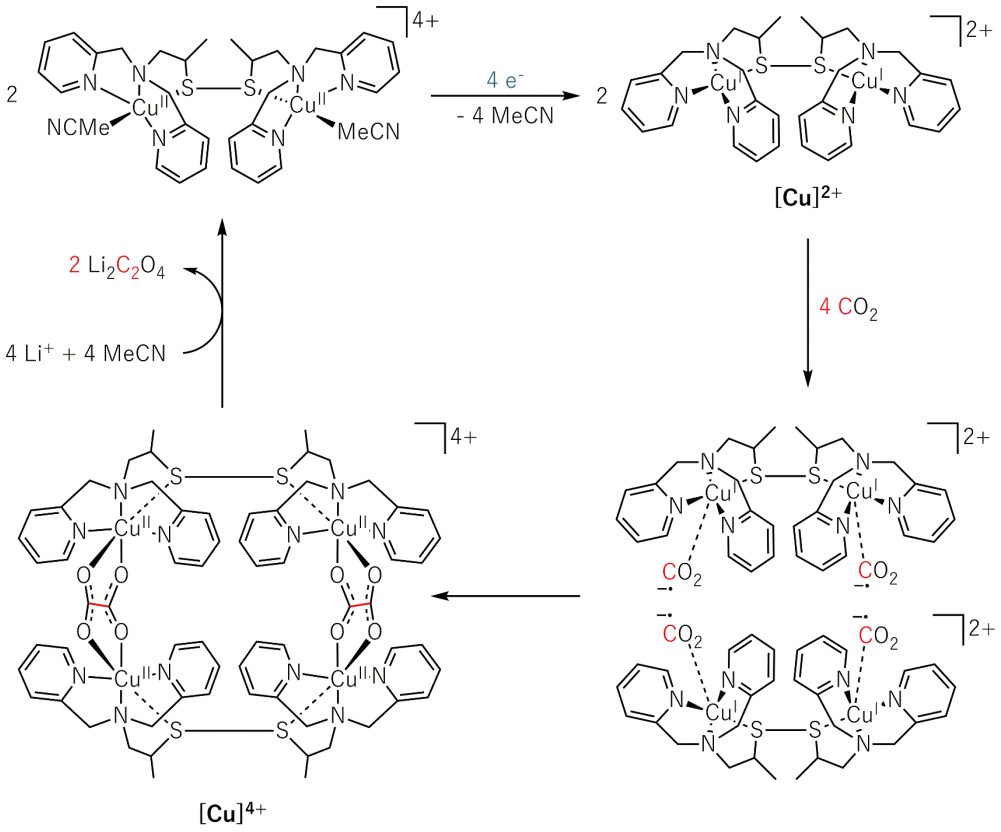

Scheme 1.10. Electrocatalytic cycle for oxalate formation by a copper dimer proposed by ANGAMUTHU et al. Reprinted from ref. [61] with permission from AAAS.

CPE at the potential of the irreversible reduction peak found at –0.03 V_{NHE} revealed the reduction of the starting complex followed by dimerization and the liberation of oxalate. The product precipitates as the lithium salt since $LiClO_4$ is used to ensure the conductivity of the solution. The authors reported a current efficiency of 96% but a low TON of six after seven hours of reaction time.

To this point, higher molecular complexity seems only accessible by immobilized molecular species (Figure 1.10). For example, the polyethylene glycol (PEG)-derivatized Mn and Co corroles reported by the SCHÖFBERGER group (Figure 1.10A) show remarkable product selectivity when used on carbon paper electrodes.[89] They each produce methanol with a maximum FE of 23% at $\eta \approx -530$ mV (Mn) and 59% (Co), as well as acetate (Mn, $FE_{max} = 61\%$ at $\eta \approx -560$ mV) or ethanol (Co, $FE_{max} = 48\%$), respectively.

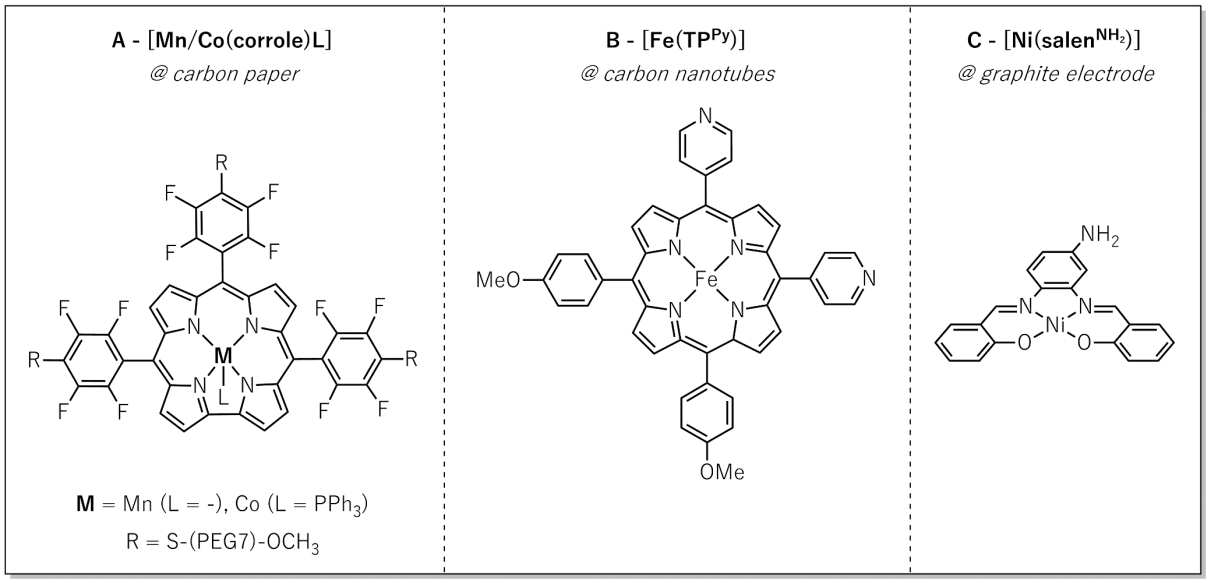

Figure 1.10. (A) Mn and Co corroles reported by the SCHÖFBERGER group,[89-90] (B) iron porphyrin-pyridine by ABDINEJAD et al.,[91] and (C) nickel aminosalen by BOSE et al.[92]

Immobilizing the iron porphyrin-pyridine complex [Fe(TP^{Py})] on carbon nanotubes (Figure 1.10B) allowed the transfer of eight electrons and the formation of methane. The maximum faradaic efficiency of 20% was achieved at E_{app} = –1.4 V_{RHE} with 5% water in DMF.[91]

BOSE et al. immobilized the amino-functionalized [Ni(salen^{NH_2})] complex in Figure 1.10C on the surface of a graphite electrode and performed CPE experiments in 0.5 mM aq. $KHCO_3$ solution.[92] The multi-electron products ethanol (FE = 36%), methanol (FE = 16%), and acetaldehyde (FE = 7%) were produced at E_{app} = –1.8 V_{Ag}, besides formic acid and hydrogen. Reference experiments with the unfunctionalized salen complex only showed hydrogen formation and emphasized the importance of the amino group in the ligand backbone for CO_2 conversion.

In order to access these multi-electron, multi-carbon products without the necessity of immobilizing the electrocatalyst, the decisive factor(s) dictating the activity of the complexes in known reactions must be identified and tailored. One of these factors appears to be the metal center of the coordination compound (*vide infra*).

1.2.3.3 Metal Dependencies in Product Distribution

A summary of the landscape of 3d transition metal complexes for the electrocatalytic conversion of CO_2 to two-electron products is given in Figure 1.11. The plots illustrate the formation of carbon monoxide or formate and formic acid, respectively, according to the position of the metal center in the periodic table of elements. Catalysts generating both products are taken into account in each of the figures.

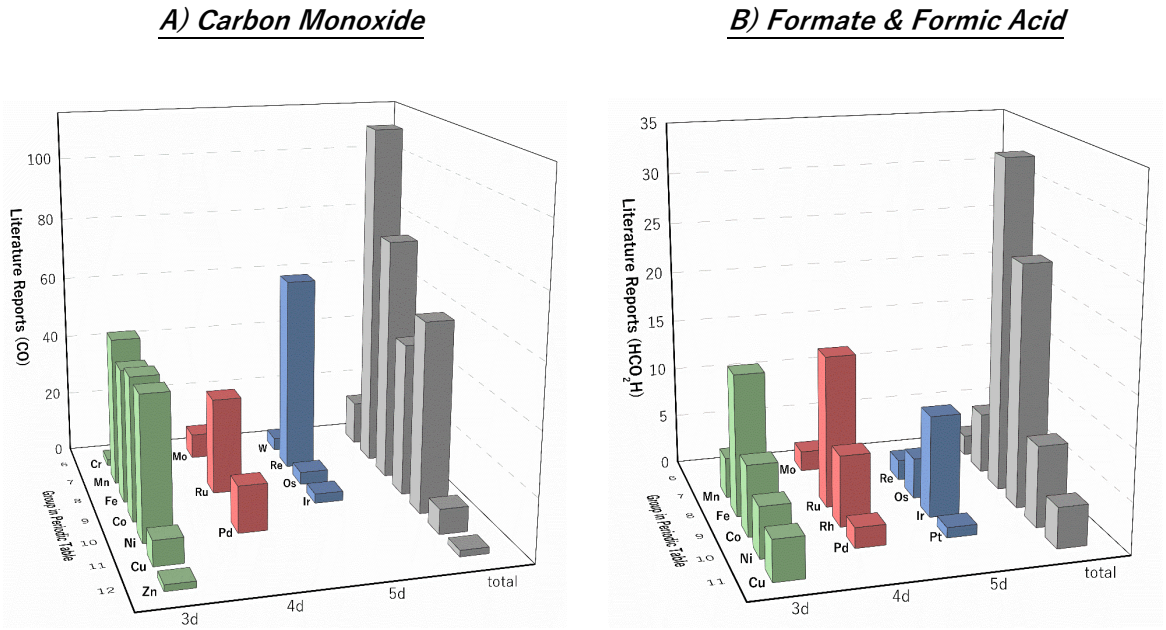

Figure 1.11. Indication of preferred formation of (A) CO and (B) formate/formic acid for different transition metals by the number of literature reports.

The diagrams emphasize the favored production of CO in groups 7 to 10 of the periodic table, in which 3d metals have by far the most significant contribution. The majority of the systems are based on either bpy (Mn, Re, and Ru), TPP (Fe), or cyclam (Ni) ligand architectures. For these catalysts, the accessible mechanistic information indicates a prevalence of the ET_M pathway.

Concomitant with the decreasing number of examples for CO in groups 8 and 9, an increasing number of reports for HCO_2^-/HCO_2H production is found. The metals within these well-performing electrocatalysts (Ru, Rh, and Ir) are also known to form highly efficient CO_2 hydrogenation catalysts. This observation concludes that the reactive hydride intermediates of these metals exhibit a favorable hydricity for formic acid or formate production in both areas of CO_2 reduction and point toward ET_H as the main pathway.

Hydricity is crucial in determining the preferred reaction route and was already reported for various electro- or thermocatalytic CO_2 reduction systems.[93] Additionally, Figure 1.11 indicates that hydricity not only determines the preferred formation of H_2 or HCO_2H within one mechanism but that it can even shut down the ET_M mechanism in favor of the ET_H route. Hence, modulation of the hydricity by carefully adjusting the electronic and geometric features provided by the ligand framework may thus be a promising approach to gaining control over the known reaction pathways.[88]

1.2.4 Structure-Reactivity Relationships of CO_2 Electrocatalysts

Figure 1.12 illustrates important parameters, objectives, and reaction conditions to consider and attune in the design of organometallic complexes for the electrocatalytic reduction of CO_2.

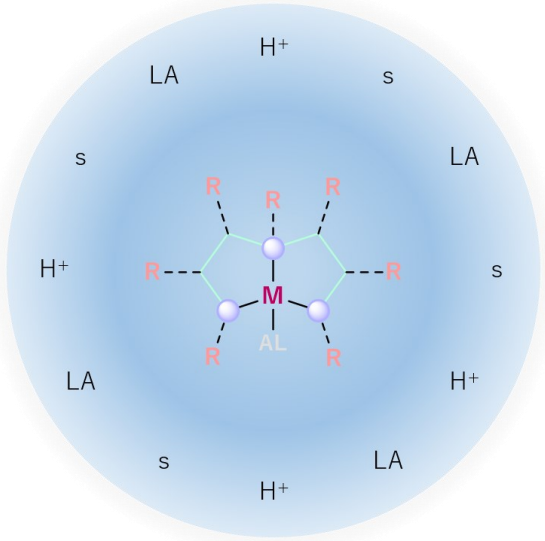

Design Parameters/Objectives:

- Metal Center (**M**)
- Coordinating Atom (●)
- Auxiliary Ligand (AL)
- Ligand Backbone (—)
- Functional Group (R)

Reaction Conditions:

- (Coordinating) solvent (s)
- Additive (e.g., H^+ or LA)
- Oxygen/Water

Figure 1.12. Objectives and parameters affecting the design of molecular transition metal complexes for the electrocatalytic reduction of CO_2.

1.2.4.1 Tailoring Catalysts for Reductive Electrochemistry

The essential requirement for an electrocatalyst to operate via one of the inner-sphere pathways ET_M or ET_H is the ability of the complex to generate a free coordination site for the formation of an **M**-C or **M**-H bond. Therefore, ligand systems saturating all possible coordination sites of a metal center in the catalytically active oxidation state can only be used for outer-sphere electron shuttles.[94]

If a free coordination site is available, the electron density constitutes the crucial factor determining potential reductive abilities at the metal center. For a homogeneous electron transfer, the highest occupied molecular orbital (HOMO) of the reducing agent must be higher in energy than the lowest unoccupied molecular orbital (LUMO) of the substrate.[95]

Reduction of the metal center to the typically required low oxidation states renders the coordination sphere an increasingly important factor. Only if the electronic and steric properties of the ligand sufficiently stabilize the reduced intermediate state can the lifetime of the species reach a scale in which substrates such as CO_2 or H^+ can be attacked to induce further conversion. However, excessive stabilization of an intermediate would decelerate the subsequent reaction steps toward the products and the regeneration of the active species (analogous to the SABATIER

principle in heterogeneous chemistry). Hence, the stability of an intermediate impacts the preferred reaction route, e.g., displayed by the hydricity in the case of an **M**-H species.[96]

Classically, incorporating aromatic moieties that allow the delocalization of electrons from the metal center helps stabilize a highly reduced species. This effect can be supported when electron-withdrawing substituents (exhibiting inductive and mesomeric effects) are applied or by incorporating electrophilic auxiliary ligands. Carbonyl ligands constitute an option since "excess" electrons can be transferred to the antibonding π* orbital by back-bonding interactions. In the extreme case, the stabilization of the metal by withdrawing electron density is represented by redox non-innocent ligands. Here, the ligand does not only remove electron density but is reduced itself (*vide supra*).

The atoms coordinating the metal center (e.g., C, N, O, P, or S) allow attunement of electron density, bond order, as well as the type and degree of functionalization. The ligand backbone between the coordinating atoms significantly influences the flexibility or rigidity of the whole system, with the latter being modifiable by the number of atoms in the resulting metallacycle and the incorporated bond orders (e.g., aliphatic or aromatic). Functional groups, specifically those bound to the coordinating atoms, allow direct adjustment of the reduction potential and control of the steric shielding around the metal center.

Besides the core structure of the complex, external influences affecting the catalyst-to-be under reaction conditions need to be anticipated. The sensitivity to ambient oxygen or water as a common proton source (e.g., when considering oxophilic metal centers or phosphine-based ligand structures) must be probed to avoid restrictions in reaction conditions. The same applies to potentially labile auxiliary ligands (AL) in the inner coordination sphere of the complex, which may exchange with commonly used solvents for electrochemical applications (e.g., MeCN[85k] and DMF[79o, 97]). In the simplest case, the exchange alters the electron density of the metal center, and hence its reducibility, but it could also wholly solvolyze the complex (*vide infra*).

1.2.4.2 Identification of Catalytic Key Components

The presented variety of components influencing a molecular electrocatalyst's electronic and geometric features evokes the inevitable question of which part of the complex is (mainly) responsible for its activity, stability, or selectivity. Moreover: is the product trend proposed based on Figure 1.11 genuinely caused by the various metal centers, or is it a mere coincidence resulting from the intertwinement of intrinsic (complex) and extrinsic (reaction conditions) factors?

A reliable answer to this question can only be given by strict application of the basic scientific principle *ceteris paribus*, i.e., only one parameter of an experiment must be varied at a time to

ensure that said parameter is the cause for a variation in the result. Regarding the role of the metal center of a complex in a catalytic reaction, reaction conditions and the inner coordination sphere surrounding the metal center must be kept constant. For eCO_2r, in particular, the ligand system's redox- and chemical innocence must be guaranteed. However, the few studies reporting the systematic variation of the metal center while retaining a single ligand framework mostly rely on non-innocent ligands (Figure 2.1).[98] The inherent intertwinement of ligand- and metal-centered processes therein yet complicates the deconvolution of individual contributions.[99]

Although this fundamental requirement of redox-innocence is fulfilled by existing ligand frameworks such as cyclam, potential adjustments to assure the applicability of the complex in the desired reaction (e.g., solubility, steric bulk, and electron donation/withdrawal) are synthetically challenging in a cyclic system. Pincer systems, however, can be designed to be (electro-)chemically inert under reductive conditions and are easily modifiable. This ligand type's modular conception renders it the optimal platform for the isolated investigation of the metal center – or other components within the coordination sphere – when the organometallic principles for the design of a molecular catalyst are refined toward the requirements of reductive electrochemistry.

Within the group of pincer structures, the N^2,N^6-bis(diphenylphosphaneyl)-N^2,N^6-diphenylpyridine-2,6-diamine ligand **L** in Figure 1.13 comprises relevant features to allow an isolated view on the effect of the metal center.

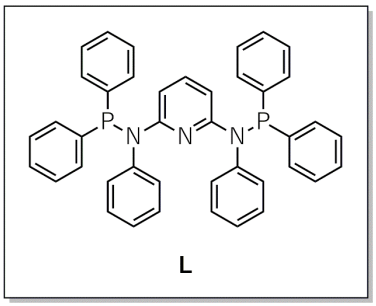

Figure 1.13. Structure of N^2,N^6-bis(diphenylphosphaneyl)-N^2,N^6-diphenylpyridine-2,6-diamine (**L**).

The PNP ligand displays a moderate steric demand to shield the metal center in the formed coordination compounds but still allows coordination of the substrate. The high degree of aromaticity is supposed to interfere only marginally in the metal-centered redox processes but still provide sufficient π back bonding for stabilizing low-valent species. A pyridinic core structure linked by nitrogen bridges proved efficient in CO_2 electroreduction complexes before.[63, 100] The pincer shape induced by the addition of strongly coordinating phosphines grants coordinative stability.

L hence forms the basis for the studies conducted in this work, as presented in the next section.

1.3 Aim of the Thesis

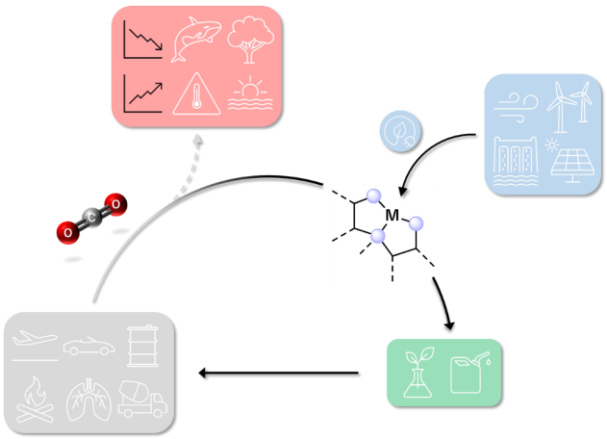

Although the transition metal in the center of a coordination complex for the electrocatalytic reduction of carbon dioxide is crucial in determining the traversed pathway and, hence, the generated product, its role in the reaction is still insufficiently investigated. The isolated consideration of the metal center affords careful design of the coordination complex's inner coordination sphere, e.g., by ensuring the redox-innocence of the coordinated chelating ligands. This approach, in turn, requires meticulous adjustment of the design principles known from organometallic chemistry toward the needs of reductive electrochemistry.

Therefore, in chapter 2 of this work, the synthesis and structural characterization of the redox-inert N^2,N^6-bis(diphenylphosphaneyl)-N^2,N^6-diphenylpyridine-2,6-diamine ligand **L** and a library of corresponding mid to late 3d transition metal complexes (Mn to Zn) are developed. These complexes' spatial and electronic structures will be discussed through spectroscopic techniques such as NMR, EPR, and MÖSSBAUER combined with SQUID analysis and single-crystal XRD. Besides the comparative analysis among the different metal centers, the effect of changing the auxiliary ligands from chloride to acetonitrile will be addressed and put into context with the observed coordination geometries and electron configurations.

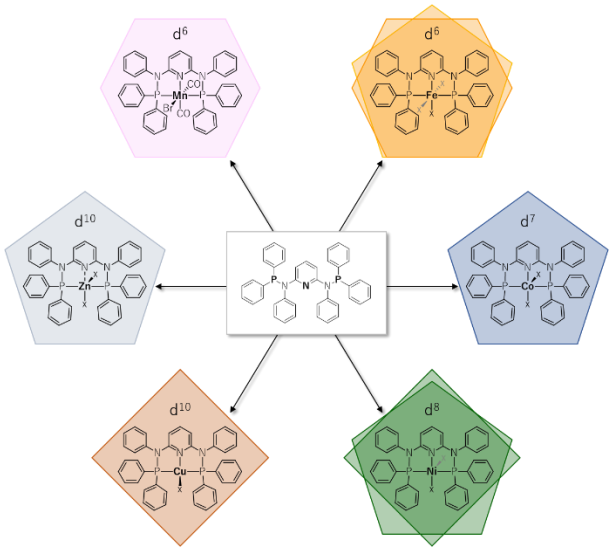

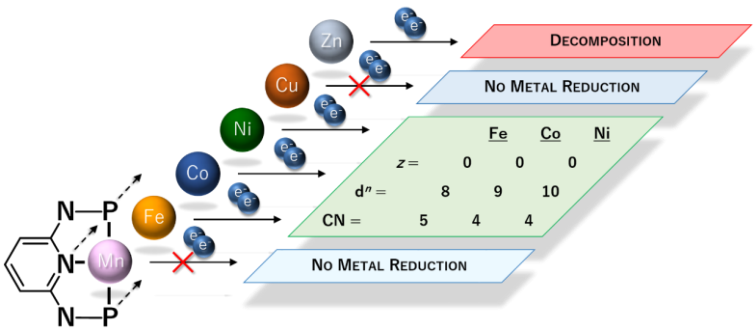

With these initial features known, the complexes' redox and chemical processes during electrochemistry under inert conditions are investigated in the first part of chapter 3.

After probing the reducibility of the respective 3d transition metal center, part two of the chapter will focus on exchange processes between acetonitrile and chloride spectator ligands during reduction. CV and NMR studies allow the postulation of the most probable reduction mechanisms and the resulting species.

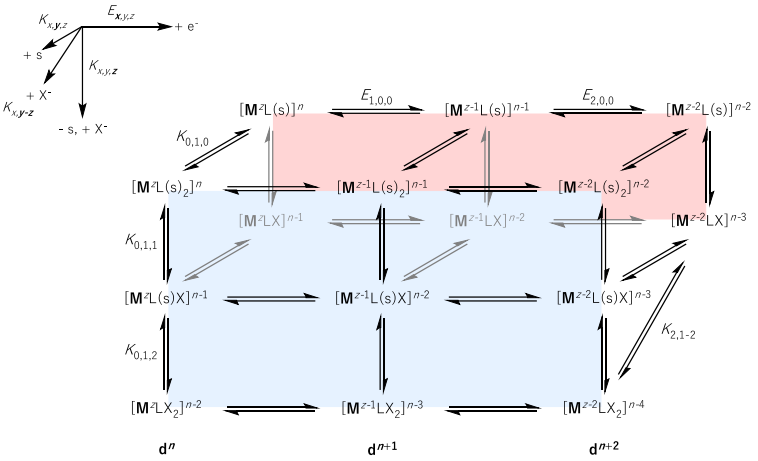

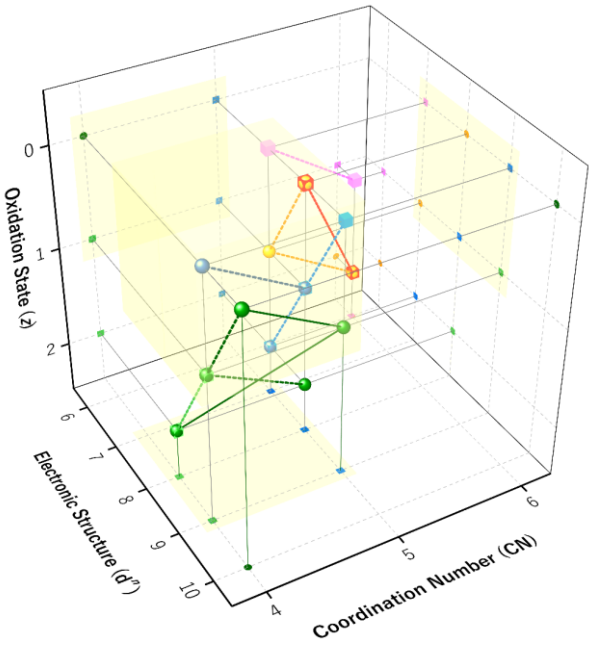

In chapter 4, CO_2 is introduced to the systems to study the coordination of the substrate to the metal center. The findings herein and in the literature are combined to propose favorable properties of 3d transition metal complexes bearing non-innocent ligand systems for electrocatalytic CO_2 reduction. In the last part, LEWIS respectively BRØNSTED acids will be added to access the catalytic CO_2 reduction cycle and find suitable electrolysis conditions. Eventually, bulk electrolysis will be performed, and the results will be related to the metal center in the subjected complexes.

1.4 References

[1] D. A. N. Ussiri, R. Lal, in *Carbon Sequestration for Climate Change Mitigation and Adaptation*, Springer, Cham, **2017**.

[2] D. M. J. S. Bowman, J. K. Balch, P. Artaxo, W. J. Bond, J. M. Carlson, M. A. Cochrane, C. M. D'Antonio, R. S. DeFries, J. C. Doyle, S. P. Harrison, F. H. Johnston, J. E. Keeley, M. A. Krawchuk, C. A. Kull, J. B. Marston, M. A. Moritz, I. C. Prentice, C. I. Roos, A. C. Scott, T. W. Swetnam, G. R. van der Werf, S. J. Pyne, *Science* **2009**, *324*, 481.

[3] J. Graber, J. Amthor, R. Dahlman, D. Drell, S. Weatherwax, *Carbon Cycling and Biosequestration: Integrating Biology and Climate Through Systems Science*, U.S. Department of Science, **2008**.

[4] B. P. Tissot, D. H. Welte, in *Petroleum Formation and Occurrence: A New Approach to Oil and Gas Exploration*, Springer, Berlin, Heidelberg, **1978**.

[5] a) C. D. Keeling, T. P. Whorf, M. Wahlen, J. van der Plichtt, *Nature* **1995**, *375*, 666; b) J. R. Petit, J. Jouzel, D. Raynaud, N. I. Barkov, J. M. Barnola, I. Basile, M. Bender, J. Chappellaz, M. Davis, G. Delaygue, M. Delmotte, V. M. Kotlyakov, M. Legrand, V. Y. Lipenkov, C. Lorius, L. Pépin, C. Ritz, E. Saltzman, M. Stievenard, *Nature* **1999**, *399*, 429; c) D. S. Lee, D. W. Fahey, P. M. Forster, P. J. Newton, R. C. N. Wit, L. L. Lim, B. Owen, R. Sausen, *Atmos. Environ.* **2009**, *43*, 3520; d) J. D. Shakun, P. U. Clark, F. He, S. A. Marcott, A. C. Mix, Z. Liu, B. Otto-Bliesner, A. Schmittner, E. Bard, *Nature* **2012**, *484*, 49.

[6] R. Schmalensee, T. M. Stoker, R. A. Judson, *Rev. Econ. Stat.* **1998**, *80*, 15.

[7] J. Woods, A. Williams, J. K. Hughes, M. Black, R. Murphy, *Phil. Trans. R. Soc. Lon. B* **2010**, *365*, 2991.

[8] a) V. Eyring, I. S. A. Isaksen, T. Berntsen, W. J. Collins, J. J. Corbett, O. Endresen, R. G. Grainger, J. Moldanova, H. Schlager, D. S. Stevenson, *Atmos. Environ.* **2010**, *44*, 4735; b) D. S. Lee, G. Pitari, V. Grewe, K. Gierens, J. E. Penner, A. Petzold, M. J. Prather, U. Schumann, A. Bais, T. Berntsen, D. Iachetti, L. L. Lim, R. Sausen, *Atmos. Environ.* **2010**, *44*, 4678; c) E. Uherek, T. Halenka, J. Borken-Kleefeld, Y. Balkanski, T. Berntsen, C. Borrego, M. Gauss, P. Hoor, K. Juda-Rezler, J. Lelieveld, D. Melas, K. Rypdal, S. Schmid, *Atmos. Environ.* **2010**, *44*, 4772; d) O. J. A. Howitt, M. A. Carruthers, I. J. Smith, C. J. Rodger, *Atmos. Environ.* **2011**, *45*, 7036; e) M. Masiol, R. M. Harrison, *Atmos. Environ.* **2014**, *95*, 409.

[9] E. Worrell, L. Price, N. Martin, C. Hendriks, L. O. Meida, *Annu. Rev. Energy Env.* **2001**, *26*, 303.

[10] P. G. Levi, J. M. Cullen, *Environ. Sci. Technol.* **2018**, *52*, 1725.

[11] S. Solomon, D. Qin, M. Manning, Z. Chen, M. Marquis, K. B. Averyt, M. Tignor, H. L. Miller, *Climate Change 2007: The Physical Science Basis. Contribution of Working Group I to the Fourth Assessment Report of the Intergovernmental Panel on Climate Change*, IPCC, Cambridge, United Kingdom and New York, NY, USA, **2007**.

[12] a) M. Wang, A. Lawal, P. Stephenson, J. Sidders, C. Ramshaw, *Chem. Eng. Res. Des.* **2011**, *89*, 1609; b) R. Monastersky, *Nature* **2013**, *497*, 13.

[13] NOAA Global Monitoring Laboratory, "Trends in Atmospheric Carbon Dioxide", can be found under https://www.esrl.noaa.gov/gmd/ccgg/trends/mlo.html, **2022**, last accessed on: 23.03.2022.

[14] H. Ritchie, M. Roser, "CO_2 and Greenhouse Gas Emissions", can be found under https://ourworldindata.org/atmospheric-concentrations, **2020**, last accessed on: 23.03.2022.

[15] B. M. Bhanage, *Transformation and Utilization of Carbon Dioxide*, Springer, Berlin, Heidelberg, **2014**.

[16] a) T. J. Meyer, *Acc. Chem. Res.* **1989**, *22*, 163; b) J. H. Alstrum-Acevedo, M. K. Brennaman, T. J. Meyer, *Inorg. Chem.* **2005**, *44*, 6802; c) D. King, J. Browne, R. Layard, G. O'Donnell, M. Rees, N. Stern, A. Turner, *A Global Apollo Programme to Combat Climate Change*, London School of Economics and Science, **2015**; d) K. Brinkert, in *Energy Conversion in Natural and Artificial Photosynthesis*, Springer, Cham, **2018**.

[17] a) M. Aresta, A. Dibenedetto, *Dalton Trans.* **2007**, 2975; b) E. E. Benson, C. P. Kubiak, A. J. Sathrum, J. M. Smieja, *Chem. Soc. Rev.* **2009**, *38*, 89; c) J. L. Inglis, B. J. MacLean, M. T. Pryce, J. G. Vos, *Coord. Chem. Rev.* **2012**, *256*, 2571; d) M. Aresta, A. Dibenedetto, A. Angelini, *Chem. Rev.* **2014**, *114*, 1709; e) D. U. Nielsen, X.-M. Hu, K. Daasbjerg, T. Skrydstrup, *Nat. Catal.* **2018**, *1*, 244.

[18] a) P. Anastas, N. Eghbali, *Chem. Soc. Rev.* **2010**, *39*, 301; b) J. B. Zimmerman, P. T. Anastas, H. C. Erythropel, W. Leitner, *Science* **2020**, *367*, 397.

[19] N. von der Assen, L. J. Müller, A. Steingrube, P. Voll, A. Bardow, *Environ. Sci. Technol.* **2016**, *50*, 1093.

[20] M. E. Vol'pin, I. S. Kolomnikov, *Pure Appl. Chem.* **1973**, *33*, 567.

[21] The source of the figure is distributed under the Creative Commons Attribution 4.0 License. F. Kaspar, M. Borsche, U. Pfeifroth, J. Trentmann, J. Drücke, P. Becker, *Adv. Sci. Res.* **2019**, *16*, 119.

[22] a) H. Offermanns, F. X. Effenberger, W. Keim, L. Plass, *Chem. Ing. Tech.* **2017**, *89*, 270; b) K. Wagemann, F. Ausfelder, *E-Fuels – Mehr als eine Option*, **2017**.

[23] a) M. Faraday, *Ann. Phys.* **1834**, *109*, 433; b) H. Lund, *J. Electrochem. Soc.* **2002**, *149*, 21.

[24] H. Kolbe, *J. prakt. Chem.* **1847**, *41*, 137.

[25] J. Tafel, H. Hahl, *Ber. Dtsch. Chem. Ges.* **1907**, *40*, 3312.

[26] C. Kingston, M. D. Palkowitz, Y. Takahira, J. C. Vantourout, B. K. Peters, Y. Kawamata, P. S. Baran, *Acc. Chem. Res.* **2020**, *53*, 72.

[27] T. F. O'Brien, T. V. Bommaraju, F. Hine, *Handbook of Chlor-Alkali Technology*, Springer, Boston, MA, **2005**.

[28] D. Pletcher, F. C. Walsh, in *Industrial Electrochemistry*, Springer, Dordrecht, **1993**.

[29] X.-B. Lu, *Carbon Dioxide and Organometallics*, Springer, Cham, **2016**.

[30] a) A. M. Bazzanella, F. Ausfelder, *Low carbon energy and feedstock for the European chemical industry*, DECHEMA Gesellschaft für Chemische Technik und Biotechnologie e.V., **2017**; b) Covestro AG, "Cardyon®: Ein ökologisch sinnvolles Polyol", can be found under https://solutions.covestro.com/de/marken/cardyon, **2017**, last accessed on: 23.03.2022; c) Econic Technologies Ltd, "How It Works", can be found under http://econic-technologies.com/how-it-works/, **2017**, last accessed on: 23.03.2022; d) Evonik Industries AG, "Evonik and Siemens to generate high-value specialty chemicals from carbon dioxide and eco-electricity", can be found under https://corporate.evonik.com/en/pages/article.aspx?articleId=106259, **2018**, last accessed on: 23.03.2022; e) Carbon Recycling International Ltd., "Carbon Dioxide Emissions to Value", can be found under https://www.carbonrecycling.is/technology, **2022**, last accessed on: 23.03.2022; f) R. Krause, D. Reinisch, C. Reller, H. Eckert, D. Hartmann, D. Taroata, K. Wiesner-Fleischer, A. Bulan, A. Lueken, G. Schmid, *Chem. Ing. Tech.* **2020**, *92*, 53.

[31] C. Song, *Catal. Today* **2006**, *115*, 2.

[32] D. A. Palmer, R. Vaneldik, *Chem. Rev.* **1983**, *83*, 651.

[33] J. Artz, T. E. Mueller, K. Thenert, J. Kleinekorte, R. Meys, A. Sternberg, A. Bardow, W. Leitner, *Chem. Rev.* **2018**, *118*, 434.

[34] a) W. Wang, S. Wang, X. Ma, J. Gong, *Chem. Soc. Rev.* **2011**, *40*, 3703; b) W. H. Wang, Y. Himeda, J. T. Muckerman, G. F. Manbeck, E. Fujita, *Chem. Rev.* **2015**, *115*, 12936; c) J. Klankermayer, S. Wesselbaum, K. Beydoun, W. Leitner, *Angew. Chem. Int. Ed.* **2016**, *55*, 7296.

[35] J. Qiao, Y. Liu, F. Hong, J. Zhang, *Chem. Soc. Rev.* **2014**, *43*, 631.

[36] a) M. Gattrell, N. Gupta, A. Co, *J. Electroanal. Chem.* **2006**, *594*, 1; b) S. Nitopi, E. Bertheussen, S. B. Scott, X. Y. Liu, A. K. Engstfeld, S. Horch, B. Seger, I. E. L. Stephens, K. Chan, C. Hahn, J. K. Norskov, T. F. Jaramillo, I. Chorkendorff, *Chem. Rev.* **2019**, *119*, 7610; c) J. Zhao, S. Xue, J. Barber, Y. Zhou, J. Meng, X. Ke, *J. Mater. Chem. A* **2020**, *8*, 4700.

[37] a) S. Schlager, A. Dibenedetto, M. Aresta, D. H. Apaydin, L. M. Dumitru, H. Neugebauer, N. S. Sariciftci, *Energy Technol.* **2017**, *5*, 812; b) P. Chiranjeevi, M. Bulut, T. Breugelmans, S. A. Patil, D. Pant, *Curr. Opin. Green Sustain. Chem.* **2019**, *16*, 65; c) F. N. Ahmad Rizal Lim, F. Marpani, V. E. Anak Dilol, S. Mohamad Pauzi, N. H. Othman, N. H. Alias, N. R. Nik Him, J. Luo, N. Abd Rahman, *Membranes* **2022**, *12*, 28.

[38] a) Y. Oh, X. Hu, *Chem. Soc. Rev.* **2013**, *42*, 2253; b) D. V. Vasilyev, P. J. Dyson, *ACS Catal.* **2021**, *11*, 1392.

[39] S. Zhang, Q. Fan, R. Xia, T. J. Meyer, *Acc. Chem. Res.* **2020**, *53*, 255.

[40] a) R. Francke, B. Schille, M. Roemelt, *Chem. Rev.* **2018**, *118*, 4631; b) L. Chen, G. Chen, C.-F. Leung, C. Cometto, M. Robert, T.-C. Lau, *Chem. Soc. Rev.* **2020**, *49*, 7271.

[41] H. Kumagai, T. Nishikawa, H. Koizumi, T. Yatsu, G. Sahara, Y. Yamazaki, Y. Tamaki, O. Ishitani, *Chem. Sci.* **2019**, *10*, 1597.

[42] E. Lamy, L. Nadjo, J.-M. Savéant, *J. Electroanal. Chem.* **1977**, *78*, 403.

[43] D. Chang, T. Malinski, A. Ulman, K. M. Kadish, *Inorg. Chem.* **1984**, *23*, 817.

[44] a) J. D. Blakemore, R. H. Crabtree, G. W. Brudvig, *Chem. Rev.* **2015**, *115*, 12974; b) S. S. Rohner, N. W. Kinzel, C. Werlé, W. Leitner, *Dalton Trans.* **2019**, *48*, 13205.

[45] a) A. J. Bard, L. R. Faulkner, *Electrochemical Methods*, 2nd ed., John Wiley & Sons, Inc., New York, **2001**; b) A. M. Appel, M. L. Helm, *ACS Catal.* **2014**, *4*, 630.

[46] a) P. Chen, M. A. Fryling, R. L. McCreery, *Anal. Chem.* **1995**, *67*, 3115; b) P. F. Barbara, T. J. Meyer, M. A. Ratner, *J. Phys. Chem.* **1996**, *100*, 13148; c) D. Bohra, J. H. Chaudhry, T. Burdyny, E. A. Pidko, W. A. Smith, *Energy Environ. Sci.* **2019**, *12*, 3380.

[47] a) E. S. Rountree, B. D. McCarthy, T. T. Eisenhart, J. L. Dempsey, *Inorg. Chem.* **2014**, *53*, 9983; b) C. Costentin, G. Passard, J.-M. Savéant, *J. Am. Chem. Soc.* **2015**, *137*, 5461.

[48] a) D. M. Feng, Y. P. Zhu, P. Chen, T. Y. Ma, *Catalysts* **2017**, *7*, 373; b) C. Costentin, J.-M. Savéant, C. Tard, *ACS Energy Lett.* **2018**, *3*, 695.

[49] J.-M. Savéant, *Chem. Rev.* **2008**, *108*, 2348.

[50] S. V. Rosokha, J. K. Kochi, *J. Am. Chem. Soc.* **2007**, *129*, 3683.

[51] C. Costentin, M. Robert, J.-M. Savéant, *Chem. Soc. Rev.* **2013**, *42*, 2423.

[52] a) J. Pacansky, U. Wahlgren, P. S. Bagus, *J. Chem. Phys.* **1975**, *62*, 2740; b) G. L. Gutsev, R. J. Bartlett, R. N. Compton, *J. Chem. Phys.* **1998**, *108*, 6756; c) M. Bonifačić, G. L. Hug, C. Schöneich, *J. Phys. Chem. A* **2000**, *104*, 1240.

[53] W. Leitner, *Coord. Chem. Rev.* **1996**, *153*, 257.

[54] a) R. Noyori, T. Ohkuma, *Angew. Chem. Int. Ed.* **2001**, *40*, 40; b) R. Noyori, *Angew. Chem. Int. Ed.* **2002**, *41*, 2008; c) C. A. Sandoval, T. Ohkuma, K. Muñiz, R. Noyori, *J. Am. Chem. Soc.* **2003**, *125*, 13490.

[55] a) I. Castro-Rodriguez, H. Nakai, L. N. Zakharov, A. L. Rheingold, K. Meyer, *Science* **2004**, *305*, 1757; b) M. Aresta, A. Dibenedetto, E. Quaranta, *Reaction mechanisms in carbon dioxide conversion*, Springer, Berlin, Heidelberg, **2015**; c) A. Paparo, J. Okuda, *Coord. Chem. Rev.* **2017**, *334*, 136.

[56] M. Aresta, R. Gobetto, E. Quaranta, I. Tommasi, *Inorg. Chem.* **1992**, *31*, 4286.

[57] a) J. P. Collin, A. Jouaiti, J. P. Sauvage, *Inorg. Chem.* **1988**, *27*, 1986; b) M. Y. Udugala-Ganehenege, N. M. Dissanayake, Y. Liu, A. M. Bond, J. Zhang, *Transition Met. Chem.* **2014**, *39*, 819.

[58] A. Paparo, J. S. Silvia, C. E. Kefalidis, T. P. Spaniol, L. Maron, J. Okuda, C. C. Cummins, *Angew. Chem. Int. Ed.* **2015**, *54*, 9115.

[59] L. Castro, O. P. Lam, S. C. Bart, K. Meyer, L. Maron, *Organometallics* **2010**, *29*, 5504.

[60] a) F. Bottomley, I. J. B. Lin, P. S. White, *J. Organomet. Chem.* **1981**, *212*, 341; b) L. Castro, S. Labouille, D. R. Kindra, J. W. Ziller, F. Nief, W. J. Evans, L. Maron, *Chem. Eur. J.* **2012**, *18*, 7886; c) A.-C. Schmidt, F. W. Heinemann, C. E. Kefalidis, L. Maron, P. W. Roesky, K. Meyer, *Chem. Eur. J.* **2014**, *20*, 13501; d) N. Tsoureas, L. Castro, A. F. R. Kilpatrick, F. G. N. Cloke, L. Maron, *Chem. Sci.* **2014**, *5*, 3777.

[61] R. Angamuthu, P. Byers, M. Lutz, A. L. Spek, E. Bouwman, *Science* **2010**, *327*, 313.

[62] M. D. Sampson, C. P. Kubiak, *J. Am. Chem. Soc.* **2016**, *138*, 1386.

[63] L. Chen, Z. Guo, X.-G. Wei, C. Gallenkamp, J. Bonin, E. Anxolabéhère-Mallart, K.-C. Lau, T.-C. Lau, M. Robert, *J. Am. Chem. Soc.* **2015**, *137*, 10918.

[64] a) C. Riplinger, E. A. Carter, *ACS Catal.* **2015**, *5*, 900; b) H. Takeda, C. Cometto, O. Ishitani, M. Robert, *ACS Catal.* **2016**, *7*, 70.

[65] B. D. McCarthy, D. J. Martin, E. S. Rountree, A. C. Ullman, J. L. Dempsey, *Inorg. Chem.* **2014**, *53*, 8350.

[66] a) F. Franco, C. Cometto, F. Ferrero Vallana, F. Sordello, E. Priola, C. Minero, C. Nervi, R. Gobetto, *Chem. Commun.* **2014**, *50*, 14670; b) G. Neri, I. M. Aldous, J. J. Walsh, L. J. Hardwick, A. J. Cowan, *Chem. Sci.* **2016**, *7*, 1521.

[67] C. Riplinger, M. D. Sampson, A. M. Ritzmann, C. P. Kubiak, E. A. Carter, *J. Am. Chem. Soc.* **2014**, *136*, 16285.

[68] a) W. Kaim, *Inorg. Chem.* **2011**, *50*, 9752; b) W. Kaim, *Eur. J. Inorg. Chem.* **2012**, *2012*, 343; c) K. A. Grice, C. Saucedo, *Inorg. Chem.* **2016**, *55*, 6240; d) N. Elgrishi, M. B. Chambers, X. Wang, M. Fontecave, *Chem. Soc. Rev.* **2017**, *46*, 761; e) B. Chatterjee, W.-C. Chang, S. Jena, C. Werlé, *ACS Catal.* **2020**, *10*, 14024; f) B. Chatterjee, W. C. Chang, C. Werlé, *ChemCatChem* **2020**, *13*, 1659; g) N. Queyriaux, *ACS Catal.* **2021**, *11*, 4024.

[69] J. Hawecker, J.-M. Lehn, R. Ziessel, *J. Chem. Soc., Chem. Commun.* **1984**, 328.

[70] E. E. Benson, M. D. Sampson, K. A. Grice, J. M. Smieja, J. D. Froehlich, D. Friebel, J. A. Keith, E. A. Carter, A. Nilsson, C. P. Kubiak, *Angew. Chem. Int. Ed.* **2013**, *52*, 4841.

[71] a) J. Kothandaraman, A. Goeppert, M. Czaun, G. A. Olah, G. K. S. Prakash, *J. Am. Chem. Soc.* **2016**, *138*, 778; b) P. Zhang, S.-F. Ni, L. Dang, *Chem. Asian J.* **2016**, *11*, 2528; c) W.-H. Wang, X. Feng, M. Bao, in *Transformation of Carbon Dioxide to Formic Acid and Methanol*, Springer, Singapore, **2018**; d) J. M. Barlow, J. Y. Yang, *ACS Cent. Sci.* **2019**, *5*, 580; e) D. P. Estes, M. Leutzsch, L. Schubert, A. Bordet, W. Leitner, *ACS Catal.* **2020**, *10*, 2990.

[72] C. W. Machan, M. D. Sampson, C. P. Kubiak, *J. Am. Chem. Soc.* **2015**, *137*, 8564.

[73] a) K.-Y. Wong, W.-H. Chung, C.-P. Lau, *J. Electroanal. Chem.* **1998**, *453*, 161; b) J. D. Froehlich, C. P. Kubiak, *Inorg. Chem.* **2012**, *51*, 3932; c) C. Costentin, M. Robert, J.-M. Savéant, A. Tatin, *Proc. Natl. Acad. Sci. USA* **2015**, *112*, 6882.

[74] M. Beley, J.-P. Collin, R. Ruppert, J.-P. Sauvage, *J. Chem. Soc., Chem. Commun.* **1984**, 1315.

[75] a) G. B. Balazs, F. C. Anson, *J. Electroanal. Chem.* **1992**, *322*, 325; b) J. D. Froehlich, C. P. Kubiak, *J. Am. Chem. Soc.* **2015**, *137*, 3565.

[76] a) P. J. Connolly, E. J. Billo, *Inorg. Chem.* **1987**, *26*, 3224; b) S. Sakaki, *J. Am. Chem. Soc.* **1990**, *112*, 7813; c) S. Sakaki, *J. Am. Chem. Soc.* **1992**, *114*, 2055; d) K. Bujno, R. Bilewicz, L. Siegfried, T. A. Kaden, *J. Electroanal. Chem.* **1998**, *445*, 47; e) J. Song, E. L. Klein, F. Neese, S. Ye, *Inorg. Chem.* **2014**, *53*, 7500.

[77] a) G. B. Balazs, F. C. Anson, *J. Electroanal. Chem.* **1993**, *361*, 149; b) K. Bujno, R. Bilewicz, L. Siegfried, T. Kaden, *Electrochim. Acta* **1997**, *42*, 1201; c) Y. Wu, B. Rudshteyn, A. Zhanaidarova, J. D. Froehlich, W. Ding, C. P. Kubiak, V. S. Batista, *ACS Catal.* **2017**, *7*, 5282.

[78] M. Rudolph, S. Dautz, E.-G. Jäger, *J. Am. Chem. Soc.* **2000**, *122*, 10821.

[79] a) M. Hammouche, D. Lexa, M. Momenteau, J.-M. Savéant, *J. Am. Chem. Soc.* **1991**, *113*, 8455; b) I. Bhugun, D. Lexa, J.-M. Savéant, *J. Am. Chem. Soc.* **1994**, *116*, 5015; c) C. Costentin, S. Drouet, M. Robert, J.-M. Savéant, *Science* **2012**, *338*, 90; d) C. Costentin, S. Drouet, G. Passard, M. Robert, J.-M. Savéant, *J. Am. Chem. Soc.* **2013**, *135*, 9023; e) E. A. Mohamed, Z. N. Zahran, Y. Naruta, *Chem. Commun.* **2015**, *51*, 16900; f) R. B. Ambre, Q. Daniel, T. Fan, H. Chen, B. Zhang, L. Wang, M. S. G. Ahlquist, L. Duan, L. Sun, *Chem. Commun.* **2016**, *52*, 14478; g) I. Azcarate, C. Costentin, M. Robert, J.-M. Savéant, *J. Am. Chem. Soc.* **2016**, *138*, 16639; h) J. Choi, T. M. Benedetti, R. Jalili, A. Walker, G. Wallace Gordon, D. L. Officer, *Chem. Eur. J.* **2016**, *22*, 14158; i) A. Maurin, M. Robert, *J. Am. Chem. Soc.* **2016**, *138*, 2492; j) A. Tatin, C. Comminges, B. Kokoh, C. Costentin, M. Robert, J.-M. Savéant, *Proc. Natl. Acad. Sci. USA* **2016**, *113*, 5526; k) A. Khadhraoui, P. Gotico, B. Boitrel, W. Leibl, Z. Halime, A. Aukauloo, *Chem. Commun.* **2018**, *54*, 11630; l) E. M. Nichols, J. S. Derrick, S. K. Nistanaki, P. T. Smith, C. J. Chang, *Chem. Sci.* **2018**, *9*, 2952; m) J. D. B. Koenig, J. Willkomm, R. Roesler, W. E. Piers, G. C. Welch, *ACS Appl. Energy Mater.* **2019**, *2*, 4022; n) B. Mondal, P. Sen, A. Rana, D. Saha, P. Das, A. Dey, *ACS Catal.* **2019**, *9*, 3895; o) B. Zhao, H. Lei, N. Wang, G. Xu, W. Zhang, R. Cao, *Chem. Eur. J.* **2020**, *26*, 4007; p) S. Amanullah, P. Saha, A. Dey, *J. Am. Chem. Soc.* **2021**, *143*, 13579; q) A. Chaturvedi, C. K. Williams, N. Devi, J. J. Jiang, *Inorg. Chem.* **2021**, *60*, 3843.

[80] a) D. Behar, T. Dhanasekaran, P. Neta, C. M. Hosten, D. Ejeh, P. Hambright, E. Fujita, *J. Phys. Chem. A* **1998**, *102*, 2870; b) S. Aoi, K. Mase, K. Ohkubo, S. Fukuzumi, *Chem. Commun.* **2015**, *51*, 10226; c) S. Lin, C. S. Diercks, Y. B. Zhang, N. Kornienko, E. M. Nichols, Y. Zhao, A. R. Paris, D. Kim, P. Yang, O. M. Yaghi, C. J. Chang, *Science* **2015**, *349*, 1208; d) K. Alenezi, *J. Chem.* **2016**, *2016*, 1; e) X.-M. Hu, M. H. Rønne, S. U.

Pedersen, T. Skrydstrup, K. Daasbjerg, *Angew. Chem. Int. Ed.* **2017**, *56*, 6468; f) M. Zhu, D.-T. Yang, R. Ye, J. Zeng, N. Corbin, K. Manthiram, *Catal. Sci. Technol.* **2019**, *9*, 974.

[81] C. K. Williams, A. Lashgari, J. Chai, J. J. Jiang, *ChemSusChem* **2020**, *13*, 3412.

[82] a) I. Bhugun, D. Lexa, J.-M. Savéant, *J. Am. Chem. Soc.* **1996**, *118*, 1769; b) I. Azcarate, C. Costentin, M. Robert, J.-M. Savéant, *J. Phys. Chem. C* **2016**, *120*, 28951; c) Y. Okabe, S. K. Lee, M. Kondo, S. Masaoka, *J. Biol. Inorg. Chem.* **2017**, *22*, 713.

[83] a) C. Costentin, M. Robert, J.-M. Savéant, *Acc. Chem. Res.* **2015**, *48*, 2996; b) J. A. Barrett, F. M. Brunner, P. L. Cheung, C. P. Kubiak, G. L. Lee, C. J. Miller, K. M. Waldie, A. Zhanaidarova, in *Carbon Dioxide Electrochemistry: Homogeneous and Heterogeneous Catalysis*, The Royal Society of Chemistry, **2021**.

[84] a) M. L. Clark, K. A. Grice, C. E. Moore, A. L. Rheingold, C. P. Kubiak, *Chem. Sci.* **2014**, *5*, 1894; b) F. Franco, C. Cometto, F. Sordello, C. Minero, L. Nencini, J. Fiedler, R. Gobetto, C. Nervi, *ChemElectroChem* **2015**, *2*, 1372; c) J. Tory, B. Setterfield-Price, R. A. W. Dryfe, F. Hartl, *ChemElectroChem* **2015**, *2*, 213.

[85] a) T. R. O'Toole, L. D. Margerum, T. D. Westmoreland, W. J. Vining, R. W. Murray, T. J. Meyer, *J. Chem. Soc., Chem. Commun.* **1985**, 1416; b) B. P. Sullivan, C. M. Bolinger, D. Conrad, W. J. Vining, T. J. Meyer, *J. Chem. Soc., Chem. Commun.* **1985**, 1414; c) M. Bourrez, F. Molton, S. Chardon-Noblat, A. Deronzier, *Angew. Chem. Int. Ed.* **2011**, *50*, 9903; d) J. A. Keith, K. A. Grice, C. P. Kubiak, E. A. Carter, *J. Am. Chem. Soc.* **2013**, *135*, 15823; e) M. Bourrez, M. Orio, F. Molton, H. Vezin, C. Duboc, A. Deronzier, S. Chardon-Noblat, *Angew. Chem. Int. Ed.* **2014**, *53*, 240; f) C. W. Machan, S. A. Chabolla, J. Yin, M. K. Gilson, F. A. Tezcan, C. P. Kubiak, *J. Am. Chem. Soc.* **2014**, *136*, 14598; g) M. D. Sampson, A. D. Nguyen, K. A. Grice, C. E. Moore, A. L. Rheingold, C. P. Kubiak, *J. Am. Chem. Soc.* **2014**, *136*, 5460; h) Y. C. Lam, R. J. Nielsen, H. B. Gray, W. A. Goddard, *ACS Catal.* **2015**, *5*, 2521; i) Y. Matsubara, D. C. Grills, Y. Kuwahara, *ACS Catal.* **2015**, *5*, 6440; j) C. W. Machan, J. Yin, S. A. Chabolla, M. K. Gilson, C. P. Kubiak, *J. Am. Chem. Soc.* **2016**, *138*, 8184; k) F. Franco, C. Cometto, L. Nencini, C. Barolo, F. Sordello, C. Minero, J. Fiedler, M. Robert, R. Gobetto, C. Nervi, *Chem. Eur. J.* **2017**, *23*, 4782; l) A. Nakada, O. Ishitani, *ACS Catal.* **2017**, *8*, 354; m) K. T. Ngo, M. McKinnon, B. Mahanti, R. Narayanan, D. C. Grills, M. Z. Ertem, J. Rochford, *J. Am. Chem. Soc.* **2017**, *139*, 2604; n) B. Reuillard, K. H. Ly, T. E. Rosser, M. F. Kuehnel, I. Zebger, E. Reisner, *J. Am. Chem. Soc.* **2017**, *139*, 14425; o) S. Sung, D. Kumar, M. Gil-Sepulcre, M. Nippe, *J. Am. Chem. Soc.* **2017**, *139*, 13993; p) M. L. Clark, A. Ge, P. E. Videla, B. Rudshteyn, C. J. Miller, J. Song, V. S. Batista, T. Lian, C. P. Kubiak, *J. Am. Chem. Soc.* **2018**, *140*, 17643; q) M. L. Clark, P. L. Cheung,

M. Lessio, E. A. Carter, C. P. Kubiak, *ACS Catal.* **2018**, *8*, 2021; r) E. Haviv, D. Azaiza-Dabbah, R. Carmieli, L. Avram, J. M. L. Martin, R. Neumann, *J. Am. Chem. Soc.* **2018**, *140*, 12451; s) S. Sato, K. Saita, K. Sekizawa, S. Maeda, T. Morikawa, *ACS Catal.* **2018**, *8*, 4452; t) D. R. Whang, D. H. Apaydin, S. Y. Park, N. S. Sariciftci, *J. Catal.* **2018**, *363*, 191; u) H. Koizumi, H. Chiba, A. Sugihara, M. Iwamura, K. Nozaki, O. Ishitani, *Chem. Sci.* **2019**, *10*, 3080.

[86] a) H. Ishida, H. Tanaka, K. Tanaka, T. Tanaka, *J. Chem. Soc., Chem. Commun.* **1987**, 131; b) H. Ishida, K. Tanaka, T. Tanaka, *Organometallics* **1987**, *6*, 181; c) H. Ishida, K. Fujiki, T. Ohba, K. Ohkubo, K. Tanaka, T. Terada, T. Tanaka, *J. Chem. Soc., Dalton Trans.* **1990**, 2155; d) J. R. Pugh, M. R. M. Bruce, B. P. Sullivan, T. J. Meyer, *Inorg. Chem.* **1991**, *30*, 86; e) M.-N. Collomb-Dunand-Sauthier, A. Deronzier, R. Ziessel, *Inorg. Chem.* **1994**, *33*, 2961; f) H. Nakajima, Y. Kushi, H. Nagao, K. Tanaka, *Organometallics* **1995**, *14*, 5093; g) H. Nakajima, K. Tanaka, *Chem. Lett.* **1995**, *24*, 891; h) S. Chardon-Noblat, A. Deronzier, R. Ziessel, D. Zsoldos, *Inorg. Chem.* **1997**, *36*, 5384; i) T. Mizukawa, K. Tsuge, H. Nakajima, K. Tanaka, *Angew. Chem. Int. Ed.* **1999**, *38*, 362; j) E. Fujita, M. Chou, K. Tanaka, *Appl. Organomet. Chem.* **2000**, *14*, 844; k) S. Ramakrishnan, C. E. D. Chidsey, *Inorg. Chem.* **2017**, *56*, 8326.

[87] a) C. M. Bolinger, B. P. Sullivan, D. Conrad, J. A. Gilbert, N. Story, T. J. Meyer, *J. Chem. Soc., Chem. Commun.* **1985**, 796; b) C. M. Bolinger, N. Story, B. P. Sullivan, T. J. Meyer, *Inorg. Chem.* **1988**, *27*, 4582; c) A. G. M. M. Hossain, T. Nagaoka, K. Ogura, *Electrochim. Acta* **1997**, *42*, 2577; d) F. D. Sypaseuth, C. Matlachowski, M. Weber, M. Schwalbe, C. C. Tzschucke, *Chem. Eur. J.* **2015**, *21*, 6564.

[88] N. W. Kinzel, C. Werlé, W. Leitner, *Angew. Chem. Int. Ed.* **2021**, *60*, 11628.

[89] S. Gonglach, S. Paul, M. Haas, F. Pillwein, S. S. Sreejith, S. Barman, R. De, S. Müllegger, P. Gerschel, U.-P. Apfel, H. Coskun, A. Aljabour, P. Stadler, W. Schöfberger, S. Roy, *Nat. Commun.* **2019**, *10*, 3864.

[90] R. De, S. Gonglach, S. Paul, M. Haas, S. S. Sreejith, P. Gerschel, U.-P. Apfel, T. H. Vuong, J. Rabeah, S. Roy, W. Schöfberger, *Angew. Chem. Int. Ed.* **2020**, *59*, 10527.

[91] M. Abdinejad, C. Dao, B. Deng, F. Dinic, O. Voznyy, X.-a. Zhang, H.-B. Kraatz, *ACS Sustain. Chem. Eng.* **2020**, *8*, 9549.

[92] P. Bose, C. Mukherjee, A. K. Golder, *Inorg. Chem. Front.* **2019**, *6*, 1721.

[93] a) B. Mondal, F. Neese, S. Ye, *Inorg. Chem.* **2015**, *54*, 7192; b) B. Mondal, F. Neese, S. Ye, *Inorg. Chem.* **2016**, *55*, 5438; c) B. M. Ceballos, J. Y. Yang, *Proc. Natl. Acad. Sci. USA*

2018, *115*, 12686; d) K. M. Waldie, A. L. Ostericher, M. H. Reineke, A. F. Sasayama, C. P. Kubiak, *ACS Catal.* **2018**, *8*, 1313.

[94] J. P. F. Rebolledo-Chávez, M. Cruz-Ramírez, R. Patakfalvi, F. J. T. Rangel, L. Ortiz-Frade, *Electrochim. Acta* **2017**, *247*, 241.

[95] N. Elgrishi, K. J. Rountree, B. D. McCarthy, E. S. Rountree, T. T. Eisenhart, J. L. Dempsey, *J. Chem. Educ.* **2018**, *95*, 197.

[96] C. Costentin, J.-M. Savéant, *J. Am. Chem. Soc.* **2017**, *139*, 8245.

[97] T. Yokoyama, H. Kitagawa, H.-a. Iwasawa, M. Zenki, *Inorg. Chim. Acta* **1996**, *253*, 1.

[98] a) S. S. Rozenel, J. B. Kerr, J. Arnold, *Dalton Trans.* **2011**, *40*, 10397; b) N. Elgrishi, M. B. Chambers, V. Artero, M. Fontecave, *PCCP* **2014**, *16*, 13635; c) C. Lescot, S. Savourey, P. Thuéry, G. Lefèvre, J.-C. Berthet, T. Cantat, *C. R. Chim.* **2016**, *19*, 57; d) K. Talukdar, A. Issa, J. W. Jurss, *Front. Chem.* **2019**, *7*.

[99] M. Loipersberger, D. G. A. Cabral, D. B. K. Chu, M. Head-Gordon, *J. Am. Chem. Soc.* **2021**, *143*, 744.

[100] a) S. Min, S. Rasul, H. Li, D. C. Grills, K. Takanabe, L.-J. Li, K.-W. Huang, *ChemPlusChem* **2016**, *81*, 166; b) G. K. Rao, W. Pell, I. Korobkov, D. Richeson, *Chem. Commun.* **2016**, *52*, 8010; c) G. Hu, J. J. Jiang, H. R. Kelly, A. J. Matula, Y. Wu, N. Romano, B. Q. Mercado, H. Wang, V. S. Batista, R. H. Crabtree, G. W. Brudvig, *Chem. Commun.* **2020**, *56*, 9126; d) N.-n. Shi, W.-j. Xie, W.-s. Gao, J.-m. Wang, S.-f. Zhang, Y.-h. Fan, M. Wang, *Appl. Organomet. Chem.* **2020**, *34*, e5551.

Chapter 2: Synthesis & Structures

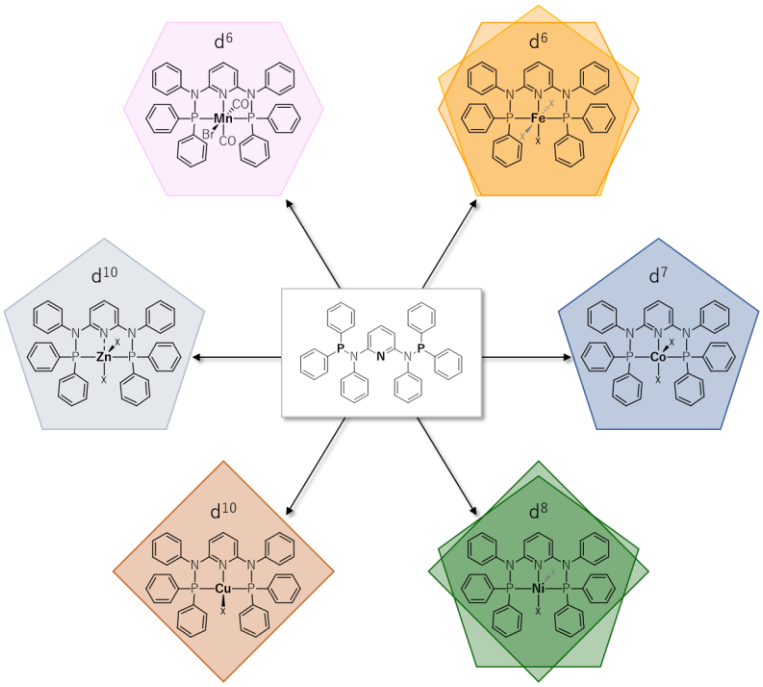

In the following chapter, the synthesis routes toward the central ligand structure of this work, N^2,N^6-bis(diphenylphosphaneyl)-N^2,N^6-diphenylpyridine-2,6-diamine, as well as the mid to late 3d transition metal complexes derived thereof are discussed.

The focus is set on the structural analysis of the received products based on nuclear magnetic resonance (NMR) spectroscopy and single-crystal X-ray diffraction (XRD). Whenever applicable, MÖSSBAUER and electron paramagnetic resonance (EPR) spectroscopic as well as superconducting quantum interference device (SQUID) data complement the analysis.

Subsequently, crystal field theory is employed to gain insight into the metal's electronic configuration and set a starting point for assessing further electron injections by electrochemical means.

Lastly, relationships between the observed geometric and electronic features of the 3d metal center are drawn to conclude crucial properties in the systematic design of potential CO_2 electroreduction catalysts.

Parts of this chapter have been published in:

N. W. Kinzel, D. Demirbas, E. Bill, T. Weyhermüller, C. Werlé, N. Kaeffer, W. Leitner, *Inorg. Chem.* **2021**, *60*, 19062.

Systematic variations of metal centers with redox-innocent ligands such as pincer-type structures[1] remain insufficiently investigated in CO_2 electroreduction (Figure 2.1). However, the involvement of a ligand inert to redox and protonation processes under common electrocatalytic conditions is a prerequisite for the isolated analysis of the metal center.

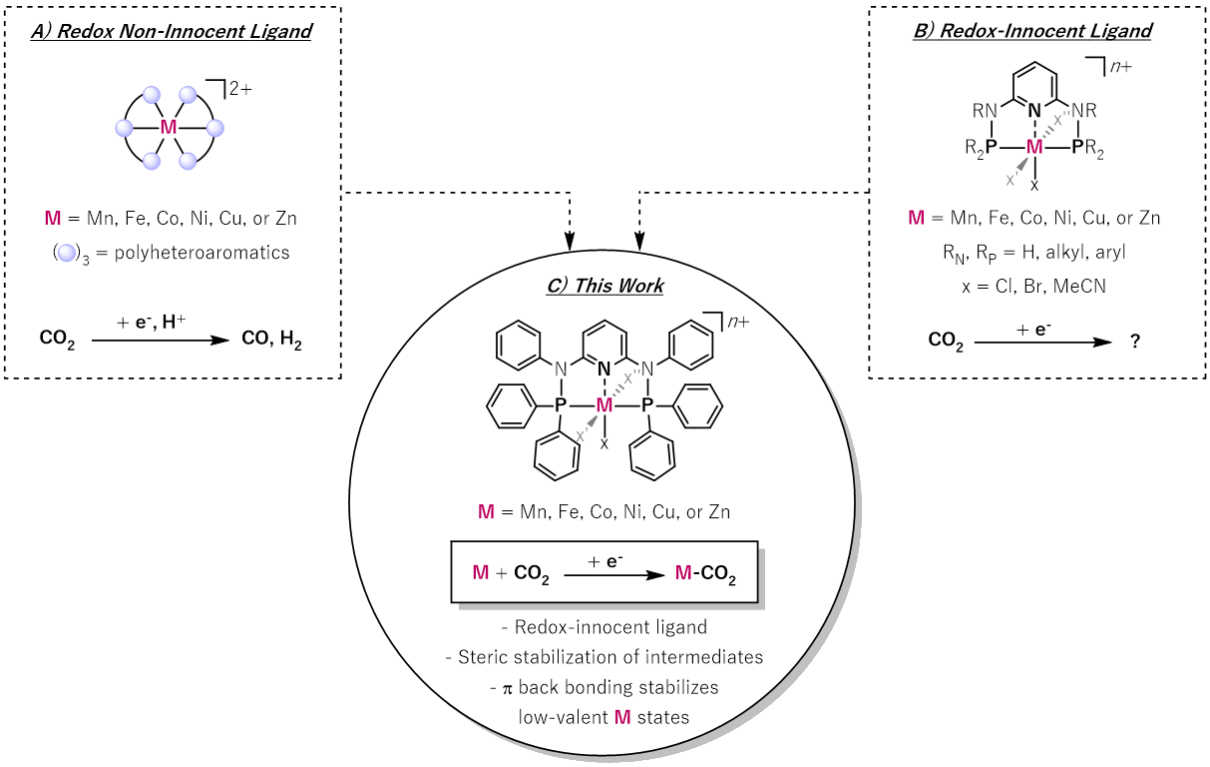

Figure 2.1. (A) Studies investigating 3d metal series in the same non-innocent ligand frameworks,[2] (B) complexes reported in literature coordinated by redox-innocent PN_3P ligand frameworks (n = charge of the complex),[1a-g] and (C) focus of this work.

In this work, the redox-innocent N^2,N^6-bis(diphenylphosphaneyl)-N^2,N^6-diphenylpyridine-2,6-diamine ligand **L**, which is surmised to stabilize reduced metal states by spatial (steric bulk) and electronic (π back bonding) effects, was singled out as the coordination framework. The following section presents the synthesis of the ligand system.

2.1 PNP Pincer Ligand

The synthetic pathway presented in Scheme 2.1 starts with a reported palladium-catalyzed BUCHWALD-HARTWIG coupling of 2,6-dibromopyridine (DBP) and aniline (An) to produce N^2,N^6-diphenylpyridine-2,6-diamine (**DPPDA**). The compound was isolated in 76% yield after purification by column chromatography on silica (see section 2.4.2.1), with the successful synthesis being confirmed by comparison of the ^{1}H and ^{13}C{^{1}H} NMR spectroscopic results with the data in the original report.[3]

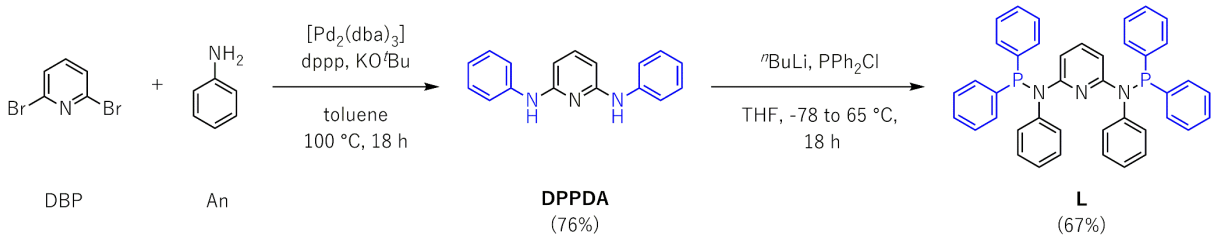

Scheme 2.1. Synthesis of **L**.

Subsequently, diphenylphosphino moieties were installed by low-temperature lithiation of the secondary amine groups in **DPPDA** at –78 °C in tetrahydrofuran (THF). Consecutively, the nitrogen-phosphorus bond was established by adding chlorodiphenylphosphine and the loss of lithium chloride during stirring at 65 °C for 18 h. NMR spectroscopy and high-resolution mass spectrometry (HRMS) confirmed the product formation. At the same time, elemental analysis (EA) validated the purity of ligand **L**, which was received in 67% yield after workup (synthetic details are given in section 2.4.2.2). The molecular structure of **L** as obtained from X-ray diffraction analysis of single crystals grown from a concentrated THF/pentane (3:1) solution at –35 °C is shown in Figure 2.2.

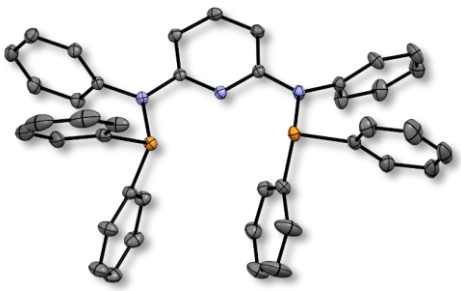

Figure 2.2. Molecular structure of **L** (color code: grey = C, blue = N, orange = P). Thermal ellipsoids are shown at a 50% probability level. H-atoms and co-crystallized solvent molecules were omitted for clarity. Selected interatomic distances (Å) and bond angles (°): N_{Py}-C_{Py} = 1.3384(16) and 1.3369(16), C_{Py}-N_{Ph} = 1.3988(16) and 1.3973(16), P-N = 1.7540(12) and 1.7430(11), P-P = 4.226, N_{Py}-C_{Py}-N_{Ph} = 115.88(11) and 114.17(11), P-N_{Ph}-C_{Py} = 119.53(9) and 115.72(8).

Even before the coordination of a metal atom, the molecular structure of the ligand exhibits the typical pincer shape, with the five atoms forming the PN_3P pincer belt nearly co-planar (PNCN torsion angles at 8.0° and −15.4°). This planarity might result from the steric hindrance of the rotation around the C-N bond linking the pyridine core and the bulky aniline moiety or from the conjugation of the lone pairs of the aniline nitrogens with the heterocycle, inferring in-plane triangular geometry at these nitrogen atoms. Notably, the *pinching* character of **L** is marked by a relatively short P-P distance ($d_{P\text{-}P}$ = 4.226 Å), likely in virtue of the steric constraint imposed at the aniline nitrogen atoms making C-N-P angles narrow (119.5°, 115.7°).

The ^{1}H NMR spectrum of **L** reflects the aromatic nature of the compound (as does the $^{13}C\{^{1}H\}$ spectrum, Figure A.1) by exhibiting peaks in the range of 5.80–7.23 ppm (see Figure 2.3). Although most aromatic signals overlap and form multiplets, the two protons in the *meta* position of the pyridine ring (PyH_m) give a characteristic doublet at 5.81 ppm with a coupling constant of J = 8.0 Hz. Only one singlet is visible in the $^{31}P\{^{1}H\}$ NMR spectrum (52.8 ppm, Figure A.2), which confirms the identical chemical environment of the two phosphorus nuclei in the structure.

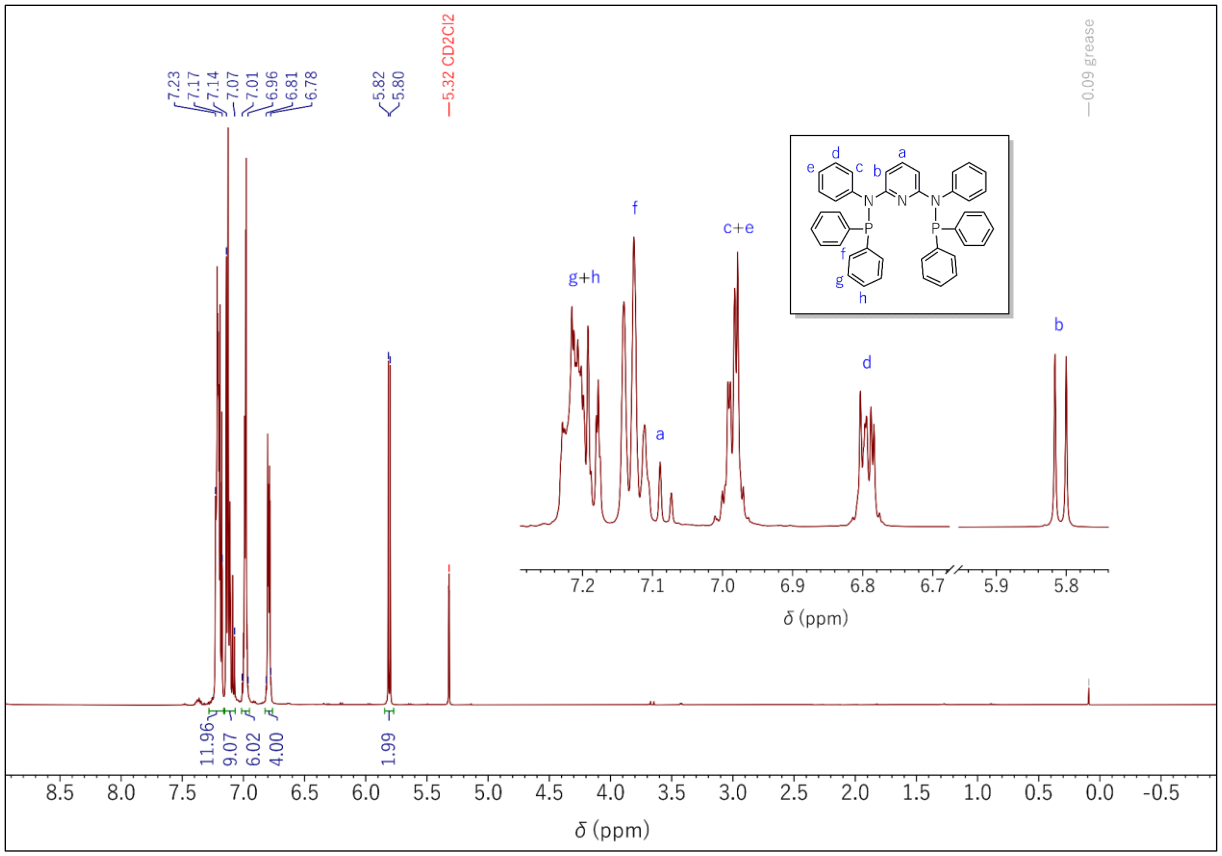

Figure 2.3. ^{1}H NMR spectrum of **L** in CD_2Cl_2 at 500 MHz and 296 K (inset: aromatic region and peak assignments).

2.2 3d Transition Metal Complexes

3d transition metal pincer complexes were obtained by metalation of **L** with the respective metal precursor in yields ranging from 52% to 96% under the conditions summarized in Table 2.1. Further synthetic details are indicated in the experimental section 2.4.

Table 2.1. Reaction conditions for the synthesis of 3d transition metal complexes in this work (reaction time = 2 h for [**ML**(MeCN)$_m$](BF$_4$)$_2$ complexes, otherwise 16 h).

Complex[a]	**Precursor**	**Solvent**	***T*** **(°C)**	***Y*** **(%)**
[Mn**L**(CO)$_2$Br]	[Mn(CO)$_5$Br]	toluene	110	74
[Fe**L**Cl$_2$]	FeCl$_2$	DCM	rt	95
[Fe**L**(MeCN)$_3$](OTf)$_2$	Fe(OTf)$_2$	MeCN	rt	87
[**ML**(MeCN)$_m$](BF$_4$)$_2$[b]	[**M**(MeCN)$_6$](BF$_4$)$_2$	MeCN	rt	88 (Fe), 96 (Co), 94 (Ni)
[Co**L**Cl$_2$]	CoCl$_2$	THF	rt	90
[Ni**L**Cl$_2$]	(dme)NiCl$_2$	DCM	rt	88
[Cu**L**Cl]	CuCl	THF	rt	65
[Cu**L**I]	CuI	THF	65	52
[Zn**L**Cl$_2$]	ZnCl$_2$	THF	rt	85
[Zn**L**(OTf)$_2$]	Zn(OTf)$_2$	MeCN	80	95

[a] Co-crystallized solvents are regarded in the experimental section. [b] **M** = Fe, Co, or Ni; *m* = 1 (Ni), 2 (Co), or 3 (Fe).

A schematic structure of the resulting $\mathbf{M}_{\mathbf{x}}^{\mathbf{z}}$ complexes [where *z* = oxidation state, and x = inner-sphere coordinating unit(s) regardless of stoichiometry], the simplified metal orbitals, as well as the abbreviation and nomenclature system applied to the complexes in this work, are summarized in Figure 2.4.

$\mathbf{M}_{\mathbf{Cl}}^{\mathbf{II}}$ complexes bearing metal centers in their +II oxidation state and bis-chloride coordination were targeted preferentially to ensure a systematic comparison. These structures were successfully obtained for Fe ($\mathbf{Fe}_{\mathbf{Cl}}^{\mathbf{II}}$), Co ($\mathbf{Co}_{\mathbf{Cl}}^{\mathbf{II}}$), Ni ($\mathbf{Ni}_{\mathbf{Cl}}^{\mathbf{II}}$), and Zn ($\mathbf{Zn}_{\mathbf{Cl}}^{\mathbf{II}}$) but not for Mn and Cu (*vide infra*). In these cases, the complexes $\mathbf{Mn}_{\mathbf{CO,Br}}^{\mathbf{I}}$ and $\mathbf{Cu}_{\mathbf{Cl}}^{\mathbf{I}}$ were synthesized from the respective **M**(I) precursors [Mn(CO)$_5$Br] and CuCl. Along with these complexes, variations in terms of electronegativity and coordinating ability of the anions were made by preparing $\mathbf{Cu}_{\mathbf{I}}^{\mathbf{I}}$, and $\mathbf{Zn}_{\mathbf{OTf}}^{\mathbf{II}}$.

Lastly, acetonitrile complexes of Fe ($\mathbf{Fe}_{\mathbf{s}}^{\mathbf{II}}$), Co ($\mathbf{Co}_{\mathbf{s}}^{\mathbf{II}}$), and Ni ($\mathbf{Ni}_{\mathbf{s}}^{\mathbf{II}}$) were synthesized to prevent perturbations in electroanalysis/-catalysis arising from the exchange of chloride ligands with the electrochemical solvent MeCN.

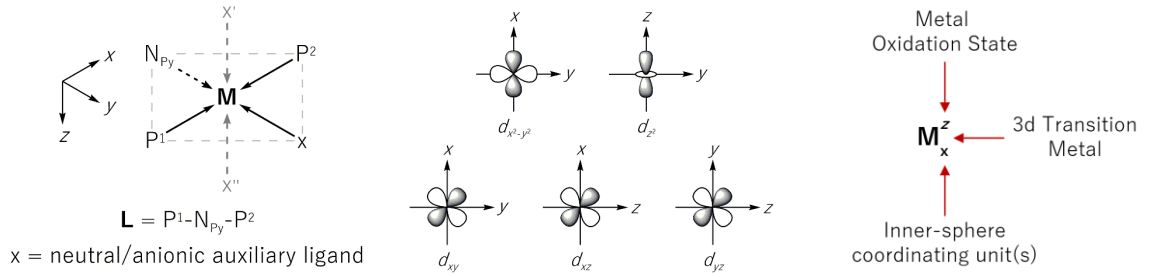

D) Nomenclature

$\mathbf{Mn^{I}_{CO,Br}}$:	[Mn**L**$(CO)_2$Br]	$\mathbf{Co^{II}_{Cl}}$:	[Co**L**Cl_2]	$\mathbf{Cu^{I}_{Cl}}$:	[Cu**L**Cl]
$\mathbf{Fe^{II}_{Cl}}$:	[Fe**L**Cl_2]	$\mathbf{Co^{II}_{s}}$:	[Co**L**$(MeCN)_2$]$(BF_4)_2$	$\mathbf{Cu^{I}_{I}}$:	[Cu**L**I]
$\mathbf{Fe^{II}_{s}}$:	[Fe**L**$(MeCN)_3$]$(BF_4)_2$	$\mathbf{Ni^{II}_{Cl}}$:	[Ni**L**Cl_2]	$\mathbf{Zn^{II}_{Cl}}$:	[Zn**L**Cl_2]
$\mathbf{Fe^{II}_{s}}$**-OTf:**	[Fe**L**$(MeCN)_3$]$(OTf)_2$	$\mathbf{Ni^{II}_{s}}$:	[Ni**L**$(MeCN)$]$(BF_4)_2$	$\mathbf{Zn^{II}_{OTf}}$:	[Zn**L**$(OTf)_2$]

Figure 2.4. (A) General structure, (B) metal orbital description, (C) abbreviation system, and (D) nomenclature of 3d transition metal complexes in this work.

Selected NMR spectroscopic data (Table 2.2), as well as characteristic features of the structures, calculated structural parameters, and coordination geometries (Table 2.3), will be discussed for each species individually in the following sections.

2.2.1 Halide & Triflate Complexes

2.2.1.1 [Mn**L**$(CO)_2$Br]

In the case of manganese, neither metalation with $MnCl_2$ at room temperature in THF as reported for related pyridine-based PNP pincers (R_N = H, R_P = ^{i}Pr)[1f] nor variations on conditions (solvents, temperatures, precursors) succeeded with **L**. The only reported [Mn$(PN_3P)Cl_2$] structure within a pyridine-based pincer framework displays an almost ideal square-based pyramidal (SBP) geometry (τ_5 = 0.04) with two phosphorous in *trans* position to the basal plane and relatively distant from Mn ($d_{Mn\text{-}P}$ = 2.574 and 2.590 Å, $d_{P\text{-}P}$ = 4.886 Å), in a high-spin, five unpaired electron configuration ($\mu_{eff} \approx 6$).[1f] Potentially, **L** does not allow sufficient elongation between the two phosphorous sites, which would likely be required in a putative [Mn**L**Cl_2] complex. The electron-withdrawing character of the phenyl substituent at the phosphines may also disfavor the coordination of a Mn(II) fragment since coordination of lower-valent [$Mn^{I}(CO)_5Br$] effectively yields the Mn(I) complex $\mathbf{Mn^{I}_{CO,Br}}$. This 18-electron species crystallizes in a distorted octahedral (O_h) coordination environment (Figure 2.5), as commonly encountered for related pincer Mn(I) carbonyl bromide complexes due to the energetically favorable occupation of the low-energy t_{2g} orbitals (Figure 2.5, right).[4]

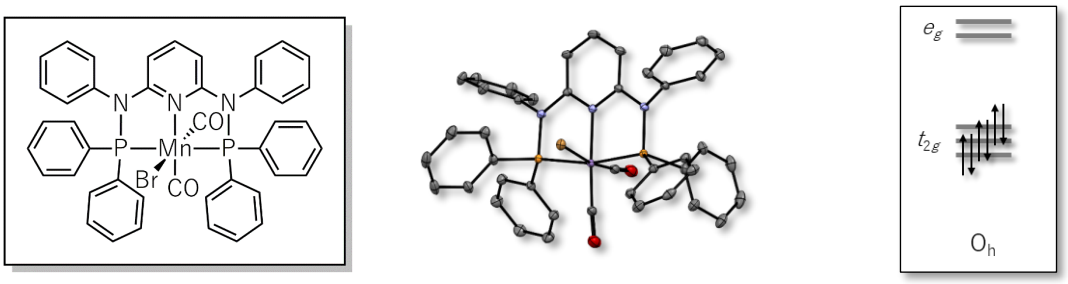

$[MnL(CO)_2Br]$ ($\mathbf{Mn}^{I}_{CO,Br}$)

Figure 2.5. Left/center: Molecular structure of *cis*-$\mathbf{Mn}^{I}_{CO,Br}$. Thermal ellipsoids are shown at a 50% probability level. H-atoms and co-crystallized solvent molecules were omitted for clarity. Right: Schematic d-block orbital diagram of a d^6 low-spin $\mathbf{M}L_6$ complex (e.g., $\mathbf{Mn}^{I}_{CO,Br}$) of octahedral geometry. Adapted with permission from ref. [5].

Single-crystal XRD analysis revealed a *cis-trans*-mixture of the CO ligands in a 95:5 ratio. The diamagnetic d^6 low-spin (ls) complex $\mathbf{Mn}^{I}_{CO,Br}$ exhibits distinguishable but overlapping sets of ^{1}H NMR signals for the chemically inequivalent aromatic protons of the R_N and R_P phenyl moieties positioned *syn* or *anti* of Br in the predominant *cis*-CO configuration (Figure 2.6).

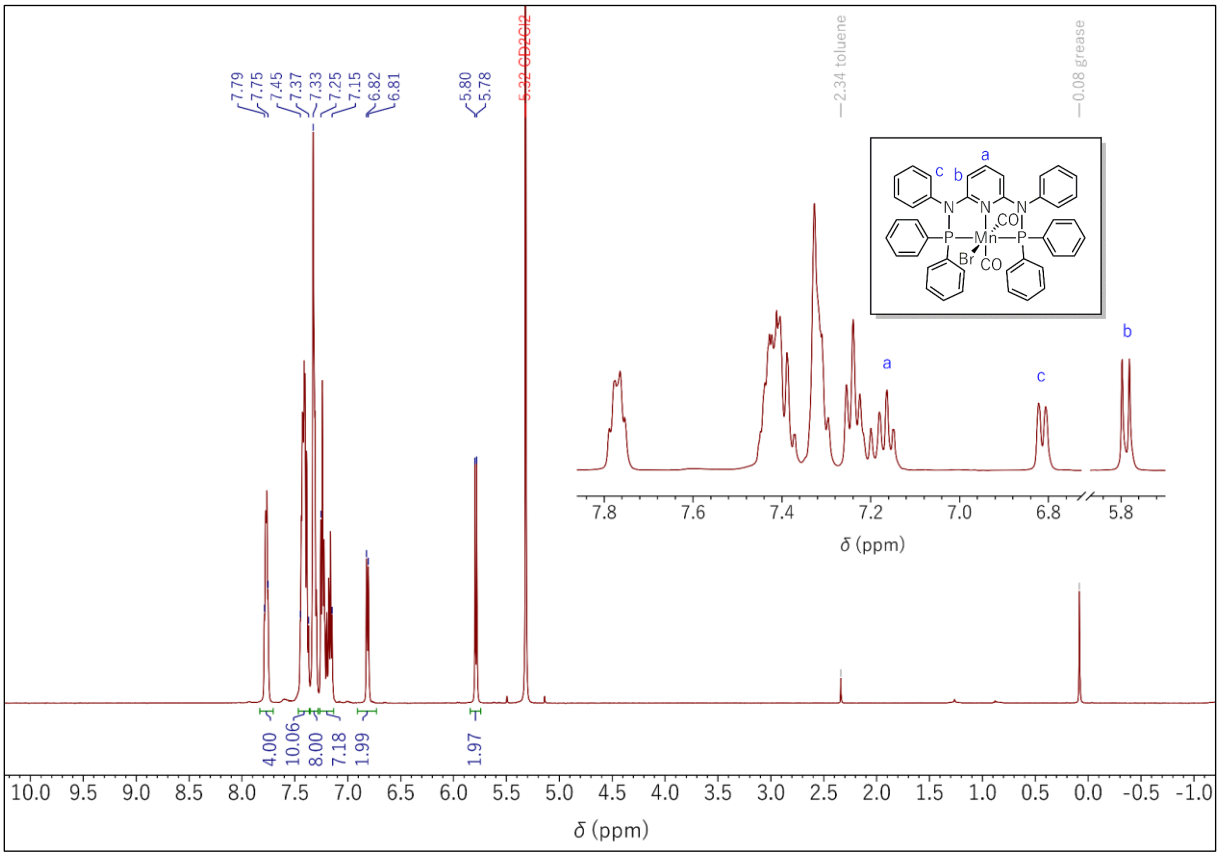

Figure 2.6. ^{1}H NMR spectrum of $\mathbf{Mn}^{I}_{CO,Br}$ in CD_2Cl_2 at 500 MHz and 296 K (inset: aromatic region and peak assignments).

While chemical inequivalence is also reflected by the increased number of peaks in the $^{13}C\{^1H\}$ NMR spectrum of the compound (Figure A.5) compared to a structure of higher symmetry, a singlet at 138.9 ppm in the $^{31}P\{^1H\}$ NMR spectrum indicates the same chemical environment around the phosphorous atoms (Figure A.6).

2.2.1.2 [Fe**L**Cl$_2$]

$\mathbf{Fe}^{\mathbf{II}}_{\mathbf{Cl}}$ crystallizes in a strongly distorted square-based pyramidal structure (Figure 2.7), as reflected by a τ_5 value of 0.38. The PNP coordination sites of **L** exhibit relatively extended bond distances of 2.327 Å for Fe-N as well as 2.429 and 2.426 Å for both Fe-P bonds. Although commonly encountered for less sterically hindered PN_3P-coordinated compounds (R_N = H),[1b] the spatial demand of the phenylamine group in **L** seems to prevent the formation of bis-PN_3P coordinated species.

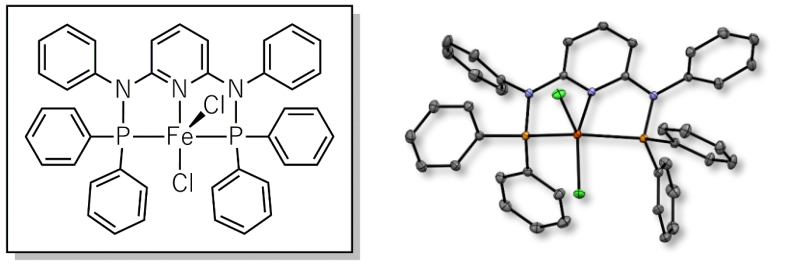

[Fe**L**Cl$_2$] ($\mathbf{Fe}^{\mathbf{II}}_{\mathbf{Cl}}$)

Figure 2.7. Molecular structure of $\mathbf{Fe}^{\mathbf{II}}_{\mathbf{Cl}}$. Thermal ellipsoids are shown at a 50% probability level. H-atoms and co-crystallized solvent molecules were omitted for clarity.

The zero-field ^{57}Fe-MÖSSBAUER spectrum of $\mathbf{Fe}^{\mathbf{II}}_{\mathbf{Cl}}$ recorded with a powder sample at 80 K showed a quadrupole doublet with high isomer shift δ = 0.80 mm·s^{-1} and large quadrupole splitting ΔE_Q of 3.33 mm·s^{-1} (Figure 2.8). The values are typical of high-spin Fe(II) with S = 2.[6]

Accordingly, the compound was EPR-silent in THF solution at X-band frequencies [because the zero-field splitting of the quintet state exceeds the microwave quantum energy, as often encountered for the 3d^6 configuration of Fe(II)].[7] Moreover, the effective magnetic moment μ_{eff} of solid $\mathbf{Fe}^{\mathbf{II}}_{\mathbf{Cl}}$ was determined at 4.9 μ_B at 270 K (Figure A.10), agreeing with the spin-only value of 4.90 μ_B expected for S = 2.[8] The axial zero-field splitting parameter D = 4 cm^{-1} obtained from the temperature variation of the magnetic susceptibility $X{\cdot}T$ vs. temperature T is in the usual range for Fe(II) with S = 2.

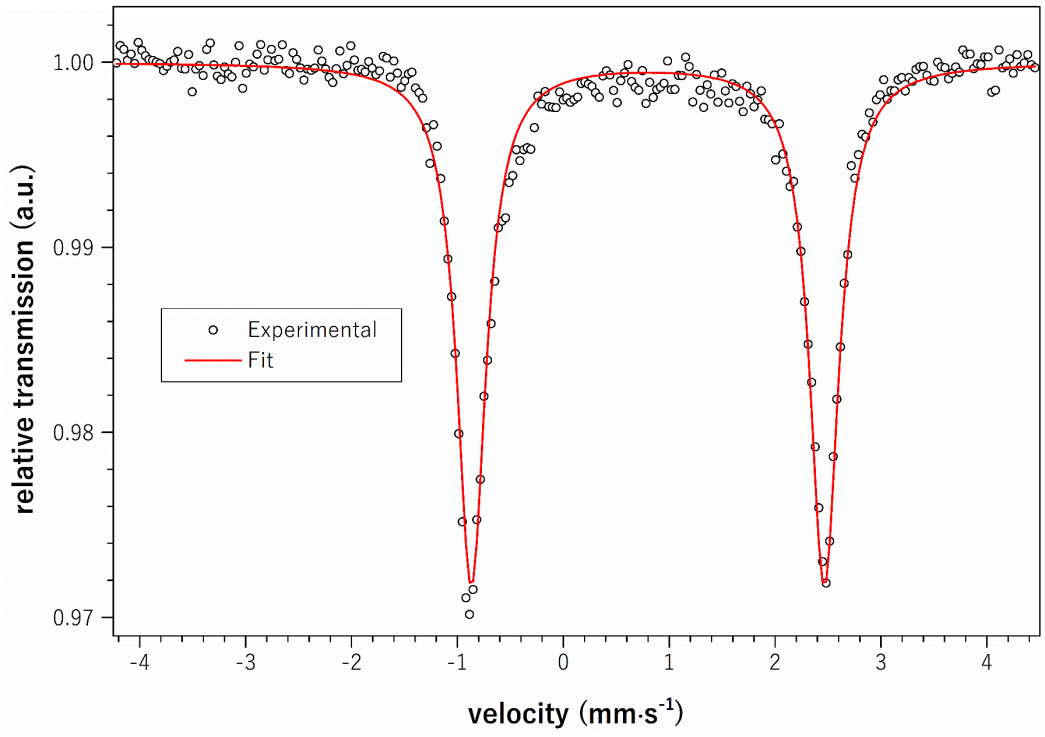

Figure 2.8. Zero-field ^{57}Fe-MÖSSBAUER spectrum of solid $\mathbf{Fe}^{\mathbf{II}}_{\mathbf{Cl}}$ recorded at 80 K. Red: LORENTZIAN doublet fit with isomer shift δ = 0.80 mm·s^{-1}, quadrupole splitting ΔE_Q = 3.33 mm·s^{-1}, and line width (full width at half maximum) Γ = 0.33 mm·s^{-1} at 100% relative intensity.

Despite the distribution of the contact-shifted signals of $\mathbf{Fe}^{\mathbf{II}}_{\mathbf{Cl}}$ between 57.5 ppm and –11.8 ppm in ^{1}H NMR analysis in CD_2Cl_2, diagnostic of a paramagnetic Fe(II) center, the assignment of these peaks is possible by integration (Figure 2.9).

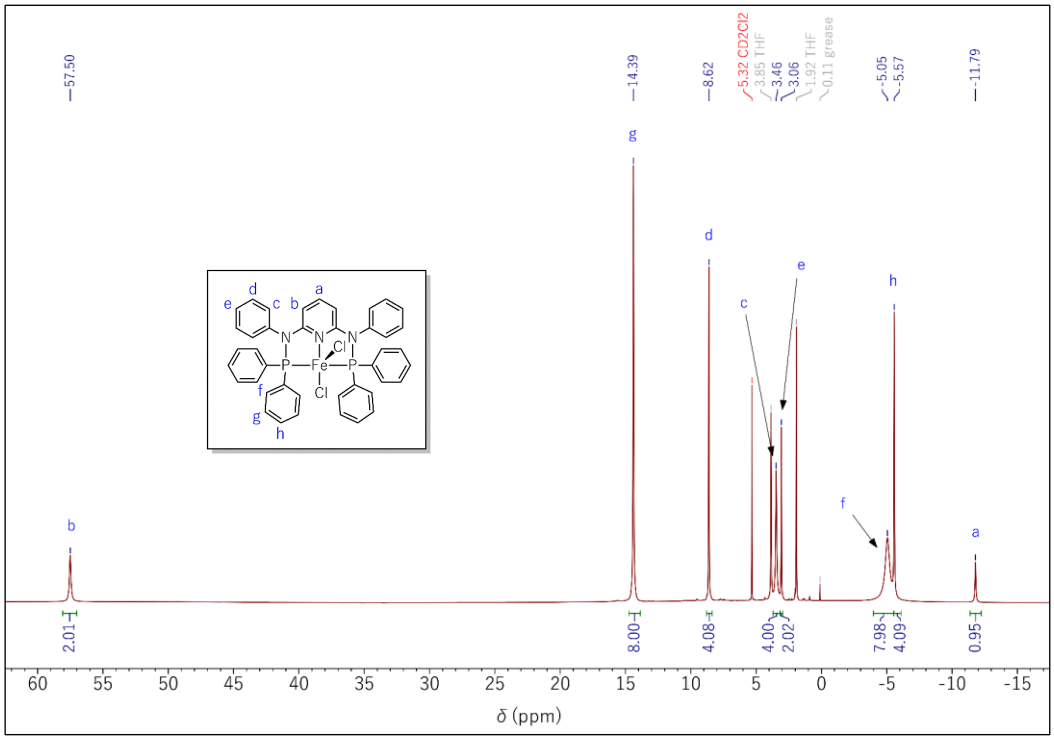

Figure 2.9. ^{1}H NMR spectrum of $\mathbf{Fe}^{\mathbf{II}}_{\mathbf{Cl}}$ in CD_2Cl_2 at 500 MHz and 296 K with peak assignments.

In the 3d^6 high-spin (hs) electronic configuration of Fe(II) in $\mathbf{Fe^{II}_{Cl}}$, the $d_{x^2-y^2}$ HOMO is expected to be stabilized by the distortion of the SBP structure to higher angles between the apical (ap) ligand and the basal plane θ_{ap} (up to 117 °, Figure 2.10A).[5] Similar distorted SBP geometries were observed for a series of related PN_3P-coordinated iron bis-chloride complexes, for which extended Fe-N and Fe-P distances were attributed to a high-spin state.[1c]

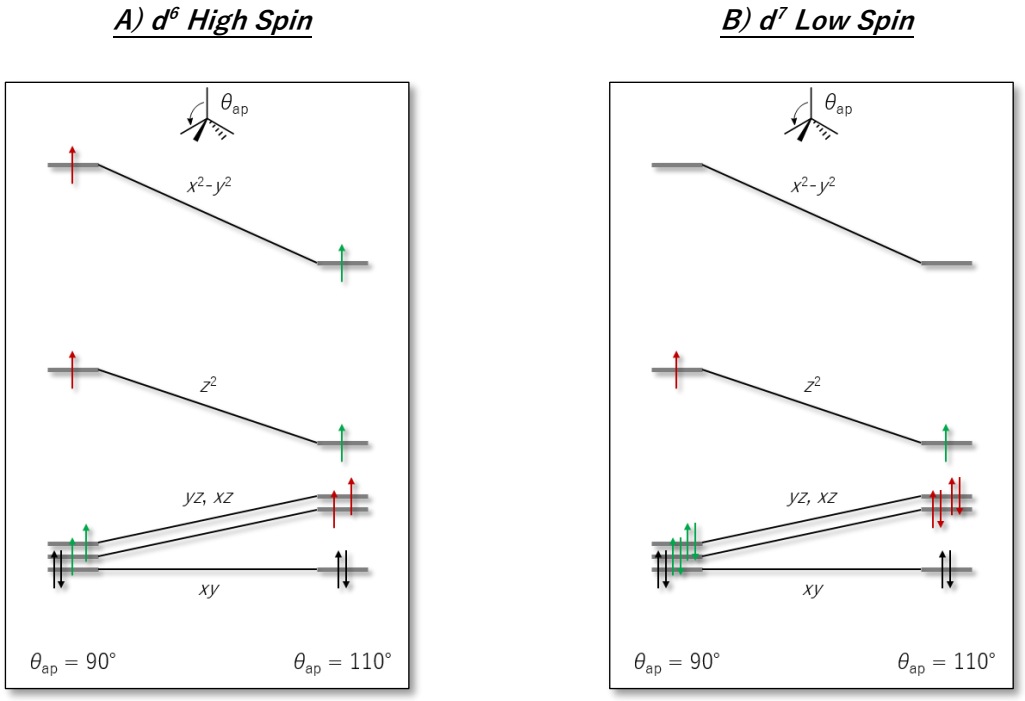

Figure 2.10. Schematic d-block orbital diagrams of (A) a d^6 high-spin $\mathbf{ML_5}$ complex (e.g., $\mathbf{Fe^{II}_{Cl}}$) and (B) a d^7 low-spin $\mathbf{ML_5}$ complex (e.g., $\mathbf{Co^{II}_{Cl}}$) of SBP geometry with θ_{ap} = 90° and 110°. Adapted with permission from ref. [5]. Electrons of lower energy compared to those in the same orbital are marked in green, those of higher energy in red.

2.2.1.3 [Co**L**Cl$_2$]

$\mathbf{Co^{II}_{Cl}}$ crystallizes in an almost ideal square-based pyramidal structure (Figure 2.7) with a τ_5 = 0.04, similar to the SBP structure reported by RÖSLER et al. with R_N = H (τ_5 = 0.01).[1e]

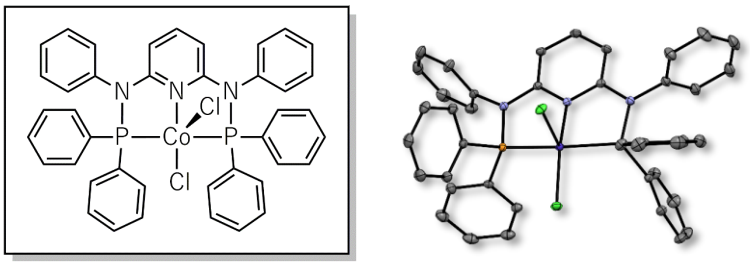

[Co**L**Cl$_2$] ($\mathbf{Co^{II}_{Cl}}$)

Figure 2.11. Molecular structure of $\mathbf{Co^{II}_{Cl}}$. Thermal ellipsoids are shown at a 50% probability level. H-atoms and co-crystallized solvent molecules were omitted for clarity.

The Co complex in this work displays a bond length of 239 pm between Co and the apical chloride atom (241 pm for the example by RÖSLER et al.[1e]), which suggests that this ligand is weakly bound. However, crystals prepared from the strongly coordinating MeCN solvent (Figure A.60) neither showed the formation of the outer-sphere chloride complex nor substitution of the ligand by a solvent molecule, but only a fractional elongation of the Co-Cl_{ap} bond to 242 pm.

$\mathbf{Co^{II}_{Cl}}$ exhibits heavily broadened ^{1}H NMR signals with chemical shifts between 5 ppm and 12 ppm (Figure 2.12) in accordance with a paramagnetic d^7 electron configuration. Although integration of the peaks sums to the expected 33 protons, the paramagnetic character of the substance prohibited further NMR spectroscopic analysis on other nuclei.

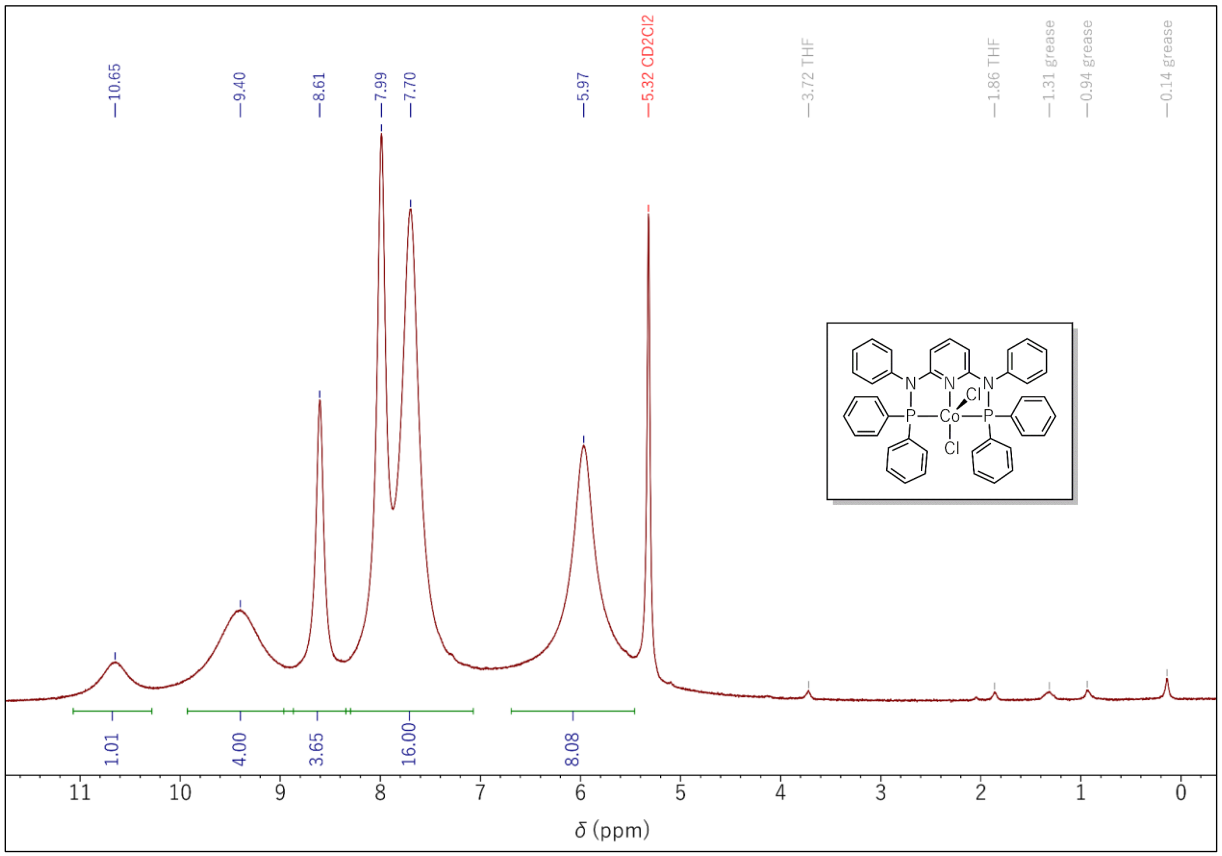

Figure 2.12. ^{1}H NMR spectrum of $\mathbf{Co^{II}_{Cl}}$ in CD_2Cl_2 at 400 MHz and 296 K.

Solid $\mathbf{Co^{II}_{Cl}}$ gave an effective magnetic moment of 1.9 μ_B at 270 K (Figure A.13), consistent with the spin-only value for S = ½ (1.73 μ_B) and in line with related complexes in literature (an effective magnetic moment of 2.3 μ_B was reported for a complex with R_N = H).[1e] The corresponding low-spin $3d^7$ configuration of $\mathbf{Co^{II}_{Cl}}$ was further corroborated by the X-band EPR spectrum of the compound in MeCN solution at 10 K, showing distinct anisotropic g splitting and ^{59}Co hyperfine splitting (Figure 2.13).

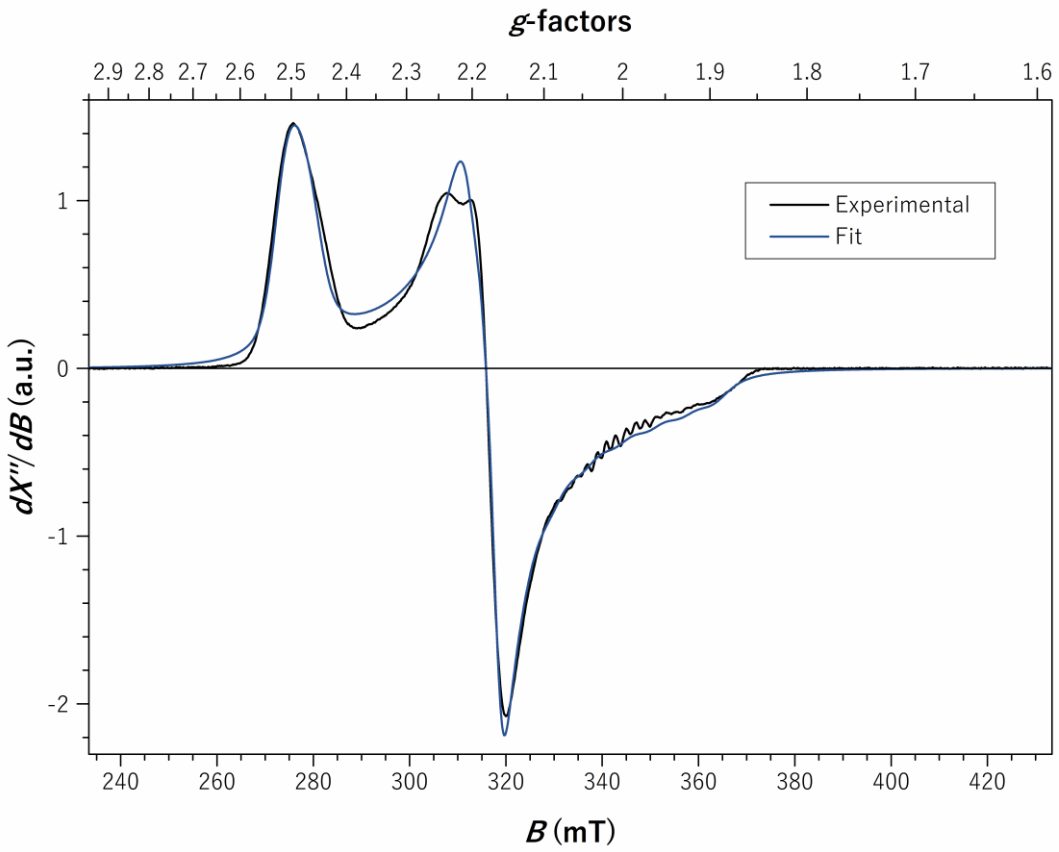

Figure 2.13. X-band EPR spectrum of ca. 1 mM $\mathbf{Co}^{\mathbf{II}}_{\mathbf{Cl}}$ in 2-methyltetrahydrofuran recorded at 10 K; microwave frequency 9.63715 GHz, power 0.2 mW, modulation 0.8 mT/100 kHz. Blue: simulation with $g_{z,y,x}$ = (2.485, 2.165, 2.030) and first-order ^{59}Co hyperfine splitting with $A_{x,y,z}$ = (63.44, 2.36, 11.89) 10^{-4} cm^{-1}.

The nearly ideal SBP geometry observed for $\mathbf{Co}^{\mathbf{II}}_{\mathbf{Cl}}$ is likely favored over distortions to higher values of τ_5 since the corresponding structures would stabilize the singly occupied d_{z^2} orbital but destabilize the fully occupied d_{yz} and d_{xz} orbitals (Figure 2.10B).[5]

2.2.1.4 [Ni**L**Cl$_2$]

$\mathbf{Ni}^{\mathbf{II}}_{\mathbf{Cl}}$ displays an SBP structure (Figure 2.14) with a distortion intermediate to $\mathbf{Fe}^{\mathbf{II}}_{\mathbf{Cl}}$ and $\mathbf{Co}^{\mathbf{II}}_{\mathbf{Cl}}$.

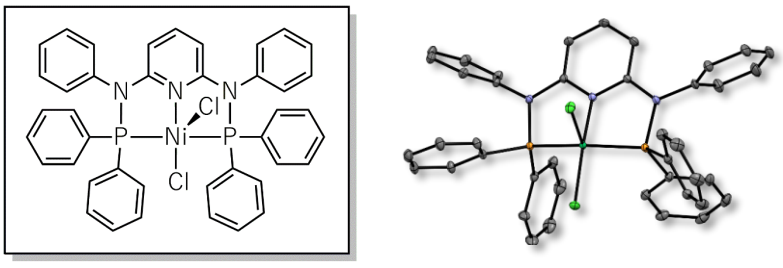

[Ni**L**Cl$_2$] ($\mathbf{Ni}^{\mathbf{II}}_{\mathbf{Cl}}$)

Figure 2.14. Molecular structure of $\mathbf{Ni}^{\mathbf{II}}_{\mathbf{Cl}}$. Thermal ellipsoids are shown at a 50% probability level. H-atoms and co-crystallized solvent molecules were omitted for clarity.

The electronic stabilization of the d_{z^2} HOMO procured by a θ_{ap} of up to 110°[5] is particularly favorable for the 18 electron d^8 configuration of $\mathbf{Ni}^{\mathbf{II}}_{\mathbf{Cl}}$ (in analogy to Figure 2.10). The apical chloride ligand is weakly bound to the metal, manifesting in a bond length of 255 pm. Although the formation of a cationic, almost ideally square planar (SP) d^8 [Ni(PN$_3$P)Br]Br complex (with R_N = H) was observed in methanol,[1a] $\mathbf{Ni}^{\mathbf{II}}_{\mathbf{Cl}}$ crystals grown from MeCN (Figure A.61) maintain the apical chloride ligand coordinated with a marginally elongated bond distance.

NMR spectroscopy revealed a single ^{31}P peak at 85.0 ppm (Figure A.16) and well-distinguished sets of ^{1}H signals (Figure A.14), most indicative of the pyridinic protons in *meta* position that exhibit a characteristic doublet at 5.73 ppm (J = 8.2 Hz, Table 2.2).

2.2.1.5 [Cu**L**Cl] & [Cu**L**I]

For copper, the reaction of **L** with $CuCl_2$ produced a diamagnetic complex, as inferred from NMR analysis, whereas a putative monomeric [Cu**L**Cl$_2$] complex is expected to be paramagnetic (d^9). Previous literature reports suggest the reduction of Cu(II) to Cu(I) upon coordination to **L** and oxidation of the ligand (additional diamagnetic signals are visible in the ^{1}H and ^{31}P{^{1}H} NMR spectra, see Figure A.24 & Figure A.25).[9]

Thus, the successfully synthesized complex $\mathbf{Cu}^{\mathbf{I}}_{\mathbf{Cl}}$ starting from CuCl was chosen as a surrogate. The identical NMR spectra of the products from $CuCl_2$ and CuCl (see Figure A.19 to Figure A.25) supported this approach. Similarly, $\mathbf{Cu}^{\mathbf{I}}_{\mathbf{I}}$ was synthesized from CuI to introduce the less electronegative iodide ligand. The tetracoordinate d^{10} complexes displayed in Figure 2.15 both exhibit a distorted tetrahedral (T_d) structure with τ_4 values of 0.78 (chloride) and 0.77 (iodide).

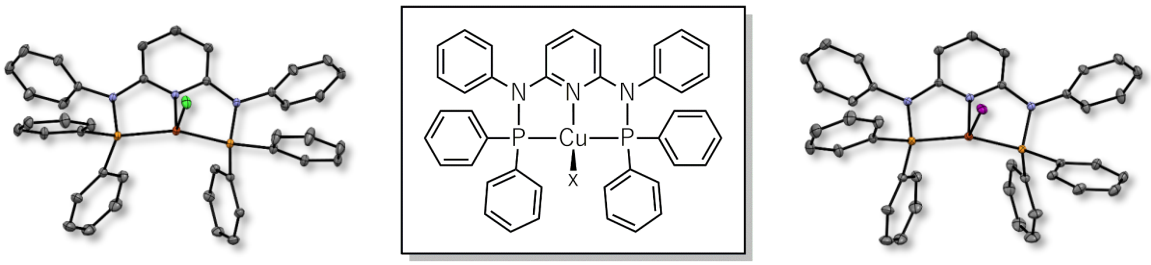

[Cu**L**Cl] ($\mathbf{Cu}^{\mathbf{I}}_{\mathbf{Cl}}$) [Cu**L**I] ($\mathbf{Cu}^{\mathbf{I}}_{\mathbf{I}}$)

Figure 2.15. Molecular structures of $\mathbf{Cu}^{\mathbf{I}}_{\mathbf{x}}$ with x = Cl (left) or I (right). Thermal ellipsoids are shown at a 50% probability level. H-atoms and co-crystallized solvent molecules were omitted for clarity.

Both structures are intermediates between the ideal tetrahedron (τ_4 = 1) and the butterfly/see-saw ($\tau_4 \approx 0.43$, Figure 2.16). The found coordination geometries comply with known bromide analogs (R_N = Me, τ_4 = 0.78) by RAO et al., who report their structure as trigonal pyramidal.[1d]

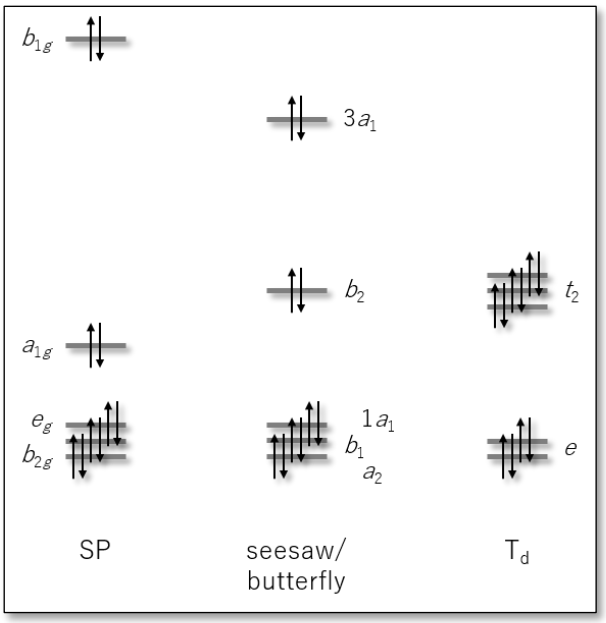

Figure 2.16. Schematic d-block orbital diagrams for d^{10} **M**L_4 complexes (e.g., $\mathbf{Cu}^{\mathbf{I}}_{\mathbf{x}}$ or $\mathbf{Zn}^{\mathbf{II}}_{\mathbf{Cl}}$) of different geometry. Adapted with permission from ref. [5].

NMR spectroscopic analyses (see Figure A.19 to Figure A.30) reflect a similar coordination structure with ^{31}P (39.9 ppm, resp. 40.0 ppm for $\mathbf{Cu}^{\mathbf{I}}_{\mathbf{Cl}}$, resp. $\mathbf{Cu}^{\mathbf{I}}_{\mathbf{I}}$) and ^{1}H peaks (e.g., 5.68 ppm, J = 8.0 Hz; resp. 5.67 ppm, J = 8.0 Hz for PyH_m in $\mathbf{Cu}^{\mathbf{I}}_{\mathbf{Cl}}$, resp. $\mathbf{Cu}^{\mathbf{I}}_{\mathbf{I}}$) only marginally deviating.

2.2.1.6 [Zn**L**Cl_2] & [Zn**L**$(OTf)_2$]

In contrast to the shared behavior of the earlier $\mathbf{M}^{\mathbf{II}}_{\mathbf{Cl}}$ complexes, the pyridine unit in $\mathbf{Zn}^{\mathbf{II}}_{\mathbf{Cl}}$ is not bound to the metal center, leaving the species in an almost ideal tetrahedral coordination geometry (τ_4 = 0.95; Figure 2.17, left).

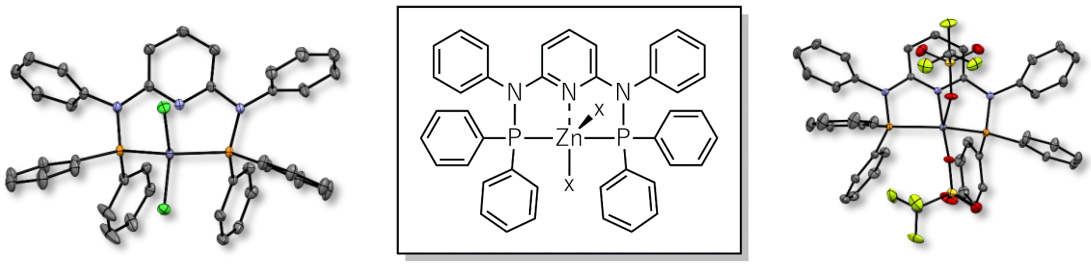

[Zn**L**Cl_2] ($\mathbf{Zn}^{\mathbf{II}}_{\mathbf{Cl}}$) [Zn**L**$(OTf)_2$] ($\mathbf{Zn}^{\mathbf{II}}_{\mathbf{OTf}}$)

Figure 2.17. Molecular structures of $\mathbf{Zn}^{\mathbf{II}}_{\mathbf{x}}$ with x = Cl (left) or OTf (right). Thermal ellipsoids are shown at a 50% probability level. H-atoms and co-crystallized solvent molecules were omitted for clarity.

The 18-electron valence of this d^{10} configuration at the Zn center likely favors tetra- over penta-coordinate structures. $\mathbf{Zn}^{\mathbf{II}}_{\mathbf{Cl}}$ preferentially adopts a tetrahedral structure over a square planar

one, possibly because the HOMOs in the former (t_2 orbitals) are significantly more stabilized than the HOMO in the latter (b_{1g} orbital, see Figure 2.16). Additionally, the structural constraints of the pincer ligand might disfavor the formation of the SP configuration. A bromide analog with R_N = Me also exhibits the tetrahedral structure.[1g]

By contrast, $\mathbf{Zn^{II}_{OTf}}$ remains pentacoordinate and forms a 20-valence electron (VE) complex of distorted trigonal bipyramidal (TBP) structure (Figure 2.17, right), as reflected in the τ_5 value of 0.82. 20-electron complexes are only accessible in very weak-field complexes, where the antibonding molecular orbital hosting two electrons is sufficiently low in energy, with TBP geometry stabilized compared to SBP (Figure 2.18).[5]

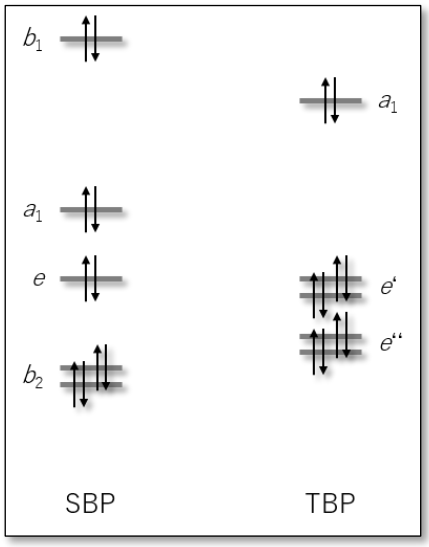

Figure 2.18. Schematic d-block orbital diagrams for d^{10} **M**L_5 complexes (e.g., $\mathbf{Zn^{II}_{OTf}}$) of different geometry. Adapted with permission from ref. [5].

$\mathbf{Zn^{II}_{OTf}}$ is the only literature example of a pyridine-based PNP pincer complex derived from the $Zn(OTf)_2$ precursor. Therefore, the closest relatable system is the terpyridine-coordinated Zn complex reported by BOCIAN et al., which crystallizes in a seesaw/butterfly structure (τ_5 = 0.47).[10] Here, the bond distance between Zn and the nitrogen atom of the pyridine core is significantly shorter than the Zn-N bond in $\mathbf{Zn^{II}_{OTf}}$ (204 pm vs. 233 pm), indicating the nitrogen is loosely coordinated in the latter system.

Distinctions in the molecular structures of $\mathbf{Zn^{II}_{Cl}}$ and $\mathbf{Zn^{II}_{OTf}}$ also displayed in the recorded NMR spectra (see Figure A.31 to Figure A.40), with a difference of 2.1 ppm for the ^{31}P nucleus (30.9 ppm, resp. 28.8 ppm for $\mathbf{Zn^{II}_{Cl}}$, resp. $\mathbf{Zn^{II}_{OTf}}$) and 0.09 ppm (5.85 ppm, J = 8.1 Hz; resp. 5.94 ppm, J = 8.2 Hz for $\mathbf{Zn^{II}_{Cl}}$, resp. $\mathbf{Zn^{II}_{OTf}}$) for the PyH_m protons.

2.2.1.7 Comparative Structural Assessment

The obtained geometric and electronic features of the $\mathbf{M}_{\mathbf{x}}^{\mathbf{z}}$ complexes, as described in the previous sections, shall now be correlated to the 3d metal center to identify the role of the metal core on these properties. First, the difference between the chemical shifts of the free vs. the coordinated ligand in $^{31}P\{^{1}H\}$ NMR spectroscopy, titled coordination chemical shift $\Delta\delta$, shall serve as metrics to describe the electron density of the metal center and is calculated according to eq. (2.1).[11]

$$\Delta\delta = \delta_P(\mathbf{M}_{\mathbf{x}}^{\mathbf{z}}) - \delta_P(\mathbf{L}) \qquad (2.1)$$

$\delta_P(\mathbf{M}_{\mathbf{x}}^{\mathbf{z}})$ abbreviates the $^{31}P\{^{1}H\}$ NMR chemical shift of the phosphine signal in an $\mathbf{M}_{\mathbf{x}}^{\mathbf{z}}$ complex while $\delta_P(\mathbf{L})$ represents the value for the free ligand **L**. δ_P and $\Delta\delta$ values of the halide complexes are summarized in Table 2.2.

Table 2.2. $^{31}P\{^{1}H\}$ NMR (δ_P) and coordination chemical shifts ($\Delta\delta$) as well as ^{1}H NMR chemical shifts of the pyridinic protons in *meta* position [$\delta_H(Py\mathit{H}_m)$; CD_2Cl_2, 500 MHz, 296 K] for diamagnetic halide complexes in this work.

	δ_P (ppm)	$\Delta\delta$ (ppm)	$\delta_H(Py\mathit{H}_m)$ (ppm)[a]
L	52.8	-	5.81 (8.0)
$\mathbf{Mn}_{\mathbf{CO,Br}}^{\mathbf{I}}$	138.9	86.1	5.79 (8.2)
$\mathbf{Ni}_{\mathbf{Cl}}^{\mathbf{II}}$	85.0	32.2	5.73 (8.2)
$\mathbf{Cu}_{\mathbf{Cl}}^{\mathbf{I}}$	39.9	–12.9	5.68 (8.0)
$\mathbf{Cu}_{\mathbf{I}}^{\mathbf{I}}$	40.0	–12.8	5.67 (8.0)
$\mathbf{Zn}_{\mathbf{Cl}}^{\mathbf{II}}$	30.9	–21.9	5.85 (8.1)
$\mathbf{Zn}_{\mathbf{OTf}}^{\mathbf{II}}$	28.8	–24.0	5.94 (8.2)

[a] Brackets: $^{3}J_{doublet}$ (Hz).

$\Delta\delta$ decreases when incrementing the electron count from early ($\mathbf{Mn}_{\mathbf{CO,Br}}^{\mathbf{I}}$) to late ($\mathbf{Zn}_{\mathbf{Cl/OTf}}^{\mathbf{II}}$) metals of the 3d row (Figure 2.19A). The observed trend is consistent with an increasing electronic density at the metal center within the same oxidation state when traversing from left to right in the 3d period. For the lowest 3d electron counts (Mn and Ni), the predominant σ-donation of the phosphine de-shields the coordinated phosphorous atom and produces positive $\Delta\delta$ values. In contrast, the highest electron counts (Cu and Zn) induce the phosphine's additional π-acceptor ability, resulting in negative $\Delta\delta$ values.

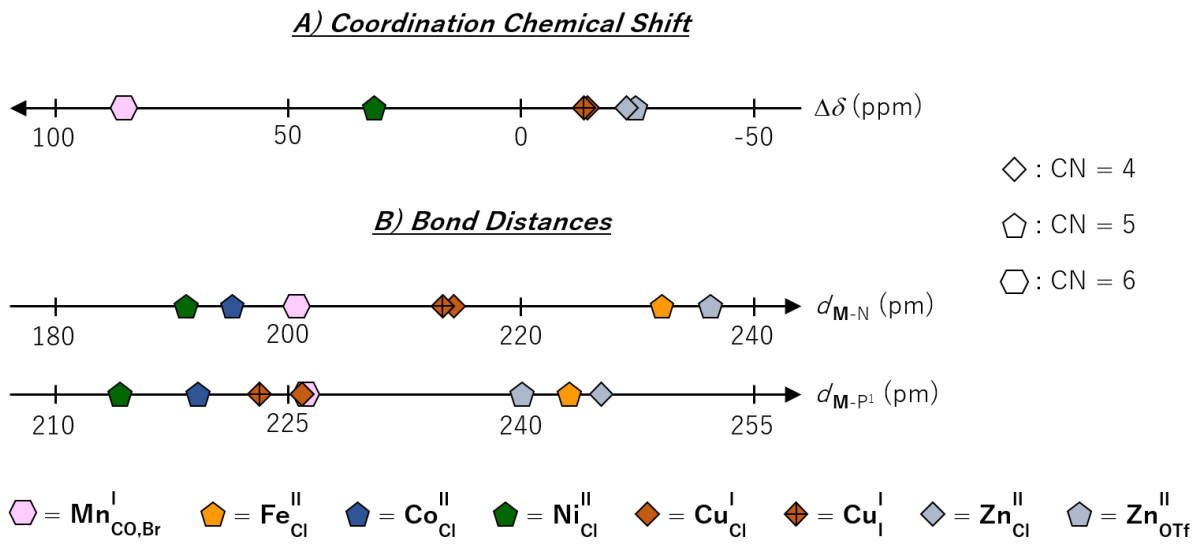

Figure 2.19. (A) $\Delta\delta$ derived from $^{31}P\{^{1}H\}$ NMR spectra in CD_2Cl_2 for diamagnetic halide complexes and (B) metal-ligand bond distances of halide complexes in this work.

Second, the ionic radii of the metal center and the coordinating atom[12], as well as the electronegativity differences between them[13], correlate to the bond distances and overall structure of the complexes. With the coordinating atoms kept identical in the bis-chloride series, variations in geometric properties are expected to be directly relatable to the metal center. The respective properties are summarized in Table 2.3.

Table 2.3. Selected interatomic distances (Å) and bond angles (°), as well as geometry indices τ and idealized coordination geometries for the halide and triflate complexes $\mathbf{M}^{z}_{x}$ in this work.

	M-N$_{Py}$	M-P^1	M-P^2	P^1-M-N$_{Py}$	P^1-M-P^2	τ_4	τ_5[14]	Idealized Geom.
$\mathbf{Mn}^{I}_{CO,Br}$	2.0391(13)	2.2623(5)	2.2273(5)	83.22(4)	166.305(18)	-	-	O_h
$\mathbf{Fe}^{II}_{Cl}$	2.3269(10)	2.4260(3)	2.4291(3)	73.77(2)	130.409(13)	-	0.38	SBP
$\mathbf{Co}^{II}_{Cl}$	1.9465(10)	2.1882(4)	2.1847(4)	84.90(3)	166.277(14)	-	0.04	SBP
$\mathbf{Ni}^{II}_{Cl}$	1.9084(11)	2.1407(4)	2.1574(4)	85.26(3)	155.509(15)	-	0.23	SBP
$\mathbf{Cu}^{I}_{Cl}$	2.1377(8)	2.2556(3)	2.2687(3)	80.89(2)	135.982(11)	0.78	-	T_d
$\mathbf{Cu}^{I}_{I}$	2.1283(7)	2.2299(2)	2.2589(2)	78.69(19)	133.215(9)	0.77	-	T_d
$\mathbf{Zn}^{II}_{Cl}$	2.7383(9)[a]	2.4489(3)	2.4182(3)	64.50(2)[a]	112.597(11)	0.95	-	T_d
$\mathbf{Zn}^{II}_{OTf}$	2.335(2)	2.3979(8)	2.3758(8)	72.38(6)	129.09(3)	-	0.82	TBP

[a] No bond between metal and nitrogen.

The bond distances between the coordination sites and the donor atoms (P and N) of the ligand scaffold in the $\mathbf{M}^{z}_{x}$ complexes are depicted in Figure 2.19B. The **M**-P and **M**-N bonds shorten

while incrementing the 3d row in the subgroup of $\mathbf{M}_{\mathbf{Cl}}^{\mathbf{II}}$ SBP complexes (**M** = Fe, Co, or Ni), as expected from decreasing metal ionic radii in the 3d block.[15] However, varying auxiliary ligands and coordination geometries overrule the trend for other complexes in the row.

2.2.2 Acetonitrile Complexes

The complexes of Fe, Co, and Ni bearing MeCN as an inner-sphere coordinating unit ($\mathbf{M}_{\mathbf{s}}^{\mathbf{II}}$, s = MeCN) are synthesized to counter the potential exchange of chloride ligands with the electrochemical solvent MeCN in the corresponding $\mathbf{M}_{\mathbf{Cl}}^{\mathbf{II}}$ series. They are scrutinized toward the influence of the metal center and the auxiliary ligands on structural and electronic properties in the following section.

The $\mathbf{M}_{\mathbf{s}}^{\mathbf{II}}$ complexes were prepared via room-temperature reaction of equimolar amounts of **L** and the respective $[\mathbf{M}(MeCN)_6](BF_4)_2$ precursor in DCM for two hours. After precipitative workup, the complexes could be isolated in excellent yields between 88 and 96% (detailed synthetic information in the experimental section). The aforementioned analytical methods confirmed their structure and purity. Selected interatomic distances and bond angles are summarized in Table A.18.

2.2.2.1 Iron-based Complexes

a) $[Fe\mathbf{L}(MeCN)_3]X_2$ (X = BF_4, OTf)

The molecular structure of $\mathbf{Fe}_{\mathbf{s}}^{\mathbf{II}}$ is a distorted octahedron in which **L** occupies the meridional position (Figure 2.20, left). The distortion is caused by almost identical P-Fe-N_{Py} bond angles of 82.31° and 82.28°, significantly deviating from the expected 90° in an ideal octahedral geometry.

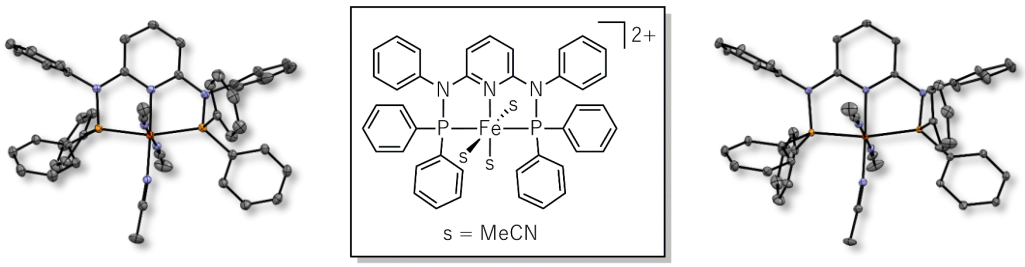

$[Fe\mathbf{L}(MeCN)_3](BF_4)_2$ ($\mathbf{Fe}_{\mathbf{s}}^{\mathbf{II}}$)

$[Fe\mathbf{L}(MeCN)_3](OTf)_2$ ($\mathbf{Fe}_{\mathbf{s}}^{\mathbf{II}}$**-OTf**)

Figure 2.20. Molecular structures of $\mathbf{Fe}_{\mathbf{s}}^{\mathbf{II}}$ (left) and $\mathbf{Fe}_{\mathbf{s}}^{\mathbf{II}}$**-OTf** (right). Thermal ellipsoids are shown at a 50% probability level. H-atoms, outer-sphere ligands, and co-crystallized solvent molecules were omitted for clarity.

Moreover, the moiety spanned by the pyridine core and the phenylamine groups of the ligand appears distorted compared to the P^1-Fe-N_{Py} plane, with torsion angles at 18.6° and 14.9°. Apart from **L**, the iron core is coordinated by three auxiliary MeCN ligands with Fe-N_{MeCN} distances of 193.4 pm for the equatorial as well as 192.6 pm and 191.5 pm for the axial positions. While the P^1-Fe-N_{MeCN} angles are close to the expected 90° for the axial ligands (91.23° and 89.86°), a more substantial deviation can be observed for the equatorial ligand (95.07°), as also reported for Fe(II) PN_3P tris-acetonitrile complexes with R_N = H and R_P = Ph.[1a]

^{1}H NMR analysis of $\mathbf{Fe_s^{II}}$ (Figure 2.21; further spectra in Figure A.41 to Figure A.44) reveals equatorial and axial MeCN signals (2.39 ppm and 1.69 ppm, integration 1:2) in CD_2Cl_2. Three strong field-splitting MeCN ligands and diamagnetism deduced from the NMR response indicate a d^6 low-spin configuration with three fully occupied t_{2g} orbitals and S = 0 (Figure 2.5, right).

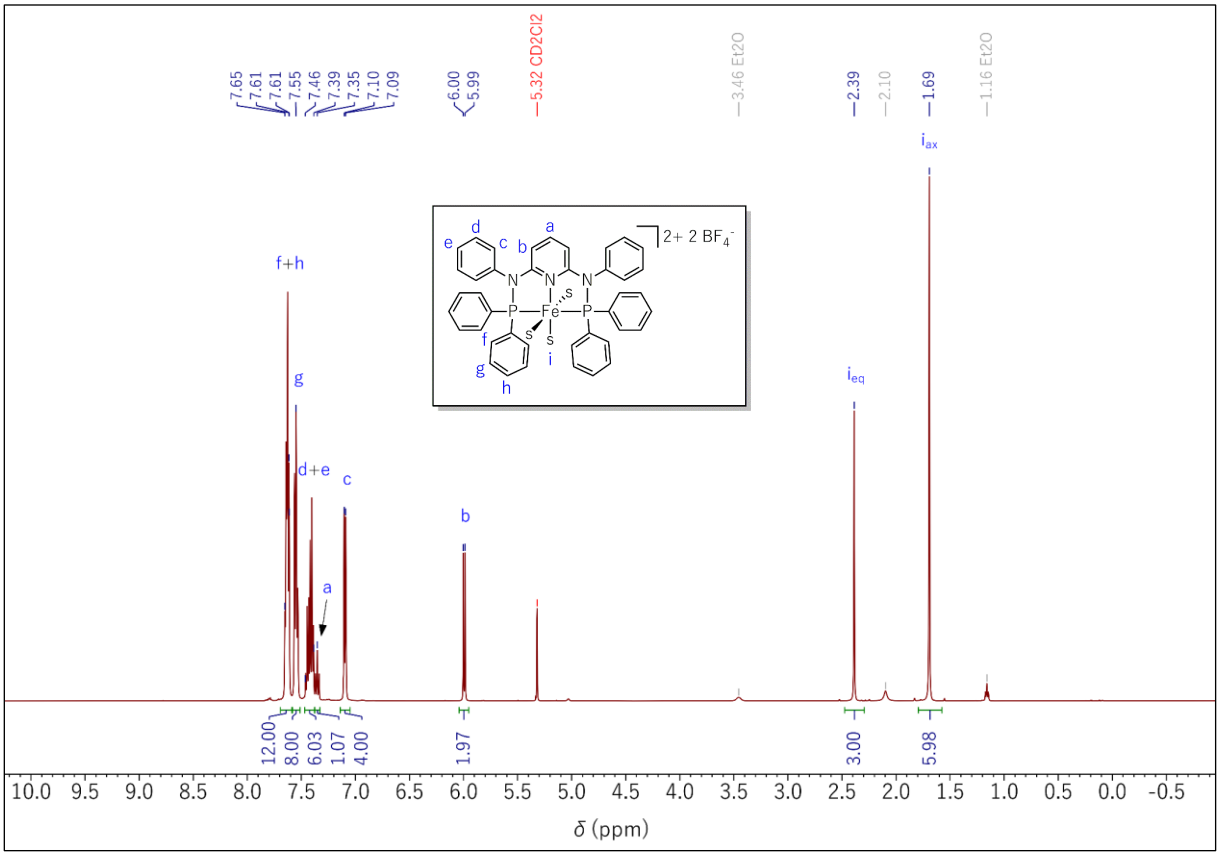

Figure 2.21. ^{1}H NMR spectrum of $\mathbf{Fe_s^{II}}$ in CD_2Cl_2 at 500 MHz and 296 K with peak assignments.

Besides $\mathbf{Fe_s^{II}}$, $\mathbf{Fe_s^{II}}$**-OTf** was synthesized by reaction of **L** with the $Fe(OTf)_2$ precursor in MeCN. The resulting complex exhibits a distorted octahedral geometry similar to that of $\mathbf{Fe_s^{II}}$ which comprises **L** in the meridional position of the inner coordination sphere and three acetonitrile ligands to complete the structure (Figure 2.20, right). The P^1-Fe-N bond angles are close to the expected 90° for the two axial solvent ligands (91.40° and 89.75°) but are significantly distorted for the equatorial acetonitrile (98.56°) as well.

The MÖSSBAUER spectrum of solid $\mathbf{Fe_s^{II}}$**-OTf** shows an isomer shift of $\delta = 0.34$ mm·s^{-1} and weak quadrupole splitting of 0.87 mm·s^{-1} (Figure A.45). These parameters readily exclude a high-spin configuration but confirm the diamagnetic low-spin d^6 configuration of $\mathbf{Fe_s^{II}}$**-OTf** with $S = 0$, further corroborated by the NMR response.

The NMR spectroscopic data of $\mathbf{Fe_s^{II}}$**-OTf** (Figure A.46 to Figure A.50) correspond to those of $\mathbf{Fe_s^{II}}$ with chemical shifts only marginally deviating due to a residual electronic effect of the counter anion. Furthermore, the coordination of MeCN was confirmed by the dissolution of $\mathbf{Fe_s^{II}}$**-OTf** in CD_3CN and subsequent NMR spectroscopic analysis, which showed that the corresponding signals had disappeared by exchange with the deuterated solvent (Figure A.51).

b) Conversion of [Fe**L**Cl_2] to [Fe**L**$(MeCN)_3]Cl_2$

Dissolving $\mathbf{Fe_{Cl}^{II}}$ in MeCN (e.g., for CV analysis) results in a color change from yellow to red (for UV/VIS spectra, see Figure A.52), indicative of a substantial change in the coordination sphere. New diamagnetic signals corroborating this hypothesis build up between 5.6 and 8.0 ppm in the ^{1}H NMR spectrum taken in CD_3CN (Figure 2.22).

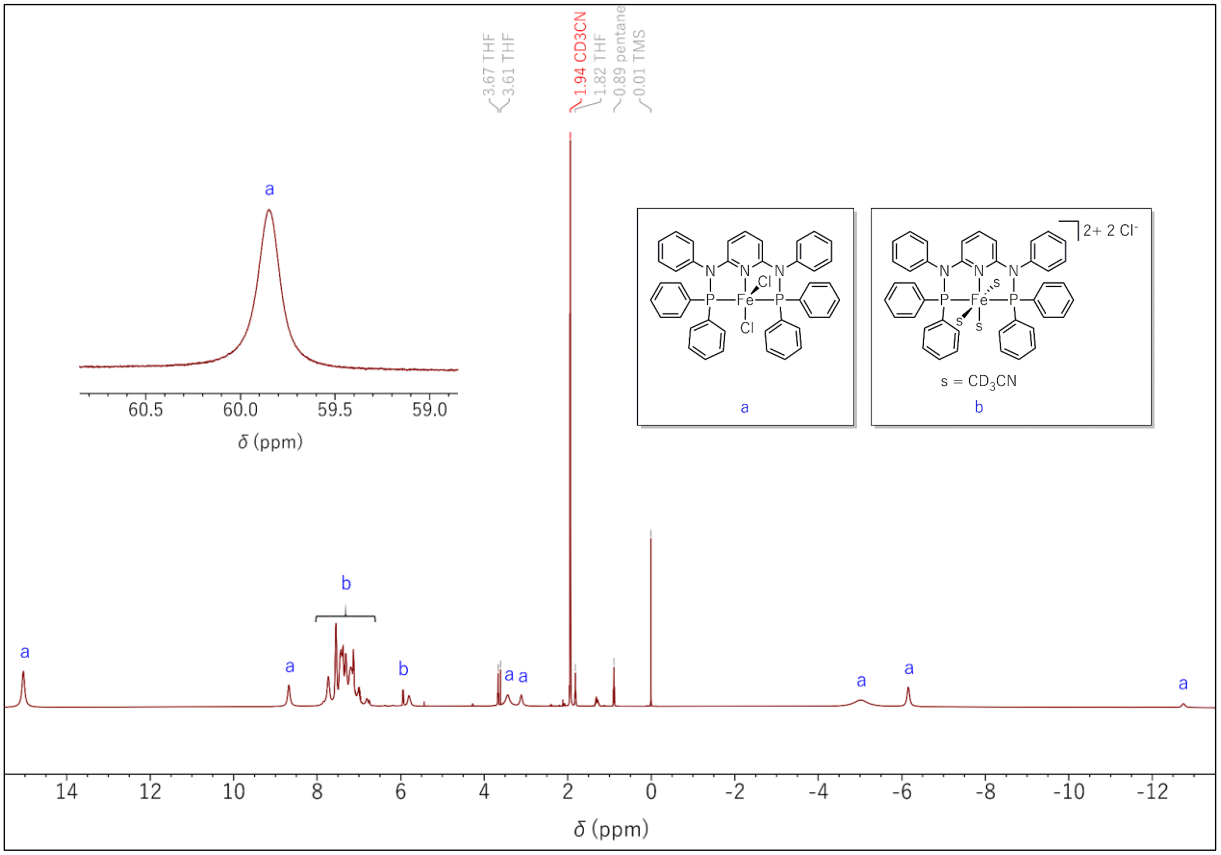

Figure 2.22. ^{1}H NMR spectrum of $\mathbf{Fe_{Cl}^{II}}$ in CD_3CN at 500 MHz and 296 K {a: $\mathbf{Fe_{Cl}^{II}}$, b: [Fe**L**$(CD_3CN)_3]Cl_2$}.

The comparison of the NMR spectra of $\mathbf{Fe}^{\mathbf{II}}_{\mathbf{Cl}}$ in CD_3CN (e.g., the $^{31}P\{^1H\}$ spectrum in Figure A.53) with those of $\mathbf{Fe}^{\mathbf{II}}_{\mathbf{s}}$**-OTf** in the same solvent point to identical coordination environments. Conversion of $\mathbf{Fe}^{\mathbf{II}}_{\mathbf{Cl}}$ in MeCN was further supported by crystals grown from an MeCN solution of $\mathbf{Fe}^{\mathbf{II}}_{\mathbf{Cl}}$ that reveal an inner-sphere molecular structure (see Figure A.59) identical to $\mathbf{Fe}^{\mathbf{II}}_{\mathbf{s}}$**(-OTf)**. The same NMR studies yet showed that the conversion of $\mathbf{Fe}^{\mathbf{II}}_{\mathbf{Cl}}$ into $\mathbf{Fe}^{\mathbf{II}}_{\mathbf{s}}$**-OTf** in MeCN is incomplete in solution; the two species are equilibrated with other intermediates (Figure 2.22).

2.2.2.2 [Co**L**(MeCN)$_2$](BF$_4$)$_2$

Single-crystal XRD of $\mathbf{Co}^{\mathbf{II}}_{\mathbf{s}}$ revealed twofold MeCN coordination and a square-based pyramidal structure (Figure 2.23) as inferred from a geometry index of $\tau_5 = 0.04$. Regarding the Co-N_{MeCN} bond distances, a significant elongation can be observed for the apical coordinating solvent (204.9 pm) compared to the basal one (189.3 pm).

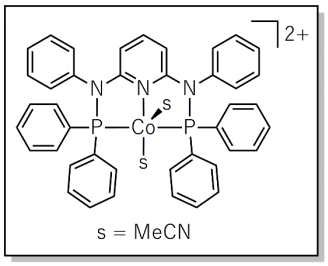

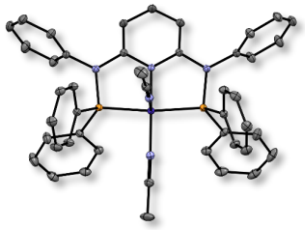

[Co**L**(MeCN)$_2$](BF$_4$)$_2$ ($\mathbf{Co}^{\mathbf{II}}_{\mathbf{s}}$)

Figure 2.23. Molecular structure of $\mathbf{Co}^{\mathbf{II}}_{\mathbf{s}}$. Thermal ellipsoids are shown at a 50% probability level. H-atoms, outer-sphere BF_4^- ligands, and co-crystallized solvent molecules were omitted for clarity.

Although a ^1H NMR spectrum of $\mathbf{Co}^{\mathbf{II}}_{\mathbf{s}}$ could be recorded (Figure A.54), the peaks ranging from ca. –20 to +15 ppm are heavily broadened and unsuitable for integration. The paramagnetic nature of the d^7 Co(II) species also prohibited recording heteronuclear NMR spectra. Simulations performed on the EPR spectrum in Figure 2.24 indicate two overlapping signals without hyperfine splitting, suggesting the presence of two rhombic low-spin ($S = ½$) Co species with one unpaired electron in the HOMO d_{z^2}, as already concluded for $\mathbf{Co}^{\mathbf{II}}_{\mathbf{Cl}}$.

The second species identified in Figure 2.24 might originate from different geometric orientations of $\mathbf{Co}^{\mathbf{II}}_{\mathbf{s}}$ or ligand association, respectively exchange, in MeCN. Impurities of the cobalt precursor can be excluded based on the lack of a singlet at $\delta_H = -2.82$ ppm in ^1H NMR analysis that is characteristic for the six acetonitrile ligands coordinated to $[Co(MeCN)_6](BF_4)_2$.

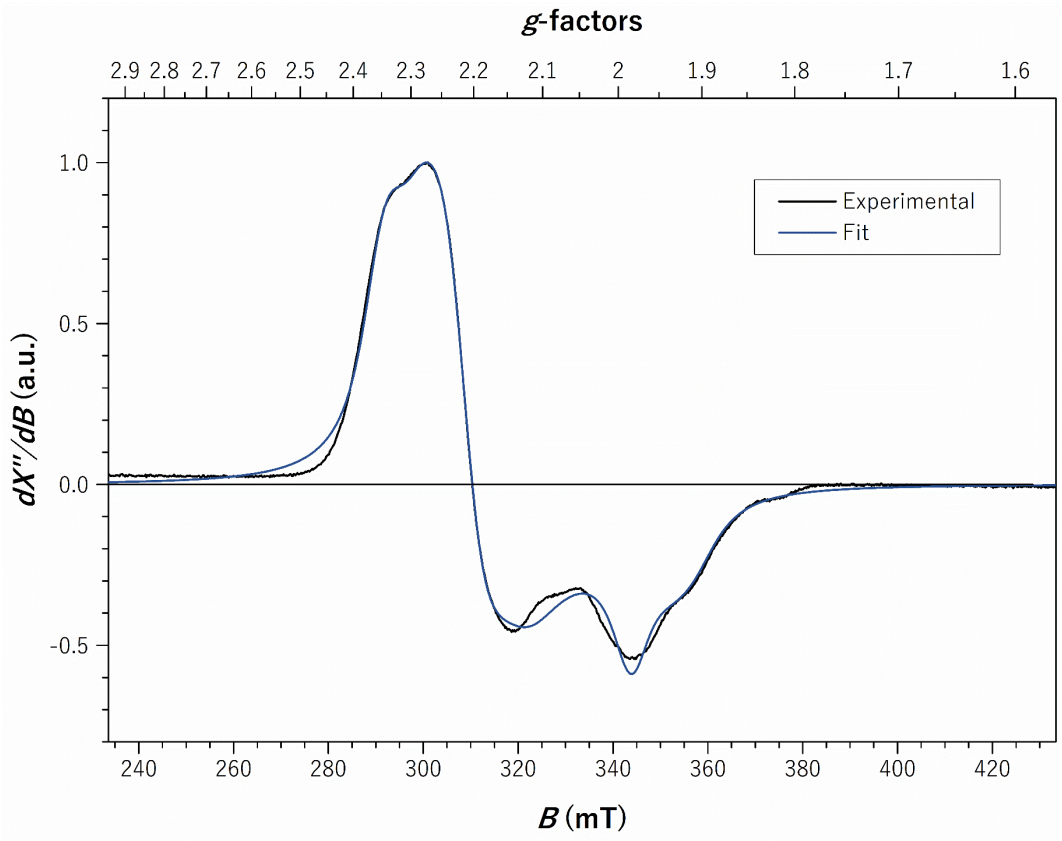

Figure 2.24. X-band EPR spectrum of ca. 1 mM $\mathbf{Co_s^{II}}$ in MeCN recorded at 10 K; microwave frequency 9.629 GHz, power 0.2 mW, modulation 0.75 mT/100 kHz. Blue: simulation with g_{z_1,y_1,x_1} = (2.196, 2.284, 1.941), Γ = 15.0655 and g_{z_1,y_1,x_1} = (2.353, 2.234, 1.999), Γ = 10.6400.

2.2.2.3 [Ni**L**(MeCN)](BF$_4$)$_2$

For $\mathbf{Ni_s^{II}}$, the pincer ligand **L** and a single equatorial acetonitrile ligand ($d_{Ni\text{-}N}$ = 185.6 pm) form a slightly distorted square plane environing the nickel core (τ_4 = 0.12, Figure 2.25).

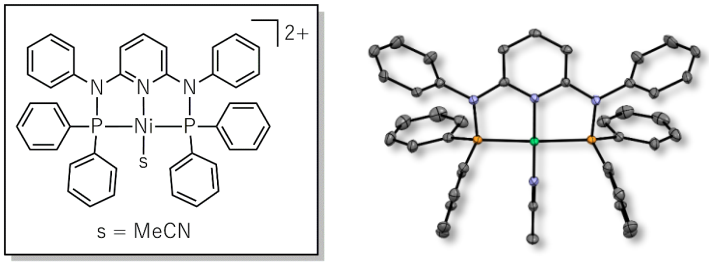

[Ni**L**(MeCN)](BF$_4$)$_2$ ($\mathbf{Ni_s^{II}}$)

Figure 2.25. Molecular structure of $\mathbf{Ni_s^{II}}$. Thermal ellipsoids are shown at a 50% probability level. H-atoms, outer-sphere BF_4^- ligands, and co-crystallized solvent molecules were omitted for clarity.

The coordinated solvent molecule is detected as a single peak (integral = 3) at 2.09 ppm in the ^{1}H NMR spectrum of the complex (Figure 2.26). Coordination of the nickel center to **L** also leads

to the deconvolution of the aromatic ^{1}H signals, which enables the determination of peak multiplicities and clear assignments to the aromatic positions. The well-resolved NMR spectra (Figure A.55 to Figure A.58) suggest a diamagnetic nature for $\mathbf{Ni_s^{II}}$, putatively a low-spin Ni(II) $3d^8$ state. This electron configuration typically yields the square planar geometry observed here due to the decreased energy of the fully occupied d_{z^2} orbital compared to other $\mathbf{M}L_4$ structures (see Figure 2.16).

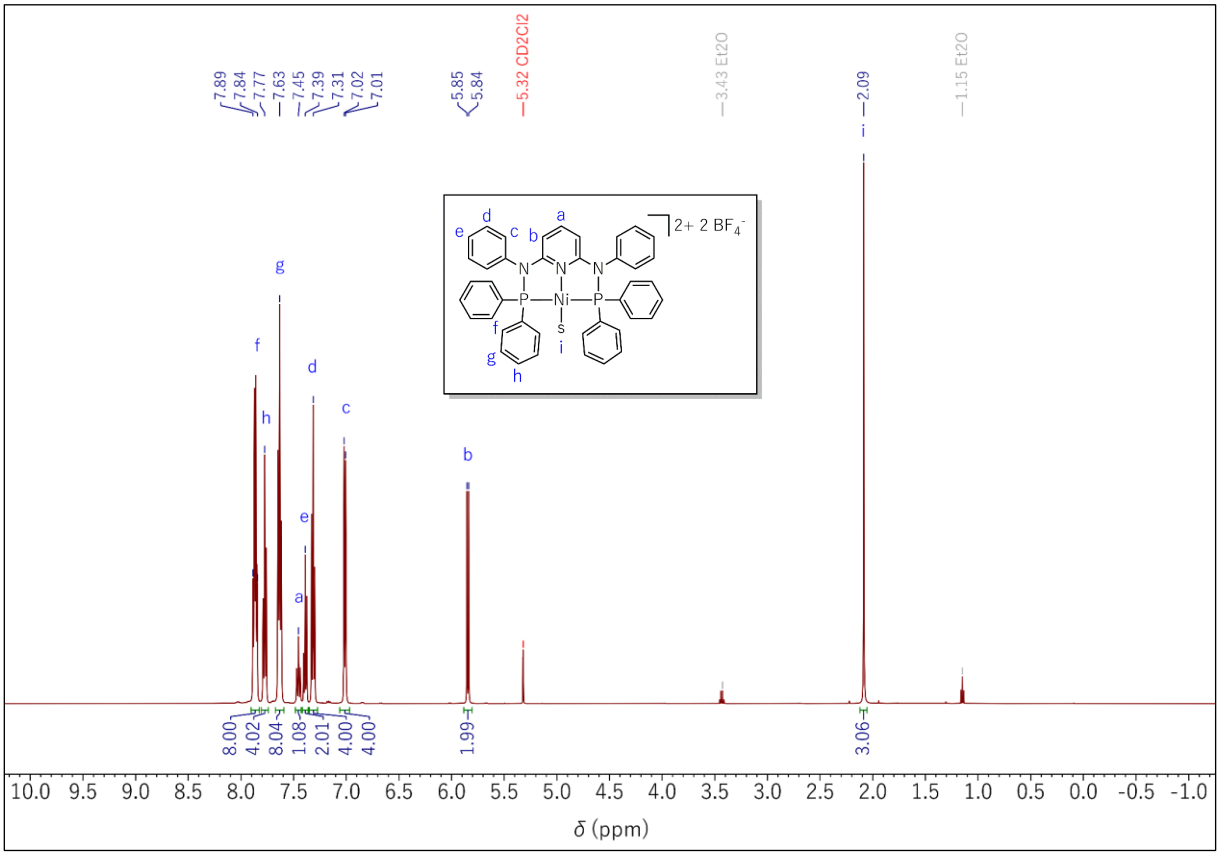

Figure 2.26. ^{1}H NMR spectrum of $\mathbf{Ni_s^{II}}$ in CD_2Cl_2 at 500 MHz and 296 K with peak assignments.

2.2.2.4 Comparative Structural Assessment

Structural comparison along the $\mathbf{M_s^{II}}$ series reveals a constant decrement of the number of auxiliary MeCN ligands (n_{MeCN}) when traversing the 3d transition metal period with n_{MeCN} = 3 for Fe, n_{MeCN} = 2 for Co, and n_{MeCN} = 1 for Ni (Table 2.4).

Table 2.4. Structural and electronic data obtained for the $\mathbf{M_s^{II}}$ complexes.

	n_{MeCN}	CN	Idealized Geometry (τ_4/τ_5)	d^n, n =	VE
$\mathbf{Fe_s^{II}}$	3	6	O_h (-)	6	18
$\mathbf{Co_s^{II}}$	2	5	SBP (0.04)	7	17
$\mathbf{Ni_s^{II}}$	1	4	SP (0.12)	8	16

Consequently, despite the gain in d electrons, the valence electron counts drop from 18 (full shell) for the d^6 Fe to 17 for the d^7 Co and 16 for the d^8 Ni species. Similar to the VE count, the bond distances (d_{bond}) between the metal and the equatorial MeCN ligand (**M**-N_{eq}), **M**-P^1, and **M**-N_{Py} decrease in the order $\mathbf{Fe}_s^{II}$ > $\mathbf{Co}_s^{II}$ > $\mathbf{Ni}_s^{II}$. These bonds spanning the square "plane" between metal and coordinating atoms (Figure 2.4A, x = N_{eq}) are formed by hybridized $d_{x^2-y^2}$ orbitals. Since the coordinating atoms are identical for all $\mathbf{M}_s^{II}$ complexes, property variations are expected to be directly relatable to the characteristics of the metal center. The **M**-P and **M**-N bond distances in this coordination plane depend linearly on the electronegativity of the central metal (X_M), as shown in Figure 2.27 (X_{Fe} = 1.64, X_{Co} = 1.70, and X_{Ni} = 1.75)[16].

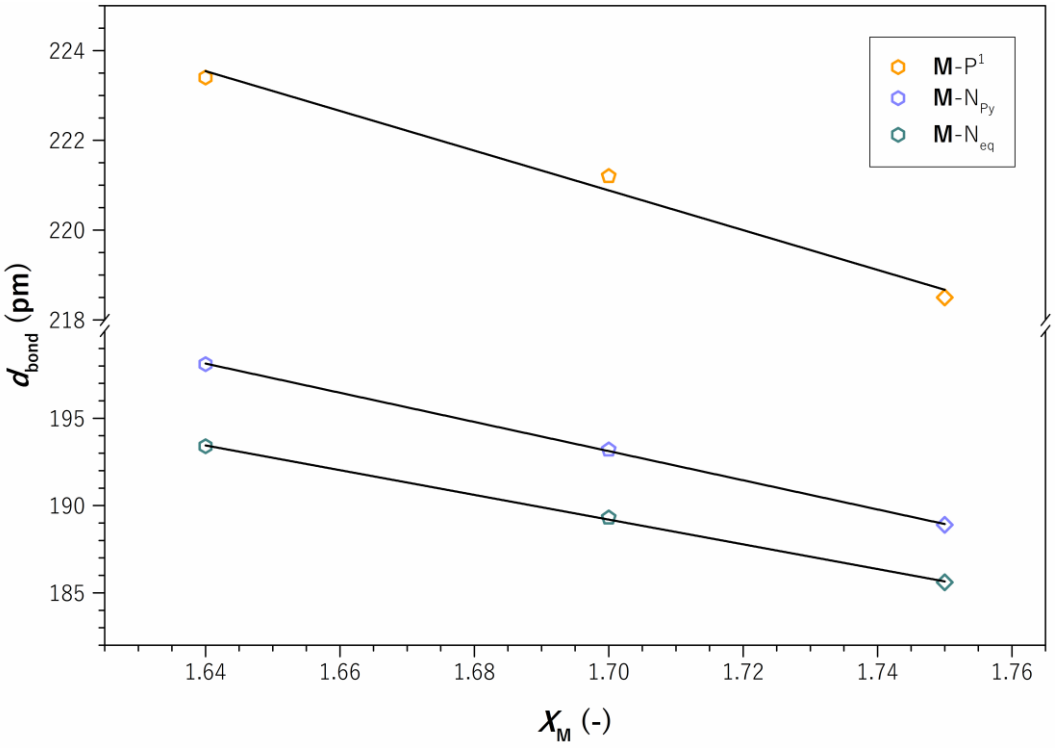

Figure 2.27. d_{bond} vs. X_M for $\mathbf{M}_s^{II}$ complexes (hexagon: Fe, pentagon: Co, square: Ni).

The increasing capability of the metal to attract (the ligating atom's) electrons causes an increased overlap with the orbital of the coordinating partner and, ultimately, a decrease in the bond distance from Fe to Ni. A simultaneous increase in complex stability is expected when switching to later metals.[13]

The correlation between bond distance and metal ionic radius as observed for the $\mathbf{M}_{Cl}^{II}$ series in section 2.2.1.7 could not be observed here, likely because of the varying coordination spheres compared to the bis-chloride complexes. The following chapter will explore further structural and electronic effects of the spectator ligands on the structure of the complexes in the $\mathbf{M}_s^{II}$ and $\mathbf{M}_{Cl}^{II}$ series for **M** = Fe, Co, and Ni.

2.3 Influence of Auxiliary Ligands – Acetonitrile vs. Chloride

Key geometric and electronic features of the chloride and acetonitrile complexes of Fe, Co, and Ni are shown in Table 2.5. Although based on the same d electron configurations, $\mathbf{M}_{s}^{II}$ and $\mathbf{M}_{Cl}^{II}$ complexes of the same metal develop substantially different coordination spheres in the solid state. While the coordination number remains at five and enables the formation of SBP complexes for $\mathbf{M}_{Cl}^{II}$, the number of AL (n_{AL}) – and consequently the order of the corresponding coordination polyhedron – decreases stepwise from Fe to Ni in $\mathbf{M}_{s}^{II}$ complexes.

Table 2.5. Comparison of structural and electronic data obtained for the $\mathbf{M}_{s}^{II}$ and $\mathbf{M}_{Cl}^{II}$ complexes of **M** = Fe, Co, and Ni.

	$\mathbf{Fe}_{s}^{II}$	$\mathbf{Fe}_{Cl}^{II}$	$\mathbf{Co}_{s}^{II}$	$\mathbf{Co}_{Cl}^{II}$	$\mathbf{Ni}_{s}^{II}$	$\mathbf{Ni}_{Cl}^{II}$
$\mathbf{d^n}$, $\boldsymbol{n}$ =	6	6	7	7	8	8
VE	18	16	17	17	16	18
CN	6	5	5	5	4	5
$\boldsymbol{n}_{AL}$	3	2	2	2	1	2
Ideal. Geom.	O_h	SBP	SBP	SBP	SP	SBP

VE numbers increase along the 3d row in the $\mathbf{M}_{Cl}^{II}$ series but decline for $\mathbf{M}_{s}^{II}$. Depending on the AL, $\mathbf{Fe}_{x}^{II}$ and $\mathbf{Ni}_{x}^{II}$ exhibit 18, respectively 16, VE complexes, whereas $\mathbf{Co}_{x}^{II}$ stays in a 17 VE radical electron configuration.

For iron, the increase in energy of occupied orbitals through the strong field-splitting of MeCN can be minimized by the population of the degenerate t_{2g} orbitals in $\mathbf{Fe}_{s}^{II}$**(-OTf)**. Conceivable pentacoordinate d^6 complexes would be destabilized to a greater extent due to further splitting of the filled orbitals. Opposed to this, the weak field-splitting chloride ligands decrease the orbital energy gap below the spin pairing energy, ultimately inducing the high-spin configuration.

The independence of the structural properties of $\mathbf{Co}_{x}^{II}$ from the AL (even τ_5 is identical) may stem from the radical character of the d^7 electron configuration, which requires at least one electron in a singly occupied molecular orbital (SOMO) of higher energy. Tetradentate $\mathbf{M}L_4$ structures would lead to an electron-deprived 15 VE complex, which appears energetically unfavorable. Further association of a ligand under the formation of a 19 VE $\mathbf{M}L_6$ compound in octahedral geometry would require the occupation of an e_g orbital of higher energy, which is assumed to be unfavorable with both ALs. The field-splitting induced by the AL is less marked in the almost ideal SBP, as observed for both low-spin d^7 Co complexes (see Figure 2.10B, left). Since only the

single electron in the hybridized d_{z^2} orbital is affected, the square-based pyramid likely constitutes the preferred coordination geometry.

The $\mathbf{Ni}_{\mathbf{x}}^{\mathbf{II}}$ complexes behave inversely to their iron congeners. With two more electrons to locate in the hybridized d orbitals, the weak field-splitting of the chloride ligands helps decrease the energy of the d_{z^2} HOMO (especially in combination with distortion of the SBP structure). Although the formation of a square planar d^8 complex with one chloride in the outer coordination sphere would likely lead to a further decrease of the energy of the HOMO (Figure 2.28, right), energetic stabilization by the formation of a full-shell complex with SBP geometry appears to be the favored option for $\mathbf{Ni}_{\mathbf{Cl}}^{\mathbf{II}}$.

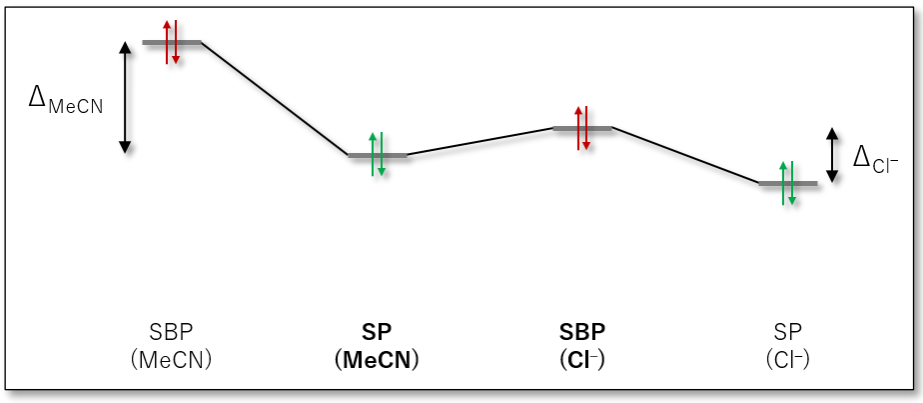

Figure 2.28. Proposed qualitative energy levels for the HOMO in SBP and SP d^8 low-spin complexes containing strong (MeCN) and weak field-splitting auxiliary ligands (Cl^-). Green shows the energetically favorable geometry, red the unfavorable. The structures observed for the $\mathbf{Ni}_{\mathbf{x}}^{\mathbf{II}}$ complexes are highlighted in bold.

With MeCN as the auxiliary ligand, the orbital energy difference (Δ) of the d_{z^2} orbital between the two possible coordination geometries likely exceeds a beneficial threshold in a pentacoordinate system. Here, a decrease in the HOMO energy is achieved by forcing the complex off the desired full-shell state and into SP geometry.

In conclusion, opposing combinations of valence and d^n electron counts are stabilized by auxiliary MeCN ligands, whereas correlating valence and d^n electron numbers are favored with Cl^- ligands due to the differences in their crystal field splitting abilities.

The obtained knowledge of the initial electronic and spatial configurations of the $\mathbf{M}_{\mathbf{x}}^{\mathbf{z}}$ complexes will serve as the starting point for further electron addition upon electrochemical reduction in cyclic voltammetry.

2.4 Experimental

2.4.1 General Considerations

All synthetic manipulations were performed under an argon atmosphere either in an MBRAUN UNILAB PLUS glovebox or using standard SCHLENK techniques in oven-dried glassware, ensuring rigorously inert conditions. Organic solvents were dried and degassed by passage over an MBRAUN SPS-7 solvent purification system, handled under an argon atmosphere, and stored over molecular sieves. Commercially available chemicals were purchased from MERCK, CARL ROTH, TCI, or ABCR and used without further purification if not otherwise stated. NMR solvents were degassed by three freeze-pump-thaw cycles and dried over molecular sieves. Aniline was dried over molecular sieves and degassed by purging with argon.

NMR spectra were recorded on a BRUKER AVANCE NEO 400 MHz or a BRUKER AVANCE III HD 500 MHz NMR spectrometer (the latter operated by Dr. THOMAS WEYHERMÜLLER and LUKAS SCHUBERT) with a BRUKER PRODIGY probe at the indicated temperature. Chemical shifts (δ) are given in ppm related to tetramethylsilane (TMS) and the coupling constants (J) in Hz. The solvent signal was used as the reference, and the chemical shift was converted to the TMS scale ($CDCl_3$: δ_H = 7.26 ppm and δ_C = 77.16 ppm, CD_2Cl_2: δ_H = 5.32 ppm and δ_C = 53.84 ppm, CD_3CN: δ_H = 1.94 ppm and δ_C = 1.32 ppm).[17] First-order spin multiplicities are abbreviated as singlet (s), doublet (d), triplet (t), and quadruplet (q). Couplings of higher order or overlapped signals are denoted as multiplet (m) and broadened signals as (br). The positions of protons and carbon atoms in aromatic rings are given as *ortho* (o), *meta* (m), *para* (p), and quaternary (q).

HRM spectra were recorded on a THERMO SCIENTIFIC Q EXACTIVE PLUS HYBRID QUADRUPOLE-ORBITRAP mass spectrometer at the MAX-PLANCK-INSTITUT FÜR KOHLENFORSCHUNG.

UV/VIS measurements were conducted on an AGILENT TECHNOLOGIES CARY 8454 UV/Visible spectroscopy system.

Elemental analysis (CHN) was performed by ANNIKA GUROWSKI on an ELEMENTAR UNICUBE fitted with a thermal conductivity detector.

Single crystals were selected by Dr. THOMAS WEYHERMÜLLER and BERND MIENERT under a microscope in polarized light with an applied nitrogen cryostream at approx. –40 °C and were covered with polyfluorinated polyether. The crystals were picked up with nylon loops and rapidly mounted in the nitrogen cold gas stream of the diffractometer at 100 K to prevent solvent loss. A BRUKER D8 VENTURE diffractometer equipped with an IμS 3.0 DIAMOND source, INCOATEC HELIOS mirror optics (Mo-K_α radiation; λ = 0.71073 Å), and PHOTON III detector was used for

data collection. Data were processed using the BRUKER APEX 3 software suite. The final cell constants are based upon the refinement of the XYZ-centroids of several thousand reflections above 20 $\sigma(I)$. Structures were solved and refined using the embedded BRUKER SHELXTL software package. All non-hydrogen atoms were anisotropically refined; hydrogen atoms were placed at calculated positions and refined as riding atoms with isotropic displacement parameters.

Magnetic susceptibility data were recorded by DERYA DEMIRBAS and Dr. ECKHARD BILL with powder samples in the temperature range 2–270 K using a SQUID susceptometer with a field of 1.0 T (MPMS-3, QUANTUM DESIGN, calibrated with a standard palladium reference sample, error < 2%). Multiple-field variable-temperature magnetization measurements were done at 1 T, 4 T, and 7 T in the range of 2–260 K, with the magnetization equidistantly sampled on a $1/T$ temperature scale. Sample holders of quartz with O-ring sealings were used. The SQUID response curves (raw data) have been corrected for holder and solvent contributions by subtracting the corresponding response curves obtained from separate measurements without sample material. The experimental magnetization data obtained from independent simulation of the corrected SQUID response curves were corrected for underlying diamagnetism (using tabulated PASCAL's constants) and temperature-independent paramagnetism. Handling and simulation of the SQUID raw data, as well as spin HAMILTONIAN simulation of the susceptibility and magnetization data, were done with the JULX.SL package for exchange-coupled systems.

^{57}Fe-MÖSSBAUER spectra were recorded by DERYA DEMIRBAS and Dr. ECKHARD BILL with non-enriched powder samples on a conventional spectrometer with an alternating constant acceleration of the γ-source (^{57}Co/Rh, 1.8 GBq). The source was kept at room temperature, and the sample temperature was maintained constant in an OXFORD INSTRUMENTS VARIOX cryostat. The raw data (512 channels) were folded to merge the recorded two mirror images of the spectra, which also eliminates the parabolic background. The minimum experimental line width was 0.24 mm·s^{-1} (full width at half maximum). Isomer shifts are quoted relative to iron metal at 300 K as the spectrometer was calibrated by recording the MÖSSBAUER spectrum of a 12 μm thick foil of α-Fe at room temperature, with the center of the six-line pattern being taken as zero velocity. Spectra were simulated with LORENTZIAN doublets or doublet VOIGT profiles using the MF.SL package (version 2.2) and least-squares parameter optimization.

X-band EPR derivative spectra of frozen-solution samples (ca. 1 mM) were recorded by DERYA DEMIRBAS and Dr. ECKHARD BILL on a BRUKER ELEXSYS E500 spectrometer equipped with a BRUKER dual-mode cavity (ER4116DM), a helium flow cryostat (OXFORD INSTRUMENTS ESR 910), and a BRUKER high-sensitivity SUPER-X BRIDGE (ER-049X) microwave unit with an integrated microwave frequency counter. The magnetic field controller (ER032T) was externally calibrated

with a BRUKER NMR field probe (ER035M). The spectra were simulated with the program ESIMX.SL for calculating powder spectra with effective *g* values, first-order hyperfine splitting, and anisotropic line widths (GAUSSIAN line shapes).

2.4.2 PNP Pincer Ligand

2.4.2.1 N^2,N^6-diphenylpyridine-2,6-diamine

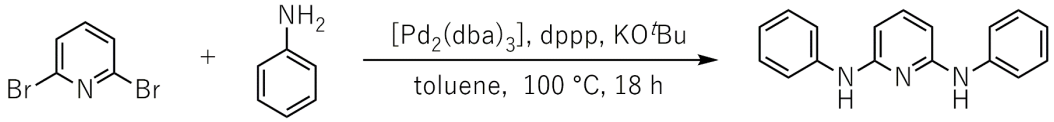

DBP	An	**DPPDA**
$C_5H_3Br_2N$	C_6H_7N	$C_{17}H_{15}N_3$
236.89 g·mol^{-1}	93.13 g·mol^{-1}	261.33 g·mol^{-1}

N^2,N^6-diphenylpyridine-2,6-diamine was synthesized following a modified procedure of WAGAW and BUCHWALD.[3]

2,6-Dibromopyridine (DBP, 497.8 mg, 2.0 mmol, 1.0 equiv.), aniline (An, 372.5 mg, 0.37 mL, 4.0 mmol, 2.0 equiv.), tris(dibenzylideneacetone)dipalladium {[$Pd_2(dba)_3$], 36.6 mg, 0.04 mmol, 0.02 equiv.}, 1,3-bis(diphenylphosphino)propane (dppp, 33.0 mg, 0.08 mmol, 0.04 equiv.) and potassium *tert*-butoxide (628.4 mg, 5.6 mmol, 2.8 equiv.) were placed into a SCHLENK tube in the glovebox, and toluene (15 mL) was added. The suspension was stirred at 100 °C for 18 h and cooled to rt before adding DCM (10 mL). The organic phase was washed with brine (20 mL), the resulting aqueous phase was extracted with DCM (3 x 10 mL), and the combined organic layers were dried over anhydrous magnesium sulfate. After removing the organic solvents *in vacuo*, the crude product was purified by column chromatography on silica using an 85:15 mixture of pentane and ethyl acetate.

Orange solid. *Y* = 397 mg, 1.52 mmol, 76%.

The obtained analytical data are consistent with those previously reported in the literature.[3]

^{1}H NMR (500 MHz, $CDCl_3$, 298 K): δ_H = 7.37–7.29 (m, PhH_o + PhH_m + PyH_p, 9H), 7.03 (tt, *J* = 1.5, 3.9, PhH_p, 2H), 6.38 (br s, N*H*, 2H), 6.32 (d, *J* = 8.0 Hz, PyH_m, 2H).

^{13}C{^{1}H} NMR (126 MHz, $CDCl_3$, 298 K): δ_C = 155.0 (PyC_o), 140.7 (PhC_{NH}), 139.6 (PyC_p), 129.3 (PhC_m), 122.7 (PhC_p), 120.5 (PhC_o), 99.0 (PyC_m).

Retardation factor: 0.55 in pentane/ethyl acetate (85:15).

2.4.2.2 N^2,N^6-bis(diphenylphosphaneyl)-N^2,N^6-diphenylpyridine-2,6-diamine

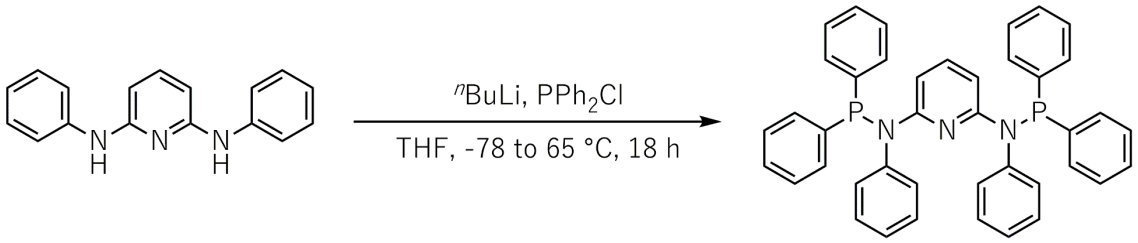

DPPDA
$C_{17}H_{15}N_3$
261.33 g·mol^{-1}

L
$C_{41}H_{33}N_3P_2$
629.68 g·mol^{-1}

n-Butyllithium (2.5 M in hexanes, 4.0 mL, 10.0 mmol, 2.0 equiv.) was added dropwise to an orange solution of **DPPDA** (1.3067 g, 5.0 mmol, 1.0 equiv.) in THF (35 mL) at –78 °C. The solution was allowed to warm up to rt and stirred for 1 h before cooling to 0 °C once more and dropwise addition of chlorodiphenylphosphine (1.84 mL, 10.0 mmol, 2.0 equiv.). The solution was allowed to warm up to rt and stirred for 1 h, then at 65 °C for 18 h. After cooling to rt, the solvents were removed *in vacuo*, and the brown residue was washed with MeOH (4 x 10 mL), Et_2O (3 x 5 mL), and pentane (3 x 5 mL). Removal of residual solvents *in vacuo* yielded the desired product.

White solid. *Y* = 2.1 g, 3.3 mmol, 67%.

Crystals suitable for X-ray diffraction were obtained from a concentrated THF/pentane (3:1) solution at –35 °C.

^{1}H NMR (500 MHz, CD_2Cl_2, 296 K): δ_H = 7.28–7.16 (m, 12H, PPhH_m + PPhH_p), 7.15–7.07 (m, 9H, PPhH_o + PyH_p), 7.02–6.95 (m, 6H, NPhH_m + NPhH_p), 6.82–6.76 (m, 4H, NPhH_o), 5.81 (d, 2H, *J* = 8.0, PyH_m).

^{13}C{^{1}H} NMR (126 MHz, CD_2Cl_2, 296 K): δ_C = 160.3–159.7 (m, PyC_q), 143.1–142.8 (m, NPhC_q), 139.5–138.8 (m, PPhC_q), 138.6 (PyC_p), 133.9–133.3 (m, PPhC_m), 130.9 (NPhC_o), 129.1 (NPhC_m), 128.8 (PPhC_p), 128.0 (t, *J* = 2.9, PPhC_o), 126.4 (NPhC_p), 101.5 (PyC_m).

^{31}P{^{1}H} NMR (202 MHz, CD_2Cl_2, 296 K): δ_P = 52.8.

HRMS (ESI$^+$): *m*/*z* calcd for $C_{41}H_{33}N_3P_2 + H^+$ = 630.22225, found = 630.22213.

EA: calcd for $C_{41}H_{33}N_3P_2$ = C: 78.21, H: 5.28, N: 6.67; found = C: 78.36, H: 5.15, N: 6.64.

2.4.3 Bis-Chloride Complexes

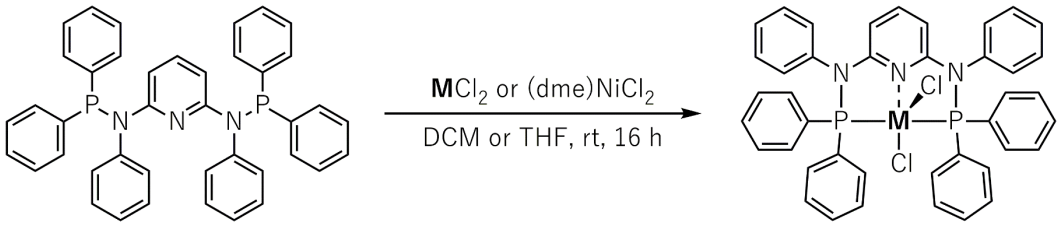

L

$C_{41}H_{33}N_3P_2$

629.68 g·mol^{-1}

$\mathbf{M}^{II}_{Cl}$

M = Fe, Co, Ni, or Zn

L (31.5 mg, 0.05 mmol, 1.0 equiv.) and the respective bis-chloride metal precursor **M**Cl_2 (**M** = Fe, Co, or Zn) or (dme)$NiCl_2$ (11.0 mg, 0.05 mmol, 1.0 equiv.) were placed into a SCHLENK tube in the glovebox, and DCM (**M** = Fe or Ni, 2 mL) or THF (**M** = Co or Zn, 2 mL) was added. The resulting solution was stirred at rt for 16 h before removing the solvent *in vacuo*.

The crude product was purified by precipitation from a DCM solution with pentane, washing the precipitate with pentane (3 x 2 mL), and removing the solvent *in vacuo*.

Deviations from the purification procedure are explicated for the individual complexes.

2.4.3.1 [Fe**L**Cl_2]

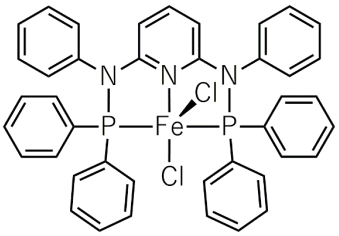

Fe^{II}_{Cl}

$C_{41}H_{33}Cl_2FeN_3P_2$

756.43 g·mol^{-1}

Yellow solid. *Y* = 30.8 mg, 0.048 mmol, 95%.

Crystals suitable for X-ray diffraction were obtained from a concentrated DCM/pentane (3:1) solution at −35 °C.

^{1}H NMR (500 MHz, CD_2Cl_2, 296 K): δ_H = 57.14 (br s, 2H, PyH_m), 14.38 (br s, 8H, PPhH_m), 8.61 (br s, 4H, NPhH_m), 3.52 (br s, 4H, NPhH_o), 3.13 (br s, 2H, NPhH_p), −4.92 (br s, 8H, PPhH_o), −5.45 (br s, 4H, PPhH_p), −11.61 (br s, 1H, PyH_p).

^{13}C{^{1}H} NMR (126 MHz, CD_2Cl_2, 296 K): δ_C = 282.7, 258.5, 199.5, 155.0, 152.1, 116.9, 108.6.

HRMS (ESI$^+$): *m*/*z* calcd for $[C_{41}H_{33}Cl_2FeN_3P_2 - Cl^-]^+$ = 720.11821, found = 720.11849.

EA: calcd for $C_{41}H_{33}Cl_2FeN_3P_2$ = C: 65.10, H: 4.40, N: 5.56; found = C: 65.31, H: 4.79, N: 5.28.

Crystals of [Fe**L**$(MeCN)_3$]$(Cl_3FeOFeCl_3)$ were obtained from a concentrated MeCN/Et_2O (3:1) solution of **Fe^{II}_{Cl}** at −30 °C under air.

2.4.3.2 [Co**L**Cl_2]

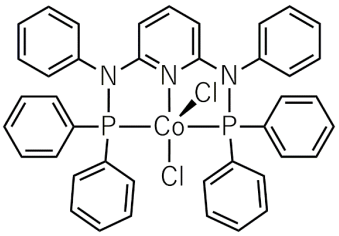

Co^{II}_{Cl}

$C_{41}H_{33}Cl_2CoN_3P_2$

759.52 g·mol^{-1}

The desired product was precipitated from a THF solution.

Dark red solid. *Y* = 34.0 mg, 0.045 mmol, 90%.

Crystals suitable for X-ray diffraction were obtained from vapor diffusion of pentane into a concentrated THF solution at rt or from a concentrated MeCN/Et_2O (3:1) solution at –35 °C.

^{1}H NMR (400 MHz, CD_2Cl_2, 296 K): δ_H = 10.65 (br s, 1H), 9.40 (br s, 4H), 8.61 (br s, 4H), 8.34–7.07 (m, 16H), 5.97 (br s, 8H).

HRMS (ESI$^+$): *m*/*z* calcd for $[C_{41}H_{33}Cl_2CoN_3P_2]^+$ = 758.08533: found = 758.08561.

EA: calcd for $C_{41}H_{33}Cl_2CoN_3P_2$ = C: 64.84, H: 4.38, N: 5.53; found = C: 64.56, H: 4.27, N: 5.48.

2.4.3.3 [Ni**L**Cl_2]

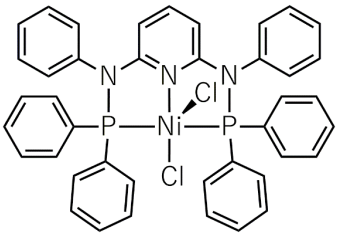

Ni^{II}_{Cl}

$C_{41}H_{33}Cl_2NiN_3P_2$

759.28 g·mol^{-1}

Red solid. Y = 34.2 mg, 0.044 mmol, 88% (including 0.2 CH_2Cl_2).

Crystals suitable for X-ray diffraction were obtained from a concentrated DCM/pentane (3:1) solution or a concentrated MeCN/Et_2O (3:1) solution at –35 °C.

^{1}H NMR (500 MHz, CD_2Cl_2, 296 K): δ_H = 7.90 (d, 8H, J = 6.3, PPhH_o), 7.63 (t, 4H, J = 7.4, PPhH_p), 7.48 (t, 8H, J = 7.5, PPhH_m), 7.41–7.31 (m, 3H, NPhH_p + PyH_p), 7.27 (t, 4H, J = 7.5, NPhH_m), 6.92 (d, 4H, J = 7.6, NPhH_o), 5.73 (d, 2H, J = 8.2, PyH_m).

^{13}C{^{1}H} NMR (126 MHz, CD_2Cl_2, 296 K): δ_C = 163.8 (PyC_q), 142.8 (PyC_p), 137.9 (NPhC_q), 134.7 (PPhC_o), 133.1 (PPhC_p), 130.6 (NPhC_o), 130.1 (NPhC_m), 129.6 (NPhC_p), 129.2 (PPhC_m), 126.2 (t, J = 23.7, PPhC_q), 103.4 (PyC_m).

^{31}P{^{1}H} NMR (202 MHz, CD_2Cl_2, 296 K): δ_P = 85.0.

HRMS (ESI$^+$): m/z calcd for $[C_{41}H_{33}Cl_2N_3NiP_2 - Cl^-]^+$ = 722.11862, found = 722.11871.

EA: calcd for $C_{41}H_{33}Cl_2N_3NiP_2 \cdot 0.2\ CH_2Cl_2$ = C: 63.75, H: 4.34, N: 5.41; found = C: 63.55, H: 4.57, N: 5.43.

2.4.3.4 [Zn**L**Cl_2]

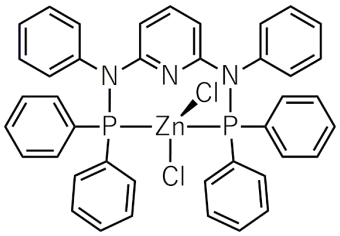

Zn^{II}_{Cl}

$C_{41}H_{33}Cl_2N_3P_2Zn$

765.96 g·mol^{-1}

White solid. *Y* = 33.3 mg, 0.042 mmol, 85% (including 0.25 CH_2Cl_2).

Crystals suitable for X-ray diffraction were obtained from a concentrated THF/pentane (3:1) solution at –35 °C.

^{1}H NMR (500 MHz, CD_2Cl_2, 296 K): δ_H = 7.46–7.39 (m, 8H, PPhH_o), 7.34–7.28 (m, 5H, PPhH_p + PyH_p), 7.24–7.08 (m, 14H, PPhH_m + NPhH_m + NPhH_p), 7.03–6.90 (m, 4H, NPhH_o), 5.85 (d, 2H, *J* = 8.1, PyH_m).

^{13}C{^{1}H} NMR (126 MHz, CD_2Cl_2, 296 K): δ_C = 157.4 (t, *J* = 7.3, PyC_q), 141.4 (PyC_p), 138.7 (NPhC_q), 133.8 (PPhC_o), 131.6 (PPhC_p), 131.2 (NPhC_o), 129.9 (NPhC_m), 128.9 (t, *J* = 4.9, PPhC_m), 128.4 (NPhC_p), 101.8 (PyC_m).

^{31}P{^{1}H} NMR (202 MHz, CD_2Cl_2, 296 K): δ_P = 30.9.

HRMS (ESI$^+$): *m*/*z* calcd for $[C_{41}H_{33}Cl_2N_3P_2Zn - Cl^-]^+$ = 728.11242, found = 728.11180.

EA: calcd for $C_{41}H_{33}Cl_2N_3P_2Zn \cdot 0.25\ CH_2Cl_2$ = C: 62.94, H: 4.29, N: 5.34; found = C: 62.67, H: 4.30, N: 5.33.

2.4.4 Further Halide & Triflate Complexes

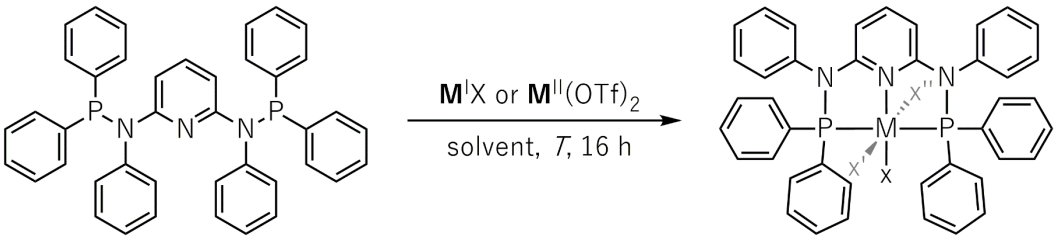

L

$C_{41}H_{33}N_3P_2$

629.68 g·mol^{-1}

M^{I}_{x} or M^{II}_{OTf}

M = Mn, Cu, or Zn

L (31.5 mg, 0.05 mmol, 1.0 equiv.) and the respective metal precursor (0.05 mmol, 1.0 equiv.) were placed into a SCHLENK tube in the glovebox, and the respective solvent (2 mL) was added. The resulting solution was stirred at the indicated temperature for 16 h before removing the solvent *in vacuo*.

The crude product was purified by precipitation from a DCM solution with pentane, washing the precipitate with pentane (3 x 2 mL), and removing the solvent *in vacuo*.

Deviations from the general procedure are explicated for the individual complexes.

2.4.4.1 [Mn**L**(CO)$_2$Br]

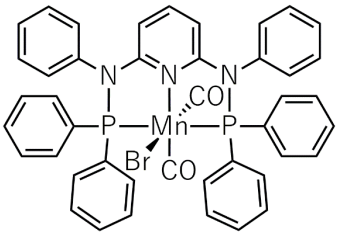

Mn$^{I}_{CO,Br}$

$C_{43}H_{33}BrMnN_3O_2P_2$

820.55 g·mol^{-1}

Reaction conditions: [Mn(CO)$_5$Br], toluene, 110 °C.

The desired product was obtained after washing the residue with DCM (2 mL) and pentane (3 x 2 mL) and removing the solvent *in vacuo*.

Yellow solid. *Y* = 30.8 mg, 0.037 mmol, 74% (including 0.1 C_7H_8).

A color change to brown was observed in concentrated DCM solutions under exposure to light, possibly upon CO loss and dimerization. Crystals suitable for X-ray diffraction were obtained from vapor diffusion of pentane into a concentrated DCM solution at rt under the exclusion of light.

^{1}H NMR (500 MHz, CD_2Cl_2, 296 K): δ_H = 7.77 (dd, 4H, *J* = 5.8, 5.1), 7.47–7.36 (m, 10H), 7.36–7.27 (m, 8H), 7.26–7.13 (m, 7H, PyH_p), 6.81 (d, 2H, *J* = 8.0, NPhH_o), 5.79 (d, 2H, *J* = 8.2, PyH_m).

^{13}C{^{1}H} NMR (126 MHz, CD_2Cl_2, 296 K): δ_C = 178.0 (*C*O), 164.1 (t, *J* = 12.9, PyC_q), 141.3 (NPhC_q), 139.9 (t, *J* = 23.4, PPhC_q), 139.1 (PyC_p), 137.5 (t, *J* = 6.3), 132.5, 131.8, 131.7 (t, *J* = 5.7), 131.5, 130.6, 130.3, 130.2, 130.1, 128.8, 128.2 (t, *J* = 4.6), 127.4 (t, *J* = 5.0), 102.9 (PyC_m).

^{31}P{^{1}H} NMR (202 MHz, CD_2Cl_2, 296 K): δ_P = 138.9.

HRMS (ESI$^+$): *m*/*z* calcd for $[C_{43}H_{33}BrMnN_3O_2P_2]^+$ = 819.06064, found = 819.06076.

EA: calcd for $C_{43}H_{33}BrMnN_3O_2P_2$ · 0.1 C_7H_8 = C: 63.26, H: 4.11, N: 5.06; found = C: 63.66, H: 4.44, N: 4.99.

2.4.4.2 [Cu**L**Cl]

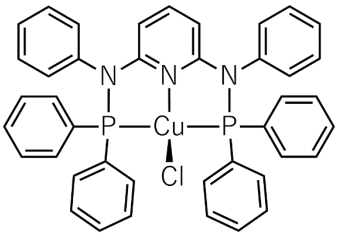

Cu^{I}_{Cl}

$C_{41}H_{33}ClCuN_3P_2$

728.68 g·mol^{-1}

Reaction conditions: CuCl, THF, rt.

Light yellow solid. *Y* = 23.9 mg, 0.033 mmol, 65% (including 0.05 CH_2Cl_2).

Crystals suitable for X-ray diffraction were obtained from a concentrated DCM/pentane (3:1) solution at –35 °C.

^{1}H NMR (500 MHz, CD_2Cl_2, 296 K): δ_H = 7.50 (dd, 8H, *J* = 5.8, 5.3, PPhH_o), 7.31 (t, 4H, *J* = 7.4, PPhH_p), 7.24 (t, 1H, *J* = 8.0, PyH_p), 7.17 (t, 8H, *J* = 7.6, PPhH_m), 7.15–7.08 (m, 6H, NPhH_m + NPhH_p), 6.93–6.83 (m, 4H, NPhH_o), 5.68 (d, 2H, *J* = 8.0, PyH_m).

^{13}C{^{1}H} NMR (126 MHz, CD_2Cl_2, 296 K): δ_C = 157.8 (t, *J* = 9.4, PyC_q), 141.6 (PyC_p), 140.1 (t, *J* = 3.0, NPhC_q), 133.6 (PPhC_o), 132.9 (t, *J* = 11.4, PPhC_q), 130.9 (NPhC_o), 130.4 (PPhC_p), 129.7 (NPhC_m), 128.5 (t, *J* = 4.4, PPhC_m), 127.9 (NPhC_p), 101.1 (PyC_m).

^{31}P{^{1}H} NMR (202 MHz, CD_2Cl_2, 296 K): δ_P = 39.9.

HRMS (ESI$^+$): *m*/*z* calcd for $[C_{41}H_{33}ClCuN_3P_2]^+$ = 727.11288, found = 727.11272.

EA: calcd for $C_{41}H_{33}ClCuN_3P_2 \cdot 0.05\ CH_2Cl_2$ = C: 67.27, H: 4.55, N: 5.73; found = C: 67.02, H: 4.75, N: 5.48.

2.4.4.3 [Cu**L**I]

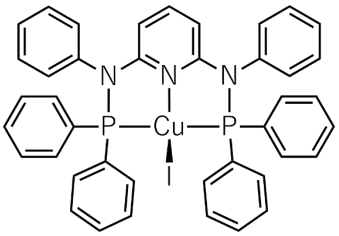

Cu^{I}_{I}

$C_{41}H_{33}ICuN_3P_2$

820.13 g·mol^{-1}

Reaction conditions: CuI, THF, 65 °C.

White solid. *Y* = 21.3 mg, 0.026 mmol, 52%.

Crystals suitable for X-ray diffraction were obtained from a concentrated THF solution at –35 °C.

^{1}H NMR (500 MHz, CD_2Cl_2, 296 K): δ_H = 7.62–7.41 (m, 8H, PPhH_o), 7.36–7.23 (m, 5H, PPhH_p + PyH_p), 7.21–7.06 (m, 14H, PPhH_m + NPhH_m + NPhH_p), 7.01–6.89 (m, 4H, NPhH_o), 5.67 (d, 2H, *J* = 8.0, PyH_m).

^{13}C{^{1}H} NMR (126 MHz, CD_2Cl_2, 296 K): δ_C = 157.7 (t, *J* = 9.2, PyC_q), 141.6 (PyC_p), 140.0 (t, *J* = 2.7, NPhC_q), 133.7 (PPhC_o), 132.6 (t, *J* = 11.7, PPhC_q), 130.9 (NPhC_o), 130.4 (PPhC_p), 129.7 (NPhC_m), 128.4 (t, *J* = 4.4, PPhC_m), 127.9 (NPhC_p), 101.2 (PyC_m).

^{31}P{^{1}H} NMR (202 MHz, CD_2Cl_2, 296 K): δ_P = 40.0.

HRMS (ESI$^+$): *m*/*z* calcd for $[C_{41}H_{33}CuIN_3P_2]^+$ = 819.04849, found = 819.04742.

EA: calcd for $C_{41}H_{33}CuIN_3P_2$ = C: 60.05, H: 4.06, N: 5.12; found = C: 59.82, H: 4.18, N: 5.06.

2.4.4.4 [Zn**L**(OTf)$_2$]

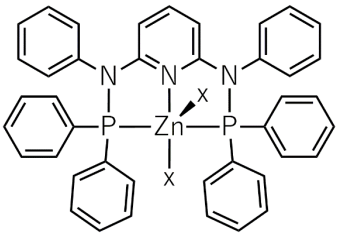

Zn^{II}_{OTf}

x = OTf

$C_{43}H_{33}F_6N_3O_6P_2S_2Zn$

993.19 g·mol^{-1}

Reaction conditions: $Zn(OTf)_2$, MeCN, 80 °C.

White solid. *Y* = 47.4 mg, 0.048 mmol, 95%.

Crystals suitable for X-ray diffraction were obtained from a concentrated THF solution at –35 °C.

^{1}H NMR (500 MHz, CD_2Cl_2, 296 K): δ_H = 7.45–7.36 (m, 13H, PPhH_o + PPhH_p + PyH_p), 7.25 (t, 8H, *J* = 7.7, PPhH_m), 7.22–7.14 (m, 6H, NPhH_m + NPhH_p), 7.03 (br s, 4H, NPhH_o), 5.94 (d, 2H, *J* = 8.2, PyH_m).

^{13}C{^{1}H} NMR (126 MHz, CD_2Cl_2, 296 K): δ_C = 157.5 (t, *J* = 6.8, PyC_q), 143.2 (PyC_p), 138.0 (t, *J* = 2.4, NPhC_q), 133.9 (br, PPhC_q), 132.5 (PPhC_o), 130.7 (br, NPhC_o), 130.3 (NPhC_m), 129.2 (t, *J* = 5.2, PPhC_m), 129.0 (PPhC_p), 126.0 (NPhC_p), 120.1 (q, *C*F_3), 102.9 (PyC_m).

^{31}P{^{1}H} NMR (202 MHz, CD_2Cl_2, 296 K): δ_P = 28.8.

HRMS (ESI$^+$): *m*/*z* calcd for $[C_{43}H_{33}F_6N_3O_6P_2S_2Zn - CF_3SO_3^-]^+$ = 842.09559, found = 842.09613.

EA: calcd for $C_{43}H_{33}F_6N_3O_6P_2S_2Zn$ = C: 52.00, H: 3.35, N: 4.23; found = C: 52.26, H: 3.68, N: 4.32.

2.4.5 Acetonitrile Complexes

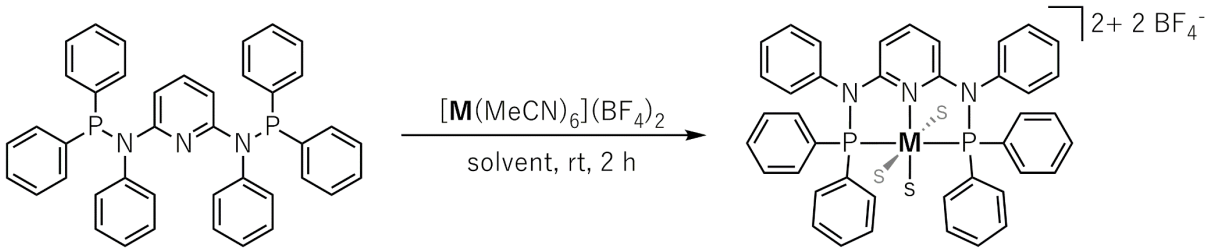

L

$C_{41}H_{33}N_3P_2$

629.68 g·mol^{-1}

$\mathbf{M}_s^{II}$

s = MeCN

M = Fe, Co, or Ni

The precursors [**M**(MeCN)$_6$](BF$_4$)$_2$ (**M** = Fe, Co, or Ni) were synthesized according to a procedure reported by SEN et al.[18]

L (125.9 mg, 0.20 mmol, 1.0 equiv.) and the respective [**M**(MeCN)$_6$](BF$_4$)$_2$ (**M** = Fe, Co, or Ni) precursor (0.20 mmol, 1.0 equiv.) were placed into a SCHLENK tube in the glovebox, and DCM (5 mL) was added. The resulting solution was stirred for 2 h at rt before removing the solvent *in vacuo*. The crude product was dissolved in MeCN and precipitated with Et$_2$O. The $\mathbf{M}_s^{II}$ complexes (**M** = Fe, Co, or Ni; s = MeCN) were isolated by washing the precipitate with Et$_2$O (3 x 3 mL) and removing the residual solvent *in vacuo*.

Crystals suitable for X-ray diffraction were obtained from a concentrated solution in MeCN/Et$_2$O at –35 °C.

2.4.5.1 [Fe**L**(MeCN)$_3$](BF$_4$)$_2$

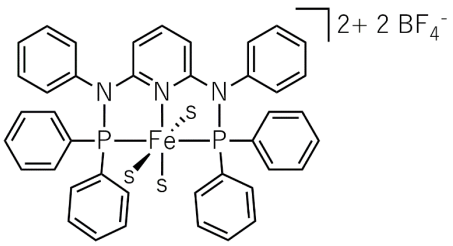

Fe$_s^{II}$

s = MeCN

$C_{47}H_{42}B_2F_8FeN_6P_2$

982.29 g·mol^{-1}

Orange solid. *Y* = 173 mg, 0.18 mmol, 88% (including 0.05 $C_4H_{10}O$).

^{1}H NMR (500 MHz, CD_2Cl_2, 296 K): δ_H = 7.68–7.59 (m, 12H, PPh*H*$_o$ + PPh*H*$_p$), 7.55 (t, *J* = 7.9, 8H, PPh*H*$_m$), 7.47–7.38 (m, 6H, NPh*H*$_m$ + NPh*H*$_p$), 7.35 (tt, *J* = 8.2, 1.5, 1H, Py*H*$_p$), 7.13–7.05 (m, 4H, NPh*H*$_o$), 5.99 (d, *J* = 8.2, 2H, Py*H*$_m$), 2.39 (s, 3H, C*H*$_3$CN$_{eq}$), 1.69 (s, 6H, C*H*$_3$CN$_{ax}$).

^{13}C{^{1}H} NMR (126 MHz, CD_2Cl_2, 296 K): δ_C = 166.1 (t, *J* = 11.1, Py*C*$_q$), 141.8 (Py*C*$_p$), 139.2 (t, *J* = 2.7, NPh*C*$_q$), 138.7 (CH$_3$*C*N$_{eq}$), 138.1 (CH$_3$*C*N$_{ax}$), 134.1 (t, *J* = 6.3, PPh*C*$_o$), 132.9 (PPh*C*$_p$), 131.1 (NPh*C*$_m$), 130.5 (NPh*C*$_o$), 129.9 (NPh*C*$_p$), 129.7 (t, *J* = 2.7, PPh*C*$_m$), 129.5 (PPh*C*$_q$), 129.3, 104.5 (t, *J* = 2.3, Py*C*$_m$), 5.0 (*C*H$_3$CN$_{eq}$), 4.3 (*C*H$_3$CN$_{ax}$).

^{31}P{^{1}H} NMR (202 MHz, CD_2Cl_2, 296 K): δ_P = 129.3.

HRMS (ESI$^+$): *m*/*z* calcd for [$C_{47}H_{42}B_2F_8FeN_6P_2$ – 2 BF_4^-]$^{2+}$ = 404.11423, found = 404.11406.

EA: calcd for $C_{47}H_{42}B_2F_8FeN_6P_2$ · 0.05 $C_4H_{10}O$ = C: 57.50, H: 4.34, N: 8.52; found = C: 57.83, H: 4.72, N: 8.69.

2.4.5.2 [Co**L**(MeCN)$_2$](BF$_4$)$_2$

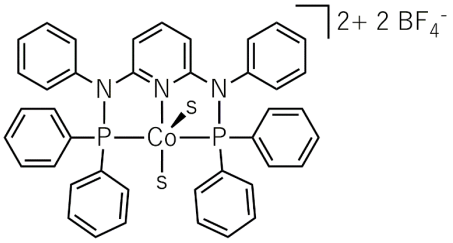

Co$_s^{II}$

s = MeCN

$C_{45}H_{39}B_2CoF_8N_5P_2$

944.33 g·mol^{-1}

Orange/brown solid. *Y* = 182 mg, 0.19 mmol, 96% (including 0.1 $C_4H_{10}O$).

^{1}H NMR (500 MHz, CD_2Cl_2, 296 K): δ_H = 9.02 (br s), 8.91 (br s), 7.49 (br s), 7.07 (br s), 1.40 (br s), –1.24 (br s), –14.2 (br s).

HRMS (ESI$^+$): *m*/*z* calcd for $[C_{45}H_{39}B_2CoF_8N_5P_2 - 2\ BF_4^- - CH_3CN]^{2+}$ = 364.58681, found = 364.58707.

EA: calcd for $C_{45}H_{39}B_2CoF_8N_5P_2 \cdot 0.1\ C_4H_{10}O$ = C: 57.57, H: 4.24, N: 7.36; found = C: 57.57, H: 4.61, N: 7.56.

2.4.5.3 [Ni**L**(MeCN)](BF$_4$)$_2$

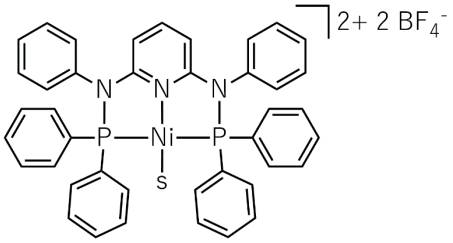

Ni$^{II}_{s}$

s = MeCN

$C_{43}H_{36}B_2F_8N_4NiP_2$

903.04 g·mol^{-1}

Orange solid. *Y* = 171 mg, 0.19 mmol, 94%.

^{1}H NMR (500 MHz, CD_2Cl_2, 296 K): δ_H = 7.91–7.83 (m, 8H, PPh*H*$_o$), 7.77 (t, *J* = 7.5, 4H, PPh*H*$_p$), 7.63 (tt, *J* = 7.7, 1.7, 8H, PPh*H*$_m$), 7.45 (tt, *J* = 8.3, 1.8, 1H, Py*H*$_p$), 7.39 (t, *J* = 7.4, 2H, NPh*H*$_p$), 7.31 (t, *J* = 7.7, 4H, NPh*H*$_m$), 7.01 (d, *J* = 7.6, 4H, NPh*H*$_o$), 5.85 (d, *J* = 8.3, 2H, Py*H*$_m$), 2.09 (s, 3H, C*H*$_3$CN).

^{13}C{^{1}H} NMR (126 MHz, CD_2Cl_2, 296 K): δ_C = 164.9 (t, *J* = 12.2, Py*C*$_q$), 144.8 (Py*C*$_p$), 136.4 (NPh*C*$_q$), 134.8 (PPh*C*$_p$), 134.3 (t, *J* = 7.3, PPh*H*$_o$), 131.0 (NPh*C*$_m$), 130.4 (t, *J* = 6.0, PPh*C*$_m$), 130.0 (NPh*C*$_o$), 123.5 (t, *J* = 29.0, PPh*C*$_q$), 104.7 (t, *J* = 3.2, Py*C*$_m$), 4.3 (*C*H$_3$CN).

^{31}P{^{1}H} NMR (202 MHz, CD_2Cl_2, 296 K): δ_P = 92.5.

HRMS (ESI$^+$): *m*/*z* calcd for [$C_{43}H_{36}B_2F_8N_4NiP_2$ – 2 BF_4^-]$^{2+}$ = 364.08789, found = 364.08769.

EA: calcd for $C_{43}H_{36}B_2F_8N_4NiP_2$ = C: 57.19, H: 4.02, N: 6.20; found = C: 57.47, H: 4.32, N: 6.54.

2.4.5.4 [Fe**L**(MeCN)$_3$](OTf)$_2$

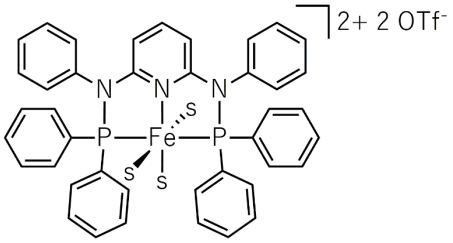

Fe^{II}_s-OTf

s = MeCN

$C_{49}H_{42}F_6FeN_6O_6P_2S_2$

1106.81 g·mol^{-1}

L (31.5 mg, 0.05 mmol, 1.0 equiv.) and Fe(OTf)$_2$ (17.7 mg, 0.05 mmol, 1.0 equiv.) were placed into a SCHLENK tube in the glovebox, and MeCN (2 mL) was added. The resulting orange solution was stirred at rt for 16 h before removing the solvent *in vacuo*. The desired product **Fe^{II}_s-OTf** was obtained after washing with Et$_2$O (2 mL), pentane (3 x 2 mL), and removing the solvent *in vacuo*.

Orange solid. *Y* = 48.9 mg, 0.043 mmol, 87% (including 0.25 $C_4H_{10}O$).

Crystals suitable for X-ray diffraction were obtained from a concentrated MeCN/Et$_2$O (3:1) solution at –35 °C.

^{1}H NMR (500 MHz, CD_2Cl_2, 296 K): δ_H = 7.75–7.59 (m, 12H, PPhH_o + PPhH_p), 7.60–7.50 (m, 8H, PPhH_m), 7.48–7.37 (m, 6H, NPhH_m + NPhH_p), 7.34 (t, 1H, *J* = 8.2, PyH_p), 7.10 (d, 4H, *J* = 7.4, NPhH_o), 5.99 (d, 2H, *J* = 8.2, PyH_m), 2.43 (s, 3H, CH_3CN$_{eq}$), 1.73 (s, 6H, CH_3CN$_{ax}$).

^{13}C{^{1}H} NMR (126 MHz, CD_2Cl_2, 296 K): δ_C = 166.0 (t, *J* = 11.1, PyC_q), 141.8 (PyC_p), 139.2 (t, *J* = 2.7, NPhC_q), 138.7 (CH$_3$*C*N$_{eq}$), 138.1 (CH$_3$*C*N$_{ax}$), 134.1 (t, *J* = 6.3, PPhC_o), 132.9 (PPhC_p), 131.1 (NPhC_m), 130.5 (NPhC_o), 129.9 (NPhC_p), 129.7 (t, *J* = 2.7, PPhC_m), 129.5 (PPhC_q), 129.3, 104.5 (t, *J* = 2.3, PyC_m), 5.4 (*C*H$_3$CN$_{eq}$), 4.7 (*C*H$_3$CN$_{ax}$).

^{31}P{^{1}H} NMR (202 MHz, CD_2Cl_2, 296 K): δ_P = 129.2.

HRMS (ESI$^+$): *m*/*z* calcd for [$C_{49}H_{42}F_6FeN_6O_6P_2S_2$ – 2 $CF_3SO_3^-$ – 2 CH_3CN]$^{2+}$ = 363.08768, found = 363.08752.

EA: calcd for $C_{49}H_{42}F_6FeN_6O_6P_2S_2$ · 0.25 $C_4H_{10}O$ = C: 53.37, H: 3.99, N: 7.47; found = C: 53.04, H: 4.33, N: 7.12.

2.4.5.5 [Ni**L**(MeCN)$_2$]BF$_4$

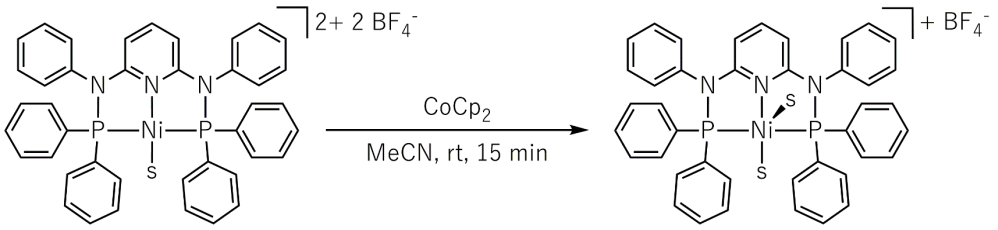

Ni$_s^{II}$
$C_{43}H_{36}B_2F_8N_4NiP_2$
903.04 g·mol^{-1}

s = MeCN

Ni$_s^{I}$
$C_{45}H_{39}BF_4N_5NiP_2$
857.29 g·mol^{-1}

Ni$_s^{II}$ (9.0 mg, 0.01 mmol, 1.0 equiv.) and cobaltocene (2.0 mg, 0.01 mmol, 1.0 equiv.) were placed into a 4 mL vial in the glovebox, and MeCN (ca. 0.8 mL) was added. The resulting dark red solution was stirred at rt for 15 min.

Crystals of **Ni$_s^{I}$** suitable for X-ray diffraction were obtained by adding Et_2O to the MeCN solution at –35 °C.

2.5 References

[1] a) D. Benito-Garagorri, E. Becker, J. Wiedermann, W. Lackner, M. Pollak, K. Mereiter, J. Kisala, K. Kirchner, *Organometallics* **2006**, *25*, 1900; b) M. Glatz, B. Bichler, M. Mastalir, B. Stöger, M. Weil, K. Mereiter, E. Pittenauer, G. Allmaier, L. F. Veiros, K. Kirchner, *Dalton Trans.* **2015**, *44*, 281; c) M. Glatz, C. Holzhacker, B. Bichler, M. Mastalir, B. Stöger, K. Mereiter, M. Weil, L. F. Veiros, N. C. Mösch-Zanetti, K. Kirchner, *Eur. J. Inorg. Chem.* **2015**, *2015*, 5053; d) G. K. Rao, S. I. Gorelsky, I. Korobkov, D. Richeson, *Dalton Trans.* **2015**, *44*, 19153; e) S. Rösler, J. Obenauf, R. Kempe, *J. Am. Chem. Soc.* **2015**, *137*, 7998; f) M. Mastalir, M. Glatz, B. Stöger, M. Weil, E. Pittenauer, G. Allmaier, K. Kirchner, *Inorg. Chim. Acta* **2017**, *455*, 707; g) G. K. Rao, W. Pell, B. Gabidullin, I. Korobkov, D. Richeson, *Chem. Eur. J.* **2017**, *23*, 16763; h) R. Arevalo, P. J. Chirik, *J. Am. Chem. Soc.* **2019**, *141*, 9106.

[2] a) N. Elgrishi, M. B. Chambers, V. Artero, M. Fontecave, *PCCP* **2014**, *16*, 13635; b) K. Talukdar, A. Issa, J. W. Jurss, *Front. Chem.* **2019**, *7*.

[3] S. Wagaw, S. L. Buchwald, *J. Org. Chem.* **1996**, *61*, 7240.

[4] M. Garbe, K. Junge, M. Beller, *Eur. J. Org. Chem.* **2017**, *2017*, 4344.

[5] Y. Jean, *Molecular Orbitals of Transition Metal Complexes*, Oxford University Press, New York, **2005**.

[6] a) R. M. Golding, K. F. Mok, J. F. Duncan, *Inorg. Chem.* **1966**, *5*, 774; b) E. Kuzmann, Z. Homonnay, Z. Klencsár, R. Szalay, *Molecules* **2021**, *26*, 1062.

[7] G. Mathies, S. D. Chatziefthimiou, D. Maganas, Y. Sanakis, S. Sottini, P. Kyritsis, E. J. J. Groenen, *J. Magn. Reson.* **2012**, *224*, 94.

[8] S. F. A. Kettle, in *Physical Inorganic Chemistry: A Coordination Chemistry Approach*, Springer, Berlin, Heidelberg, **1996**.

[9] a) M. R. Malachowski, M. Adams, N. Elia, A. L. Rheingold, R. S. Kelly, *J. Chem. Soc., Dalton Trans.* **1999**, 2177; b) C.-Y. Su, S. Liao, M. Wanner, J. Fiedler, C. Zhang, B.-S. Kang, W. Kaim, *Dalton Trans.* **2003**, 189; c) O. A. Fedorova, N. E. Shepel, S. D. Tokarev, E. V. Lukovskaya, Y. A. Sotnikova, A. A. Moiseeva, A. D'Aléo, F. Fages, F. Maurel, Y. V. Fedorov, *New J. Chem.* **2019**, *43*, 2817; d) S. Kumari, S. Muthuramalingam, A. K. Dhara, U. P. Singh, R. Mayilmurugan, K. Ghosh, *Dalton Trans.* **2020**, *49*, 13829.

[10] A. Bocian, D. Brykczyńska, M. Kubicki, Z. Hnatejko, M. Wałęsa-Chorab, A. Gorczyński, V. Patroniak, *Polyhedron* **2019**, *157*, 249.

[11] O. Kühl, in *Phosphorus-31 NMR Spectroscopy: A Concise Introduction for the Synthetic Organic and Organometallic Chemist*, Springer, Berlin, Heidelberg, **2008**.

[12] a) P. F. Lang, B. C. Smith, *Dalton Trans.* **2014**, *43*, 8016; b) E. Blokker, X. Sun, J. Poater, J. M. van der Schuur, T. A. Hamlin, F. M. Bickelhaupt, *Chem. Eur. J.* **2021**, *27*, 15616.

[13] D. Chapman, *Nature* **1954**, *174*, 887.

[14] A. W. Addison, T. N. Rao, J. Reedijk, J. van Rijn, G. C. Verschoor, *J. Chem. Soc., Dalton Trans.* **1984**, 1349.

[15] R. D. Shannon, *Acta Cryst. A* **1976**, *32*, 751.

[16] A. L. Allred, E. G. Rochow, *J. lnorg. Nucl. Chem.* **1958**, *5*, 264.

[17] G. R. Fulmer, A. J. M. Miller, N. H. Sherden, H. E. Gottlieb, A. Nudelman, B. M. Stoltz, J. E. Bercaw, K. I. Goldberg, *Organometallics* **2010**, *29*, 2176.

[18] a) B. J. Hathaway, D. G. Holah, A. E. Underhill, *J. Chem. Soc.* **1962**, 2444; b) A. Sen, T.-W. Lai, R. R. Thomas, *J. Organomet. Chem.* **1988**, *358*, 567.

Chapter 3: Electrochemistry under Inert Conditions

Part 1: General Redox Behavior

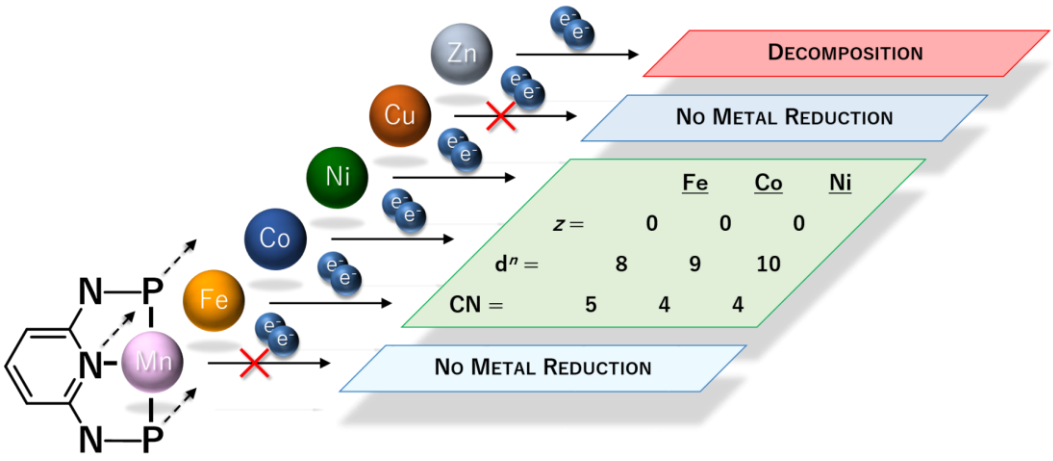

Part 1 of the following chapter comprises the electrochemical analysis of the previously synthesized chemical compounds to assess their redox behavior.

Since electron uptake is a prerequisite for the homogeneously catalyzed activation of CO_2, this analysis shall examine the reducibility of the transition metal complexes presented herein. The origin of the redox events (ligand- or metal-centered) and concomitant structural changes are discussed. Eventually, the electron configuration of the metal center is correlated to the behavior in cyclic voltammetry to derive a broader view of the aptitude of a specific metal center in CO_2 electroreduction.

Parts of this chapter have been published in:

N. W. Kinzel, D. Demirbas, E. Bill, T. Weyhermüller, C. Werlé, N. Kaeffer, W. Leitner, *Inorg. Chem.* **2021**, *60*, 19062.

CV measurements in this chapter were conducted under an argon atmosphere with an analyte concentration of 1 mM on a glassy carbon working electrode (circular surface with a diameter of 3.0 mm) and in a 0.1 M solution of tetrabutylammonium hexafluorophosphate ($TBAPF_6$) in acetonitrile at a scan rate (ν) of 100 $mV \cdot s^{-1}$. Deviations from these conditions are noted with the respective voltammogram. A brief introduction to the method is given in Appendix D.

3.1 PNP Pincer Ligand

In order to determine the capability of the ligand to take up electrons, cyclic voltammetry measurements were performed on **L** (Figure 3.1). The ligand was found electrochemically inactive in the potential window between –2.5 and –0.1 V_{Fc} in MeCN and DMF.

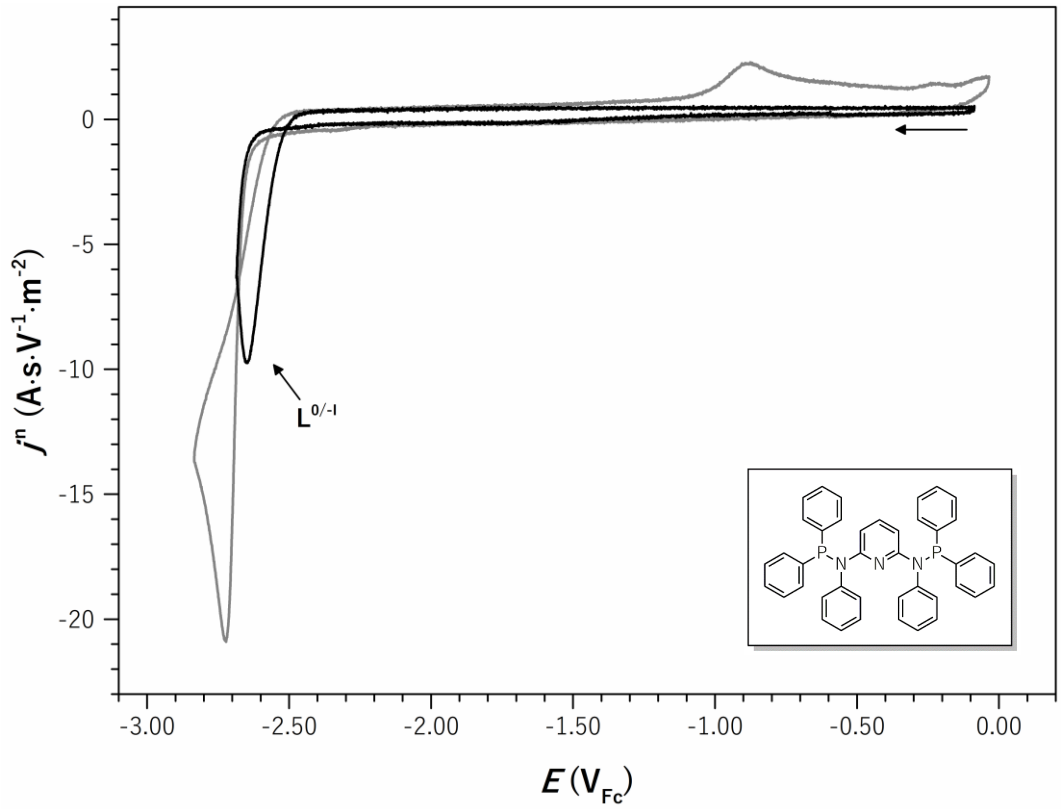

Figure 3.1. CVs of **L** in MeCN (black) and DMF (grey).

An irreversible reduction wave can be observed at potentials below –2.5 V_{Fc} in both solvents. Nevertheless, **L** can be classified as a redox-innocent system since the reduction is located on the far negative side of the potential scale exceeding the potential threshold for metal-centered reduction processes that could lead to efficient conversion of CO_2. For the same reason, little involvement of the ligand in the redox events of the $\mathbf{M}_x^z$ complexes is expected.

3.2 3d Transition Metal Complexes

3.2.1 Halide & Triflate Complexes

3.2.1.1 [Mn**L**(CO)$_2$Br]

$\mathbf{Mn}^{\mathbf{I}}_{\mathbf{CO,Br}}$ shows a primary irreversible reduction wave at $E_{p,c}$ = –2.64 V_{Fc} and minor additional waves at $E_{p,c}$ ≈ –2.45 V_{Fc} and $E_{p,a}$ ≈ –1.10 V_{Fc} in DMF (Figure 3.2). The poor solubility rendered attempts to analyze the complex in MeCN impossible.

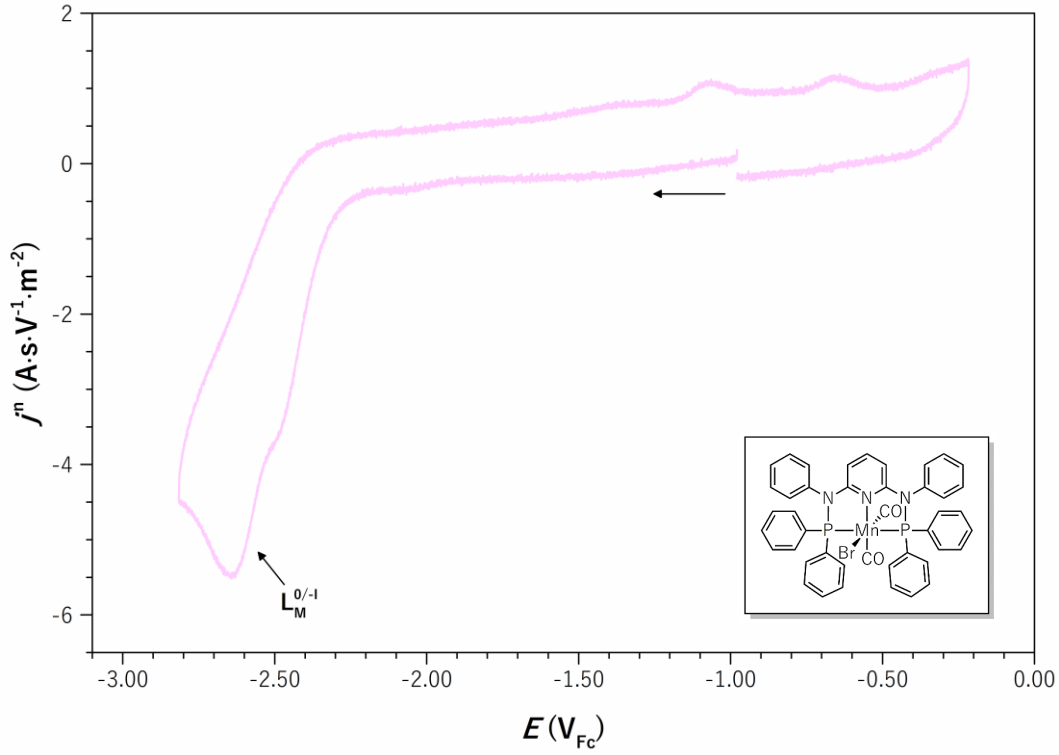

Figure 3.2. CV of 0.5 mM $\mathbf{Mn}^{\mathbf{I}}_{\mathbf{CO,Br}}$ in DMF.

The KUBIAK group proposes a metal-centered reduction to a Mn(0) species with concomitant halide loss and subsequent fast dimerization for the related [Mn(tpy)(CO)$_2$Br] complex.[1] However, the lack of a substantial re-oxidation wave indicative of a reduced $\mathbf{Mn}^{\mathbf{I}}_{\mathbf{CO,Br}}$ dimer makes such a metal-centered reduction event appear unlikely. In addition, $\mathbf{Mn}^{\mathbf{I}}_{\mathbf{CO,Br}}$ already exists in an 18 valence electron d^6 low-spin configuration, and reduction would populate a high-lying e_g orbital. Hence, the reduction of the coordinated ligand $\mathbf{L_M}$ is proposed to be favored at the strongly cathodic potential identified here [eq. (3.1)].

E: $$[Mn^{I}\mathbf{L}(CO)_2Br] + e^- \rightleftarrows [Mn^{I}\mathbf{L}^{(-I)}(CO)_2Br]^- \qquad (3.1)$$

Previous NMR studies showed the conversion of $\mathbf{Mn}^{\mathbf{I}}_{\mathbf{CO,Br}}$ in concentrated CD_2Cl_2 solutions (Figure A.7). So far, this is attributed to a light-induced sequence of carbonyl decoordination and

dimerization. According to this hypothesis, partial conversion of the analyte in the diluted DMF solution may be the origin of the minor additional waves recorded in CV.

3.2.1.2 [Fe**L**Cl$_2$]

Unambiguous cyclic voltammograms were inaccessible for $\mathbf{Fe}_{\mathbf{Cl}}^{\mathbf{II}}$ due to its partial conversion into [Fe**L**(MeCN)$_3$]Cl$_2$ and potential further products of different MeCN/Cl$^-$ stoichiometries in MeCN (see section 2.2.1.2). Attempts to analyze the compound in other solvents were impeded by various factors, e.g., a limited electrochemical potential window (DCM), insufficient solubility (THF), or fast transformation of the analyte (DMF, see Figure B.17).

The exchange of MeCN and chloride ligands under electroreductive conditions will be reviewed in more detail in part 2 of this chapter.

3.2.1.3 [Co**L**Cl$_2$]

Two partially reversible redox events at E^0 = –0.17 V_{Fc} (ΔE_p = 216 mV, $Co^{III/II}$) and E^0 = –1.21 V_{Fc} (ΔE_p = 94 mV, $Co^{II/I}$) as well as two irreversible waves at $E_{p,c}$ = –1.98 V_{Fc} ($Co^{I/0}$) and $E_{p,c}$ = –2.61 V_{Fc} ($\mathbf{L}_{\mathbf{M}}^{\mathbf{0/-I}}$) can be observed in the cyclic voltammogram of $\mathbf{Co}_{\mathbf{Cl}}^{\mathbf{II}}$ (Figure 3.3).

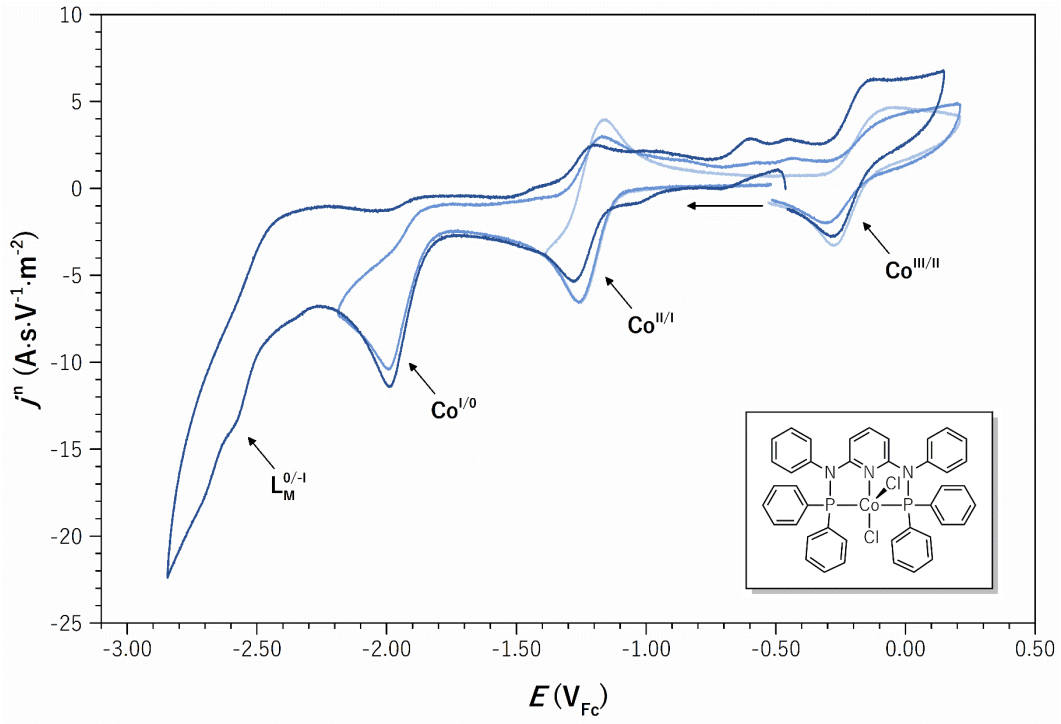

Figure 3.3. CVs of $\mathbf{Co}_{\mathbf{Cl}}^{\mathbf{II}}$ at varying potential windows.

Although a molecular structure of $\mathbf{Co}_{\mathbf{Cl}}^{\mathbf{II}}$ obtained from an acetonitrile solution confirms the retention of the inner-sphere coordination of both chloride ligands in the solid state (Figure A.60),

the formation of a cationic $[Co^{II}\mathbf{L}(MeCN)Cl]^+$ complex upon dissolution of $\mathbf{Co^{II}_{Cl}}$ in MeCN is supported by findings of BROWN et al. for similar complexes.[2] Applying a potential of ca. −1.2 V_{Fc} leads to the reduction and conversion of $[Co^{II}\mathbf{L}(MeCN)Cl]^+$ into a neutral $[Co^{I}\mathbf{L}Cl]$ species in an electrochemical-chemical (**EC**) sequence (cf. Appendix D) broken down in eq. (3.2) and (3.3).

E: $$[Co^{II}\mathbf{L}(MeCN)Cl]^+ + e^- \rightleftarrows [Co^{I}\mathbf{L}(MeCN)Cl] \quad (3.2)$$

C: $$[Co^{I}\mathbf{L}(MeCN)Cl] \rightleftarrows [Co^{I}\mathbf{L}Cl] + MeCN \quad (3.3)$$

Further reduction results in a second **EC** mechanism to Co(0), the chemical step of which can be attributed to the substitution of a chloride ligand with a solvent molecule under the formation of a putative $[Co^{0}\mathbf{L}(MeCN)]$ complex, as shown in eq. (3.4) and (3.5).

E: $$[Co^{I}\mathbf{L}Cl] + e^- \rightleftarrows [Co^{0}\mathbf{L}Cl]^- \quad (3.4)$$

C: $$[Co^{0}\mathbf{L}Cl]^- + MeCN \rightleftarrows [Co^{0}\mathbf{L}(MeCN)] + Cl^- \quad (3.5)$$

Scanning to more cathodic potentials reveals a third irreversible reduction wave at $E_{p,c}$ = −2.61 V_{Fc}, likely indicating the reduction of the coordinated ligand system.

A singly occupied d_{z^2} orbital constitutes the HOMO at the d^7 configuration of the initial paramagnetic Co(II) species (Scheme 3.1). The first reduction is expected to fill this d_{z^2} orbital, producing a diamagnetic $[Co^{I}\mathbf{L}(MeCN)Cl]$ complex. Release of the apical ligand would stabilize the now fully occupied d_{z^2} orbital in a square planar $[Co^{I}\mathbf{L}Cl]$ 16-electron complex, as found for the related pincer complex $[Co^{I}(PN_3P)(MeCN)]^+$ (R_N = H, R_P = ^{t}Bu).[3]

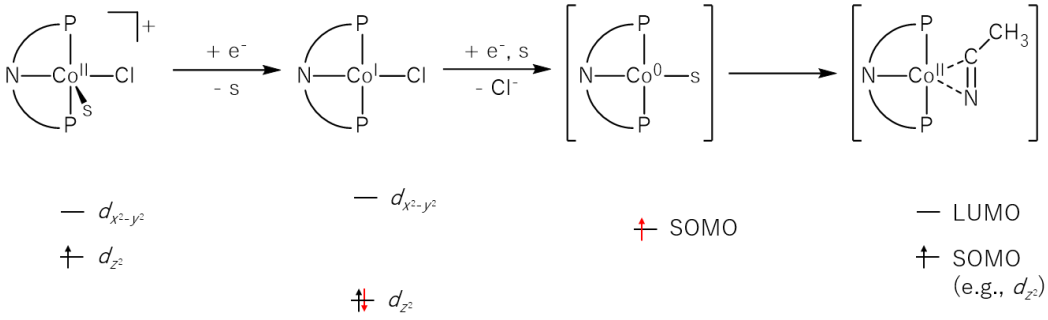

Scheme 3.1. Proposed electrochemical pathway and schematic frontier orbital diagrams for the reduction of $\mathbf{Co^{II}_{Cl}}$ in MeCN under argon atmosphere (s = MeCN).

The sizeable potential gap to the second reduction into a Co(0) species $E_{p,c}(Co^{I/0}) - E^0(Co^{II/I})$ = −670 mV is consistent with the injection of the second electron into a high-lying antibonding $d_{x^2-y^2}$ orbital. This second electron transfer is followed by an irreversible chemical step (**EC**), most probably the substitution of Cl^- with MeCN to generate a neutral

[Co^0**L**(MeCN)] complex. Calculations on similar complexes suggest an η^2 π-bonded MeCN in a structure best described as a Co(II) cycloimine.[3]

3.2.1.4 [Ni**L**Cl$_2$]

$\mathbf{Ni}^{II}_{Cl}$ shows a voltamperometric pattern similar to $\mathbf{Co}^{II}_{Cl}$ with a reversible reduction wave at E^0 = −1.16 V_{Fc} followed by an irreversible process at $E_{p,c}$ = −1.65 V_{Fc} (Figure 3.4), assigned to $Ni^{II/I}$ and $Ni^{I/0}$ events, respectively. Two more irreversible reduction waves appear at $E_{p,c}$ = −2.41 V_{Fc} and −2.75 V_{Fc}. The wave at −2.41 V_{Fc} can be attributed to a ligand-centered reduction, but the second reduction wave remains unassigned.

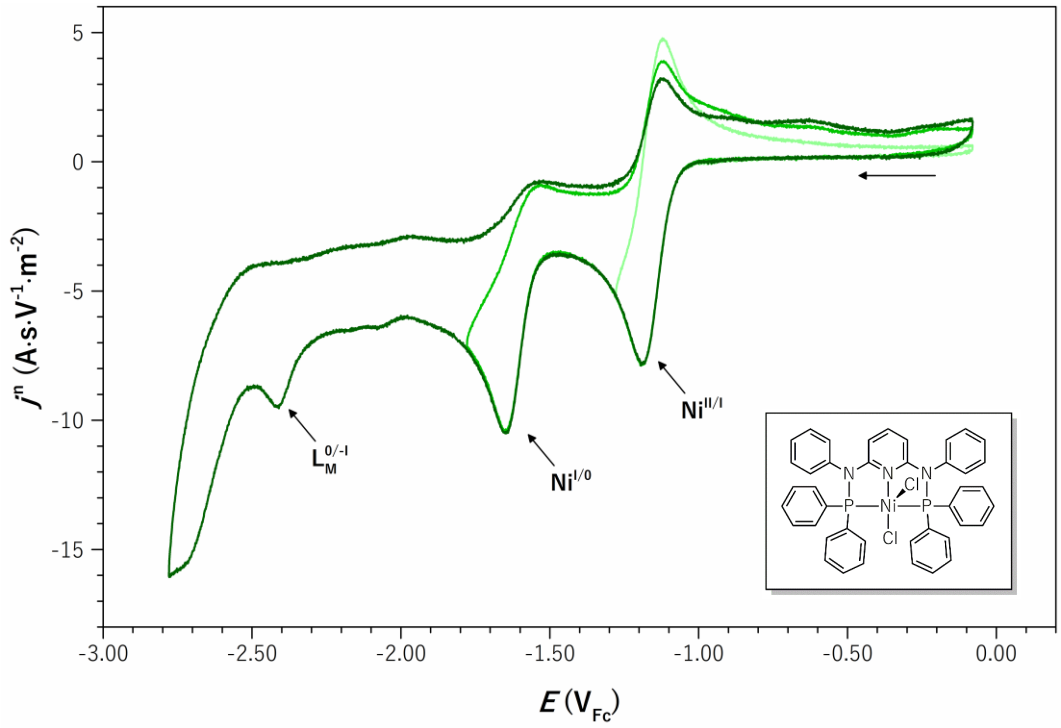

Figure 3.4. CVs of $\mathbf{Ni}^{II}_{Cl}$ at varying potential windows.

With a weakly coordinated apical chloride ligand in the solid state (Figure A.61), decoordination toward a cationic [Ni^{II}**L**Cl]$^+$ complex in the MeCN solution is conceivable. Reduction of [Ni^{II}**L**Cl]$^+$ is then proposed to generate a neutral [Ni^{I}**L**Cl] species [eq. (3.6)]. Tetradentate geometries were found for similar [Ni^{I}(PNP)] complexes.[4]

E: $$[Ni^{II}\mathbf{L}Cl]^+ + e^- \rightleftarrows [Ni^{I}\mathbf{L}Cl] \qquad (3.6)$$

As stems from the irreversibility of the $Ni^{I/0}$ event at ν = 100 mV·s^{-1}, the formation of a Ni(0) species is also coupled to a chemical step (**EC**) – likely a Cl^-/MeCN exchange producing a low valent [Ni^0**L**(MeCN)] complex [eq. (3.7) and (3.8)].

E: $[Ni^{I}LCl] + e^{-} \rightleftarrows [Ni^{0}LCl]^{-}$ (3.7)

C: $[Ni^{0}LCl]^{-} + MeCN \rightleftarrows [Ni^{0}L(MeCN)] + Cl^{-}$ (3.8)

The reversibility of the $Ni^{I/0}$ wave can be recovered by elevating the scan rate (Figure 3.5A), suggesting a slow chemical step. A standard potential of $E^{0}(Ni^{I/0}) = -1.59\ V_{Fc}$ is extracted at fast scan rates. The $E_{p,c}$ vs. log(v) graph for this wave decays linearly in the irreversible, pure kinetics (KP) zone of the kinetic zone diagram (cf. Figure D.4). A slope of $-21.2\ mV{\cdot}log(v)^{-1}$ (Figure 3.5B) reasonably agrees with the theoretical value for an **EC** mechanism.[5]

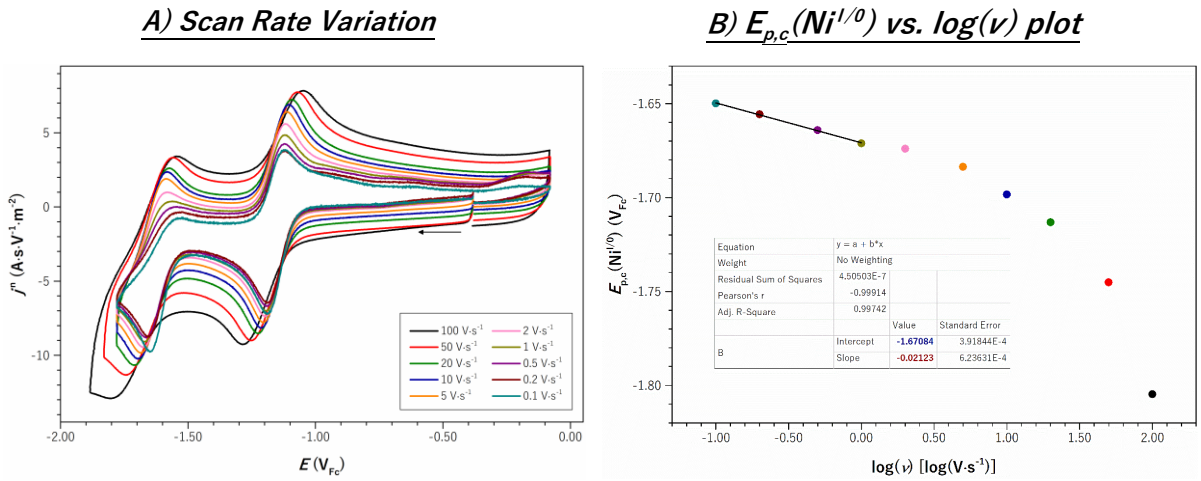

Figure 3.5. (A) CVs at varying scan rates and (B) $E_{p,c}(Ni^{I/0})$ vs. log(v) plot of $\mathbf{Ni^{II}_{Cl}}$.

$\mathbf{Ni^{II}_{Cl}}$ is reduced to a Ni(0) species by two consecutive electron injections expected to fill the $d_{x^2-y^2}$ orbital (Scheme 3.2) as corroborated by reduced states computed on a $[Ni(PN_3P)Br_2]$ complex bearing a close PN_3P ligand (R_N = H or Me, R_P = Ph).[6]

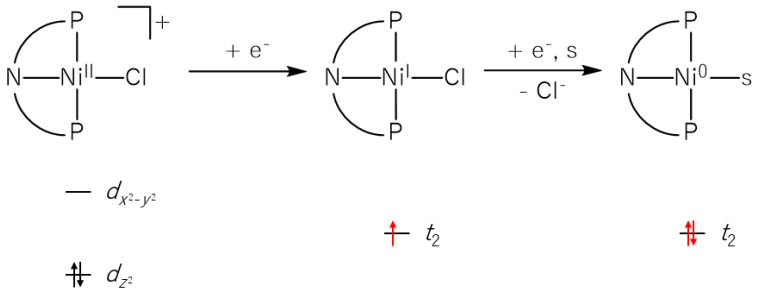

Scheme 3.2. Proposed electrochemical pathway and schematic frontier orbital diagrams for the reduction of $\mathbf{Ni^{II}_{Cl}}$ in MeCN under argon atmosphere (s = MeCN).

The potential gap between the +I and 0 oxidation states [$E^{0}(Ni^{I/0}) - E^{0}(Ni^{II/I}) = -430$ mV] is tighter compared to $\mathbf{Co^{II}_{Cl}}$, consistent with a two-fold electronic increment in the same high-lying $d_{x^2-y^2}$ orbital. Upon reduction to the Ni(0) state, Cl^{-}/MeCN substitution would likely form an energetically favorable tetrahedral d^{10} 18 VE $[Ni^{0}L(MeCN)]$ complex.

3.2.1.5 [Cu**L**Cl] & [Cu**L**I]

$\mathbf{Cu}^{I}_{Cl}$ exhibits a reversible redox event at E^0 = –0.09 V_{Fc} and an irreversible reduction wave at $E_{p,c}$ = –2.35 V_{Fc} (Figure 3.6, solid line). $\mathbf{Cu}^{I}_{I}$ shows almost identical redox features at slightly shifted potentials (E^0 = –0.03 V_{Fc} and $E_{p,c}$ = –2.27 V_{Fc}; Figure 3.6, dashed line). Hence, similar electrochemical processes are expected for both complexes.

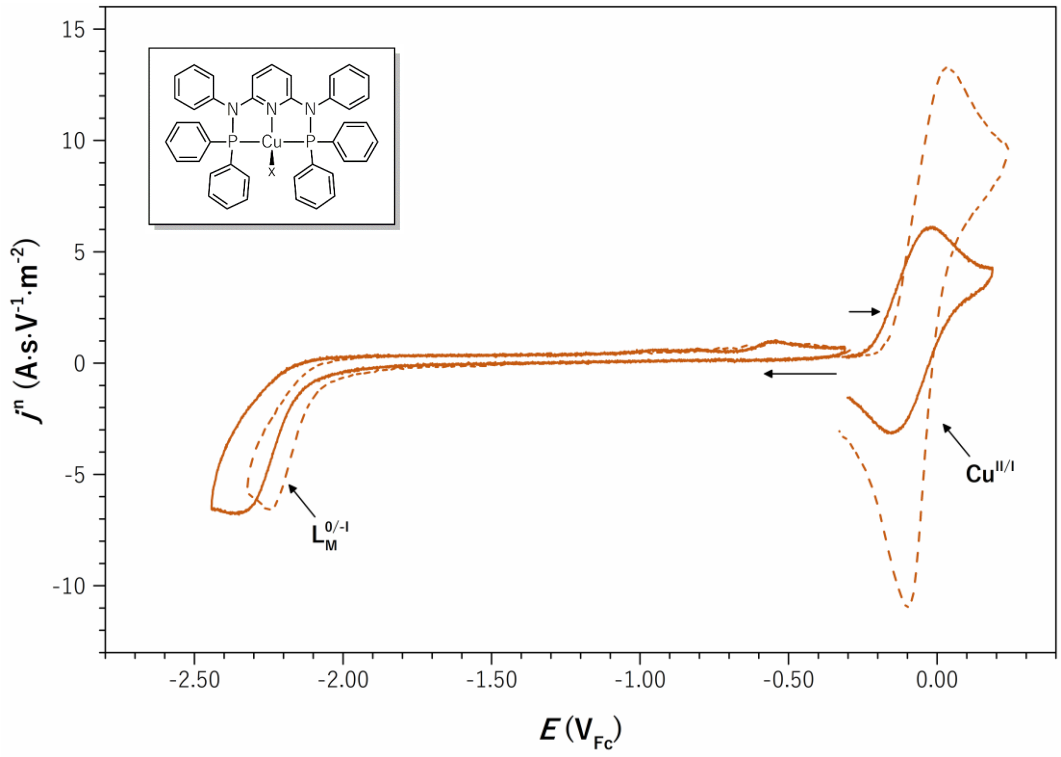

Figure 3.6. CVs of $\mathbf{Cu}^{I}_{x}$ with x = Cl (solid line) or I (dashed line) in cathodic (←) and anodic (→) directions.

Assignment of the reversible wave to the $Cu^{II/I}$ couple indicates that the +II oxidation state can be accessed by electrochemical means. This finding is in stark contrast to the challenging synthesis of the Cu(II) species in section 2.2.1.5. The Cu(II) state is possibly only stable in the time scale of the CV experiment and decomposes within the reaction time of the synthesis.

Putative Cu(0) complexes, as the products of metal-centered reduction processes, are likely to decompose into heterogeneous Cu(0) deposits at the electrode surface. However, no substantial oxidative desorption peak (for reference, see Figure 3.7, dashed line) commonly accounting for the oxidation of such Cu(0) deposits could be observed in the backward scan of the investigated potential window, regardless of the scan rate. Moreover, the Cu(I) species already exist in a d^{10} electron configuration with all d orbitals fully occupied. Therefore, the irreversible reduction waves are more likely to represent a ligand- rather than metal-centered reduction [eq. (3.9)].

E: $$[Cu^{I}\mathbf{L}X] + e^- \rightleftarrows [Cu^{I}\mathbf{L}^{(-I)}X]^- \ (X = Cl, I) \qquad (3.9)$$

3.2.1.6 [Zn**L**Cl$_2$] & [Zn**L**(OTf)$_2$]

CV analysis of $\mathbf{Zn}^{\mathbf{II}}_{\mathbf{Cl}}$ revealed an irreversible reduction wave at $E_{p,c}$ = –2.56 V_{Fc} (Figure 3.7, solid line). d^{10} Zn ions are usually redox-innocent in accessible reduction windows, and the corresponding complexes are thus commonly used to identify the redox behavior of the coordinated ligand system.[7]

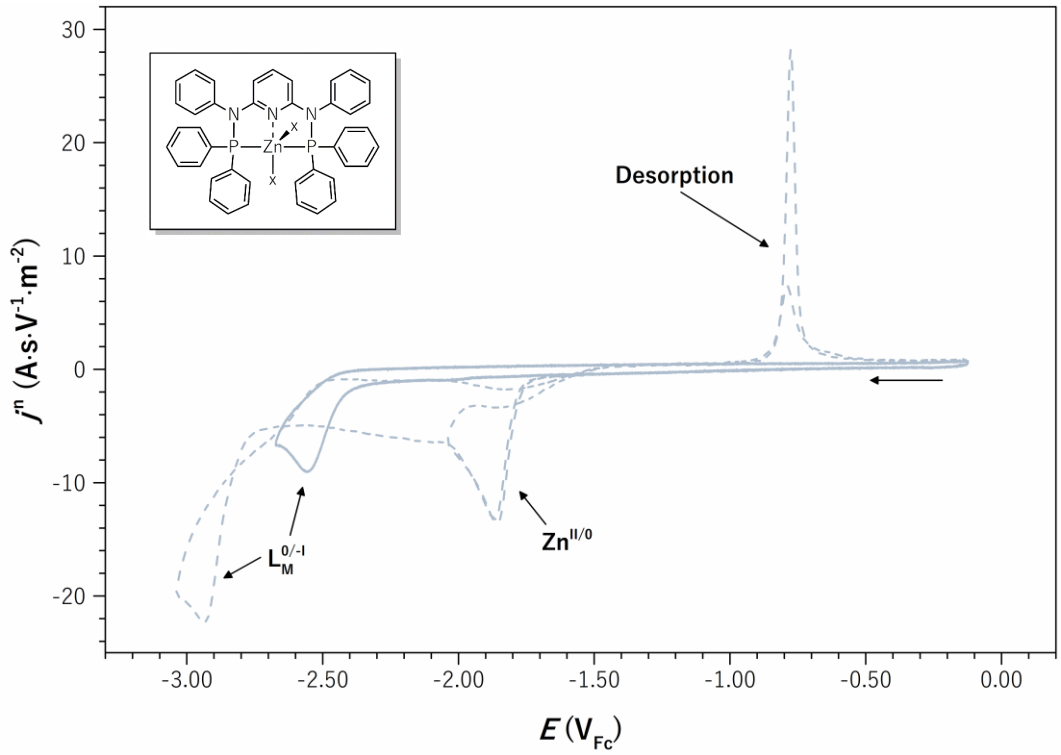

Figure 3.7. CVs of $\mathbf{Zn}^{\mathbf{II}}_{\mathbf{x}}$ with x = Cl (solid line) or OTf (dashed line) at varying potential windows.

The fact that $\mathbf{Zn}^{\mathbf{II}}_{\mathbf{Cl}}$ already exists in a stable 18 electron configuration with the 3d orbitals fully occupied renders a metal-centered reduction unlikely. The similarity to the $\mathbf{Cu}^{\mathbf{I}}_{\mathbf{x}}$ d^{10} complexes with a single irreversible reduction wave at low potential suggests an electron transfer to the ligand [eq. (3.10)].

E: $$[Zn^{II}\mathbf{L}Cl_2] + e^- \rightleftarrows [Zn^{II}\mathbf{L}^{(-I)}Cl_2]^- \qquad (3.10)$$

The cathodic scan of $\mathbf{Zn}^{\mathbf{II}}_{\mathbf{OTf}}$ displays two irreversible reduction waves at $E_{p,c}$ = –1.86 V_{Fc} and $E_{p,c}$ = –2.94 V_{Fc} (Figure 3.7, dashed lines). The trace of the former wave is crossed by that of the backward anodic scan and followed by a sharp oxidative desorption peak at a higher potential ($E_{p,a}$ = –0.79 V_{Fc}). Observing a line crossing and a desorption wave are diagnostic of electrodeposition upon reduction. Therefore, $\mathbf{Zn}^{\mathbf{II}}_{\mathbf{OTf}}$ likely undergoes a two-electron reduction to Zn(0) and decomposition into (nanoparticulate) Zn(0) deposits on the electrode surface [eq. (3.11)

and (3.12)]. Solution dissociation of $\mathbf{Zn}^{\mathbf{II}}_{\mathbf{OTf}}$ into a dicationic complex would rationalize the positive shift in reduction potential compared to $\mathbf{Zn}^{\mathbf{II}}_{\mathbf{Cl}}$.

E: $$[Zn^{II}\mathbf{L}(MeCN)_2]^{2+} + 2\ e^- \rightleftarrows [Zn^0\mathbf{L}(MeCN)_2] \quad (3.11)$$

C: $$[Zn^0\mathbf{L}(MeCN)_2] \rightleftarrows Zn(0)\downarrow + \mathbf{L} + 2\ MeCN \quad (3.12)$$

The more negatively shifted reduction wave could correspond to an electron transfer to the residual coordinated ligand.

3.2.2 Acetonitrile Complexes

The cyclic voltammograms of the $\mathbf{M}^{\mathbf{II}}_{\mathbf{s}}$ complexes at 100 mV·s^{-1} under argon are discussed below.

3.2.2.1 $[Fe\mathbf{L}(MeCN)_3](BF_4)_2$

The CV responses of $\mathbf{Fe}^{\mathbf{II}}_{\mathbf{s}}$ and $\mathbf{Fe}^{\mathbf{II}}_{\mathbf{s}}$**-OTf** proved to be similar since both complexes comprise an identical inner coordination sphere. Explanations will be based on $\mathbf{Fe}^{\mathbf{II}}_{\mathbf{s}}$ to rule out the effects of the outer coordination sphere when comparing the iron species to other $\mathbf{M}^{\mathbf{II}}_{\mathbf{s}}$ complexes.

$\mathbf{Fe}^{\mathbf{II}}_{\mathbf{s}}$ exhibits two narrowly separated irreversible reduction waves at $E_{p,c} = -1.72\ V_{Fc}$ and $-1.97\ V_{Fc}$ (Figure 3.8). These events are attributed to the $Fe^{II/I}$ and $Fe^{I/0}$ reductions accompanied by chemical steps, i.e., loss of acetonitrile ligands and significant structural changes.

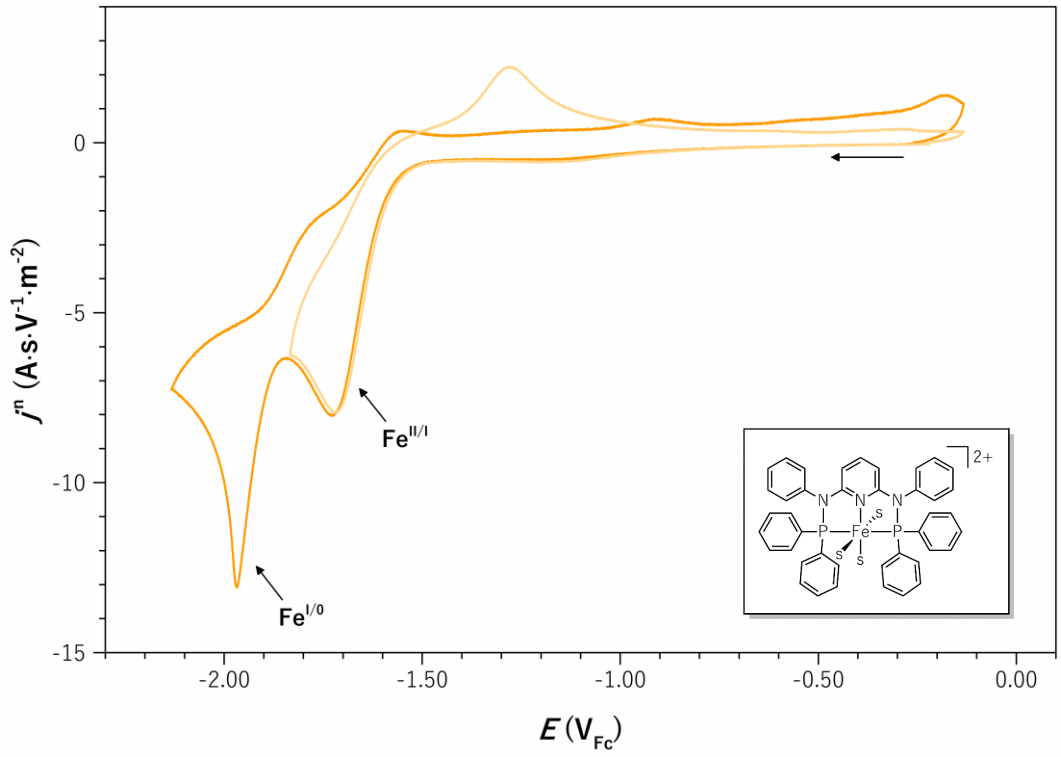

Figure 3.8. CVs of $\mathbf{Fe}^{\mathbf{II}}_{\mathbf{s}}$ at varying potential windows.

The corresponding back-oxidation wave of the $Fe^{I/0}$ couple stays inaccessible for scan rates up to 100 $V \cdot s^{-1}$, suggesting that the follow-up chemical events are fast. The re-oxidation wave located at a considerably more positive potential ($E_{p,a}$ = –1.28 V_{Fc}) when reversing the potential scan between the first and second reduction wave (Figure B.3) supports the occurrence of structural reorganization upon reduction. This oxidation wave vanishes at low scan rates when the scan is reversed after the second reduction wave (Figure B.4).

The sharp, peak-like appearance of the $Fe^{I/0}$ wave significantly diverts from the diffusion-controlled shape of a typical cyclic voltammetry wave. Hence, a more detailed analysis of the underlying processes supported by literature precedents is presented below.

a) Monomeric Pathway

With $\mathbf{Fe_s^{II}}$ adopting a distorted octahedral geometry in a d^6 low-spin configuration, the electron added upon reduction from Fe(II) to Fe(I) [eq. (3.13)] would populate an energy-rich e_g antibonding orbital. An energetically more beneficial possibility comprises the release of a solvent ligand and the formation of a d^7 $[Fe^{I}\mathbf{L}(MeCN)_2]^+$ complex in SBP geometry [eq. (3.14)] as obtained for the isoelectronic $\mathbf{Co_s^{II}}$.

$$\mathbf{E}: \quad [Fe^{II}\mathbf{L}(MeCN)_3]^{2+} + e^- \rightleftarrows [Fe^{I}\mathbf{L}(MeCN)_3]^+ \tag{3.13}$$

$$\mathbf{C}: \quad [Fe^{I}\mathbf{L}(MeCN)_3]^+ \rightleftarrows [Fe^{I}\mathbf{L}(MeCN)_2]^+ + MeCN \tag{3.14}$$

Further reduction of the resulting Fe(I) complex would lead to the formation of an Fe(0) d^8 species. Although coordinated by carbonyl ligands, the KIRCHNER group presented several examples of pyridine-based Fe(0) pincer complexes in pentacoordinate structures.[8] Under the assumption of a similar $\mathbf{M}L_5$ structure in this case [eq. (3.15)], a mere one-electron reduction and geometric changes of the already pentacoordinate $[Fe^{I}\mathbf{L}(MeCN)_2]^+$ species would not justify the observed CV behavior. Hence such a monomeric pathway can be excluded.

$$\mathbf{E}: \quad [Fe^{I}\mathbf{L}(MeCN)_2]^+ + e^- \rightleftarrows [Fe^{0}\mathbf{L}(MeCN)_2] \tag{3.15}$$

b) Dimerization

The WIEGHARDT group reported the chemical reduction of $[Fe(tim)(MeCN)_2]^{2+}$ (tim = 2,3,9,10-tetramethyl-1,4,8,11-tetraazacyclotetradeca-1,3,8,10-tetraene, Figure 3.9A) to the $[\{Fe(tim)\}_2]$ dimer based on computational and spectroscopic evidence as well as X-ray structure determination.[9] Cyclic voltammetry performed on the starting complex revealed a reduction pattern and wave shapes similar to those of $\mathbf{Fe_s^{II}}$ (Figure 3.9B) which supports the hypothesis of dimerization for the latter example as well. Their investigations yet revealed that the reduction of

$[Fe(tim)(MeCN)_2]^{2+}$ is purely ligand-centered, which poses a severe difference to the redox-inert **L** (*vide supra*).

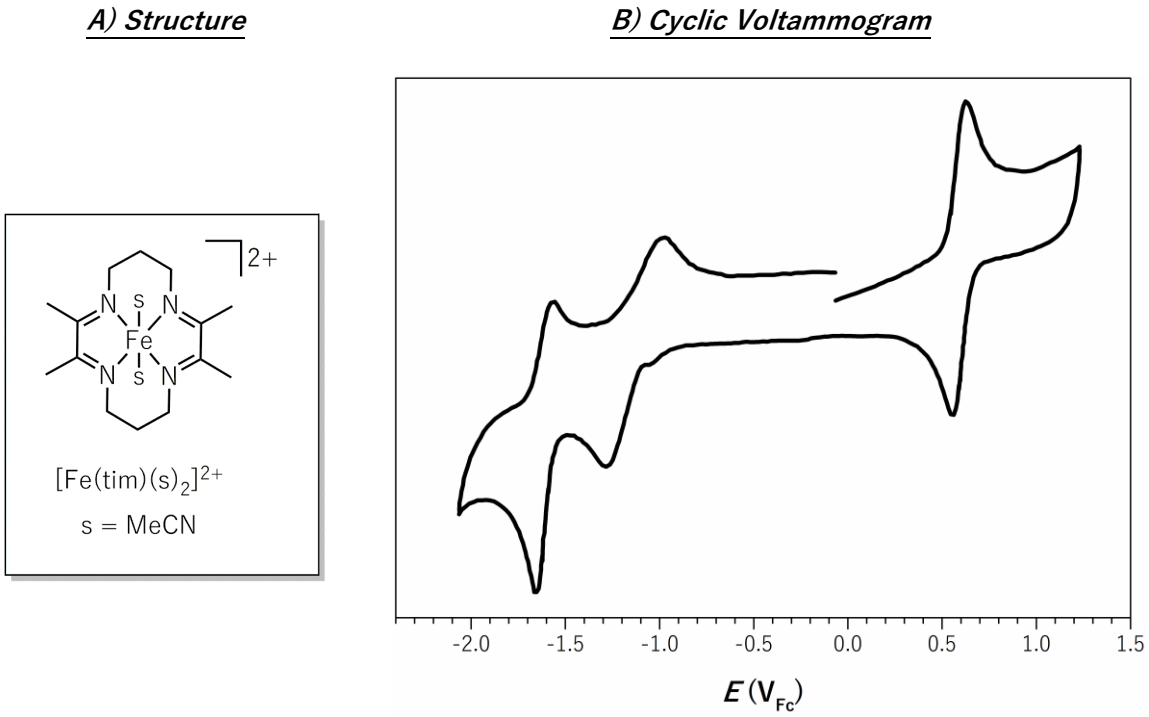

Figure 3.9. (A) Structure and (B) cyclic voltammogram of $[Fe(tim)(MeCN)_2]^{2+}$ reported by HESS et al. Adapted with permission from ref. [9].

c) Dimerization + Dimer Break-Up

Based on the analysis of the waves above, the **E** step in eq. (3.13) could also be followed by the generation of a dimeric $[Fe^{I}_2\mathbf{L}_2(MeCN)_{2m}]^{2+}$ compound, either as an Fe-Fe bonded or an MeCN-bridged one [eq. (3.16)].

$$\mathbf{C}: \quad 2\,[Fe^{I}\mathbf{L}(MeCN)_3]^{+} \rightleftarrows [Fe^{I}_2\mathbf{L}_2(MeCN)_{2m}]^{2+} + x\,MeCN \tag{3.16}$$

The oxidation wave at $-1.28\ V_{Fc}$ is tentatively attributed to the oxidation of such dimeric species. The second reduction wave can then be assigned to the reduction of the putative $[Fe^{I}_2\mathbf{L}_2(MeCN)_{2m}]^{2+}$ dimer into an $[Fe^{0}_2\mathbf{L}_2(MeCN)_{2m'}]$ species [eq. (3.17) and (3.18)].

$$\mathbf{E}: \quad [Fe^{I}_2\mathbf{L}_2(MeCN)_{2m}]^{2+} + 2\,e^{-} \rightleftarrows [Fe^{0}_2\mathbf{L}_2(MeCN)_{2m}] \tag{3.17}$$

$$\mathbf{C}: \quad [Fe^{0}_2\mathbf{L}_2(MeCN)_{2m}] \rightleftarrows [Fe^{0}_2\mathbf{L}_2(MeCN)_{2m'}] + y\,MeCN \tag{3.18}$$

When the scan reversal is cathodic to this second reduction, the disappearance of the re-oxidation wave at $-1.28\ V_{Fc}$ for low sweep rates suggests the transformation of the postulated $[Fe^{0}_2\mathbf{L}_2(MeCN)_{2m'}]$ dimer into monomeric Fe(0) species or other degradation products [e.g., Fe(0) deposits].

d) Disproportionation

Another potential reaction route upon reduction of $\mathbf{Fe_s^{II}}$ was reported by SONG et al. for the pyridine-based $[Fe(NNN)(^tBuCN)_3]^{2+}$ pincer complex shown in Figure 3.10.[10]

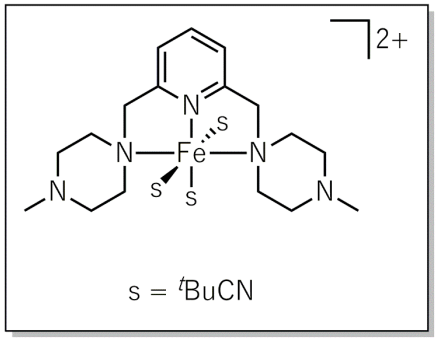

Figure 3.10. Structure of $[Fe(NNN)(^tBuCN)_3]^{2+}$ reported by SONG et al.[10]

NMR analysis after chemical reduction of the Fe(II) species with 1 equiv. of Na(Hg) revealed two sets of diamagnetic signals, which were assigned to the starting material and the two-electron reduced $[Fe^0(NNN)(^tBuCN)_2]$ complex. Hence, the authors deduced the disproportionation (DISP) mechanism described in eq. (3.19) and (3.20) at the Fe(I) stage.

$$\mathbf{E}: \quad [Fe^{II}(NNN)(^tBuCN)_3]^{2+} + e^- \rightleftarrows [Fe^{I}(NNN)(^tBuCN)_3]^{+} \tag{3.19}$$

$$\mathbf{C}: \quad [Fe^{I}(NNN)(^tBuCN)_3]^{+} \rightleftarrows \tfrac{1}{2}\,[Fe^{0}(NNN)(^tBuCN)_2] + \tfrac{1}{2}\,[Fe^{II}(NNN)(^tBuCN)_3]^{2+} + \tfrac{1}{2}\,{}^tBuCN \tag{3.20}$$

A similar mechanism is conceivable for $\mathbf{Fe_s^{II}}$, although CV analysis of $[Fe(NNN)(^tBuCN)_3]^{2+}$ revealed two quasi-reversible reduction events instead of, e.g., the sharp $Fe^{I/0}$ wave observed for $\mathbf{Fe_s^{II}}$. This discrepancy, however, could be explained by the different auxiliary ligands (MeCN vs. ^{t}BuCN). SONG et al. report the instability of $[Fe(NNN)(MeCN)_3]^{2+}$ under electrochemical conditions but neither specify the reason nor the observed CV response.

Although the dimeric pathways presented above cannot be excluded completely, the DISP mechanism appears favored because the observations were made on a pyridine-based pincer structure. In this context, it is intriguing to substitute MeCN with ^{t}BuCN in $\mathbf{Fe_s^{II}}$ to achieve a better comparison with the results of SONG et al.

3.2.2.2 $[Co\mathbf{L}(MeCN)_2](BF_4)_2$

The CV response of $\mathbf{Co_s^{II}}$ consists of a reversible reduction wave at $E^0 = -0.93\ V_{Fc}$ ($\Delta E_p = 65$ mV) and an irreversible process at a more negative potential of $E_{p,c} = -1.98\ V_{Fc}$ (Figure 3.11), attributed to the two one-electron reduction couples $Co^{II/I}$ and $Co^{I/0}$, respectively. Extension of the

potential range reveals an additional irreversible reduction wave at $E_{p,c}$ = –2.56 V_{Fc}, suggested to originate from the reduction of the coordinated ligand system.

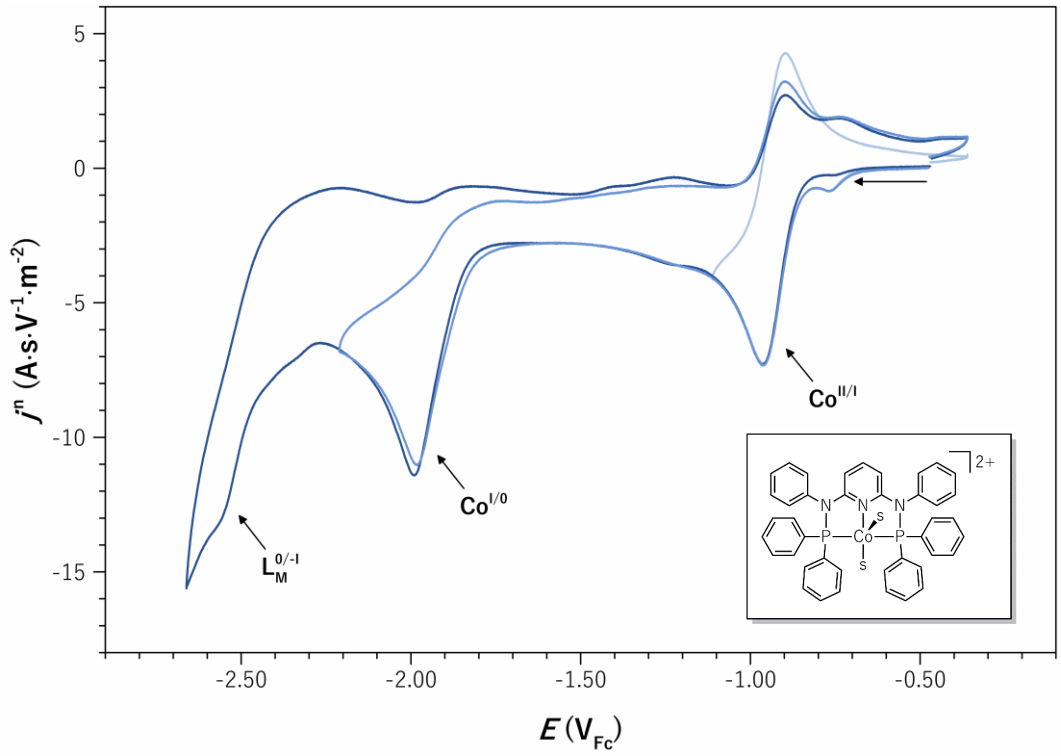

Figure 3.11. Cyclic voltammograms of $\mathbf{Co_s^{II}}$ at varying potential windows.

The $Co^{II/I}$ wave stays reversible up to the maximum applied scan rate of 100 V·s^{-1} (Figure B.5). Although this behavior could indicate a single **E** step without substantial alterations in the coordination sphere, the addition of another electron into a high-lying d_{z^2} orbital of a potential square-based pyramidal $[Co^{I}\mathbf{L}(MeCN)_2]^+$ species appears unlikely concerning the strong field-splitting ability of the MeCN ligands. In contrast to this, the loss of a solvent and the formation of a square planar $[Co^{I}\mathbf{L}(MeCN)]^+$ d^8 16 VE complex $\mathbf{Co_s^{I}}$ in an **EC** sequence would be energetically favorable [see Scheme 3.3, eq. (3.21) and (3.22)].

E: $$[Co^{II}\mathbf{L}(MeCN)_2]^{2+} + e^- \rightleftarrows [Co^{I}\mathbf{L}(MeCN)_2]^+ \quad (3.21)$$

C: $$[Co^{I}\mathbf{L}(MeCN)_2]^+ \rightleftarrows [Co^{I}\mathbf{L}(MeCN)]^+ + MeCN \quad (3.22)$$

The structure found for the isoelectronic $\mathbf{Ni_s^{II}}$ (section 3.2.2.3) and a literature report by SHAFFER et al. for the related pincer complex $[Co^{I}(PN_3P)(MeCN)]^+$ (R_N = H, R_P = ^{t}Bu) support this conclusion.[3] Moreover, retention of the reversibility of the wave in the predominant **EC** sequence presented above is only possible in the DE zone of the kinetic zone diagram (further explanations are given in Appendix D, Figure D.4) and with the equilibrium constant K for the

chemical step in eq. (3.22) being small. *K* likely fulfills this criterion regarding the excess solvent that rather shifts the acetonitrile equilibrium in the direction of the bis-MeCN species.

The irreversibility of the subsequent reduction wave of $\mathbf{Co_s^I}$ even at sweep rates of up to 100 $V \cdot s^{-1}$ (Figure B.6) hints toward another **EC** sequence [eq. (3.23) and (3.24)].

E: $$[Co^{I}\mathbf{L}(MeCN)]^{+} + e^{-} \rightleftarrows [Co^{0}\mathbf{L}(MeCN)] \quad (3.23)$$

C: $$[Co^{0}\mathbf{L}(MeCN)] \rightleftarrows [Co^{0}\mathbf{L}(\eta^{2}\text{-}MeCN)] \quad (3.24)$$

Further loss of a ligand during the chemical step would lead to a d^9 15 VE complex $[Co^{0}\mathbf{L}]$ of questionable stability. Hence, the irreversible wave rather constitutes the CV response to a significant geometric change. Upon reduction, the additional electron would be forced to populate an energetically very high-lying $d_{x^2-y^2}$ orbital in the SP structure proposed for $\mathbf{Co_s^I}$. Orbital reorganization into a cycloimine structure (Scheme 3.3) similar to that of $\mathbf{Co_{Cl}^{II}}$ avoids this high-energy state, hence, posing the more favorable option. The supposedly fast bond rearrangement might then induce the independence of the $Co^{I/0}$ wave shape from the scan rate in CV analysis.

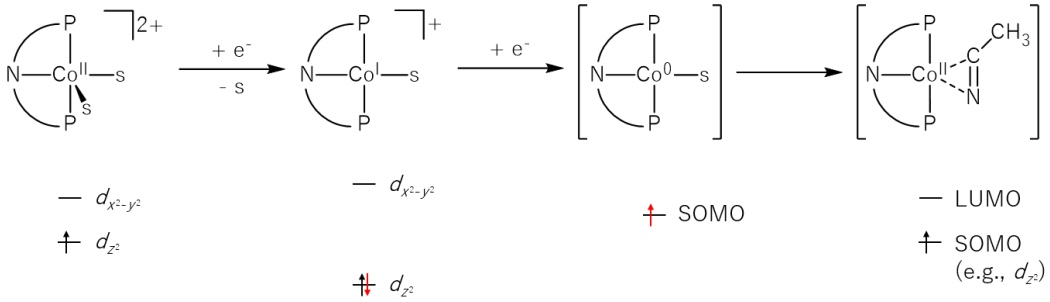

Scheme 3.3. Proposed electrochemical pathway and schematic frontier orbital diagrams for the reduction of $\mathbf{Co_s^{II}}$ in MeCN under argon atmosphere (s = MeCN).

3.2.2.3 [Ni**L**(MeCN)](BF$_4$)$_2$

$\mathbf{Ni_s^{II}}$ exhibits a similar but anodically shifted reduction sequence with a reversible reduction wave at $E^0 = -0.75\ V_{Fc}$ ($\Delta E_p = 66$ mV) and two irreversible processes at $E_{p,c} = -1.63\ V_{Fc}$ and $E_{p,c} = -2.43\ V_{Fc}$ (Figure 3.12). The first two electrons are likely transferred to the metal, whereas $\mathbf{L_M}$ takes up the third one (see section 3.2.1.4).

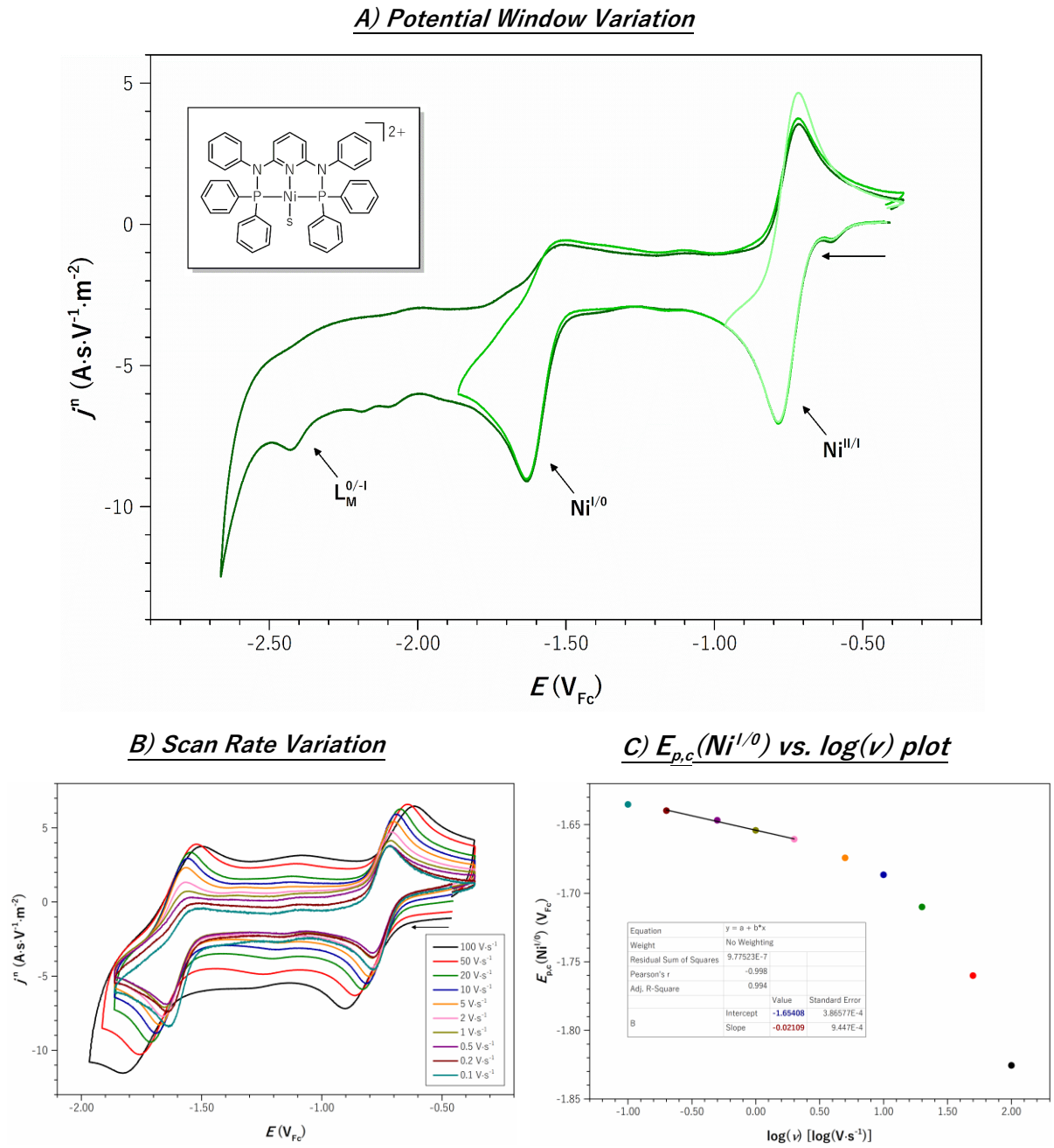

Figure 3.12. Cyclic voltammograms under variation of (A) potential window and (B) scan rate, as well as (C) $E_{p,c}(Ni^{I/0})$ vs. log(ν) plot of $\mathbf{Ni_s^{II}}$.

Reduction at the $Ni^{II/I}$ wave is coupled to the association of a solvent molecule as corroborated by a molecular structure (Figure A.62) isolated after the chemical reduction of $\mathbf{Ni_s^{II}}$ with cobaltocene in MeCN at a potential of –0.94 V_{SCE}[11] (corrected to approx. –1.32 V_{Fc}[12]). The **CE** sequence in eq. (3.25) and (3.26) is proposed based on the scan-rate dependent measurements and further analyses in section 3.5.3.

C: $$[Ni^{II}\mathbf{L}(MeCN)]^{2+} + MeCN \rightleftarrows [Ni^{II}\mathbf{L}(MeCN)_2]^{2+} \quad (3.25)$$

E: $$[Ni^{II}\mathbf{L}(MeCN)_2]^{2+} + e^- \rightleftarrows [Ni^{I}\mathbf{L}(MeCN)_2]^{+} \quad (3.26)$$

The geometry index τ_5 = 0.51 locates $\mathbf{Ni_s^I}$ intermediate to the ideal SBP or TBP geometries. Based on the SBP geometry, strong distortion from the basal plane decreases the energy of the fully occupied d_{z^2} orbital and lowers the $d_{x^2-y^2}$ SOMO in the d^9 electron configuration (Scheme 3.4).

This gain in energy might also explain the preferred formation of a 19 VE complex over a putative 17 VE T_d structure. In the latter, the high field splitting would have increased the energy level of the degenerate d_{xy}, d_{xz}, and d_{yz} orbitals populated with five electrons in sum.

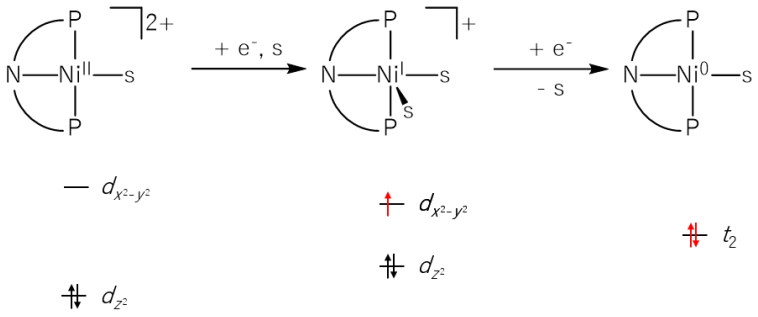

Scheme 3.4. Proposed electrochemical pathway and schematic frontier orbital diagrams for the reduction of $\mathbf{Ni_s^{II}}$ in MeCN under argon atmosphere (s = MeCN).

Further potential reduction grants access to the irreversible $Ni^{I/0}$ wave, the reversibility of which can be restored at scan rates above 5 $V \cdot s^{-1}$ (ΔE_p = 109 mV, Figure 3.12B). The $E_{p,c}$ vs. log(ν) plot decays linearly with a slope of –21.1 $mV \cdot \log(\nu)^{-1}$ (Figure 3.12C) in the KP zone, suggesting an **EC** mechanism.

Upon reduction, $\mathbf{Ni_s^I}$ likely expels one of its AL and generates the $[Ni^0\mathbf{L}(MeCN)]$ species, putatively in a tetrahedral geometry favored for d^{10} $\mathbf{M}L_4$ complexes [eq. (3.27) and (3.28)].[13]

E: $$[Ni^I\mathbf{L}(MeCN)_2]^+ + e^- \rightleftarrows [Ni^0\mathbf{L}(MeCN)_2] \quad (3.27)$$

C: $$[Ni^0\mathbf{L}(MeCN)_2] \rightleftarrows [Ni^0\mathbf{L}(MeCN)] + MeCN \quad (3.28)$$

3.3 Reducibility of 3d Transition Metal Centers

The potentials of the redox events found for the $\mathbf{M}_{\mathbf{x}}^{\mathbf{z}}$ complexes from cyclic voltammetry under an inert atmosphere are summarized in Table 3.1.

Table 3.1. Redox potentials and shapes of the CV waves of the $\mathbf{M}_{\mathbf{x}}^{\mathbf{z}}$ complexes. E^0 values are reported for reversible (rev.), $E_{p,c}$ values for irreversible (irrev.) waves.

	$\mathbf{M}^{\mathbf{II/I}}$			$\mathbf{M}^{\mathbf{I/0}}$			$\mathbf{L}_{\mathbf{M}}^{\mathbf{0/-I}}$
	$E^0/E_{p,c}$ (V_{Fc})	shape	ΔE_p (mV)	$E^0/E_{p,c}$ (V_{Fc})	shape	ΔE_p (mV)	$E_{p,c}$ (V_{Fc})
$\mathbf{Mn}_{\mathbf{CO,Br}}^{\mathbf{I}}$ [a]	-	-	-	-	-	-	–2.64
$\mathbf{Fe}_{\mathbf{s}}^{\mathbf{II}}$	–1.72	irrev.	-	–1.97	irrev.	-	-
$\mathbf{Co}_{\mathbf{Cl}}^{\mathbf{II}}$	–1.21	rev.	94	–1.98	irrev.	-	–2.61
$\mathbf{Co}_{\mathbf{s}}^{\mathbf{II}}$	–0.93	rev.	65	–1.98	irrev.	-	–2.56
$\mathbf{Ni}_{\mathbf{Cl}}^{\mathbf{II}}$	–1.16	rev.	69	–1.59[b]	rev.	114	–2.41
$\mathbf{Ni}_{\mathbf{s}}^{\mathbf{II}}$	–0.75	rev.	66	–1.63[b]	rev.	109	–2.43
$\mathbf{Cu}_{\mathbf{Cl}}^{\mathbf{I}}$	–0.09	rev.	130	-	-	-	–2.35
$\mathbf{Cu}_{\mathbf{I}}^{\mathbf{I}}$	–0.03	rev.	128	-	-	-	–2.27
$\mathbf{Zn}_{\mathbf{Cl}}^{\mathbf{II}}$	-	-	-	-	-	-	–2.56
$\mathbf{Zn}_{\mathbf{OTf}}^{\mathbf{II}}$	–1.86[c]	irrev.	-	-	-	-	–2.94

[a] Recorded in DMF, 0.5 mM $\mathbf{Mn}_{\mathbf{CO,Br}}^{\mathbf{I}}$. [b] ν = 5 V·s^{-1}. [c] Likely $Zn^{II/0}$ reduction.

In the series of complexes under scrutiny, metal-centered reductions are inaccessible for d^{10} configurations ($\mathbf{Cu}_{\mathbf{Cl/I}}^{\mathbf{I}}$ and $\mathbf{Zn}_{\mathbf{Cl}}^{\mathbf{II}}$), likely because of the combined saturation of the 3d metal orbitals and the valence shell (Table 3.2). Reducing the ligand within the complexes' coordination sphere is yet possible and produces a CV response even for the otherwise redox-inactive Cu and Zn metal centers. Nonetheless, **L** remains a redox-innocent ligand since reduction requires very negative potentials below –2.2 V_{Fc}.

Although deviating from a d^{10} configuration, such a ligand-centered reduction event is the only CV response of the low-spin d^6 $\mathbf{Mn}_{\mathbf{CO,Br}}^{\mathbf{I}}$ complex as well. The strong field-splitting carbonyl ligands likely destabilize the unoccupied e_g orbitals of the metal center to an extent at which ligand reduction is energetically favored over metal reduction, though at very cathodic potentials (< –2.5 V_{Fc}). A generalization of this hypothesis would then conclude that CO-coordinated Mn complexes generally require redox-active ligands (e.g., bipyridine[14]) or a cationic state[15]

to be active in CO_2 electroreduction at low overpotential. This point is in sharp contrast to thermochemical CO_2 hydrogenation passing through the Mn-H pathway, where Mn(I) carbonyl complexes based on redox-innocent ligands are highly efficient catalysts.[16]

Table 3.2. Observed electronic properties and electrochemical behavior of $\mathbf{M}_{\mathbf{x}}^{\mathbf{z}}$ complexes.

	$\mathbf{d}^{n}$, n =	VE	$\mathbf{M}^{II/I}$	$\mathbf{M}^{I/0}$	$\mathbf{L}_{\mathbf{M}}^{0/-I}$	Dec.[a]
$\mathbf{Mn}_{\mathbf{CO,Br}}^{\mathbf{I}}$	6 (ls)	18	-	-	✓	-
$\mathbf{Fe}_{\mathbf{Cl}}^{\mathbf{II}}$[b]	6 (hs)	16	-	-	-	-
$\mathbf{Fe}_{\mathbf{s}}^{\mathbf{II}}$	6 (ls)	18	✓	✓	✓	-
$\mathbf{Co}_{\mathbf{s/Cl}}^{\mathbf{II}}$	7 (ls)	17	✓	✓	✓	-
$\mathbf{Ni}_{\mathbf{Cl}}^{\mathbf{II}}$	8 (ls)	16	✓	✓	✓	-
$\mathbf{Ni}_{\mathbf{s}}^{\mathbf{II}}$	8 (ls)	18	✓	✓	✓	-
$\mathbf{Cu}_{\mathbf{Cl/I}}^{\mathbf{I}}$	10	18	✓	-	✓	-
$\mathbf{Zn}_{\mathbf{Cl}}^{\mathbf{II}}$	10	18	-	-	✓	-
$\mathbf{Zn}_{\mathbf{OTf}}^{\mathbf{II}}$	10	20	-	-	-	✓

[a] Dec. = decomposition. [b] $\mathbf{Fe}_{\mathbf{Cl}}^{\mathbf{II}}$ partially converts in MeCN and was not electrochemically analyzed in the solvent.

A deviation from the d^{10} state unlocks metal-centered reduction processes for complexes with unsaturated d orbitals and less pronounced crystal field splitting, as observed in the cases of $\mathbf{Fe}_{\mathbf{s}}^{\mathbf{II}}$, $\mathbf{Co}_{\mathbf{x}}^{\mathbf{II}}$, and $\mathbf{Ni}_{\mathbf{x}}^{\mathbf{II}}$ (x = MeCN or Cl; Table 3.2). Notably, Fe, Co, and Ni complexes are among the most prominent eCO_2r catalysts.[17] Ligand-centered reductions at mildly negative potentials are commonly proposed for complexes synthesized from these metals (e.g., with polypyridine ligands having delocalized, low-energy π* orbitals).[17-18] Here, however, comparison with the Mn, Cu, or Zn complexes allows the assignment of the first two reductions solely to metal-centered events.

Dimer formation differentiates the CV pattern of $\mathbf{Fe}_{\mathbf{s}}^{\mathbf{II}}$ from those of the Co and Ni complexes. The latter two likely undergo similar reduction sequences down to their **M**(0) state but via different intermediates depending on the starting structure (see $\mathbf{Co}_{\mathbf{s}}^{\mathbf{II}}$ and $\mathbf{Ni}_{\mathbf{s}}^{\mathbf{II}}$). The d^7 vs. d^8 electron configurations of $\mathbf{Co}_{\mathbf{Cl}}^{\mathbf{II}}$ and $\mathbf{Ni}_{\mathbf{Cl}}^{\mathbf{II}}$ (sharing the same initial geometry) cause the population of different orbitals upon electron uptake and, hence, different energy barriers as reflected by the potentials required for the reduction steps.

Comparing complexes of the same metal but differing auxiliary ligands (i.e., Cl^- vs. MeCN) similarly reveals shifting potentials. Therefore, exchange equilibria between the anionic halide ligand Cl^- and the coordinating but labile, neutral solvent ligand MeCN are investigated for their influence on the processes in cyclic voltammetry. Since metal-centered reductions at moderate potentials were observed solely for Fe, Co, and Ni, the analysis of spectator ligand phenomena in the next chapter will be limited to complexes comprising these metals.

Part 2: Dynamic Ligand Equilibria

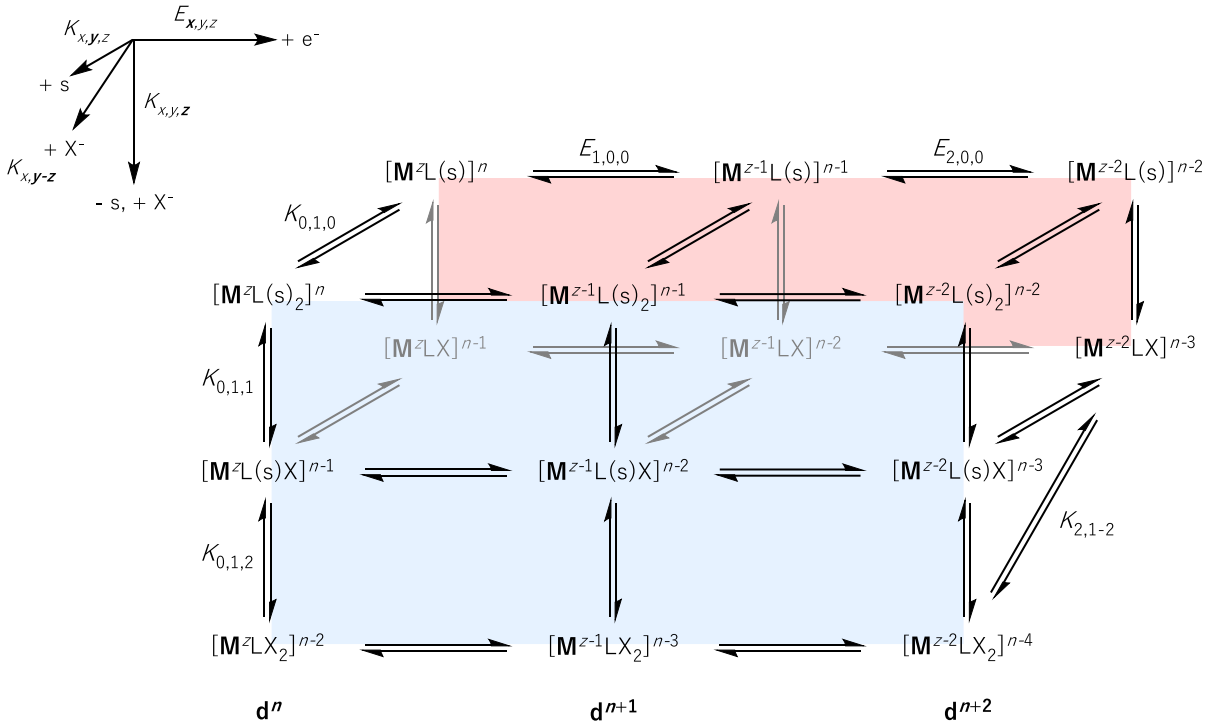

In part 2 of chapter 3, the ligand equilibria affecting the $\mathbf{M_x^{II}}$ (x = MeCN or Cl) complexes of Fe, Co, and Ni under electrochemical conditions will be discussed.

Chloride ligands are added to the $\mathbf{M_s^{II}}$ complexes to understand the electrochemical behavior of the $\mathbf{M_{Cl}^{II}}$ analogs in MeCN. The cyclic voltammetry and NMR spectroscopic analyses are supported by X-ray diffraction of intermediate structures whenever isolable.

Both approaches are combined to assess the degree of displacement of the chemical equilibria linked to electrochemical reduction. Ultimately, this approach allows proposing the most favorable reaction pathways for the $\mathbf{M_x^{II}}$ (x = MeCN or Cl) complexes of Co and Ni under inert conditions in a “cube scheme”.

Additionally, the analysis elucidates the influence of auxiliary ligand effects on the complexes’ reduction behaviors. Switching the CV solvent from MeCN to DMF probes the coordinating ability of the solvent and renders an estimation of the lability of inner-sphere ligands possible.

Since metal halides are readily available precursors for transition metal complexes, many molecular electrocatalysts (e.g., for CO_2 reduction)[2, 19] rely on them. However, contacting these complexes with MeCN – a frequently used solvent in electrochemical applications due to its wide potential window – may lead to (de-)coordination or exchange of the weak field-splitting halides with stronger field-splitting acetonitrile. The modified inner coordination sphere can yet have a severe influence on the electron density of the metal center and its overall redox behavior, which is directly linked to the catalytic performance of the compound.

The analysis of this ligand exchange for the $\mathbf{M}_x^{II}$ series begins with the gradual addition of the chloride source tetrabutylammonium chloride (TBACl) to the MeCN-coordinated $\mathbf{M}_s^{II}$ complexes. As observed in Figure 3.13, the obtained CV results are also applicable to the $\mathbf{M}_{Cl}^{II}$ series, since (almost) identical compositions are achieved after adding two equivalents of Cl^-.

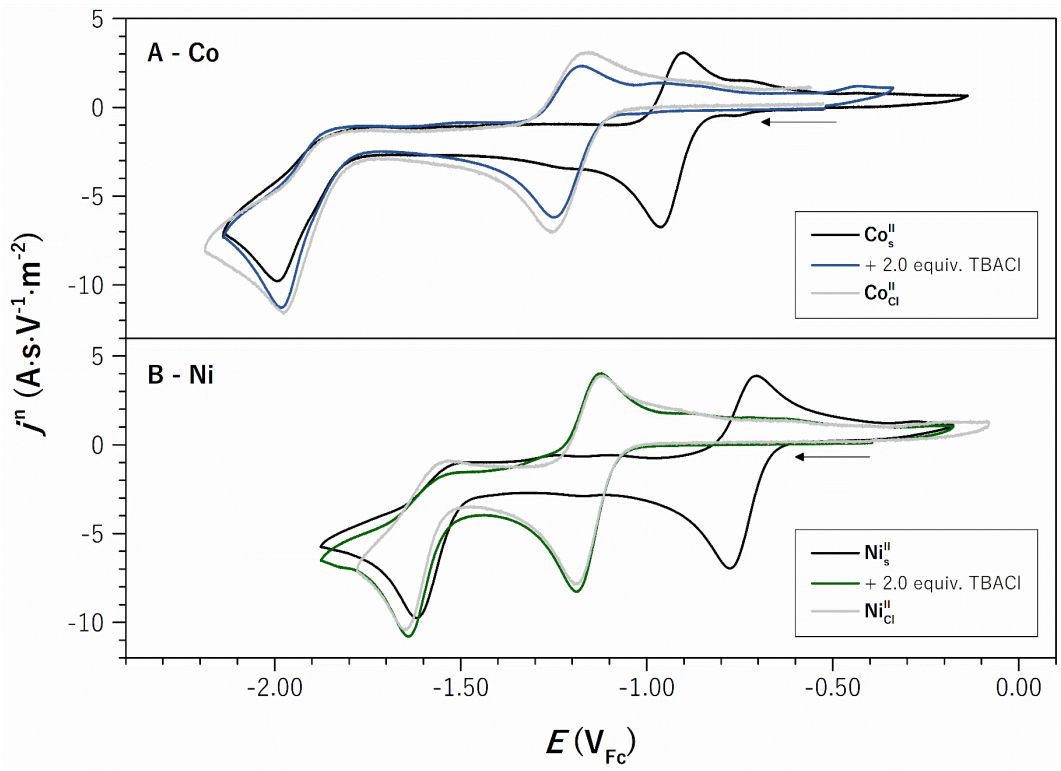

Figure 3.13. CVs of (A) $\mathbf{Co}_s^{II}$ and $\mathbf{Co}_{Cl}^{II}$, (B) $\mathbf{Ni}_s^{II}$ and $\mathbf{Ni}_{Cl}^{II}$, and after adding two equivalents of TBACl to the $\mathbf{M}_s^{II}$ complexes.

This equivalence is likely not applicable to the iron complexes due to the ill-defined composition of $\mathbf{Fe}_{Cl}^{II}$ in MeCN and the putative dimeric reduction pathway for $\mathbf{Fe}_s^{II}$. Nevertheless, the analysis of the ligand equilibria will be conducted analogously to Ni and Co for completeness.

The interconversion of acetonitrile and chloride species in the inner coordination sphere of the $\mathbf{M}_x^{II}$ complexes will be studied by NMR spectroscopy at the initial +II oxidation state before investigating the speciation at reduced states via cyclic voltammetry.

3.4 NMR Spectroscopic Ligand Tracking at the M(II) Stage

When investigating diamagnetic complexes, the association and dissociation of moieties containing NMR active nuclei can be directly described by changes in the chemical shift and coupling pattern/constant of the ligand signal (e.g., MeCN ligands in $\mathbf{Fe_s^{II}}$ and $\mathbf{Ni_s^{II}}$). Moreover, even in paramagnetic complexes (e.g., $\mathbf{Co_x^{II}}$ and $\mathbf{Fe_{Cl}^{II}}$) and for NMR silent auxiliary ligands such as chlorides, chemical shift differences of the NMR active nuclei in the ligand framework can be used to identify different coordinated species. The varying electronic effects of chloride and acetonitrile ligands on the metal center are passed on to the proton and phosphorus atoms in the ligand backbone and can be used to describe the exchange of the auxiliary ligands.

Therefore, NMR studies were performed under the sequential addition of TBACl – a chloride source soluble in organic media and with the same non-coordinating cation as the $TBAPF_6$ electrolyte salt – to the $\mathbf{M_s^{II}}$ complexes in CD_2Cl_2 and CD_3CN. Performing NMR studies in weakly coordinating CD_2Cl_2 prevents the coordinative competition between the deuterated solvent and the chloride ligands and allows the observation of coordinated and free acetonitrile. Although CD_3CN compromises the direct detection of ligand exchange phenomena by exchanging the coordinated acetonitrile, the complementary NMR analysis simulates the conditions during a CV experiment and the competition between acetonitrile(-d_3) and chloride ligands.

3.4.1 $[\mathbf{FeL(MeCN)_3](BF_4)_2}$

Figure 3.14 summarizes the ^{1}H NMR spectra of $\mathbf{Fe_s^{II}}$ recorded in CD_2Cl_2 with added TBACl. Already at half an equivalent of TBACl, a new singlet with a 1:1 integral ratio to the signal of equatorial MeCN emerges at 2.00 ppm (in reasonable agreement with the chemical shift of free MeCN). Moreover, paramagnetically shifted signals identical to those of $\mathbf{Fe_{Cl}^{II}}$ and of a third undefined species appear. Therefore, the partial conversion of $\mathbf{Fe_s^{II}}$ into $\mathbf{Fe_{Cl}^{II}}$ under concomitant dissociation of MeCN is likely. The reaction appears to proceed quantitatively at an overall of 3 equiv. of TBACl, at which mainly $\mathbf{Fe_{Cl}^{II}}$ is present according to eq. (3.29).

$$\mathbf{C}: \quad [Fe^{II}\mathbf{L}(MeCN)_3](BF_4)_2 + 2\ TBACl \rightleftarrows [Fe^{II}\mathbf{L}Cl_2] + 2\ TBABF_4 + 3\ MeCN \qquad (3.29)$$

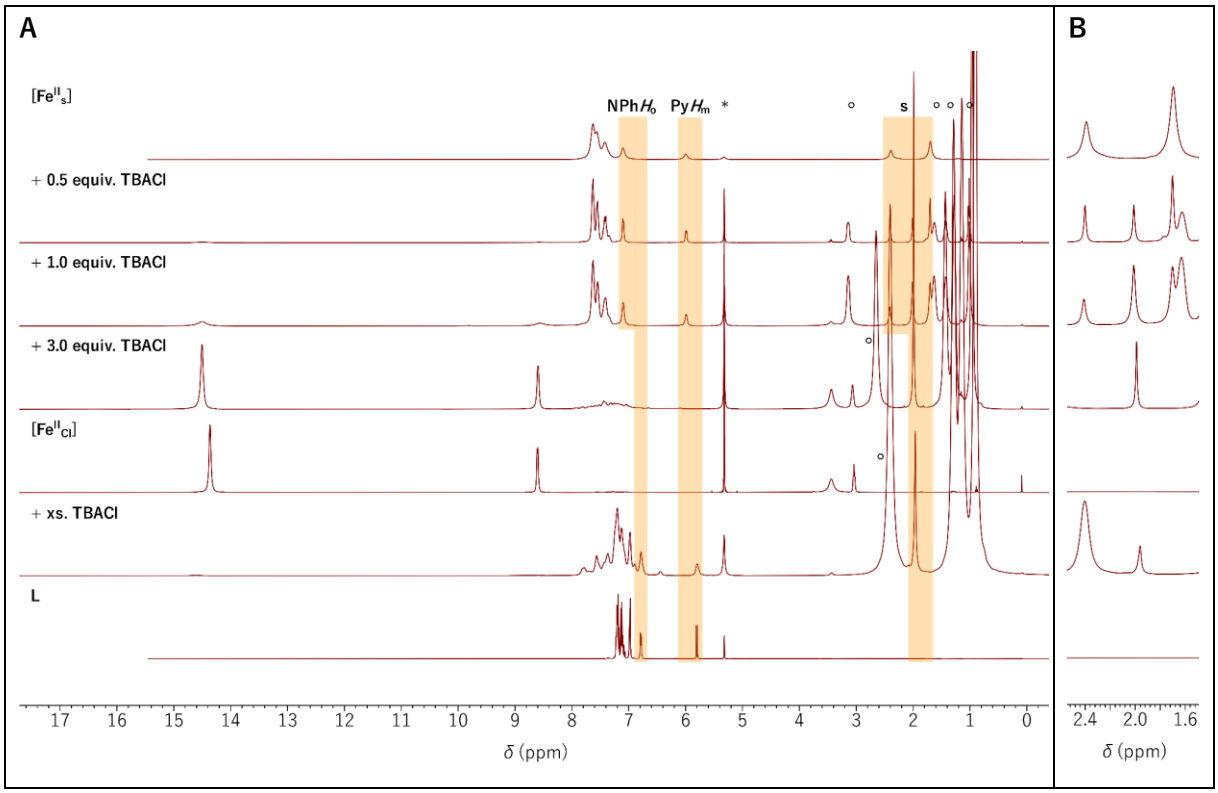

Figure 3.14. (A) ^{1}H NMR study of $\mathbf{Fe^{II}_s}$ at varying amounts of TBACl in CD_2Cl_2 at 400 MHz and 296 K and (B) zoom on the MeCN signals. Spectra of $\mathbf{Fe^{II}_{Cl}}$ and **L** are shown as references (* = residual proton signal of CD_2Cl_2, ° = TBA^+ signals, and s = MeCN).

Simultaneously, the dark orange/red solution of $\mathbf{Fe^{II}_s}$ in CD_2Cl_2 gradually turns to light yellow, resembling a pristine solution of $\mathbf{Fe^{II}_{Cl}}$ in DCM. Minor signals of free ligand **L** and other undefined signals appear in the aromatic region of the ^{1}H spectrum.

As inferred from the complete discoloration of the solution in higher excess of TBACl, $\mathbf{Fe^{II}_{Cl}}$ disintegrates into **L** and an unidentified colorless iron compound in the presence of one spare equivalent of chloride ions [eq. (3.30)]. Although "cream-colored"[20] $[Fe^{II}Cl_4]^{2-}$ could form, the iron-containing species has not been unambiguously identified so far.

$$\mathbf{C}: \quad [Fe^{II}\mathbf{L}Cl_2] \xrightarrow{+\,m\ Cl^-} [Fe^{II}Cl_{2+m}]^{(m-)} + \mathbf{L} \qquad (3.30)$$

A decomposition of the iron complex is also reflected in the phosphorus NMR in Figure B.9. The free ligand marks the main species with a peak at 52.8 ppm but is accompanied by several other signals attributed to other degradation products.

Based on the conversion of $\mathbf{Fe^{II}_s}$ into $\mathbf{Fe^{II}_{Cl}}$ already in the presence of half an equiv. of TBACl, the affinity of the complex to substitute acetonitrile with chloride ions can be estimated as high. $\mathbf{Fe^{II}_{Cl}}$ is yet unstable itself, as inferred from the partial decomposition at only one excessive equivalent of chloride ions.

The ^{1}H NMR spectra recorded for the addition of TBACl to $\mathbf{Fe_s^{II}}$ in CD_3CN are shown in Figure 3.15. $\mathbf{Fe_s^{II}}$ exhibits the same behavior in CD_3CN as in CD_2Cl_2, but higher amounts of TBACl are required for the single reaction steps. For instance, signals of $\mathbf{Fe_{Cl}^{II}}$ only emerge starting from one equivalent of TBACl in CD_3CN, whereas 0.5 equiv. suffice in CD_2Cl_2. This deviation can be attributed to the shift of the equilibrium in eq. (3.29) toward $\mathbf{Fe_s^{II}}$ by the excess of MeCN(-d_3).

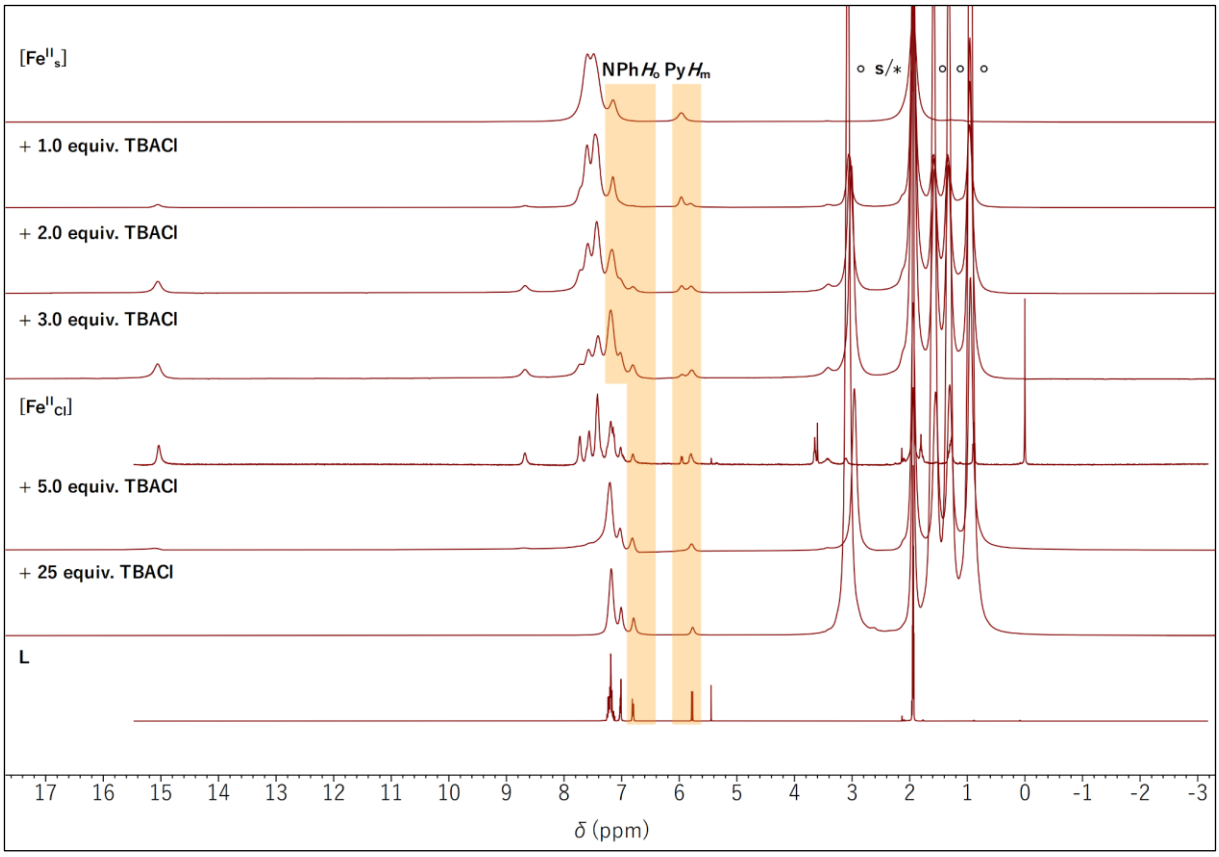

Figure 3.15. ^{1}H NMR study of $\mathbf{Fe_s^{II}}$ with varying amounts of TBACl in CD_3CN at 400 MHz and 296 K. Spectra of $\mathbf{Fe_{Cl}^{II}}$ and **L** are shown as references (* = residual proton signal of CD_3CN, ° = TBA^+ signals, and s = MeCN).

Ligand signals likely originating from the decomposition proposed in eq. (3.30) become visible in the $^{31}P\{^1H\}$ NMR spectra already at 2 equiv. of TBACl (Figure B.11). Further chloride addition only leads to increasing intensities of the ligand signals until they are the only peaks visible in the NMR spectra. Hence, the Fe complexes are assumed to disintegrate completely.

3.4.2 $[CoL(MeCN)_2](BF_4)_2$

The ^{1}H NMR spectroscopic study of $\mathbf{Co_s^{II}}$ with added TBACl is depicted in Figure 3.16. The sequential addition of up to two equivalents of TBACl variates the appearance of the proton signals in the aromatic region. Broad signals caused by the paramagneticity of the involved Co d^7 species yet impede their detailed analysis. No free acetonitrile is observable up to 3 equiv. of TBACl.

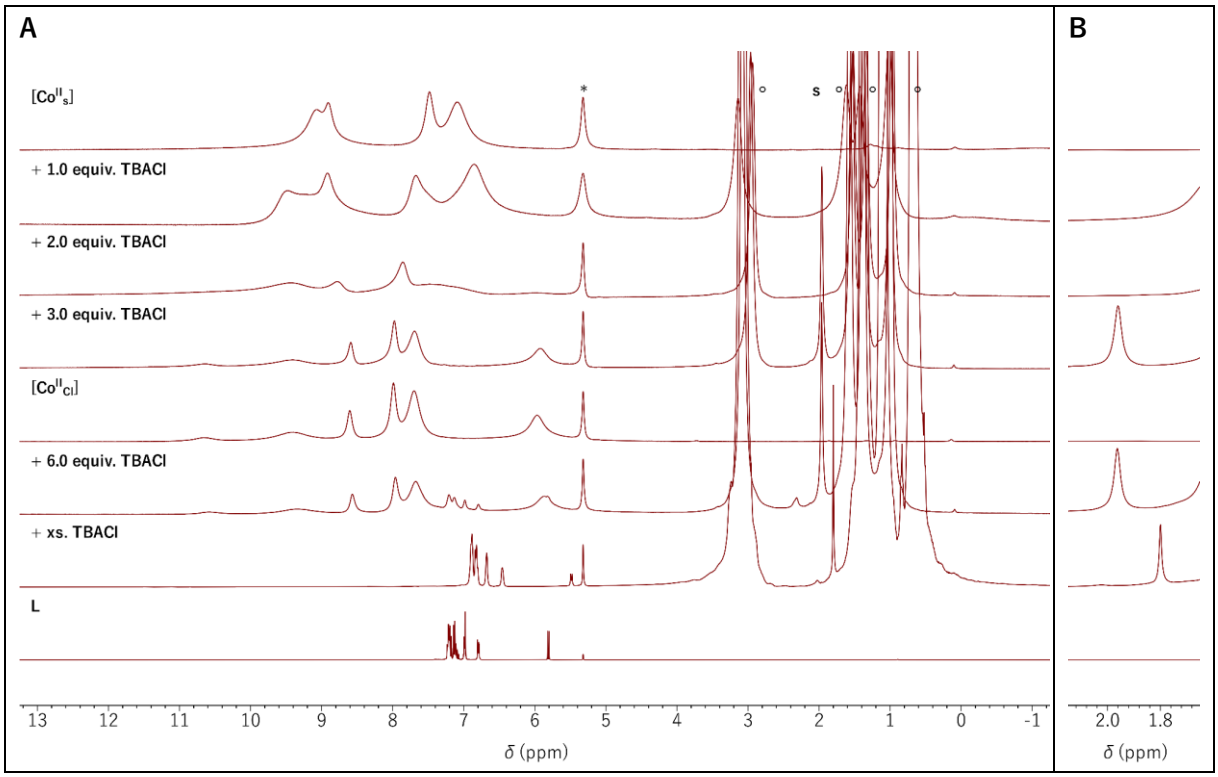

Figure 3.16. (A) ^{1}H NMR study of $\mathbf{Co^{II}_{s}}$ at varying amounts of TBACl in CD_2Cl_2 at 400 MHz and 296 K and (B) zoom on the MeCN signals (right). Spectra of $\mathbf{Co^{II}_{Cl}}$ and **L** are shown as references (* = residual proton signal of CD_2Cl_2, ° = TBA^+ signals, and s = MeCN).

In contrast, the molecular structure obtained from the addition of one equiv. of TBACl to $\mathbf{Co^{II}_{s}}$ (Figure 3.17) shows the formation of a heteroleptic complex. Although the poor quality of the crystal hindered the extraction of exact geometric parameters, the structure suggests $[Co^{II}\mathbf{L}(MeCN)Cl]^+$, with the chloride ion substituting the MeCN ligand in the basal plane.

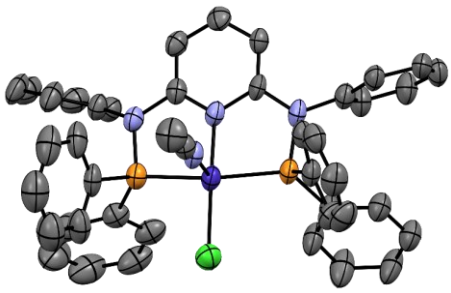

Figure 3.17. Molecular structure of $[Co^{II}\mathbf{L}(MeCN)Cl]^+$ received from crystals obtained from a concentrated MeCN/Et_2O (3:1) solution at −35 °C. H-atoms, outer-sphere ligands, solvents, and TBA^+ molecules were omitted for clarity.

Therefore, the lack of a peak for free acetonitrile is attributed to the association of chloride [eq. (3.31)] and fast exchange of coordinated and free solvent at the Co center [eq. (3.32)].

$$\mathbf{C}: \quad [Co^{II}\mathbf{L}(MeCN)_2](BF_4)_2 + TBACl \rightleftarrows [Co^{II}\mathbf{L}(MeCN)_2Cl]BF_4 + TBABF_4 \qquad (3.31)$$

$$\mathbf{C}: \quad [Co^{II}\mathbf{L}(MeCN)_2Cl]BF_4 \rightleftarrows [Co^{II}\mathbf{L}(MeCN)Cl]BF_4 + MeCN \qquad (3.32)$$

The NMR pattern of the aromatic protons at 3 equiv. of TBACl is identical to that of pure $\mathbf{Co^{II}_{Cl}}$, therefore indicating the formation of the bis-chloride complex [eq. (3.33)].

$$\mathbf{C}: \quad [Co^{II}\mathbf{L}(MeCN)Cl]BF_4 + TBACl \rightleftarrows [Co^{II}\mathbf{L}Cl_2] + TBABF_4 + MeCN \qquad (3.33)$$

This hypothesis is corroborated by a new singlet appearing at 1.97 ppm, attributed to the release of free acetonitrile from the complex. Integration of the signal to the TBA^+ peaks suggests the decoordination of both solvent molecules from the complex. The substitution of MeCN seems unfavored since it requires an excess of one equivalent of TBACl for the conversion of $\mathbf{Co^{II}_{s}}$ into $\mathbf{Co^{II}_{Cl}}$.

Up to this point, the initially orange solution of $\mathbf{Co^{II}_{s}}$ turned to a deeper red with each addition step. Beginning at 6 equiv. of TBACl, new peaks at chemical shifts identical to that of **L** can be observed in the ^1H (Figure 3.16, bottom) and the so-far silent $^{31}P\{^1H\}$ spectrum (Figure B.10), indicating disintegration of the starting complex.

Excess of TBACl leads to strongly shifting signals and an abrupt color change to blue. The complete loss of the complex peaks relates to the quantitative decoordination of the ligand from the metal center and putative formation of $(TBA)_2[Co^{II}Cl_4]$ as inferred from the change of color [eq. (3.34)].[20-21] The paramagneticity of the newly-formed Co(II) d^7 species is likely causing the shift of the free ligand peaks.

$$\mathbf{C}: \quad [Co^{II}\mathbf{L}Cl_2] + 2\ TBACl \rightleftarrows (TBA)_2[Co^{II}Cl_4] + \mathbf{L} \qquad (3.34)$$

The ^1H NMR spectra of $\mathbf{Co^{II}_{s}}$ upon TBACl addition in CD_3CN are presented in Figure 3.18. Twofold addition of 0.5 equiv. TBACl gradually converts the starting complex, most evident from the loss of signals at 8.84 ppm and 7.40 ppm. At one equivalent of chloride source, minor amounts of the initial complex remain visible in the ^1H NMR spectrum. This fact indicates the incomplete conversion of the complex, yet experimental error cannot be entirely excluded as the cause.

Further addition of TBACl spreads the broad proton signals in the aromatic region until a spectrum similar to that of $\mathbf{Co^{II}_{Cl}}$ is reached at three equivalents. Minor signals of the free ligand are observable in the respective ^1H and ^{31}P NMR spectra (Figure B.12). Hence, the coordination of two chloride ligands to $\mathbf{Co^{II}_{s}}$ is likely achieved between 2 and 3 equiv. of TBACl, after which decomposition of the complex occurs according to eq. (3.34). The decomposition, indicated by a color change to blue, becomes almost quantitative at 25 equiv. of TBACl.

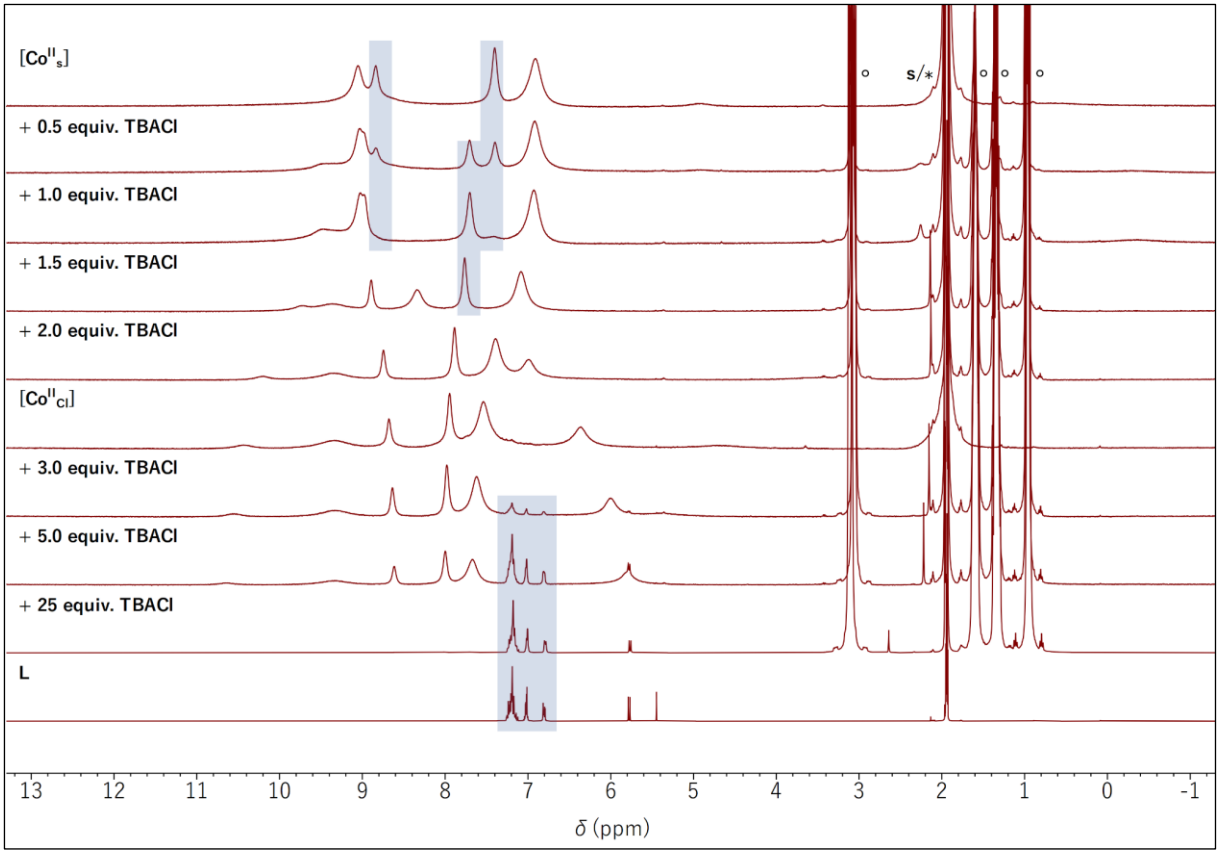

Figure 3.18. ^{1}H NMR study of $\mathbf{Co^{II}_{s}}$ at varying amounts of TBACl in CD_3CN at 400 MHz and 296 K. Spectra of $\mathbf{Co^{II}_{Cl}}$ and **L** are shown as references. (* = residual proton signal of CD_3CN, ° = TBA^+ signals, and s = MeCN).

3.4.3 [NiL(MeCN)](BF$_4$)$_2$

A new signal at 87.2 ppm emerges in the ^{31}P NMR spectrum of $\mathbf{Ni^{II}_{s}}$ in CD_2Cl_2 (Figure 3.19) when 0.5 equivalents of TBACl are added. Integration of the peak compared to the residual signal of the starting complex (δ_P = 92.5 ppm) shows a 1:1 ratio. The corresponding ^{1}H NMR spectrum in Figure 3.20 exhibits an identical behavior for the signal of the protons in the *ortho* position of the nitrogen-bound phenyl ring (NPhH_o). Although two species were identified, only one acetonitrile peak can be observed at 2.03 ppm. Since the peak is located precisely in the middle of the signals of coordinated (2.08 ppm) and free MeCN (1.97 ppm)[22], it likely arises from the exchange of both molecules at the remaining half equivalent of MeCN-coordinated species. The spectroscopic behavior hence indicates the conversion of TBACl and substitution of the solvent coordinated to $\mathbf{Ni^{II}_{s}}$ with the chloride ions into a single new nickel species. This ligand exchange is reflected by the orange starting solution turning red.

The $\mathbf{Ni^{II}_{s}}$ phosphorous signal entirely vanishes when another half equiv. of the chloride source is added, leaving the peak at 87.2 ppm as the sole signal. The NPhH_o peak of $\mathbf{Ni^{II}_{s}}$ is lost equally and the singlet MeCN signal shifts further to 1.97 ppm, attributed to free acetonitrile in CD_2Cl_2.

Hence, according to eq. (3.35), the coordinated acetonitrile ligand was quantitatively substituted by chloride ions.

$$\mathbf{C}: \quad [Ni^{II}\mathbf{L}(MeCN)](BF_4)_2 + TBACl \rightleftarrows [Ni^{II}\mathbf{L}Cl]BF_4 + TBABF_4 + MeCN \qquad (3.35)$$

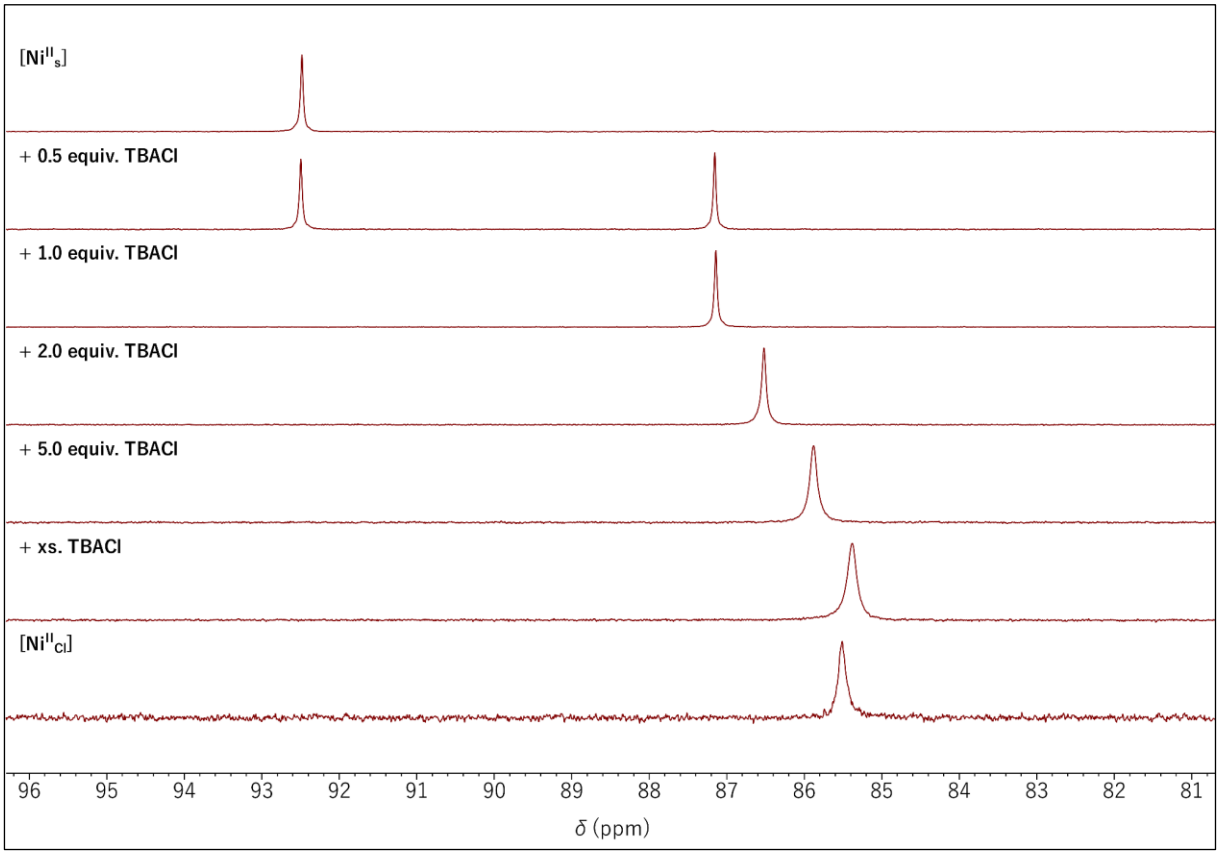

Figure 3.19. $^{31}P\{^1H\}$ NMR study of $\mathbf{Ni}^{\mathbf{II}}_{\mathbf{s}}$ at varying amounts of TBACl in CD_2Cl_2 at 162 MHz and 296 K. The spectrum of $\mathbf{Ni}^{\mathbf{II}}_{\mathbf{Cl}}$ is shown as a reference.

Adding a second equivalent of TBACl leads to an upfield shift of the aromatic proton signals and the phosphorus peak as well as the intensification of the red color of the solution. The aromatic signals are in good agreement with those of a pristine $\mathbf{Ni}^{\mathbf{II}}_{\mathbf{Cl}}$ reference sample (Figure 3.20, bottom), which reflects quantitative consumption of the second chloride equivalent by association to the mono-chloride and formation of $\mathbf{Ni}^{\mathbf{II}}_{\mathbf{Cl}}$ [eq. (3.36)].

$$\mathbf{C}: \quad [Ni^{II}\mathbf{L}Cl]BF_4 + TBACl \rightleftarrows [Ni^{II}\mathbf{L}Cl_2] + TBABF_4 \qquad (3.36)$$

The quantitative coordination of the chloride ions to the complex indicates the substitution/coordination equilibria being shifted far to the product side.

Increasing the amount of TBACl above two equivalents leads to a further upfield shift of the signals in the ^1H and $^{31}P\{^1H\}$ NMR, potentially caused by the further displacement of the equi-

librium in eq. (3.36) to the bis-chloride species (summarized in Figure B.8). Moreover, no additional color change indicating ongoing modifications of the inner coordination sphere could be observed.

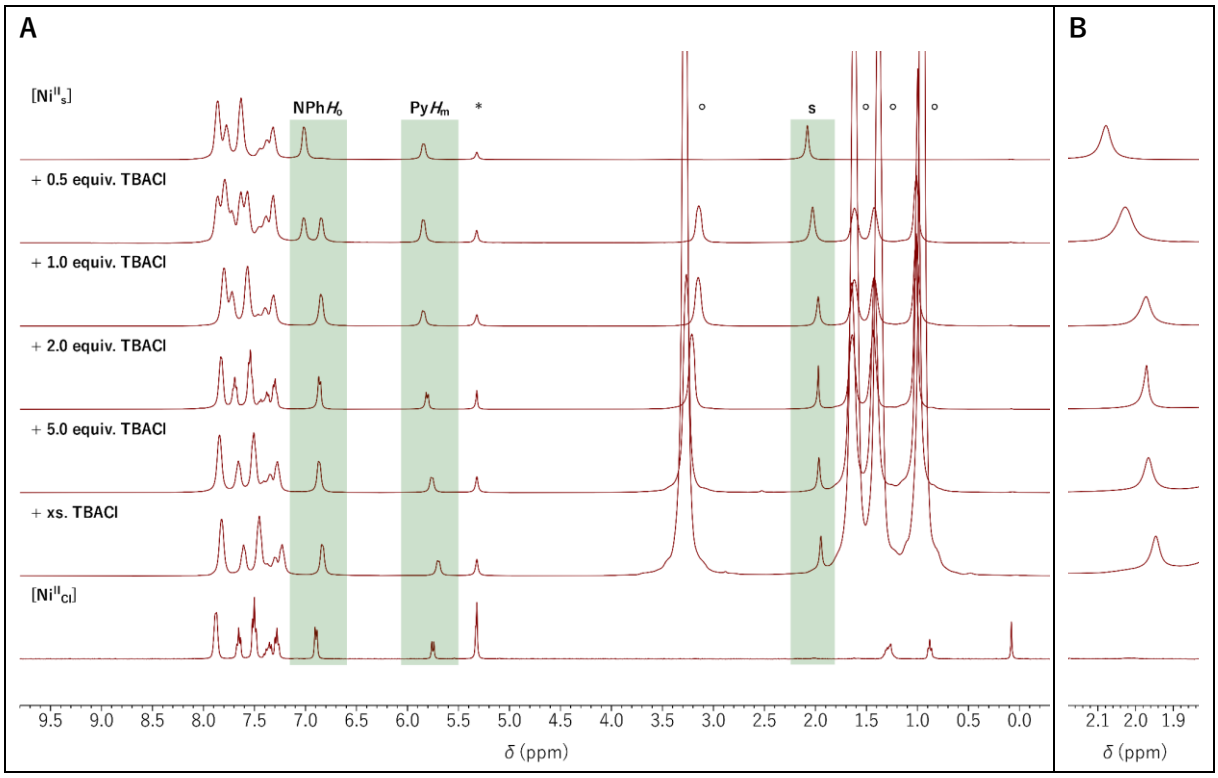

Figure 3.20. (A) ^{1}H NMR study of $\mathbf{Ni}^{II}_{s}$ at varying amounts of TBACl in CD_2Cl_2 at 400 MHz and 296 K and (B) zoom on the MeCN signals (right). The spectrum of $\mathbf{Ni}^{II}_{Cl}$ is shown as a reference (* = residual proton signal of CD_2Cl_2, ° = TBA^+ signals, and s = MeCN).

Addition of 0.5 equiv. of TBACl in CD_3CN induces the formation of a new peak at 86.3 ppm in the $^{31}P\{^{1}H\}$ NMR spectrum (Figure B.13). The broad singlet of pristine $\mathbf{Ni}^{II}_{s}$ at 92.3 ppm decreases and is only partly visible in the baseline. A second set of signals, identified from the isolated NPhH_o and PyH_m peaks, emerges in the ^{1}H NMR spectrum with integral ratios of slightly less than 1:1 compared to the starting complex signals (Figure 3.21). These ratios indicate the formation of the mono-chloride species as described in eq. (3.35), but partially inhibited by competition of the chloride ligand with the excess solvent molecules.

Further increasing the TBACl concentration induces a complete conversion of $\mathbf{Ni}^{II}_{s}$ and upfield shifts of the aromatic signals in the proton NMR as well as the phosphorus peak. The spectra of pristine $\mathbf{Ni}^{II}_{Cl}$ agree best with those of $\mathbf{Ni}^{II}_{s}$ obtained in the presence of 3.0 equiv. of TBACl, indicating that an excess of 1 equiv. is necessary to shift the equilibrium for the association of the second chloride when in coordinative competition with MeCN.

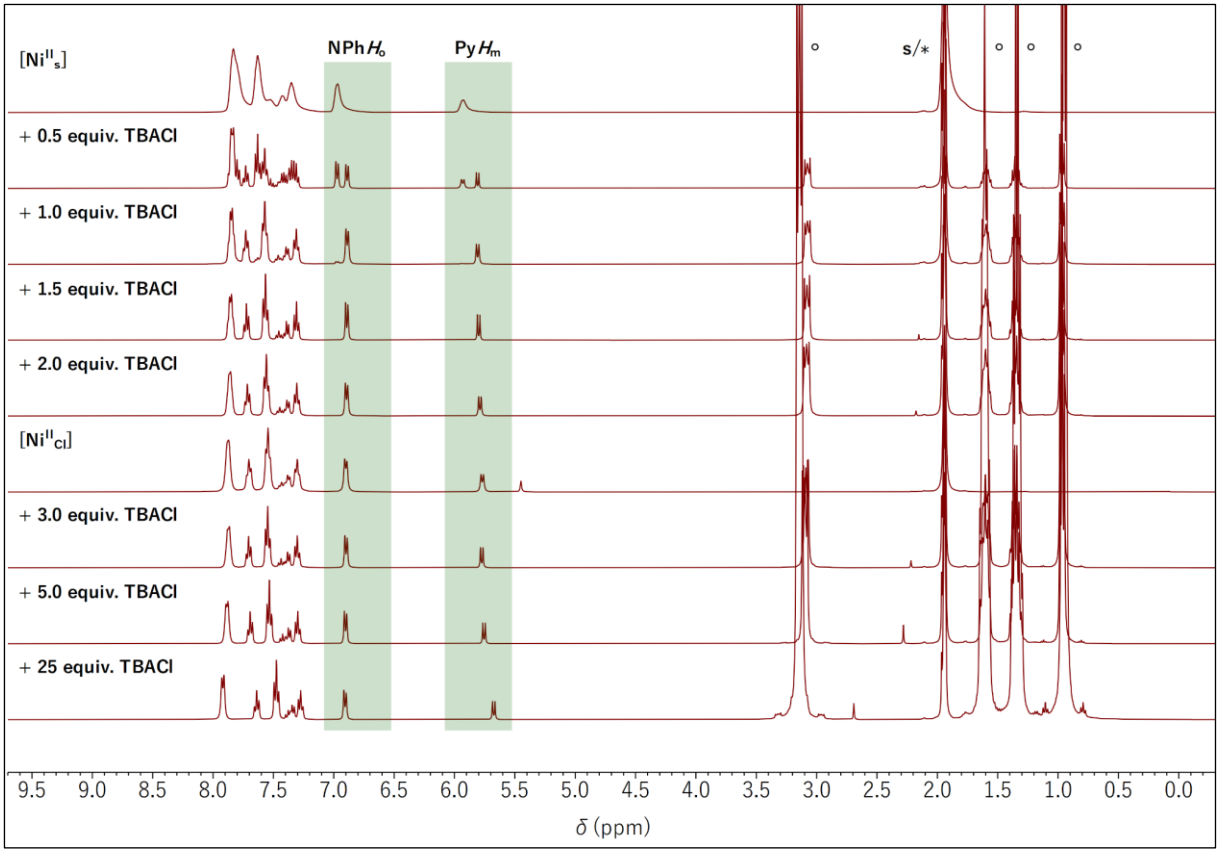

Figure 3.21. ^{1}H NMR study of $\mathbf{Ni}^{II}_{s}$ at varying amounts of TBACl in CD_3CN at 400 MHz and 296 K. The spectrum of $\mathbf{Ni}^{II}_{Cl}$ is shown as a reference (* = residual proton signal of CD_3CN, ° = TBA^+ signals).

3.4.4 Comparative Assessment

The NMR analysis under sequential addition of the chloride source TBACl concludes that each of the $\mathbf{M}^{II}_{s}$ complexes exchanges the labile MeCN ligand with chloride anions in CD_2Cl_2 and CD_3CN (Scheme 3.5). Comparison among the two deuterated solvents showed stronger competition between Cl^- and acetonitrile(-d_3) in CD_3CN, as expected by the equilibrium shift to the MeCN-bound complexes based on LE CHATELIER's principle.

Already substoichiometric amounts of TBACl suffice for the partial conversion of $\mathbf{Fe}^{II}_{s}$ into $\mathbf{Fe}^{II}_{Cl}$ and minor quantities of other unassigned species (Scheme 3.5A). Emerging ligand signals in the ^{1}H and ^{31}P NMR spectra already at two equivalents of Cl^- in CD_3CN indicate the favored disintegration of the complex structure toward potential polychloro ferrate species.

$\mathbf{Co}^{II}_{s}$ undergoes a two-fold exchange of MeCN with Cl^- to [Co**L**(MeCN)Cl]$^+$ and $\mathbf{Co}^{II}_{Cl}$ respectively in the presence of 3 equivalents of TBACl (Scheme 3.5B). Higher Cl^-/complex ratios favor the decomposition of the bis-chloro complex into putative $[CoCl_4]^{2-}$.

In the case of $\mathbf{Ni}_{\mathbf{s}}^{\mathbf{II}}$, a sequence of acetonitrile substitution to a presumably SP 16 VE d^8 mono-chloride species and chloride coordination to $\mathbf{Ni}_{\mathbf{Cl}}^{\mathbf{II}}$ can be observed (Scheme 3.5C).

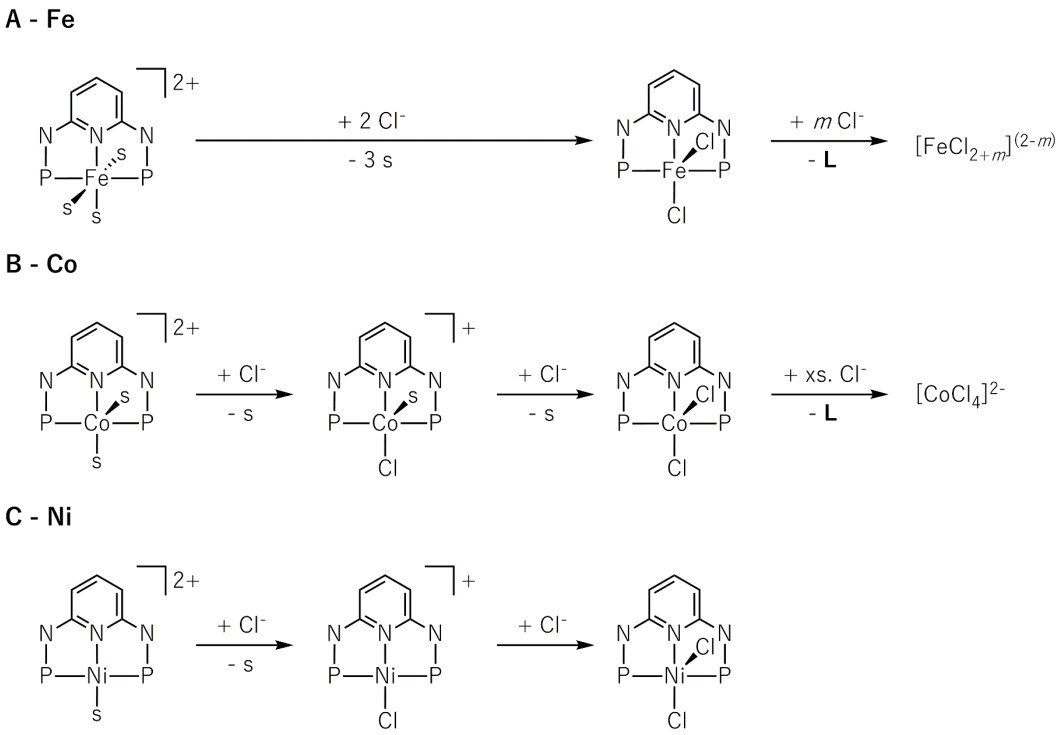

Scheme 3.5. Proposed changes in the inner coordination sphere of $\mathbf{M}_{\mathbf{s}}^{\mathbf{II}}$ complexes of (A) Fe, (B) Co, and (C) Ni upon addition of TBACl. N- and P-substituents were omitted for clarity.

The reactivity of the $\mathbf{M}_{\mathbf{s}}^{\mathbf{II}}$ complexes in the presence of ≥ 2 equivalents of chloride ions reflects their different stabilities. While $\mathbf{Ni}_{\mathbf{s}}^{\mathbf{II}}$ does not show any signs of complex degradation even at superstoichiometric amounts of TBACl, 3 equivalents suffice for $\mathbf{Co}_{\mathbf{s}}^{\mathbf{II}}$ and 2 equivalents for $\mathbf{Fe}_{\mathbf{s}}^{\mathbf{II}}$ to initiate the disintegration of the resulting bis-chloride complexes. Hence, the behavior in the presence of chloride ligands corroborates Fe < Co < Ni as the order of increasing stability predicted from the bond lengths in section 2.2.2.4.

The following variations of the chloride-to-complex ratio in cyclic voltammetry put the redox behavior of the $\mathbf{M}_{\mathbf{s}}^{\mathbf{II}}$ complexes *vis-à-vis* to the ligand exchange.

3.5 Ligand Exchange at Reduced Metal States

Extending the "one-dimensional" chemical exchange equilibria to further oxidation states adds a second electrochemical dimension to the overall behavior of the complexes under reductive conditions. Such interplay of chemical (**C**) and electrochemical (**E**) steps is best described by so-called square schemes, as reported by LAVIRON[23] and SAVÉANT[24]. A schematic square scheme for six chemical and six electrochemical equilibria is shown in Scheme 3.6.

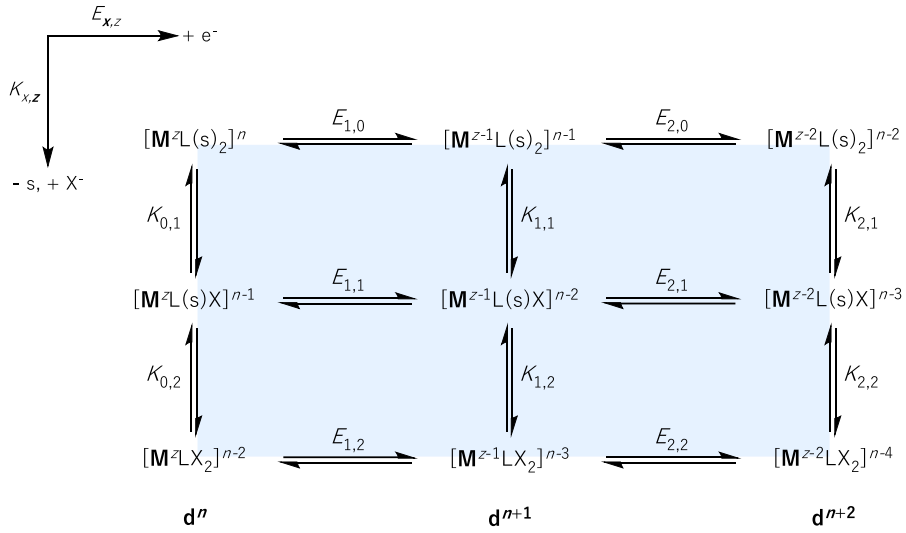

Scheme 3.6. Generalized square scheme of a molecular metal species coordinated by a tridentate ligand L, neutral solvent ligands s, and anionic ligands X^- (CN = 5).

The horizontal **E** steps (*x*-direction) reflect single-electron transfers at the metal center [eq. (3.37)] described by the standard potentials E^0. The vertical **C** steps [*z*-direction, eq. (3.38)] further represent the exchange of a neutral coordinated solvent with an anionic ligand, quantified by the respective equilibrium constants *K* as the quotient of the forward (k^+) and backward (k^-) rate constants [eq. (3.39)]. Eq. (3.37) and (3.38) exemplify both steps starting from the top-left corner of the square scheme.

E: $$[\mathbf{M}^{z}\mathrm{L(s)_2}]^{n} + \mathrm{e}^- \rightleftarrows [\mathbf{M}^{z-1}\mathrm{L(s)_2}]^{n-1} \tag{3.37}$$

C: $$[\mathbf{M}^{z}\mathrm{L(s)_2}]^{n} + \mathrm{X}^- \rightleftarrows [\mathbf{M}^{z}\mathrm{L(s)X}]^{n-1} + \mathrm{s} \tag{3.38}$$

$$K = \frac{k^+}{k^-} \tag{3.39}$$

The two standard potentials and equilibrium constants necessary to describe a tile of the square scheme (here: top-left in Scheme 3.6) can be related using eq. (3.40).[23b]

$$\frac{K_{1,1}}{K_{0,1}} = \exp\left[\left(\frac{\mathrm{F}}{\mathrm{R}T}\right)\left(E_{1,1} - E_{1,0}\right)\right] \tag{3.40}$$

In the original reports, **C** steps referred to a single reaction type, e.g., ligand substitution (*vide supra*), which keeps the coordination number of the considered species constant. Since the $\mathbf{M_s^{II}}$ and $\mathbf{M_{Cl}^{II}}$ complexes likely switch between coordination numbers via ligand (de-)coordination, the two-dimensional square schemes need to be expanded to a third dimension accounting for these elementary steps. This expansion yields the so-called "cube scheme" in Scheme 3.7.

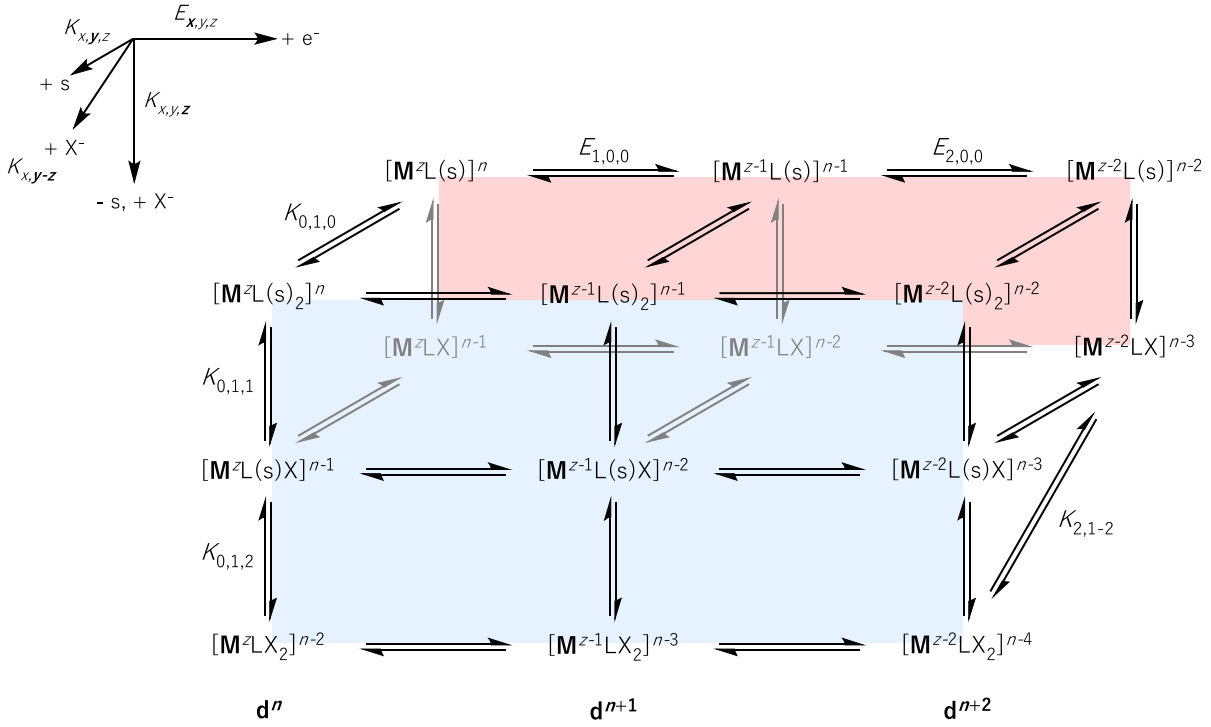

Scheme 3.7. Generalized cube scheme of a molecular metal species coordinated by a tridentate ligand L, neutral solvent ligands s, and anionic ligands X^- for CN = 4 (red) and CN = 5 (blue).

The equilibria in the *y*-direction of the cube scheme describe the association/dissociation of a solvent molecule, while the diagonals in the vertical planes do the same for X^- (exemplarily shown for $K_{2,1\text{-}2}$). In the following sections, the most likely pathways to the zero-valent state taken by the $\mathbf{M_s^{II}}$ and $\mathbf{M_{Cl}^{II}}$ complexes under electrochemical conditions in MeCN are determined by extracting the standard potentials for E steps from the CV analysis and estimating the equilibrium constants for the **C** steps within their respective cube schemes.

3.5.1 Iron

Since $\mathbf{Fe_s^{II}}$ exists in an octahedral geometry, a plane accounting for this structure ($y = 2$) had to be added to the cube scheme (Scheme 3.8). Only the putatively involved species are shown in this plane to retain the clarity of the scheme. Moreover, CV analysis of $\mathbf{Fe_s^{II}}$ in MeCN revealed the potential formation of dimeric structures upon reducing the complex. Since dimers would significantly complicate the cube scheme, the top layer structures need to be understood as the

species comprising half of the dimer. Apart from the lack of further spectroscopic or structural information, the dashed equilibria thus give an overview of the possible reduction routes for $\mathbf{Fe_s^{II}}$.

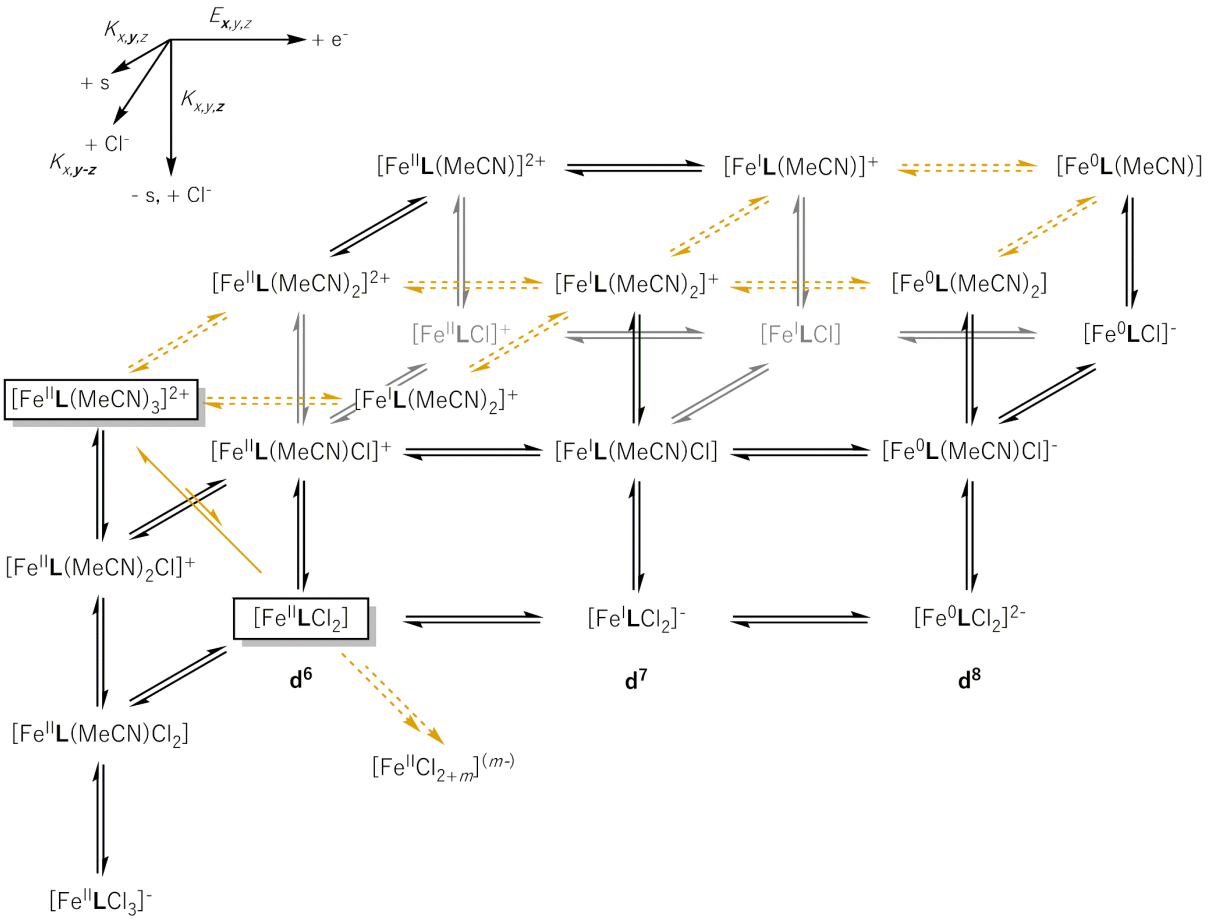

Scheme 3.8. Proposed cube scheme for the two-fold reduction of $\mathbf{Fe_s^{II}}$ and $\mathbf{Fe_{Cl}^{II}}$ in acetonitrile. Framed structures were confirmed by X-ray diffraction.

Switching to the less coordinating solvent DMF was surmised to avoid the dimeric pathways of $\mathbf{Fe_s^{II}}$ and allow a clearer picture of the processes in the cube scheme. The orange $\mathbf{Fe_s^{II}}$ complex dissolves instantly upon addition of the colorless electrolyte solution, but the solution remains colorless. The CV at ν = 100 mV·s^{-1} (Figure B.14A) shows an irreversible reduction wave with crossing lines at $E_{p,c}$ = –1.89 V_{Fc}, followed by a broad oxidative wave at $E_{p,a}$ = –0.60 V_{Fc} in the reverse scan. These observations speak in favor of a rapid disintegration of $\mathbf{Fe_s^{II}}$ in DMF and reduction of the decomposition products to Fe(0) species adsorbed on the WE when scanning in the cathodic direction. The adsorbed species are oxidatively removed from the electrode surface after reversal of the scan direction, as indicated by the shape of the corresponding wave.

Adding TBACl to $\mathbf{Fe_s^{II}}$ in MeCN during CV analysis results in decreasing current densities of the complex waves under the simultaneous rise of a new irreversible wave at $E_{p,c}$ = –2.13 V_{Fc} and a reversible one at E^0 ≈ –0.4 V_{Fc} (Figure B.15). The reversible wave was isolated for $\mathbf{Fe_{Cl}^{II}}$ and shifts

cathodically with increasing TBACl concentrations (Figure B.16). The inverse behavior of the normalized current density j^n compared to the one of the starting complex suggests the wave stems from the redox-active decomposition products of $\mathbf{Fe}_{\mathbf{Cl}}^{\mathbf{II}}$. When considering polychloro ferrate species as such products, the irreversible reduction wave at $E_{p,c}$ = –2.13 V_{Fc} could constitute the $Fe^{II/0}$ couple accompanied by the decomposition of Fe(0) species at the electrode surface. The oxidative desorption wave at $E_{p,a}$ ≈ –0.85 V_{Fc} in Figure B.15 and the potential $Fe^{III/II}$ couple of the desorbed iron(II) species at E^0 ≈ –0.4 V_{Fc} corroborate this theory.

Apparently, $\mathbf{Fe}_{\mathbf{Cl}}^{\mathbf{II}}$ undergoes rapid multi-ligand exchange when dissolved in acetonitrile. Vice versa, adding chloride ions to $\mathbf{Fe}_{\mathbf{s}}^{\mathbf{II}}$ in the NMR experiments reveals the formation of $\mathbf{Fe}_{\mathbf{Cl}}^{\mathbf{II}}$ even at substoichiometric amounts of TBACl. Hence, these means could not determine the exact route of ligand exchange. CV analysis of $\mathbf{Fe}_{\mathbf{Cl}}^{\mathbf{II}}$ in DMF indicates the compound's decomposition (Figure B.17A), similar to $\mathbf{Fe}_{\mathbf{s}}^{\mathbf{II}}$.

3.5.2 Cobalt

Scheme 3.9 shows the cube scheme for the reduction patterns of $\mathbf{Co}_{\mathbf{s}}^{\mathbf{II}}$ and $\mathbf{Co}_{\mathbf{Cl}}^{\mathbf{II}}$ in acetonitrile.

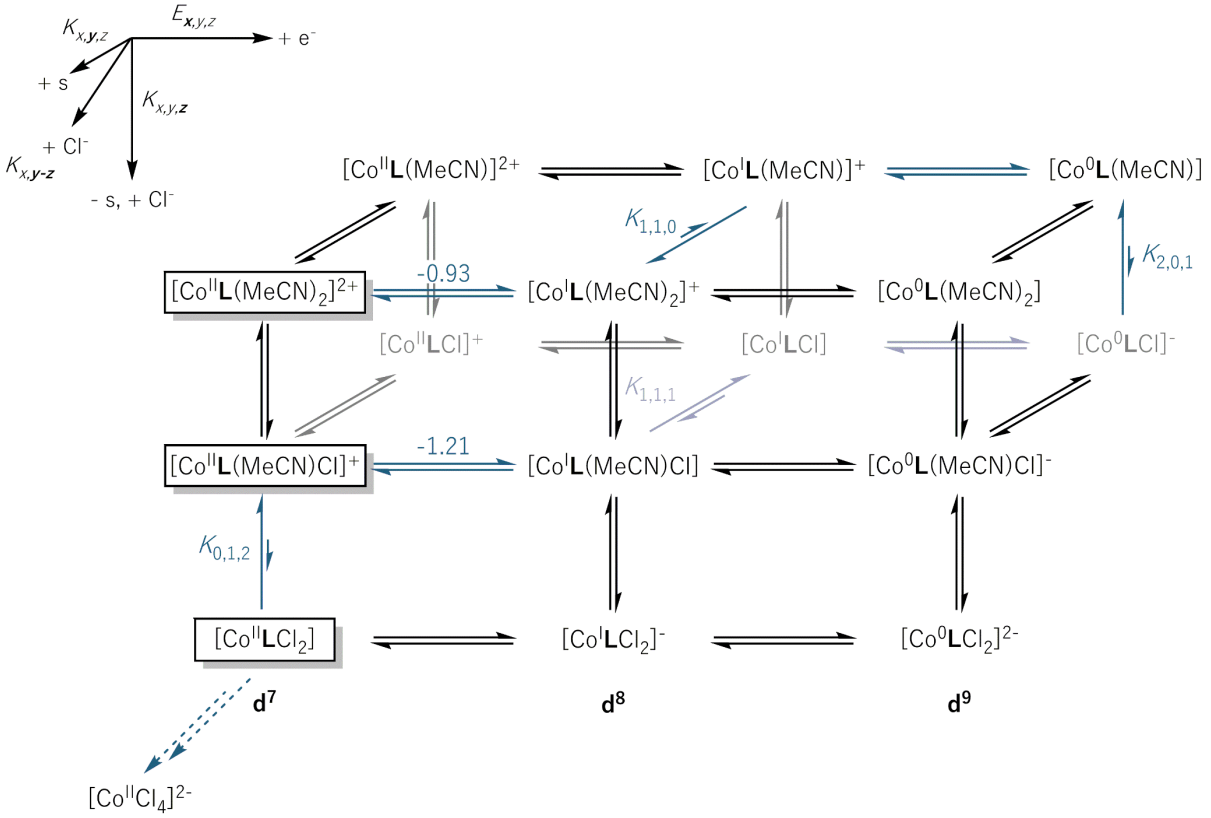

Scheme 3.9. Proposed cube scheme for the two-fold reduction of $\mathbf{Co}_{\mathbf{s}}^{\mathbf{II}}$ and $\mathbf{Co}_{\mathbf{Cl}}^{\mathbf{II}}$ in acetonitrile. Framed structures were confirmed by X-ray diffraction. Potentials are given in V_{Fc}.

3.5.2.1 $[Co\mathbf{L}(MeCN)_2](BF_4)_2$

For $[Co^{II}\mathbf{L}(MeCN)_2]^{2+}$ ($\mathbf{Co_s^{II}}$), the reversible reduction wave at $E^0_{1,1,0}$ = –0.93 V_{Fc} and applied scan rates of up to 100 $V \cdot s^{-1}$ indicate a one-electron reduction and formation of $[Co^{I}\mathbf{L}(MeCN)_2]^{+}$. However, calculations performed on a related $[Co(PN_3P)]$ pincer complex by BROWN et al. showed that the apical ligand likely dissociates upon reduction. The loss of the ligand allows the resulting $[Co^{I}\mathbf{L}(MeCN)]^{+}$ complex to exist in a square planar geometry energetically favorable for d^8 16 VE compounds.[2] As inferred from the scan rate-independent CV response of the $Co^{II/I}$ couple, the equilibrium constant for the expulsion of acetonitrile in the **C** step [eq. (3.22)] must be small (and both associated rate constants must be very fast). This behavior is reasonable regarding the equilibrium shift to the favored bis-acetonitrile species in excess MeCN.

Scan rate-varied CVs performed on the irreversible second reduction wave of the $Co^{I/0}$ couple failed to recover its reversibility but identified an **EC** mechanism. The **EC** sequence is attributed to the reduction of $[Co^{I}\mathbf{L}(MeCN)]^{+}$ to $[Co^{0}\mathbf{L}(MeCN)]$, which exists in a square planar geometry before very fast structural reorganization to the tetrahedral coordination polyhedron.

The attempt to record CVs of $\mathbf{Co_s^{II}}$ in DMF produces a colorless solution. The complex shows a sharp reduction wave with crossing lines at $E_{p,c} \approx -1.9$ V_{Fc}, followed by a broad desorption wave in the oxidative half cycle (Figure B.14B). Similar to $\mathbf{Fe_s^{II}}$ in DMF, this hints toward complex decomposition upon dissolution, followed by a sequence of reductive adsorption and oxidative desorption of the formed species.

The CV monitoring of the $Co^{II/I}$ wave of $\mathbf{Co_s^{II}}$ in MeCN at varying concentrations of TBACl is shown in Figure 3.22. For $0 < c_{TBACl} < 1$ mM (= 1 equiv. compared to $\mathbf{Co_s^{II}}$), a decrease in the peak current density of the $[Co^{II}\mathbf{L}(MeCN)_2]^{2+}/[Co^{I}\mathbf{L}(MeCN)]^{+}$ wave at $E^0_{1,0,0}$ = –0.93 V_{Fc} under concomitant rise of the $[Co^{II}\mathbf{L}(MeCN)Cl]^{+}/[Co^{I}\mathbf{L}(MeCN)Cl]$ wave at $E^0_{1,0,1}$ = –1.21 V_{Fc} can be observed up to the full loss of the more anodic redox event.

The wave's peak current densities decrease drastically, starting at approx. 2.91 mM of TBACl (= 3 equiv.). This trend agrees with the association of more than two halide ligands at these concentrations of TBACl, as observed from the previous NMR studies. The respective equilibrium for the formation of putative $[Co^{II}Cl_4]^{2-}$ and loss of **L** seems to be shifted to the substrate side without an additional chloride source but is strongly affected by superstoichiometric TBACl.

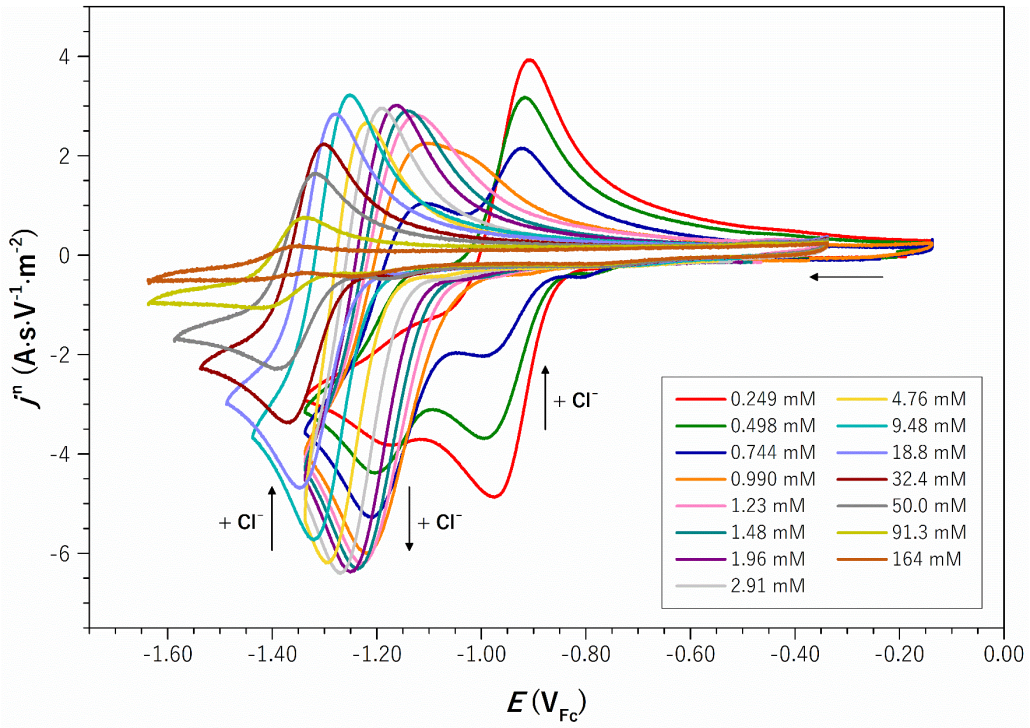

Figure 3.22. CVs of the $Co^{II/I}$ wave of $\mathbf{Co_s^{II}}$ at varying concentrations of TBACl.

3.5.2.2 [Co**L**Cl$_2$]

Dissolving $\mathbf{Co_{Cl}^{II}}$ in MeCN likely yields $[Co^{II}\mathbf{L}(MeCN)Cl]^+$, as equally observed by BROWN et al.[2] Scan rate variations on the $Co^{II/I}$ wave (Figure 3.23) reveal a quasi-reversible wave at ν = 100 mV·s^{-1} gradually losing the current density of the back-oxidation part at $E_{p,a}$ = −1.16 V_{Fc}.

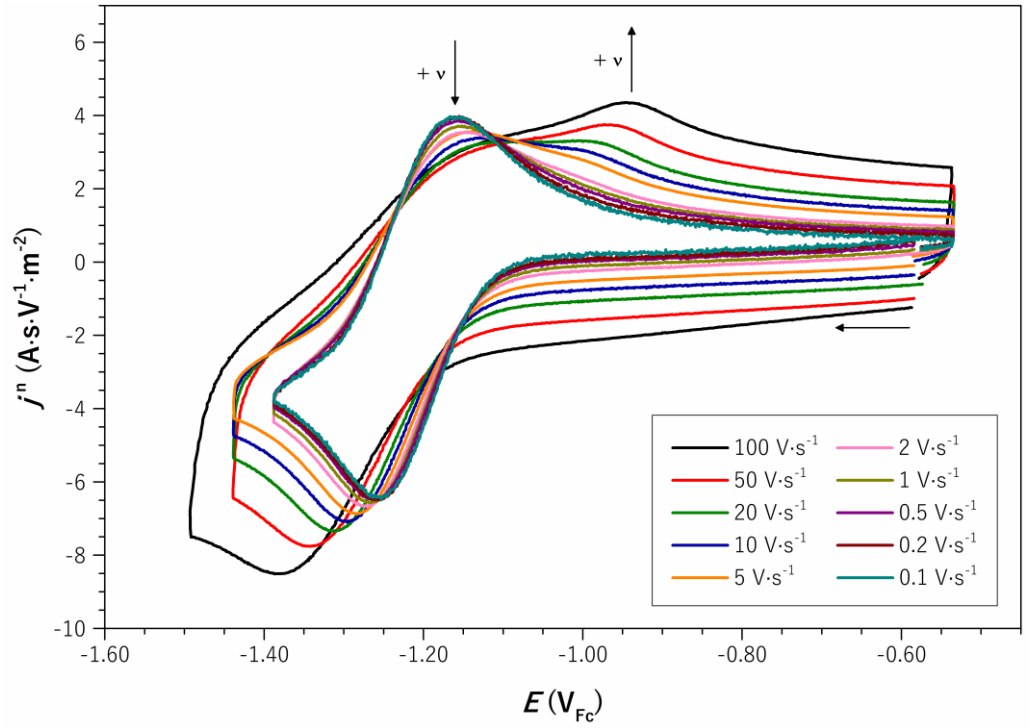

Figure 3.23. CVs of the $Co^{II/I}$ wave of $\mathbf{Co_{Cl}^{II}}$ at varying scan rates.

A second, more cathodic oxidation wave of increasing current density emerges at $E_{p,a}$ = –0.94 V_{Fc} (ν = 100 $V \cdot s^{-1}$) when exceeding 5 $V \cdot s^{-1}$. This observation concludes with an **EC** mechanism at the $Co^{II/I}$ wave, in which $[Co^{II}\mathbf{L}(MeCN)Cl]^+$ is first reduced to $[Co^{I}\mathbf{L}(MeCN)Cl]$ before losing the apical acetonitrile ligand.[2] The emergence of two different oxidation waves probably originates from the diverging forward and backward rate constants within the solvent association-dissociation equilibrium described by $K_{1,1,1}$ in eq. (3.41).

C: $$[Co^{II}\mathbf{L}(MeCN)Cl]^+ \rightleftarrows [Co^{II}\mathbf{L}Cl]^+ + MeCN \qquad (3.41)$$

$k^-_{1,1,1}$ (representing the rate of ligand decoordination) is likely too high and impedes observation of the process at the applied scan rates. However, the competition between diffusion and chemical step (solvent association with rate constant $k^+_{1,1,1}$) renders a detection of the re-oxidation of $[Co^{I}\mathbf{L}Cl]$ at $E_{p,a} \approx$ –0.94 V_{Fc} possible at scan rates > 5 $V \cdot s^{-1}$.

A complementary CV analysis of $\mathbf{Co^{II}_{Cl}}$ in DMF (Figure 3.24) revealed two predominant redox events at $E^0(Co^{II/I})$ = –1.29 V_{Fc} (reversible, ΔE_p = 96 mV) and at $E_{p,c}(Co^{I/0})$ = –2.18 V_{Fc} (irreversible). A detailed analysis of the waves by variation of the scan rate proved impossible due to intense diffusion currents and poor resolution of the recorded voltammograms.

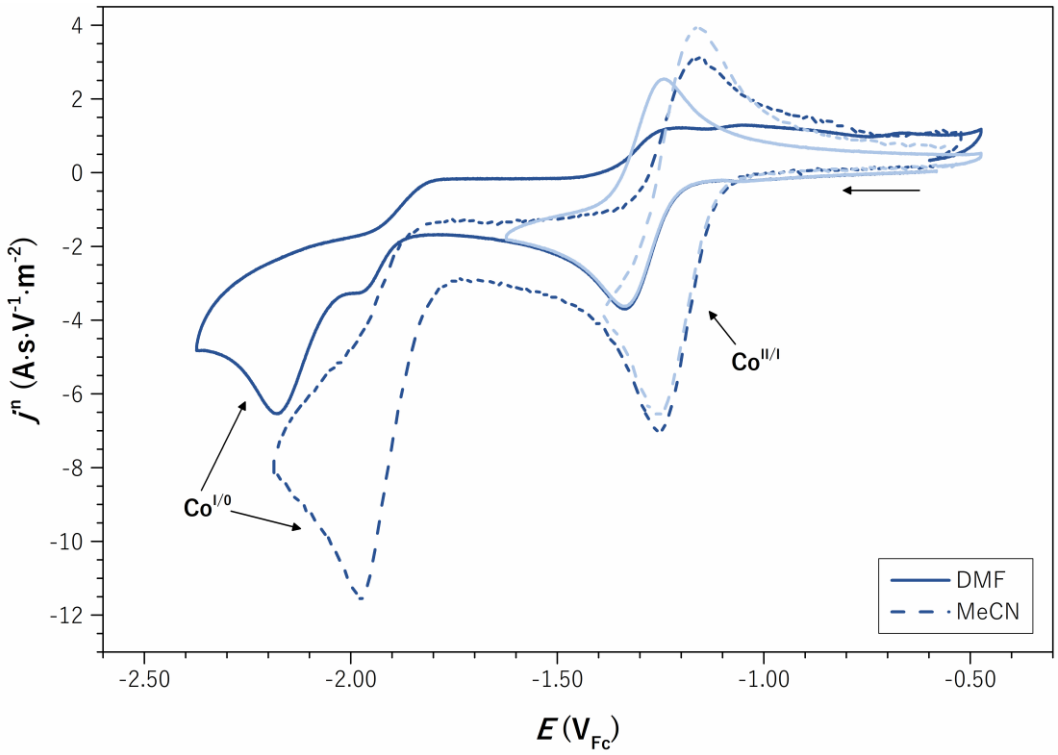

Figure 3.24. CVs of $\mathbf{Co^{II}_{Cl}}$ in DMF (solid line) and MeCN (dashed line) at varying potential windows.

Comparison with data extracted from CVs in MeCN [$E^0(Co^{II/I})$ = –1.21 V_{Fc} with ΔE_p = 94 mV and $E_{p,c}(Co^{I/0})$ = –1.98 V_{Fc}] shows a cathodic shift of both waves in DMF, but a similar peak-to-peak

potential difference ΔE_p at the $Co^{II/I}$ wave. This shift to more negative potentials in DMF could be caused by solvent coordination and less marked π back bonding compared to MeCN. The concomitant increase in electron density at the metal center affords more negative reduction potentials and induces a cathodic wave shift in CV. These findings support the theory of a solvent molecule being involved in the first redox event of $\mathbf{Co}_{Cl}^{II}$ and extend it to DMF.

In MeCN, [Co^{I}**L**Cl] is reduced to Co(0) in an **EC** fashion as deduced from the slope of the peak reduction potential in scan rate-varied measurements. [Co^{I}**L**Cl] likely undergoes reduction to [Co^{0}**L**Cl]$^-$ before substitution of chloride by MeCN and formation of tetrahedral [Co^{0}**L**(MeCN)]. The same $E_{p,c}(Co^{I/0}) = -1.98$ V_{Fc} in the CVs of $\mathbf{Co}_{s}^{II}$ and $\mathbf{Co}_{Cl}^{II}$ could evidence the same species at the Co(0) state for both complexes. The substitution equilibrium constant $K_{2,0,1}$ must be large, considering the retention of the irreversibility of the wave in the KP zone. Concurrently, $k_{2,0,1}^{+}$ must be large as well (or $k_{2,0,1}^{-}$ small) as inferred from the minor effect of increasing TBACl concentrations (apart from the loss of peak current density originating from the decomposition of the cobalt complex at higher oxidation states, Figure B.18).

3.5.3 Nickel

The proposed cube scheme for the reduction patterns of $\mathbf{Ni}_{s}^{II}$ and $\mathbf{Ni}_{Cl}^{II}$ in acetonitrile is shown in Scheme 3.10.

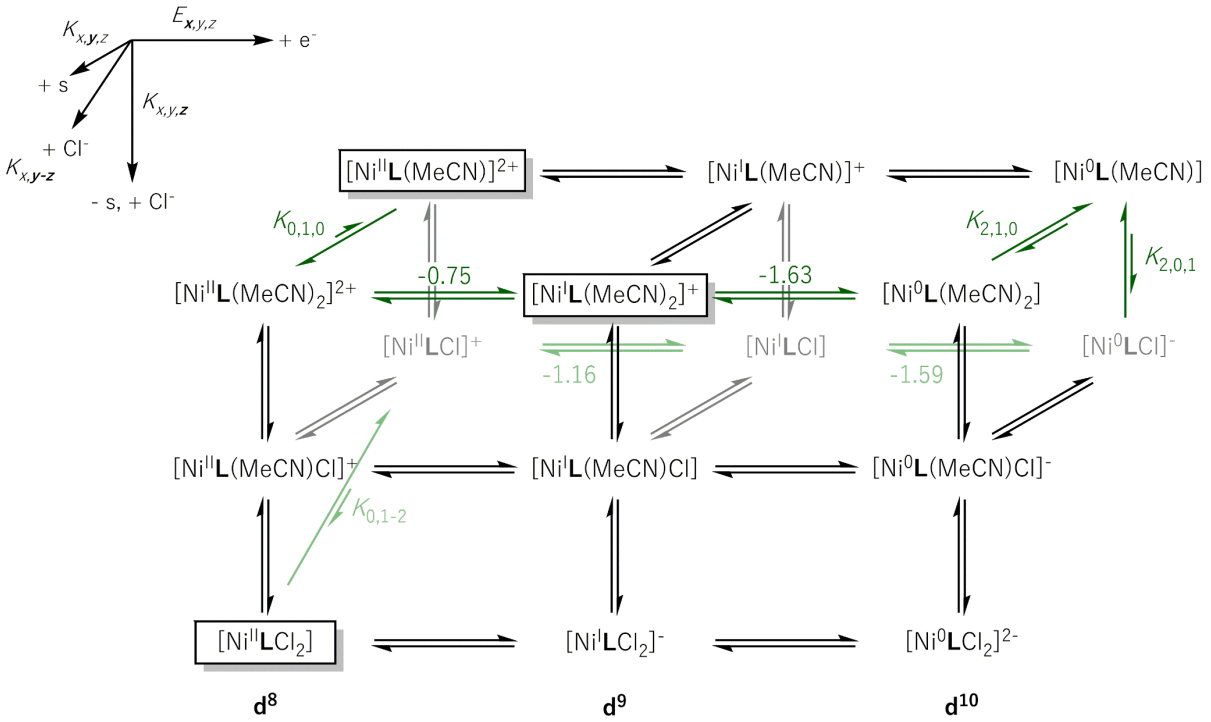

Scheme 3.10. Proposed cube scheme for the two-fold reduction of $\mathbf{Ni}_{s}^{II}$ and $\mathbf{Ni}_{Cl}^{II}$ in acetonitrile. Framed structures were confirmed by X-ray diffraction. Potentials are given in V_{Fc}.

3.5.3.1 [Ni**L**(MeCN)](BF$_4$)$_2$

Regarding $[Ni^{II}\mathbf{L}(MeCN)]^{2+}$ ($\mathbf{Ni_s^{II}}$) as the starting point, the reversible reduction wave at $E^0_{1,0,0} = -0.75\ V_{Fc}$ up to scan rates of 100 $V \cdot s^{-1}$ (Figure B.7) hints toward a single one-electron reduction forming $[Ni^{I}\mathbf{L}(MeCN)]^{+}$. However, the actual molecular structure at the Ni(I) state determined by single-crystal X-ray diffraction is $[Ni^{I}\mathbf{L}(MeCN)_2]^{+}$. A **CE** sequence is proposed based on the reversibility of the wave over several orders of magnitude in scan rate and a supposedly large MeCN association equilibrium constant $K_{1,1,0}$ in excess MeCN [eq. (3.25) and (3.26)]. Probably, both underlying rate constants ($k^{+}_{1,1,0}$ and $k^{-}_{1,1,0}$) are fast compared to the maximum applied scan rate. Hence, the observed reduction wave likely displays a fastly equilibrated mixture with $E^0 = -0.75\ V_{Fc}$ being the weighted average of the standard potentials of the electron transfer to $[Ni^{II}\mathbf{L}(MeCN)]^{2+}$ respectively $[Ni^{II}\mathbf{L}(MeCN)_2]^{2+}$.

A further reduction to the zero-valent nickel complex occurs at $E^0_{2,1,0} = -1.63\ V_{Fc}$, with the reoxidation wave recovered only at scan rates > 5 $V \cdot s^{-1}$. The **C** step in the **EC** mechanism is sufficiently slow [$k^{-}_{2,1,0}$ was determined at $3.9 \cdot 10^{1}\ s^{-1}$ from the slope of the $E_{p,c}$ vs. log(ν) plot and eq. (D.11)] to be accessed at elevated scan rates, consistent with a reduction of $[Ni^{I}\mathbf{L}(MeCN)_2]^{+}$ to $[Ni^{0}\mathbf{L}(MeCN)_2]$ before the loss of MeCN gives the 18 VE $[Ni^{0}\mathbf{L}(MeCN)]$ species.

In contrast to this, two major irreversible reduction waves attributed to two-fold one-electron reductions from Ni(II) to Ni(0) can be observed for $\mathbf{Ni_s^{II}}$ in DMF at $E_{p,c} = -0.87\ V_{Fc}$ and $-1.85\ V_{Fc}$ (Figure B.14C). The irreversible nature of the $Ni^{II/I}$ wave and the cathodic shift of $\Delta E^{MeCN \rightarrow DMF}_{p,c} \approx -80$ mV indicate a chemical reaction connected to the reduction step, likely the exchange of the acetonitrile ligand with DMF or association of another solvent molecule [eq. (3.42) and (3.43)].

C: $$[Ni^{II}\mathbf{L}(MeCN)]^{2+} + DMF \rightleftarrows [Ni^{II}\mathbf{L}(dmf)]^{2+} + MeCN \quad (3.42)$$

E: $$[Ni^{II}\mathbf{L}(dmf)]^{2+} + e^- + m\ DMF \rightarrow [Ni^{I}\mathbf{L}(dmf)_{m+1}]^{+}\ (m = 0 \text{ or } 1) \quad (3.43)$$

Reduction at the second wave is then surmised to give the putatively tetrahedral d^{10} 18 VE complex $[Ni^{0}\mathbf{L}(dmf)]$, either by loss of a DMF ligand and geometric reorganization or solely by the latter [eq. (3.44) and (3.45)].

E: $$[Ni^{I}\mathbf{L}(dmf)_{m+1}]^{+} + e^- \rightarrow [Ni^{0}\mathbf{L}(dmf)_{m+1}]\ (m = 0 \text{ or } 1) \quad (3.44)$$

C: $$[Ni^{0}\mathbf{L}(dmf)_{m+1}] \rightleftarrows [Ni^{0}\mathbf{L}(dmf)] + m\ DMF \quad (3.45)$$

Addition of up to ca. 1 mM of TBACl to $\mathbf{Ni_s^{II}}$ in MeCN (Figure 3.25) induces a similar CV behavior compared to that of $\mathbf{Co_s^{II}}$ indicating conversion of $[Ni^{II}\mathbf{L}(MeCN)]^{2+}$ to $[Ni^{II}\mathbf{L}Cl]^{+}$. The maximum

peak current density of the $Ni^{II/I}$ wave at $E^0_{1,0,1}$ = −1.16 V_{Fc} is reached at TBACl concentrations of 1.96 mM (= 2 equiv.). The subsequent drop at higher excess of TBACl indicates a **CE** mechanism in which the product of the **C** step is redox-inert at the considered potential.

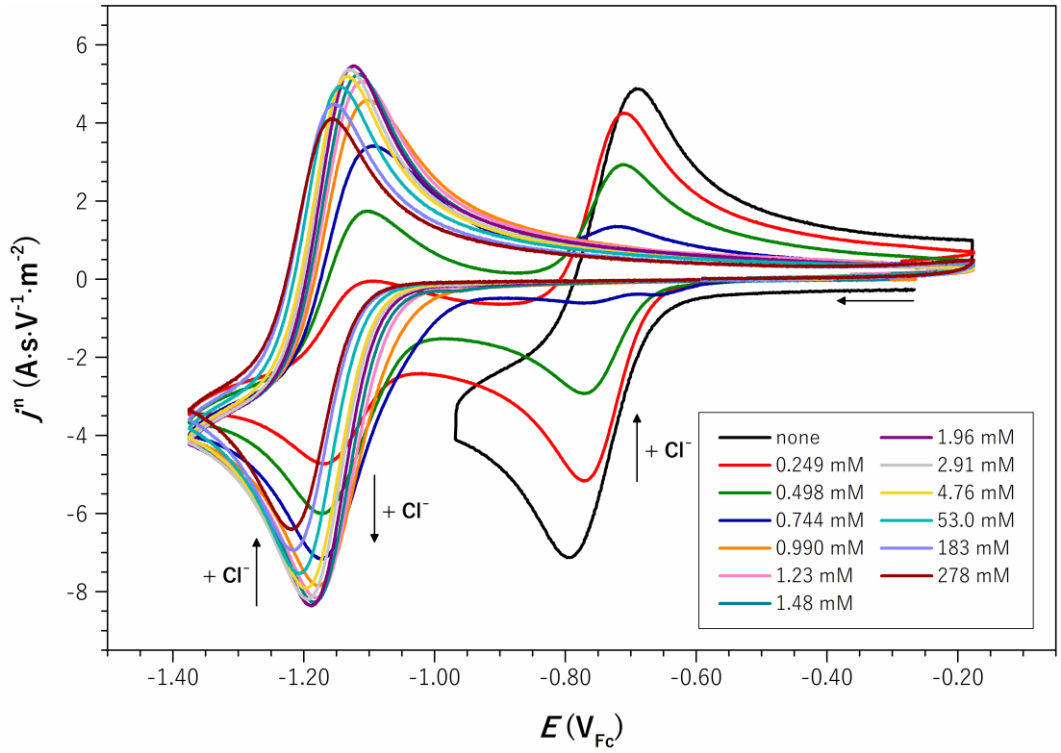

Figure 3.25. CVs of the $Ni^{II/I}$ wave of $\mathbf{Ni_s^{II}}$ at varying concentrations of TBACl.

Although NMR spectroscopy in CD_2Cl_2 indicates a quantitative association of the second chloride ligand when 2 equiv. of TBACl are added, the same experiment in CD_3CN suggests the necessity of a superstoichiometric amount of the Cl^- source for bis-chlorination. Apart from the coordinative competition between chloride and acetonitrile, the stronger polarity of MeCN supports the dissociation of ionic species and shifts the equilibrium toward the mono-chloride.

The equilibrium in eq. (3.36) is increasingly shifted to $\mathbf{Ni_{Cl}^{II}}$ at $c_{TBACl} \geq 3$ mM, which likely constitutes said CV-silent species. $K_{0,1\text{-}2}$ for the association of the second chloride ligand [eq. (3.46)] is surmised to be small compared to $K_{0,0,1}$ for exchanging MeCN with Cl^- [eq. (3.47)] considering the substantial remaining peak current density at more than 250 equiv. of TBACl.

C: $$[Ni^{II}\mathbf{L}Cl]^+ + Cl^- \rightleftarrows [Ni^{II}\mathbf{L}Cl_2] \quad (3.46)$$

C: $$[Ni^{II}\mathbf{L}(MeCN)]^{2+} + Cl^- \rightleftarrows [Ni^{II}\mathbf{L}Cl]^+ + MeCN \quad (3.47)$$

The CVs of $\mathbf{Ni_s^{II}}$ at ν = 10 V·s^{-1} under variation of the TBACl concentration allow the analysis of the $Ni^{I/0}$ wave in its reversible state (Figure 3.26).

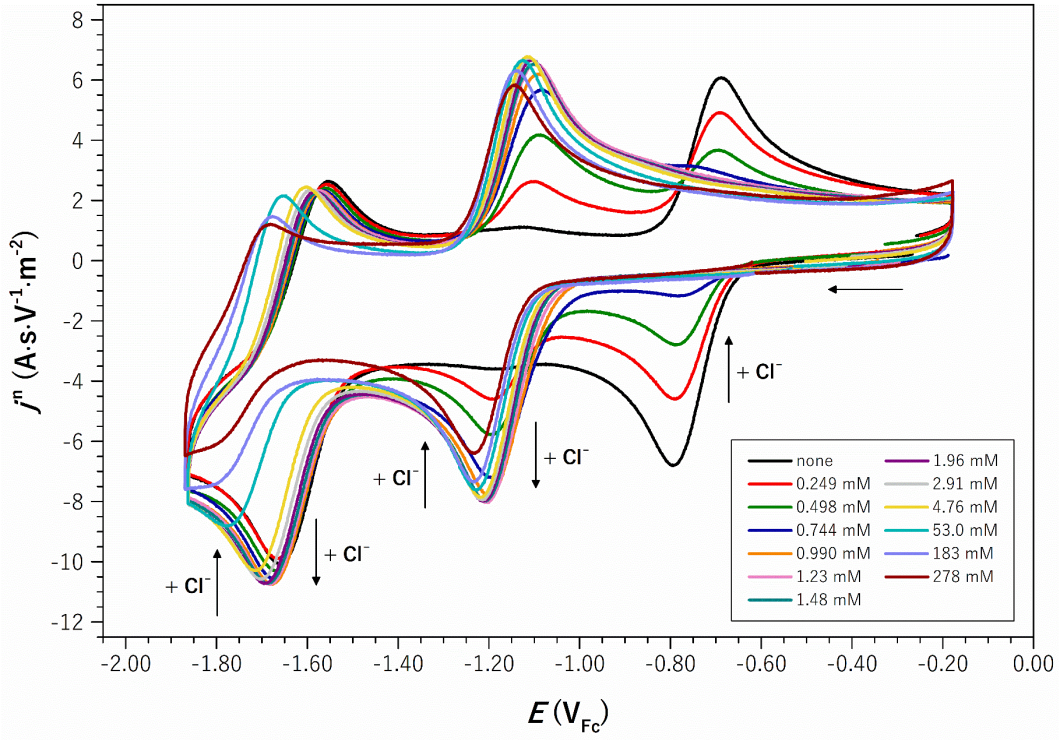

Figure 3.26. CVs of $\mathbf{Ni}_{\mathbf{s}}^{\mathbf{II}}$ at ν = 10 V·s^{-1} and varying concentrations of TBACl.

The $Ni^{I/0}$ wave exhibits a significant cathodic shift of the standard potential accompanied by loss of peak current density at c_{TBACl} > ~ 5 mM, likely reflecting the association of chloride at the Ni(I) stage and subsequent reduction via the **CE** steps in eq. (3.48) and (3.49).

C: $$[Ni^{I}\mathbf{L}Cl] + Cl^- \rightleftarrows [Ni^{I}\mathbf{L}Cl_2]^- \quad (3.48)$$

E: $$[Ni^{I}\mathbf{L}Cl_2]^- + e^- \rightleftarrows [Ni^{0}\mathbf{L}Cl_2]^{2-} \quad (3.49)$$

Formation of redox-inert $[Ni^{I}\mathbf{L}Cl_2]^-$ at the considered potentials leads to the gradual loss of current density at this wave. The associated equilibrium constant $K_{1,1\text{-}2}$ is likely relatively small regarding the required concentrations of TBACl.

3.5.3.2 [Ni**L**Cl$_2$]

The first reduction wave of $\mathbf{Ni}_{\mathbf{Cl}}^{\mathbf{II}}$ at $E^0_{1,0,1}$ = −1.16 V_{Fc} stays fully reversible in the applied range of scan rates of 0.1 V·s^{-1} to 100 V·s^{-1} (Figure B.2). Analyzing $\mathbf{Ni}_{\mathbf{s}}^{\mathbf{II}}$ by NMR spectroscopy revealed a rapid exchange of MeCN with Cl$^-$ at 1 equiv. of TBACl, which identifies $[Ni^{II}\mathbf{L}Cl]^+$ as a possible species in CV. Although coordination of MeCN is possible for $\mathbf{Ni}_{\mathbf{Cl}}^{\mathbf{II}}$ (similar to $\mathbf{Ni}_{\mathbf{s}}^{\mathbf{II}}$) CVs in the less coordinating solvent DMF (Figure 3.27) suggest a different behavior.

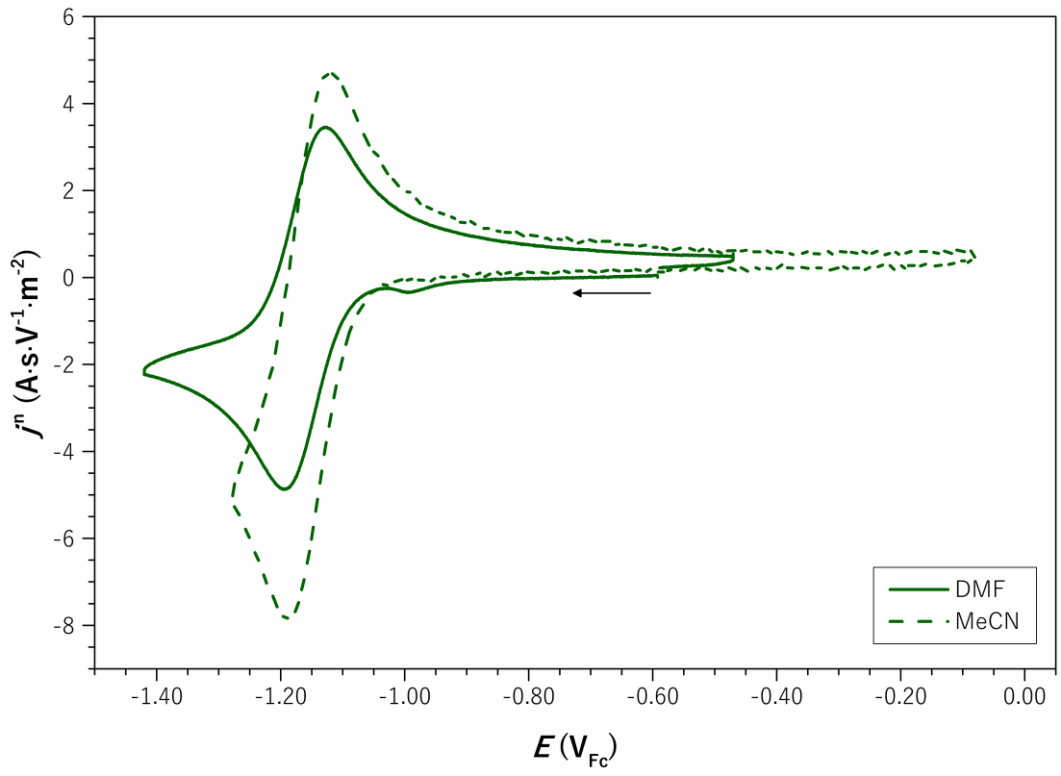

Figure 3.27. CVs of the $Ni^{II/I}$ wave of $\mathbf{Ni}^{\mathbf{II}}_{\mathbf{Cl}}$ in DMF (solid line) and MeCN (dashed line).

The CV pattern of $\mathbf{Ni}^{\mathbf{II}}_{\mathbf{Cl}}$ in DMF begins with a reversible wave at $E^0 = -1.16$ V_{Fc} ($\Delta E_p = 67$ mV) prior to a broad, irreversible wave at $E_{p,c} = -1.96$ V_{Fc} (Figure B.17C) assigned to the $Ni^{II/I}$ and $Ni^{I/0}$ couples, respectively. Scan rate-dependent CVs reveal retention of the reversibility of the $Ni^{II/I}$ wave and the irreversibility of the $Ni^{I/0}$ one throughout the whole range of applied scan rates (Figure B.19 and Figure B.20). $\mathbf{Ni}^{\mathbf{II}}_{\mathbf{Cl}}$ exhibits a $Ni^{II/I}$ wave at an almost identical standard potential of $E^0 = -1.16$ V_{Fc} ($\Delta E_p = 67$ mV, Figure 3.27) in DMF and MeCN. Since the wave's potential stays unaffected by the solvent exchange, the involvement of DMF and MeCN are excluded at this stage. The reversible $Ni^{II/I}$ wave thus reflects an isolated **E** step from $[Ni^{II}\mathbf{L}Cl]^+$ to $[Ni^{I}\mathbf{L}Cl]$ [eq. (3.6)].

The subsequent $Ni^{I/0}$ wave behaves similarly to that of $\mathbf{Ni}^{\mathbf{II}}_{\mathbf{s}}$ but at an anodically shifted potential $E^0_{2,0,1} = -1.59$ V_{Fc}. Its cathodic peak potential decays logarithmically of scan rate (KP zone) with an intercept of $a = -1.67$ V_{Fc} (Figure 3.5, right). From this data, the apparent forward rate constant of the follow-up chemical step was estimated at $k^+_{2,0,1} = 3.6{\cdot}10^{-1}$ s^{-1} using equation (D.11). Hence, the $Ni^{I/0}$ wave of $\mathbf{Ni}^{\mathbf{II}}_{\mathbf{Cl}}$ is attributed to the **EC** sequence comprising the reduction of $[Ni^{I}\mathbf{L}Cl]$ to $[Ni^{0}\mathbf{L}Cl]^-$ and moderately fast chloride exchange yielding $[Ni^{0}\mathbf{L}(MeCN)]$ from eq. (3.7) and (3.8).

Less stabilization from π back bonding of the auxiliary ligand in [Ni^0**L**(dmf)] compared to [Ni^0**L**(MeCN)] and the necessity of a more potent driving force for the reduction might explain the drastic anodic shift of the Ni$^{I/0}$ wave in DMF by $\Delta E_{p,c}^{MeCN\rightarrow DMF} \approx -300$ mV.

3.5.4 Electrochemical Influence of the Auxiliary Ligands

The CVs of the $\mathbf{M}_x^{II}$ complexes (**M** = Ni or Co, x = MeCN or Cl) in Figure 3.13 are scrutinized in more detail to emphasize the significance of the auxiliary ligand for the reducibility and reduction strength of a complex.

For Co, the Co$^{II/I}$ wave is shifted by $\Delta E_{Cl\rightarrow s}^{0}(Co^{II/I}) = 0.32$ V between chloride and MeCN as auxiliary ligands. This potential difference reflects the far easier reducibility of the acetonitrile species compared to the chloride one at the Co$^{II/I}$ wave. Scheme 3.9 depicts that **EC** sequences of [Co^{II}**L**(MeCN)Cl]$^+$ to [Co^{I}**L**Cl] and [Co^{II}**L**(MeCN)$_2$]$^{2+}$ to [Co^{I}**L**(MeCN)]$^+$ underlie the respective Co$^{II/I}$ wave. Hence, both substrates and products only differ by one auxiliary ligand, making the latter the defining factor for the deviation in standard potential.

In general, chloride ligands only serve as σ-donors, whereas nitriles are known to provide (limited) π back bonding as well.[25] Hence, the additional electron density located at the metal center is better compensated for in the presence of MeCN ligands, which makes them (weakly) stabilizing auxiliary ligands for metals in low-valent oxidation states. The lesser π-accepting character of the chloride ligand and the lowered charge of the complex require a higher driving force for the electron transfer to [Co^{II}**L**(MeCN)Cl]$^+$ compared to [Co^{II}**L**(MeCN)$_2$]$^{2+}$, which manifests itself in the observed potential difference.

The difference in peak potential of $\Delta E_{p,c}^{Cl\rightarrow s} = -0.02$ V at the second wave, ascribed to the Co$^{I/0}$ redox event, is insignificant in relation to the one for Co$^{II/I}$. Despite different Co(I) compounds, reducing both species requires a similar driving force. Subsequent reorganization yields [Co^0**L**(MeCN)] as the favored zero-valent species for both starting complexes.

The CVs of the nickel-based compounds in Figure 3.13 show a related behavior; however, with varied potential differences of $\Delta E_{Cl\rightarrow s}^{0}(Ni^{II/I}) = 0.41$ V and $\Delta E_{p,c}^{Cl\rightarrow s}(Ni^{I/0}) = 0.02$ V. Adding an electron to the diamagnetic d^8 Ni(II) species [Ni^{II}**L**Cl]$^+$ and [Ni^{II}**L**(MeCN)]$^+$ yields tetracoordinate [Ni^{I}**L**Cl] and pentacoordinate [Ni^{I}**L**(MeCN)$_2$]$^+$, respectively. Here, the stronger field splitting of MeCN renders the formation of a putatively tetrahedral d^9 species unfavorable and hence forms $\mathbf{Ni}_s^{I}$ (CN = 5).

In summary, the π-accepting character of MeCN diminishes the electron density at the metal center and shifts the reduction potential of the complex anodically, which facilitates the reduction of the complex. However, this decrease in driving force goes in parallel with a loss of reduction strength.

The direct comparison of the $\mathbf{M}_{x}^{II}$ complex series (x = MeCN or Cl) of Fe, Co, and Ni by cyclic voltammetry in more (MeCN) or less (DMF) coordinating solvents can give an impression of the lability of chloride and MeCN ligands. Table 3.3 summarizes the qualitative assessment of the behavior of $\mathbf{M}_{x}^{II}$ complexes (**M** = Fe, Co, or Ni; x = MeCN or Cl) inferred from CV in DMF and MeCN electrolyte solution.

Table 3.3. Qualitative assessment of the behavior of $\mathbf{M}_{x}^{II}$ complexes in DMF and MeCN electrolyte solution, as inferred from CV (= : stable, ⇄ : conversion, – : decomposition).

	$\mathbf{Fe}_{Cl}^{II}$	$\mathbf{Fe}_{s}^{II}$	$\mathbf{Co}_{Cl}^{II}$	$\mathbf{Co}_{s}^{II}$	$\mathbf{Ni}_{Cl}^{II}$	$\mathbf{Ni}_{s}^{II}$
DMF	–	–	⇄	–	⇄	⇄
MeCN	⇄	=	⇄	=	⇄	=

While $\mathbf{Fe}_{Cl}^{II}$ (partly) decomposes in both solvents, $\mathbf{Co}_{Cl}^{II}$ only exchanges one chloride ligand in MeCN (as inferred from the potential shift at the first reduction wave), and Ni is not affected at all at the $Ni^{II/I}$ couple. Hence this row of CVs indicates an incrementing influence of the solvent in the series Ni < Co < Fe. In DMF, the $\mathbf{M}_{s}^{II}$ complexes of Fe and Co decompose completely, whereas Ni possibly exchanges its coordinated solvent. Among the chloride analogs, only iron decomposes in DMF, while cobalt and nickel are converted.

This analysis confirms the expectation of the solvent ligand acetonitrile to be more labile than chloride when contacted with an excess of DMF. Put in perspective to the individual metal center, the general stability of the complexes and the metal-auxiliary ligand bond strength appear to increase in the row of Fe < Co < Ni. This trend is well in line with decreasing bond lengths (as a proxy for the bond strength) toward later central metals in the 3d row, as discussed in section 2.2.1.7 for $\mathbf{M}_{Cl}^{II}$ and in section 2.2.2.4 for $\mathbf{M}_{s}^{II}$.

For the stable complexes, the switch to DMF almost exclusively leads to anodically shifting potentials of the reduction waves (in particular $\mathbf{M}^{I/0}$) induced by the electronic effect of the solvent when coordinated to the metal center. The potential shift again emphasizes the auxiliary ligand's influence on the reducibility and, hence, the reducing strength of the complexes.

3.6 Experimental

3.6.1 NMR Studies

3.6.1.1 NMR Studies in Deuterated Dichloromethane

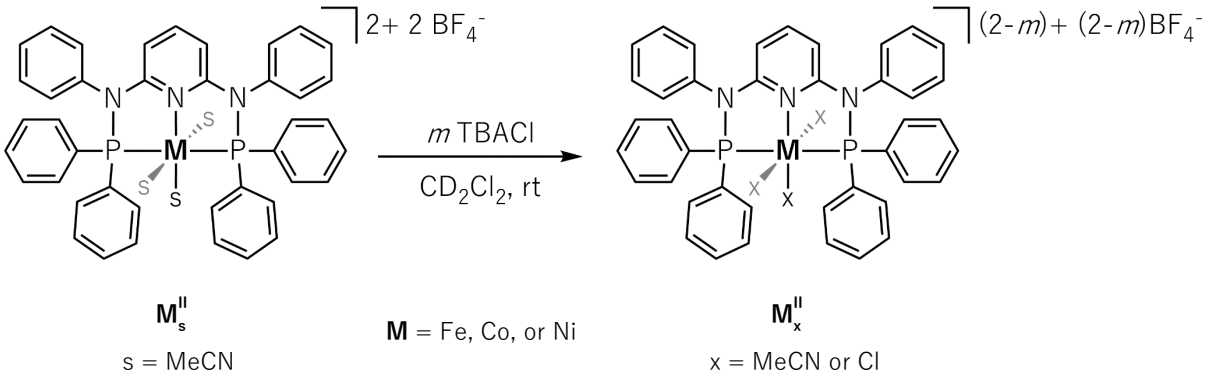

$\mathbf{M_s^{II}}$ (0.01 mmol, 1.00 equiv.) was placed into a J. YOUNG NMR tube in the glovebox, and CD_2Cl_2 (0.5 mL) was added. ^1H and $^{31}P\{^1H\}$ NMR spectra were recorded. Solid TBACl was added stepwise, and NMR spectra were recorded after each addition.

3.6.1.2 NMR Studies in Deuterated Acetonitrile

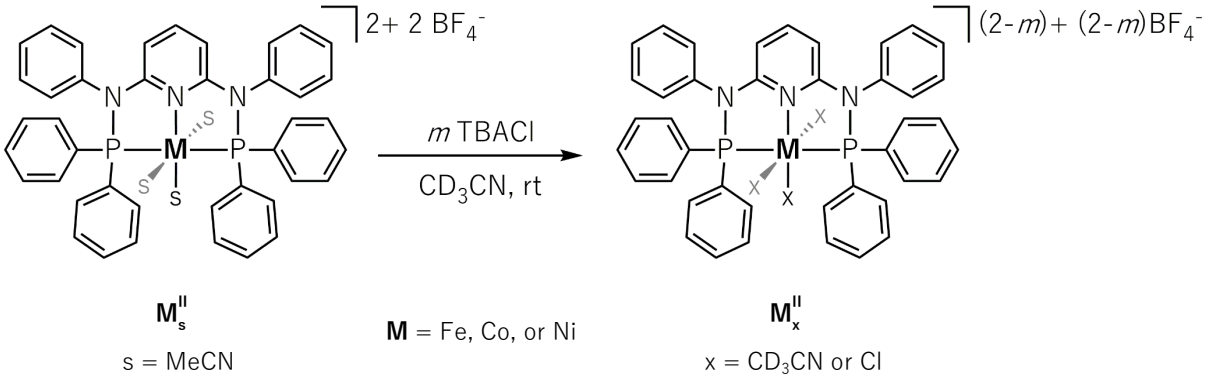

$\mathbf{M_s^{II}}$ (0.005 mmol, 1.00 equiv.) was placed into a J. YOUNG NMR tube in the glovebox, and CD_3CN (0.5 mL) was added. ^1H and $^{31}P\{^1H\}$ NMR spectra were recorded. A solution of TBACl in CD_3CN (0.1 M) was added stepwise, and NMR spectra were recorded after each addition.

3.6.2 Cyclic Voltammetry

Cyclic voltammetry was performed on a BIOLOGIC VSP-300 potentiostat equipped with an analog ramp generator for high potential scan rate analysis (Figure 3.28A) using a standard three-electrode setup (Figure 3.28B). The setup contains a glassy carbon working electrode (WE), a platinum wire counter electrode (CE), and a custom-made $AgNO_3$/Ag (10 mM $AgNO_3$ in a solution of 0.1 M $^nBu_4NPF_6$ in the electrochemical solvent) or an Innovative Instruments LF-5 leak-free AgCl/Ag (3.4 M KCl in H_2O) reference electrode (RE, Figure 3.28C). The working electrode was polished over a velvet polishing pad using an alumina suspension before rinsing with ultrapure water from a MILLIQ ADVANTAGE A10 water purification system and ethanol. Reference and counter electrodes were rinsed with ultrapure water and ethanol. Lastly, each electrode was dried under a stream of argon before insertion into the hot cell (stored at 120 °C). The OHMIC drop of the electrochemical cell was estimated and compensated (85%) by the iR compensation loop embedded in the potentiostat.

A dry and degassed solution of 1 mM analyte and 0.1 M $^nBu_4NPF_6$ was prepared in the electrochemical solvent. Tetrabutylammonium hexafluorophosphate was dried and degassed *in vacuo* at 80 °C for 12 h. The electrolyte solution was purged by bubbling a solvent-saturated argon flow through a silicone tubing under vigorous stirring before adding the analyte. Cyclic voltammograms were typically recorded at a scan rate of 0.1 $V \cdot s^{-1}$, with the scanned potential window adjusted according to the visible redox waves. Parameter variations are indicated in the respective measurements.

TBACl was dried and degassed in the molten state *in vacuo* at 110 °C for 4 h. For CV studies, TBACl was first added as a 0.1 M solution in MeCN, then as a 1 M solution, and lastly in the solid state directly from the glovebox.

1 mM Fc was added after the last measurement of a row as the internal potential reference.

A) CV Setup

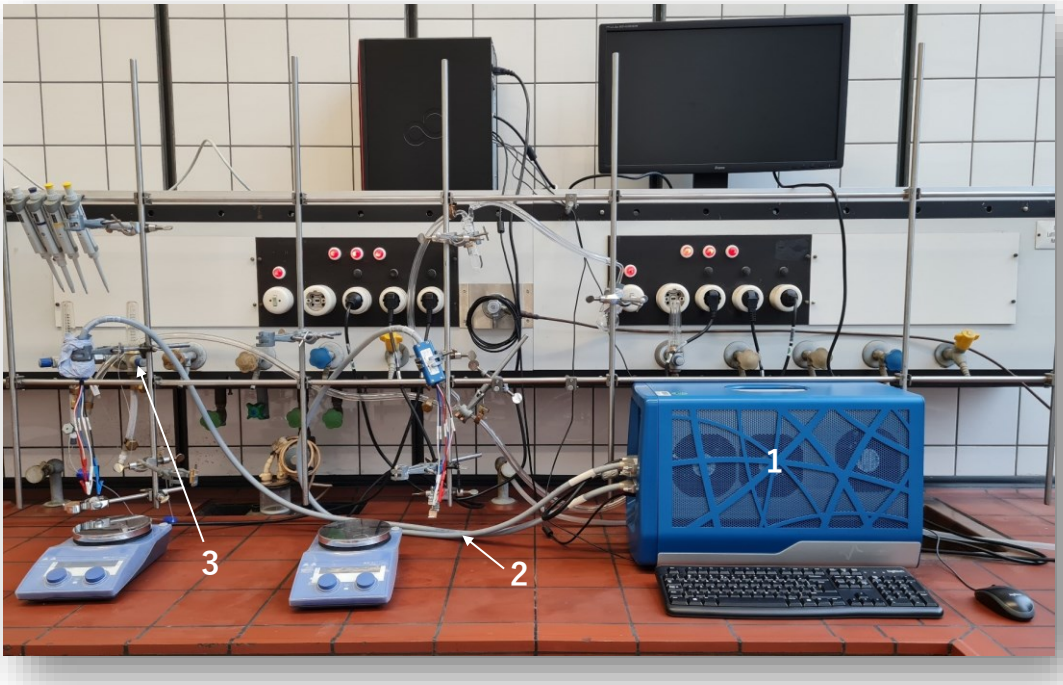

1 – Potentiostat + analog ramp generator, **2** – Electrode cables, **3** – Argon supply

B) CV Cell

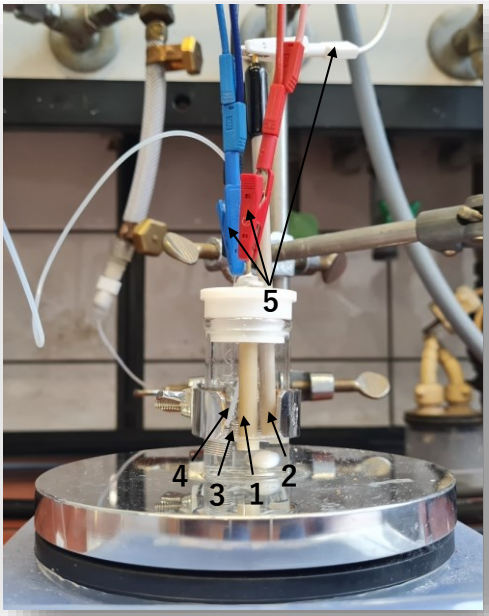

1 – GC WE, **2** – AgCl/Ag RE, **3** – Pt wire CE,
4 – Silicone tubing, **5** – Electrode cables

C) CV Electrodes

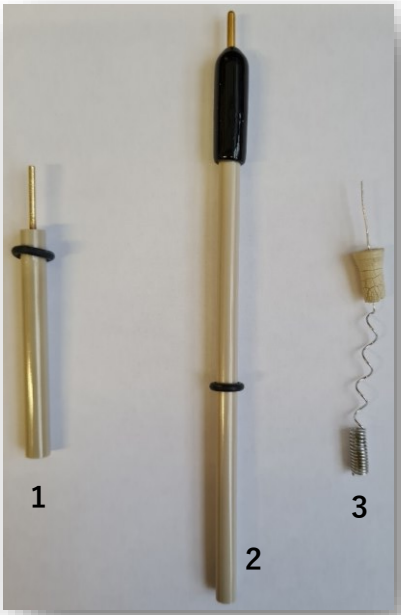

1 – GC rod WE, **2** – AgCl/Ag RE,
3 – Pt wire CE

Figure 3.28. (A) CV setup, (B) CV cell with electrodes and electrolyte, and (C) close-up of CV electrodes.

3.7 References

[1] C. W. Machan, C. P. Kubiak, *Dalton Trans.* **2016**, *45*, 17179.

[2] J. Brown, J. Ovens, D. Richeson, *ChemSusChem* **2022**, *15*, e202102542.

[3] D. W. Shaffer, S. I. Johnson, A. L. Rheingold, J. W. Ziller, W. A. Goddard, R. J. Nielsen, J. Y. Yang, *Inorg. Chem.* **2014**, *53*, 13031.

[4] S. Lapointe, E. Khaskin, R. R. Fayzullin, J. R. Khusnutdinova, *Organometallics* **2019**, *38*, 1581.

[5] J.-M. Savéant, C. Costentin, *Elements of Molecular and Biomolecular Electrochemistry: An Electrochemical Approach to Electron Transfer Chemistry*, 2nd ed., John Wiley & Sons Inc., Hoboken, NJ, **2019**.

[6] S. Norouziyanlakvan, G. K. Rao, J. Ovens, B. Gabidullin, D. Richeson, *Chem. Eur. J.* **2021**, *27*, 13518.

[7] a) H. Arora, C. Philouze, O. Jarjayes, F. Thomas, *Dalton Trans.* **2010**, *39*, 10088; b) Y. Wu, J. Jiang, Z. Weng, M. Wang, D. L. J. Broere, Y. Zhong, G. W. Brudvig, Z. Feng, H. Wang, *ACS Cent. Sci.* **2017**, *3*, 847; c) M. E. Ahmed, A. Rana, R. Saha, S. Dey, A. Dey, *Inorg. Chem.* **2020**, *59*, 5292.

[8] M. Glatz, N. Gorgas, B. Stöger, E. Pittenauer, L. Ferreira, L. F. Veiros, M. J. Calhorda, K. Kirchner, *Z. Anorg. Allg. Chem.* **2021**, *647*, 1429.

[9] C. R. Hess, T. Weyhermüller, E. Bill, K. Wieghardt, *Angew. Chem. Int. Ed.* **2009**, *48*, 3703.

[10] S. Song, J. Lee, J.-H. Choi, J. Seo, *Chem. Commun.* **2021**, *57*, 7497.

[11] W. E. Geiger, *J. Am. Chem. Soc.* **1974**, *96*, 2632.

[12] V. V. Pavlishchuk, A. W. Addison, *Inorg. Chim. Acta* **2000**, *298*, 97.

[13] Y. Jean, *Molecular Orbitals of Transition Metal Complexes*, Oxford University Press, New York, **2005**.

[14] M. D. Sampson, A. D. Nguyen, K. A. Grice, C. E. Moore, A. L. Rheingold, C. P. Kubiak, *J. Am. Chem. Soc.* **2014**, *136*, 5460.

[15] G. K. Rao, W. Pell, I. Korobkov, D. Richeson, *Chem. Commun.* **2016**, *52*, 8010.

[16] a) F. Bertini, M. Glatz, N. Gorgas, B. Stöger, M. Peruzzini, L. F. Veiros, K. Kirchner, L. Gonsalvi, *Chem. Sci.* **2017**, *8*, 5024; b) S. Kar, A. Goeppert, J. Kothandaraman, G. K. S. Prakash, *ACS Catal.* **2017**, *7*, 6347; c) C. Erken, A. Kaithal, S. Sen, T. Weyhermüller, M.

Hölscher, C. Werlé, W. Leitner, *Nat. Commun.* **2018**, *9*, 4521; d) A. Kumar, P. Daw, N. A. Espinosa-Jalapa, G. Leitus, L. J. W. Shimon, Y. Ben-David, D. Milstein, *Dalton Trans.* **2019**, *48*, 14580.

[17] N. W. Kinzel, C. Werlé, W. Leitner, *Angew. Chem. Int. Ed.* **2021**, *60*, 11628.

[18] a) N. Elgrishi, M. B. Chambers, V. Artero, M. Fontecave, *PCCP* **2014**, *16*, 13635; b) X. Su, K. M. McCardle, J. A. Panetier, J. W. Jurss, *Chem. Commun.* **2018**, *54*, 3351; c) X. Su, K. M. McCardle, L. Chen, J. A. Panetier, J. W. Jurss, *ACS Catal.* **2019**, *9*, 7398; d) N. Queyriaux, K. Abel, J. Fize, J. Pécaut, M. Orio, L. Hammarström, *Sustain. Energy Fuels* **2020**, *4*, 3668; e) M. Loipersberger, D. G. A. Cabral, D. B. K. Chu, M. Head-Gordon, *J. Am. Chem. Soc.* **2021**, *143*, 744; f) N. Queyriaux, *ACS Catal.* **2021**, *11*, 4024.

[19] a) T. Yokoyama, H. Kitagawa, H.-a. Iwasawa, M. Zenki, *Inorg. Chim. Acta* **1996**, *253*, 1; b) F. Franco, C. Cometto, L. Nencini, C. Barolo, F. Sordello, C. Minero, J. Fiedler, M. Robert, R. Gobetto, C. Nervi, *Chem. Eur. J.* **2017**, *23*, 4782; c) L. Iffland, D. Siegmund, U.-P. Apfel, *Z. Anorg. Allg. Chem.* **2020**, *646*, 746.

[20] N. S. Gill, F. B. Taylor, W. E. Hatfield, W. E. Parker, C. S. Fountain, F. L. Bunger, in *Inorg. Synth.*, **1967**.

[21] F. A. Cotton, D. M. L. Goodgame, M. Goodgame, *J. Am. Chem. Soc.* **1961**, *83*, 4690.

[22] G. R. Fulmer, A. J. M. Miller, N. H. Sherden, H. E. Gottlieb, A. Nudelman, B. M. Stoltz, J. E. Bercaw, K. I. Goldberg, *Organometallics* **2010**, *29*, 2176.

[23] a) Y. Mugnier, C. Moise, E. Laviron, *J. Organomet. Chem.* **1981**, *204*, 61; b) E. Laviron, L. Roullier, *J. Electroanal. Chem.* **1985**, *186*, 1.

[24] D. Lexa, P. Rentien, J.-M. Savéant, F. Xu, *J. Electroanal. Chem.* **1985**, *191*, 253.

[25] a) B. N. Storhoff, H. C. Lewis Jr., *Coord. Chem. Rev.* **1977**, *23*, 1; b) G. Bresciani, L. Biancalana, G. Pampaloni, S. Zacchini, G. Ciancaleoni, F. Marchetti, *Molecules* **2021**, *26*, 7088.

Chapter 4: Electrochemical Carbon Dioxide Activation

Part 1: Aprotic Conditions

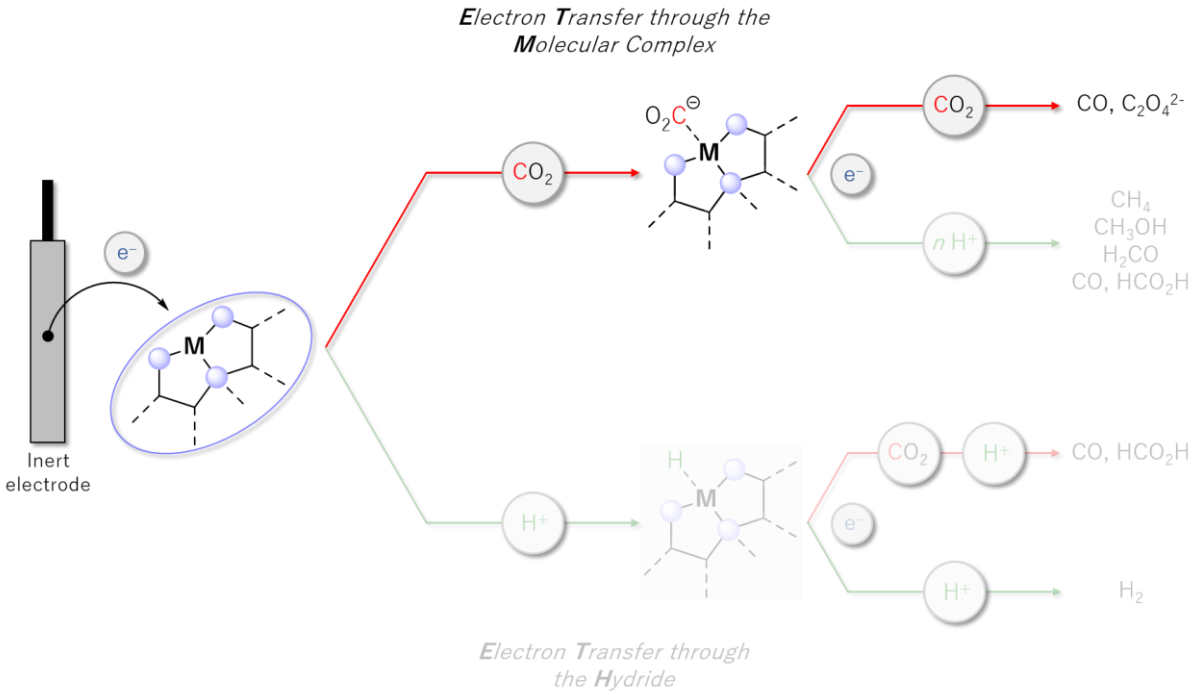

CV investigations under a CO_2 atmosphere probe the complexes' ability to coordinate the substrate in the first part of chapter 4. Reaction pathways under electrochemical conditions are proposed, and rate constants for the association of CO_2 are determined when accessible. Comparing the obtained results with literature reports identifies favorable properties for the molecularly catalyzed electrochemical CO_2 reduction.

Subsequently, experiments under the addition of Mg^{2+} ions are conducted to gain insight into the reductive disproportionation of CO_2 catalyzed by $\mathbf{M_x^{II}}$ via the ET_M mechanism. Promising reaction conditions are transferred to the controlled potential electrolysis of CO_2.

Parts of this chapter have been published in:

N. W. Kinzel, D. Demirbas, E. Bill, T. Weyhermüller, C. Werlé, N. Kaeffer, W. Leitner, *Inorg. Chem.* **2021**, *60*, 19062.

4.1 Addition of Carbon Dioxide

With the metal-centered electrochemical reducibility shown for the $\mathbf{Fe}_s^{II}$, $\mathbf{Co}_x^{II}$, and $\mathbf{Ni}_x^{II}$ complexes, CO_2 reduction requires coordination and activation of the substrate in the next step. The ET_H route is purposely hindered by depriving the system of protons to observe the **M**-CO_2 interaction as the entry into an electrocatalytic CO_2 reduction cycle via the ET_M pathway.

4.1.1 Bis-Chloride Complexes

The cyclic voltammograms of $\mathbf{Co}_{Cl}^{II}$ and $\mathbf{Ni}_{Cl}^{II}$ under argon, respectively, carbon dioxide atmosphere, are depicted in Figure 4.1. $\mathbf{Fe}_{Cl}^{II}$ is excluded due to partial conversion into a species similar to $\mathbf{Fe}_s^{II}$ (see section 2.2.2.1b) that is discussed with the acetonitrile complexes of Ni and Co.

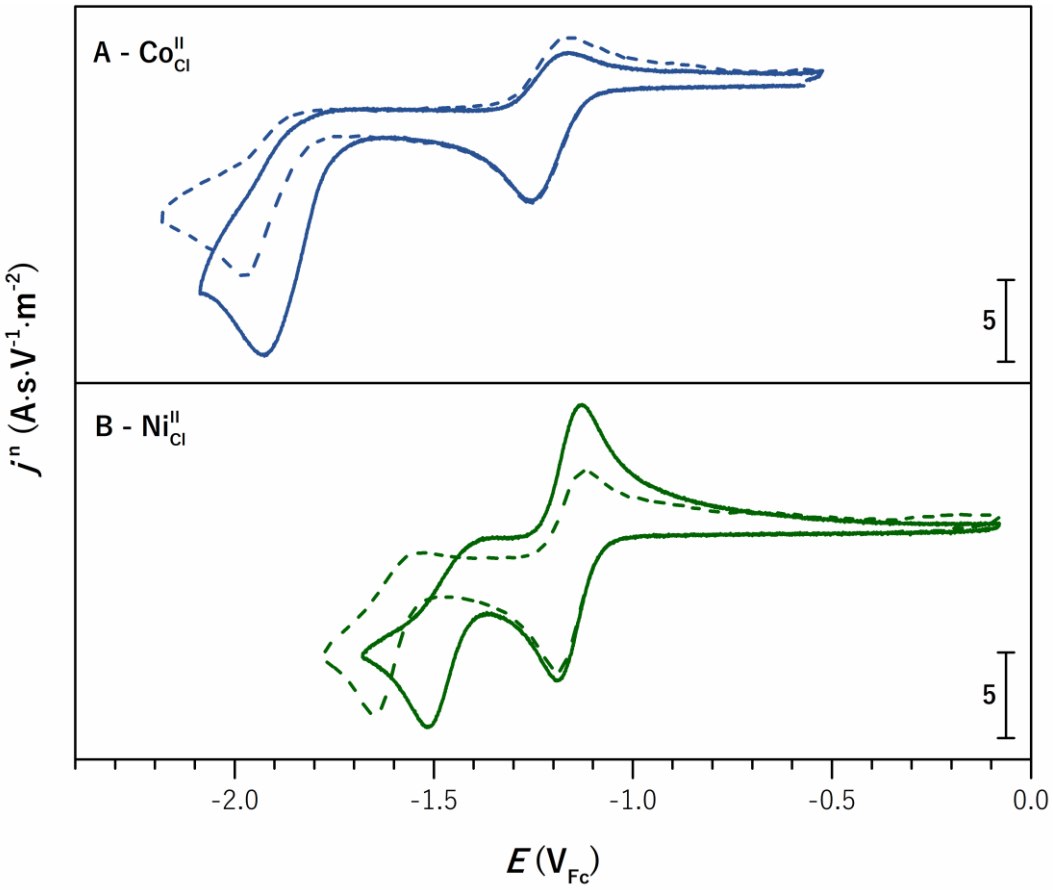

Figure 4.1. CVs of (A) $\mathbf{Co}_{Cl}^{II}$ and (B) $\mathbf{Ni}_{Cl}^{II}$ under argon (dashed line) and CO_2 atmosphere (solid line).

The $Co^{II/I}$ redox wave of $\mathbf{Co}_{Cl}^{II}$ remains unaffected by CO_2, discarding the reaction with this substrate at the Co(II) and Co(I) states. By contrast, the irreversible $Co^{I/0}$ wave shifts by approx. 50 mV in the anodic direction after CO_2 saturation. This observation evidences CO_2 coordination upon reduction to Co(0) in an **EC** mechanism, with the **E** step described in eq. (3.4) and the chemical reaction in eq. (4.1).

C: $[Co^0\mathbf{L}(MeCN)] + CO_2 \leftrightarrows [Co^0\mathbf{L}(CO_2)] + MeCN$ (4.1)

The displacement of the equilibrium in eq. (4.1) is described by $K(CO_2)$, defined as the ratio of the CO_2 association $[k^+(CO_2)]$ and dissociation $[k^-(CO_2)]$ rate constants in eq. (4.2).

$$K(CO_2) = \frac{k^+(CO_2)}{k^-(CO_2)} \tag{4.2}$$

The $Co^{I/0}$ wave remains irreversible even at elevated scan rates (Figure C.1). Hence, the rate of CO_2 association appears to be high but could not be further quantified due to the lack of knowledge of $E^0_{Ar}(Co^{I/0})$. A slight increase in the cathodic peak current (ratio $j^n_{p,c} = 1.4$) suggests electrocatalytic activity. Although reductive disproportionation of CO_2 into CO and CO_3^{2-} is conceivable under dry conditions, traces of protons from residual water or HOFFMAN degradation of the $^n Bu_4N^+$ cation possibly enable CO_2 electroreduction.

In the case of $\mathbf{Ni}^{II}_{Cl}$, the $Ni^{II/I}$ couple is also left unaffected by CO_2, discarding coordination at the corresponding +II and +I oxidation states. $\mathbf{Ni}^{II}_{Cl}$ exhibits an intense anodic shift (~130 mV) at the $Ni^{I/0}$ wave under CO_2. At variance with observations under Ar, the reversibility of the $Ni^{I/0}$ reduction wave cannot be recovered by a faster scan rate (up to 100 $V \cdot s^{-1}$, Figure 4.2).

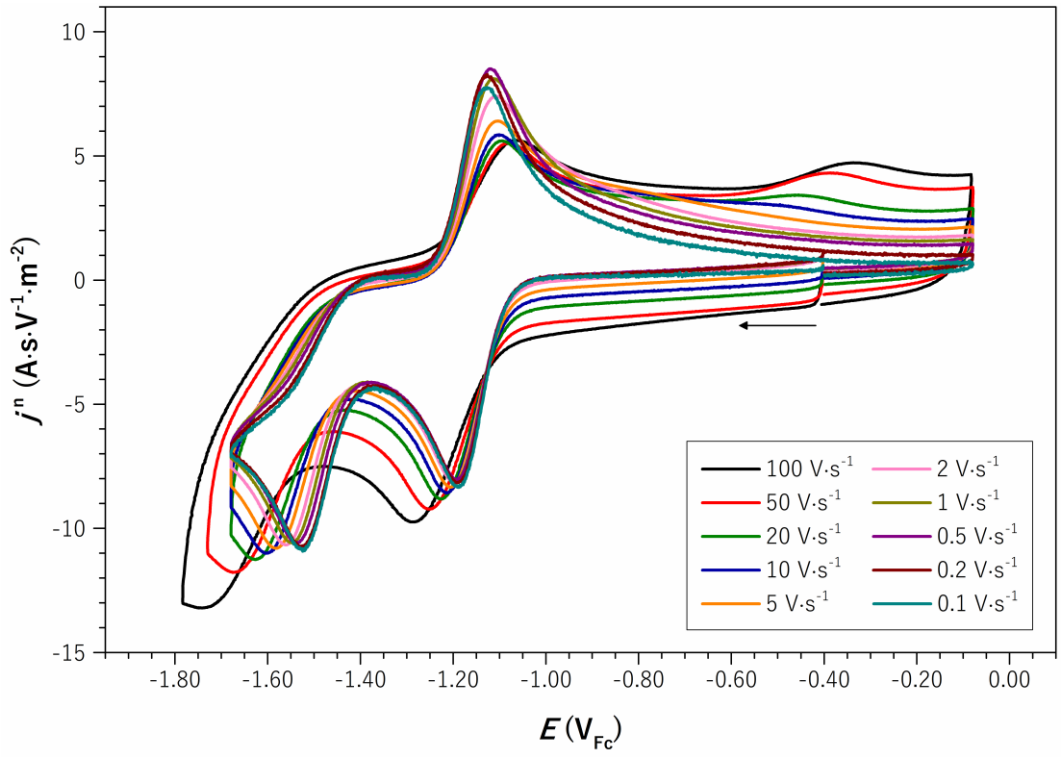

Figure 4.2. CVs of $\mathbf{Ni}^{II}_{Cl}$ under CO_2 atmosphere at varying scan rates.

These observations indicate a fast CO_2 association at the Ni(0) stage [eq. (4.3)] and are supported by the $E_{p,c} = f[\log(\nu)]$ plot linearly decaying by –28.4 mV·log(ν)$^{-1}$ (Figure 4.3, red) in the KP zone (see Figure D.4).

C: $$[Ni^0\mathbf{L}(MeCN)] + CO_2 \leftrightarrows [Ni^0\mathbf{L}(CO_2)] + MeCN \quad (4.3)$$

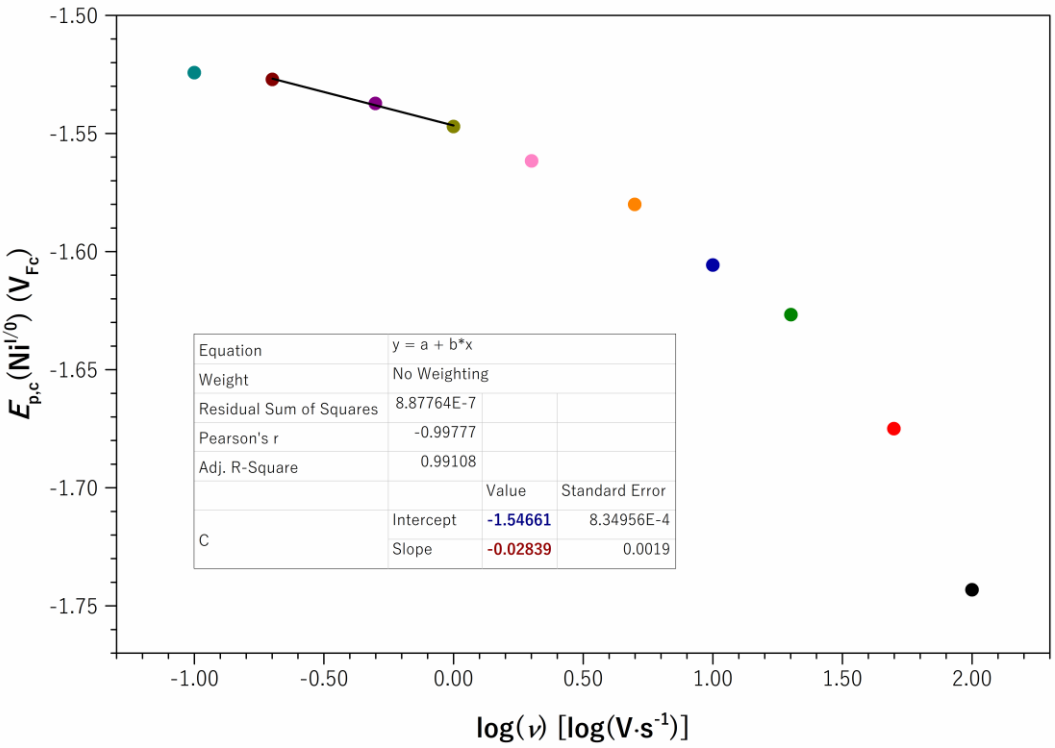

Figure 4.3. $E_{p,c}(Ni^{I/0})$ vs. log(ν) plot of $\mathbf{Ni}^{II}_{Cl}$ under CO_2 atmosphere.

Eq. (D.11) yields an apparent CO_2 association rate constant $k^+_{app}(CO_2) = 4.2{\cdot}10^3$ s^{-1}. A saturation concentration of [CO_2] = 0.28 M at 1 atmosphere of CO_2 in acetonitrile solution[1] gives the bimolecular rate constant $k^+(CO_2) = 1.5{\cdot}10^4$ M^{-1}·s^{-1} [eq. (4.4)].

$$k^+(CO_2) = \frac{k^+_{app}(CO_2)}{[CO_2]} \quad (4.4)$$

Moreover, scan rates above 10 V·s^{-1} reveal an additional oxidation wave at $E_{p,a}$ = –0.39 V_{Fc} (for ν = 50 V·s^{-1}). This wave is proposed to be associated with the oxidation of a $[Ni^{II}\mathbf{L}(MeCN)_m(COOH)]^+$ or $[Ni^{II}\mathbf{L}(MeCN)_m(CO)]^{2+}$ (m = 1 or 2) adduct generated upon reduction and protonation that is only accessible at elevated scan rates due to the limited lifetime of the species. However, the formation of a putative $[Ni^{II}\mathbf{L}(MeCN)_mH]^+$ species formed by the reaction of a Ni(0) intermediate with residual protons cannot be excluded unequivocally.

4.1.2 Acetonitrile Complexes

The cyclic voltammograms of the $\mathbf{M_s^{II}}$ complexes under argon and carbon dioxide atmosphere are reported in Figure 4.4.

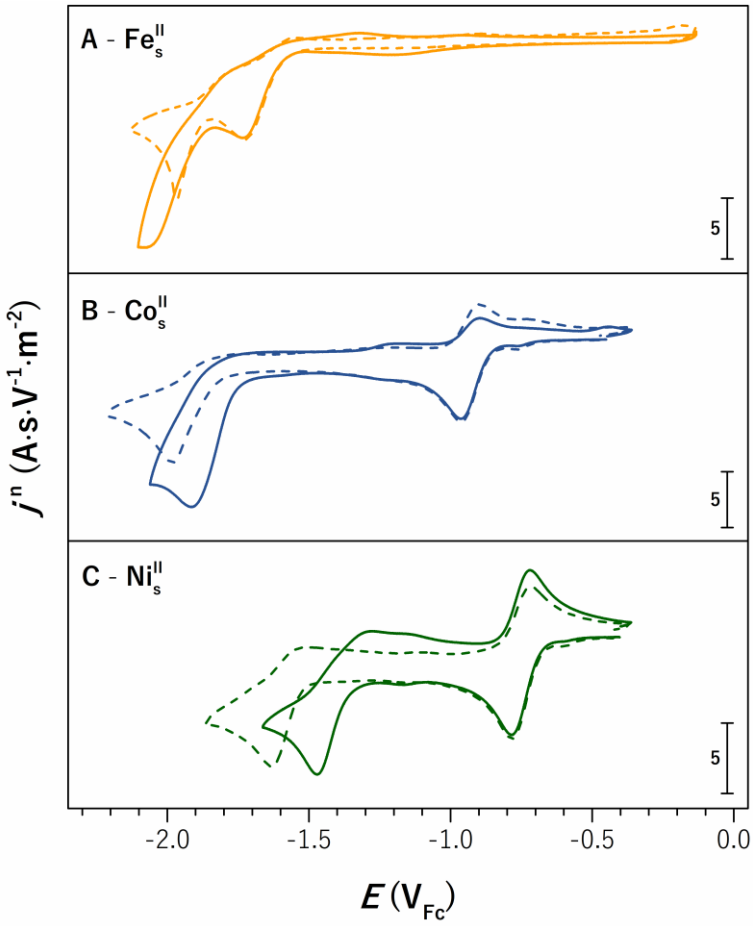

Figure 4.4. CVs of (A) $\mathbf{Fe_s^{II}}$, (B) $\mathbf{Co_s^{II}}$, and (C) $\mathbf{Ni_s^{II}}$ under argon (dashed line) and CO_2 atmosphere (solid line).

The reversibility of the two metal-centered waves of $\mathbf{Fe_s^{II}}$ under argon atmosphere at a scan rate of 100 V·s^{-1} is not retained to the same extent under CO_2 (Figure B.4 and Figure C.2). Only the potential of the $Fe^{I/0}$ wave is shifted by $\Delta E_{p,c}^{Ar \rightarrow CO_2} \approx -100$ mV under CO_2 atmosphere compared to data under argon. Moreover, a significant variation in the peak shape indicates a noticeable change in the reaction mechanism. While dimerization or disproportionation are likely under argon, these pathways might be inhibited by the coordination of carbon dioxide at this stage. The increase of the current density when introducing CO_2 (ratio $j_{p,c}^n = 1.3$) may indicate catalytic activity here as well.

For $\mathbf{Co_s^{II}}$, solely the irreversible $Co^{I/0}$ wave shifts by approx. 70 mV in the anodic direction when CO_2 is present. The retention of the irreversibility at the $Co^{I/0}$ wave for elevated scan rates (Figure C.3) and an increase in the cathodic peak current $j_{p,c}^n$ with a factor of approximately 1.4 can

be observed, similar to $\mathbf{Co}_{\mathbf{Cl}}^{\mathbf{II}}$. The combined observations hint toward an identical mechanism (**EC**) for CO_2 activation/conversion without additives.

While the $Ni^{II/I}$ wave of $\mathbf{Ni}_{\mathbf{s}}^{\mathbf{II}}$ does not exhibit any change in the presence of CO_2, the $Ni^{I/0}$ wave shifts cathodically by $\Delta E_{p,c}^{Ar \rightarrow CO_2} \approx -160$ mV. A fast association of CO_2 is supported by the loss of reversibility of the $Ni^{I/0}$ wave even at high scan rates compared to measurements under an argon atmosphere. The slope of -32.0 mV·log(ν)$^{-1}$ of the $E_{p,c}$ = f[log(ν)] plot in the KP zone suggests an **EC** mechanism (Figure 4.5) with a CO_2 association rate constant of $k_{app}^{+}(CO_2) = 4.6 \cdot 10^6$ s^{-1}, calculated from eq. (D.11). This data converts into the respective bimolecular rate constant $k^{+}(CO_2) = 1.7 \cdot 10^7$ M^{-1}·s^{-1}.

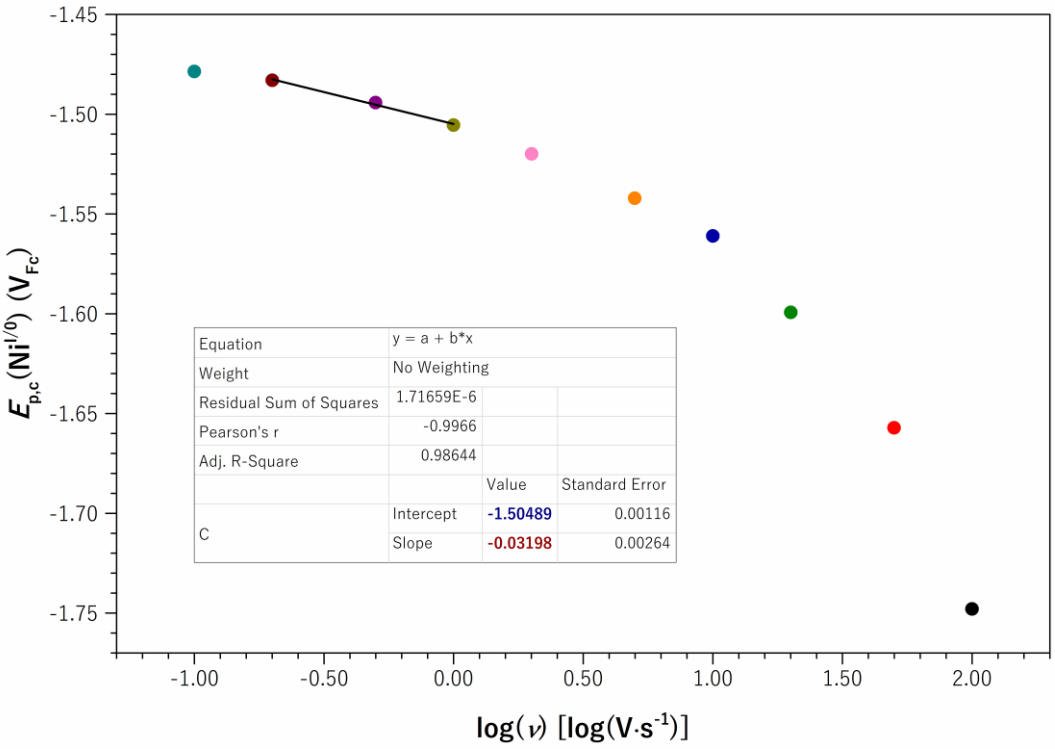

Figure 4.5. $E_{p,c}(Ni^{I/0})$ vs. log(ν) plot of $\mathbf{Ni}_{\mathbf{s}}^{\mathbf{II}}$ under CO_2 atmosphere.

4.1.3 Mechanistic Proposal for CO_2 Activation

The $\mathbf{Fe}_{\mathbf{s}}^{\mathbf{II}}$ complex shows a voltamperometric $Fe^{I/0}$ wave strongly affected by CO_2, indicating coordination at the Fe(0) state. In the presence of CO_2, the rapid chemical step deduced from the irreversibility of the $Fe^{I/0}$ wave is consistent with the high reactivity of Fe(0) species. The activation of CO_2 at Fe(0) centers reported previously, namely in eCO_2r, has been mainly observed with complexes bearing redox-active ligands[2] that are thus best described as doubly ligand-reduced Fe(II) complexes.[3] For the redox-inactive pincer ligand used here, binding of carbon dioxide to the zero-valent metal center might form [Fe^0**L**(MeCN)(CO_2)] as the primary intermediate. The subsequent reaction steps, however, remain elusive so far.

For $\mathbf{Co_x^{II}}$ (x = MeCN or Cl), CO_2 activation occurs only at the zero-valent state as well. The positive shift of the irreversible $Co^{I/0}$ wave under a CO_2 atmosphere in the pure kinetic regime indicates that the associated chemical equilibrium is more shifted or accelerated forward with that substrate. The electrophilic nature of the CO_2 carbon atom likely makes the association faster than that of MeCN under an argon atmosphere [e.g., in eq. (3.4)]. Although formally metal radical, Co(0) species do not commonly exhibit single-electron-transfer reactivity but undergo two-electron oxidative chemistry.[4] Formulation of the CO_2 activation product as a $[Co^{II}\mathbf{L}(CO_2)]$ d^7 complex is thus favored. The potential at which this intermediate is accessed is low enough for further reduction into a 16-electron $[Co^{I}\mathbf{L}(CO_2)]^-$ complex, refilling the low-lying d_{z^2} orbital (Figure 4.6A).

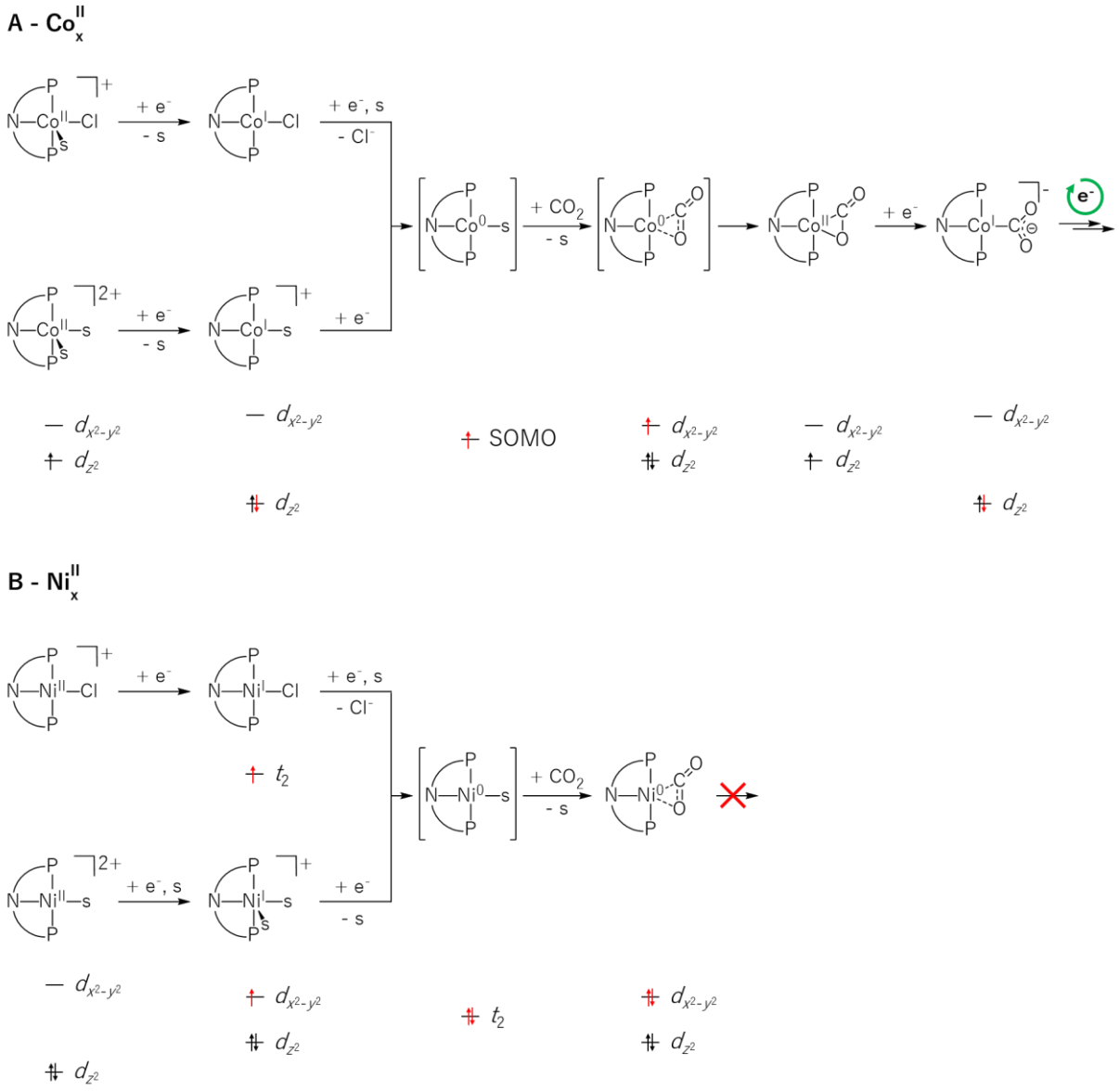

Figure 4.6. Proposed electrochemical pathways and schematic frontier orbital diagrams for the reduction of (A) $\mathbf{Co_x^{II}}$ and (B) $\mathbf{Ni_x^{II}}$ complexes with x = MeCN or Cl under CO_2 atmosphere (s = MeCN).

This species could directly enter into a catalytic cycle for CO_2 reduction, as supported by an increased magnitude of current density at the $Co^{I/0}$ wave. Notably, however, the current enhancement observed in the presence of CO_2 may also result from a faradaic (and not catalytic) two-electron reduction from $[Co^{I}\mathbf{L}Cl]$ or $[Co^{I}\mathbf{L}(MeCN)]^{+}$ to $[Co^{I}\mathbf{L}(CO_2)]^{-}$.

$\mathbf{Ni_s^{II}}$ and $\mathbf{Ni_{Cl}^{II}}$ display a SP, respectively SBP, coordination geometry, and interact with CO_2 only at the zero-valent oxidation state. The binding of CO_2 at this stage is, however, heavily favored, with $\mathbf{Ni_x^{II}}$ displaying cathodic shifts $\Delta E_{p,c}^{Ar\rightarrow CO_2}(\mathbf{M}^{I/0})$ of 160 (x = MeCN) and 130 mV (x = Cl), respectively. This shift translates into a follow-up chemical step several orders of magnitude faster upon CO_2 addition, corresponding to the binding of the electrophilic CO_2 substrate. The $k_{app}^{+}(CO_2)$ of $\mathbf{Ni_s^{II}}$ is ca. three orders of magnitude higher than that of $\mathbf{Ni_{Cl}^{II}}$ ($4.6\cdot10^{6}$ s^{-1} vs. $4.2\cdot10^{3}$ s^{-1}, Table 4.1).

Table 4.1. Apparent rate constants for MeCN association under argon atmosphere and CO_2 association under carbon dioxide atmosphere at the Ni(0) stage of $\mathbf{Ni_s^{II}}$ and $\mathbf{Ni_{Cl}^{II}}$.

	$\mathbf{Ni_s^{II}}$	$\mathbf{Ni_{Cl}^{II}}$	$\mathbf{Ni_s^{II}/Ni_{Cl}^{II}}$
$\boldsymbol{k_{app}^{+}}$**(MeCN)**	$3.9\cdot10^{1}$ s^{-1}	$3.6\cdot10^{-1}$ s^{-1}	~10^{2}
$\boldsymbol{k_{app}^{+}}$**(CO_2)**	$4.6\cdot10^{6}$ s^{-1}	$4.2\cdot10^{3}$ s^{-1}	~10^{3}

The difference in CO_2 association rate constants might stem from the preceding association of MeCN, the rate constants of which were determined at $3.6\cdot10^{-1}$ s^{-1} ($\mathbf{Ni_{Cl}^{II}}$) and $3.9\cdot10^{1}$ s^{-1} ($\mathbf{Ni_s^{II}}$) – a difference of two orders of magnitude. The more labile MeCN ligand presumably dissociates more readily and constitutes a lower barrier for CO_2 coordination than the chloride. Errors of only ±10 mV in the standard potential and the ordinate intercept during the calculation of the rate constants might cause the remaining difference in k_{app}^{+} of one order of magnitude between the two consecutive steps.

CO_2 activation at a Ni(0) center supported by a neutral PPP ligand built a five-coordinate Ni(0) species displaying η^2-CO_2 binding[5] as crystallographically shown in the famous ARESTA complex.[6] Such species are better described as Ni(0) species with marginal electron transfer to the bound CO_2 molecule, which, applied to the $\mathbf{Ni_x^{II}}$ complexes would result in similar $[Ni^{0}\mathbf{L}(CO_2)]$ adducts (Figure 4.6B). The re-oxidation wave at $E_{p,a}$ = –0.39 V_{Fc} observed at an elevated scan rate of ν = 50 $V\cdot s^{-1}$ for $\mathbf{Ni_{Cl}^{II}}$ could then relate to the oxidation of a subsequent intermediate, for instance, a $[Ni^{II}\mathbf{L}(COOH)]^{+}$ hydroxycarbonyl complex formed by protonation of $[Ni^{0}\mathbf{L}(CO_2)]$. Admittedly, the same wave cannot be observed for $\mathbf{Ni_s^{II}}$, possibly due to a lower lifetime of the CO_2 adduct that prevents reoxidation of the species.

4.1.4 Comparative Assessment

The groups of LEWIS and FUJITA have emphasized the relation between metal-centered reduction and CO_2 coordination on series of Ni(II) and Co(II) cyclam-like complexes.[1, 7] CO_2 coordinates to these complexes at the formal **M**(I) state, at which the CO_2 association equilibrium [$K(CO_2)$] and forward rate constants [$k^+(CO_2)$] were found to increase as the $\mathbf{M}^{II/I}$ standard potential becomes more negative.[7c] The present series of complexes $\mathbf{Co}_x^{II}$ and $\mathbf{Ni}_x^{II}$ (x = MeCN or Cl) exhibit reduction potentials sufficiently negative to afford CO_2 coordination. Each of the complexes requires reduction to a formal **M**(0) state to proceed to CO_2 activation, which stands in sharp contrast to the cyclam complexes of the same metals.

In particular, $[Ni(cyclam)]^+$, which has a $Ni^{II/I}$ reduction potential [$E^0(Ni^{II/I}) = -1.14\ V_{NHE}$[7d] corrected to approx. $-1.77\ V_{Fc}$[8]] close to the $Ni^{I/0}$ one of $\mathbf{Ni}_{Cl}^{II}$ [$E^0(Ni^{I/0}) = -1.59\ V_{Fc}$], exhibits a Ni(I)-$CO_2$ association rate constant [$k^+(CO_2) = 3.2\cdot10^7\ M^{-1}\cdot s^{-1}$, in aqueous solution[7b]] exceeding by several orders of magnitude that found for Ni(0)-CO_2 with $\mathbf{Ni}_{Cl}^{II}$ [$k^+(CO_2) = 1.5\cdot10^4\ M^{-1}\cdot s^{-1}$, in acetonitrile solution]. On the other hand, the value is relatively close to the one for $\mathbf{Ni}_s^{II}$ at $E^0(Ni^{I/0}) = -1.63\ V_{Fc}$ [$k^+(CO_2) = 1.7\cdot10^7\ M^{-1}\cdot s^{-1}$].

Notably, equilibrium and rate constants for CO_2 association at 3d centers in their 0 oxidation state are scarcely reported, with only one example in the order of magnitude of 10^2-$10^3\ s^{-1}$ for the CO_2 association rate constant at the electroreduced zero-valent state of a $[Co^{II}(PN_3P)(MeCN)_2]^{2+}$ complex.[9] Nevertheless, the difference to the cyclam series likely reflects the higher kinetic barrier for CO_2 association at the closed-shell $[Ni^0\mathbf{L}(MeCN)]$ complex as compared to the open-shell 17 VE $[Ni^I(cyclam)]^+$, underlining the importance of the electronic configuration for binding and activating CO_2.

The 17 VE complex $[Co^0\mathbf{L}(MeCN)]$ binds CO_2 at faster rates than 18 VE $[Ni^0\mathbf{L}(MeCN)]$, which is in agreement with this consideration. The increasing $Co^{I/0}$ cathodic peak current suggests a greater CO_2 activation upon contacting the substrate. This interpretation is in line with findings for the series of cyclam-like complexes in which Co(I) transfers up to two electrons to the bound CO_2, whereas Ni(I) does not substantially activate the substrate.[7d] The electrochemical CO_2 activation by $\mathbf{Co}_x^{II}$ and $\mathbf{Ni}_x^{II}$ within the redox-innocent ligand structure appears to follow the same trend. The two-electron reduction of $\mathbf{Ni}_x^{II}$ at mildly negative potential generates a $[Ni^0\mathbf{L}(\eta^2\text{-}CO_2)]$ complex irreducible at the potential of the $Ni^{I/0}$ wave. In contrast, $[Co^{II}\mathbf{L}(\eta^2\text{-}CO_2)]$ can be reduced at the potential of the $Co^{I/0}$ event and initiate electrocatalytic turnover.

From an organometallic view on the case of $\mathbf{Ni_x^{II}}$, these points relate to the coordination of CO_2 at Ni(0), characterized by weak to moderate back bonding according to the DEWAR-CHATT-DUNCANSON model of π bond coordination. The Ni center then remains in the formally zero-valent oxidation state. By contrast, with $\mathbf{Co_x^{II}}$, the more pronounced electron transfer from the Co(0) metal into the antibonding orbitals of the C=O bond of CO_2 results in a metallaoxirane-type structure. Consequently, the Co(0) center is oxidized to Co(II), and subsequent uptake of another electron can generate the Co(I) metallacarboxylate as a potential intermediate for catalytic CO_2 reduction.

The interplay between the electronic and structural properties of 3d metal complexes based on redox-innocent ligands with their electrochemical CO_2 activation properties is graphically summarized in Figure 4.7.

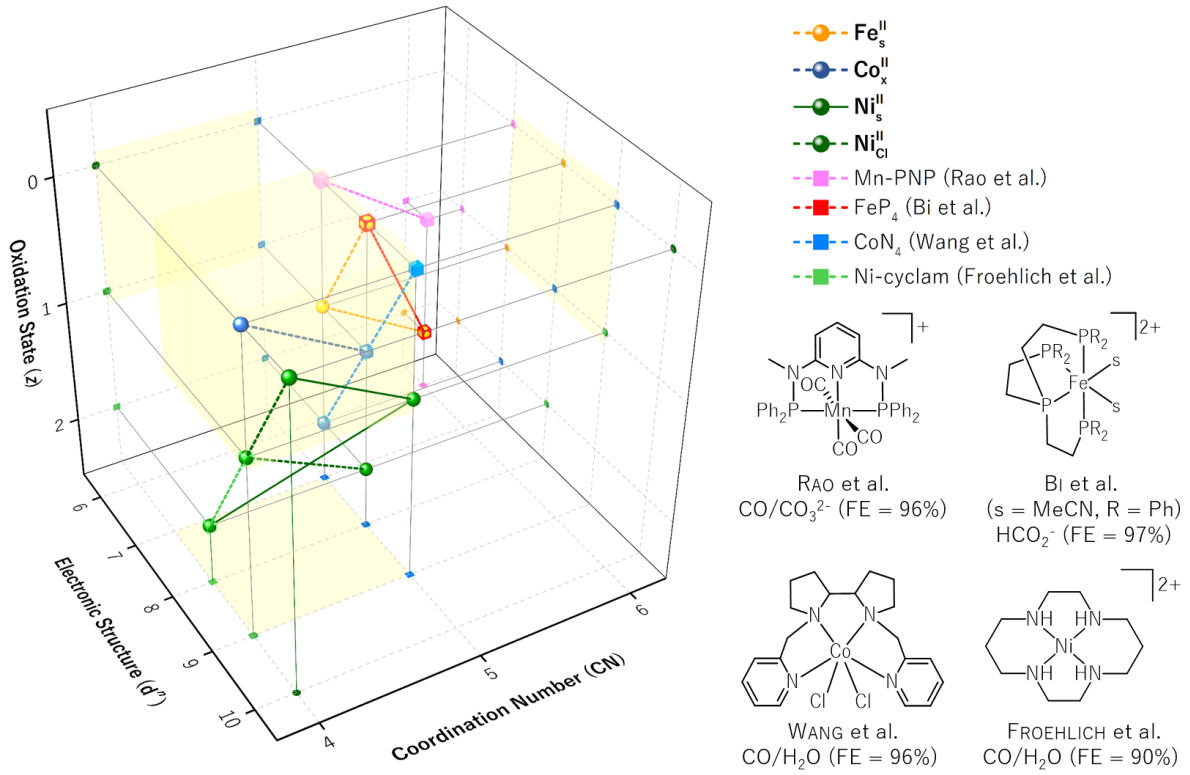

Figure 4.7. Electronic and geometric properties of $\mathbf{Fe_s^{II}}$, $\mathbf{Co_x^{II}}$, $\mathbf{Ni_x^{II}}$, and selected catalysts that contain redox-innocent ligand systems and traverse the ET_M mechanism in eCO2r (except BI et al.).[10] The diagonal lines indicate metal-centered reduction processes. The yellow area covers electronic and structural core properties favoring electrochemical CO_2 activation.

The graph comprises $\mathbf{Fe_s^{II}}$, $\mathbf{Co_x^{II}}$, and $\mathbf{Ni_x^{II}}$ as well as literature examples of active CO_2 reduction electrocatalysts. The diagonal lines represent the metal-based redox steps connecting the starting complex and the active species. All complexes showing activity toward CO_2 activation under

electrocatalytic conditions comprise common features covered by the yellow box, i.e., coordinative unsaturation with CN = 4 or 5, an open shell structure of metal electron configuration d^7 to d^9, and low oxidation states +I or 0.

Consequently, meeting these three parameters simultaneously upon accessing the active species is a design element for potential CO_2 electroreduction catalysts. Although this combination appears to be a prerequisite, it is insufficient to guarantee electrocatalytic performance. Hence, electrocatalytic activity will be investigated in the next section.

4.2 Addition of a LEWIS Acid

The reductive disproportionation of CO_2 to CO and CO_3^{2-} is one possible reaction route within the ET_M mechanism (Scheme 1.3), commonly accessible under aprotic conditions when supported by a LEWIS acid (Scheme 1.4). Based on the report of KUBIAK's group, $Mg(OTf)_2$ was chosen as the LEWIS acid source to identify candidates for the reaction.[11] However, in contrast to the literature, the triflate's solubility in MeCN electrolyte proved to be poor. Hence, a saturated solution of $Mg(OTf)_2$ in the electrolyte (0.1 M $TBAPF_6$/MeCN) was added to the complexes under a CO_2 atmosphere. Volumes of the LA solution are reported instead of concentrations for the same reason. Since the $\mathbf{M_s^{II}}$ complexes are stable in MeCN this series of compounds is subjected to CV analysis.

4.2.1 CV Studies

4.2.1.1 $[Fe\mathbf{L}(MeCN)_3](BF_4)_2$

Adding small volumes of the saturated $Mg(OTf)_2$ solution to $\mathbf{Fe_s^{II}}$ in the MeCN electrolyte solution provokes an additional reduction wave at potentials located between the previously identified $Fe^{II/I}$ and $Fe^{I/0}$ waves (Figure 4.8).

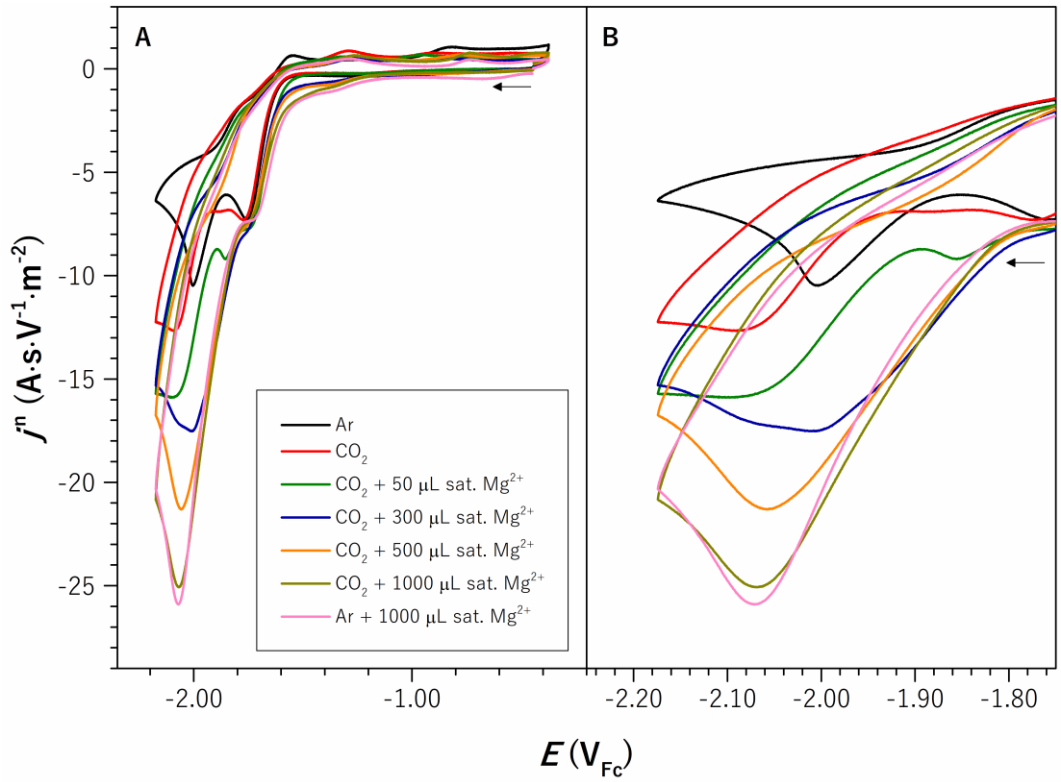

Figure 4.8. (A) CVs of $\mathbf{Fe_s^{II}}$ at varying concentrations of $Mg(OTf)_2$ under argon or CO_2 atmosphere and (B) zoom on the reduction events mainly affected.

A gradual cathodic shift is observed from an initial value of $E_{p,c} \approx -1.85$ V_{Fc} with increasing LEWIS acid concentrations. Simultaneously, the $Fe^{I/0}$ wave shifts in the anodic potential direction, eventually merging both waves at added volumes ≥ 500 µL, and the current density rises. The joining waves could indicate the gradual conversion of the pristine Fe(0) species, e.g., $[Fe^0\mathbf{L}(MeCN)_m]$ (m = 1 or 2) into $[Fe^0\mathbf{L}(MeCN)_m(OTf)]^-$ (m = 0 or 1) at increasing additive concentrations. Despite the noticeable increase in current density at the "new" $Fe^{I/0}$ wave, exchanging CO_2 with argon does not substantially affect this behavior. A decreasing current density upon substrate deprivation is yet a prime indicator of catalytic conversion since it renders the electron transfer to the molecule impossible. Therefore, catalytic conversion of CO_2 can be discarded at this stage.

Apart from co-catalyzing the reductive disproportionation of CO_2, Mg^{2+} could enhance the autoprotolysis of residual water by the formation of $[Mg(OH_2)_6]^{2+}$ [eq. (4.5)].

$$Mg^{2+} + 6\ H_2O \rightleftarrows [Mg(OH_2)_6]^{2+} \rightleftarrows [Mg(OH_2)_5OH]^+ + H^+ \qquad (4.5)$$

The DFT calculations performed by KATZ et al. support this hypothesis by reporting that the deprotonation of an aqua ligand coordinated to the magnesium center requires less free energy than the deprotonation of a free molecule.[12] Removing electron density from the coordinated oxygen atoms weakens the O-H bond, ultimately leading to deprotonation and the formation of magnesium hydroxide species, as shown in eq. (4.5). The increased proton concentration by the reaction of Mg^{2+} with water could be the origin of the increase in current density when considering $\mathbf{Fe_s^{II}}$ a hydrogen evolution catalyst.

4.2.1.2 $\underline{[Co\mathbf{L}(MeCN)_2](BF_4)_2}$

The CVs under the addition of $Mg(OTf)_2$ to a solution of $\mathbf{Co_s^{II}}$ in MeCN electrolyte are shown in Figure 4.9. The $Co^{II/I}$ wave shifts in the negative potential direction and exhibits slightly increasing current densities beginning at 300 µL of sat. LEWIS acid solution. This shift could indicate triflate coordination or MeCN substitution at the Co(II) or Co(I) oxidation states.

A slight cathodic potential shift but a significant change in current density (ratio ~1.9, corrected by the diffusion current) is observable for the $Co^{I/0}$ wave at 1 mL of $Mg(OTf)_2$ solution. The shift of the peak potential and simultaneous loss of current density after sparging with argon indicate catalytic activity for CO_2 conversion. Hence, $\mathbf{Co_s^{II}}$ proves to reduce CO_2 along the LA-assisted disproportionation route.

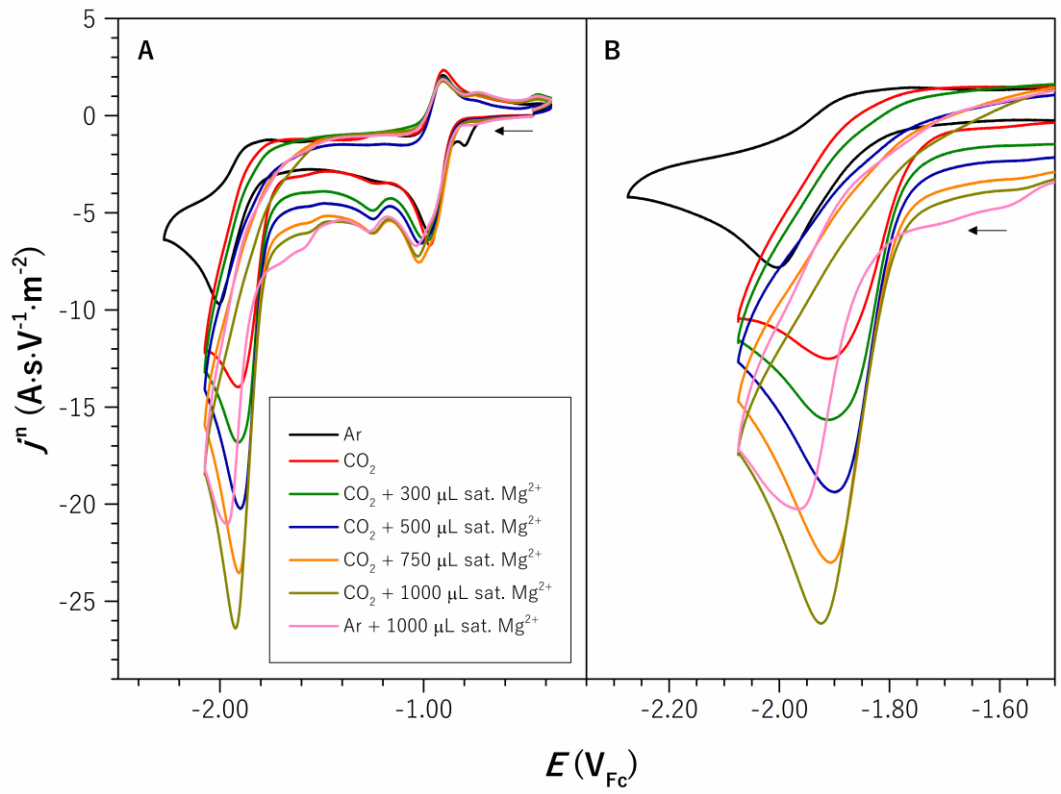

Figure 4.9. (A) CVs of $\mathbf{Co_s^{II}}$ at varying concentrations of $Mg(OTf)_2$ under argon or CO_2 atmosphere and (B) zoom on the $Co^{I/0}$ wave.

4.2.1.3 [Ni**L**(MeCN)](BF$_4$)$_2$

Figure 4.10 shows the sequential addition of saturated $Mg(OTf)_2$ to $\mathbf{Ni_s^{II}}$ in the electrolyte. The steady decrease of the normalized current densities observed for both reduction waves can be explained by the dilution of the complex upon addition of the LA solution.

A reduction wave at ca. –1.30 V_{Fc} begins to build up at a volume of 750 µL of Mg^{2+} solution, which indicates the conversion of the Ni(I) species into a potential Ni-CO_2-Mg intermediate. However, the general lack of a significant current enhancement in the presence of CO_2 and Mg^{2+} excludes a catalytic conversion via reductive disproportionation at this stage.

In summary, only $\mathbf{Co_s^{II}}$ shows indications of catalyzing the reductive disproportionation of CO_2 within the $\mathbf{M_s^{II}}$ complex series and will hence be applied in controlled potential electrolysis experiments.

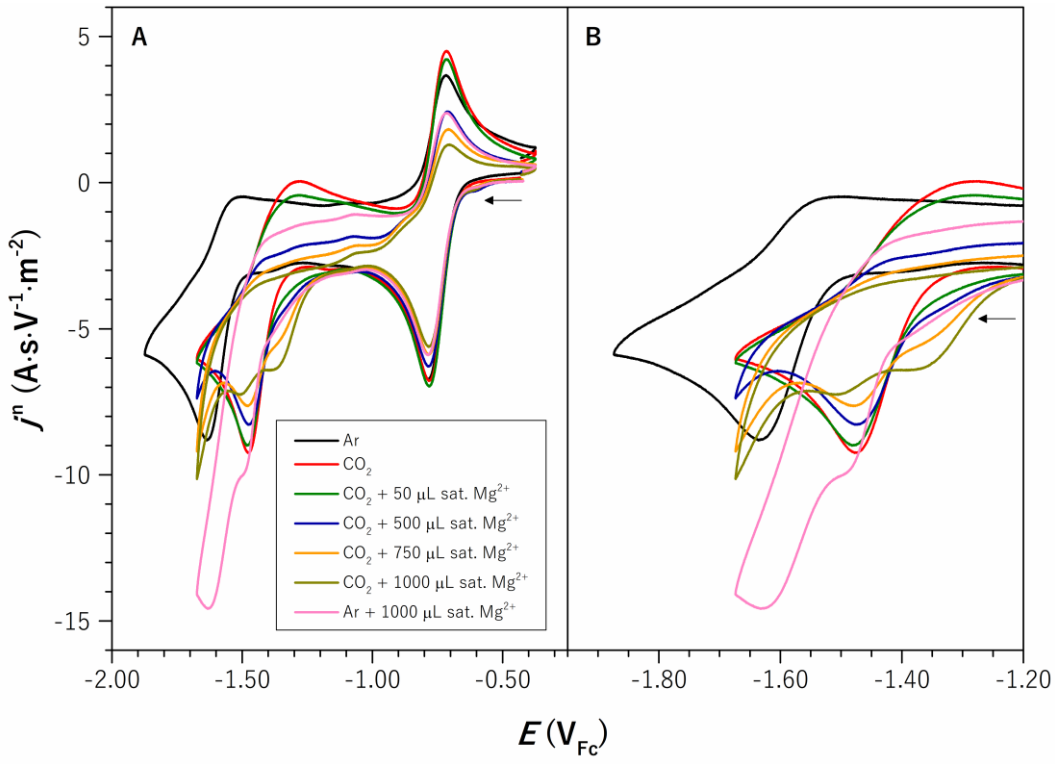

Figure 4.10. (A) CVs of $\mathbf{Ni_s^{II}}$ at varying concentrations of $Mg(OTf)_2$ under argon or CO_2 atmosphere and (B) zoom on the $Ni^{I/0}$ wave.

4.2.2 Controlled Potential Electrolysis

The CPE conditions applied to $\mathbf{Co_s^{II}}$ are summarized in Table 4.2. Product-time profiles are appended as Figure C.5.

Table 4.2. Conditions and results for CPE with $\mathbf{Co_s^{II}}$ under CO_2 atmosphere and addition of $Mg(OTf)_2$.

Entry	Additive[a]	E (V_{Fc})	FE_{max}(CO) (%)[b]	Q (C)	Dec.
1	–	–2.2	2 (3.5)	8.2	Yes
2	$Mg(OTf)_2$ (sat.)	–2.05	6 (1)	9.9	Yes
3	Sat. aq. $Mg(OTf)_2$ (10 vol%)	–1.94 to –2.24	–	< 5	Yes

[a] Brackets: additive concentration. [b] Brackets: t (h) required to reach FE_{max}.

A preliminary control experiment at the potential of the $Co^{I/0}$ wave under a CO_2 atmosphere (–2.2 V_{Fc}, entry 1) should serve as a reference for the experiments with the additive. This attempt resulted in a maximum FE for CO of approx. 2% after 3.5 h reaction time. Bulk electrolysis in the presence of sat. $Mg(OTf)_2$ (entry 2) increases the maximum FE for CO to ca. 6% after one hour of reaction time but only marginally influences the transferred charge Q.

The limited Mg^{2+} concentration in the reaction mixture was increased by adding 10 vol% of a saturated aqueous $Mg(OTf)_2$ solution, albeit knowing that H_2O can serve as a proton source.

However, controlled potential electrolyses at potentials of –1.94, –2.04, and –2.24 V_{Fc} (entry 3) did not yield any products detectable by GC (headspace) or HPLC (liquid phase), respectively. Slow discoloration of the reaction solution was observed over time, as was for entries 1 and 2. This fact and the silent CVs recorded after the electrolysis suggest complex decomposition under the applied conditions. A transferred charge of less than 5 C (equaling 0.05 mmol of electrons) supports decomposition. Approx. 40% of the electrons are consumed to reduce the entire amount of the complex (0.01 mmol) in the cathodic half-cell to the active Co(0) state. Further multi-electron reduction of CO_2 is therefore limited.

In conclusion, the CV and CPE studies in the presence of $Mg(OTf)_2$ indicate that the reductive disproportionation of CO_2 does not constitute the CO_2 conversion route traversed by the $\mathbf{M_s^{II}}$ complexes, albeit the results might be influenced by the poor solubility of the LEWIS acid. CPE experiments with $\mathbf{Co_s^{II}}$ further hinted toward complex instability under catalytic conditions.

Subsequent investigations on the $\mathbf{M_s^{II}}$ complexes' interactions with protons shall expand the picture of their reactivity to conditions that allow the formation of hydroxycarbonyl intermediates in the ET_M route or active metal hydride species to enter an ET_H catalytic cycle. Hence, the $\mathbf{M_s^{II}}$ complexes are studied in the presence of BRØNSTED acids in the next part.

Part 2: Protic Conditions

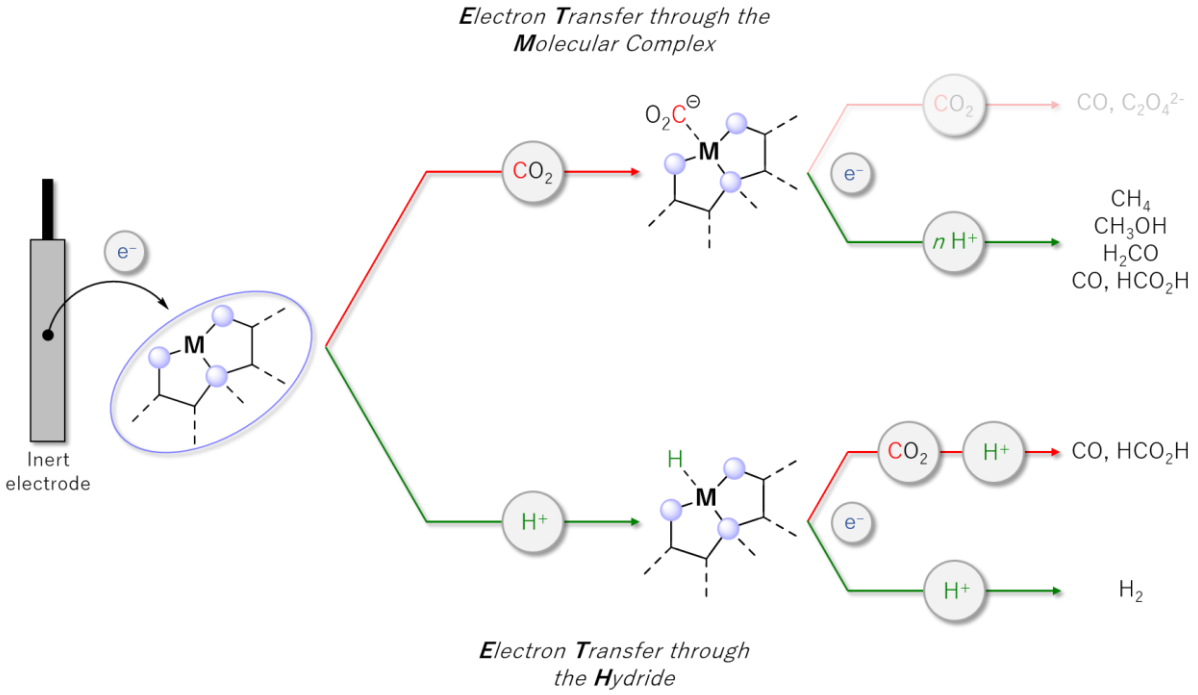

Part 2 of chapter 4 investigates the $\mathbf{M}_s^{II}$ complexes in their affinity to catalyze the electrochemical reduction of carbon dioxide in the presence of protons, i.e., via the hydroxycarbonyl route of the ET_M pathway or the ET_H mechanism.

In the first step, CV studies under the addition of proton sources of varying strength and concentration are used to assess reaction conditions for the $\mathbf{M}_s^{II}$ complexes in terms of type and concentration of proton donor.

Consecutively, the identified combinations of complex and proton source (concentration) are transferred to the bulk electrolysis of CO_2 to evaluate the complexes' catalytic properties.

4.3 CV Studies

The proton donor strength is of prime importance in the electrocatalytic reduction of CO_2. It can influence the reaction pathway by benefitting the formation of a hydroxycarbonyl species along the ET_M pathway or a metal hydride within the ET_H route. The hydride can reduce CO_2 to formic acid or protons to hydrogen, with the selectivity shifting strongly toward hydrogen when increasing the acid strength.[13] Hence, various proton sources (H_2O, MeOH, TFE, PhOH, and BA) spanning several orders of magnitude in donor strength (Scheme 4.1) are screened to identify the most favorable CO_2 reduction parameters. A general overview of the CV behavior of the $\mathbf{M_s^{II}}$ complexes at increasing acid concentrations is given before discussing conditions for the bulk electrolysis of CO_2.

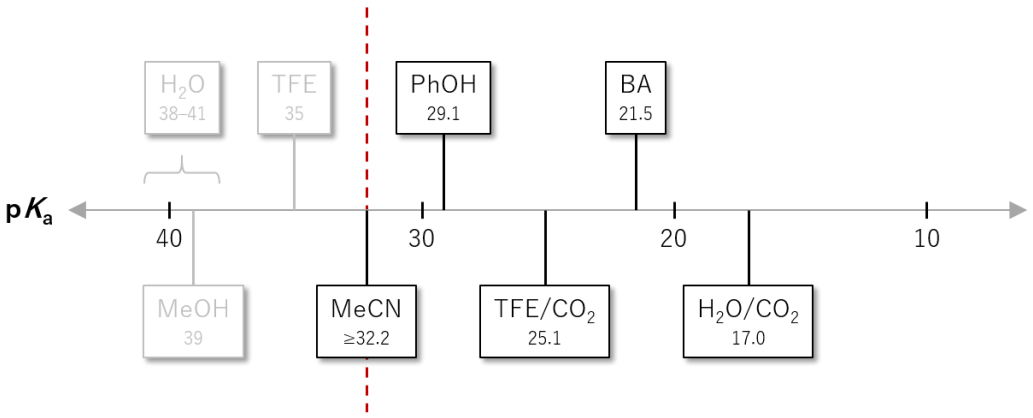

Scheme 4.1. pK_a scale in MeCN of selected proton sources used in this work.[14]

Homoassociation (also referred to as homoconjugation) of an acid and its conjugated base in organic solvents favors deprotonation and increases the acid's strength. Among others, this effect is reported for phenol and benzoic acid (BA), likely locating their homoconjugation products at lower values on the pK_a scale.[14c]

Additionally, some weak proton sources (e.g., H_2O and TFE) react with CO_2 to form carbonate products (HA/CO_2 on the pK_a scale) that are often more potent acids than the initial proton donor. The effect of the reaction might be small due to the limited concentrations of the involved species, but the unknown equilibrium constants render its assessment difficult.

It has to be noted that the pK_a values given for water, methanol, and trifluoroethanol exceed those for the solvent MeCN (red line) and must therefore be taken with care. The values for the previous two were converted from empirical factors in other solvents and might be imprecise.

Based on the pK_a values in Scheme 4.1, standard potentials (representing the minimum required thermodynamic driving force) were calculated for the accessible redox couples (Table 4.3), which will evaluate the complexes' aptitude to catalyze the respective reaction.

Table 4.3. Standard potentials of redox couples accessible under reductive conditions in the presence of BRØNSTED acids of varying pK_a values.

	pK_a[14]	E^0(CO_2/CO)[14b]	E^0(CO_2/HCO_2H)[15]	E^0(H^+/H_2)[16]
H_2O	41	–2.71	–2.73	–2.45
MeOH	39	–2.59	–2.61	–2.34
TFE	35	–2.35	–2.38	–2.10
MeCN	32.2	–2.19	–2.21	–1.93
PhOH	29.1	–2.00	–2.03	–1.75
TFE/CO_2	25.1	–1.77	–1.79	–1.51
BA	21.5	–1.55	–1.58	–1.30
H_2O/CO_2	17.0	–1.29	–1.31	–1.03

4.3.1 $[FeL(MeCN)_3](BF_4)_2$

The qualitative analysis of the CV studies of Fe_s^{II} under BRØNSTED acid addition (shown in this section or Figure C.6 to Figure C.8) is summarized in Table 4.4.

Table 4.4. Electrochemical response of Fe_s^{II} under addition of proton sources in CV analysis (= : constant and → : anodic potential shift, ↑ : increase and ↓ : decrease of magnitude).

	$M^{I/0}$		Other Events	
	$E_{p,c}$ (V_{Fc})	$j_{p,c}^n$	$E_{p,c}$ (V_{Fc})	$j_{p,c}^n$
H_2O	→	c_{HA} ≤ 4.7 M: ↑ c_{HA} ≥ 8.6 M: ↓ CO_2 removal: =	-	-
MeOH	=	↑ No CO_2: ↓	-	-
TFE	=	c_{HA} ≤ 0.46 M: ↑ c_{HA} ≥ 1.2 M: ↓ CO_2 removal: =	-	-
PhOH	=	c_{HA} ≤ 0.091 M: ↑ c_{HA} ≥ 0.19 M: = CO_2 removal: ↑	-	-
BA	=	c_{HA} ≤ 0.010 M: ↑ c_{HA} ≥ 0.010 M: = CO_2 removal: ↑	≈ –2.5	↑ CO_2 removal: =

None of the proton sources in any chosen concentration affect the $Fe^{II/I}$ wave, which confirms the results without additive and suggests that the electron densities at the Fe(II) and Fe(I) stages are insufficient for CO_2 activation.

Each proton source affects the more cathodic $Fe^{I/0}$ wave, i.e., the cathodic peak potential shifts significantly in the anodic direction, indicating substrate coordination. The removal of electron density from the metal center allows the electron transfer to occur at less negative potentials and could hint toward the substitution of CO_2 by a more electrophilic ligand such as H^+.

The normalized peak current density at the $Fe^{I/0}$ wave generally increases up to a specific, proton source-dependent concentration (except for MeOH, *vide infra*). When exceeding this threshold, the maximum peak current density plateaus for PhOH and BA (Figure C.7 and Figure C.8) or even declines in the cases of H_2O and TFE (Figure 4.11 and Figure C.6). This behavior is best observable with 15 M water and can be traced back to the dilution of the complex. At this point, the complex concentration is decreased by one third (Figure 4.11). Hence, dilution effects must be considered when interpreting the CVs depending on the complex's catalytic activity.

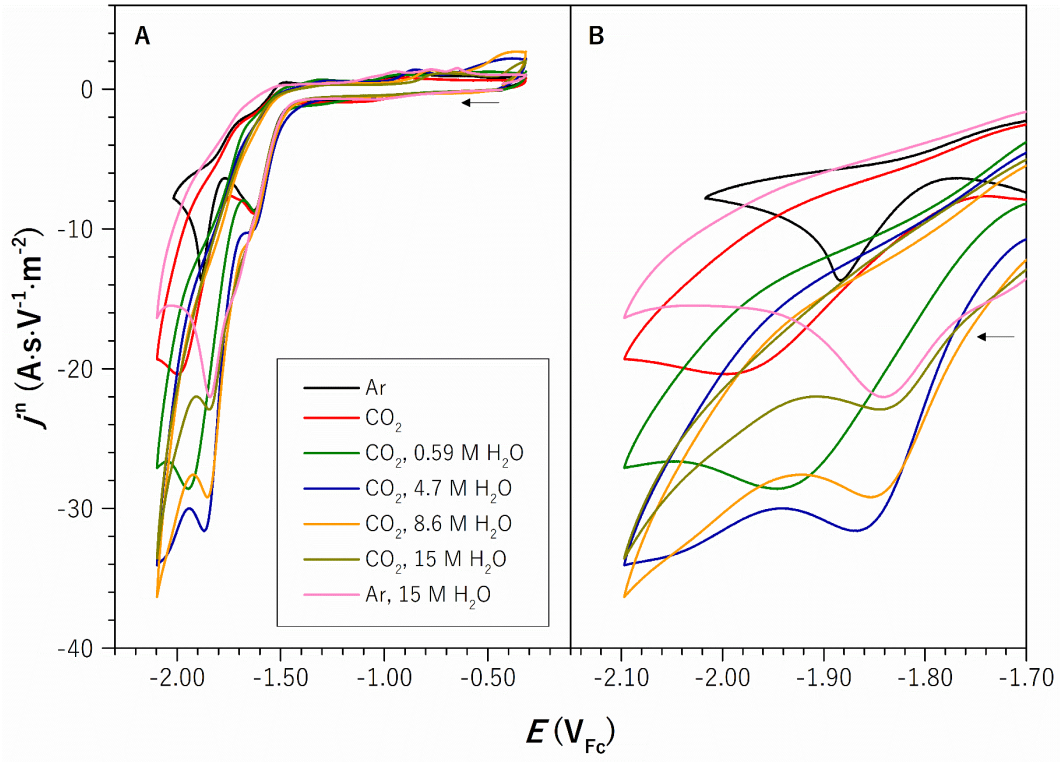

Figure 4.11. (A) CVs of $\mathbf{Fe_s^{II}}$ at varying concentrations of H_2O under argon or CO_2 atmosphere and (B) zoom on the $Fe^{I/0}$ wave.

The BRØNSTED acid concentration required to reach the highest peak current density increases with the pK_a value, reflecting the displacement of the acid equilibrium to the deprotonated side for more potent acids.

Substituting CO_2 with argon either leaves $j_{p,c}^n$ unaffected (H_2O and TFE) or increases the value (PhOH and BA). CO_2 reduction to CO or HCO_2H with Fe(0) is therefore assumed to be strongly disfavored compared to hydrogen evolution via the ET_H pathway.

A new wave exhibiting the same behavior as the $Fe^{I/0}$ wave emerges at $E_{p,c} \approx -2.5$ V_{Fc} upon the addition of benzoic acid (Figure C.8). Such a reduction wave was also observed for $\mathbf{Co_s^{II}}$ and $\mathbf{Ni_s^{II}}$ and is likely attributed to hydrogen evolution catalyzed by the glassy carbon electrode surface at very negative potentials.

Opposed to the previous proton sources, the addition of MeOH to a CO_2-saturated solution of $\mathbf{Fe_s^{II}}$ in MeCN leaves the peak potential of the $Fe^{I/0}$ wave unchanged but gradually increases the peak current density (Figure 4.12).

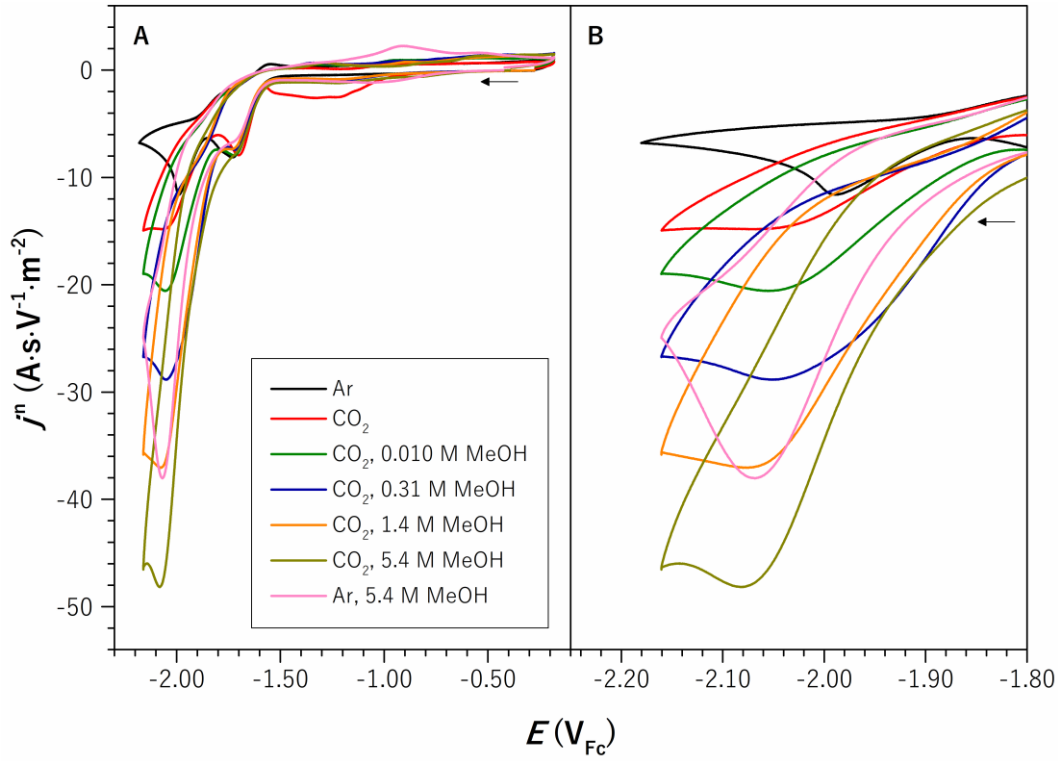

Figure 4.12. (A) CVs of $\mathbf{Fe_s^{II}}$ at varying concentrations of MeOH under argon or CO_2 atmosphere and (B) zoom on the $Fe^{I/0}$ wave.

More importantly, the removal of CO_2 leads to a decrease of $j_{p,c}^n$ of approx. 10 A·s·V^{-1}·m^{-2} indicative of catalytic conversion of carbon dioxide at this peak. However, competition with hydrogen evolution is likely since removing CO_2 does not reduce $j_{p,c}^n$ to the initial value observed under argon without additives. MeOH and CO_2 could form a more potent acid in the same manner as H_2O and TFE, which enhances proton reduction in the presence of carbon dioxide. $\mathbf{Fe_s^{II}}$ will be subjected to CPE experiments with MeOH to identify the product(s) of the reaction.

4.3.2 $[CoL(MeCN)_2](BF_4)_2$

The qualitative analysis of the analogous CV studies performed on $\mathbf{Co_s^{II}}$ (to be found below and in Figure C.9 to Figure C.11) are gathered in Table 4.5.

Table 4.5. Electrochemical response of $\mathbf{Co_s^{II}}$ under addition of proton sources in CV analysis (= : constant, → : anodic, and ← : cathodic potential shift, ↑ : increase and ↓ : decrease of magnitude).

	$M^{II/I}$			$M^{I/0}$	Other Events	
	E^0 (V_{Fc})	$j^n_{p,c}$	$E_{p,c}$ (V_{Fc})	$j^n_{p,c}$	$E_{p,c}$ (V_{Fc})	$j^n_{p,c}$
H_2O	=	↓ CO_2 removal: =	=	$c_{HA} \leq 4.6$ M: ↑ $c_{HA} \geq 8.5$ M: ↓ CO_2 removal: ↓	-	-
MeOH	=	↓ CO_2 removal: =	=	↑ CO_2 removal: ↓	-	-
TFE	=	↓ CO_2 removal: ↓	→	$c_{HA} \leq 0.31$ M/1.2 M: ↑ 0.31 M < c_{HA} < 1.2 M: ↓ CO_2 removal: ↑	-	-
PhOH	=	↓ CO_2 removal: =	→	↑ CO_2 removal: ↑	-	-
BA	←	↑ CO_2 removal: =	→	↑ CO_2 removal: ↓	≈ –2.3 ←	↑ CO_2 removal: =

While the $Co^{II/I}$ wave's current density decreases upon sequential addition of water due to dilution (and possible formation of an aqua complex), the $Co^{I/0}$ wave behaves inversely and $j^n_{p,c}$ approximately doubles at c_{H_2O} = 4.6 M. Removal of CO_2 leads to a significant loss of current density and an intense anodic wave shift. Consequently, CO_2 electroreduction is assumed for $\mathbf{Co_s^{II}}$ in the presence of water as a proton source.

When adding MeOH, CVs of $\mathbf{Co_s^{II}}$ show a similar but more marked behavior at the $Co^{I/0}$ wave. $j^n_{p,c}$ more than doubles at the maximum MeOH concentration of 2.1 M but falls back almost to the level recorded under argon atmosphere without additives after sparging out CO_2. The behavior indicates the strongly favored catalytic conversion of CO_2 over H^+, rendering H_2O and MeOH potential proton donors for the bulk electrolysis of carbon dioxide.

TFE and phenol induce declining current densities at the $Co^{II/I}$ wave, which is not explainable by dilution alone. A species redox-innocent at the considered potentials in a **CE** mechanism may

be formed. The increase in current density simultaneously induced at the $Co^{I/0}$ wave is not reversed by deprivation from the CO_2 substrate and therefore discards CO_2 reduction.

For TFE, the $Co^{I/0}$ wave's peak current density increases up to a concentration of 0.31 M, then decreases up to c_{TFE} = 1.2 M, and eventually increases again (Figure 4.13). The simultaneous loss of the $Co^{II/I}$ wave might indicate the more substantial formation of a hydride species and a concomitant shift of the reactivity from CO_2 reduction to hydrogen evolution at higher proton concentrations. An additional increase of $j^n_{p,c}$ after sparging the cell with argon supports H_2 formation.

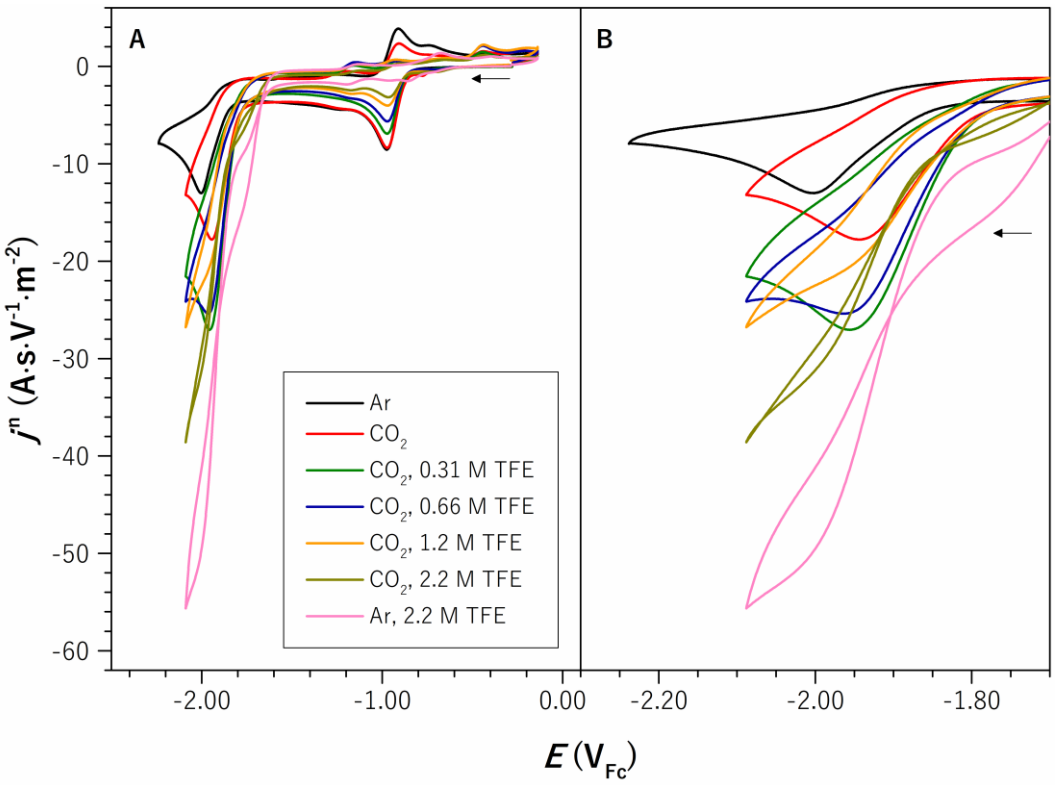

Figure 4.13. (A) CVs of $\mathbf{Co_s^{II}}$ at varying concentrations of TFE under argon or CO_2 atmosphere and (B) zoom on the $Co^{I/0}$ wave.

BA affects the shapes and heights of the two metal-centered reduction waves, and a third one observed at $E_{p,c} \approx -2.3$ V_{Fc}, but CO_2 removal only causes a marginal loss in current density (Figure C.11). The behavior opposes CO_2 conversion in favor of proton reduction.

CVs of the $Co^{II/I}$ wave upon BA addition in Figure 4.14 show a cathodic potential shift and a catalytic increase of the current density. Hence, BA's proton donor ability appears strong enough to induce hydrogen evolution at the Co(I) stage. *Vice versa*, the preference for hydrogen evolution excludes benzoic acid as a suitable acid for CO_2 reduction.

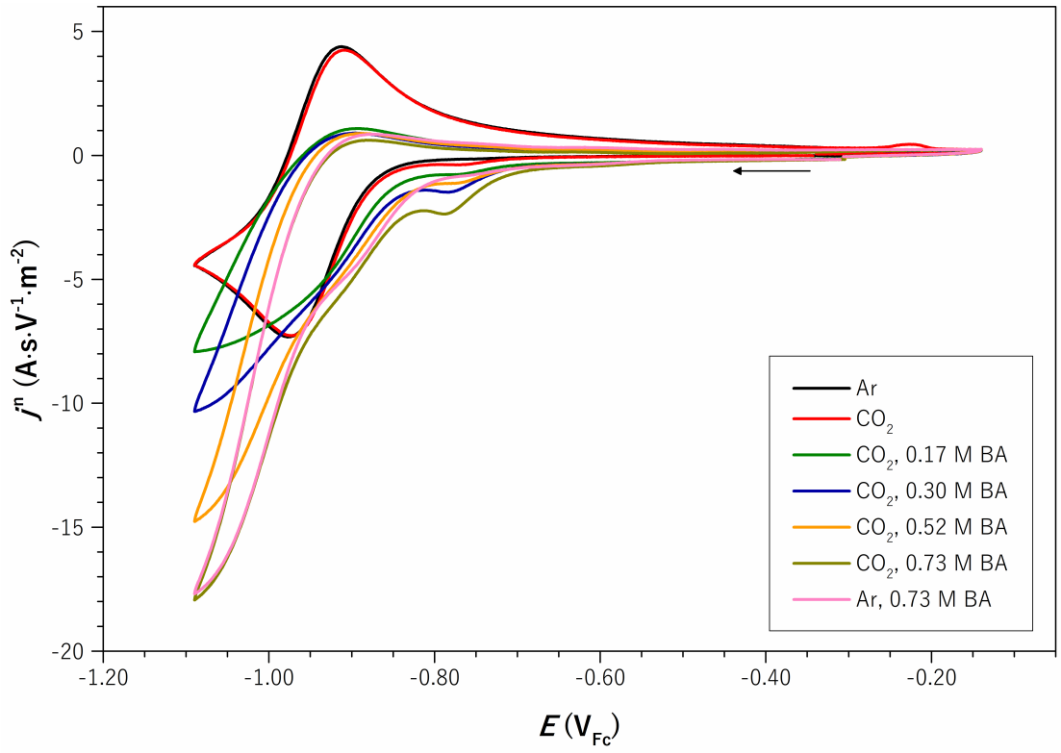

Figure 4.14. CVs of the $Co^{II/I}$ wave of $\mathbf{Co_s^{II}}$ at varying concentrations of BA under argon or CO_2 atmosphere.

4.3.3 [NiL(MeCN)](BF$_4$)$_2$

The CVs upon addition of proton sources to CO_2-sparged solutions of $\mathbf{Ni_s^{II}}$ in MeCN electrolyte are shown hereafter and in Figure C.12 to Figure C.14. Their qualitative description in terms of peak/standard potentials and normalized peak current densities is condensed in Table 4.6.

Water, methanol, and 2,2,2-trifluoroethanol (Figure C.12) do not induce a current enhancement on any of the reduction waves of $\mathbf{Ni_s^{II}}$ but instead, lead to decreasing current densities due to dilution or partial decomposition of the complex.

Table 4.6. Electrochemical response of $\mathbf{Ni_s^{II}}$ under addition of proton sources in CV analysis (= : constant, → : anodic, and ← : cathodic potential shift, ↑ : increase and ↓ : decrease of magnitude).

		$\mathbf{M^{II/I}}$		$\mathbf{M^{I/0}}$		**Other Events**
	E^0 (V_{Fc})	$j^n_{p,c}$	$E_{p,c}$ (V_{Fc})	$j^n_{p,c}$	$E_{p,c}$ (V_{Fc})	$j^n_{p,c}$
H_2O	=	↓ CO_2 removal: ↓	→	↓ CO_2 removal: ↓	-	-
MeOH	=	↓ CO_2 removal: ↓	→	↓ CO_2 removal: =	≈ −0.95	CO_2 removal: ↑
TFE	=	↓	→	↓	-	-
PhOH	=	↓ CO_2 removal: =	→	↓ CO_2 removal: ↑	≈ −1.58 →	c_{HA} ≤ 0.38 M: ↑ c_{HA} ≥ 0.68 M: ↓ CO_2 removal: ↑
BA	=	↓ CO_2 removal: =	→	↓ CO_2 removal: =	≈ −1.58 →	↓

While the standard potential of the $Ni^{II/I}$ couple remains largely unaltered by increasing proton donor strength and concentration, the $Ni^{I/0}$ wave exhibits a substantial anodic shift in each of the cases. Possibly, Ni forms hydride species (or methoxides with MeOH) dependent on the acid (Figure 4.15).

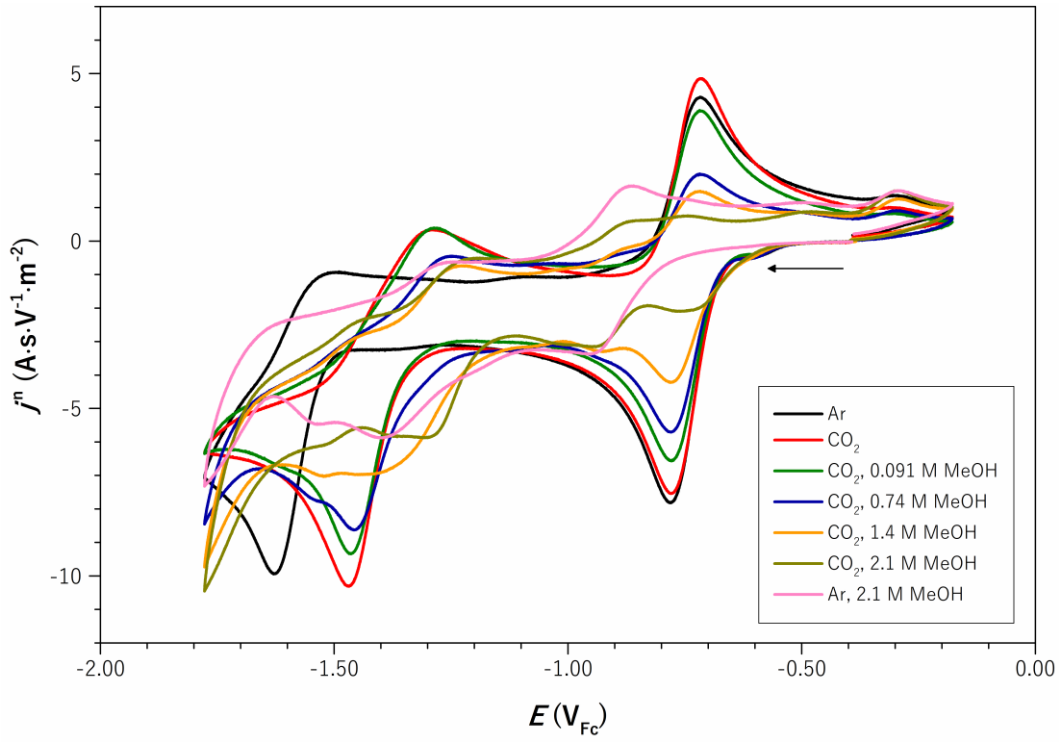

Figure 4.15. CVs of $\mathbf{Ni_s^{II}}$ at varying concentrations of MeOH under argon or CO_2 atmosphere.

A similar behavior can be observed when PhOH or BA are introduced to the analyte solution. The standard potential of the $Ni^{II/I}$ couple is not affected, but the wave loses peak current density at increased acid concentrations.

Two reduction waves are observable in the vicinity of the $Ni^{I/0}$ wave for both proton donors at low concentrations. The more cathodic wave at $E_{p,c} \approx -1.58\ V_{Fc}$ shifts anodically for higher c_{HA} and eventually vanishes completely, whereas the more anodic one only shifts in peak potential but remains at higher acid concentrations.

Both proton donors, but particularly BA, induce the build-up of a corresponding oxidation wave ($E_{p,a} \approx -1.03\ V_{Fc}$ at 0.015 M BA) that shifts in the anodic potential direction at increased acid concentrations (Figure C.13). The formation of metal hydride species favored upon proton addition could explain this behavior. Moreover, the hydride stability is supported by the mild potential of the $Ni^{I/0}$ wave that does not offer a sufficient driving force for the catalytic conversion of CO_2 or protons.

Further waves of increasing current densities arise at potentials < $-2.0\ V_{Fc}$ for PhOH and BA but were omitted from Table 4.6 since their peak current densities do not decrease when CO_2 is removed (Figure C.14).

4.3.4 Comparative Assessment

When $\mathbf{Fe_s^{II}}$ is contacted with protons at the zero-valent state, the proposed activity in the hydrogen evolution reaction necessitates hydride formation, which appears to be the preferred pathway. This preference is evident for BA, PhOH, and TFE but remains to be tested in bulk electrolysis for MeOH and water. The typical behavior for eCO_2r catalysts was observed with MeOH (current density increases with proton concentration and decreases upon CO_2 removal). However, the limited markedness of these effects suggests competition between CO_2 and proton reduction. When water is introduced as an even less acidic proton source, the "peaking" of the current density at $c_{H_2O} \approx 4.7$ M instead of the expected saturation may indicate a concentration-dependent switch from CO_2 reduction to hydrogen evolution.

Compared to this, CVs of $\mathbf{Co_s^{II}}$ putatively existing in an open-shell 17 VE electron configuration at the active Co(0) state, show clear indications of catalytic activity in the electroreduction of CO_2 when water or MeOH are chosen as the proton donor. In particular, the rising peak current densities of the $Co^{I/0}$ wave when increasing the proton donor concentration and the loss of this current density upon removal of CO_2 support this proposal. However, a switch in selectivity to proton reduction is suggested with more potent acids. This behavior agrees with literature reports on eCO_2r catalysts due to the favored formation of metal hydride species with increasing

proton availability as the prerequisite for hydrogen evolution via the ET_H pathway.[13a] Interestingly, benzoic acid is potent enough to induce a catalytic current density for proton reduction already at the Co(I) oxidation state.

The $\mathbf{Ni_s^{II}}$ complex does not show any current enhancement when purposefully introducing protons under a CO_2 atmosphere, putatively caused by the formation of a stable d^{10} 18 VE ARESTA-type η^2-CO_2 complex. The substitution of CO_2 with a proton and formation of an **M**-H complex seems favored, as inferred from the shift of the peak potential at the $Ni^{I/0}$ wave and the appearance of a corresponding re-oxidation wave at more anodic potentials.

While the catalytic waves of $\mathbf{Fe_s^{II}}$ and $\mathbf{Co_s^{II}}$ are only located slightly anodic to the required potentials for catalytic conversion as calculated from the pK_a values of the respective proton sources (Table 4.3), those of $\mathbf{Ni_s^{II}}$ are not sufficiently cathodic to show activity. Nevertheless, the contribution of homoconjugation and the formation of more acidic species upon reaction with CO_2 would decrease the required standard potential. Hence, CPE is performed to identify the outcome of the observed catalytic waves in the following section.

4.4 Controlled Potential Electrolysis

Type and concentration of the proton source used in bulk electrolysis were extracted from the respective cyclic voltammograms with the highest observed current densities. However, other potentially promising data points, e.g., those surmised to provide higher current densities for CO than for H_2, were investigated too. In the following sections, the CPE experiments in carbon dioxide-saturated electrolyte solutions are summarized in tabular form, comprising the used acid, its concentration, and the applied potentials.

The overpotential [eq. (1.1)] is given as metrics of driving force; the selectivity of the reaction is described by maximum FEs (Table 1.2, entry 4). Both extreme values for the overpotential are given for proton sources theoretically capable of forming more potent acids by chemical conversion (e.g., water and CO_2 forming bicarbonate, which is stronger than water itself, Table 4.3). Although the overpotential is usually denoted as an absolute number, in this work, only a negative value represents an actual overpotential and sufficient driving force for the reduction. In contrast, a positive value indicates an underpotential that does not provide the thermodynamically required energy threshold to initiate the reaction.

CV measurements after the electrolysis as well as ^{1}H and $^{31}P\{^{1}H\}$ NMR spectroscopic analyses were used to assess the stability of a complex under CPE conditions.

4.4.1 $[FeL(MeCN)_3](BF_4)_2$

The conditions and results for CPE experiments with $\mathbf{Fe_s^{II}}$ are reported in Table 4.7. Product-time profiles are given in Figure C.15.

Table 4.7. Conditions and results for CPE experiments with $\mathbf{Fe_s^{II}}$ under CO_2 atmosphere and addition of proton donors.

Entry	HA[a]	E (V_{Fc})	η (V)[b]		FE_{max} (%)[c]		Q (C)	Dec.
			CO	H_2	CO	H_2		
1	MeCN	–2.3	–0.11	–0.37	1 (3)	-	6.3	Yes
2	MeOH (2.5)	–2.2	0.39/–0.01	0.14/–0.27	-	95 (3)	193	Yes

[a] Brackets: c_{HA} (M). [b] Min. (left) and max. η (right). [c] Brackets: t (h) required to reach FE_{max}.

A control experiment without additive at the potential of the $Fe^{I/0}$ wave (entry 1) formed minor amounts of CO following passage of 6.3 C. Opposed to this, CPE performed in the presence of 2.5 M MeOH (entry 2) led to the multiplication of the transferred charge to 193 C and the primary formation of hydrogen with a maximum FE of 95% after 3 h of reaction time. The negative

overpotential for proton reduction but (almost) neutral one for eCO_2r can explain the selectivity toward hydrogen.

Discoloration of the reaction solution, loss of complex signatures in the NMR spectra, and the CV after the reaction hint toward complex decomposition under the reaction conditions. Hence it is likely, that heterogeneous decomposition products [e.g., Fe(0) nanoparticles] catalyze the reduction of protons. The ROBERT group showed that iron nanoparticles formed from decomposed iron quaterpyridine complexes perform very well in the electrocatalytic reduction of protons with FEs > 90%.[17] Moreover, the reductive decomposition of $\mathbf{Fe_s^{II}}$ may yield iron phosphide nanoparticles, a class of very active catalysts for the hydrogen evolution reaction.[18]

4.4.2 $[CoL(MeCN)_2](BF_4)_2$

The CPE results using $\mathbf{Co_s^{II}}$ in the presence of CO_2 are summarized in Table 4.8. Product-time profiles can be found appended in Figure C.16.

Table 4.8. Conditions and results for CPE experiments with $\mathbf{Co_s^{II}}$ under CO_2 atmosphere and addition of proton donors.

Entry	HA[a]	E (V_x)		η (V)[b]		FE_{max} (%)[c]		Q (C)	Dec.
		Ag	Fc	CO	H_2	CO	H_2		
1	MeCN	–1.7	–2.2	–0.01	–0.27	2 (3.5)	-	8.2	Yes
2	H_2O (4.5)	–1.5	–1.85	0.86/–0.56	0.60/–0.82	4 (0.5)	18 (0.5)	74.2	Yes
3	MeOH (1)	–2.1	*n. d.*	0.41/0.0	0.15/–0.25	2 (1.5)	25 (2)	20.7	Yes
4	TFE (0.2)	–1.8	–1.95	0.40/–0.18	0.15/–0.45	4 (0.5)	-	16.4	Yes
5	PhOH (1)	–1.8	–1.95	0.06	–0.20	-	94 (1)	96.6	Yes
6	BA (sat.)	–0.95	–1.1	0.45	0.20	-	-	2.6	Yes
7	BA (0.1)	–1.8	–1.95	–0.40	–0.65	-	> 100 (1)	36.5	Yes
8	PhOH (1), no [Co]	–1.9	*n. d.*	0.02	–0.24	17 (1)	66 (1)	16.1	-

[a] Brackets: c_{HA} (M). [b] Min. (left) and max. η (right). [c] Brackets: t (h) required to reach FE_{max}.

The blank experiment without a proton source (entry 1) gave a maximum FE of 2% after 3.5 h. In contrast, adding water doubled this value but is accompanied by 18% FE for H_2 (entry 2), as presented exemplarily in Figure 4.16. The FE_{max} for both products was reached after ca. 30 min, likely marking the turning point at which complex decomposition prevents further product formation.

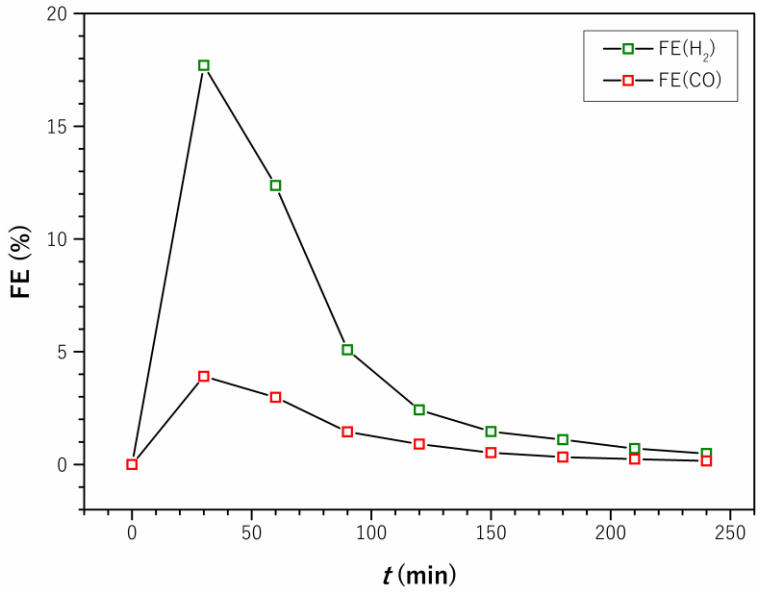

Figure 4.16. FE vs. time profile for CPE with $\mathbf{Co_s^{II}}$ and 4.5 M H_2O.

The ratio of maximum faradaic efficiencies for hydrogen to CO even increased with methanol (entry 3) but led to the sole formation of CO in a FE of 4% with TFE (entry 4). More potent acids induced the exclusive evolution of hydrogen (entries 5 and 7) by favoring the generation of Co-H species in the ET_H route. However, formate and formic acid (producible from the same route) could not be observed in HPLC analysis. When the potential was set to the $Co^{II/I}$ wave in the presence of saturated BA (entry 6), no product could be detected, despite the evident rise of the peak current density in CV.

A control experiment without $\mathbf{Co_s^{II}}$ but with added PhOH exhibited the highest FE for CO of 17% (entry 8), suggesting that the complex shifts the kinetics away from CO_2 reduction to hydrogen evolution.

Solution discoloration, loss of NMR signals, and the vanishing of the redox pattern in CV are observed in every experiment performed with $\mathbf{Co_s^{II}}$. These results suggest (nanoparticulate) Co(0) species adsorbed at the electrode surface to be responsible for most of the product. For reference, cobalt phosphide nanoparticles are reported to be well-performing catalysts in the electrochemical reduction of protons.[19]

4.4.3 $[NiL(MeCN)](BF_4)_2$

Although CV experiments suggested the reduction potentials of $\mathbf{Ni_s^{II}}$ too anodic for catalytic activity in eCO_2r or hydrogen evolution, CPE was performed to identify the products at the observed catalytic waves. Table 4.9 summarizes the performed experiments. Product-time profiles are attached in Figure C.17.

Table 4.9. Conditions and results for CPE experiments with $\mathbf{Ni_s^{II}}$ under CO_2 atmosphere and addition of proton donors.

Entry	HA[a]	E (V_x)		η (V)[b]		FE_{max} (%)[c]		Q (C)	Dec.
		Ag	Fc	CO	H_2	CO	H_2		
1	MeCN	–1.3	–1.8	0.39	0.13	4 (1)	-	6	Yes
2	H_2O (4.5)	–1.2	–1.3	1.41/–0.01	1.15/–0.27	4 (1)	-	8.9	Yes
3	PhOH (1)	–1.75	–1.95	0.06	–0.20	-	90 (2)	57.2	Yes
4	PhOH (1), no [Ni]	–1.9	*n. d.*	0.02	–0.23	17 (1)	66 (1)	16.1	-

[a] Brackets: c_{HA} (M). [b] Min. (left) and max. η (right). [c] Brackets: t (h) required to reach FE_{max}.

A maximum faradaic efficiency of 4% for CO after one hour of reaction time was observed without additives (entry 1). The FE is retained, while the passed charge increases by 50% when adding 4.5 M water. PhOH completely shifts the product selectivity to H_2 with 90% FE after two hours.

Similar to Fe and Co, discoloration as well as the loss of NMR and CV signals suggest that the nickel complex decomposes during electrolysis. Nickel phosphide nanostructures are reported to catalyze the electrochemical reduction of protons to hydrogen in strongly acidic media, which may explain the hydrogen evolution in entry 3.[20]

Summarizing the CPE results under CO_2 atmosphere for the series of $\mathbf{M_s^{II}}$ complexes, their reactivity, as inferred from CV experiments, could not be transferred to quantitative electrolysis. The complex stability under CPE conditions appears to be the central issue preventing molecular catalytic activity. Hence, the next section will discuss the reasons and mechanisms for the complex decomposition, followed by approaches to prevent it.

4.4.4 Complex Stability under CPE Conditions

The unsatisfying transfer of reactivity from CV to CPE for the $\mathbf{M_s^{II}}$ complexes is likely caused by the insufficient reduction strength of the **M**(0) species and the accumulation of decomposition and side reactions to off-cycle species throughout the experiment. Inhibition or even complete shutdown of these reactions is hence necessary to receive a clear picture of the catalytic performance of the $\mathbf{M_s^{II}}$ systems. The stabilization of the metal centers in low oxidation states mainly depends on the properties of the ligand system. Since the ligand's high degree of aromaticity induces a strong electron-withdrawing effect, the electronic structure is generally surmised to support low oxidation states.

From a steric point of view, the phenyl substituents bound to the coordinating phosphines provide only moderate shielding of the metal center. Moreover, the mainly aromatic nature of the ligand backbone might lack the flexibility to allow for the many reorganization steps during (electro)catalytic cycles. Hence, the loss of **L** and formation of **M**(0) nanoparticles might be favorable for the metal center under CPE conditions.

The position *para* to the pyridinic nitrogen could also constitute a weak point in the system, as observed in the groups of JONES and KHUSNUTDINOVA for comparable [Ni(PNP)] pincer complexes.[21] One equivalent of $LiBEt_3H$ gives a dearomatized product due to reduction at the pyridine *para* position as determined by single-crystal X-ray diffraction. Moreover, when switching to the more potent reducing agent KC_8 without a proton or hydride source, the analogous Ni(II) methyl complex dimerizes at the *para* position, likewise identified by single-crystal X-ray diffraction. Scheme 4.2 shows the possible products of these reactions applied to $\mathbf{Ni_s^{II}}$.

A) Dearomatization ***B) Dearomatization + Dimerization***

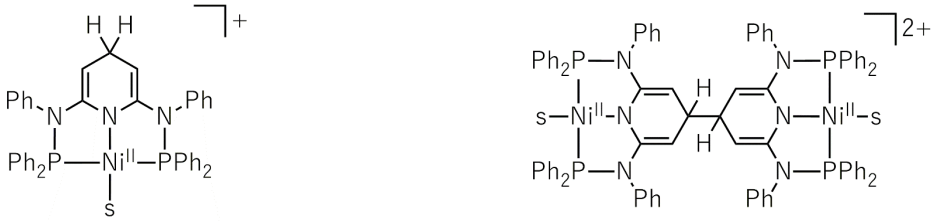

Scheme 4.2. (A) Dearomatization and (B) dimerization at the pyridine *para* position of $\mathbf{Ni_s^{II}}$ under reductive conditions analogous to those reported by LAPOINTE et al.[21b]

A similar dearomatization might be conceivable under electroreductive conditions in the presence of protons. Any dearomatized ligand formed during CPE would provide less stabilization of reduced metal oxidation states and hence renders the complex prone to decomposition. Protection of the pyridinic *para* position might stabilize the ligand system and, ultimately, the complex under CPE conditions in the presence of proton sources.

Another approach is based on the reported activity of Co and Ni complexes in CO_2 electroreduction in their **M**(I) state {*vide supra* for [Ni/Co(cyclam)]}.[7a] Reaching activity at z = +I could combine this activity with stability improvements by avoiding the putatively unstable zero-valent state.

In order to achieve this for the $\mathbf{M_s^{II}}$ complexes, the driving force for the electron transfer to the CO_2 molecule must be increased at the **M**(I) stage. Therefore, the reduction potential of the $\mathbf{M}^{II/I}$ wave requires a drastic shift in the cathodic direction by providing enhanced electron density at the metal center in its initial oxidation state. Since auxiliary ligands might decoordinate

or be substituted during reduction, **L** is the primary starting point for modifications. The electronic attunement of the phosphines by replacing the electron-withdrawing phenyl groups with electron-donating alkyls (e.g., *iso*-propyl, cyclohexyl, or *tert*-butyl) could be promising. Functionalizing the *para* position in the pyridine ring, e.g., by methoxy groups, could grant additional electron density and simultaneously protect the position under reducing conditions. These measures should displace the first reduction wave to more negative potentials and enable reduction activity for the **M**(I) complexes under a concomitant increase of stability compared to their **M**(0) analogs.

4.5 Experimental

4.5.1 Cyclic Voltammetry

CV experiments were performed as described in section 3.6.2. The electrolyte solution was sparged with solvent-saturated CO_2 for 20 min before performing measurements under a CO_2 atmosphere.

Anhydrous $Mg(OTf)_2$ was used as received and stored under an inert atmosphere.

Ultrapure water from a MILLIQ ADVANTAGE A10 water purification system, MeOH, and TFE were degassed by sparging with argon. MeOH and TFE were dried by storage over a 3 Å molecular sieve. Phenol was dried by distillation from a benzene solution which removes the water/benzene azeotrope, before distilling phenol at reduced pressure under an inert atmosphere.[22] Benzoic acid was sublimated *in vacuo* at 80 °C under an inert atmosphere.[22] All proton sources were stored under an inert atmosphere.

1 M solutions of the dried (except H_2O) and degassed proton source (H_2O, MeOH, TFE, PhOH, or BA) in MeCN electrolyte were gradually added for proton source screenings. The addition of neat substances (not subjected to the purification steps mentioned above) allowed for testing higher proton concentrations.

4.5.2 Controlled Potential Electrolysis

CPE was performed with a BIOLOGIC SP-300 potentiostat equipped with a $\pm$ 1 A/$\pm$ 48 V booster card (Figure 4.17A, no. 1) in a custom-made, gas-tight electrochemical H-cell manufactured by ADAMS & CHITTENDEN SCIENTIFIC GLASS (Figure 4.17A, no. 2 and Figure 4.17B) with both half-cells divided by a no. 3 glass frit (Figure 4.17B, no. 5). The cell comprised a standard three-electrode setup with a glassy carbon foam WE from GOODFELLOW GmbH, a platinum mesh CE, and a $AgNO_3$/Ag or AgCl/Ag RE (Figure 4.17C). The working electrodes were stored at 120 °C, used without further purification, and disposed of after one run. Reference and counter electrodes were rinsed with ultrapure water and ethanol before drying under a stream of argon and insertion into the cell. ACE threads (Figure 4.17B, no. 6) combined with two layers of punctured PTFE septa for the RE and CE, as well as epoxy resin for the WE, allowed a gas-tight connection of the electrodes. The OHMIC drop of the electrochemical cell was compensated as stated in section 3.6.2.

A) CPE Setup

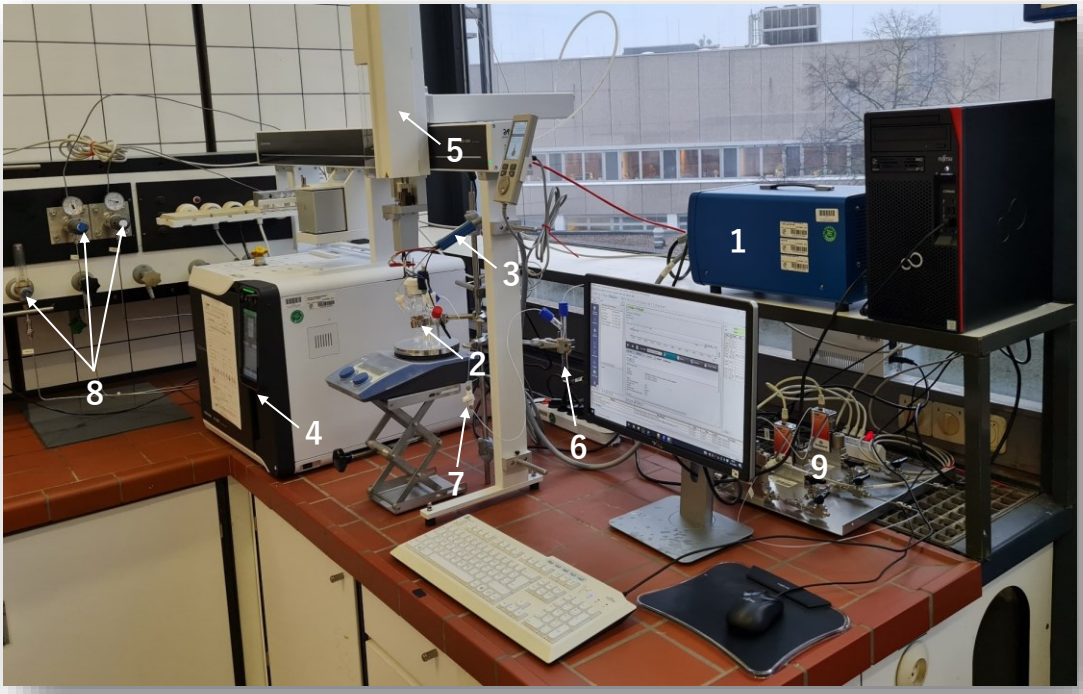

1 – Potentiostat + booster card, **2** – H-cell, **3** – Electrode cables, **4** – GC, **5** — Auto sampler, **6** – Prebubbler, **7** – Gas valve, **8** – Gas supply (from left: Ar, CO_2, He), **9** – MFC board

B) H-Cell

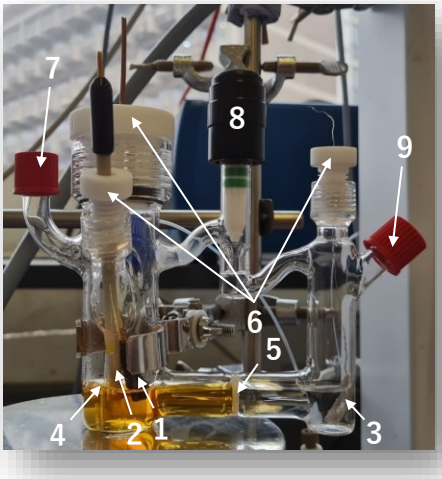

1 – GC foam WE, **2** – AgCl/Ag RE, **3** – Pt mesh CE, **4** – Silicone tubing, **5** – P3 glass frit, **6** – ACE threads, **7** – PTFE septum, **8** – ROTAFLO valve, **9** – GL14 cap

C) CPE Electrodes

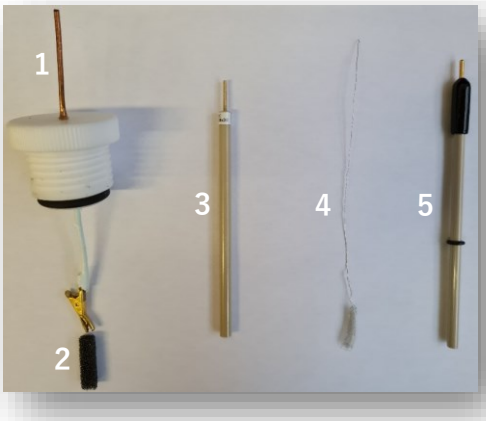

1 – #25 ACE thread + copper wire and crocodile clamp (wrapped with PTFE tape), **2** – GC foam WE, **3** – GC rod WE, **4** – Pt mesh CE, **5** – AgCl/Ag RE

Figure 4.17. (A) CPE setup, (B) H-cell with electrodes and analyte, and (C) close-up of CPE electrodes.

A piping and instrumentation diagram (P&ID) of the CPE setup is presented in Scheme 4.3.

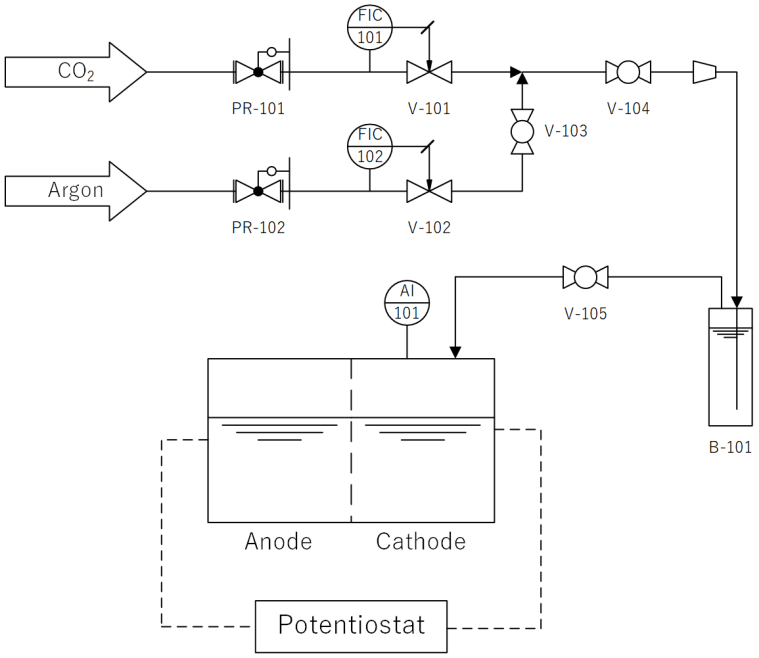

Scheme 4.3. P&ID of the CPE setup used in this work.

The CPE cell with the components displayed in Figure 4.17B was assembled still hot from storage at 120 °C and under continuous purging with solvent-saturated argon through a silicone tubing (Figure 4.17B, no. 4) to avoid the introduction of oxygen and moisture from the air. The custom-made BRONKHORST mass flow controller (MFC) board in Figure 4.17A, no. 9, and the upper part of Scheme 4.3 allowed control of the gas flow. The board is positioned between the gas supply (Figure 4.17A, no. 8) and the prebubbler used to saturate the gas with the electrolyte solvent (Scheme 4.3, B-101 and Figure 4.17A, no. 6). Differential pressure build-up was prevented by opening the ROTAFLO valve connecting the two half-cells (Figure 4.17B, no. 8) and the GL14 cap at the anodic side (Figure 4.17B, no. 9). The fully assembled H-cell was further purged with argon for 20 min. Subsequently, a 1 mM solution of the respective complex and the additive in the desired concentration (if applicable) was prepared in a dry and degassed solution of 0.1 M $^{n}Bu_4NPF_6$ in MeCN. 10 mL of the analyte solution and the electrolyte were added to the cathodic and the anodic half-cells, respectively. Argon was substituted with CO_2 by switching the gases at the MFC board (using V-103) and sparging the electrolyte solution with the solvent-saturated CO_2 flow for 20 min under vigorous stirring.

Subsequently, the silicone tubing was removed from the analyte solution, the stirring was stopped, and a CV was recorded at a scan rate of 0.1 $V \cdot s^{-1}$ to define the potential applied in CPE. The GL14 cap was closed, the CO_2 flow was stopped, and the three-way valve (Figure 4.17A, no. 7 and V-105 in Scheme 4.3) connecting the cell and the prebubbler was closed. An initial analysis of the gas phase inside the cell was performed by a SHIMADZU AOC-6000 auto sampling

system (Figure 4.17A, no. 5) penetrating the PTFE septum of the cathodic half-cell (Figure 4.17B, no. 7) with a gas-tight syringe. The sample was injected into a SHIMADZU NEXIS GC-2030 (Figure 4.17A, no. 4 and AI-101 in Scheme 4.3) with a CARBOXEN®-1010 PLOT Capillary GC column (30 m x 0.32 mm) and thermal conductivity detector (see Table 4.10, for the separation program).

The CPE was started at the desired potential and performed for 4 h or until manual abortion, with samples taken approximately every 30 min.

At the end of the electrolysis, a cyclic voltammogram was recorded at a scan rate of 0.1 $V \cdot s^{-1}$ before opening the cell. A sample of the liquid phase of the cathodic half-cell was taken, filtered through a syringe filter, and subjected to HPLC analysis. The custom SHIMADZU HPLC setup consists of a CBM-20A system controller, LC-20AD pump, DGU-20A5r degassing unit, DIL-20AC HT auto-sampler, CTO-10ASvp column oven, and an RID-10A refractive index detector equipped with a CS organic acid resin column (440 x 8 mm; see Table 4.10 for the separation program). An aliquot of the filtered solution was analyzed by NMR spectroscopy.

Table 4.10. GC and HPLC separation parameters.

	GC	**HPLC**
Cell Temperature (°C)	-	40
Column Temperature (°C)	See "Method"	25
Injector Temperature (°C)	250	-
Detector Temperature (°C)	100	-
Detector Current (mA)	100	-
Eluent	Helium	50 mM aq. H_2SO_4
Linear Velocity (cm/s)	30	-
Split Ratio	5.0	-
Injection Volume (µL)	400	70
Method	1. 40 °C for 2 min 2. 10 °C/min for 16 min to 200 °C 3. 200 °C for 8 min	1. 1 mL/min for 20 min 2. 0.3 mL/min for 15 min

Lastly, the cathodic solution was removed and substituted with fresh electrolyte before 1 mM Fc was added as the internal potential reference. The respective cyclic voltammogram was recorded at a scan rate of 0.1 $V \cdot s^{-1}$ using a GC disk WE (Figure 4.17C).

4.6 References

[1] E. Fujita, C. Creutz, N. Sutin, D. J. Szalda, *J. Am. Chem. Soc.* **1991**, *113*, 343.

[2] a) M. Hammouche, D. Lexa, J.-M. Savéant, M. Momenteau, *J. Electroanal. Chem.* **1988**, *249*, 347; b) L. Chen, Z. Guo, X.-G. Wei, C. Gallenkamp, J. Bonin, E. Anxolabéhère-Mallart, K.-C. Lau, T.-C. Lau, M. Robert, *J. Am. Chem. Soc.* **2015**, *137*, 10918.

[3] C. Römelt, J. Song, M. Tarrago, J. A. Rees, M. van Gastel, T. Weyhermüller, S. DeBeer, E. Bill, F. Neese, S. Ye, *Inorg. Chem.* **2017**, *56*, 4745.

[4] C. Chan, A. E. Carpenter, M. Gembicky, C. E. Moore, A. L. Rheingold, J. S. Figueroa, *Organometallics* **2019**, *38*, 1436.

[5] Y.-E. Kim, J. Kim, Y. Lee, *Chem. Commun.* **2014**, *50*, 11458.

[6] M. Aresta, R. Gobetto, E. Quaranta, I. Tommasi, *Inorg. Chem.* **1992**, *31*, 4286.

[7] a) M. H. Schmidt, G. M. Miskelly, N. S. Lewis, *J. Am. Chem. Soc.* **1990**, *112*, 3420; b) C. A. Kelly, Q. G. Mulazzani, M. Venturi, E. L. Blinn, M. A. J. Rodgers, *J. Am. Chem. Soc.* **1995**, *117*, 4911; c) A. J. Morris, G. J. Meyer, E. Fujita, *Acc. Chem. Res.* **2009**, *42*, 1983; d) J. Schneider, H. Jia, J. T. Muckerman, E. Fujita, *Chem. Soc. Rev.* **2012**, *41*, 2036.

[8] V. V. Pavlishchuk, A. W. Addison, *Inorg. Chim. Acta* **2000**, *298*, 97.

[9] D. W. Shaffer, S. I. Johnson, A. L. Rheingold, J. W. Ziller, W. A. Goddard, R. J. Nielsen, J. Y. Yang, *Inorg. Chem.* **2014**, *53*, 13031.

[10] a) J. D. Froehlich, C. P. Kubiak, *Inorg. Chem.* **2012**, *51*, 3932; b) G. K. Rao, W. Pell, I. Korobkov, D. Richeson, *Chem. Commun.* **2016**, *52*, 8010; c) F. Wang, B. Cao, W.-P. To, C.-W. Tse, K. Li, X.-Y. Chang, C. Zang, S. L.-F. Chan, C.-M. Che, *Catal. Sci. Technol.* **2016**, *6*, 7408; d) J. Bi, P. Hou, F.-W. Liu, P. Kang, *ChemSusChem* **2019**, *12*, 2195.

[11] M. D. Sampson, C. P. Kubiak, *J. Am. Chem. Soc.* **2016**, *138*, 1386.

[12] A. K. Katz, J. P. Glusker, G. D. Markham, C. W. Bock, *J. Phys. Chem. B* **1998**, *102*, 6342.

[13] a) N. P. Liyanage, H. A. Dulaney, A. J. Huckaba, J. W. Jurss, J. H. Delcamp, *Inorg. Chem.* **2016**, *55*, 6085; b) R. Francke, B. Schille, M. Roemelt, *Chem. Rev.* **2018**, *118*, 4631.

[14] a) G. A. N. Felton, A. K. Vannucci, N. Okumura, L. T. Lockett, D. H. Evans, R. S. Glass, D. L. Lichtenberger, *Organometallics* **2008**, *27*, 4671; b) C. Costentin, S. Drouet, M. Robert, J.-M. Savéant, *Science* **2012**, *338*, 90; c) B. D. McCarthy, D. J. Martin, E. S. Rountree, A. C. Ullman, J. L. Dempsey, *Inorg. Chem.* **2014**, *53*, 8350; d) Y. C. Lam, R. J. Nielsen, H. B. Gray, W. A. Goddard, *ACS Catal.* **2015**, *5*, 2521.

[15] S. Roy, B. Sharma, J. Pécaut, P. Simon, M. Fontecave, P. D. Tran, E. Derat, V. Artero, *J. Am. Chem. Soc.* **2017**, *139*, 3685.

[16] A. M. Appel, M. L. Helm, *ACS Catal.* **2014**, *4*, 630.

[17] C. Cometto, L. Chen, D. Mendoza, B. Lassalle-Kaiser, T.-C. Lau, M. Robert, *ChemSusChem* **2019**, *12*, 4500.

[18] L. Tian, X. Yan, X. Chen, *ACS Catal.* **2016**, *6*, 5441.

[19] a) E. J. Popczun, C. G. Read, C. W. Roske, N. S. Lewis, R. E. Schaak, *Angew. Chem. Int. Ed.* **2014**, *53*, 5427; b) D.-H. Ha, B. Han, M. Risch, L. Giordano, K. P. C. Yao, P. Karayaylali, Y. Shao-Horn, *Nano Energy* **2016**, *29*, 37.

[20] E. J. Popczun, J. R. McKone, C. G. Read, A. J. Biacchi, A. M. Wiltrout, N. S. Lewis, R. E. Schaak, *J. Am. Chem. Soc.* **2013**, *135*, 9267.

[21] a) S. Kundu, W. W. Brennessel, W. D. Jones, *Inorg. Chem.* **2011**, *50*, 9443; b) S. Lapointe, E. Khaskin, R. R. Fayzullin, J. R. Khusnutdinova, *Organometallics* **2019**, *38*, 4433.

[22] W. L. F. Armarego, C. L. L. Chai, in *Purification of Laboratory Chemicals (Sixth Edition)*, Butterworth-Heinemann, Oxford, **2009**.

Chapter 5: Conclusion & Outlook

The electrochemical reduction of carbon dioxide holds the potential to recycle the C_1 building block into the chemical value chain by using renewable energies. 3d transition metal complexes can catalyze this reaction and lead toward more complex and valuable products, which marks a pivotal step for a broader impact of the process and its expansion to an industrial scale.

The present work addressed the so-far insufficiently investigated influence of a molecular electrocatalysts' metal center on the traversed reaction pathway and the products accessible therein.

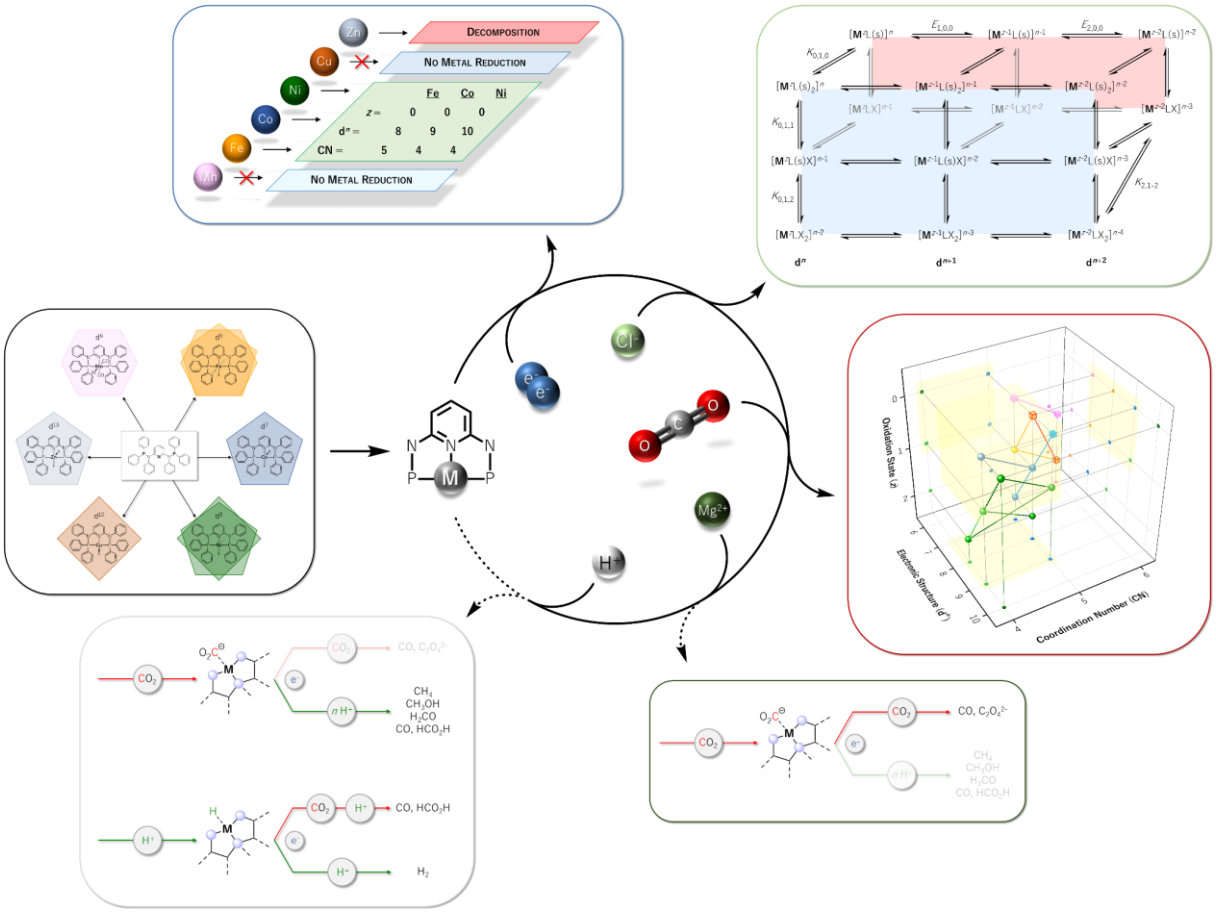

Therefore, a series of comparable mid to late 3d transition metal complexes (Mn to Zn) was synthesized from the redox-innocent N^2,N^6-bis(diphenylphosphaneyl)-N^2,N^6-diphenylpyridine-2,6-diamine pincer ligand **L**. The synthesis was successful for Fe, Co, Ni, and Zn bis-chloride metal precursors in the +II oxidation state but failed for Mn and Cu, which required a switch to the +I state for the latter. Acetonitrile-coordinated complexes of Fe, Co, and Ni were synthesized from **L** to counter a possible influence of the coordinating acetonitrile solvent used for electrochemical investigations.

Various spectroscopic techniques as well as single-crystal XRD structurally and electronically characterized each complex. This analysis formed the foundation to correlate the structure and

electronic configuration of the metal via the crystal field theory. A qualitative increase in electronic density at the metal center could be observed from the ^{31}P NMR coordination chemical shift. The bond distances between metal and coordinating atoms correlated linearly with the electronegativity of the metal center for the acetonitrile complexes and indicated increasing stabilities in the order Fe < Co < Ni.

Mn-, Cu-, and Zn-based compounds only showed ligand-centered redox activity at potentials < –2.2 V_{Fc}, whereas Fe, Co, and Ni exhibited two metal-centered redox waves representing the $\mathbf{M}^{II/I}$ and $\mathbf{M}^{I/0}$ couples, respectively. While Co and Ni partially exchanged their auxiliary ligands during this pathway, Fe was surmised to either dimerize or disproportionate.

The ligand exchange between chloride and acetonitrile, specifically at Co and Ni cores, was analyzed by NMR spectroscopy and cyclic voltammetry, which allowed the deconvolution of the electrochemical and chemical processes under reductive conditions. Independent from the auxiliary ligand in the starting complex, Co and Ni are coordinated by a single solvent ligand at the zero-valent state [$\mathbf{M}^0\mathbf{L}$(MeCN)] in acetonitrile, as graphically summarized within the so-called cube schemes. With the qualitative analysis of the electrochemical processes achieved already, quantification of equilibrium constants is planned as future work.

CV analysis also identified the auxiliary ligand as an influencing parameter on the reducibility and stability of a molecular complex under electroreductive conditions. While chloride ligands increased the stability compared to the labile acetonitrile, the latter facilitated complex reduction.

The effect of the metal center is clearly evidenced when considering CO_2 activation. Each transition metal complex coordinates CO_2 at the zero-valent state; however, an electron transfer to the substrate is only surmised for Fe and Co. The Ni(0) complex likely forms an η^2-CO_2 ARESTA-like species with minor CO_2 activation, whereas the Co(0) radical potentially provides sufficient electron transfer to CO_2 to unlock the catalytic cycle. Relating these findings to literature examples of potent eCO_2r catalysts identified coordinative unsaturation (coordination numbers 4 or 5), an open 3d shell (metal electron configuration d^7 to d^9), and low oxidation states (+I or 0) as prerequisites to be comprised in species initiating CO_2 activation. These results, hence, provide key objectives for designing molecular complexes in the electrocatalytic activation of CO_2.

The addition of LEWIS or BRØNSTED acids in cyclic voltammetry identified Co as a promising metal for the electrochemical reduction of CO_2 when environed by **L**. Acids stronger than methanol, however, induced the primary reduction of protons. The subsequent transfer of activity

from cyclic voltammetry to the quantitative conversion of CO_2 yet proved challenging since controlled potential electrolyses in the presence of proton sources only yielded minor amounts of the two-electron reduction product CO. In contrast, H_2 was generated with high faradaic efficiency.

This discrepancy to the CV results was assigned to two factors. Firstly, catalytically active, heterogeneous species may have formed due to complex decomposition observed during the reaction. The origin of the decomposition was traced to the hydrogenation of the ligand backbone in the pyridinic *para* position or destabilization of the coordination scaffold by excessively reducing conditions in the zero-valent metal state. Secondly, using a non-innocent, mainly electron-withdrawing ligand environment comes at the expense of the metal reduction potentials likely being too anodic for CO_2 reduction, which favors the thermodynamically less demanding hydrogen evolution. This characteristic renders redox-innocent ligand systems suitable for describing the role of the central metal but marks the difference to non-innocent systems preferable for catalytic activity. In contrast to **L**, the redox-innocent cyclam ligand framework donates electron density, enhances the metal center's reduction strength, and enables CO_2 reduction.

As a future perspective, the modular design of the pincer system chosen in the present work can be exploited to modify the ligand and tackle the complex instability facilely. On the one hand, protection of the putatively unstable pyridinic *para* position can hinder the attack of a hydride. On the other hand, inducing catalytic activity at the +I oxidation state by providing more electron density at the metal center (e.g., by adjusting the phosphine substituents) avoids the excessively reducing zero-valence. Both approaches combined eventually constitute a promising strategy to expand the knowledge gained herein to the electrocatalytic dimension.

Appendix A: Structural & Electronic Characterization

NMR, EPR, Mössbauer, SQUID & UV/VIS

a) PNP Pincer Ligand

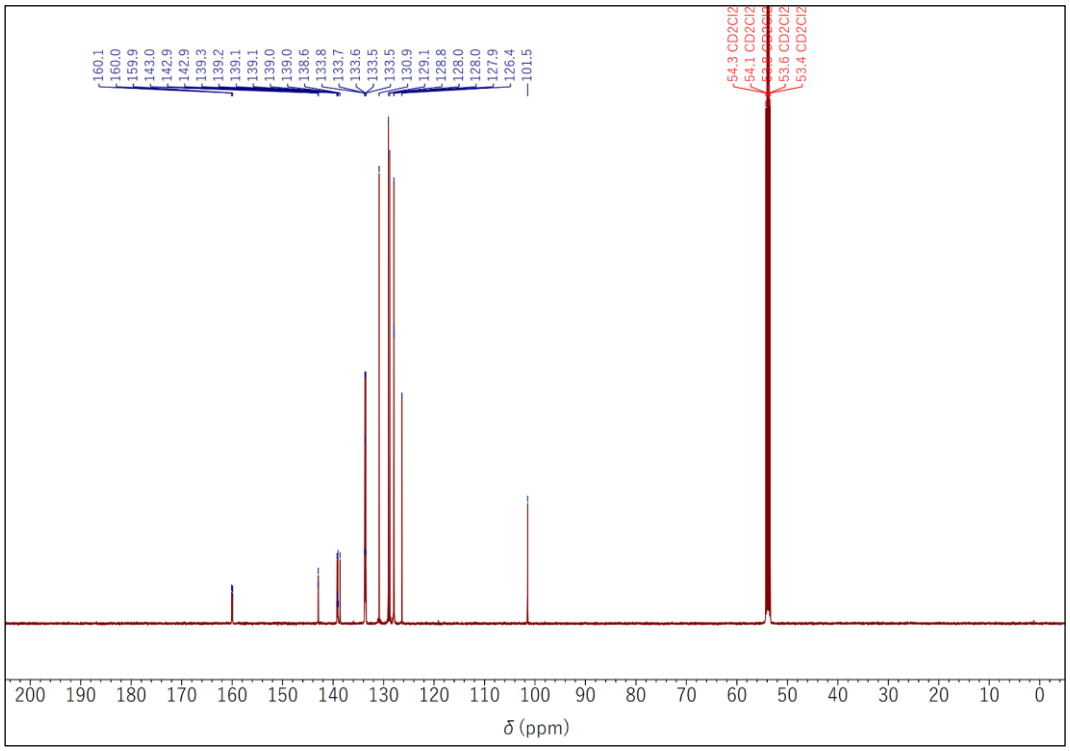

Figure A.1. $^{13}C\{^{1}H\}$ NMR spectrum of **L** in CD_2Cl_2 at 126 MHz and 296 K.

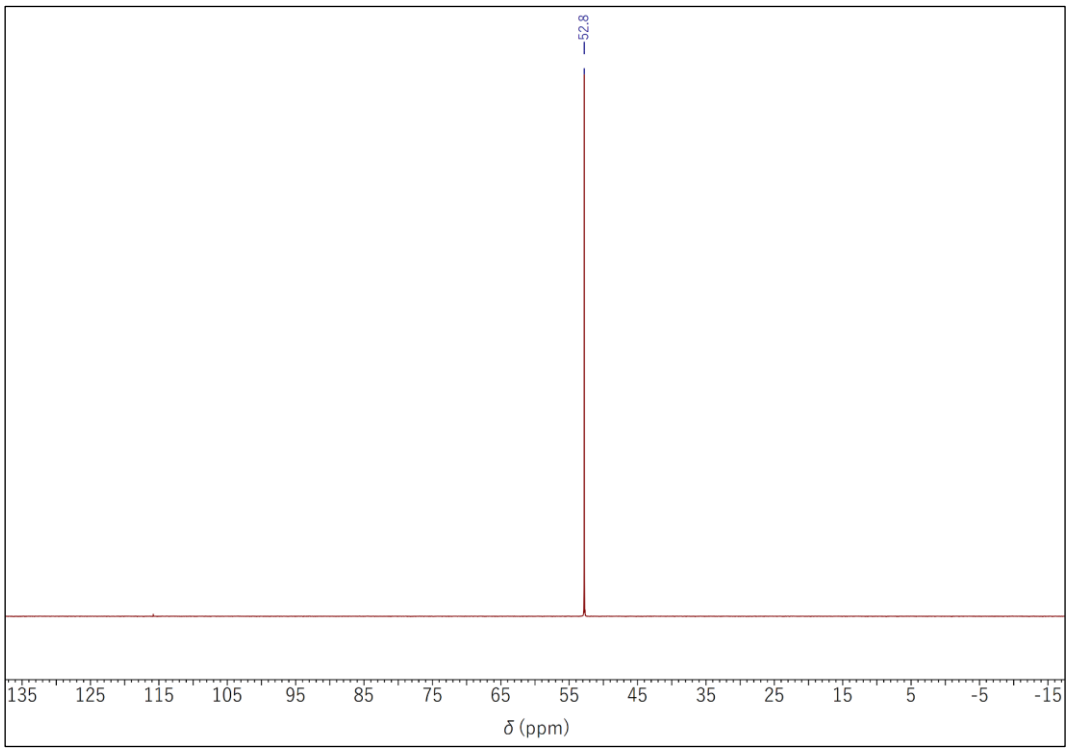

Figure A.2. $^{31}P\{^{1}H\}$ NMR spectrum of **L** in CD_2Cl_2 at 202 MHz and 296 K.

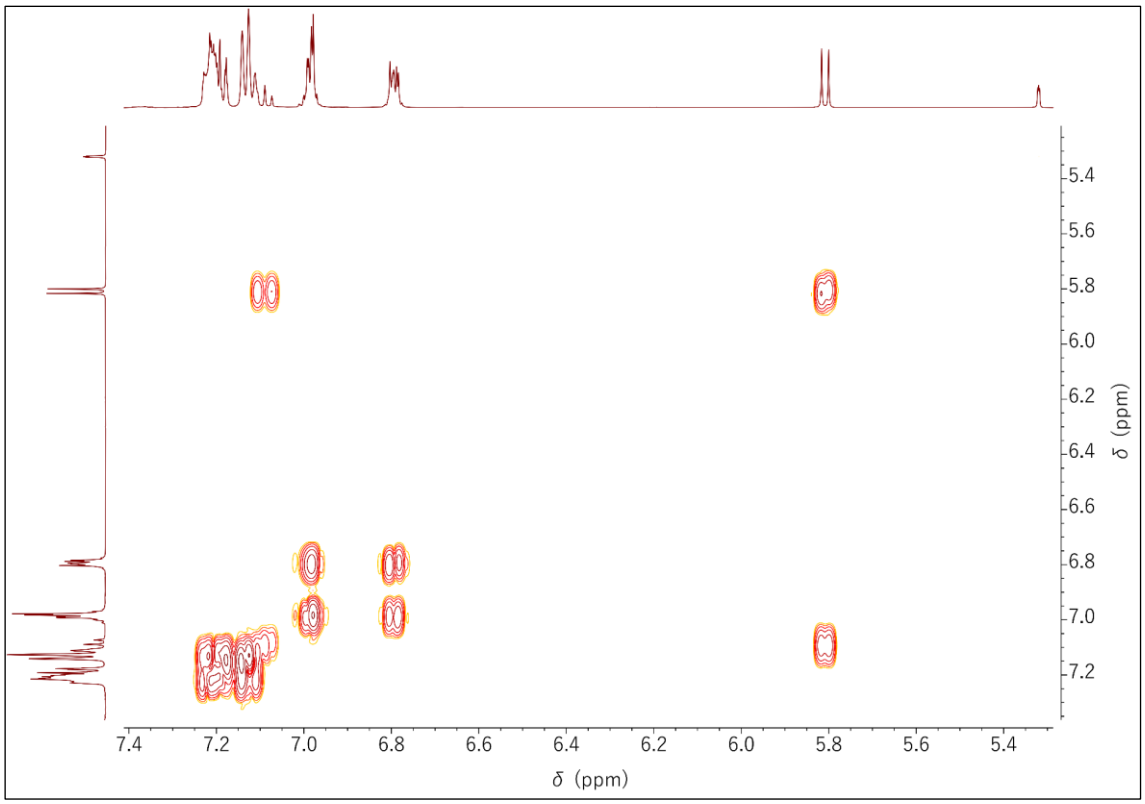

Figure A.3. $^{1}H,^{1}H$ COSY NMR spectrum of **L** in CD_2Cl_2 at 500 MHz and 296 K.

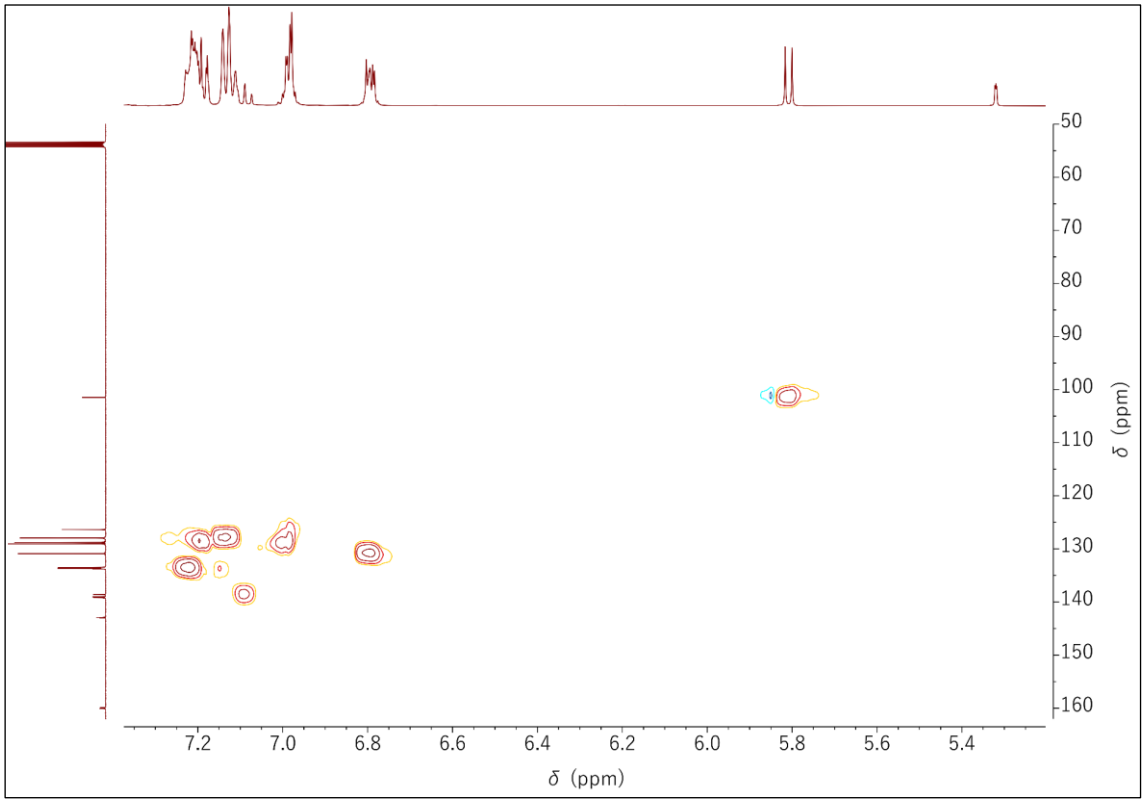

Figure A.4. $^{1}H,^{13}C$ HSQC NMR spectrum of **L** in CD_2Cl_2.

b) Halide & Triflate Complexes

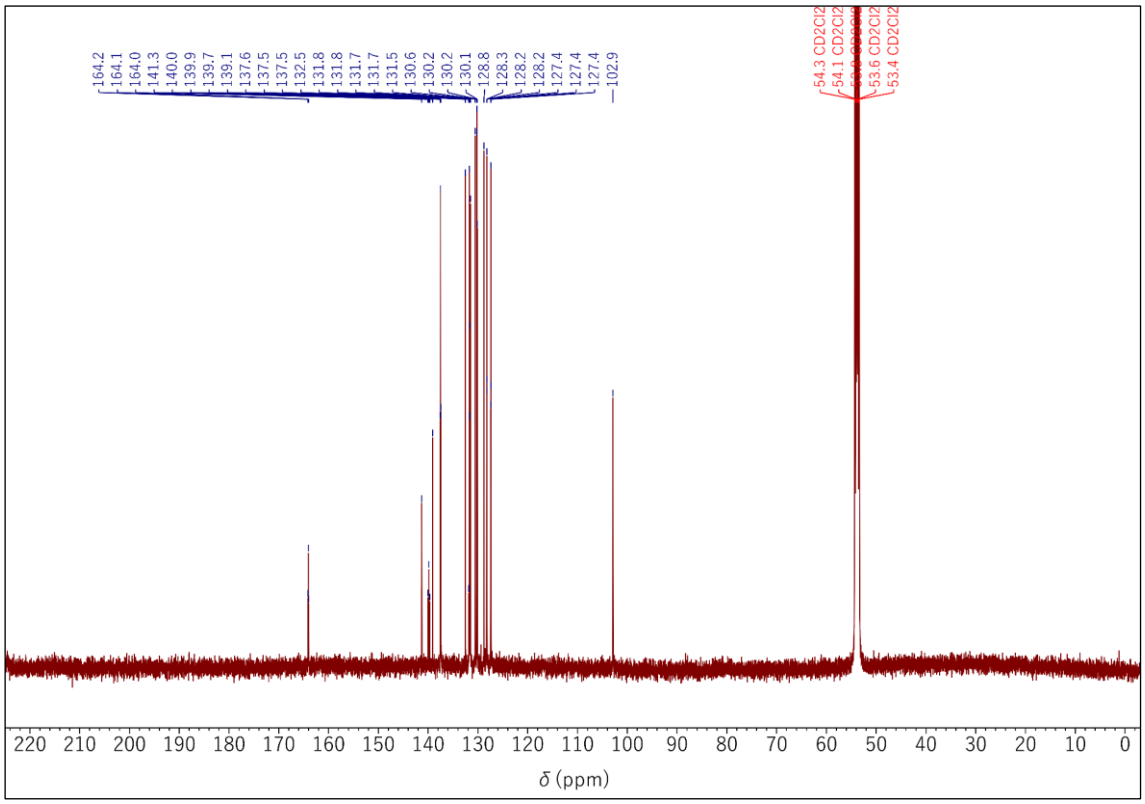

Figure A.5. $^{13}C\{^{1}H\}$ NMR spectrum of $\mathbf{Mn^{I}_{CO,Br}}$ in CD_2Cl_2 at 126 MHz and 296 K.

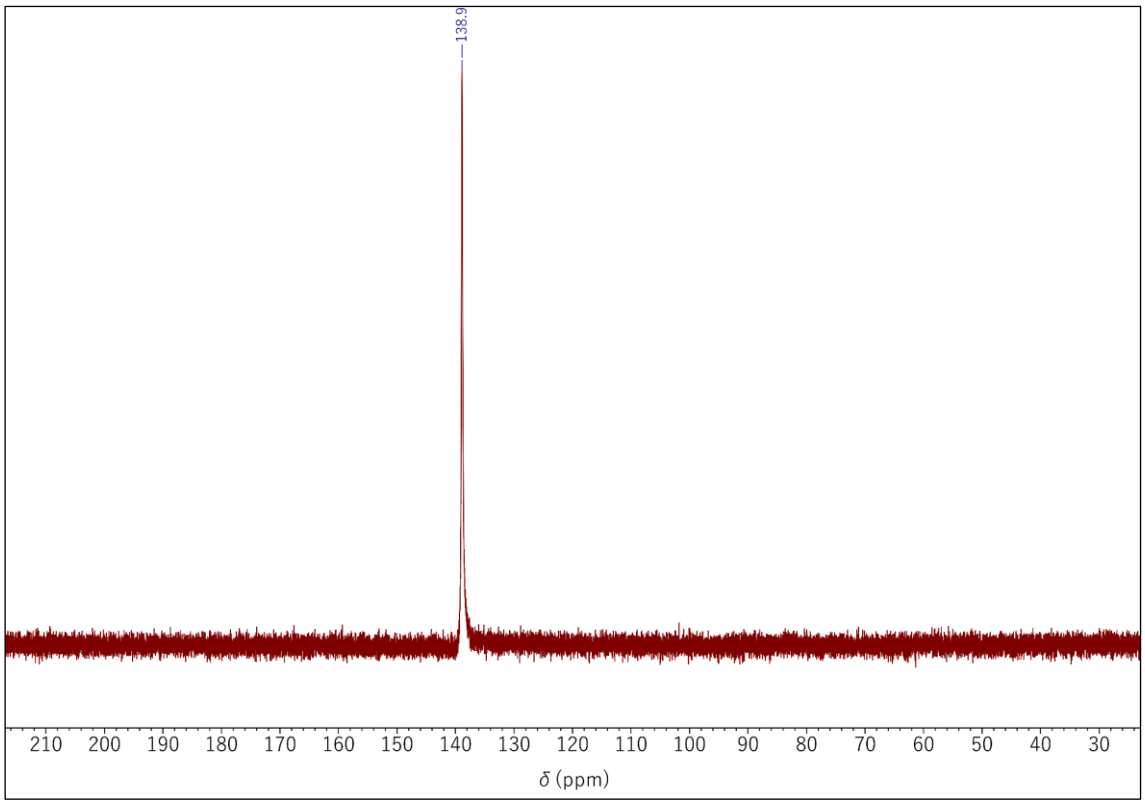

Figure A.6. $^{31}P\{^{1}H\}$ NMR spectrum of $\mathbf{Mn^{I}_{CO,Br}}$ in CD_2Cl_2 at 202 MHz and 296 K.

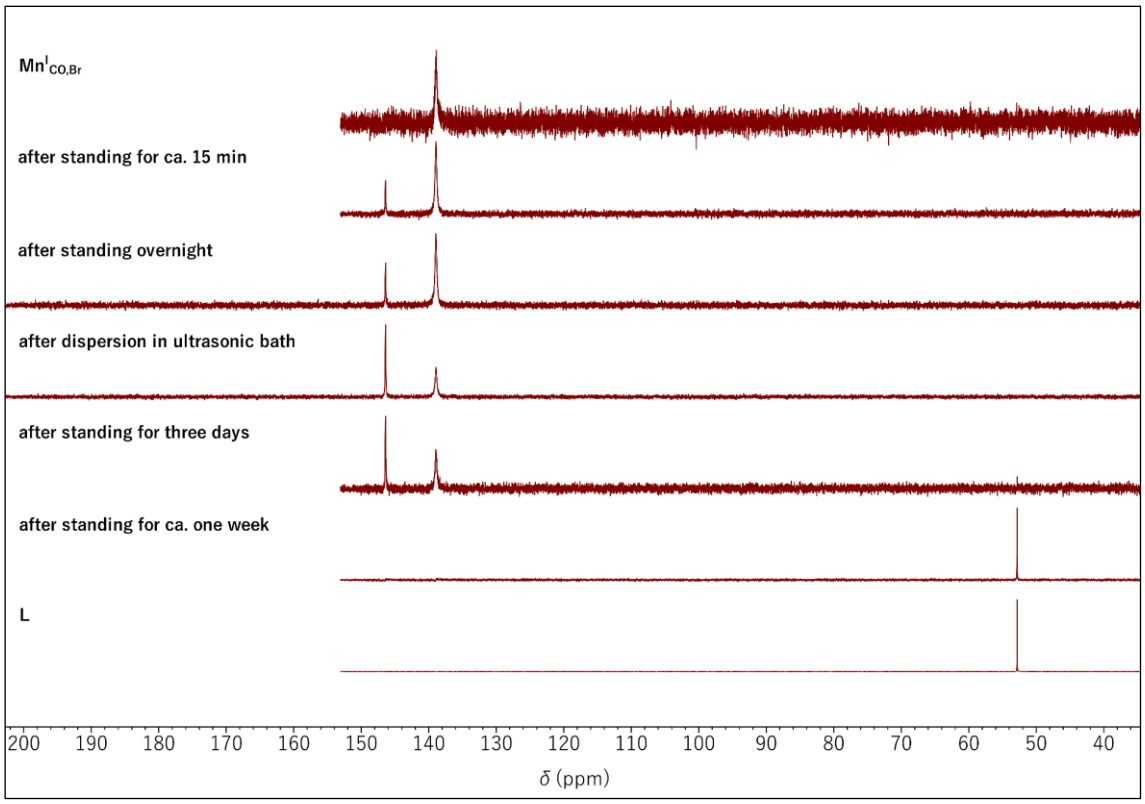

Figure A.7. Time-dependent $^{31}P\{^{1}H\}$ NMR spectra of $\mathbf{Mn^{I}_{CO,Br}}$ in CD_2Cl_2 at 162 MHz and 296 K. The spectrum of **L** is shown as a reference.

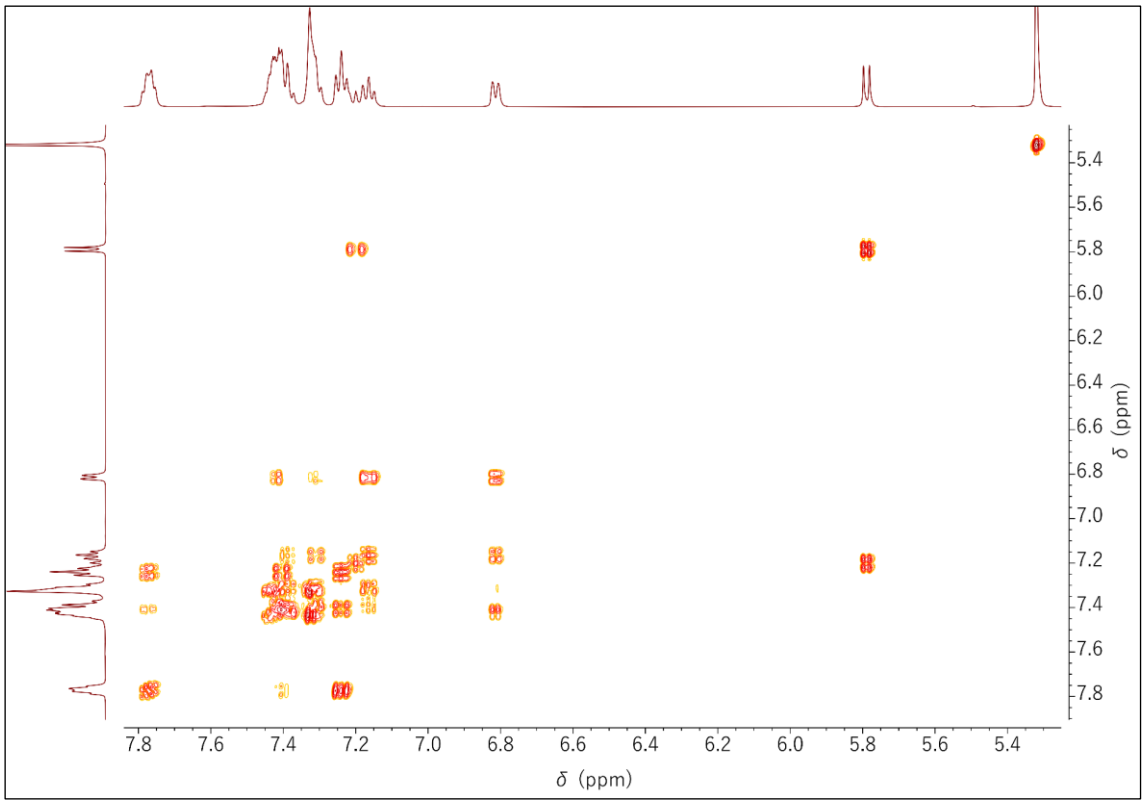

Figure A.8. $^{1}H,^{1}H$ COSY NMR spectrum of $\mathbf{Mn^{I}_{CO,Br}}$ in CD_2Cl_2 at 500 MHz and 296 K.

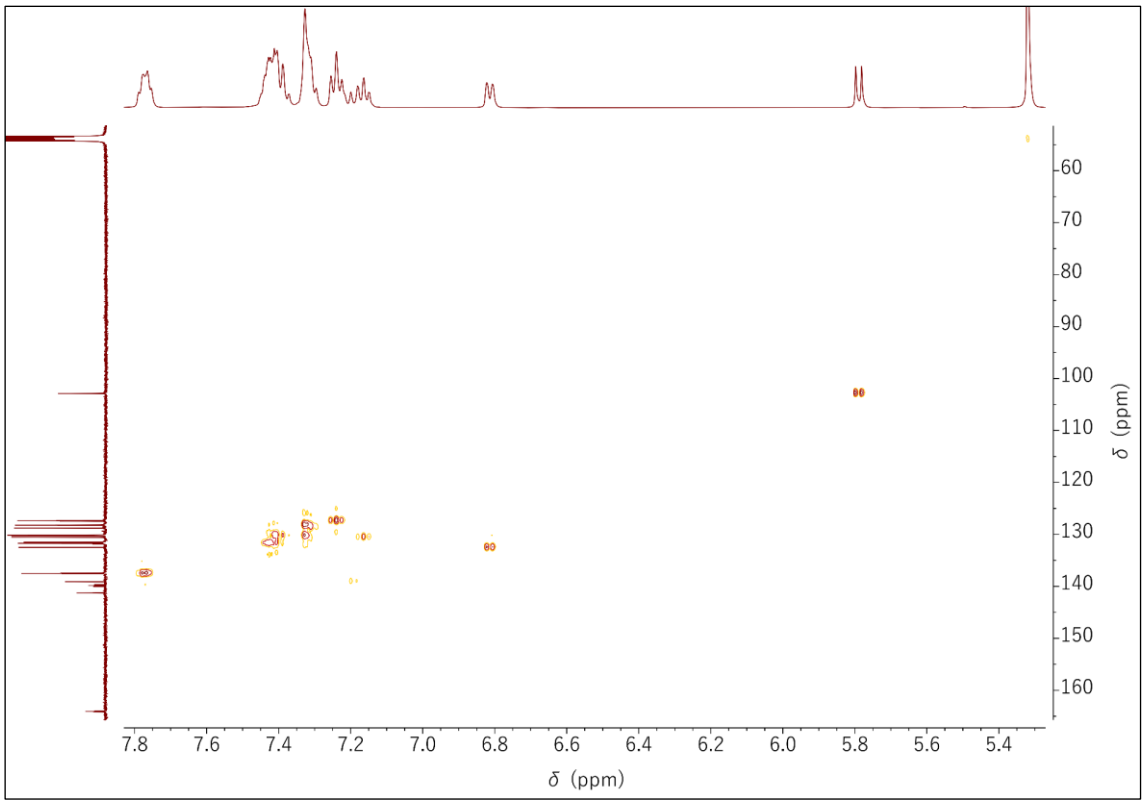

Figure A.9. $^{1}H,^{13}C$ HSQC NMR spectrum of $\mathbf{Mn}^{\mathbf{I}}_{\mathbf{CO,Br}}$ in CD_2Cl_2.

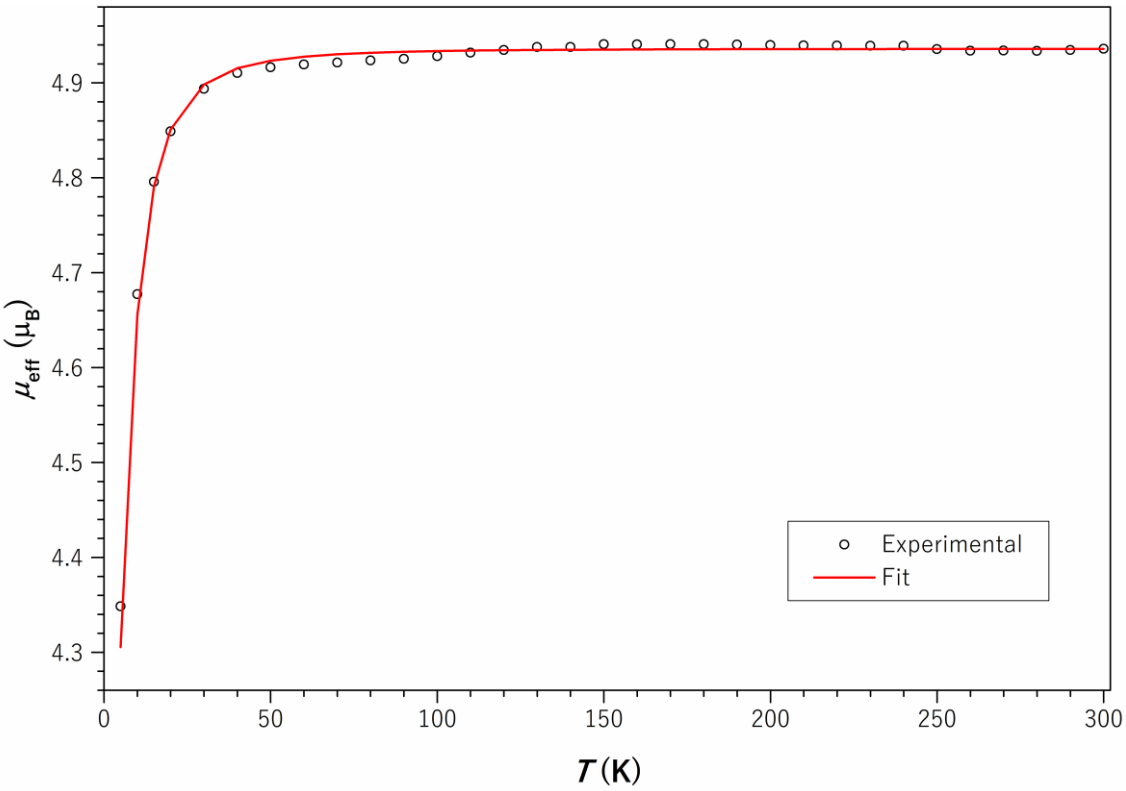

Figure A.10. Effective magnetic moment of a solid powder sample of $\mathbf{Fe}^{\mathbf{II}}_{\mathbf{Cl}}$. μ_{eff} vs. T recorded with a field of B = 1 T. The data were corrected for a diamagnetic contribution of $X_{dia} = -375 \cdot 10^{-6}$ emu. Solid line: spin HAMILTONIAN simulation with S = 2, D = 4.27 cm^{-1}, $g_{average}$ = 2.021.

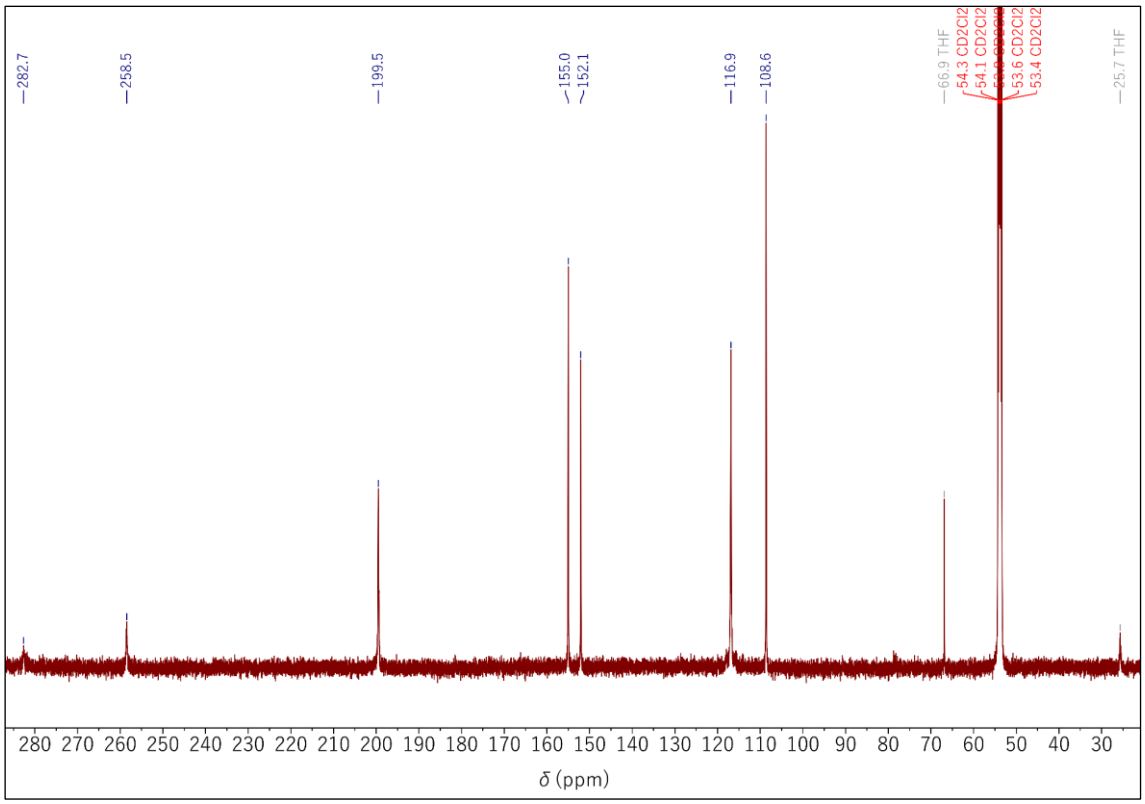

Figure A.11. $^{13}C\{^{1}H\}$ NMR spectrum of $\mathbf{Fe}^{\mathbf{II}}_{\mathbf{Cl}}$ in CD_2Cl_2 at 126 MHz and 296 K.

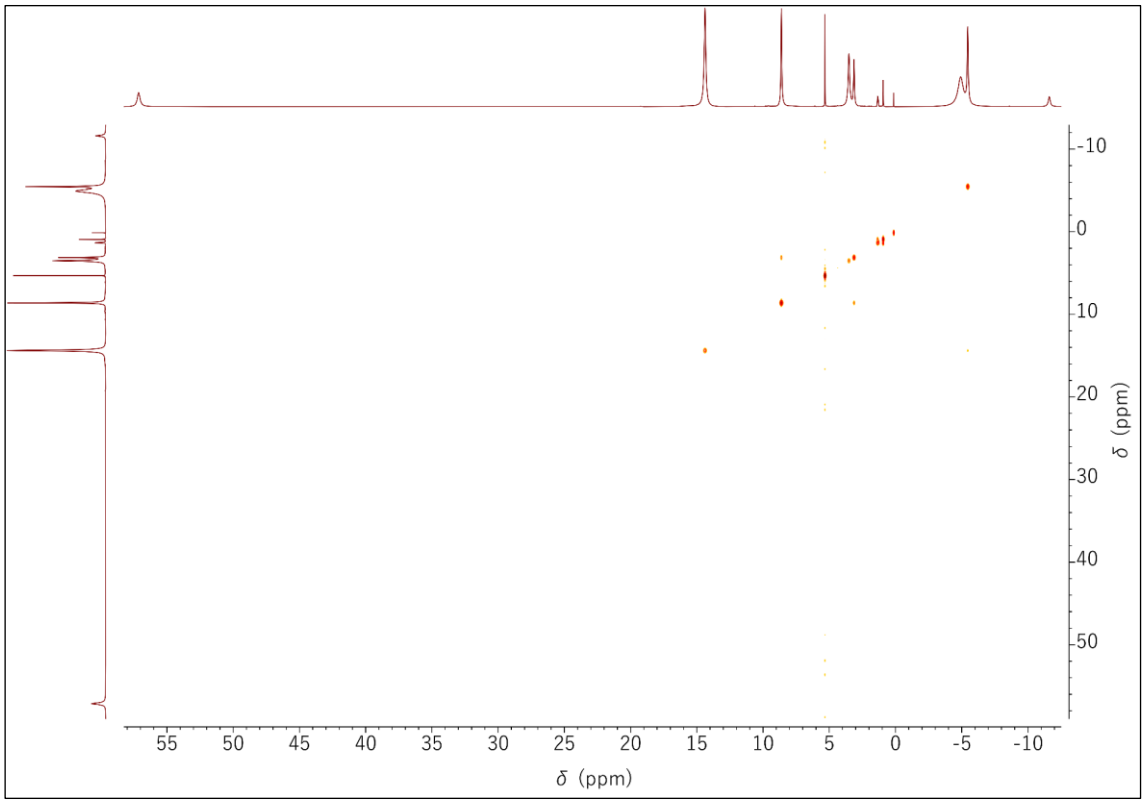

Figure A.12. $^{1}H,^{1}H$ COSY NMR spectrum of $\mathbf{Fe}^{\mathbf{II}}_{\mathbf{Cl}}$ in CD_2Cl_2 at 500 MHz and 296 K.

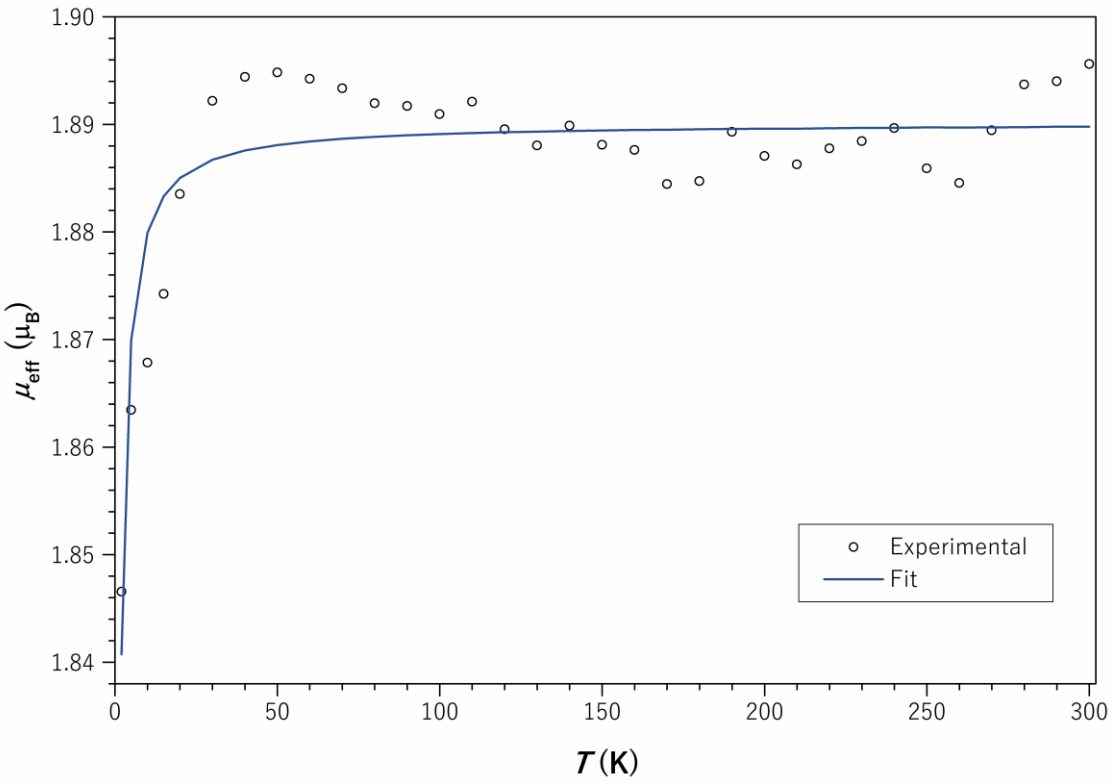

Figure A.13. Effective magnetic moment of a solid powder sample of $\mathbf{Co}^{\mathbf{II}}_{\mathbf{Cl}}$. μ_{eff} vs. T recorded with a field of B = 1 T. The data were corrected for a diamagnetic contribution of $X_{dia} = -360 \cdot 10^{-6}$ emu. Solid line: spin HAMILTONIAN simulation with S = ½, $g_{average}$ = 2.183, intermolecular coupling (2zJ) = −4.3 cm^{-1}.

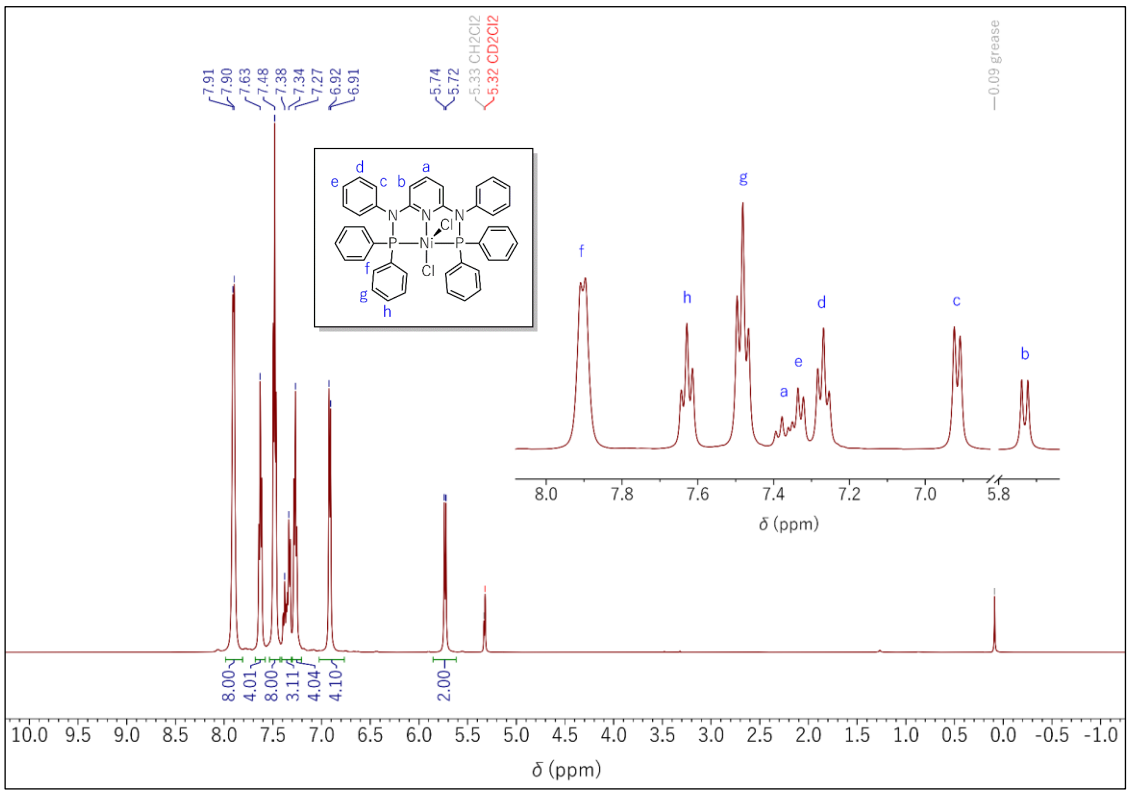

Figure A.14. ^{1}H NMR spectrum of $\mathbf{Ni}^{\mathbf{II}}_{\mathbf{Cl}}$ in CD_2Cl_2 at 500 MHz and 296 K (inset: aromatic region and peak assignments).

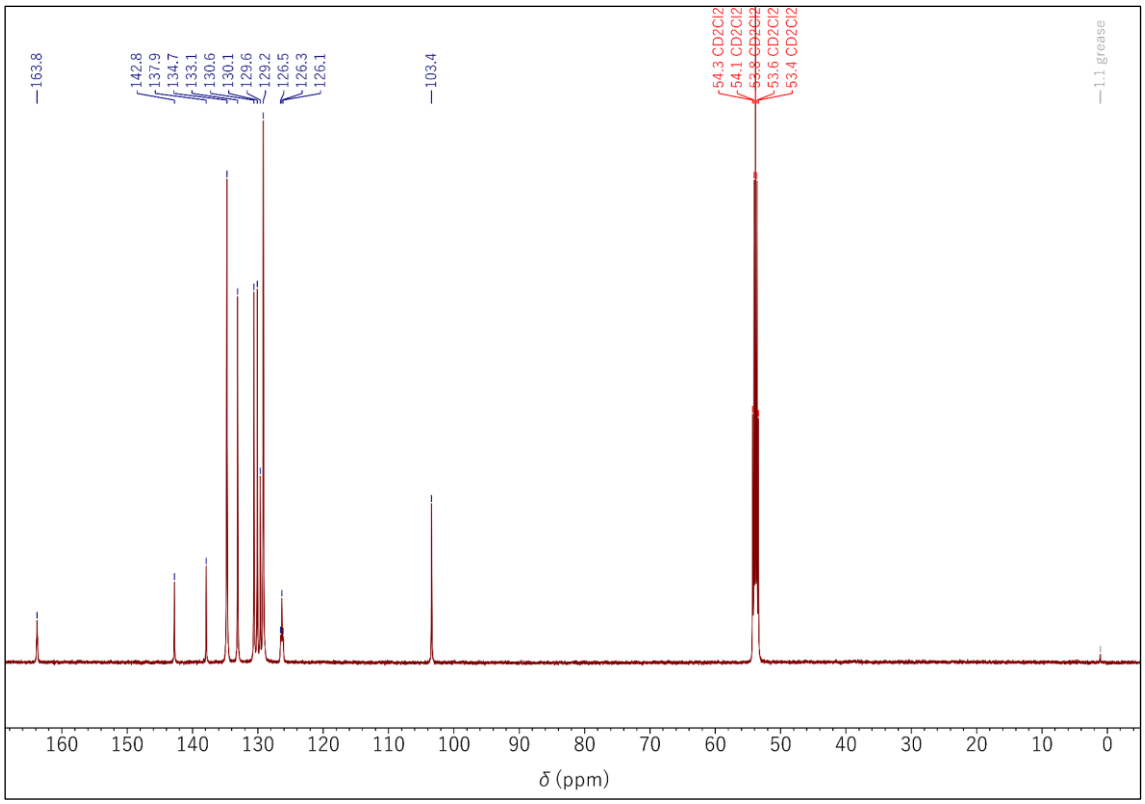

Figure A.15. $^{13}C\{^{1}H\}$ NMR spectrum of $\mathbf{Ni}^{\mathbf{II}}_{\mathbf{Cl}}$ in CD_2Cl_2 at 126 MHz and 296 K.

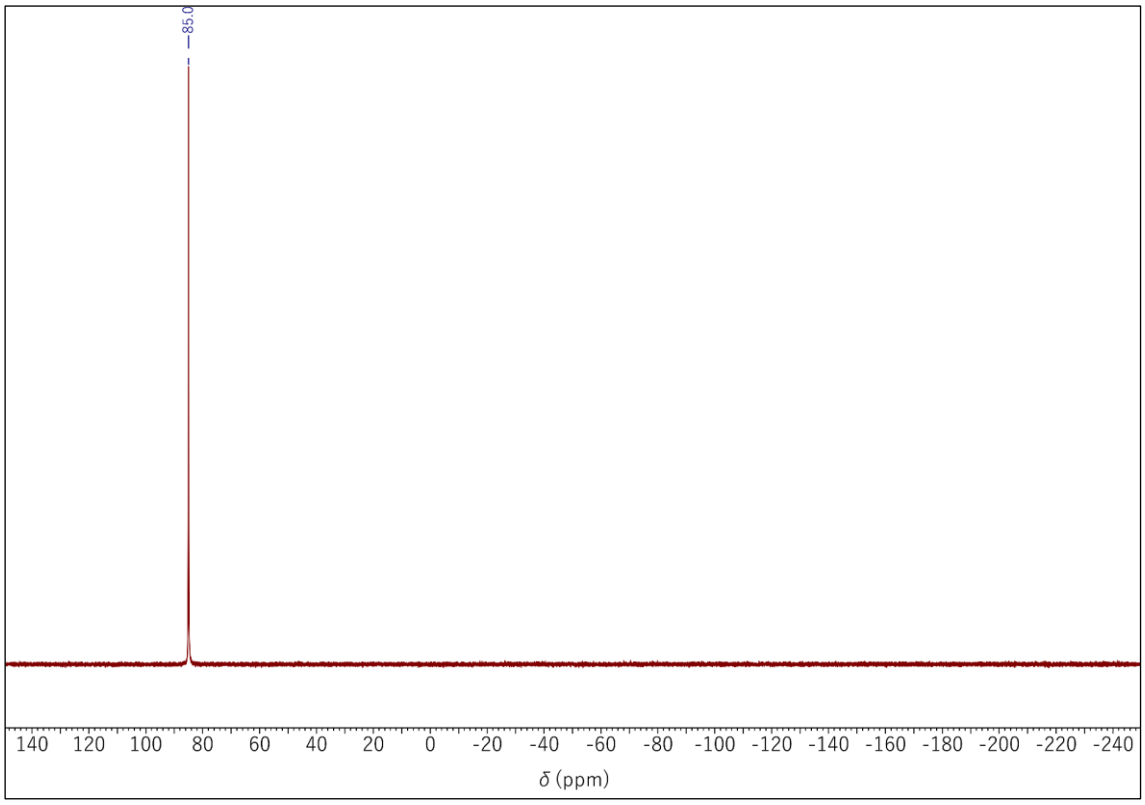

Figure A.16. $^{31}P\{^{1}H\}$ NMR spectrum of $\mathbf{Ni}^{\mathbf{II}}_{\mathbf{Cl}}$ in CD_2Cl_2 at 202 MHz and 296 K.

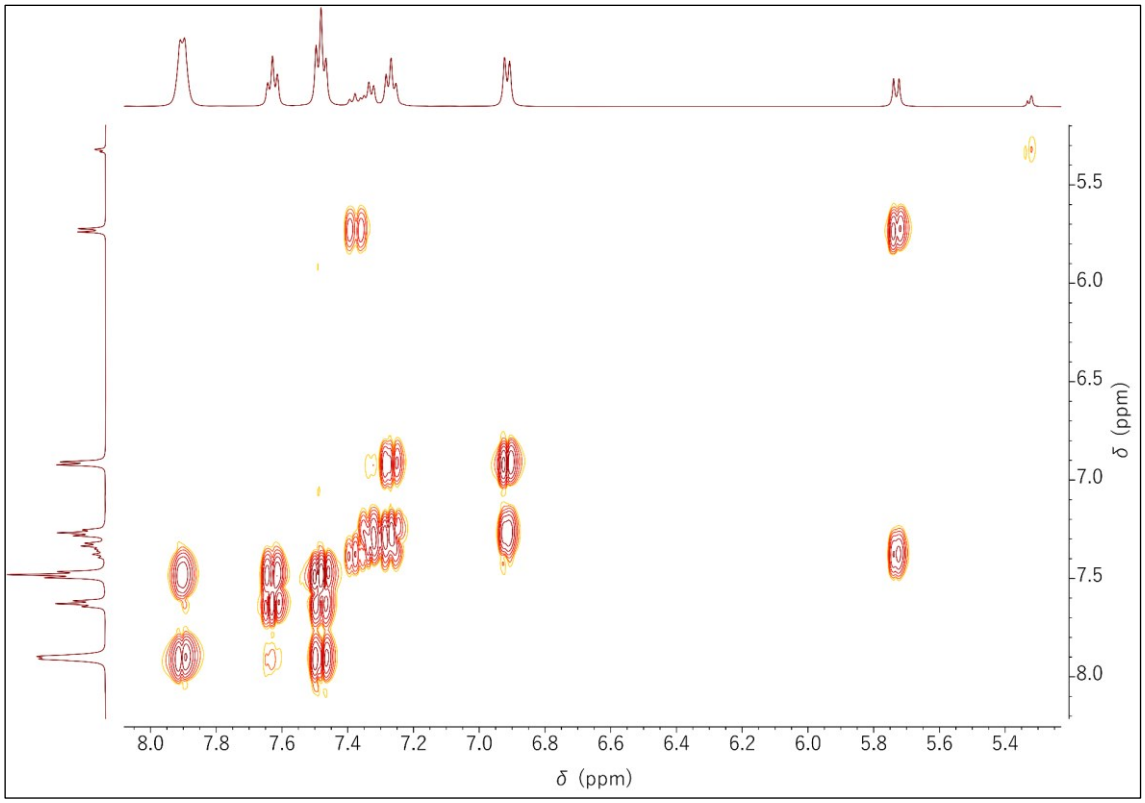

Figure A.17. $^{1}H,^{1}H$ COSY NMR spectrum of $\mathbf{Ni}^{II}_{Cl}$ in CD_2Cl_2 at 500 MHz and 296 K.

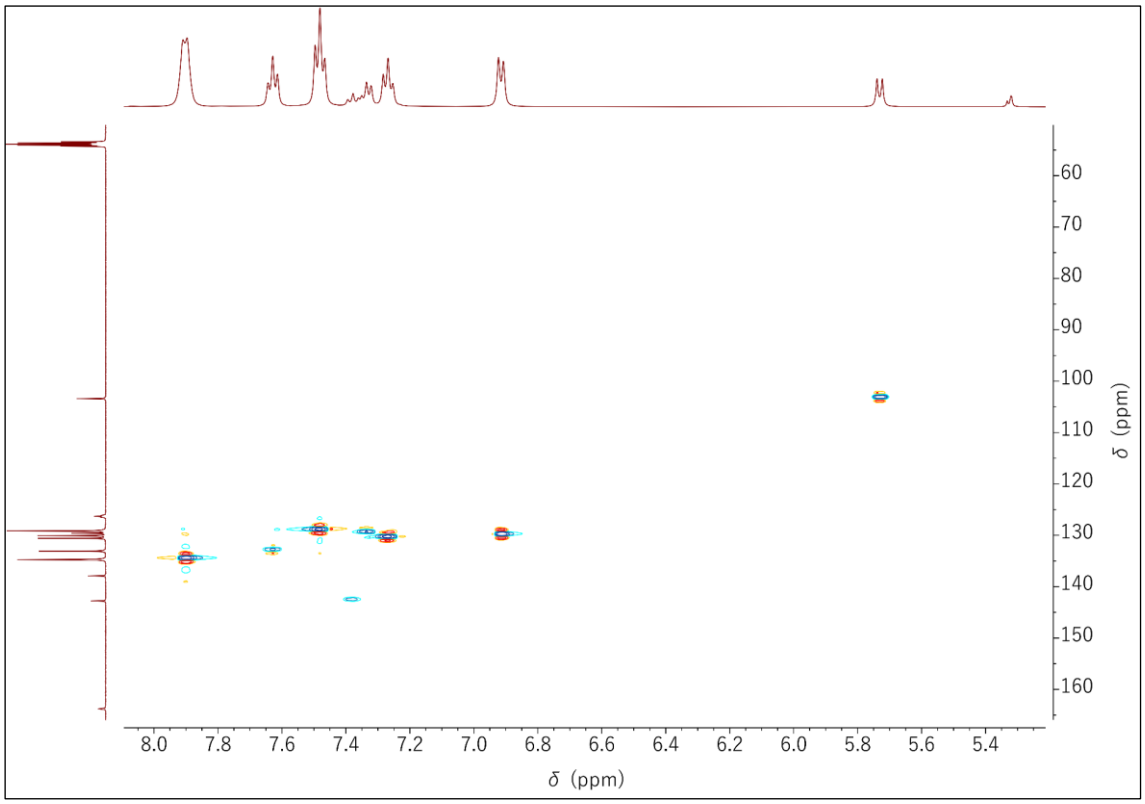

Figure A.18. $^{1}H,^{13}C$ HSQC NMR spectrum of $\mathbf{Ni}^{II}_{Cl}$ in CD_2Cl_2.

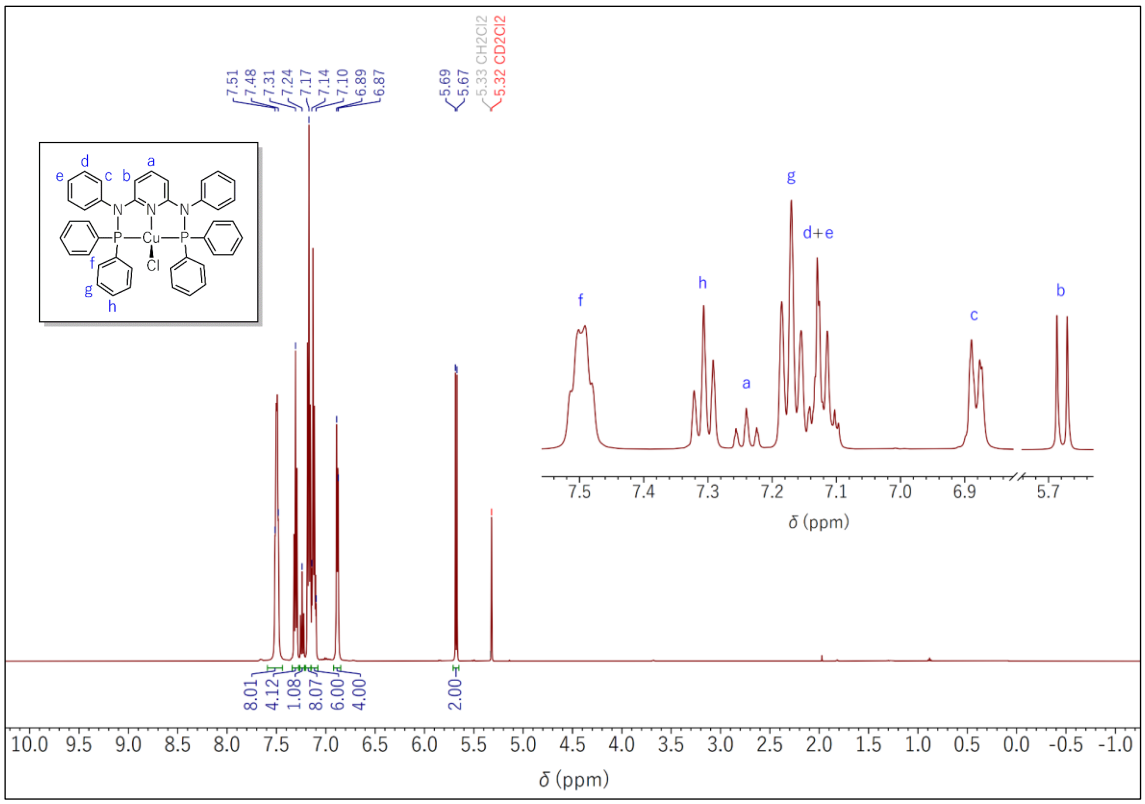

Figure A.19. ^{1}H NMR spectrum of $\mathbf{Cu^{I}_{Cl}}$ in CD_2Cl_2 at 500 MHz and 296 K (inset: aromatic region and peak assignments).

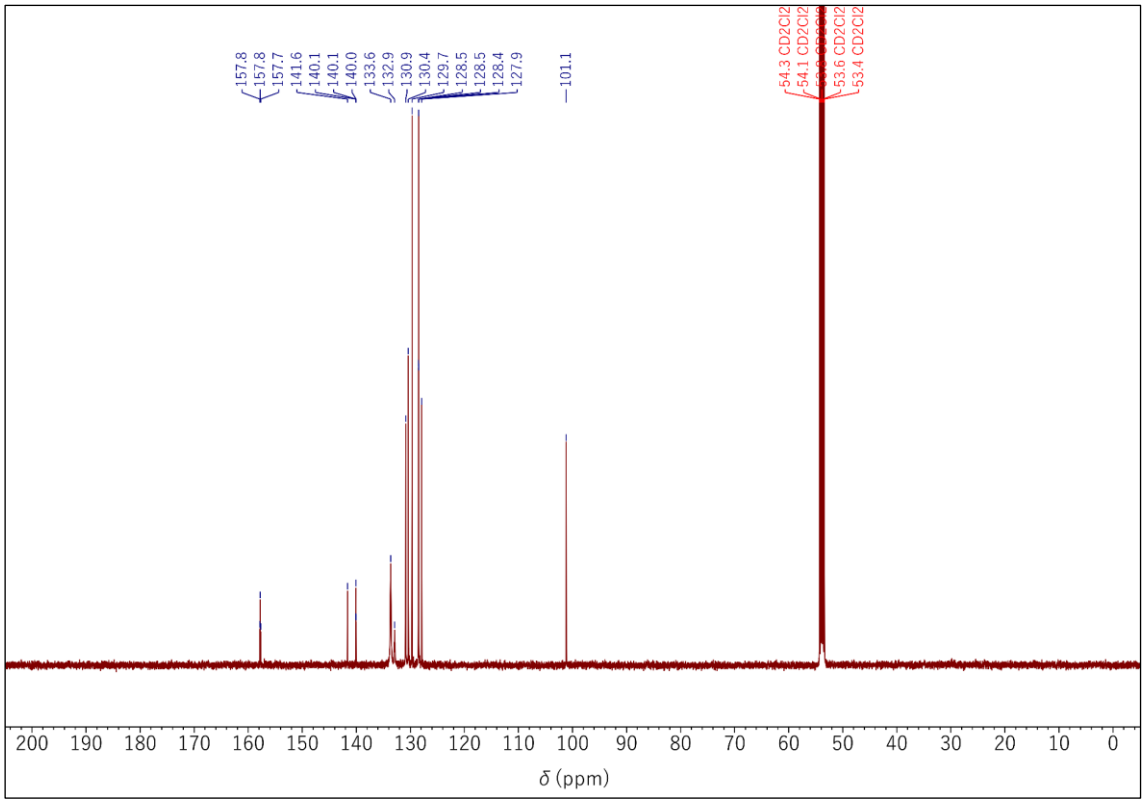

Figure A.20. ^{13}C{^{1}H} NMR spectrum of $\mathbf{Cu^{I}_{Cl}}$ in CD_2Cl_2 at 126 MHz and 296 K.

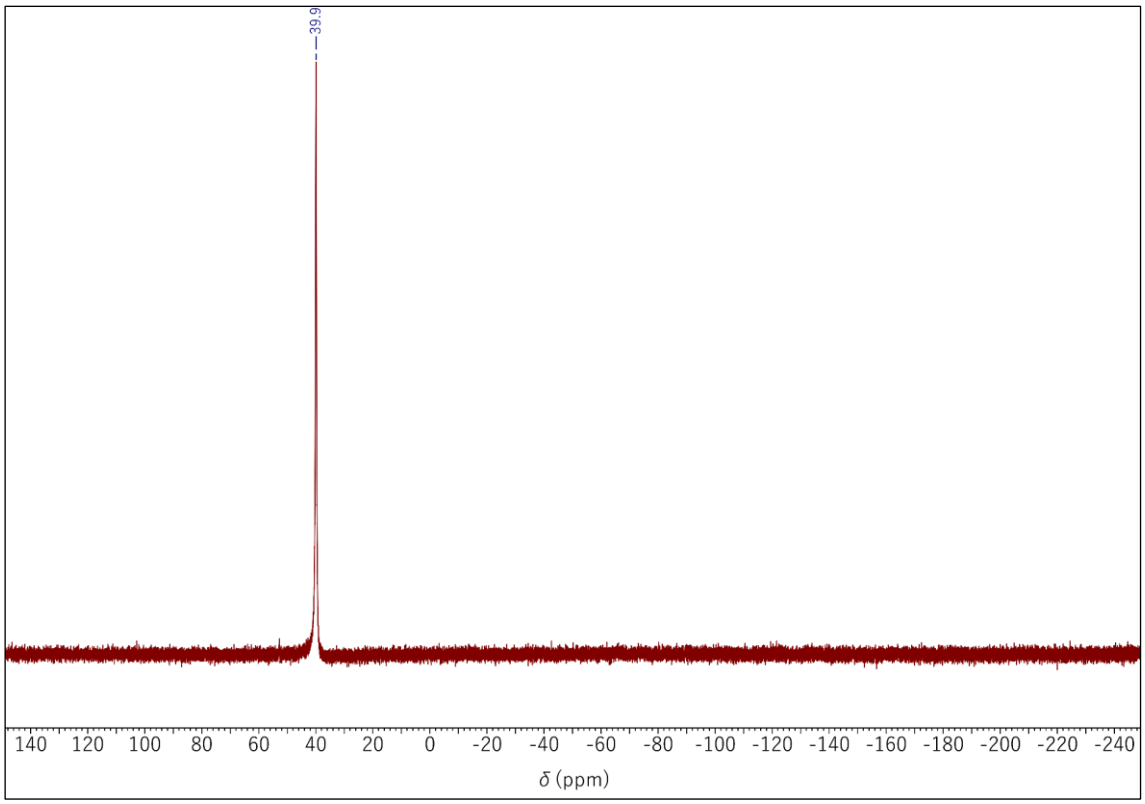

Figure A.21. $^{31}P\{^{1}H\}$ NMR spectrum of $\mathbf{Cu^{I}_{Cl}}$ in CD_2Cl_2 at 202 MHz and 296 K.

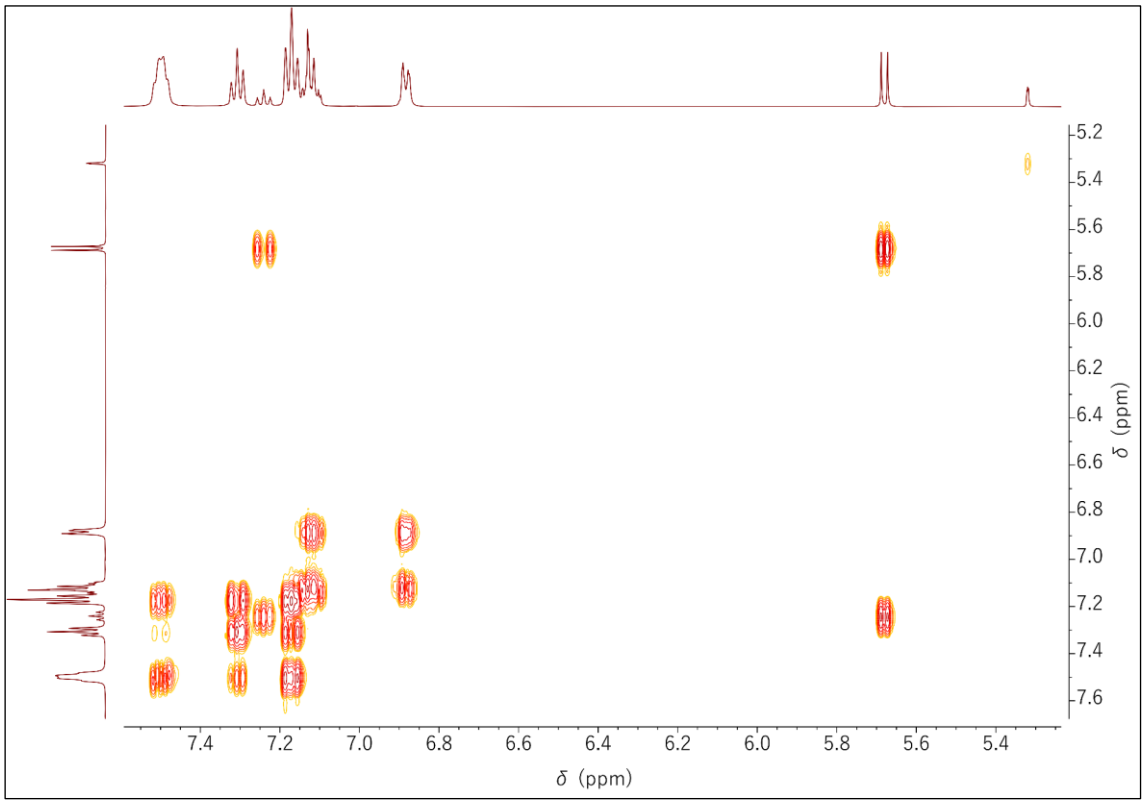

Figure A.22. $^{1}H,^{1}H$ COSY NMR spectrum of $\mathbf{Cu^{I}_{Cl}}$ in CD_2Cl_2 at 500 MHz and 296 K.

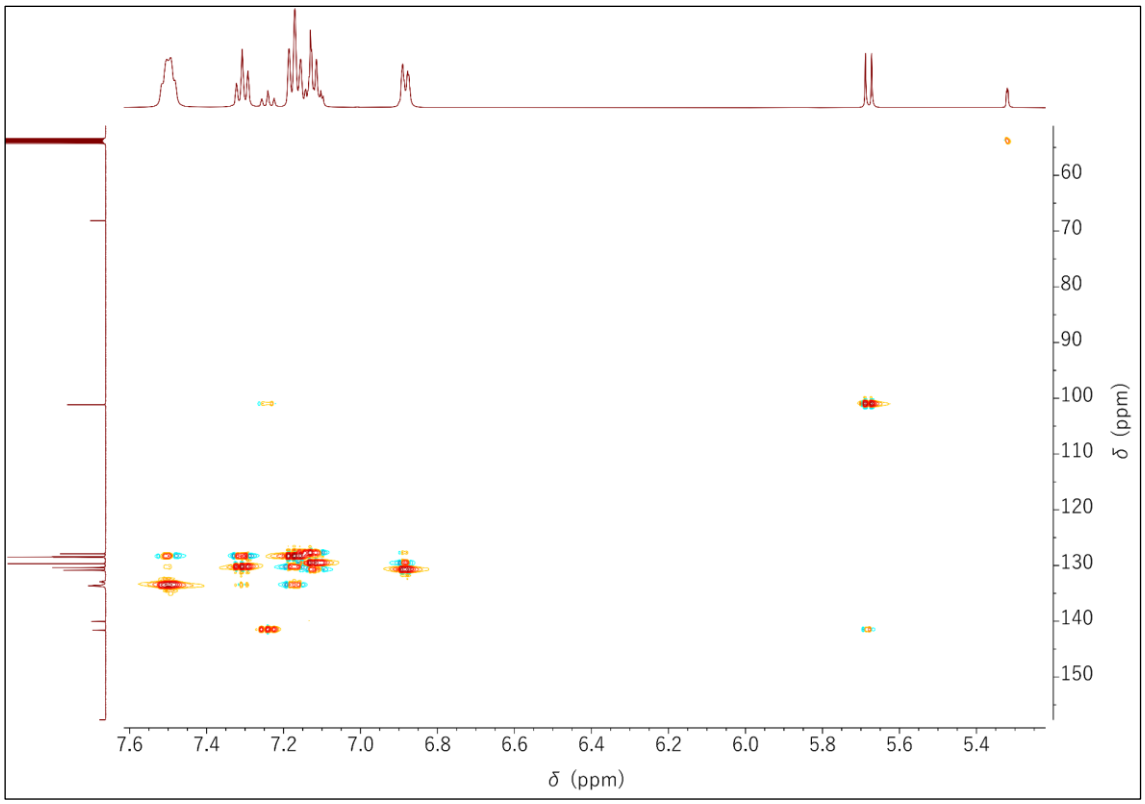

Figure A.23. $^{1}H,^{13}C$ HSQC NMR spectrum of $\mathbf{Cu}^{\mathbf{I}}_{\mathbf{Cl}}$ in CD_2Cl_2.

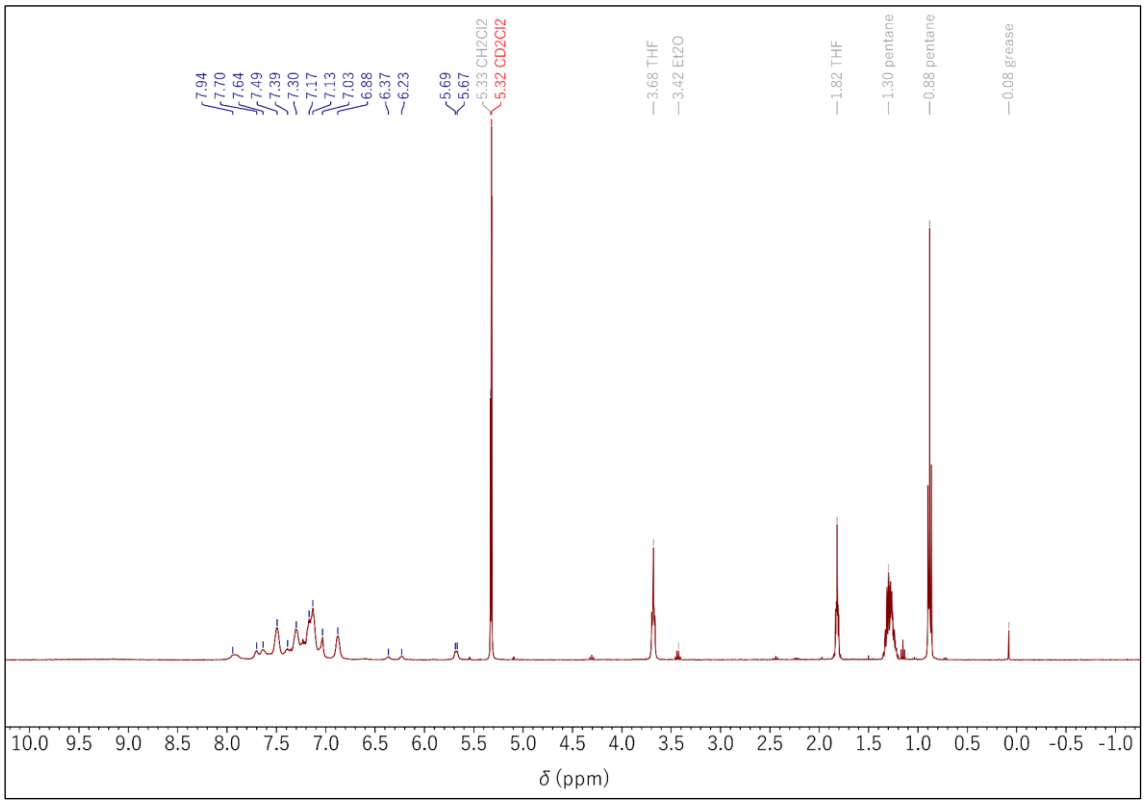

Figure A.24. ^{1}H NMR spectrum of the reaction products of $CuCl_2$ and **L** in CD_2Cl_2 at 400 MHz and 296 K.

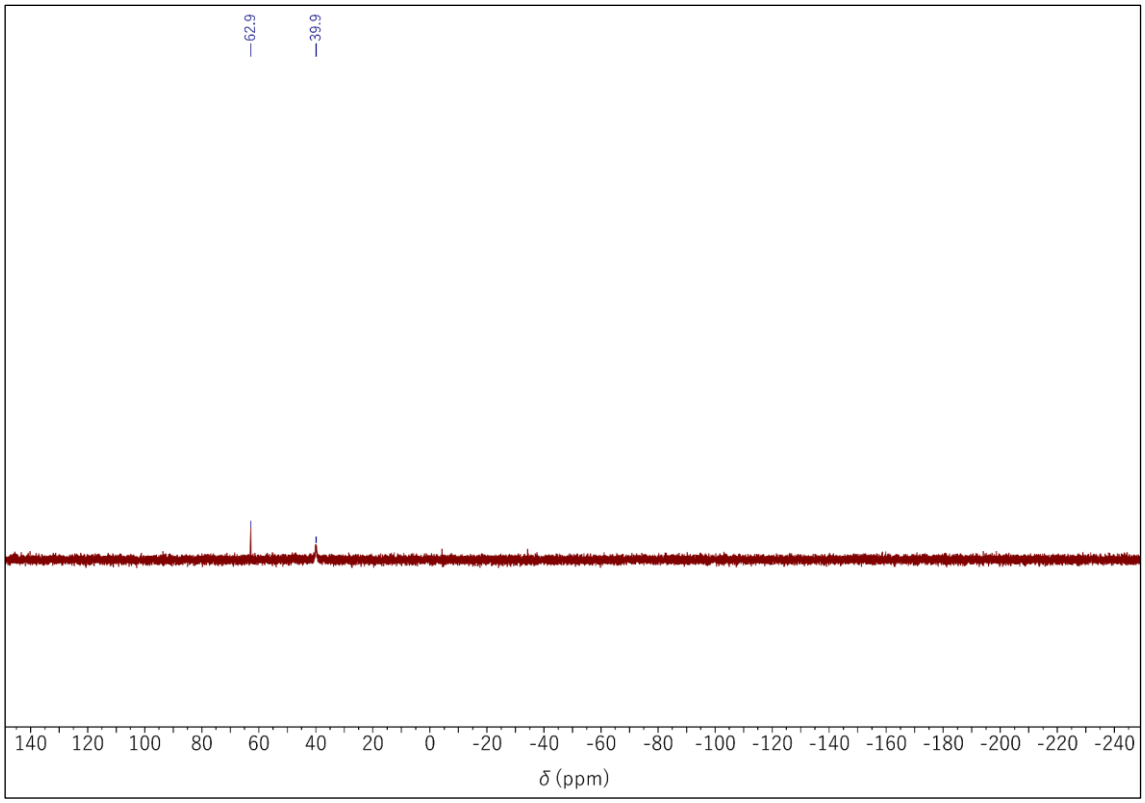

Figure A.25. $^{31}P\{^{1}H\}$ NMR spectrum of the reaction products of $CuCl_2$ and **L** in CD_2Cl_2 at 162 MHz and 296 K.

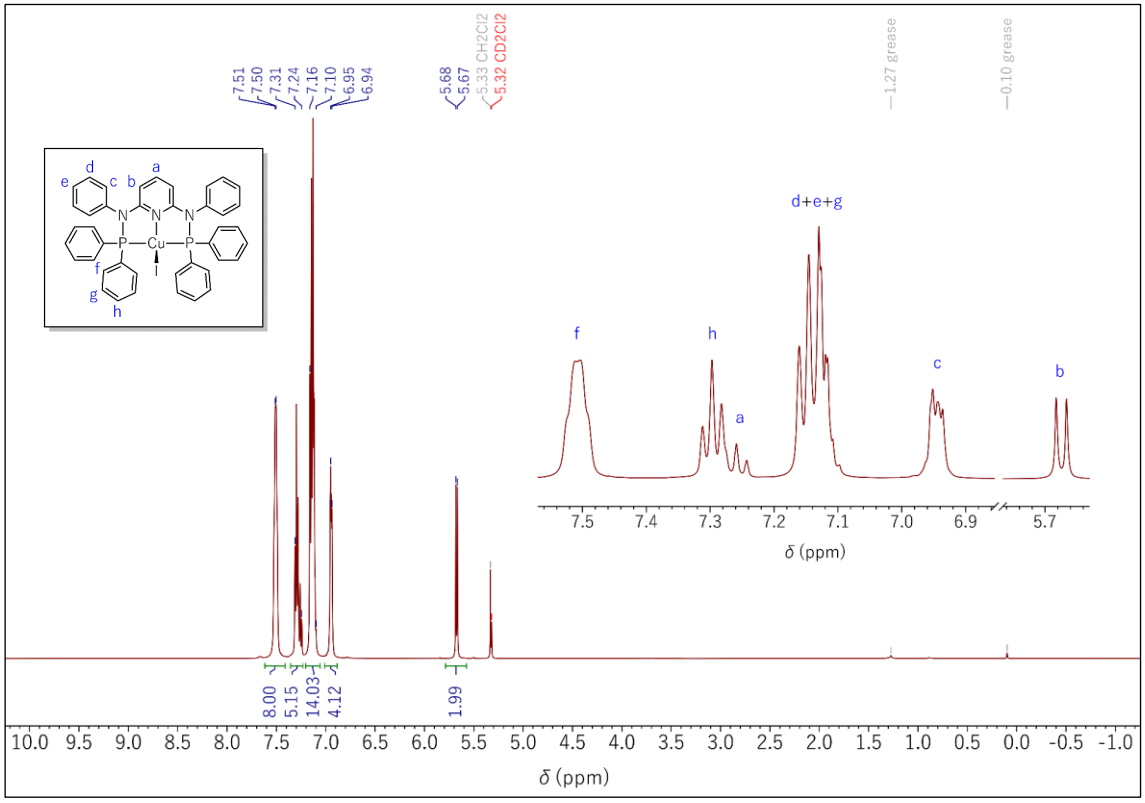

Figure A.26. ^{1}H NMR spectrum of $\mathbf{Cu_I^I}$ in CD_2Cl_2 at 500 MHz and 296 K (inset: aromatic region and peak assignments).

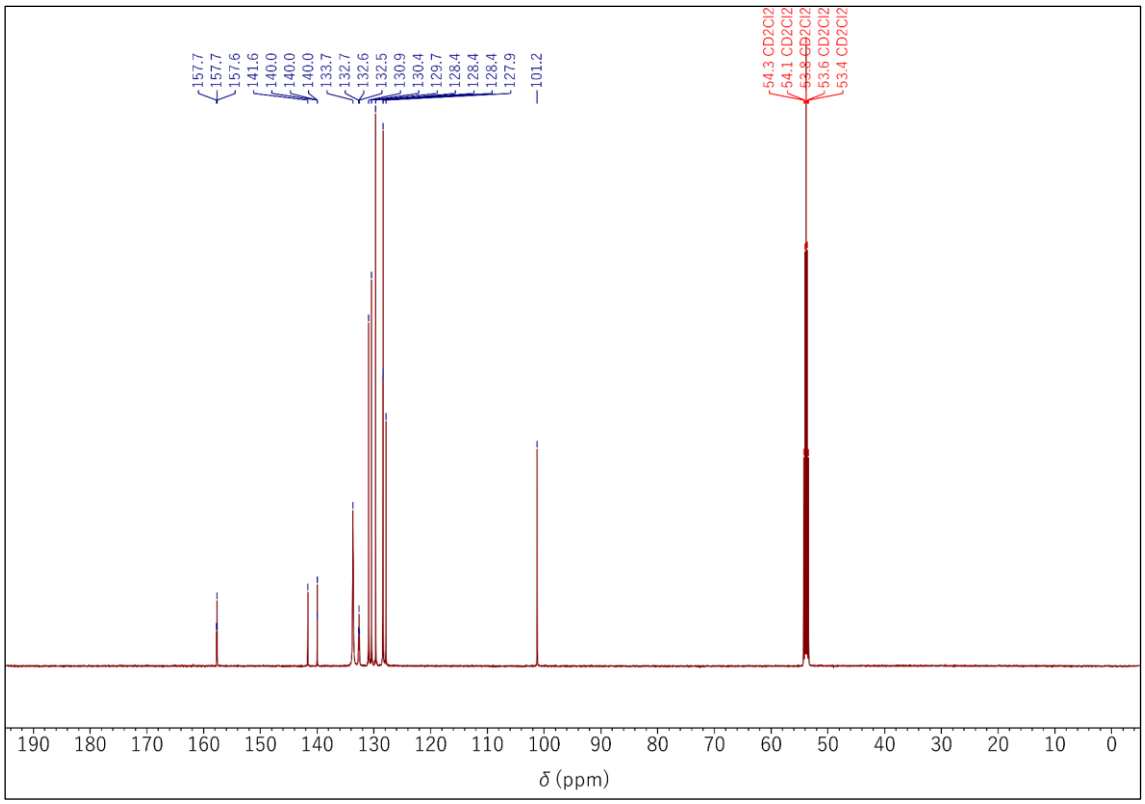

Figure A.27. $^{13}C\{^{1}H\}$ NMR spectrum of $\mathbf{Cu_I^I}$ in CD_2Cl_2 at 126 MHz and 296 K.

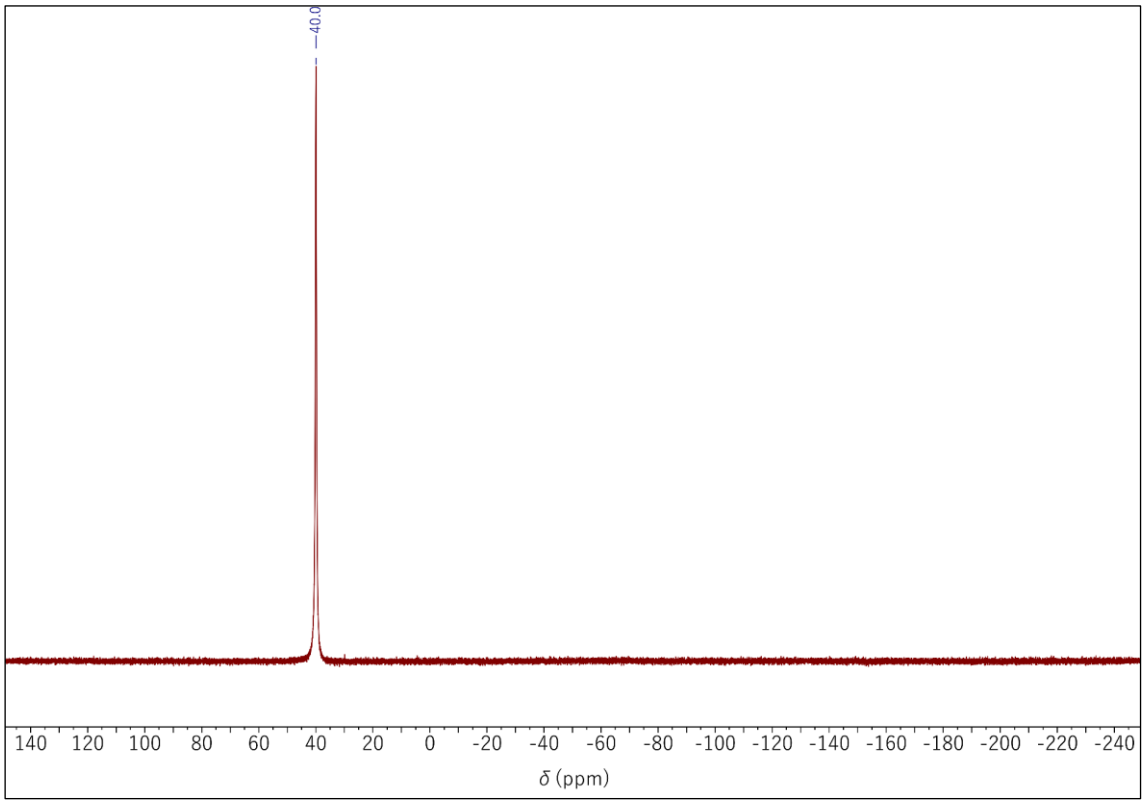

Figure A.28. $^{31}P\{^{1}H\}$ NMR spectrum of $\mathbf{Cu_I^I}$ in CD_2Cl_2 at 202 MHz and 296 K.

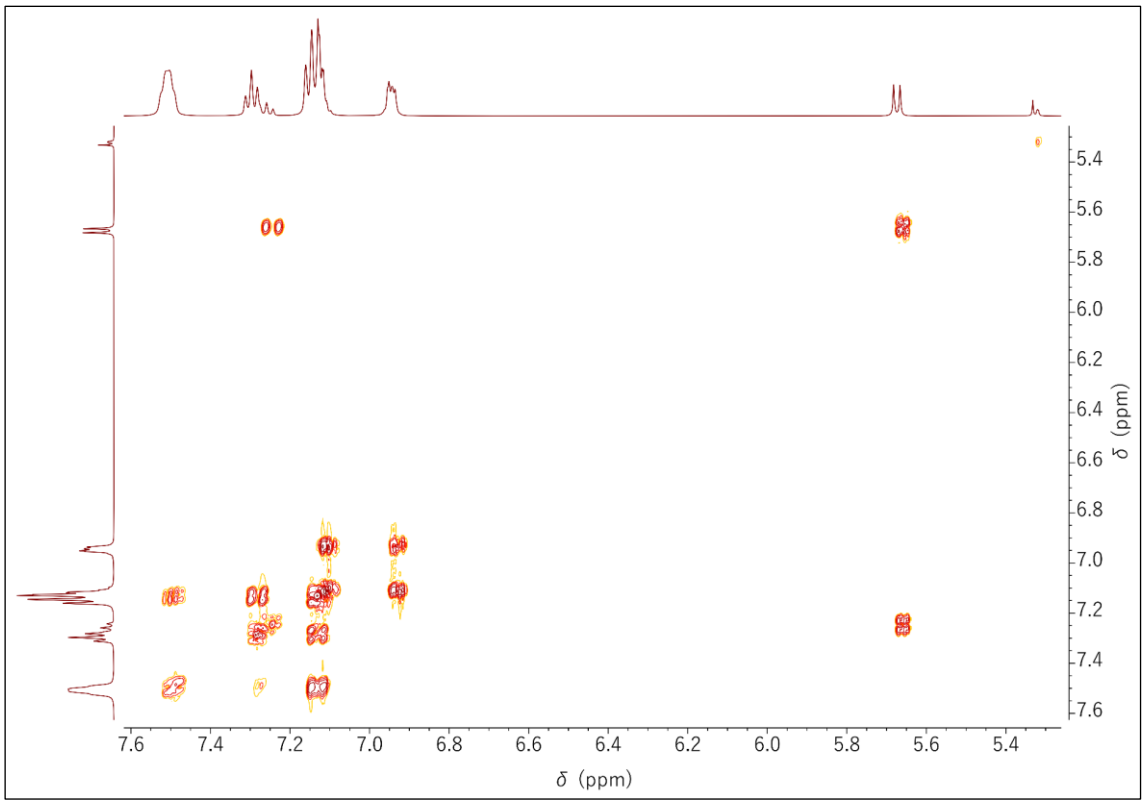

Figure A.29. $^{1}H,^{1}H$ COSY NMR spectrum of $\mathbf{Cu_I^I}$ in CD_2Cl_2 at 500 MHz and 296 K.

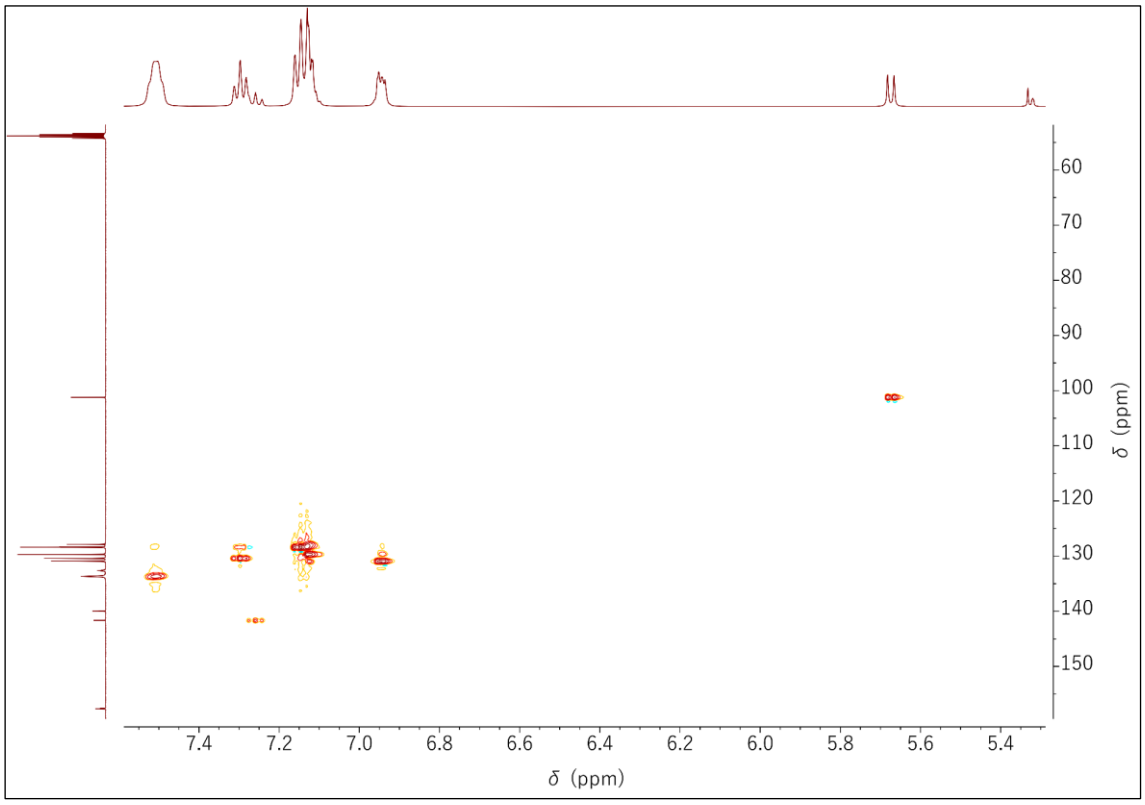

Figure A.30. $^{1}H,^{13}C$ HSQC NMR spectrum of $\mathbf{Cu_I^I}$ in CD_2Cl_2.

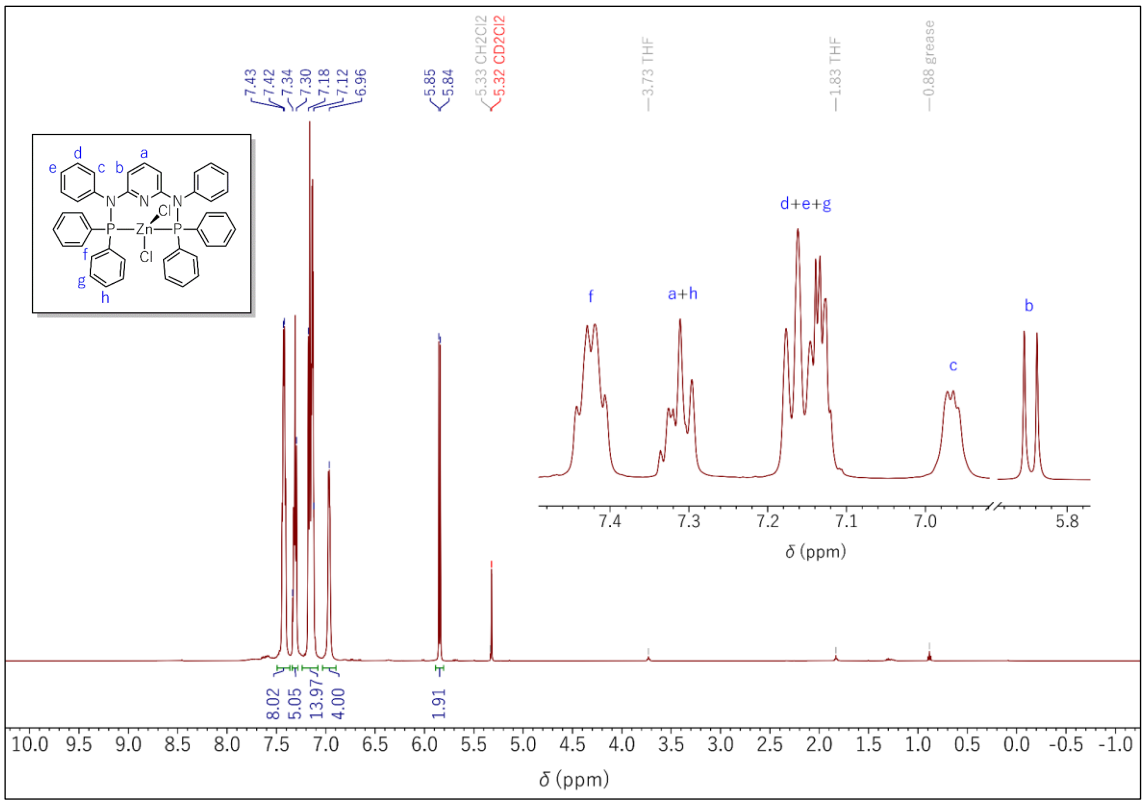

Figure A.31. ^{1}H NMR spectrum of $\mathbf{Zn}^{\mathbf{II}}_{\mathbf{Cl}}$ in CD_2Cl_2 at 500 MHz and 296 K (inset: aromatic region and peak assignments).

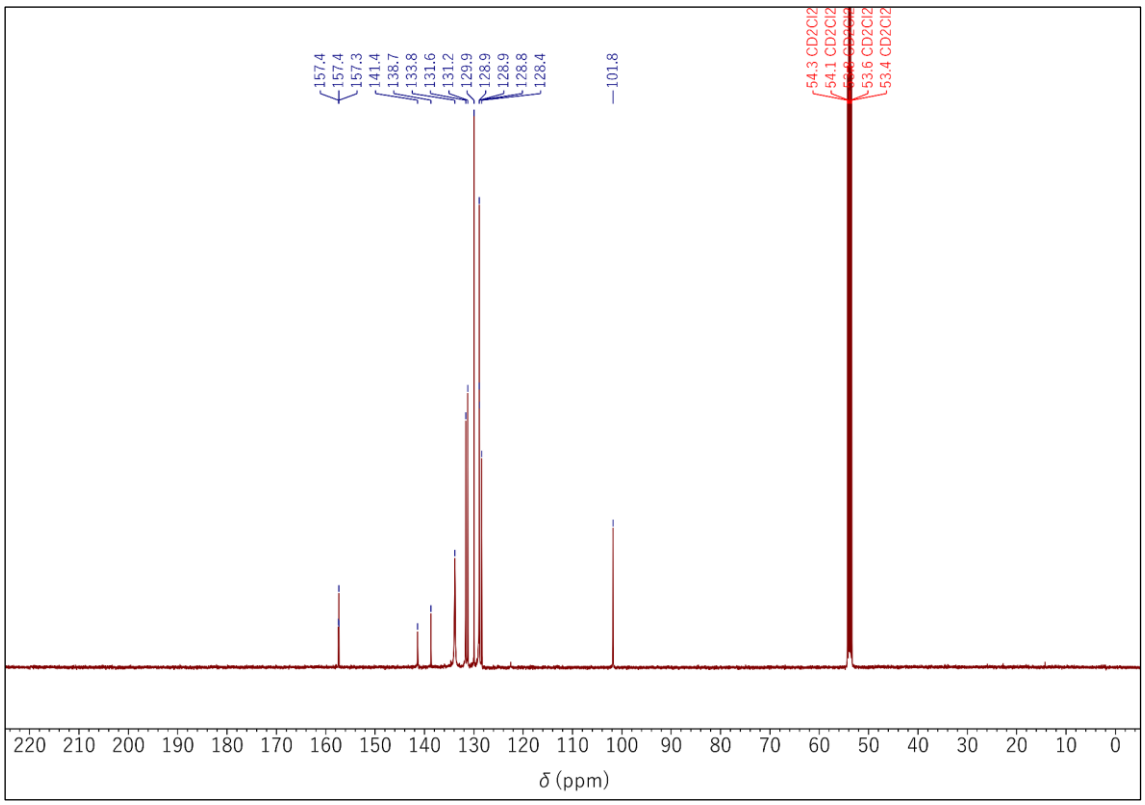

Figure A.32. ^{13}C{^{1}H} NMR spectrum of $\mathbf{Zn}^{\mathbf{II}}_{\mathbf{Cl}}$ in CD_2Cl_2 at 126 MHz and 296 K.

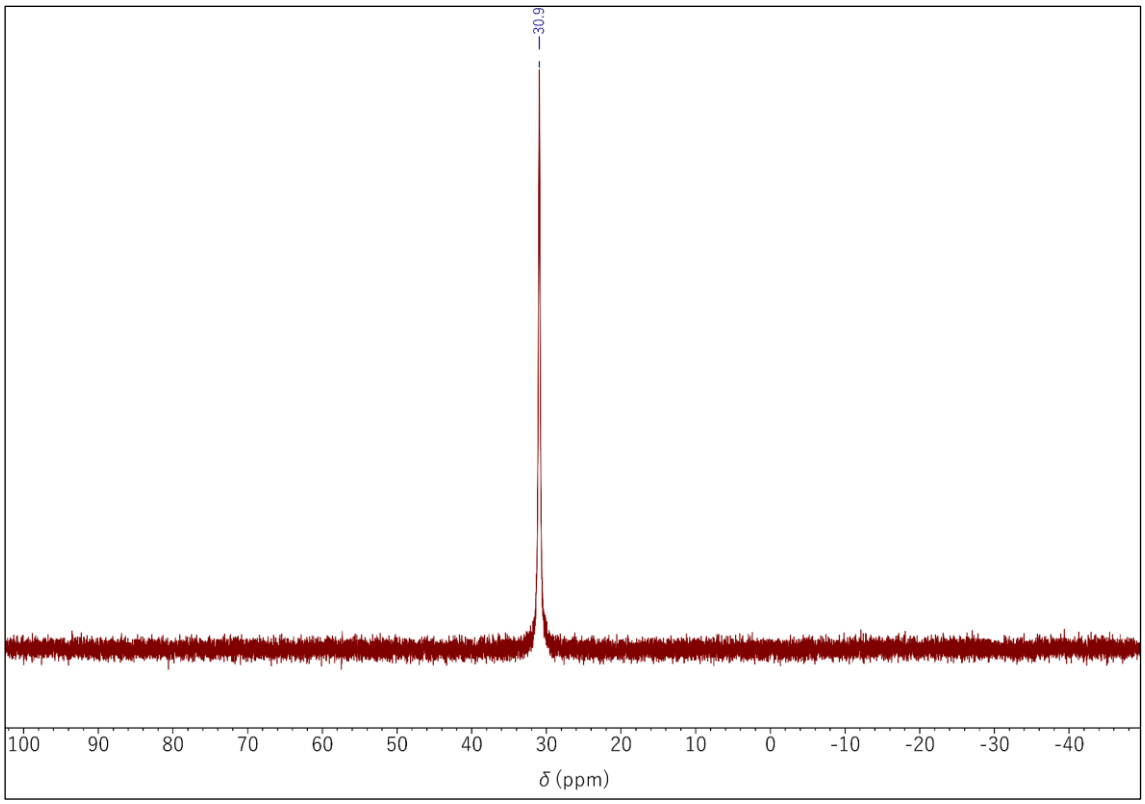

Figure A.33. $^{31}P\{^{1}H\}$ NMR spectrum of $\mathbf{Zn}^{\mathbf{II}}_{\mathbf{Cl}}$ in CD_2Cl_2 at 202 MHz and 296 K.

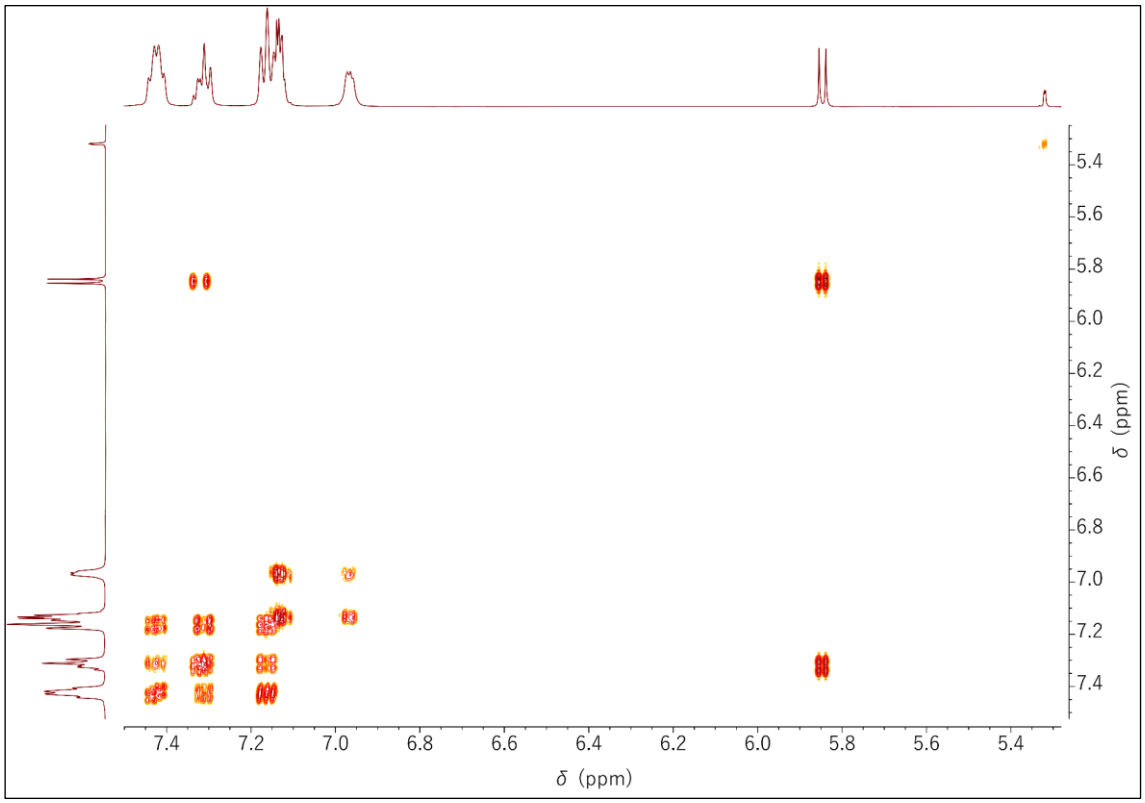

Figure A.34. $^{1}H,^{1}H$ COSY NMR spectrum of $\mathbf{Zn}^{\mathbf{II}}_{\mathbf{Cl}}$ in CD_2Cl_2 at 500 MHz and 296 K.

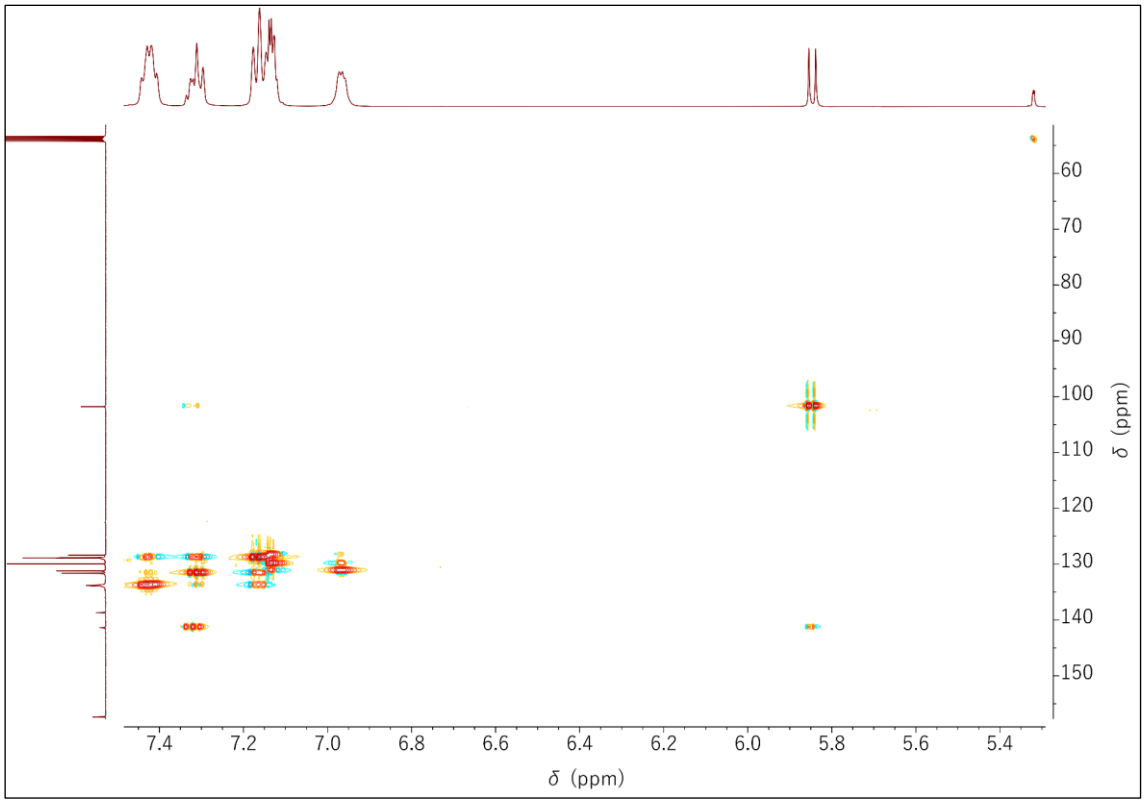

Figure A.35. $^{1}H,^{13}C$ HSQC NMR spectrum of $\mathbf{Zn}^{\mathbf{II}}_{\mathbf{Cl}}$ in CD_2Cl_2.

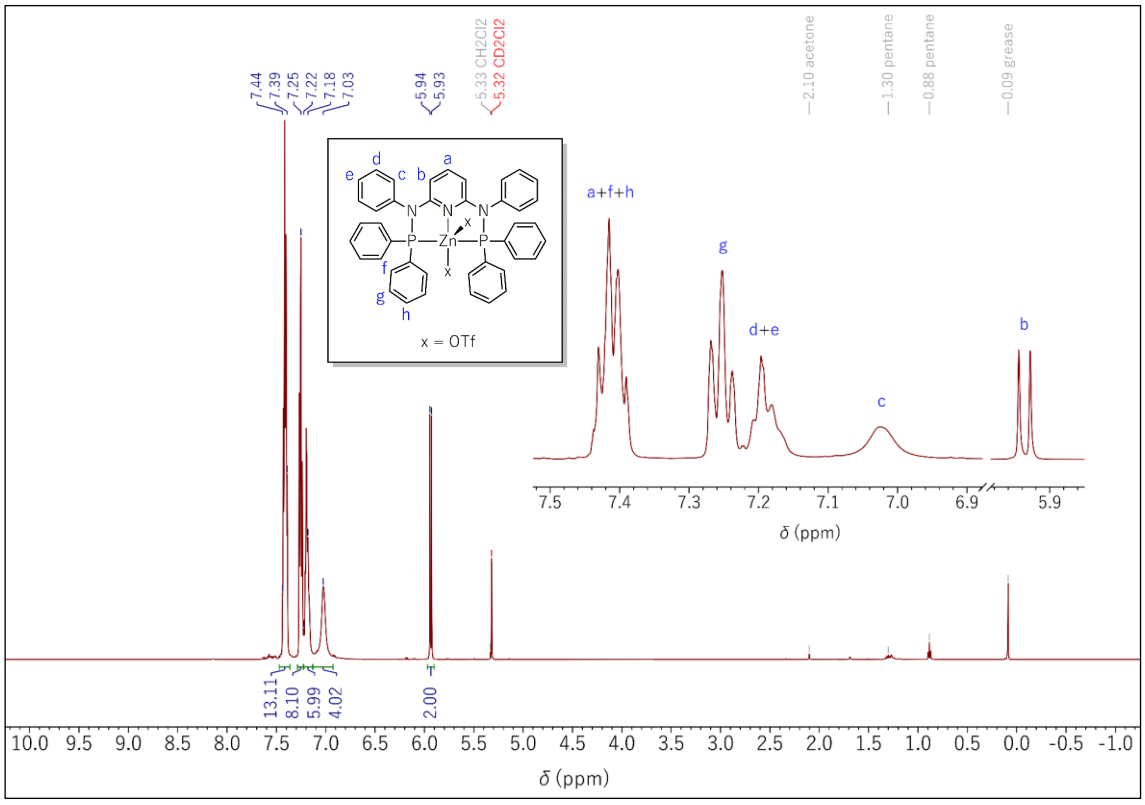

Figure A.36. ^{1}H NMR spectrum of $\mathbf{Zn}^{\mathbf{II}}_{\mathbf{OTf}}$ in CD_2Cl_2 at 500 MHz and 296 K (inset: aromatic region and peak assignments).

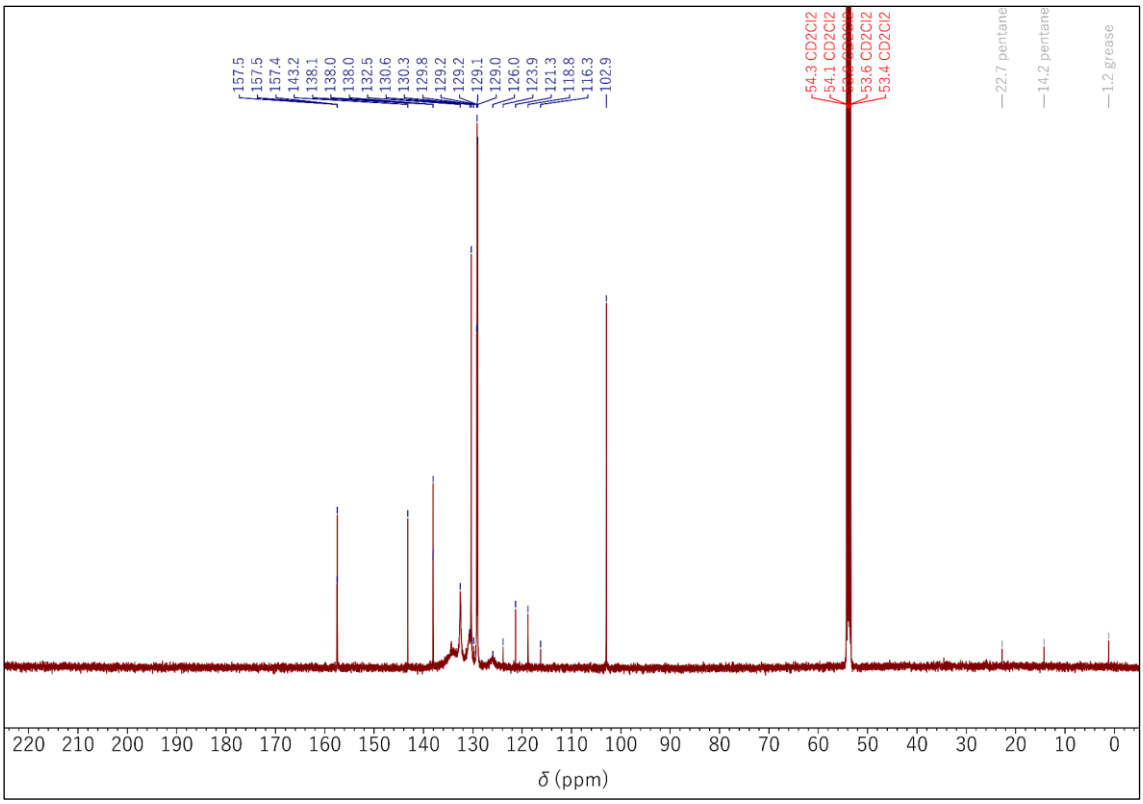

Figure A.37. $^{13}C\{^{1}H\}$ NMR spectrum of $\mathbf{Zn}^{\mathbf{II}}_{\mathbf{OTf}}$ in CD_2Cl_2 at 126 MHz and 296 K.

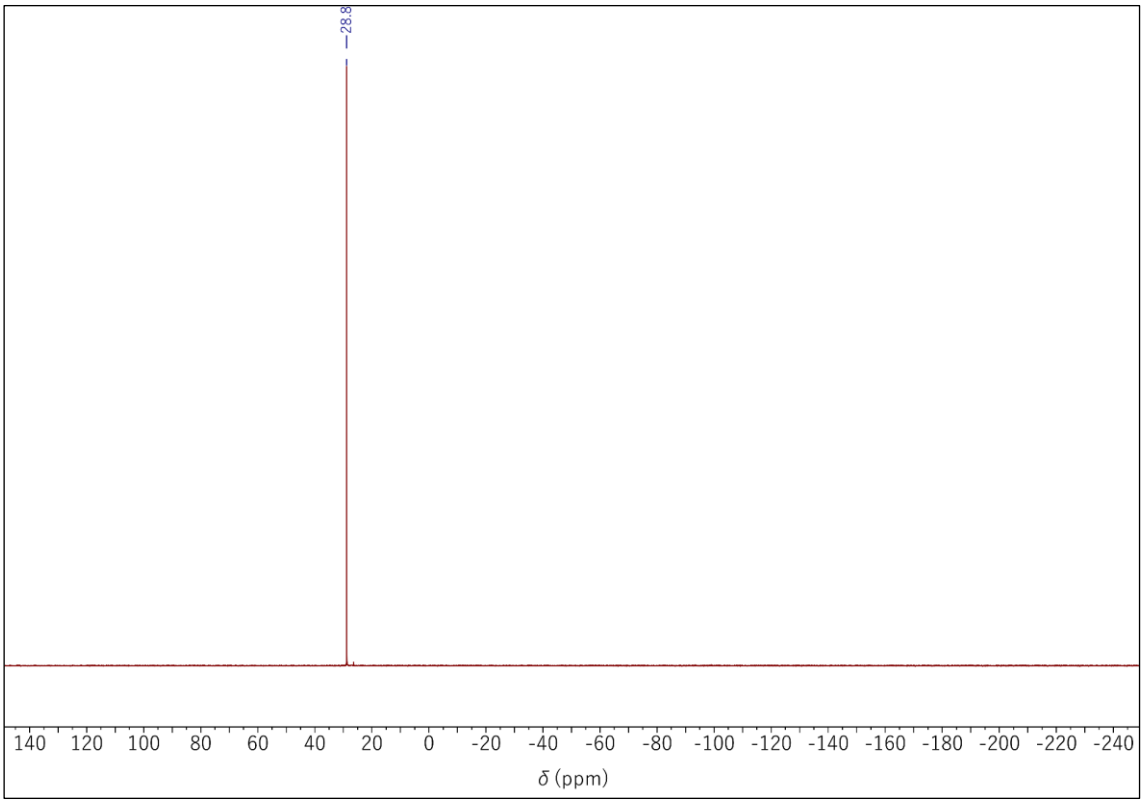

Figure A.38. $^{31}P\{^{1}H\}$ NMR spectrum of $\mathbf{Zn}^{\mathbf{II}}_{\mathbf{OTf}}$ in CD_2Cl_2 at 202 MHz and 296 K.

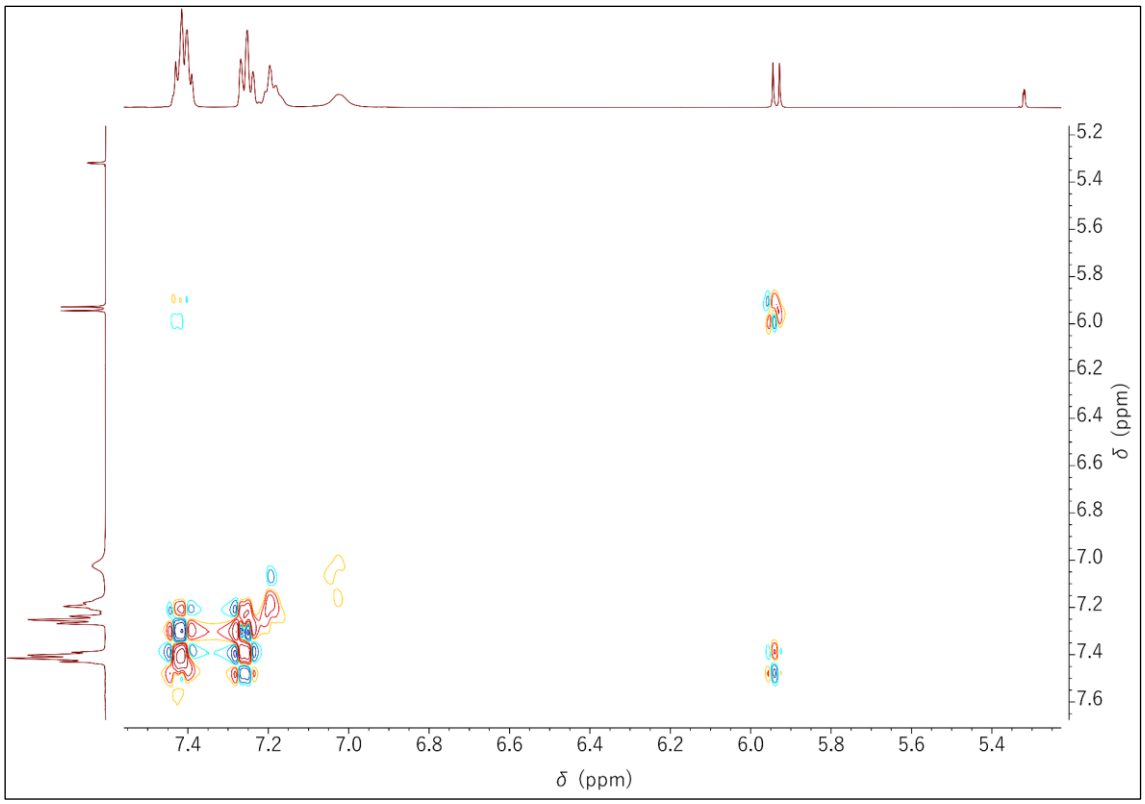

Figure A.39. $^{1}H,^{1}H$ COSY NMR spectrum of $\mathbf{Zn}^{\mathbf{II}}_{\mathbf{OTf}}$ in CD_2Cl_2 at 500 MHz and 296 K.

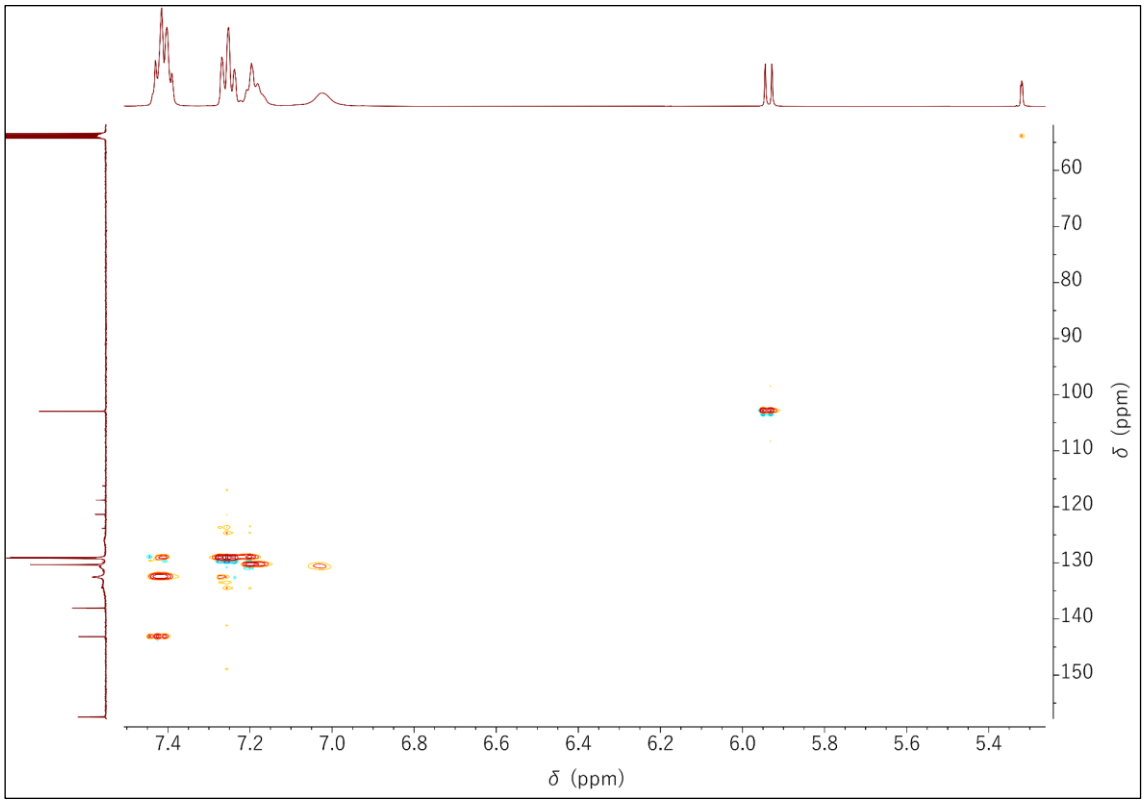

Figure A.40. $^{1}H,^{13}C$ HSQC NMR spectrum of $\mathbf{Zn}^{\mathbf{II}}_{\mathbf{OTf}}$ in CD_2Cl_2.

c) Acetonitrile Complexes

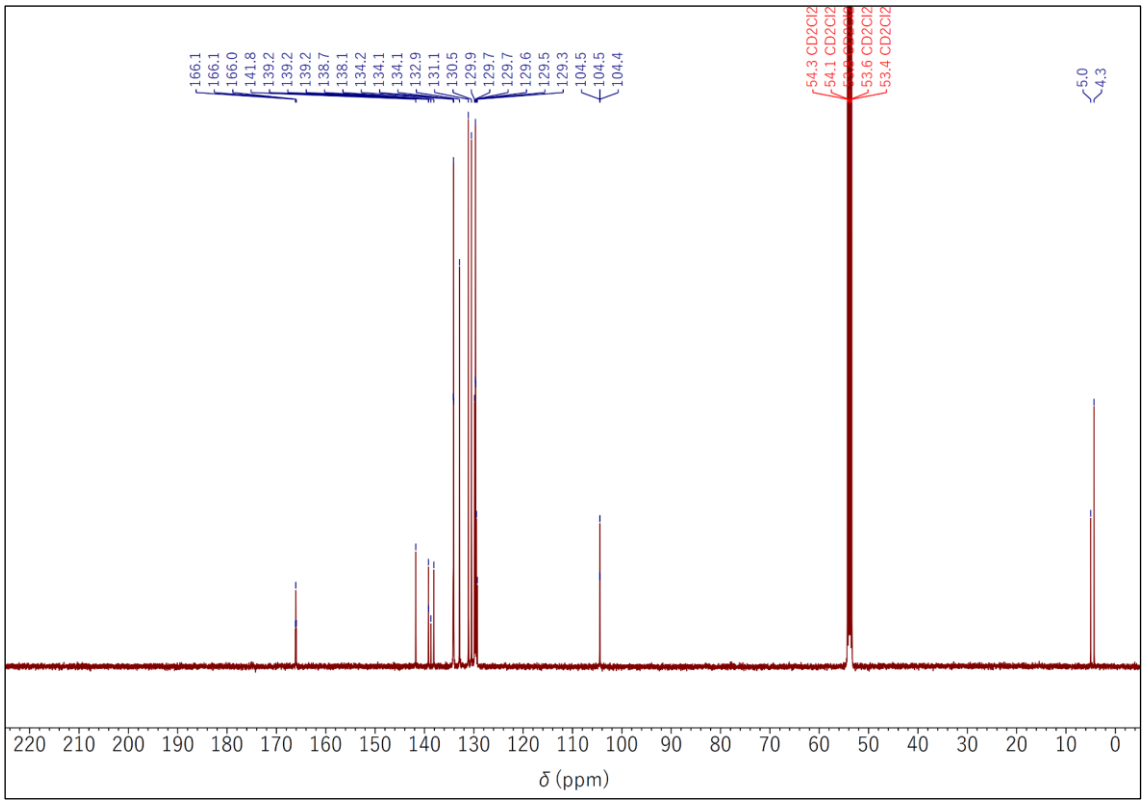

Figure A.41. $^{13}C\{^{1}H\}$ NMR spectrum of $\mathbf{Fe_s^{II}}$ in CD_2Cl_2 at 126 MHz and 296 K.

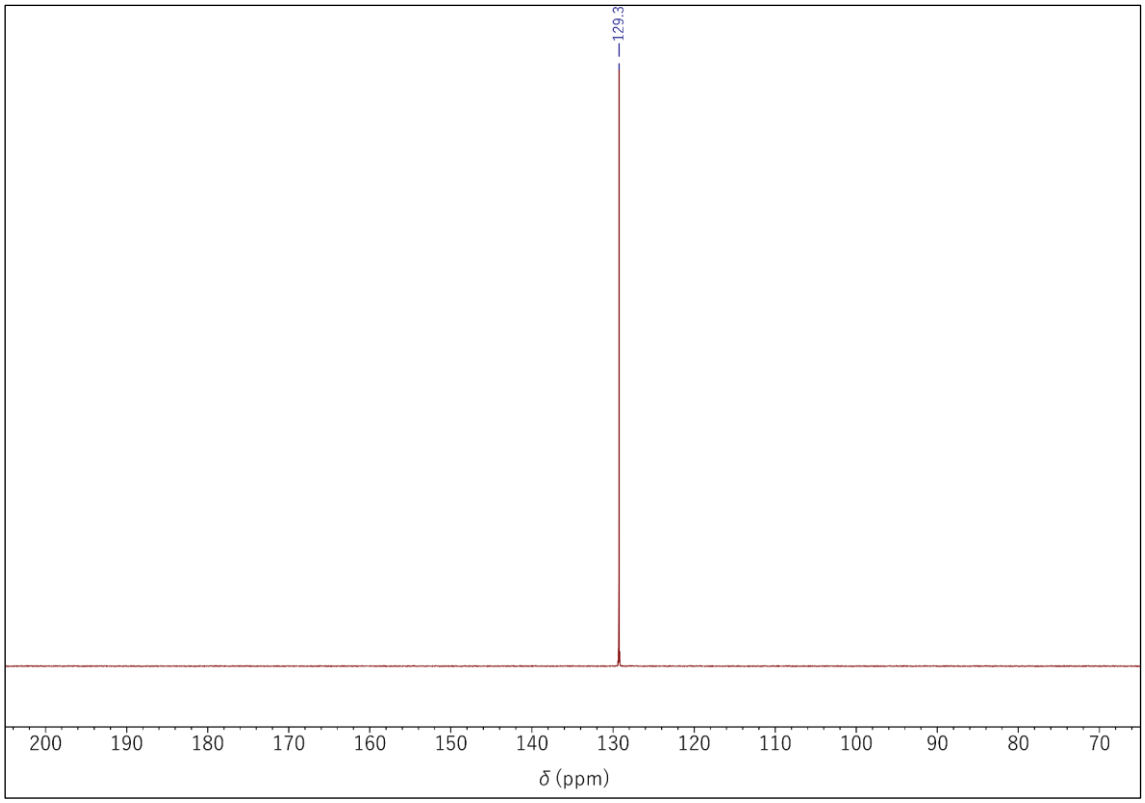

Figure A.42. $^{31}P\{^{1}H\}$ NMR spectrum of $\mathbf{Fe_s^{II}}$ in CD_2Cl_2 at 202 MHz and 296 K.

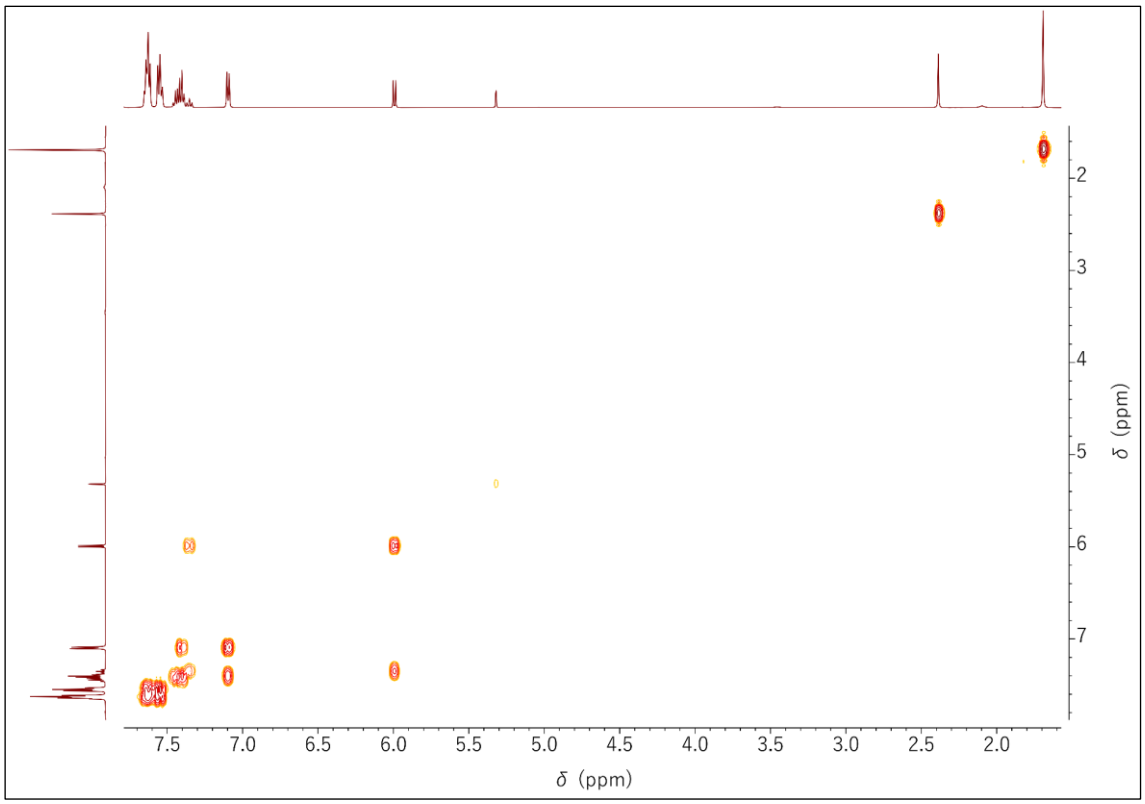

Figure A.43. $^{1}H,^{1}H$ COSY NMR spectrum of $\mathbf{Fe_s^{II}}$ in CD_2Cl_2 at 500 MHz and 296 K.

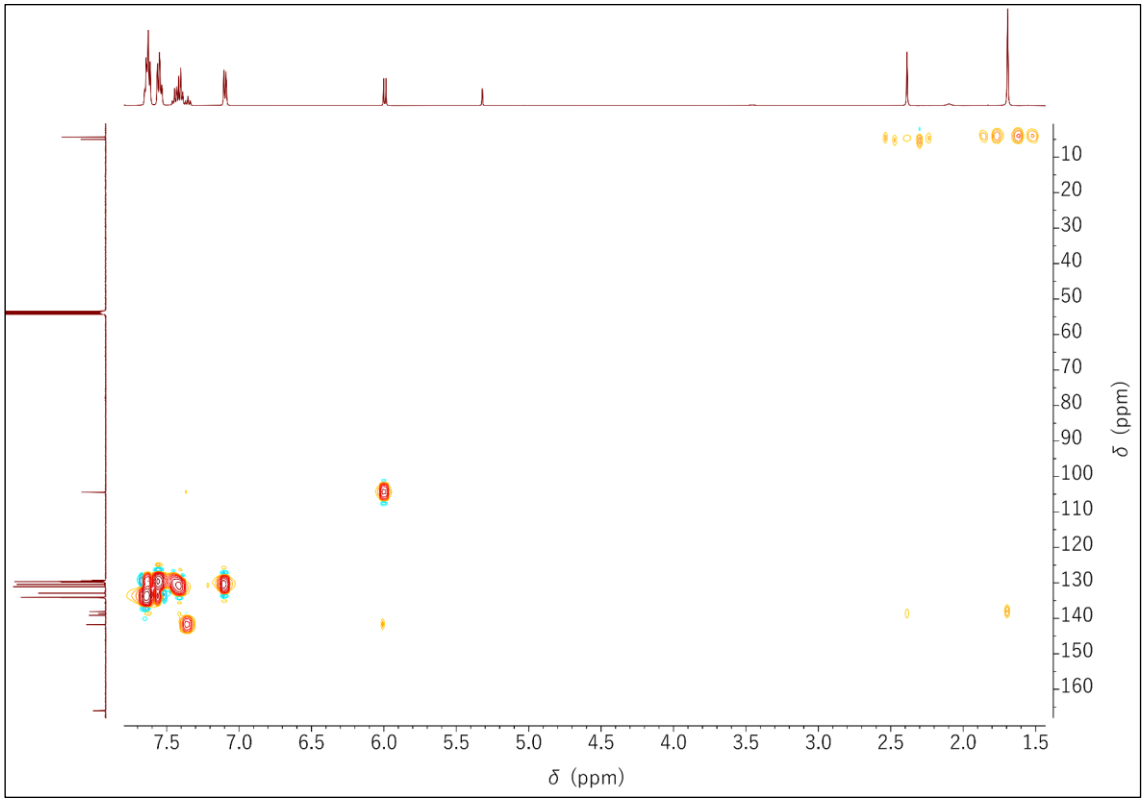

Figure A.44. $^{1}H,^{13}C$ HSQC NMR spectrum of $\mathbf{Fe_s^{II}}$ in CD_2Cl_2.

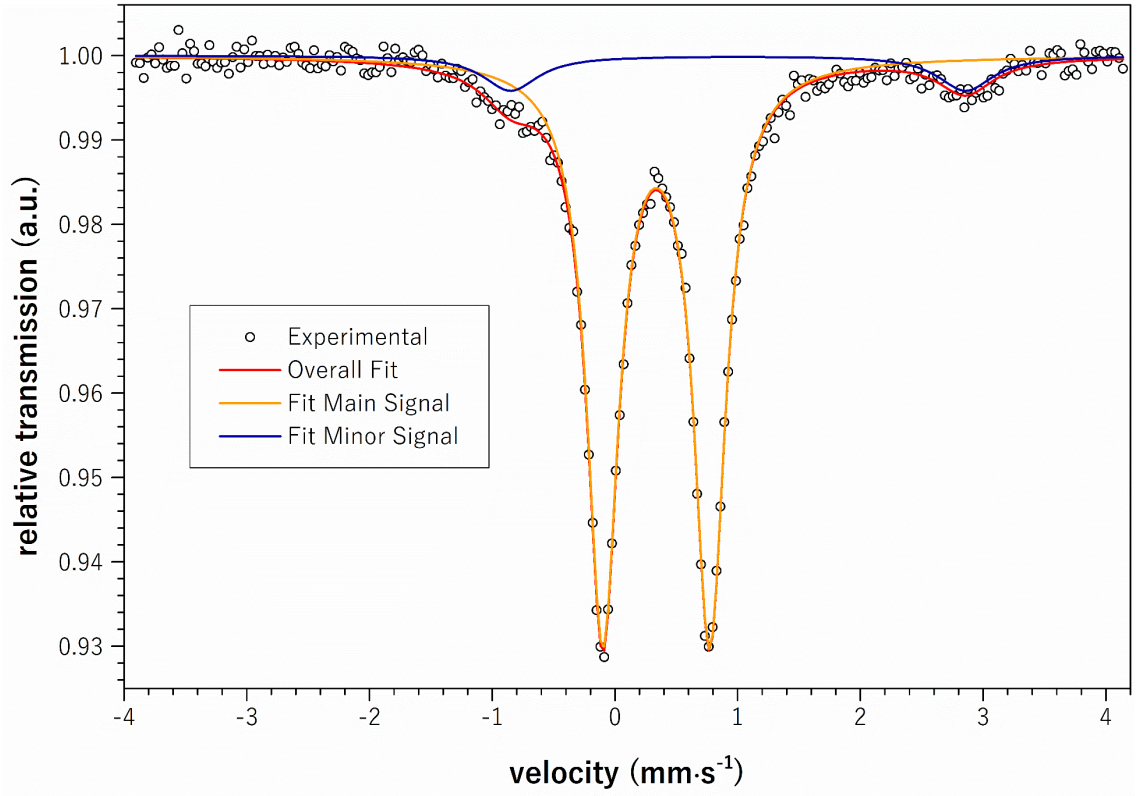

Figure A.45. Zero-field ^{57}Fe-MÖSSBAUER spectrum of solid $\mathbf{Fe_s^{II}}$**-OTf** recorded at 80 K. Red: fit with two LORENTZIAN doublets with isomer shift. Orange: main component, $\delta = 0.34$ mm·s^{-1}, $\Delta E_Q = 0.87$ mm·s^{-1}, $\Gamma = 0.31$ mm·s^{-1}, 91% relative intensity. Blue: minor component, $\delta = 1.00$ mm·s^{-1}, $\Delta E_Q = 3.71$ mm·s^{-1}, $\Gamma = 0.55$ mm·s^{-1}, 9% relative intensity.

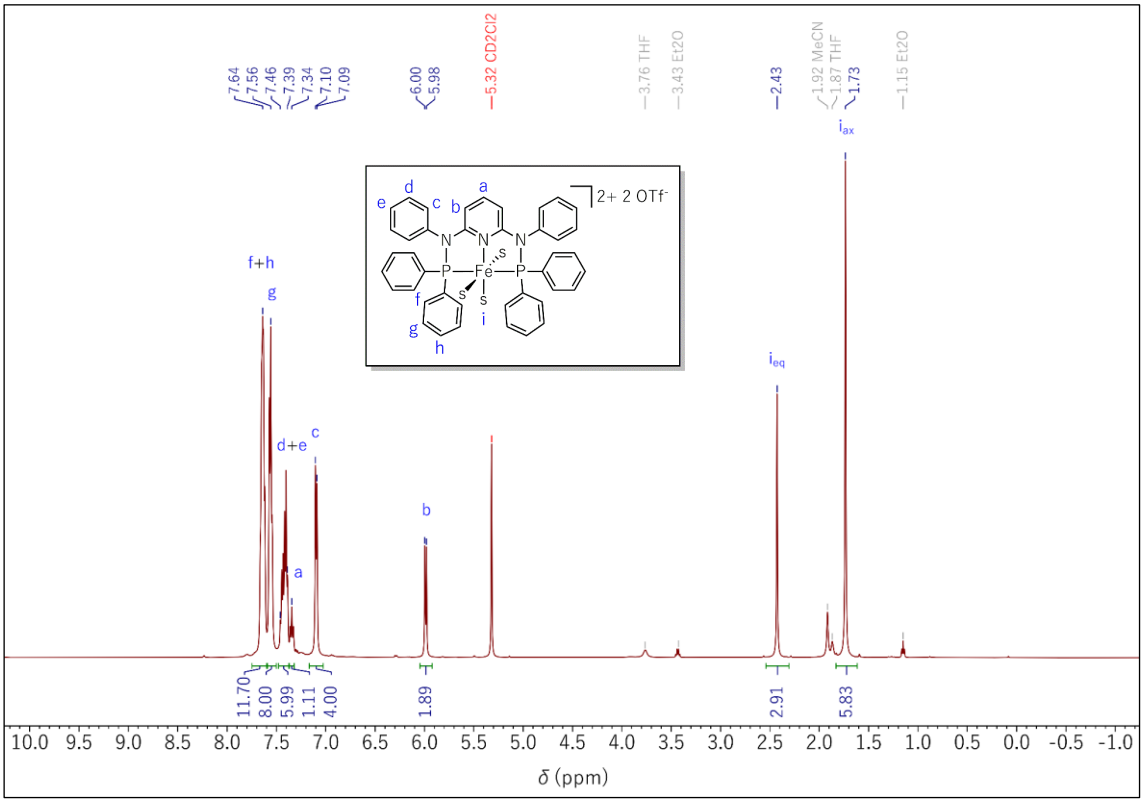

Figure A.46. ^{1}H NMR spectrum of $\mathbf{Fe_s^{II}}$**-OTf** in CD_2Cl_2 at 500 MHz and 296 K with peak assignments.

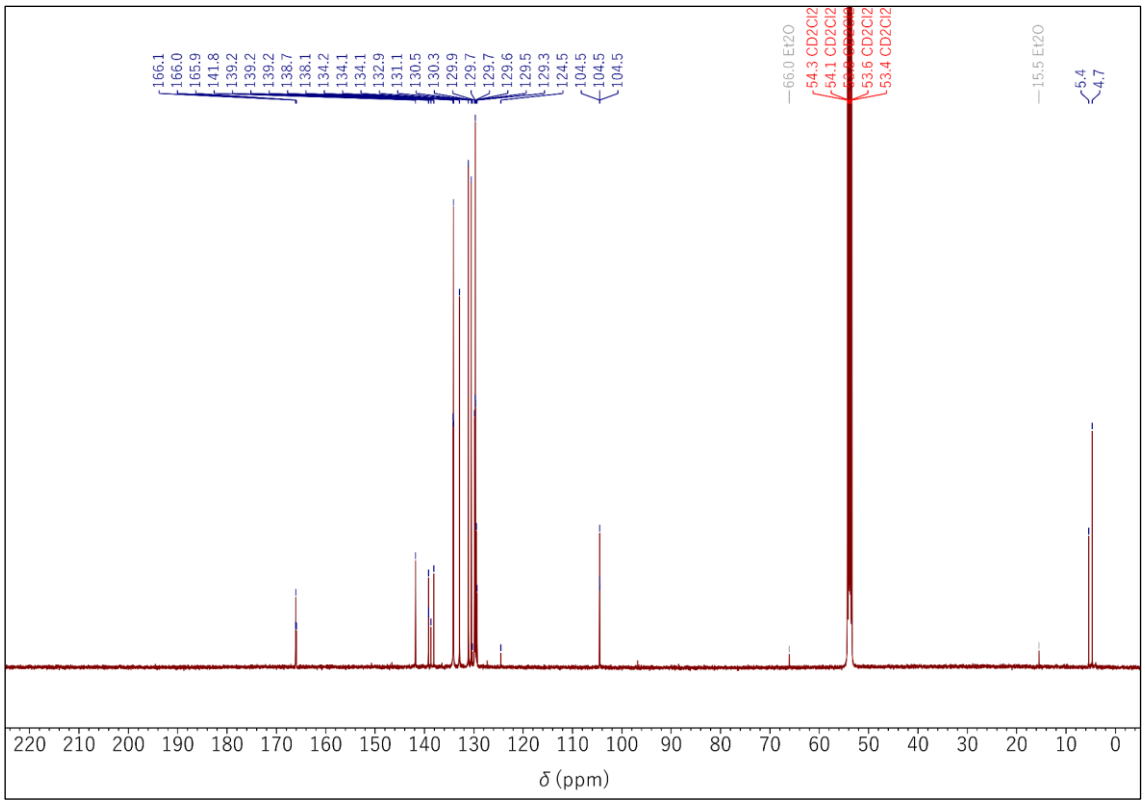

Figure A.47. $^{13}C\{^{1}H\}$ NMR spectrum of **Fe_s^{II}-OTf** in CD_2Cl_2 at 126 MHz and 296 K.

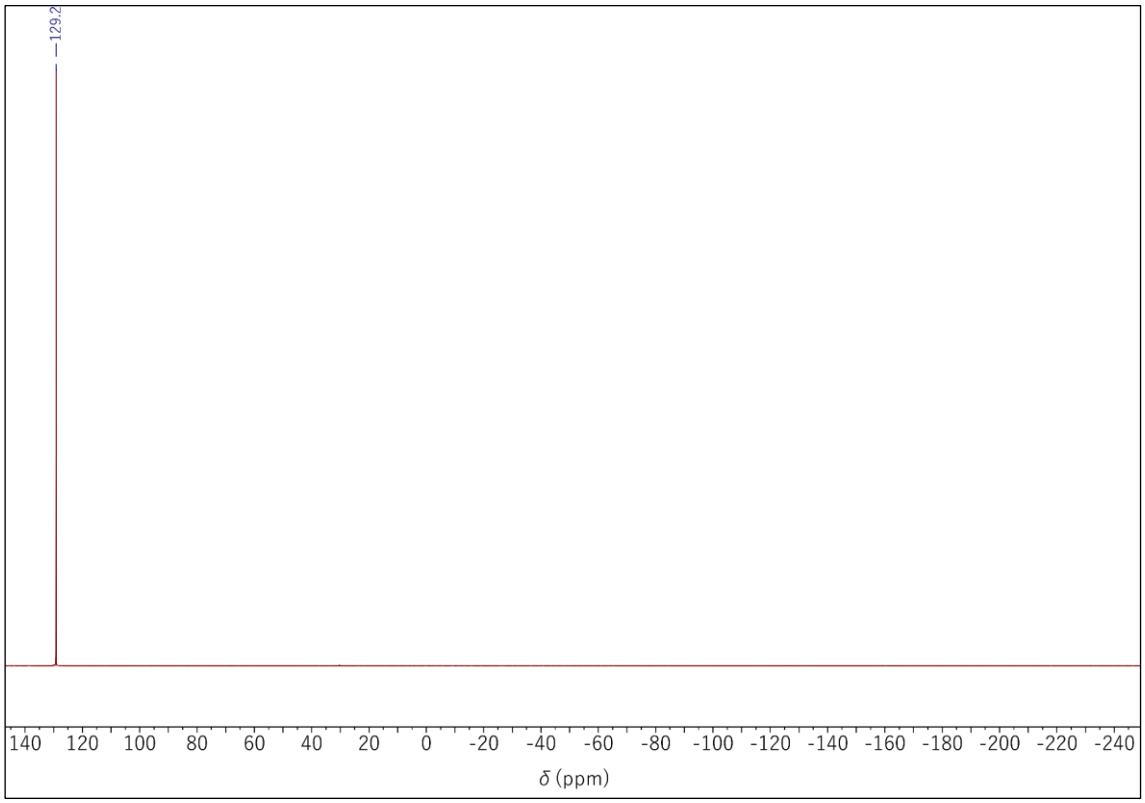

Figure A.48. $^{31}P\{^{1}H\}$ NMR spectrum of **Fe_s^{II}-OTf** in CD_2Cl_2 at 202 MHz and 296 K.

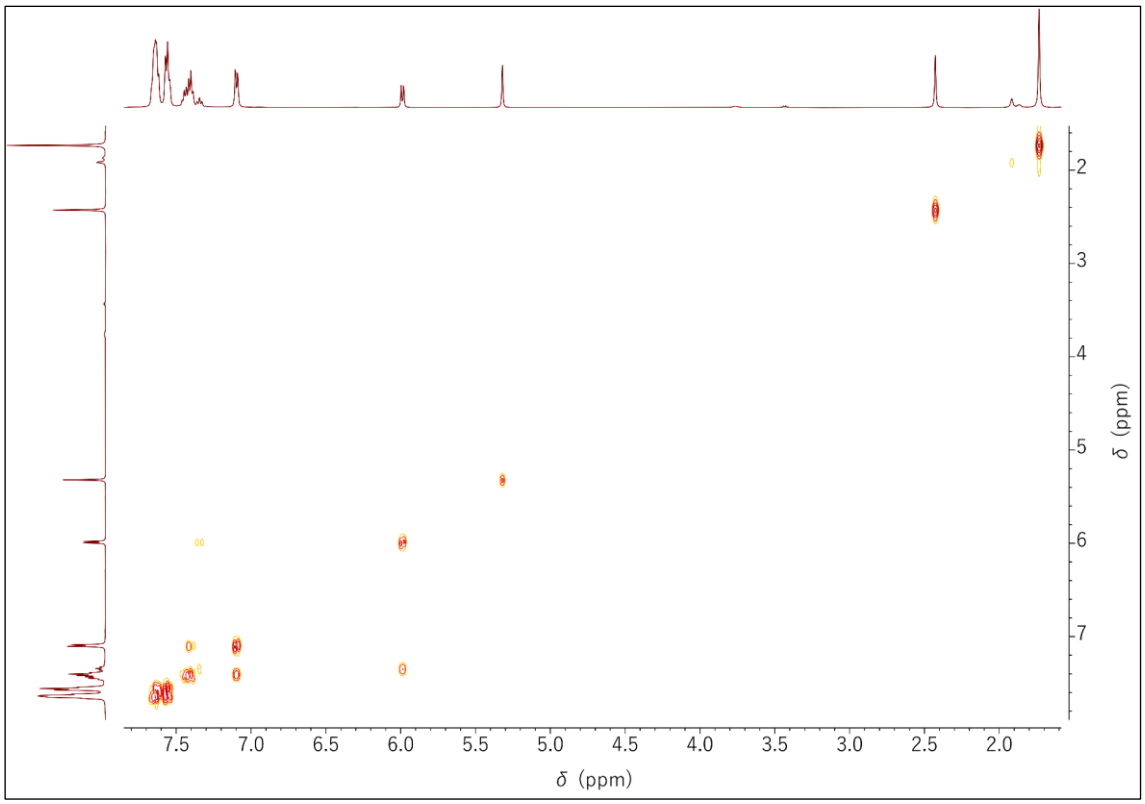

Figure A.49. $^{1}H,^{1}H$ COSY NMR spectrum of $\mathbf{Fe_s^{II}}$**-OTf** in CD_2Cl_2 at 500 MHz and 296 K.

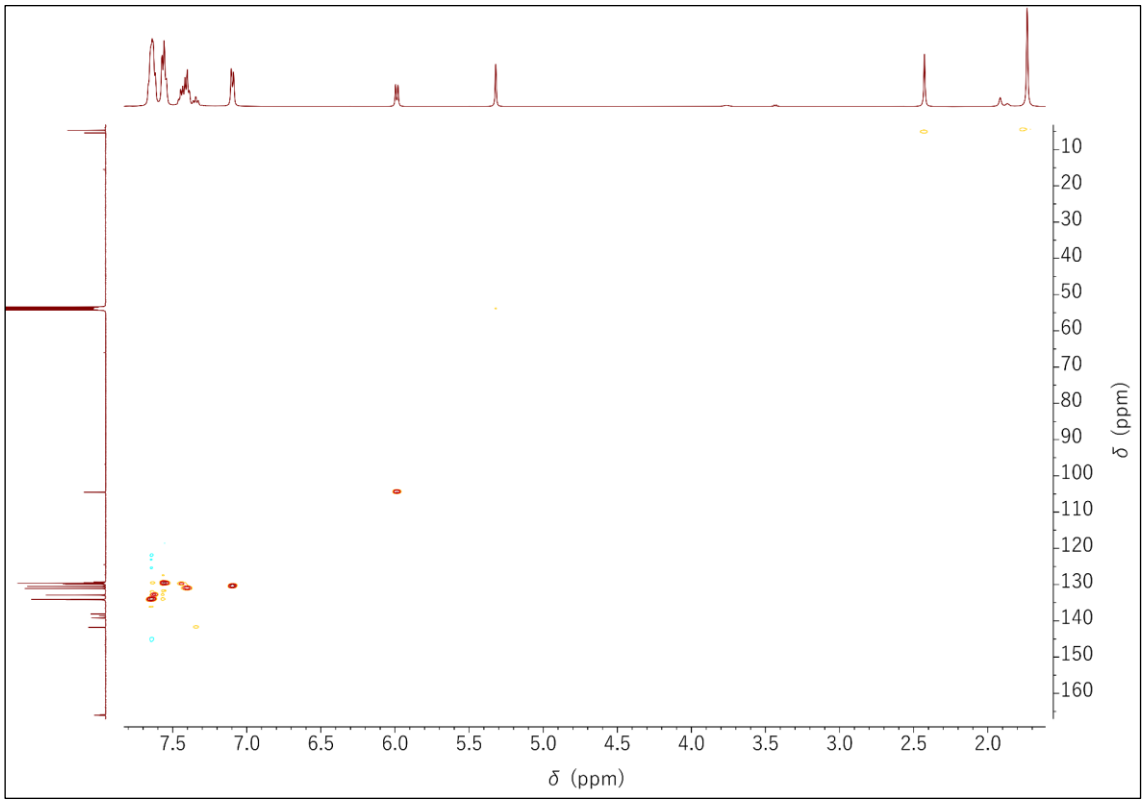

Figure A.50. $^{1}H,^{13}C$ HSQC NMR spectrum of $\mathbf{Fe_s^{II}}$**-OTf** in CD_2Cl_2.

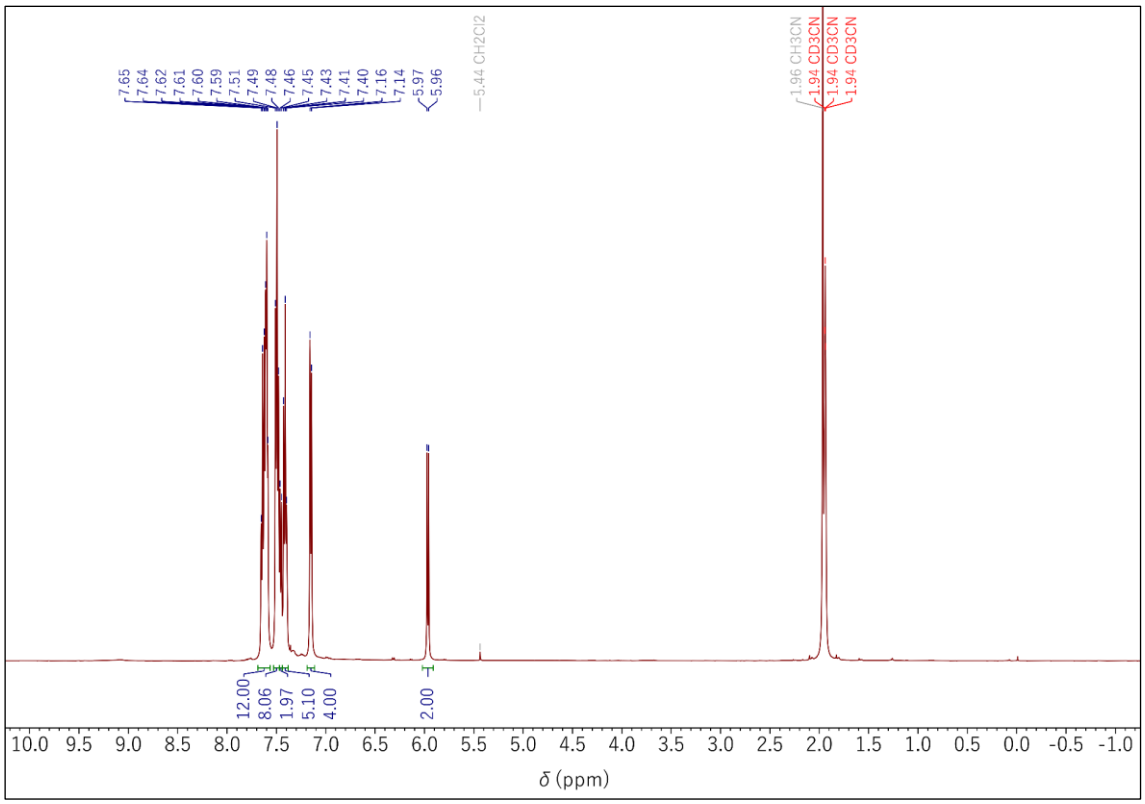

Figure A.51. ^{1}H NMR spectrum of **Fe^{II}_{s}-OTf** in CD_3CN at 500 MHz and 296 K.

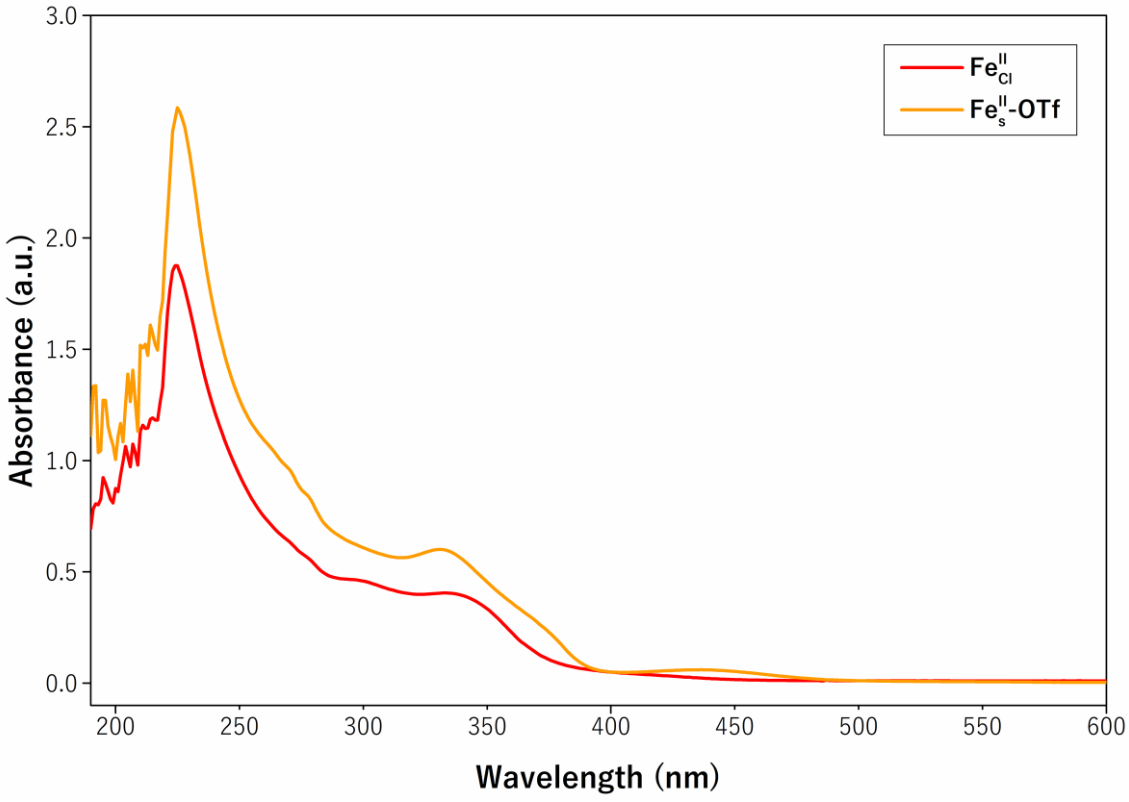

Figure A.52. UV/VIS spectra of 0.25 mM solutions of **Fe^{II}_{Cl}** and **Fe^{II}_{s}-OTf** in CH_2Cl_2.

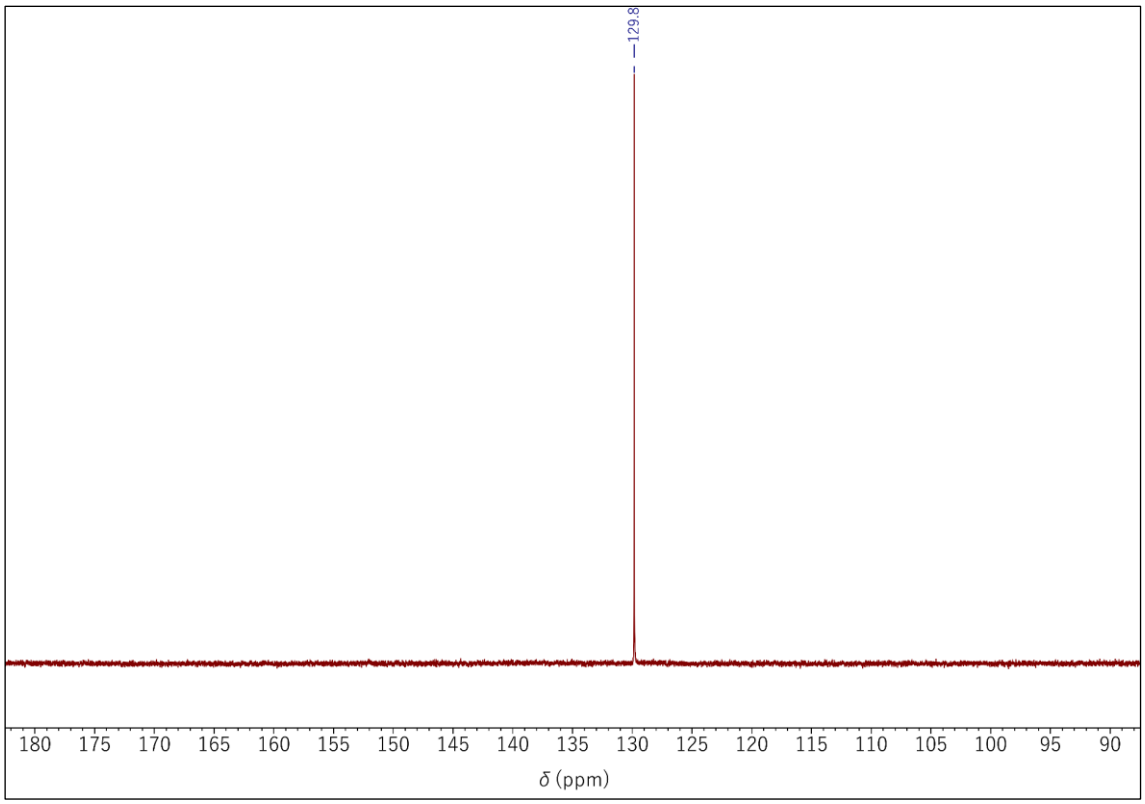

Figure A.53. $^{31}P\{^{1}H\}$ NMR spectrum of $\mathbf{Fe}_{\mathbf{Cl}}^{\mathbf{II}}$ in CD_3CN at 202 MHz and 296 K.

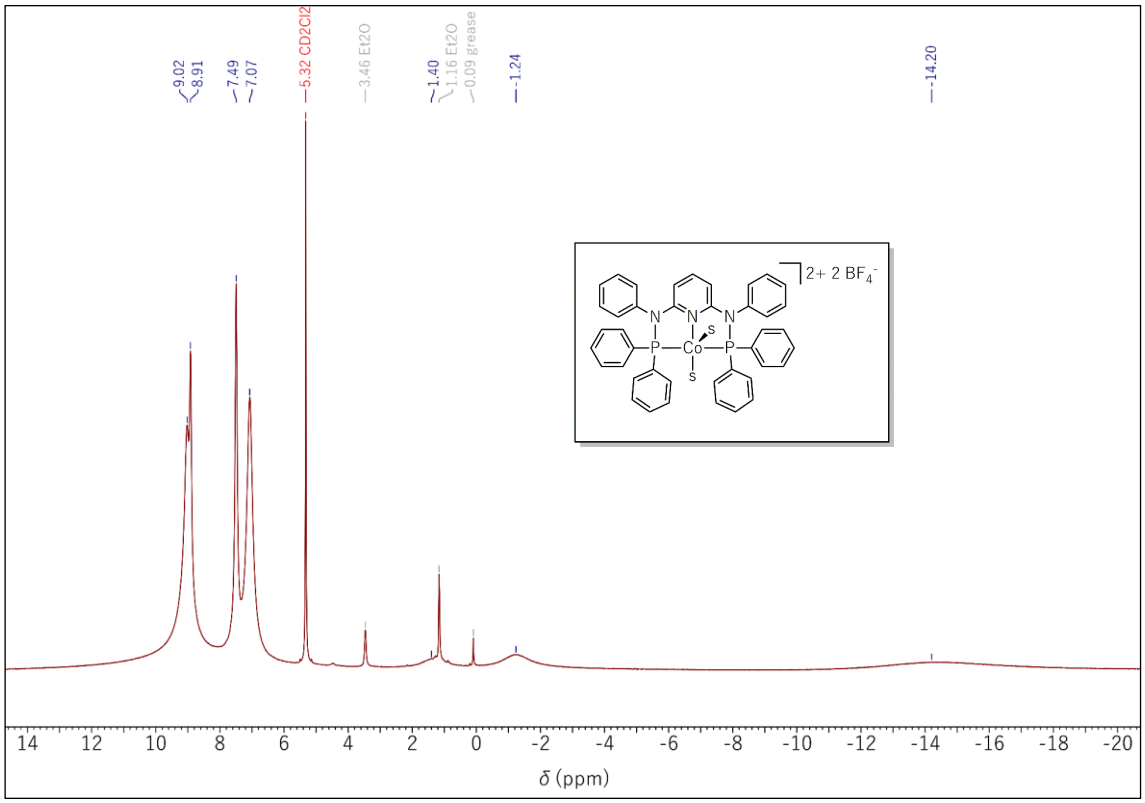

Figure A.54. ^{1}H NMR spectrum of $\mathbf{Co}_{\mathbf{s}}^{\mathbf{II}}$ in CD_2Cl_2 at 500 MHz and 296 K.

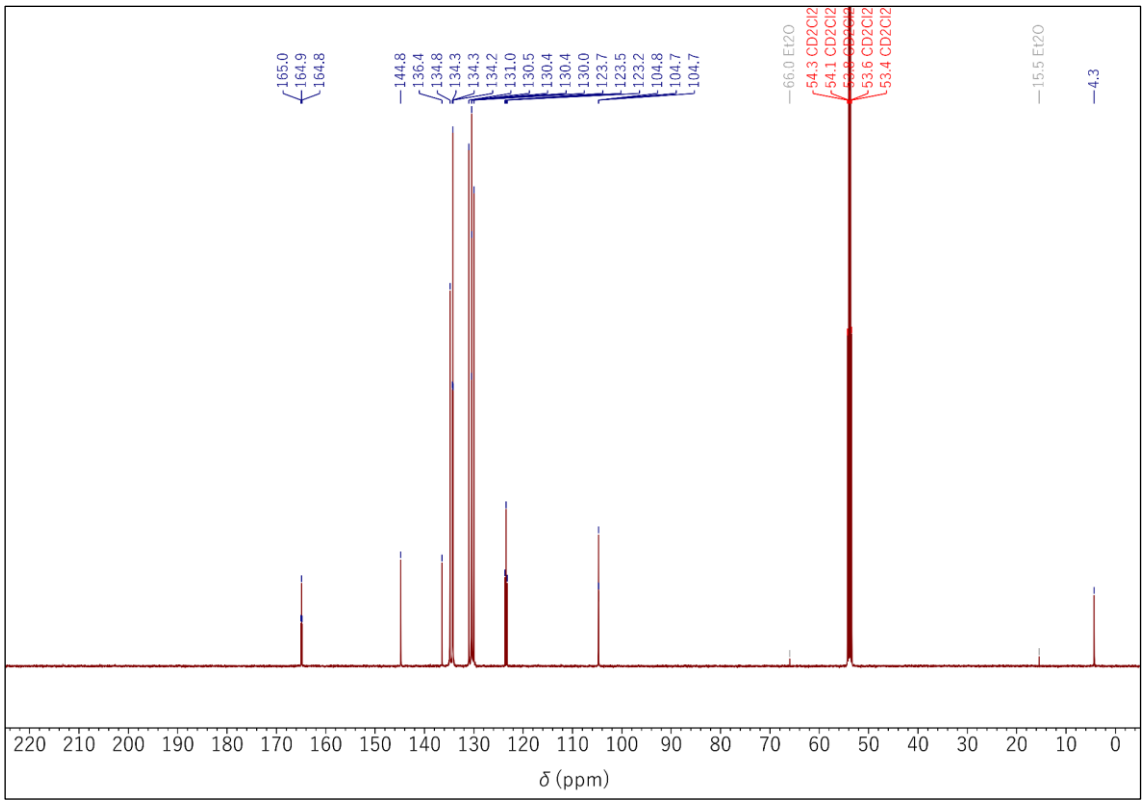

Figure A.55. $^{13}C\{^{1}H\}$ NMR spectrum of $\mathbf{Ni_s^{II}}$ in CD_2Cl_2 at 126 MHz and 296 K.

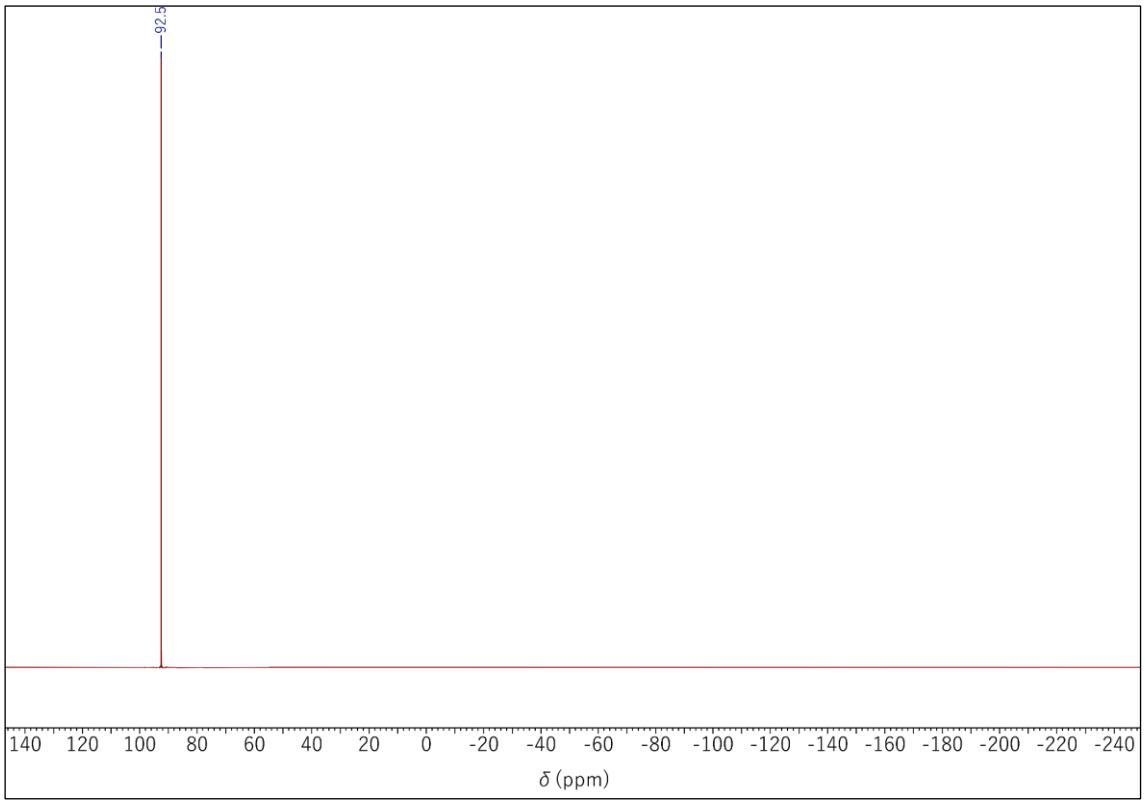

Figure A.56. $^{31}P\{^{1}H\}$ NMR spectrum of $\mathbf{Ni_s^{II}}$ in CD_2Cl_2 at 202 MHz and 296 K.

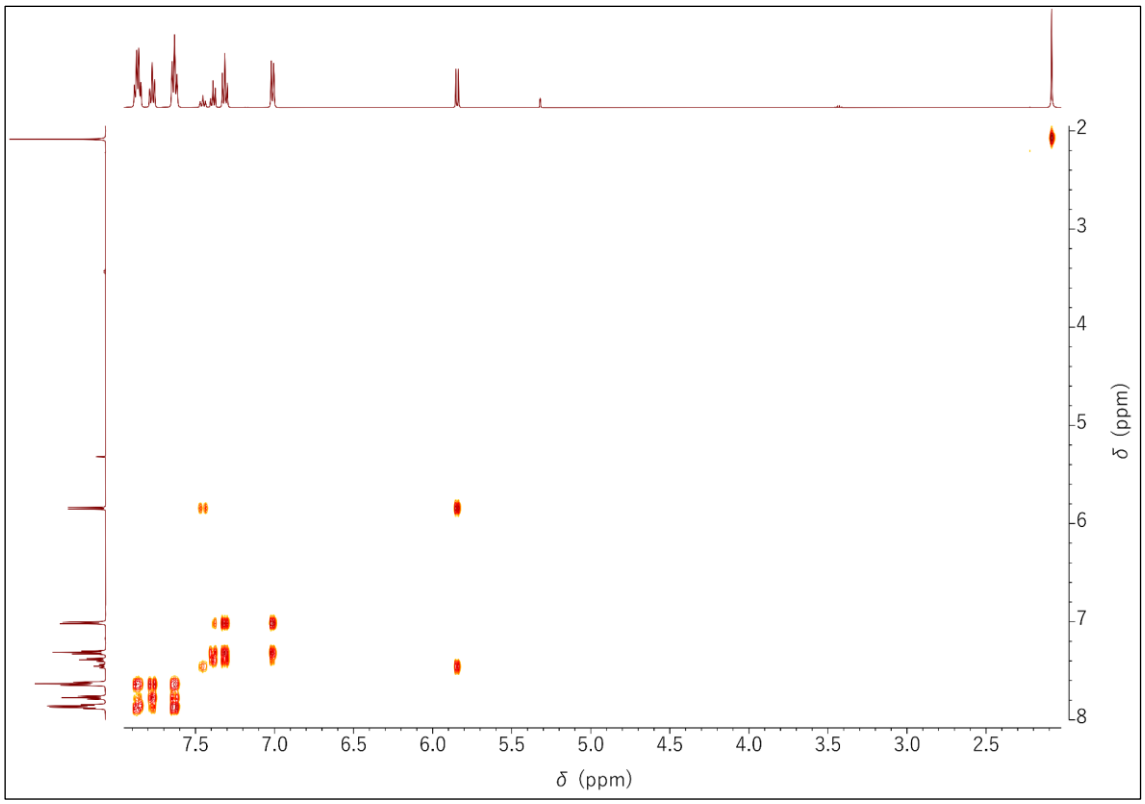

Figure A.57. $^{1}H,^{1}H$ COSY NMR spectrum of $\mathbf{Ni_s^{II}}$ in CD_2Cl_2 at 500 MHz and 296 K.

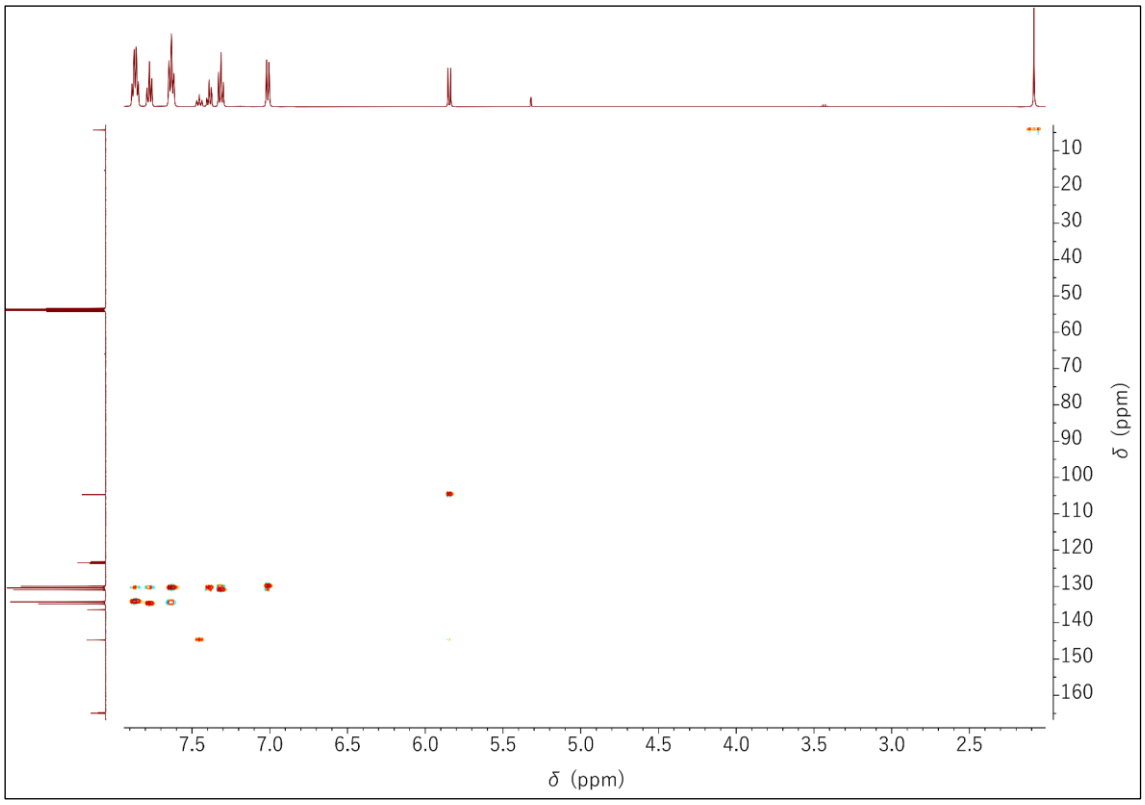

Figure A.58. $^{1}H,^{13}C$ HSQC NMR spectrum of $\mathbf{Ni_s^{II}}$ in CD_2Cl_2.

X-Ray Diffraction

a) Additional Structures

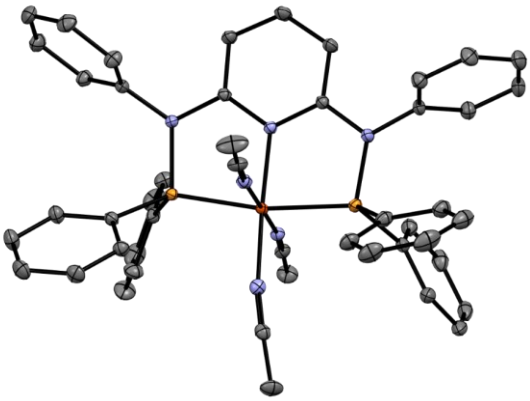

Figure A.59. Molecular structure of [Fe**L**(MeCN)$_3$](Cl$_3$FeOFeCl$_3$) received from crystals obtained from a concentrated MeCN/Et$_2$O (3:1) solution at −30 °C under air. Thermal ellipsoids are shown at a 50% probability level. H-atoms and outer-sphere ligands were omitted for clarity.

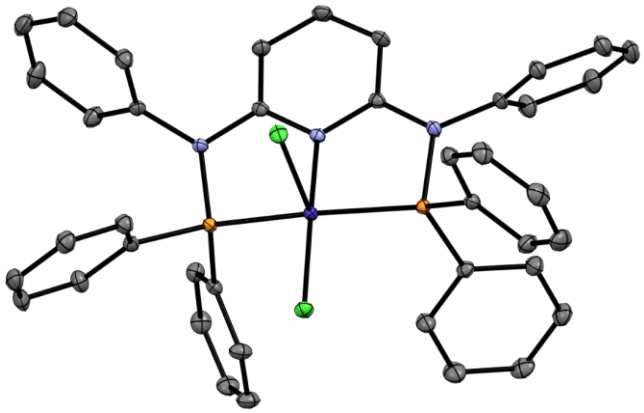

Figure A.60. Molecular structure of $\mathbf{Co}^{\mathbf{II}}_{\mathbf{Cl}}$ received from crystals obtained from a concentrated MeCN/Et$_2$O (3:1) solution at −35 °C. Thermal ellipsoids are shown at a 50% probability level. H-atoms and solvent molecules were omitted for clarity.

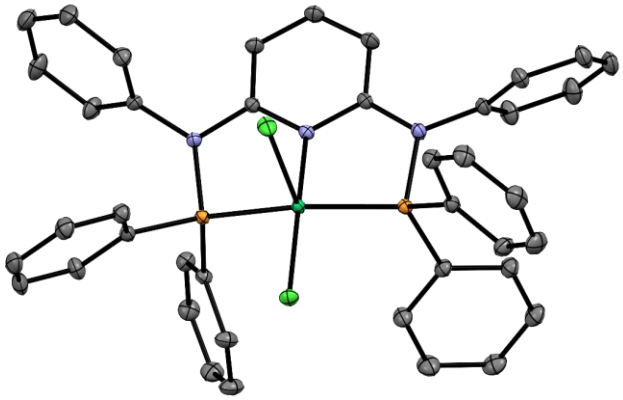

Figure A.61. Molecular structure of $\mathbf{Ni}^{\mathbf{II}}_{\mathbf{Cl}}$ received from crystals obtained from a concentrated MeCN/Et$_2$O (3:1) solution at −35 °C. Thermal ellipsoids are shown at a 50% probability level. H-atoms and solvent molecules were omitted for clarity.

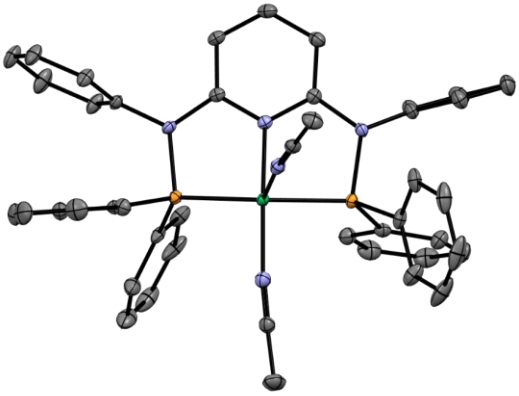

Figure A.62. Molecular structure of $\mathbf{Ni}_{\mathbf{s}}^{\mathbf{I}}$ received from crystals obtained from the crude product solution after adding Et_2O at −35 °C. Thermal ellipsoids are shown at a 50% probability level. H-atoms, solvent molecules, and the outer-sphere BF_4^- ligand were omitted for clarity.

b) Crystallographic Data

Table A.1. Crystal data and structure refinement for **L**.

CCDC No.	2109424	
Identification code	CEC0014_1	
Empirical formula	$C_{41}H_{33}N_3P_2$	
Formula weight	629.64	
Temperature	100(2) K	
Wavelength	0.71073 Å	
Crystal system	Orthorhombic	
Space group	Pbcn; No. 60	
Unit cell dimensions	a = 34.0981(10) Å	α = 90°
	b = 8.7711(2) Å	β = 90°
	c = 23.9656(8) Å	γ = 90°
Volume	7167.6(4) Å^3	
Formula units per unit cell	8	
Density (calculated)	1.167 g/cm^3	
Absorption coefficient	0.153 mm^{-1}	
F(000)	2640	
Crystal size	0.370 x 0.150 x 0.136 mm^3	
θ range for data collection	1.801 to 32.499°	
Index ranges	$-51 \le h \le 51$, $-13 \le k \le 13$, $-36 \le l \le 36$	
Reflections collected	137542	
Independent reflections	12975 [R(int) = 0.0426]	
Completeness to θ = 25.242°	100.0%	
Absorption correction	Gaussian	
Max. and min. transmission	0.838 and 0.789	
Refinement method	Full-matrix least-squares on F^2	
Data/restraints/parameters	12975/72/415	
Goodness-of-fit on F^2	1.173	
Final R indices [$I > 2\sigma(I)$]	R_1 = 0.0604, wR_2 = 0.1376	
R indices (all data)	R_1 = 0.0660, wR_2 = 0.1407	
Extinction coefficient	n/a	
Largest diff. peak and hole	0.544 and −0.436 e.Å^{-3}	

Table A.2. Crystal data and structure refinement for $\mathbf{Mn^{I}_{CO,Br}}$.

CCDC No.	2109428	
Identification code	CEC0038	
Empirical formula	$C_{43}H_{33}BrMnN_3O_2P_2$	
Formula weight	820.51	
Temperature	100(2) K	
Wavelength	0.71073 Å	
Crystal system	Monoclinic	
Space group	$P2_1/c$; No. 14	
Unit cell dimensions	a = 11.6847(9) Å	α = 90°
	b = 17.1633(13) Å	β = 104.993(3)°
	c = 18.5524(14) Å	γ = 90°
Volume	3594.0(5) Å^3	
Formula units per unit cell	4	
Density (calculated)	1.516 g/cm^3	
Absorption coefficient	1.611 mm^{-1}	
F(000)	1672	
Crystal size	0.20 x 0.20 x 0.15 mm^3	
θ range for data collection	2.160 to 40.274°	
Index ranges	$-21 \le h \le 21$, $-31 \le k \le 31$, $-32 \le l \le 33$	
Reflections collected	165160	
Independent reflections	22584 [R(int) = 0.0866]	
Completeness to θ = 25.242°	99.9%	
Absorption correction	Semi-empirical from equivalents	
Max. and min. transmission	0.7915 and 0.6979	
Refinement method	Full-matrix least-squares on F^2	
Data/restraints/parameters	22584/1/472	
Goodness-of-fit on F^2	1.205	
Final R indices [$I > 2\sigma(I)$]	R_1 = 0.0568, wR_2 = 0.1224	
R indices (all data)	R_1 = 0.0732, wR_2 = 0.1267	
Extinction coefficient	n/a	
Largest diff. peak and hole	1.473 and −1.618 e.Å^{-3}	

Table A.3. Crystal data and structure refinement for $\mathbf{Fe}^{\mathbf{II}}_{\mathbf{Cl}}$.

CCDC No.	2109421	
Identification code	CEC0020	
Empirical formula	$C_{42}H_{35}Cl_4FeN_3P_2$	
Formula weight	841.32	
Temperature	100(2) K	
Wavelength	0.71073 Å	
Crystal system	Monoclinic	
Space group	$P2_1/n$; No. 14	
Unit cell dimensions	a = 14.2736(6) Å	α = 90°
	b = 19.0907(9) Å	β = 112.610(2)°
	c = 15.2486(7) Å	γ = 90°
Volume	3835.8(3) Å^3	
Formula units per unit cell	4	
Density (calculated)	1.457 g/cm^3	
Absorption coefficient	0.791 mm^{-1}	
F(000)	1728	
Crystal size	0.300 x 0.150 x 0.120 mm^3	
θ range for data collection	1.797 to 34.999°	
Index ranges	$-23 \le h \le 20$, $-30 \le k \le 30$, $-24 \le l \le 21$	
Reflections collected	65790	
Independent reflections	16859 [R(int) = 0.0836]	
Completeness to θ = 25.242°	99.9%	
Absorption correction	Semi-empirical from equivalents	
Max. and min. transmission	0.91 and 0.83	
Refinement method	Full-matrix least-squares on F^2	
Data/restraints/parameters	16859/0/469	
Goodness-of-fit on F^2	1.059	
Final R indices [$I > 2\sigma(I)$]	R_1 = 0.0371, wR_2 = 0.0865	
R indices (all data)	R_1 = 0.0616, wR_2 = 0.0919	
Extinction coefficient	n/a	
Largest diff. peak and hole	0.749 and –0.521 e.Å^{-3}	

Table A.4. Crystal data and structure refinement for [Fe**L**(MeCN)$_3$](Cl$_3$FeOFeCl$_3$).

CCDC No.	2109425	
Identification code	CEC0018	
Chemical formula	$C_{47}H_{42}Cl_6Fe_3N_6OP_2$	
Formula weight	1149.05 g/mol	
Temperature	100(2) K	
Wavelength	0.71073 Å	
Crystal system	triclinic	
Space group	P-1	
Unit cell dimensions	a = 9.1344(5) Å	α = 85.506(2)°
	b = 12.1482(7) Å	β = 78.908(2)°
	c = 23.4429(14) Å	γ = 81.505(2)°
Volume	2521.4(3) Å^3	
Formula units per unit cell	2	
Density (calculated)	1.513 g/cm^3	
Absorption coefficient	1.275 mm^{-1}	
F(000)	1168	
θ range for data collection	1.87 to 32.50°	
Index ranges	$-13 \le h \le 13$, $-18 \le k \le 18$, $-35 \le l \le 35$	
Reflections collected	174213	
Independent reflections	18260 [R(int) = 0.0576]	
Absorption correction	Multi-Scan	
Max. and min. transmission	0.9050 and 0.7490	
Refinement method	Full-matrix least-squares on F^2	
Data/restraints/parameters	18260/0/589	
Goodness-of-fit on F^2	1.154	
Final R indices [$I > 2\sigma(I)$]	R_1 = 0.0451, wR_2 = 0.0968	
R indices (all data)	R_1 = 0.0536, wR_2 = 0.1000	
Largest diff. peak and hole	0.775 and –0.778 e.Å^{-3}	

Table A.5. Crystal data and structure refinement for $\mathbf{Co^{II}_{CI}}$.

CCDC No.	2109429	
Identification code	CEC0039	
Empirical formula	$C_{49}H_{49}Cl_2CoN_3O_2P_2$	
Formula weight	903.68	
Temperature	100(2) K	
Wavelength	0.71073 Å	
Crystal system	Monoclinic	
Space group	$P2_1/c$; No. 14	
Unit cell dimensions	a = 8.8971(4) Å	α = 90°
	b = 27.2678(13) Å	β = 90.045(2)°
	c = 17.7781(8) Å	γ = 90°
Volume	4313.0(3) Å^3	
Formula units per unit cell	4	
Density (calculated)	1.392 g/cm^3	
Absorption coefficient	0.640 mm^{-1}	
F(000)	1884	
Crystal size	0.212 x 0.121 x 0.013 mm^3	
θ range for data collection	1.882 to 34.999°	
Index ranges	$-14 \le h \le 14$, $-44 \le k \le 44$, $-28 \le l \le 27$	
Reflections collected	179352	
Independent reflections	18731 [R(int) = 0.0576]	
Completeness to θ = 25.242°	99.8%	
Absorption correction	Semi-empirical from equivalents	
Max. and min. transmission	0.9282 and 0.8728	
Refinement method	Full-matrix least-squares on F^2	
Data/restraints/parameters	18731/60/548	
Goodness-of-fit on F^2	1.109	
Final R indices [$I > 2\sigma(I)$]	R_1 = 0.0439, wR_2 = 0.0972	
R indices (all data)	R_1 = 0.0545, wR_2 = 0.1014	
Extinction coefficient	n/a	
Largest diff. peak and hole	1.006 and –0.531 e.Å^{-3}	

Table A.6. Crystal data and structure refinement for $\mathbf{Co^{II}_{Cl}}$ obtained from an MeCN/Et_2O solution.

CCDC No.	2109427	
Identification code	CEC0042	
Empirical formula	$C_{43}H_{36}Cl_2CoN_4P_2$	
Formula weight	800.53	
Temperature	100(2) K	
Wavelength	0.71073 Å	
Crystal system	Monoclinic	
Space group	$P2_1/n$; No. 14	
Unit cell dimensions	a = 14.3364(4) Å	α = 90°
	b = 18.6529(5) Å	β = 108.688(10)°
	c = 14.7075(4) Å	γ = 90°
Volume	3725.65(18) $Å^3$	
Formula units per unit cell	4	
Density (calculated)	1.427 g/cm^3	
Absorption coefficient	0.728 mm^{-1}	
F(000)	1652	
Crystal size	0.080 x 0.060 x 0.035 mm^3	
θ range for data collection	1.82 to 32.97°	
Index ranges	$-21 \le h \le 21$, $-28 \le k \le 28$, $-22 \le l \le 22$	
Reflections collected	141027	
Independent reflections	13977 [R(int) = 0.0824]	
Completeness to θ = 25.24°	99.8%	
Absorption correction	Semi-empirical from equivalents	
Max. and min. transmission	0.97 and 0.82	
Refinement method	Full-matrix least-squares on F^2	
Data/restraints/parameters	13977/0/470	
Goodness-of-fit on F^2	1.079	
Final R indices [$I > 2\sigma(I)$]	R_1 = 0.0408, wR_2 = 0.0835	
R indices (all data)	R_1 = 0.0531, wR_2 = 0.0880	
Largest diff. peak and hole	0.571 and –0.511 e.$Å^{-3}$	

Table A.7. Crystal data and structure refinement for $\mathbf{Ni}^{\mathbf{II}}_{\mathbf{Cl}}$.

CCDC No.	2109423	
Identification code	CEC0032	
Empirical formula	$C_{42}H_{35}Cl_4N_3NiP_2$	
Formula weight	844.18	
Temperature	100(2) K	
Wavelength	0.71073 Å	
Crystal system	Monoclinic	
Space group	$P2_1/c$; No. 14	
Unit cell dimensions	a = 21.9733(9) Å	α = 90°
	b = 9.2323(3) Å	β = 112.004(10)°
	c = 20.2815(8) Å	γ = 90°
Volume	3814.7(3) Å^3	
Formula units per unit cell	4	
Density (calculated)	1.470 g/cm^3	
Absorption coefficient	0.909 mm^{-1}	
F(000)	1736	
Crystal size	0.11 x 0.07 x 0.05 mm^3	
θ range for data collection	1.999 to 36.368°	
Index ranges	$-36 \le h \le 36$, $-15 \le k \le 15$, $-33 \le l \le 33$	
Reflections collected	197776	
Independent reflections	18536 [R(int) = 0.0733]	
Completeness to θ = 25.242°	100.0%	
Absorption correction	Semi-empirical from equivalents	
Max. and min. transmission	0.8625 and 0.8073	
Refinement method	Full-matrix least-squares on F^2	
Data/restraints/parameters	18536/0/469	
Goodness-of-fit on F^2	1.093	
Final R indices [$I > 2\sigma(I)$]	R_1 = 0.0458, wR_2 = 0.0936	
R indices (all data)	R_1 = 0.0578, wR_2 = 0.0980	
Extinction coefficient	n/a	
Largest diff. peak and hole	0.826 and –0.832 e.Å^{-3}	

Table A.8. Crystal data and structure refinement for $\mathbf{Ni^{II}_{Cl}}$ obtained from an MeCN/Et_2O solution.

CCDC No.	2109430	
Identification code	CEC0043	
Empirical formula	$C_{43}H_{36}Cl_2N_4NiP_2$	
Formula weight	800.31	
Temperature	100(2) K	
Wavelength	0.71073 Å	
Crystal system	Monoclinic	
Space group	$P2_1/n$; No. 14	
Unit cell dimensions	a = 14.2542(7) Å	α = 90°
	b = 18.8775(9) Å	β = 108.888(2)°
	c = 14.6589(7) Å	γ = 90°
Volume	3732.1(3) Å^3	
Formula units per unit cell	4	
Density (calculated)	1.424 g/cm^3	
Absorption coefficient	0.787 mm^{-1}	
F(000)	1656	
Crystal size	0.228 x 0.106 x 0.058 mm^3	
θ range for data collection	1.86 to 36.33°	
Index ranges	$-23 \le h \le 23$, $-31 \le k \le 31$, $-24 \le l \le 24$	
Reflections collected	203192	
Independent reflections	18091 [R(int) = 0.0582]	
Completeness to theta = 25.24°	99.9%	
Absorption correction	Semi-empirical from equivalents	
Max. and min. transmission	0.96 and 0.89	
Refinement method	Full-matrix least-squares on F^2	
Data/restraints/parameters	18091/0/470	
Goodness-of-fit on F^2	1.154	
Final R indices [$I > 2\sigma(I)$]	R_1 = 0.0421, wR_2 = 0.0892	
R indices (all data)	R_1 = 0.0509, wR_2 = 0.0924	
Largest diff. peak and hole	0.662 and –0.422 e.Å^{-3}	

Table A.9. Crystal data and structure refinement for $\mathbf{Cu^{I}_{Cl}}$.

CCDC No.	2109432	
Identification code	CEC0050	
Empirical formula	$C_{42}H_{35}Cl_3CuN_3P_2$	
Formula weight	813.56	
Temperature	100(2) K	
Wavelength	0.71073 Å	
Crystal system	Monoclinic	
Space group	$P2_1/c$; No. 14	
Unit cell dimensions	a = 15.0181(6) Å	α = 90°
	b = 13.7846(6) Å	β = 93.208(2)°
	c = 18.3831(8) Å	γ = 90°
Volume	3799.7(3) Å^3	
Formula units per unit cell	4	
Density (calculated)	1.422 g/cm^3	
Absorption coefficient	0.905 mm^{-1}	
F(000)	1672	
Crystal size	0.130 x 0.060 x 0.050 mm^3	
θ range for data collection	1.848 to 37.500°	
Index ranges	$-25 \le h \le 25$, $-23 \le k \le 23$, $-31 \le l \le 31$	
Reflections collected	310452	
Independent reflections	19998 [R(int) = 0.0517]	
Completeness to θ = 25.242°	100.0%	
Absorption correction	Semi-empirical from equivalents	
Max. and min. transmission	0.96 and 0.92	
Refinement method	Full-matrix least-squares on F^2	
Data/restraints/parameters	19998/0/460	
Goodness-of-fit on F^2	1.085	
Final R indices [$I > 2\sigma(I)$]	R_1 = 0.0403, wR_2 = 0.0903	
R indices (all data)	R_1 = 0.0470, wR_2 = 0.0933	
Extinction coefficient	n/a	
Largest diff. peak and hole	1.009 and –0.935 e.Å^{-3}	

Table A.10. Crystal data and structure refinement for $\mathbf{Cu_I^I}$.

CCDC No.	2109431	
Identification code	CEC0034	
Empirical formula	$C_{45}H_{41}CuIN_3OP_2$	
Formula weight	892.19	
Temperature	100(2) K	
Wavelength	0.71073 Å	
Crystal system	Monoclinic	
Space group	$P2_1/n$; No. 14	
Unit cell dimensions	a = 11.4338(6) Å	α = 90°
	b = 22.8575(12) Å	β = 95.401(2)°
	c = 15.3445(8) Å	γ = 90°
Volume	3992.5(4) Å^3	
Formula units per unit cell	4	
Density (calculated)	1.484 g/cm^3	
Absorption coefficient	1.439 mm^{-1}	
F(000)	1808	
Crystal size	0.200 x 0.120 x 0.060 mm^3	
θ range for data collection	2.00 to 40.00°	
Index ranges	$-20 \le h \le 20$, $-41 \le k \le 41$, $-27 \le l \le 27$	
Reflections collected	468847	
Independent reflections	24736 [R(int) = 0.0452]	
Completeness to θ = 25.24°	100.0%	
Absorption correction	Semi-empirical from equivalents	
Max. and min. transmission	0.92 and 0.82	
Refinement method	Full-matrix least-squares on F^2	
Data/restraints/parameters	24736/0/478	
Goodness-of-fit on F^2	1.133	
Final R indices [$I > 2\sigma(I)$]	R_1 = 0.0267, wR_2 = 0.0600	
R indices (all data)	R_1 = 0.0299, wR_2 = 0.0612	
Largest diff. peak and hole	1.695 and –0.901 e.Å^{-3}	

Table A.11. Crystal data and structure refinement for $\mathbf{Zn}_{\mathbf{Cl}}^{\mathbf{II}}$.

CCDC No.	2109426	
Identification code	CEC0037	
Empirical formula	$C_{45}H_{41}Cl_2N_3OP_2Zn$	
Formula weight	838.02	
Temperature	100(2) K	
Wavelength	0.71073 Å	
Crystal system	Triclinic	
Space group	P-1	
Unit cell dimensions	a = 10.9843(7) Å	α = 86.877(2)°
	b = 12.8901(8) Å	β = 73.228(2)°
	c = 15.0226(10) Å	γ = 84.511(2)°
Volume	2026.4(2) Å^3	
Formula units per unit cell	2	
Density (calculated)	1.373 g/cm^3	
Absorption coefficient	0.856 mm^{-1}	
F(000)	868	
Crystal size	0.242 x 0.201 x 0.086 mm^3	
θ range for data collection	1.94 to 33.16°	
Index ranges	$-16 \le h \le 16$, $-19 \le k \le 19$, $-23 \le l \le 23$	
Reflections collected	141741	
Independent reflections	15448 [R(int) = 0.0381]	
Completeness to θ = 25.24°	99.8%	
Absorption correction	Semi-empirical from equivalents	
Max. and min. transmission	0.93 and 0.85	
Refinement method	Full-matrix least-squares on F^2	
Data/restraints/parameters	15448/0/487	
Goodness-of-fit on F^2	1.054	
Final R indices [$I > 2\sigma(I)$]	R_1 = 0.0301, wR_2 = 0.0787	
R indices (all data)	R_1 = 0.0355, wR_2 = 0.0829	
Largest diff. peak and hole	0.802 and –0.410 e.Å^{-3}	

Table A.12. Crystal data and structure refinement for $\mathbf{Zn}^{\mathbf{II}}_{\mathbf{OTf}}$.

CCDC No.	2109420	
Identification code	CEC0006_2	
Empirical formula	$C_{51}H_{49}F_6N_3O_8P_2S_2Zn$	
Formula weight	1137.36	
Temperature	100(2) K	
Wavelength	0.71073 Å	
Crystal system	Monoclinic	
Space group	$P2_1$, No. 4	
Unit cell dimensions	a = 9.7544(6) Å	α = 90°
	b = 13.6249(8) Å	β = 96.592(2)°
	c = 19.3929(11) Å	γ = 90°
Volume	2560.3(3) Å^3	
Formula units per unit cell	2	
Density (calculated)	1.475 g/cm^3	
Absorption coefficient	0.702 mm^{-1}	
F(000)	1172	
Crystal size	0.220 x 0.130 x 0.100 mm^3	
θ range for data collection	2.114 to 33.658°	
Index ranges	$-12 \le h \le 15$, $-21 \le k \le 21$, $-30 \le l \le 30$	
Reflections collected	114914	
Independent reflections	20199 [R(int) = 0.0450]	
Completeness to θ = 33.658°	99.6%	
Absorption correction	Semi-empirical from equivalents	
Max. and min. transmission	0.93 and 0.85	
Refinement method	Full-matrix least-squares on F^2	
Data/restraints/parameters	20199/61/659	
Goodness-of-fit on F^2	1.141	
Final R indices [$I > 2\sigma(I)$]	R_1 = 0.0457, wR_2 = 0.0982	
R indices (all data)	R_1 = 0.0509, wR_2 = 0.0999	
Absolute structure parameter	0.050(8)	
Extinction coefficient	n/a	
Largest diff. peak and hole	1.166 and –0.771 e.Å^{-3}	

Table A.13. Crystal data and structure refinement for $\mathbf{Fe_s^{II}}$.

Identification code	CEC0078	
Empirical formula	$C_{49}H_{45}B_2F_8FeN_7P_2$	
Formula weight	1023.33	
Temperature	100(2) K	
Wavelength	0.71073 Å	
Crystal system	Orthorhombic	
Space group	Pbca; No. 61	
Unit cell dimensions	a = 18.9401(6) Å	α = 90°
	b = 15.6416(5) Å	β = 90°
	c = 32.6564(11) Å	γ = 90°
Volume	9674.6(5) Å^3	
Formula units per unit cell	8	
Density (calculated)	1.405 g/cm^3	
Absorption coefficient	0.452 mm^{-1}	
F(000)	4208	
Crystal size	0.185 x 0.160 x 0.053 mm^3	
θ range for data collection	1.80 to 30.00°	
Index ranges	$-26 \le h \le 26$, $-22 \le k \le 22$, $-45 \le l \le 45$	
Reflections collected	162043	
Independent reflections	14099 [R(int) = 0.0746]	
Completeness to θ = 25.24°	100.0%	
Absorption correction	Numerical Mu from Formula	
Max. and min. transmission	0.9705 and 0.8818	
Refinement method	Full-matrix least-squares on F^2	
Data/restraints/parameters	14099/84/642	
Goodness-of-fit on F^2	1.012	
Final R indices [$I > 2\sigma(I)$]	R_1 = 0.0447, wR_2 = 0.1030	
R indices (all data)	R_1 = 0.0668, wR_2 = 0.1152	
Largest diff. peak and hole	0.963 and –0.512 e.Å^{-3}	

Table A.14. Crystal data and structure refinement for $\mathbf{Co_s^{II}}$.

Identification code	CEC0074	
Empirical formula	$C_{47}H_{42}B_2CoF_8N_6P_2$	
Formula weight	985.35	
Temperature	100(2) K	
Wavelength	0.71073 Å	
Crystal system	Monoclinic	
Space group	Pn; No. 7	
Unit cell dimensions	a = 13.2577(5) Å	α = 90°
	b = 10.0882(4) Å	β = 109.7782(14)°
	c = 18.3657(7) Å	γ = 90°
Volume	2311.44(16) Å^3	
Formula units per unit cell	2	
Density (calculated)	1.416 g/cm^3	
Absorption coefficient	0.514 mm^{-1}	
F(000)	1010	
Crystal size	0.272 x 0.122 x 0.046 mm^3	
θ range for data collection	2.019 to 36.346°	
Index ranges	$-22 \le h \le 22$, $-16 \le k \le 16$, $-30 \le l \le 30$	
Reflections collected	115016	
Independent reflections	20098 [R(int) = 0.0424]	
Completeness to θ = 25.24°	99.9%	
Absorption correction	Numerical	
Max. and min. transmission	0.9783 and 0.8986	
Refinement method	Full-matrix least-squares on F^2	
Data/restraints/parameters	20098/2/598	
Goodness-of-fit on F^2	1.049	
Final R indices [$I > 2\sigma(I)$]	R_1 = 0.0371, wR_2 = 0.0893	
R indices (all data)	R_1 = 0.0411, wR_2 = 0.0911	
Absolute structure parameter	0.028(3)	
Extinction coefficient	n/a	
Largest diff. peak and hole	0.881 and –0.613 e.Å^{-3}	

Table A.15. Crystal data and structure refinement for $\mathbf{Ni_s^{II}}$.

Identification code	CEC0062	
Empirical formula	$C_{45}H_{39}B_2F_8N_5NiP_2$	
Formula weight	944.08	
Temperature	100(2) K	
Wavelength	0.71073 Å	
Crystal system	Monoclinic	
Space group	$P2_1$; No. 4	
Unit cell dimensions	a = 16.9309(10) Å	α = 90°
	b = 15.3415(9) Å	β = 92.135(2)°
	c = 17.0319(10) Å	γ = 90°
Volume	4420.9(5) Å^3	
Formula units per unit cell	4	
Density (calculated)	1.418 g/cm^3	
Absorption coefficient	0.584 mm^{-1}	
F(000)	1936	
Crystal size	0.180 x 0.180 x 0.060 mm^3	
θ range for data collection	1.792 to 33.163°	
Index ranges	$-26 \le h \le 26$, $-23 \le k \le 23$, $-26 \le l \le 26$	
Reflections collected	118366	
Independent reflections	33654 [R(int) = 0.0417]	
Completeness to θ = 25.242°	99.8%	
Absorption correction	Semi-empirical from equivalents	
Max. and min. transmission	0.9420 and 0.8606	
Refinement method	Full-matrix least-squares on F^2	
Data/restraints/parameters	33654/1/1140	
Goodness-of-fit on F^2	1.079	
Final R indices [$I > 2\sigma(I)$]	R_1 = 0.0574, wR_2 = 0.1397	
R indices (all data)	R_1 = 0.0644, wR_2 = 0.1430	
Absolute structure parameter	0.070(10)	
Extinction coefficient	n/a	
Largest diff. peak and hole	1.050 and –1.055 e.Å^{-3}	

Table A.16. Crystal data and structure refinement for **Fe^{II}_{s}-OTf**.

CCDC No.	2109422	
Identification code	CEC0024	
Chemical formula	$C_{49}H_{42}F_6FeN_6O_6P_2S_2$	
Formula weight	1106.79 g/mol	
Temperature	100(2) K	
Wavelength	0.71073 Å	
Crystal system	monoclinic	
Space group	C1c1	
Unit cell dimensions	a = 12.1381(4) Å	α = 90°
	b = 21.3273(7) Å	β = 104.6460(10)°
	c = 20.1399(7) Å	γ = 90°
Volume	5044.3(3) Å^3	
Formula units per unit cell	4	
Density (calculated)	1.457 g/cm^3	
Absorption coefficient	0.522 mm^{-1}	
F(000)	2272	
Crystal size	0.106 x 0.237 x 0.258 mm^3	
θ range for data collection	1.91 to 37.50°	
Index ranges	$-20 \le h \le 20$, $-36 \le k \le 36$, $-34 \le l \le 34$	
Reflections collected	162253	
Independent reflections	26480 [R(int) = 0.0482]	
Coverage of independent reflections	100.0%	
Absorption correction	Multi-Scan	
Max. and min. transmission	0.9470 and 0.8770	
Refinement method	Full-matrix least-squares on F^2	
Data/restraints/parameters	26480/2/652	
Goodness-of-fit on F^2	1.047	
Final R indices [$I > 2\sigma(I)$]	R_1 = 0.0255, wR_2 = 0.0621	
R indices (all data)	R_1 = 0.0269, wR_2 = 0.0626	
Largest diff. peak and hole	0.518 and –0.357 e.Å^{-3}	

Table A.17. Crystal data and structure refinement for $\mathbf{Ni_s^I}$.

Identification code	CEC0090	
Empirical formula	$C_{49}H_{49}BF_4N_5NiOP_2$	
Formula weight	931.39	
Temperature	100(2) K	
Wavelength	0.71073 Å	
Crystal system	Triclinic	
Space group	P-1; No. 2	
Unit cell dimensions	a = 9.0725(4) Å	α = 68.104(2)°
	b = 14.7988(8) Å	β = 78.956(2)°
	c = 18.8509(10) Å	γ = 80.691(2)°
Volume	2293.5(2) Å^3	
Formula units per unit cell	2	
Density (calculated)	1.349 g/cm^3	
Absorption coefficient	0.552 mm^{-1}	
F(000)	970	
Crystal size	0.12 x 0.03 x 0.01 mm^3	
θ range for data collection	2.201 to 30.000°	
Index ranges	$-12 \le h \le 12$, $-20 \le k \le 20$, $-26 \le l \le 26$	
Reflections collected	129041	
Independent reflections	13378 [R(int) = 0.0941]	
Completeness to θ = 25.242°	100.0%	
Absorption correction	Semi-empirical from equivalents	
Max. and min. transmission	0.9705 and 0.9045	
Refinement method	Full-matrix least-squares on F^2	
Data/restraints/parameters	13378/54/572	
Goodness-of-fit on F^2	1.123	
Final R indices [$I > 2\sigma(I)$]	R_1 = 0.0589, wR_2 = 0.1085	
R indices (all data)	R_1 = 0.0779, wR_2 = 0.1151	
Extinction coefficient	n/a	
Largest diff. peak and hole	0.763 and –0.693 e.Å^{-3}	

Table A.18. Selected interatomic distances (Å) and bond angles (°) for acetonitrile-coordinated complexes $\mathbf{M_s^z}$ in this work.

	M-N_{Py}	M-P^1	M-P^2	M-N_{eq}	P^1-M-N_{Py}	P^1-M-P^2
$\mathbf{Fe_s^{II}}$	1.9811(15)	2.2339(5)	2.2546(5)	1.9339(16)	82.31(5)	164.59(2)
$\mathbf{Co_s^{II}}$	1.9318(14)	2.2121(5)	2.2168(5)	1.8930(16)	85.15(4)	169.198(18)
$\mathbf{Ni_s^{II}}$	1.887(3)	2.1726(9)	2.1794(9)	1.845(3)	85.98(9)	169.37(4)
$\mathbf{Fe_s^{II}}$-OTf	1.9717(9)	2.2411(3)	2.2238(3)	1.9258(10)	83.67(3)	167.824(12)
$\mathbf{Ni_s^{I}}$	2.0694(18)	2.2479(6)	2.2162(6)	2.041(2)	81.33(5)	143.40(2)

c) Calculation of Geometry Indices

Since tetra- and pentacoordinate complexes can form polyhedra of different geometries, the geometry index τ was used to determine the closest idealized structure and the extent of the deviation. The calculation of τ is based on the two largest valence angles, α and β, of the coordination center ($\beta > \alpha$), which are summarized in Table A.19 for the tetra- and pentacoordinate complexes investigated in this work.

Table A.19. Two largest valence angles ($\beta > \alpha$) of the coordination center for tetra- and pentacoordinate complexes investigated in this study.

	α (°)	β (°)
$\mathbf{Fe_{Cl}^{II}}$	130.41(2)	153.00(3)
$\mathbf{Co_s^{II}}$	166.53(7)	169.198(18)
$\mathbf{Co_{Cl}^{II}}$	164.14(4)	166.28(2)
$\mathbf{Ni_s^{II}}$	168.37(5)	174.73(16)
$\mathbf{Ni_{Cl}^{II}}$	155.51(2)	169.44(4)
$\mathbf{Ni_s^{I}}$	143.40(2)	173.65(8)
$\mathbf{Cu_{Cl}^{I}}$	114.37(2)	135.98(2)
$\mathbf{Cu_I^{I}}$	118.90(2)	133.22(2)
$\mathbf{Zn_{Cl}^{II}}$	112.60(1)	113.82(2)
$\mathbf{Zn_{OTf}^{II}}$	129.09(3)	178.10(9)

The geometry indices τ_4 of tetracoordinate compounds $\mathbf{Ni}_{\mathbf{s}}^{\mathbf{II}}$, $\mathbf{Cu}_{\mathbf{Cl}}^{\mathbf{I}}$, $\mathbf{Cu}_{\mathbf{I}}^{\mathbf{I}}$, and $\mathbf{Zn}_{\mathbf{Cl}}^{\mathbf{II}}$ were calculated according to equation (A.1) reported by the HOUSER group (with $\theta \approx 109.5°$).[1]

$$\tau_4 = \frac{360° - (\alpha + \beta)}{360° - 2\theta} \tag{A.1}$$

Based on the result, the two extreme structures

- square plane: $\beta = \alpha = 180° \rightarrow \tau_4 = 0$,
- tetrahedron: $\beta = \alpha = \theta \approx 109.5° \rightarrow \tau_4 = 1$

and their intermediates, trigonal pyramid ($\tau_4 = 0.85$) and seesaw/butterfly ($\tau_4 \approx 0.43$), can be defined.

The geometry indices τ_5 of pentacoordinate compounds $\mathbf{Fe}_{\mathbf{Cl}}^{\mathbf{II}}$, $\mathbf{Co}_{\mathbf{s}}^{\mathbf{II}}$, $\mathbf{Co}_{\mathbf{Cl}}^{\mathbf{II}}$, $\mathbf{Ni}_{\mathbf{s}}^{\mathbf{I}}$, $\mathbf{Ni}_{\mathbf{Cl}}^{\mathbf{II}}$, and $\mathbf{Zn}_{\mathbf{OTf}}^{\mathbf{II}}$ were calculated using equation (A.2) reported by ADDISON et al.[2]

$$\tau_5 = \frac{\beta - \alpha}{60°} \tag{A.2}$$

In this case, the value enables differentiation between the

- square-based pyramid: $\beta = \alpha = 180° \rightarrow \tau_5 = 0$ and
- trigonal bipyramid: $\beta = 180°$, $\alpha = 120° \rightarrow \tau_5 = 1$.

Appendix B: NMR Studies & CVs under Inert Atmosphere

Halide & Triflate Complexes

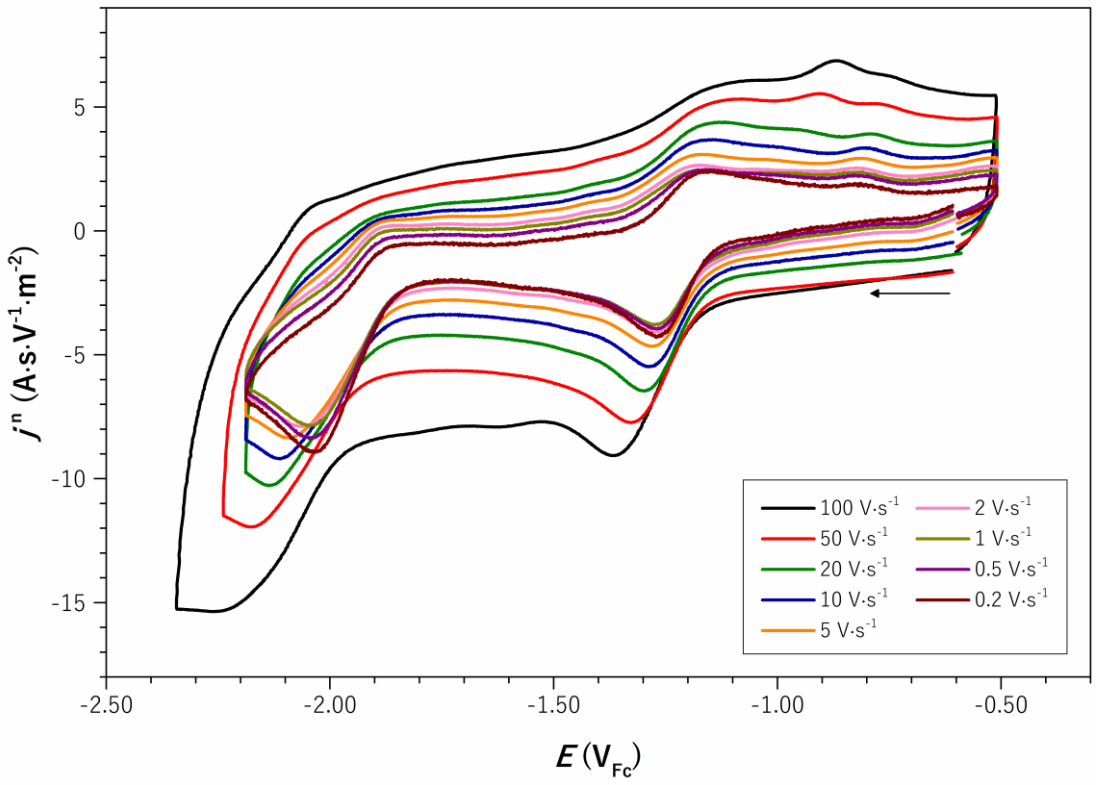

Figure B.1. CVs of $\mathbf{Co}^{\mathbf{II}}_{\mathbf{Cl}}$ at varying scan rates.

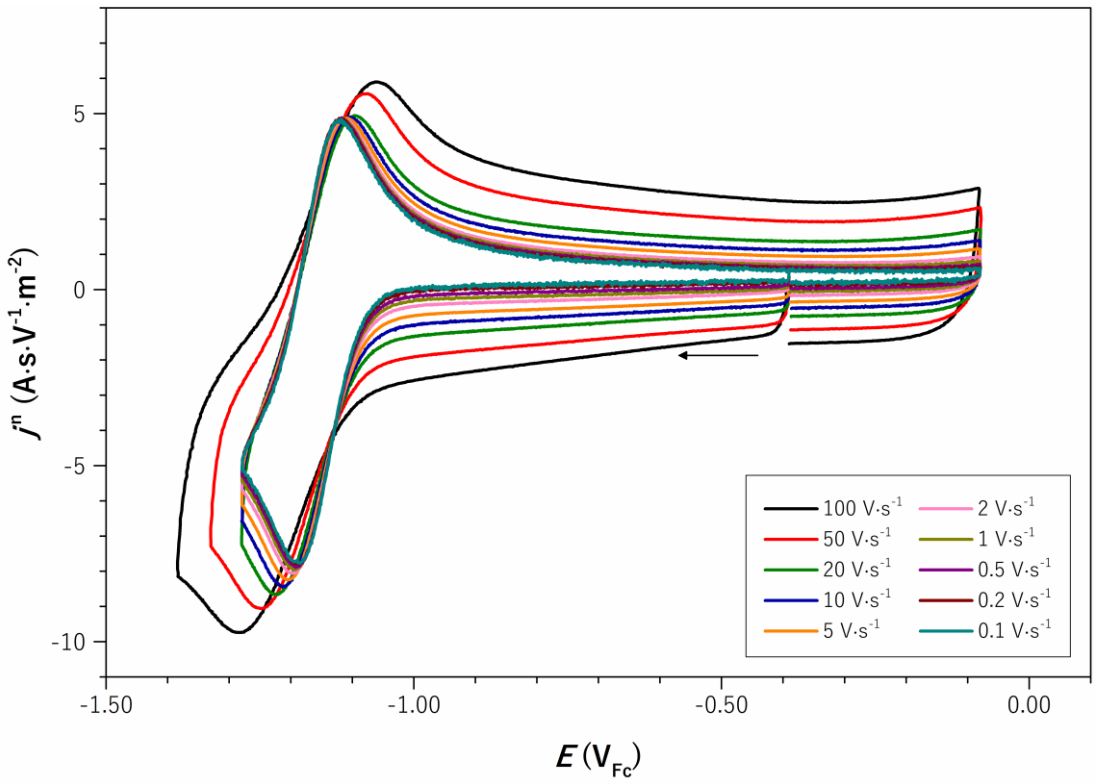

Figure B.2. CVs of the $Ni^{II/I}$ wave of $\mathbf{Ni}^{\mathbf{II}}_{\mathbf{Cl}}$ at varying scan rates.

Acetonitrile Complexes

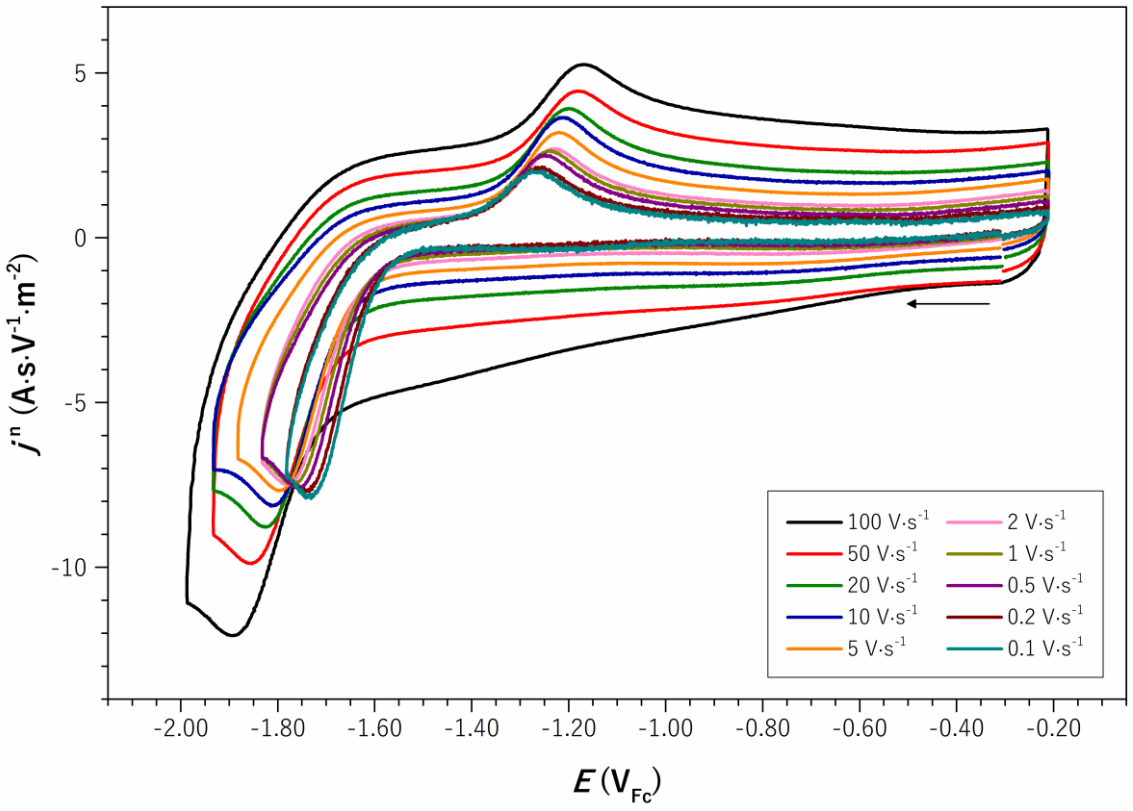

Figure B.3. CVs of the $Fe^{II/I}$ wave of $\mathbf{Fe_s^{II}}$ at varying scan rates.

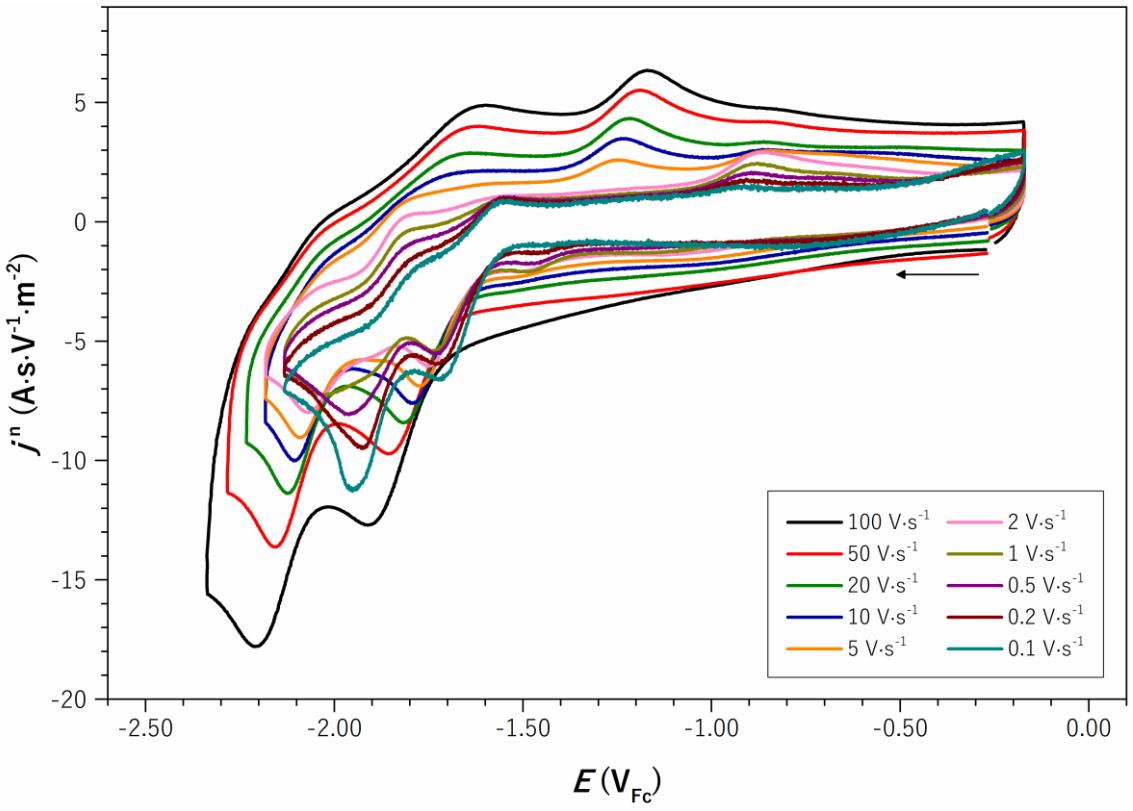

Figure B.4. CVs of $\mathbf{Fe_s^{II}}$ at varying scan rates.

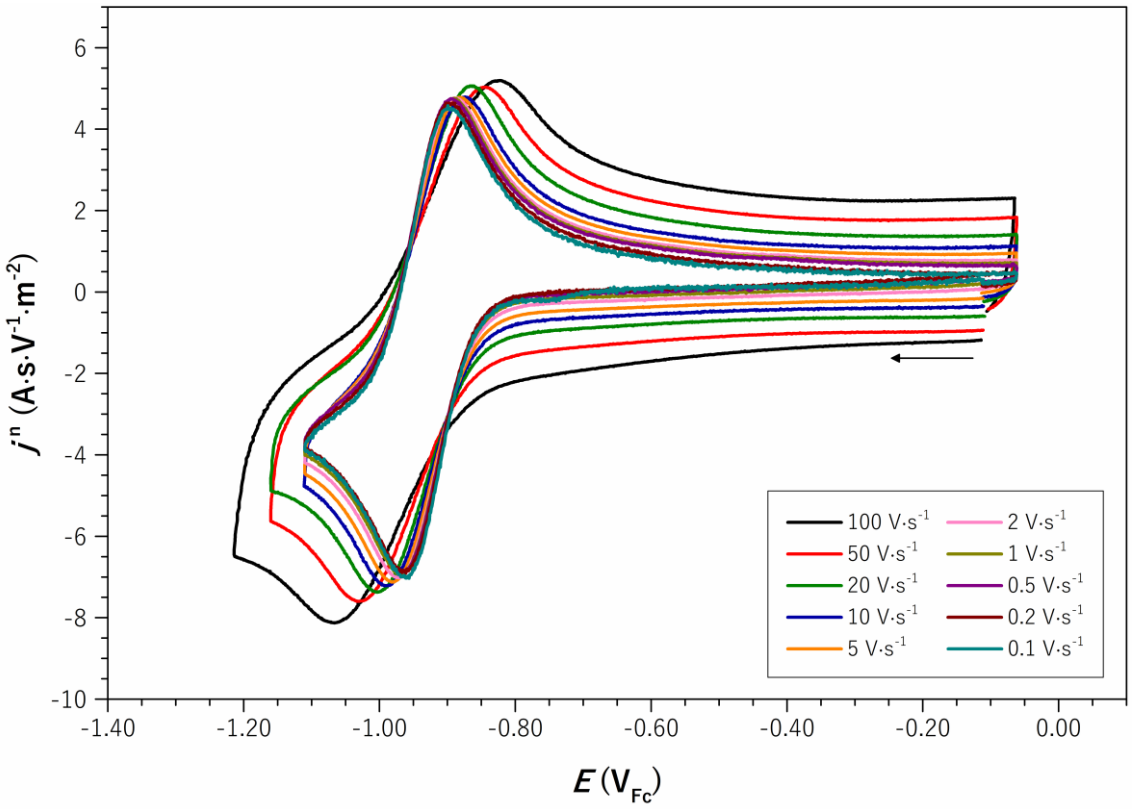

Figure B.5. CVs of the $Co^{II/I}$ wave of $\mathbf{Co_s^{II}}$ at varying scan rates.

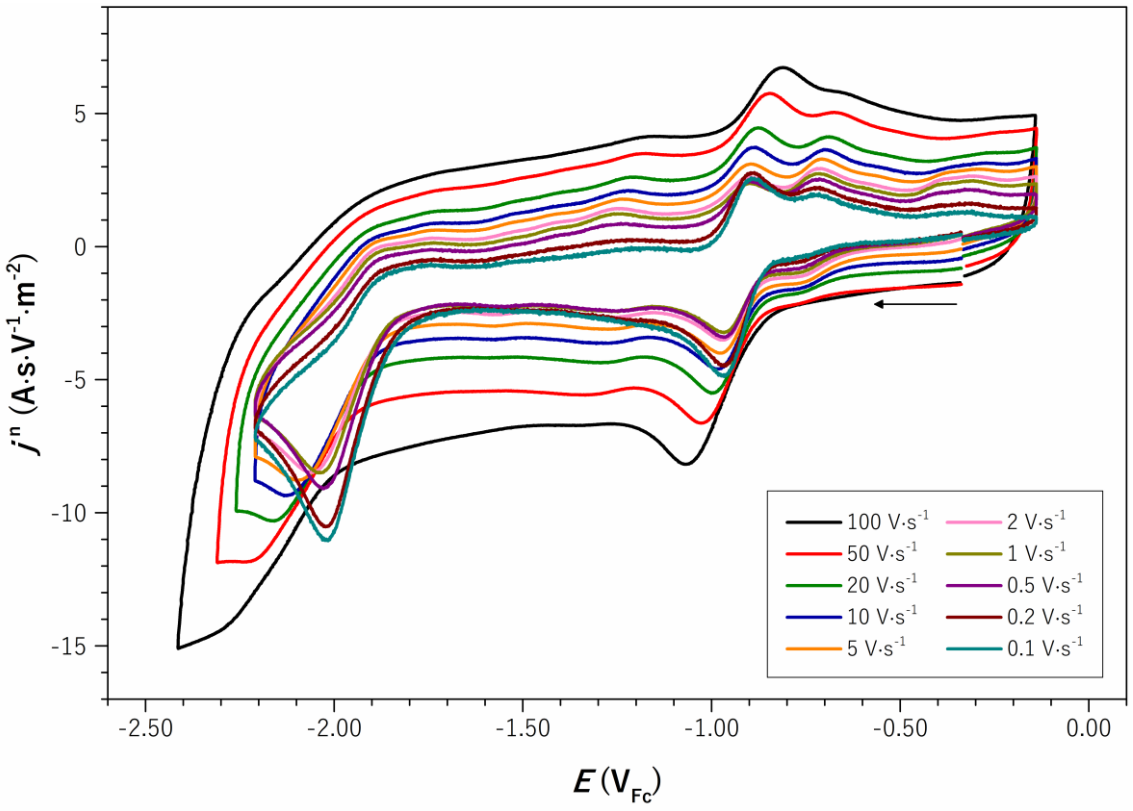

Figure B.6. CVs of $\mathbf{Co_s^{II}}$ at varying scan rates.

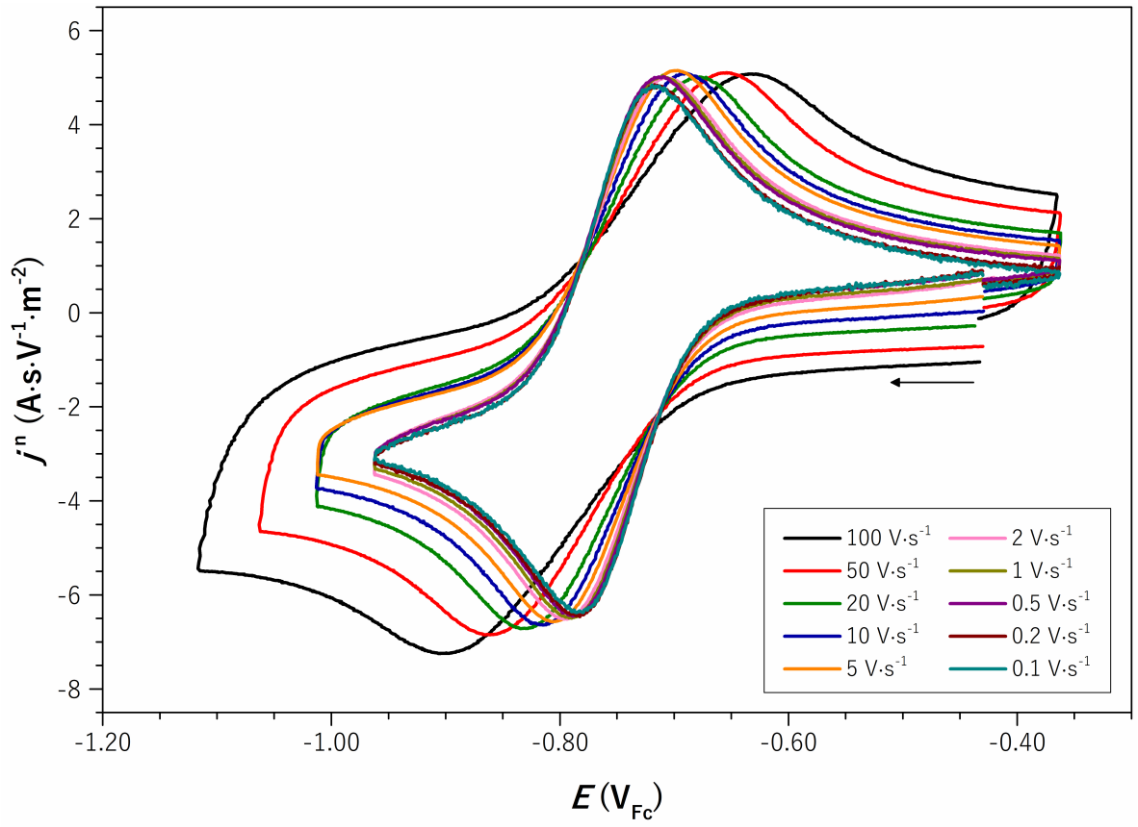

Figure B.7. CVs of the $Ni^{II/I}$ wave of $\mathbf{Ni_s^{II}}$ at varying scan rates.

NMR Studies under Addition of TBACl

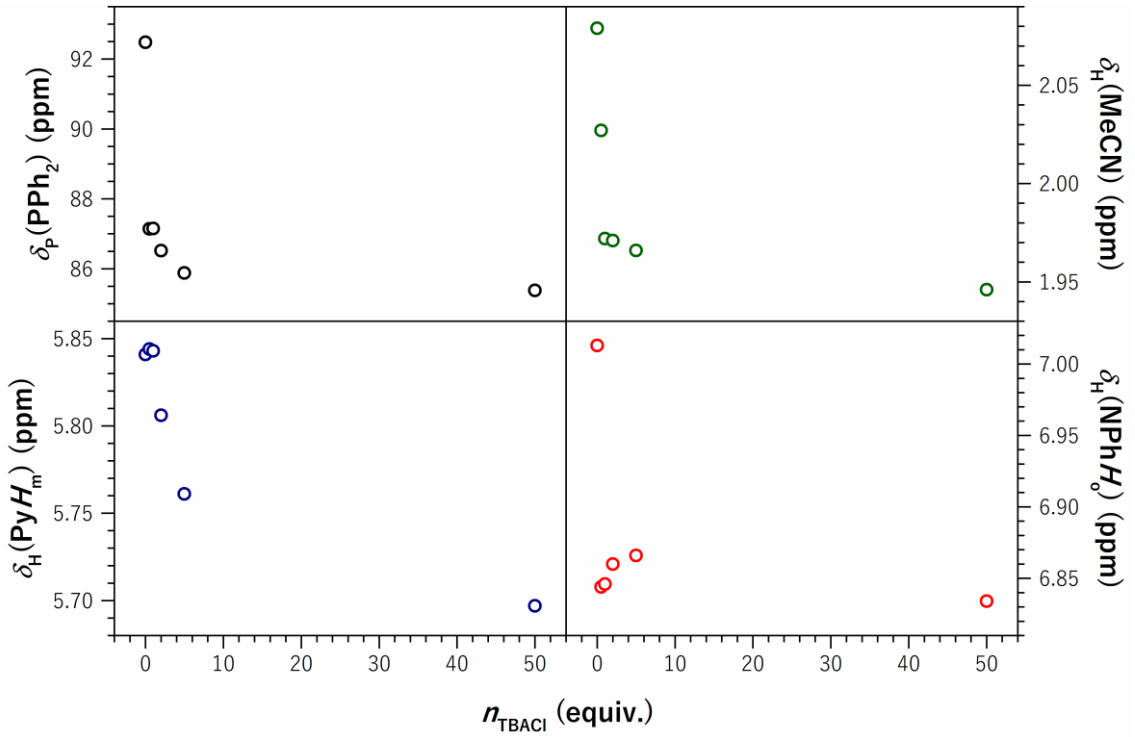

Figure B.8. Chemical shifts of selected $\mathbf{Ni_s^{II}}$ NMR peaks in CD_2Cl_2 at 162 MHz and 296 K vs. equivalents of added TBACl. A value of 50 equiv. was estimated for the data point in excess of TBACl since the exact added amount was not determined.

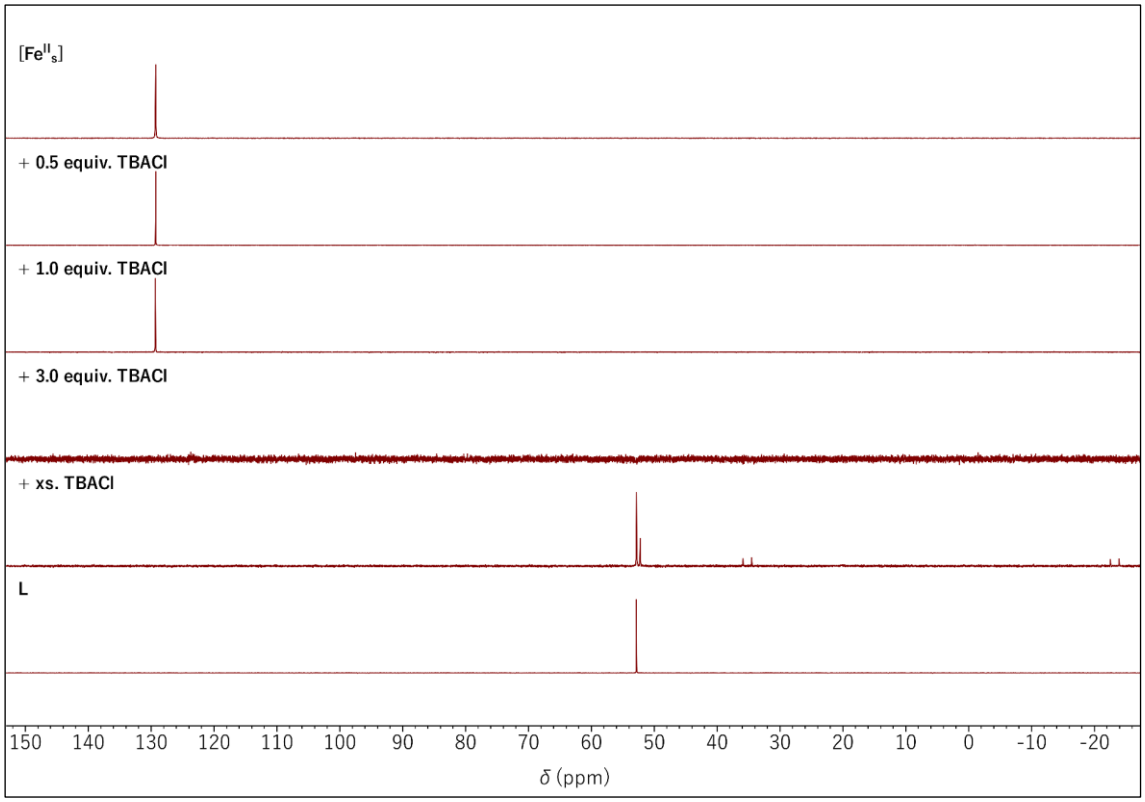

Figure B.9. $^{31}P\{^1H\}$ NMR study of $\mathbf{Fe_s^{II}}$ at varying amounts of TBACl in CD_2Cl_2 at 162 MHz and 296 K. The spectrum of **L** is shown as a reference.

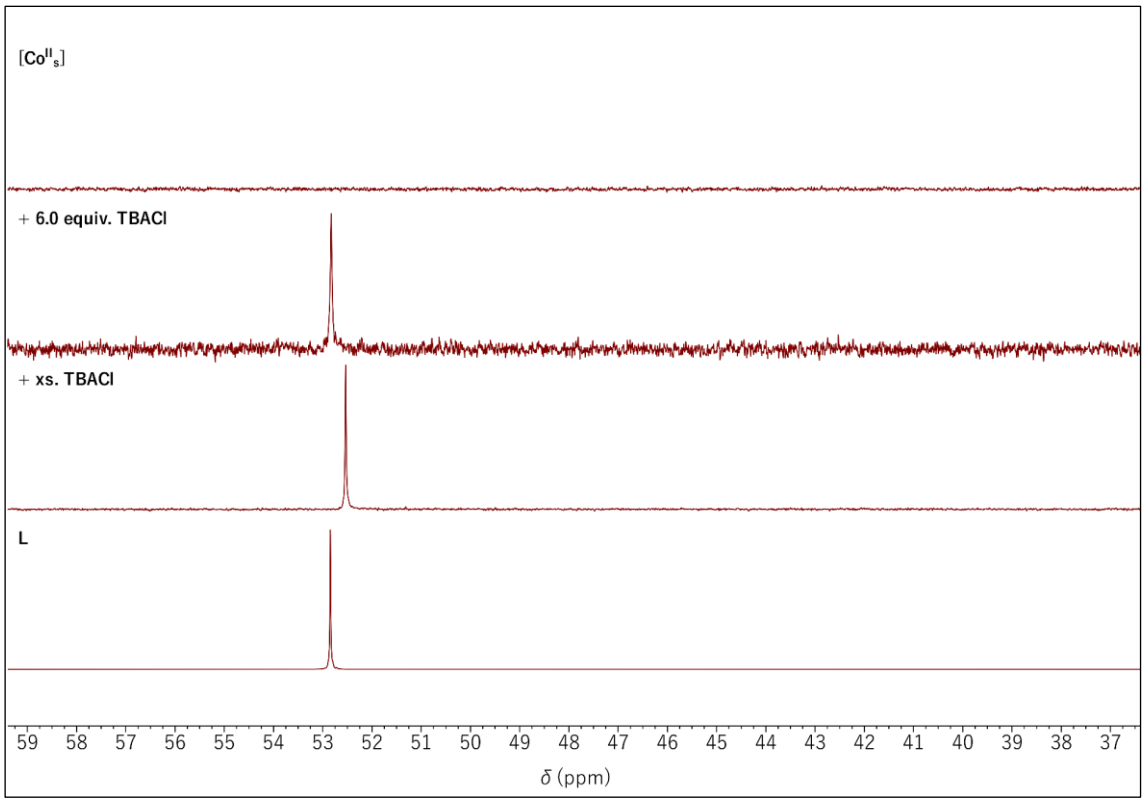

Figure B.10. $^{31}P\{^{1}H\}$ NMR study of $\mathbf{Co^{II}_s}$ at varying amounts of TBACl in CD_2Cl_2 at 162 MHz and 296 K. The spectrum of **L** is shown as a reference.

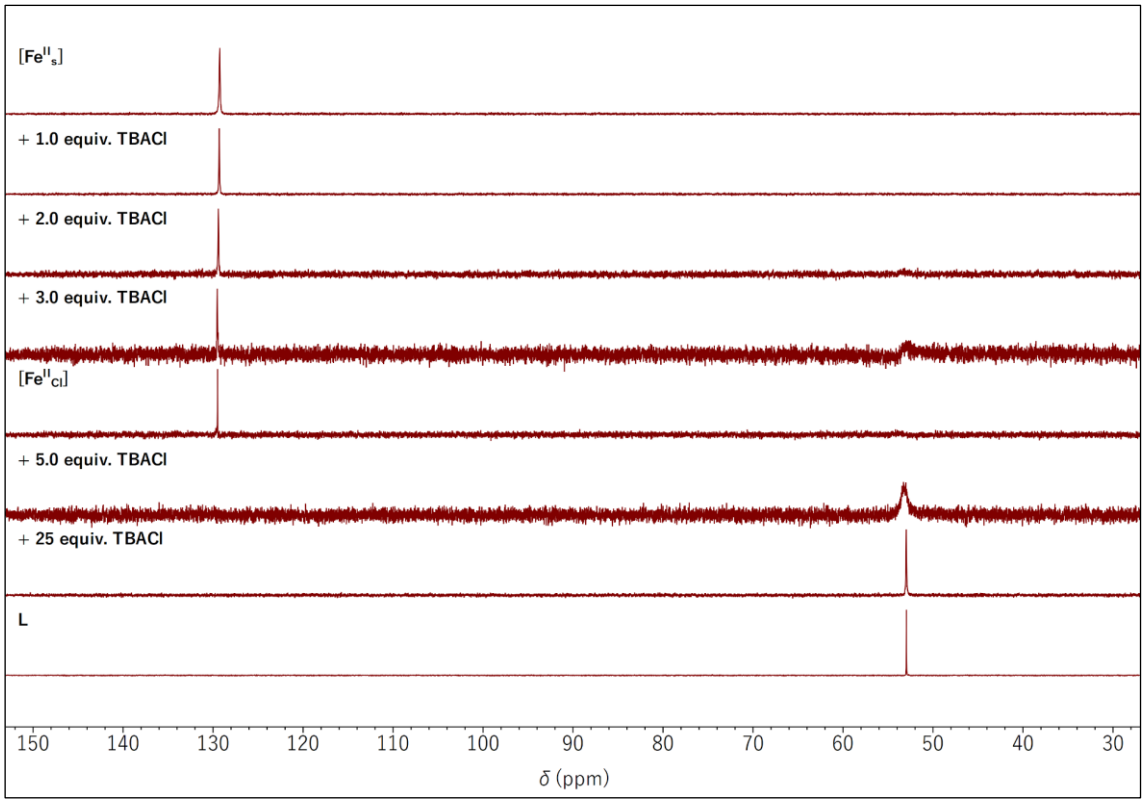

Figure B.11. $^{31}P\{^{1}H\}$ NMR study of $\mathbf{Fe^{II}_s}$ at varying amounts of TBACl in CD_3CN at 162 MHz and 296 K. Spectra of $\mathbf{Fe^{II}_{Cl}}$ and **L** are shown as references.

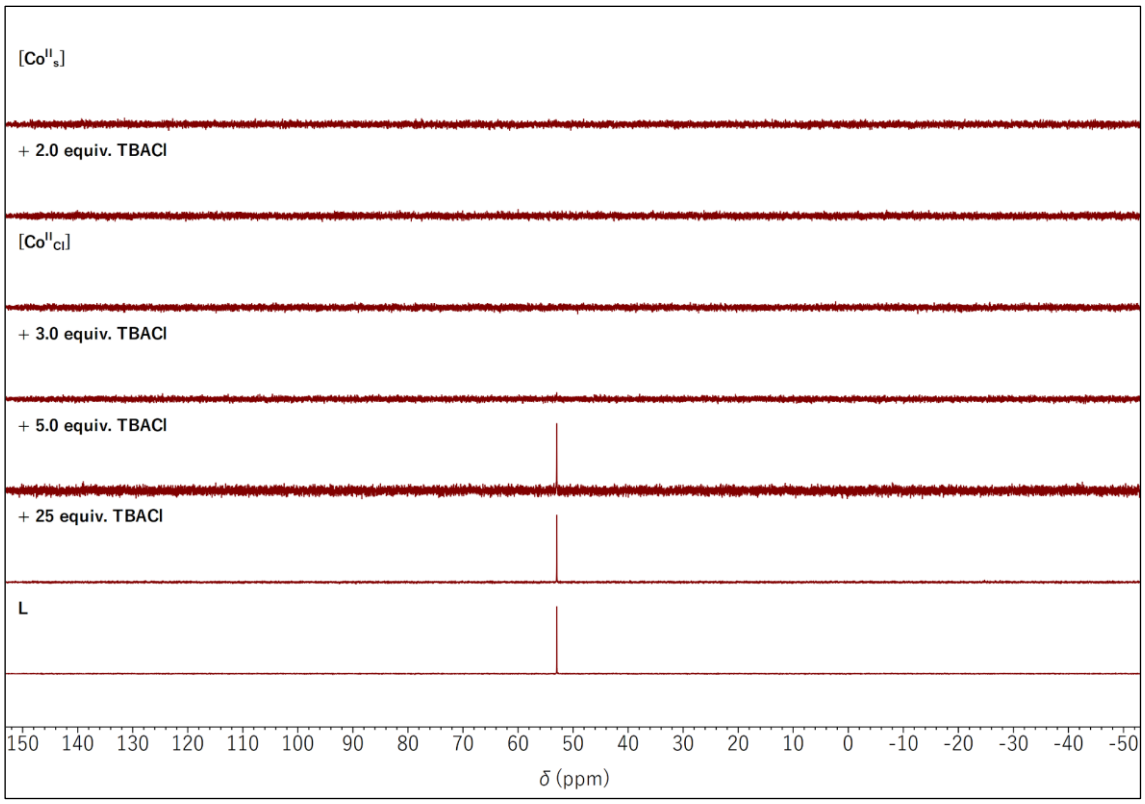

Figure B.12. $^{31}P\{^{1}H\}$ NMR study of $\mathbf{Co^{II}_{s}}$ at varying amounts of TBACl in CD_3CN at 162 MHz and 296 K. Spectra of $\mathbf{Co^{II}_{Cl}}$ and **L** are shown as references.

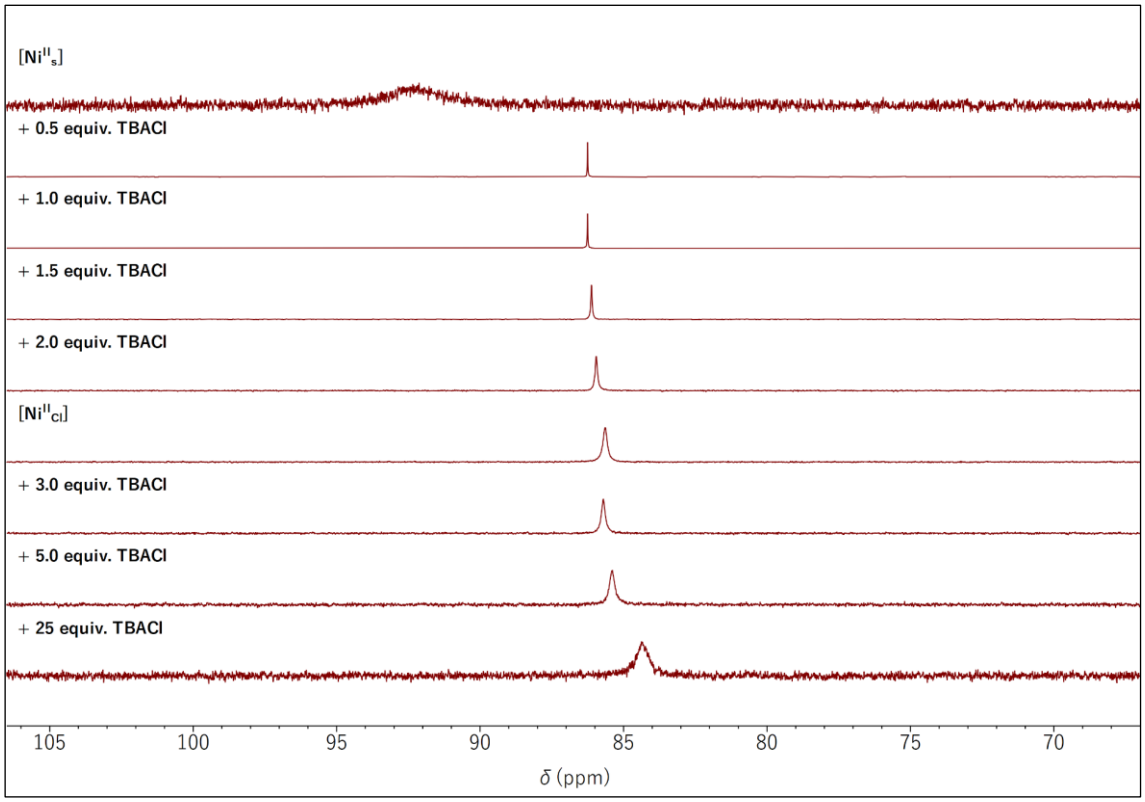

Figure B.13. $^{31}P\{^{1}H\}$ NMR study of $\mathbf{Ni^{II}_{s}}$ at varying amounts of TBACl in CD_3CN at 162 MHz and 296 K. The spectrum of $\mathbf{Ni^{II}_{Cl}}$ is shown as a reference.

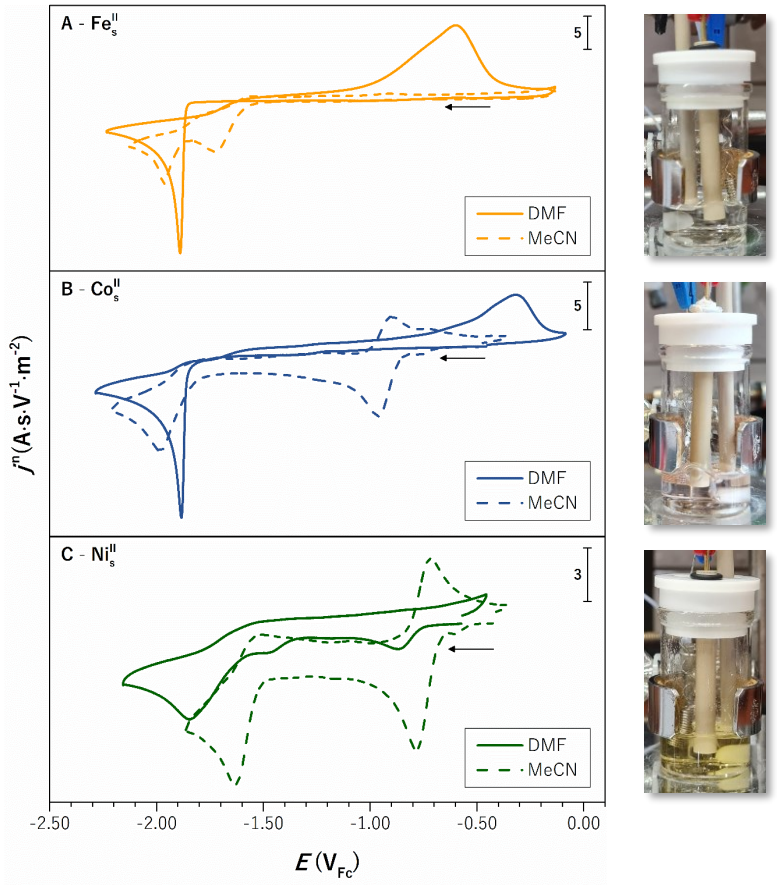

Figure B.14. Left: CVs of (A) $\mathbf{Fe_s^{II}}$, (B) $\mathbf{Co_s^{II}}$, and (C) $\mathbf{Ni_s^{II}}$ in DMF (solid line) and MeCN (dashed line). Right: Corresponding solutions in DMF electrolyte.

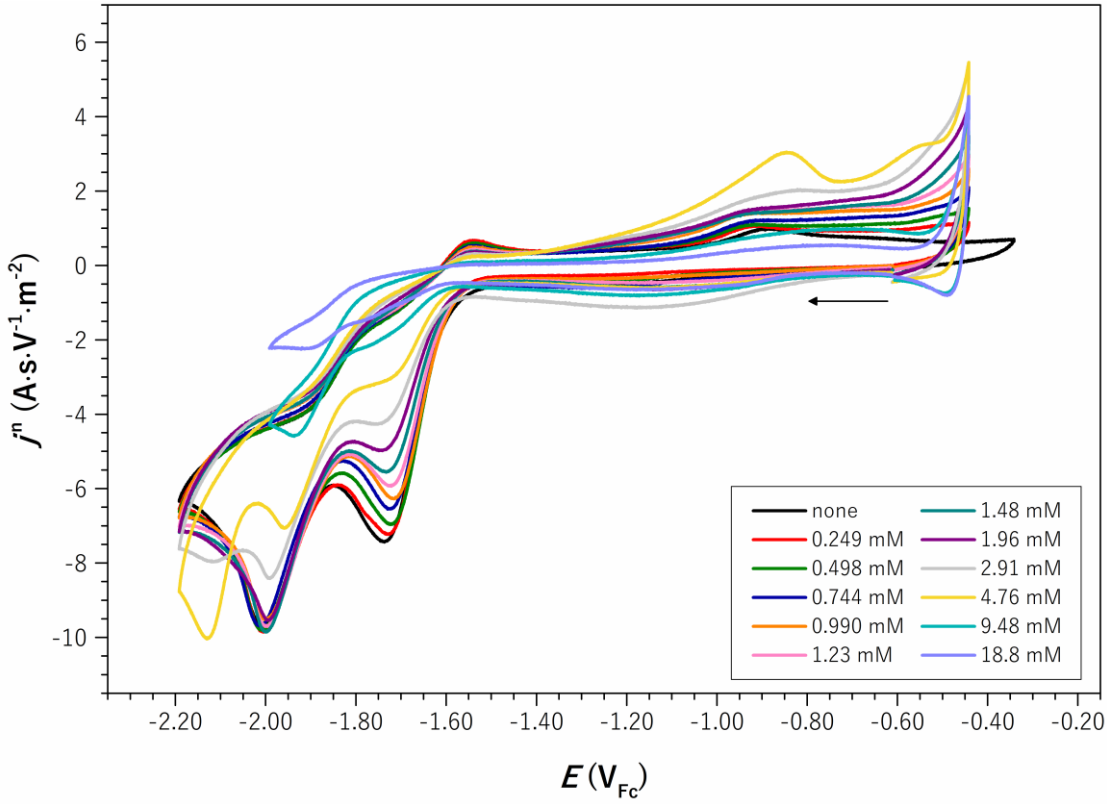

Figure B.15. CVs of $\mathbf{Fe_s^{II}}$ at varying concentrations of TBACl.

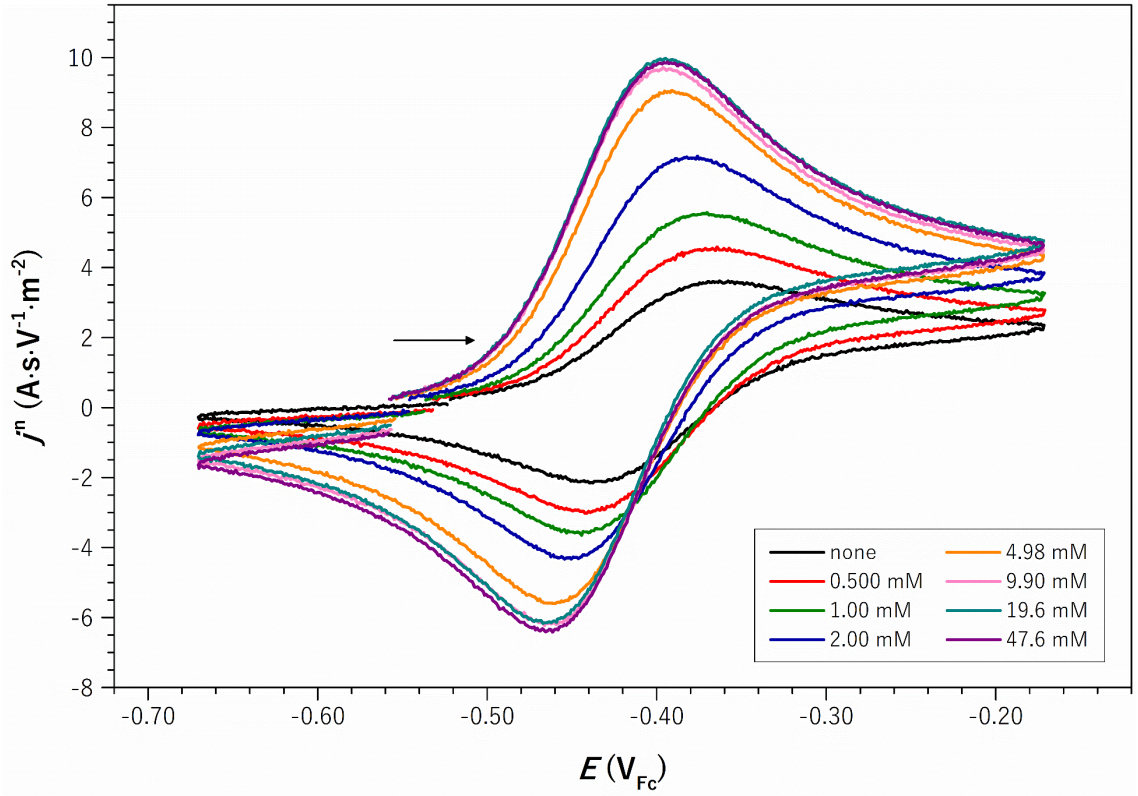

Figure B.16. CVs of the reversible wave emerging upon addition of TBACl to $\mathbf{Fe}^{\mathbf{II}}_{\mathbf{Cl}}$.

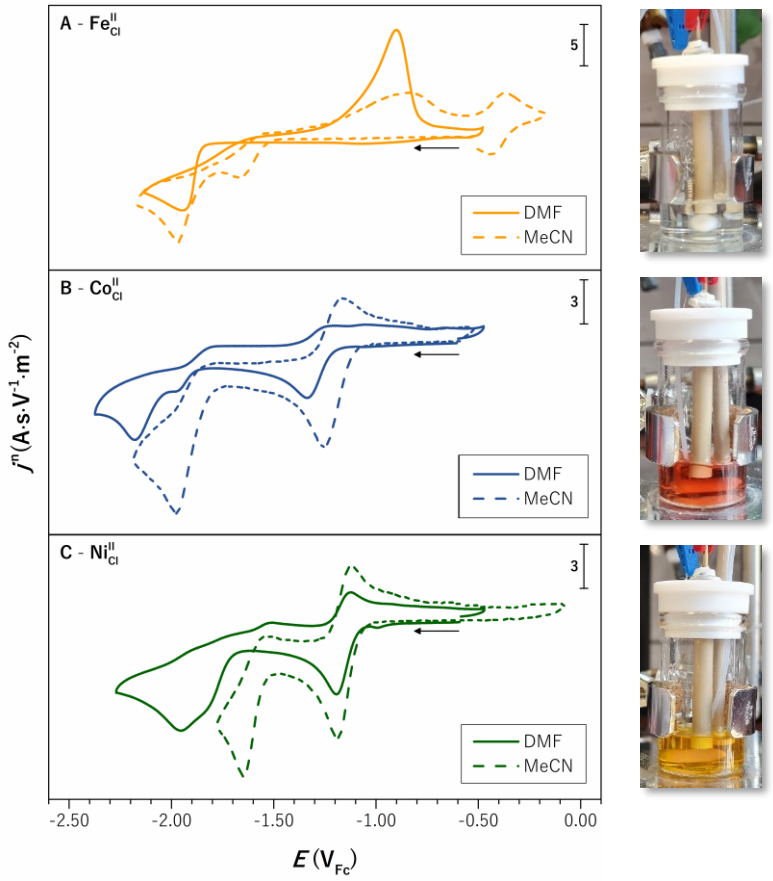

Figure B.17. Left: CVs of (A) $\mathbf{Fe}^{\mathbf{II}}_{\mathbf{Cl}}$, (B) $\mathbf{Co}^{\mathbf{II}}_{\mathbf{Cl}}$, and (C) $\mathbf{Ni}^{\mathbf{II}}_{\mathbf{Cl}}$ in DMF (solid line) and MeCN (dashed line). Right: Corresponding solutions in DMF electrolyte.

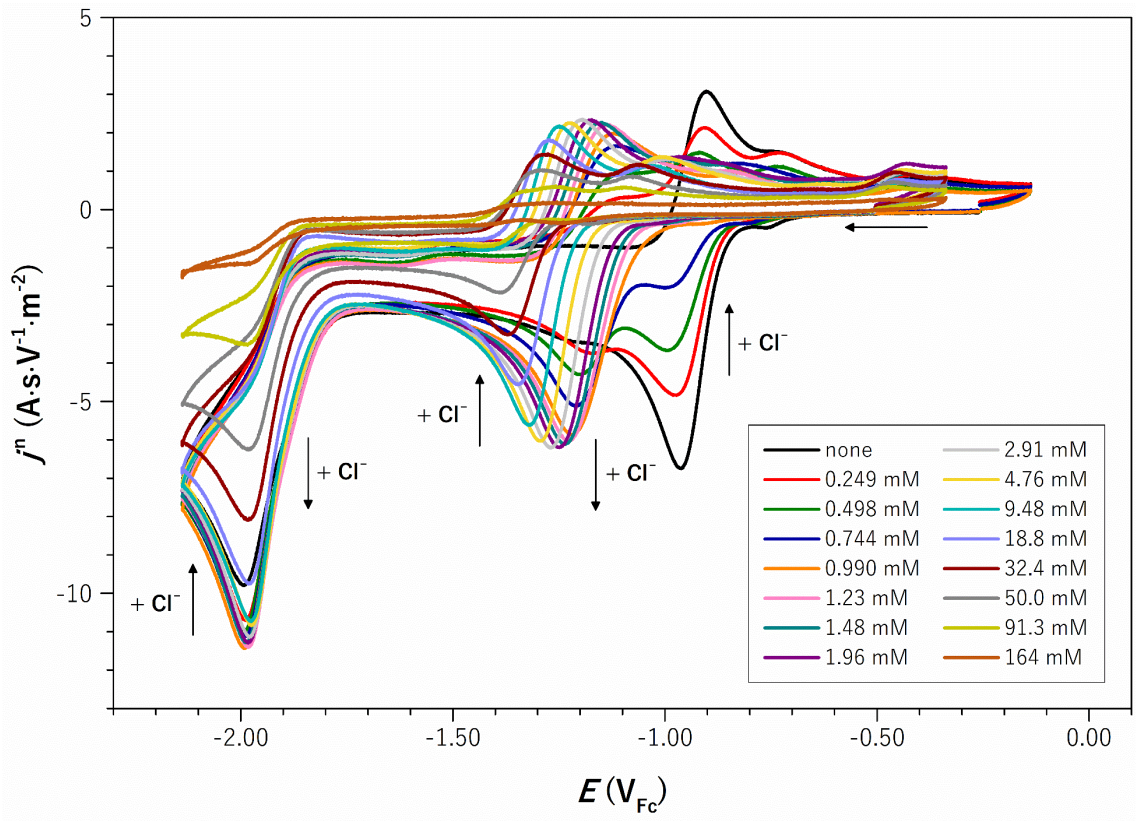

Figure B.18. CVs of $\mathbf{Co_s^{II}}$ at varying concentrations of TBACl.

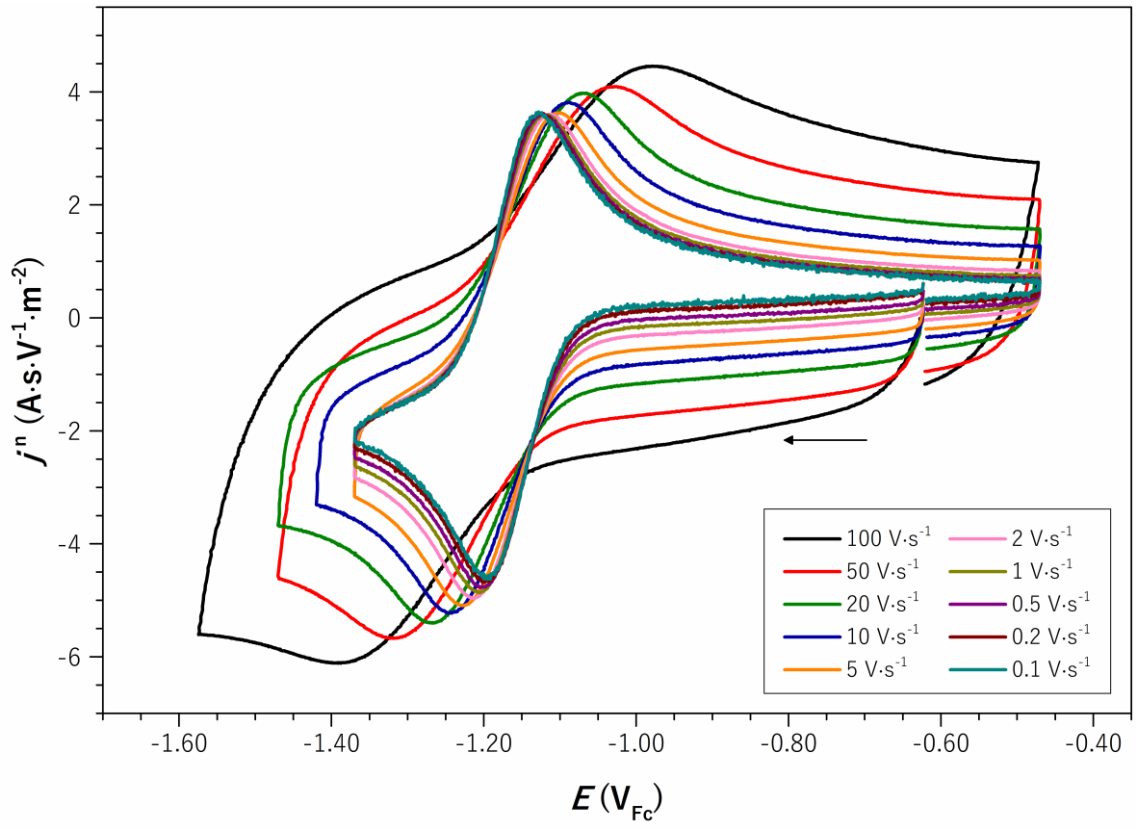

Figure B.19. CVs of the $Ni^{II/I}$ wave of $\mathbf{Ni_{Cl}^{II}}$ at varying scan rates in DMF.

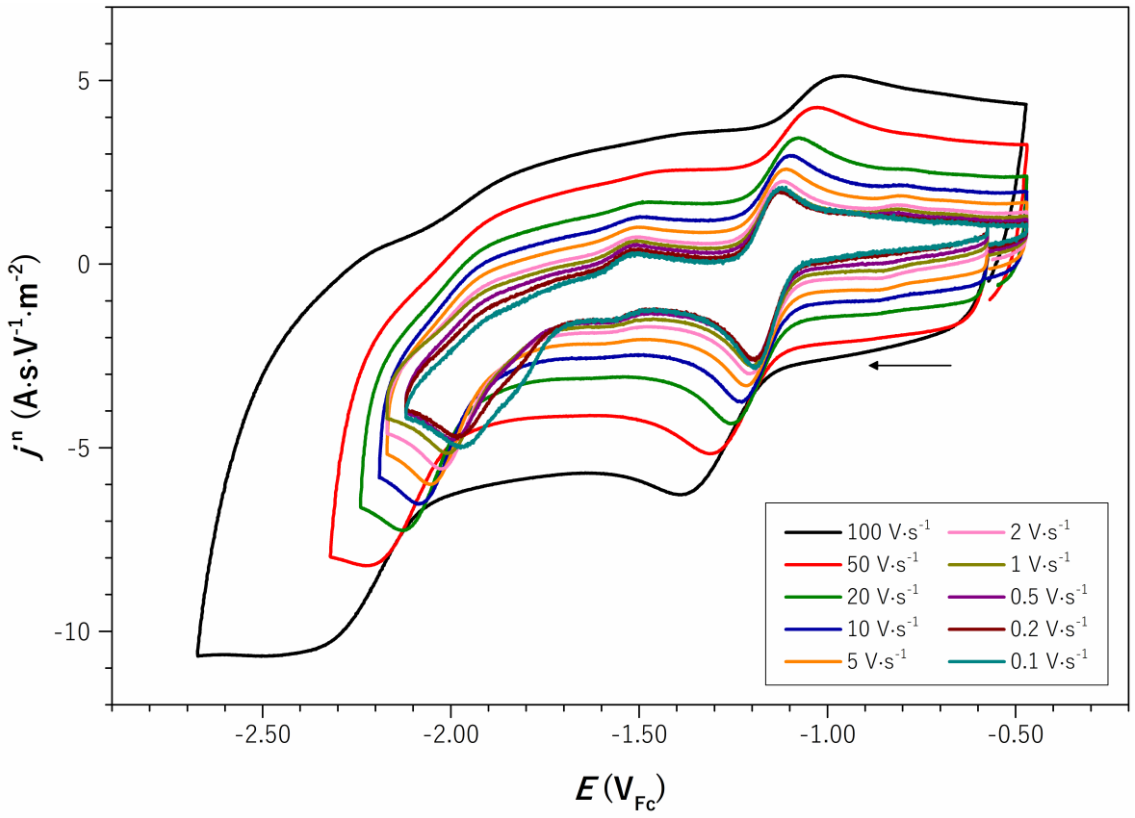

Figure B.20. CVs of $\mathbf{Ni}^{\mathbf{II}}_{\mathbf{Cl}}$ at varying scan rates in DMF.

Appendix C: CVs & Product Data under Carbon Dioxide Atmosphere

Addition of Carbon Dioxide

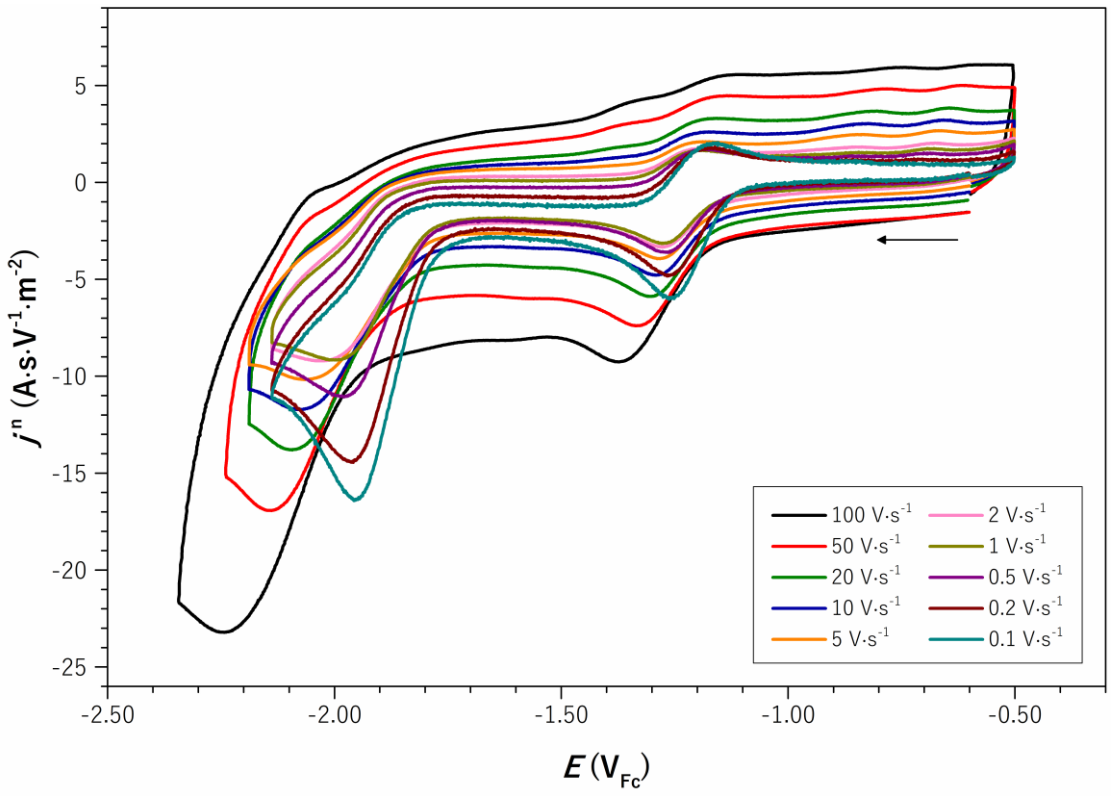

Figure C.1. CVs of $\mathbf{Co}_{Cl}^{II}$ at varying scan rates under CO_2 atmosphere.

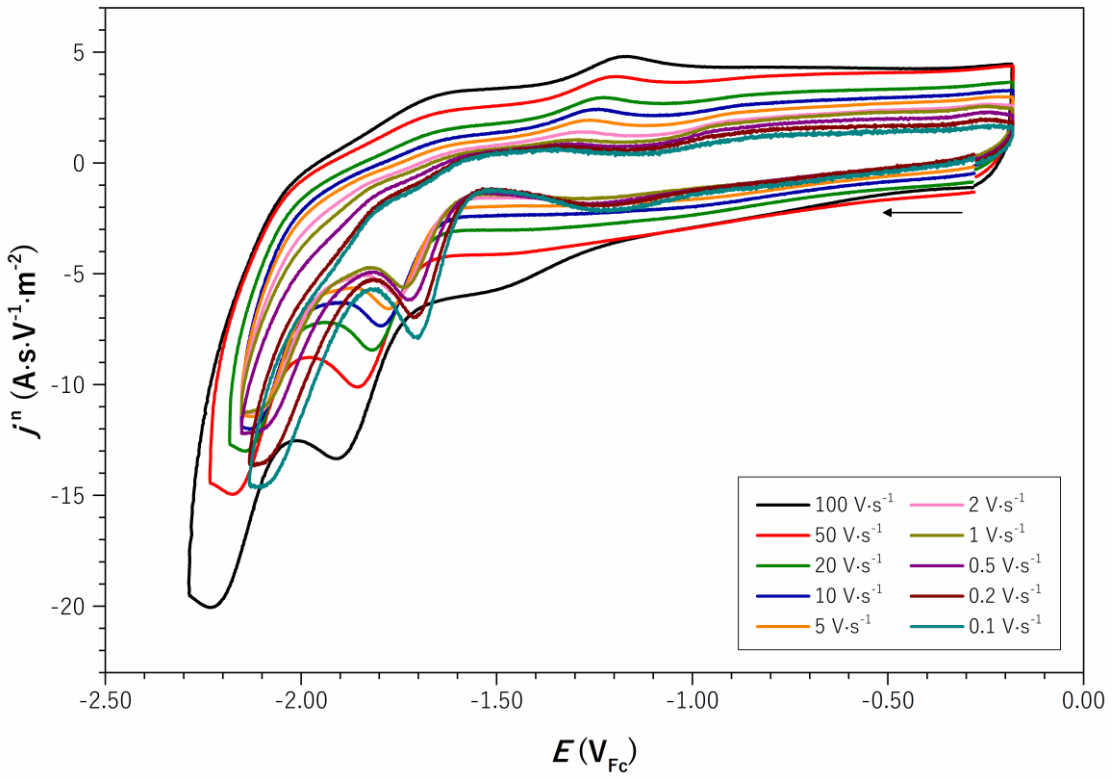

Figure C.2. CVs of $\mathbf{Fe}_{s}^{II}$ at varying scan rates under CO_2 atmosphere.

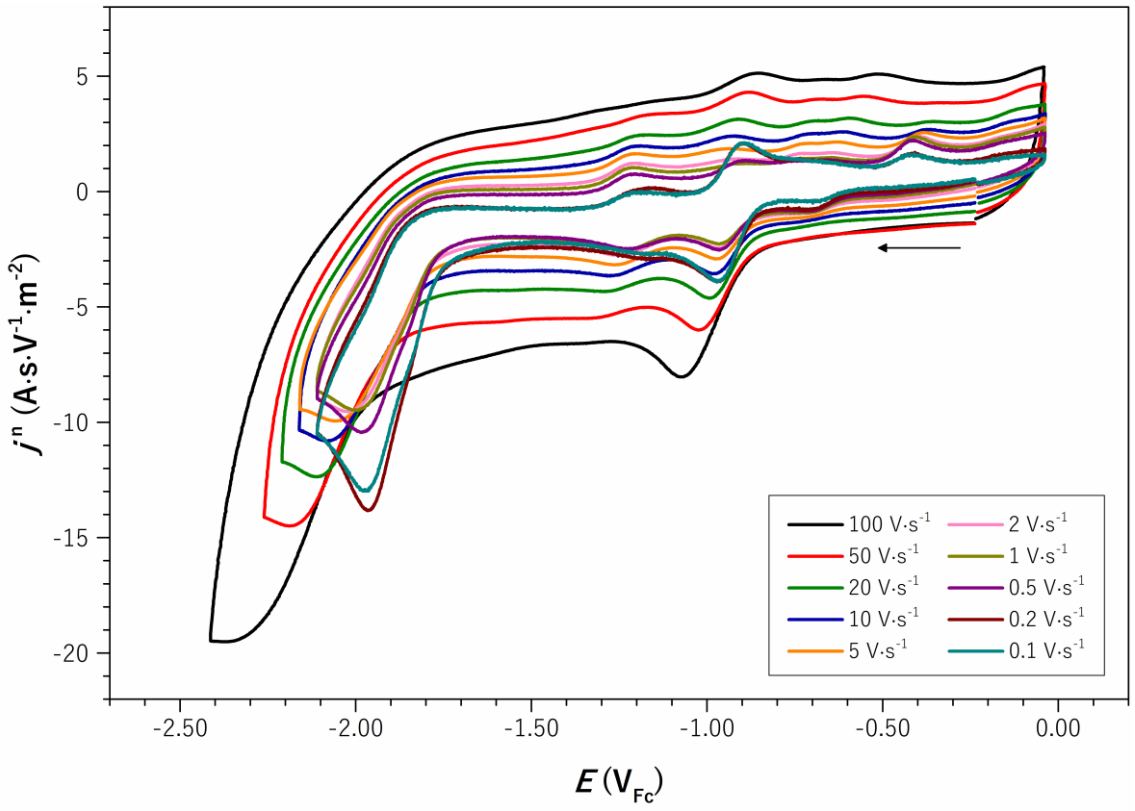

Figure C.3. CVs of $\mathbf{Co_s^{II}}$ at varying scan rates under CO_2 atmosphere.

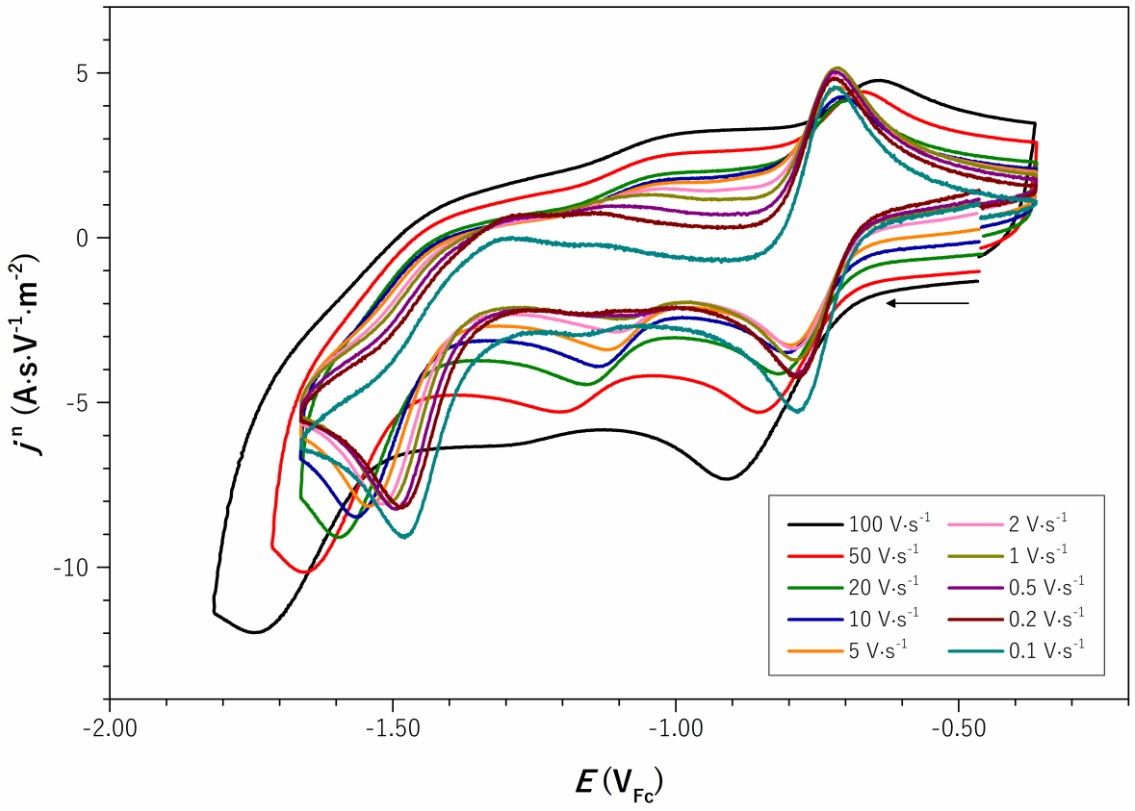

Figure C.4. CVs of $\mathbf{Ni_s^{II}}$ at varying scan rates under CO_2 atmosphere.

Addition of a LEWIS Acid

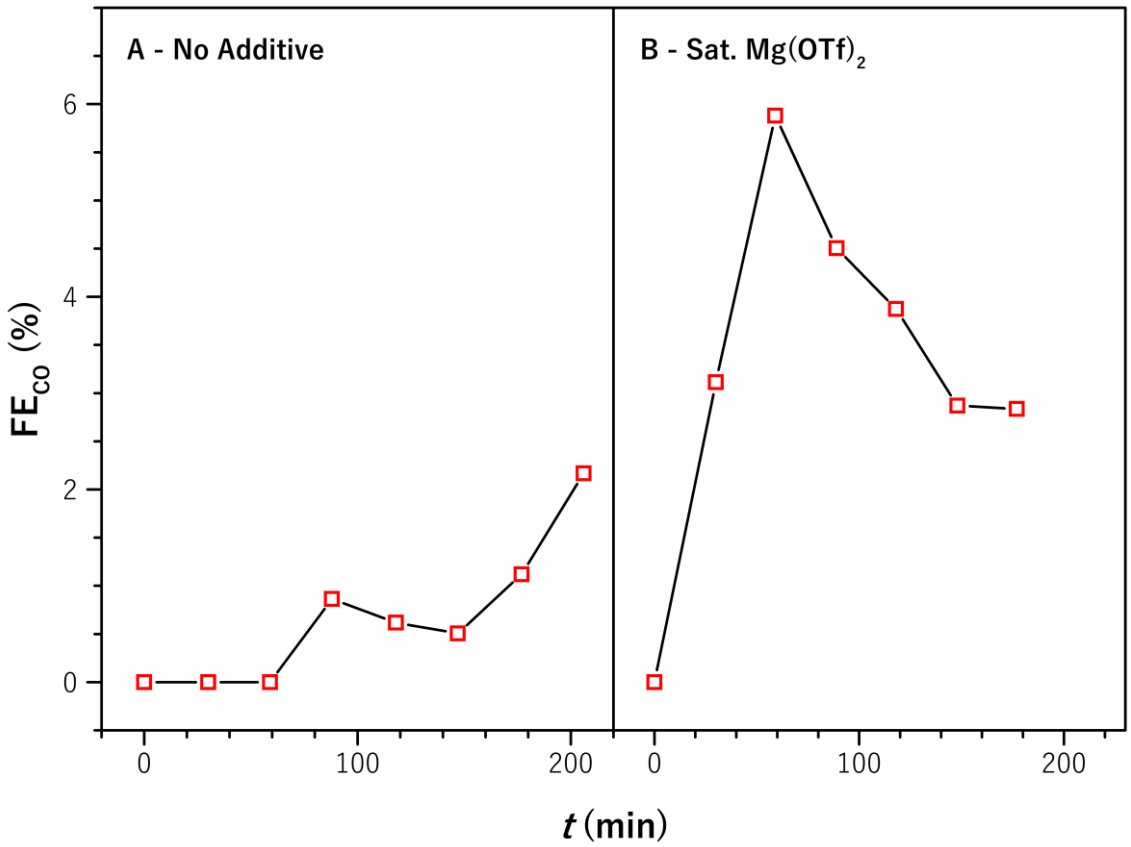

Figure C.5. FE_{CO} vs. time profile for the CPE of $\mathbf{Co_s^{II}}$ (A) without additive and (B) with saturated $Mg(OTf)_2$.

Addition of Brønsted Acids

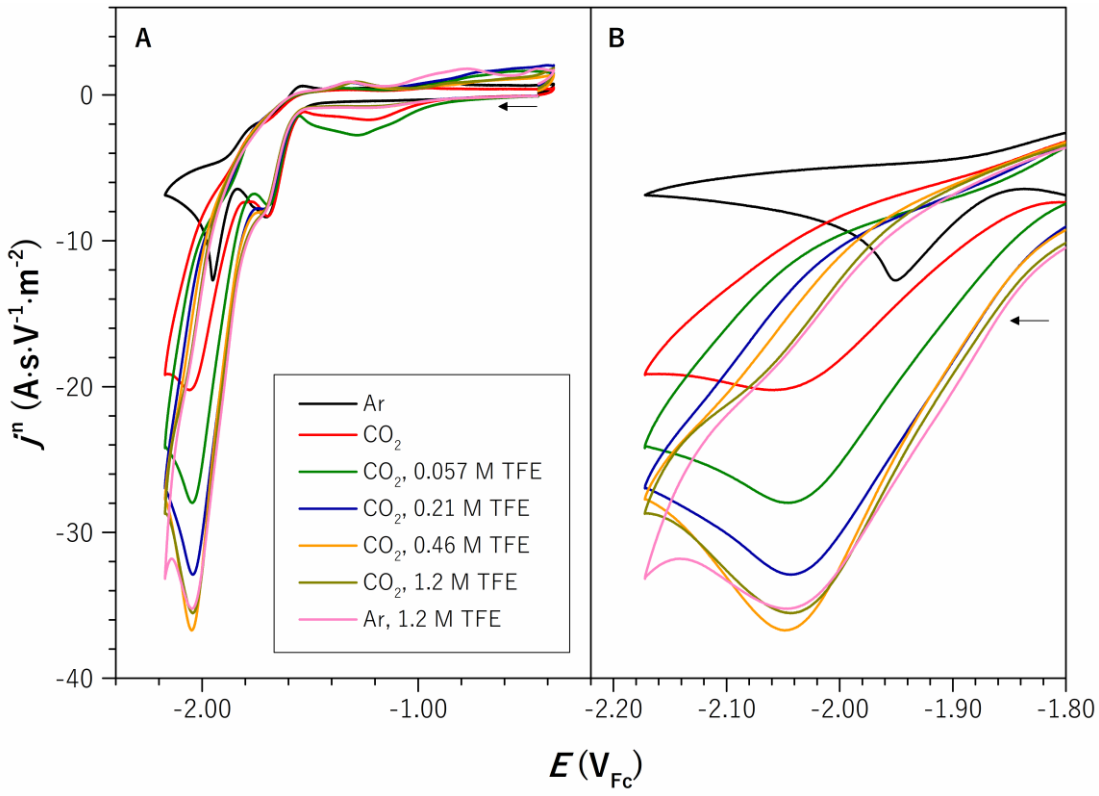

Figure C.6. (A) CVs of $\mathbf{Fe_s^{II}}$ at varying concentrations of TFE under argon or CO_2 atmosphere and (B) zoom on the $Fe^{I/0}$ wave.

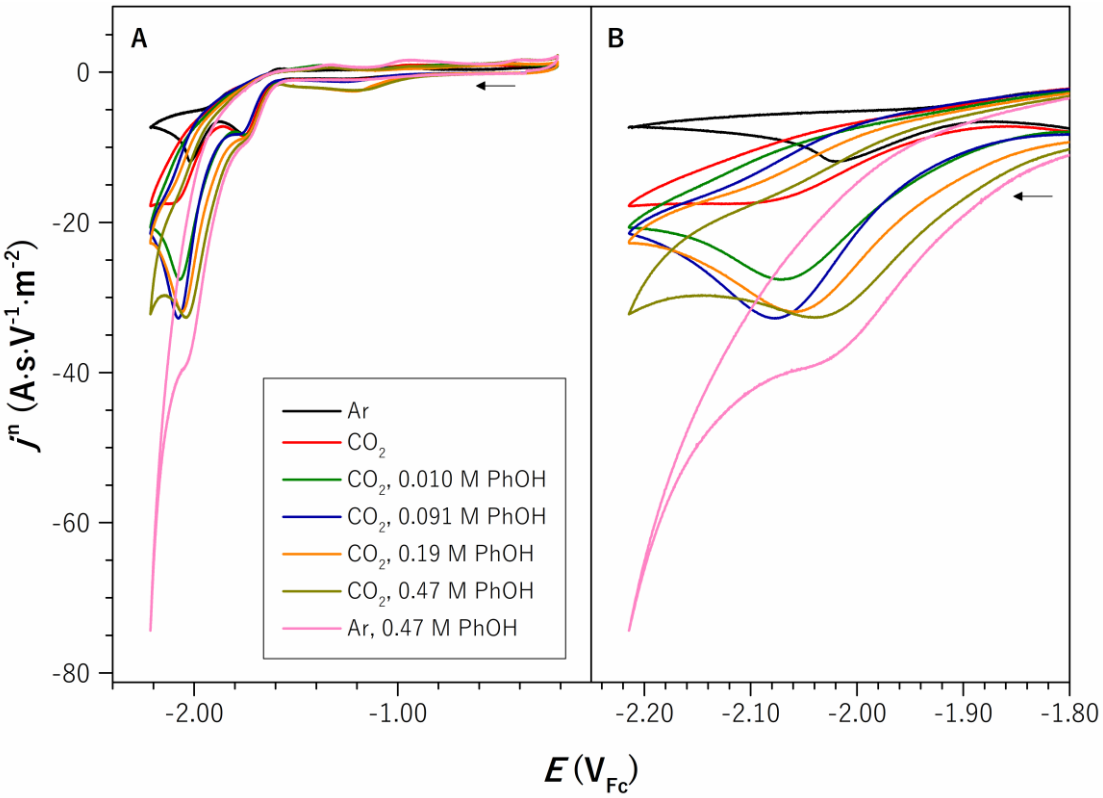

Figure C.7. (A) CVs of $\mathbf{Fe_s^{II}}$ at varying concentrations of PhOH under argon or CO_2 atmosphere and (B) zoom on the $Fe^{I/0}$ wave.

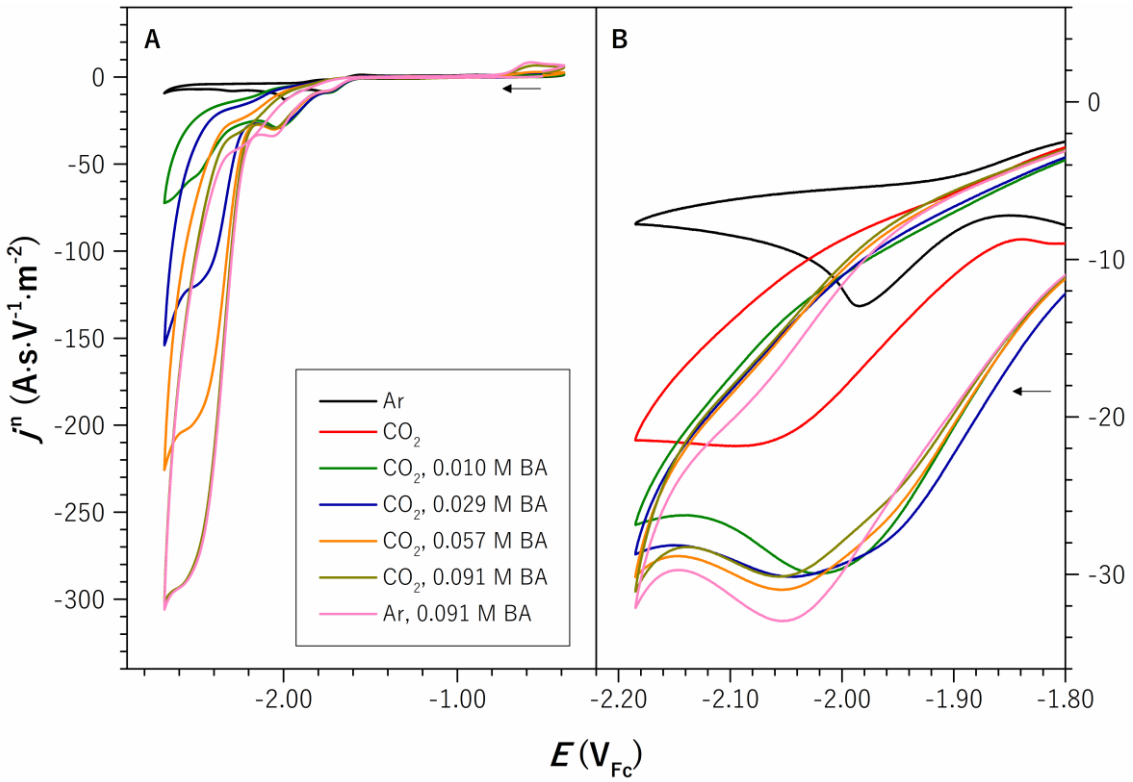

Figure C.8. (A) CVs of $\mathbf{Fe_s^{II}}$ at varying concentrations of BA under argon or CO_2 atmosphere and (B) zoom on the $Fe^{I/0}$ wave.

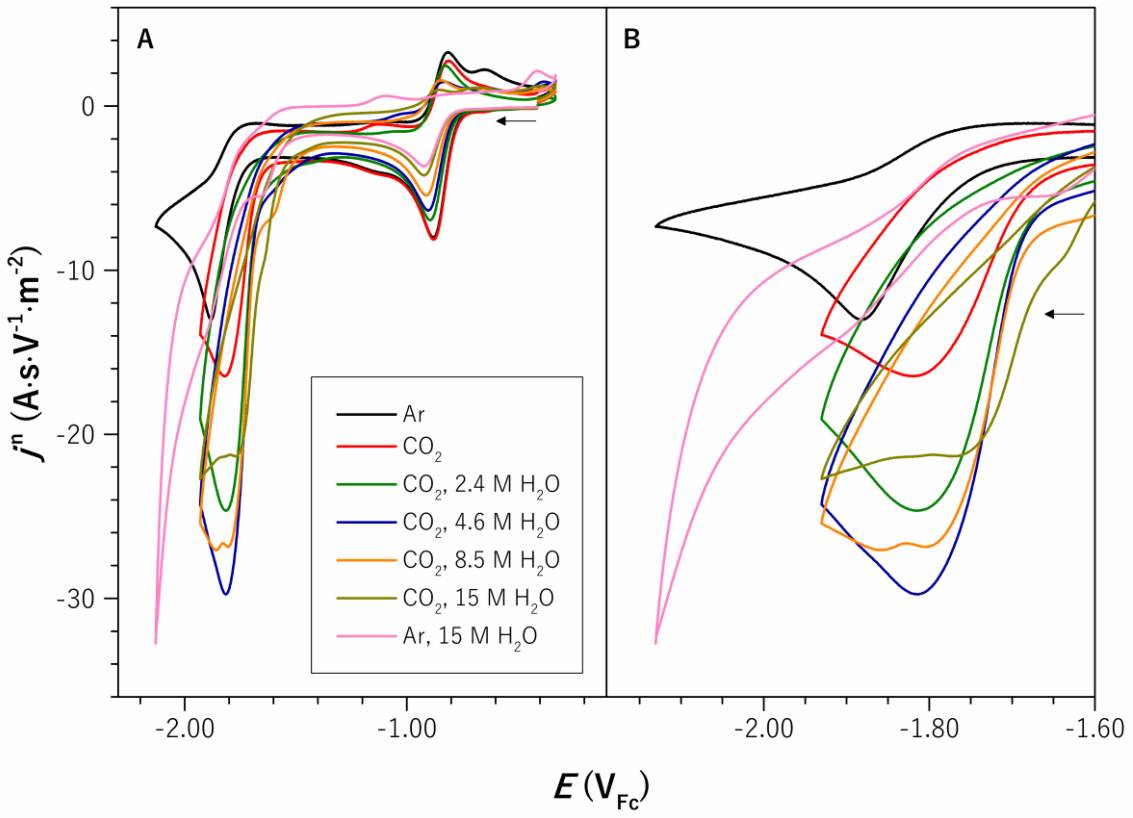

Figure C.9. (A) CVs of $\mathbf{Co_s^{II}}$ at varying concentrations of H_2O under argon or CO_2 atmosphere and (B) zoom on the $Co^{I/0}$ wave.

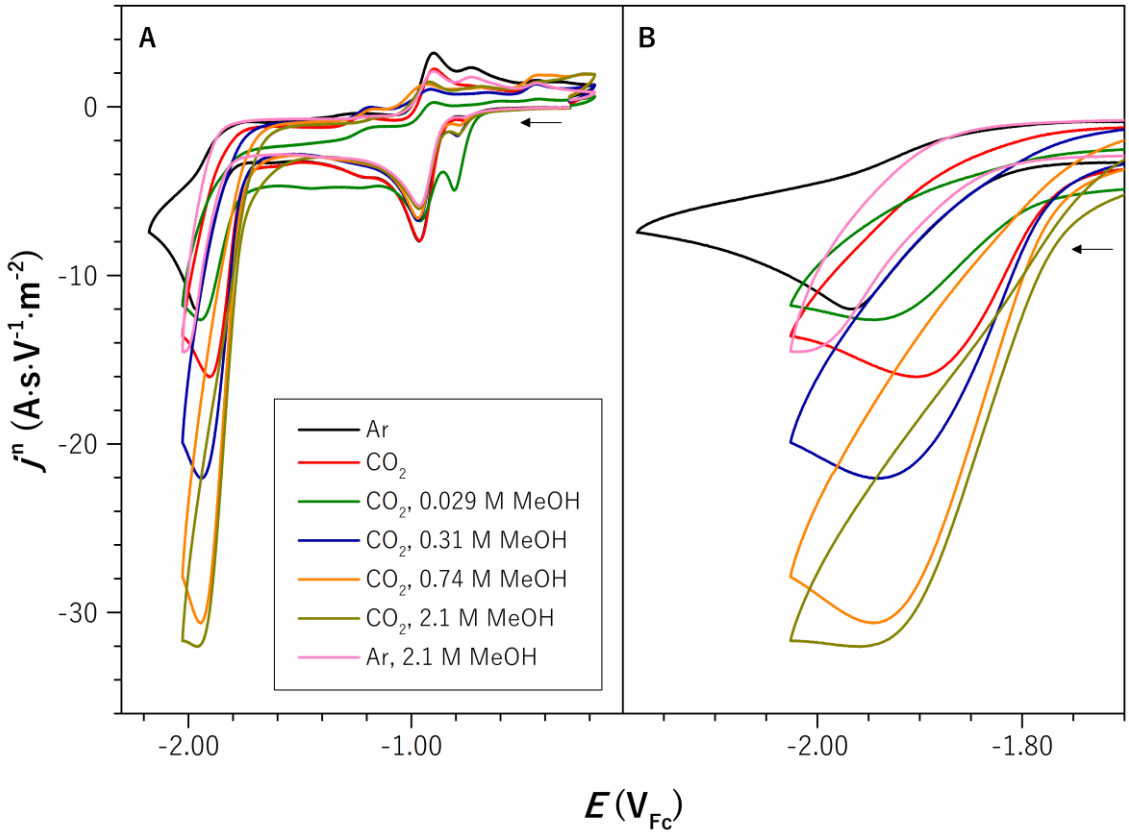

Figure C.10. (A) CVs of $\mathbf{Co_s^{II}}$ at varying concentrations of MeOH under argon or CO_2 atmosphere and (B) zoom on the $Co^{I/0}$ wave.

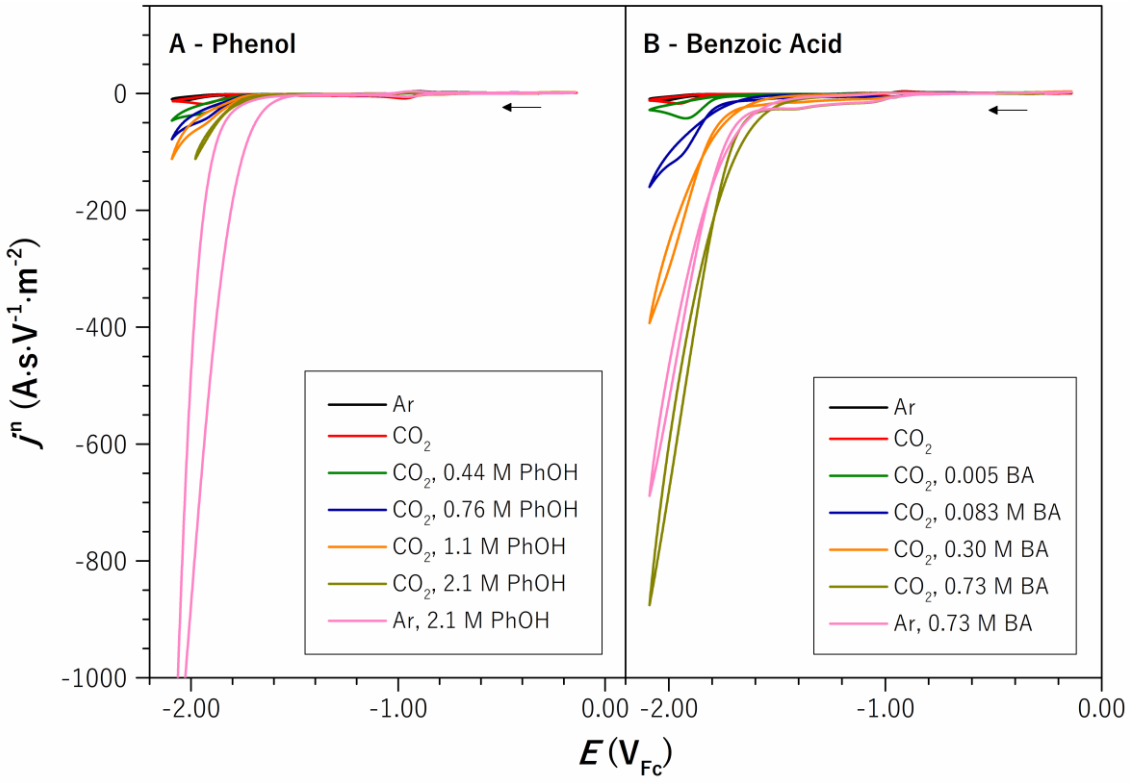

Figure C.11. CVs of $\mathbf{Co_s^{II}}$ at varying concentrations of (A) PhOH and (B) BA under argon or CO_2 atmosphere.

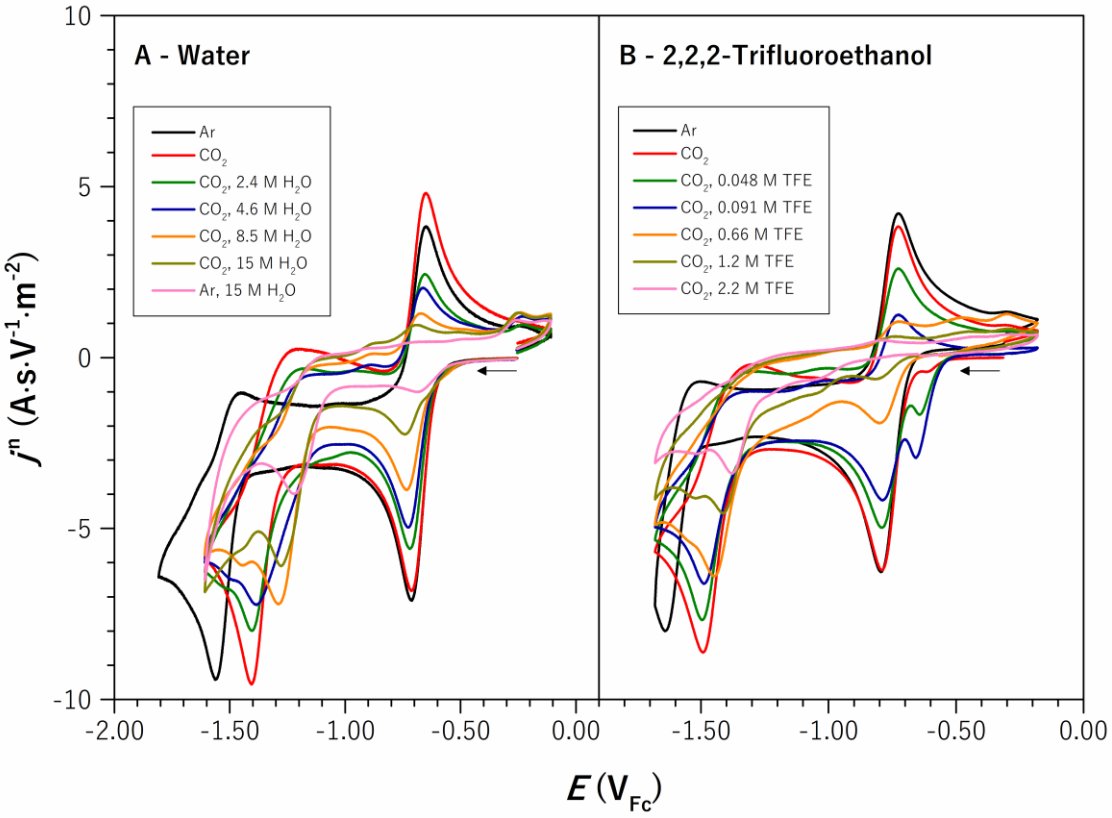

Figure C.12. CVs of Ni_s^{II} at varying concentrations of (A) H_2O and (B) TFE under argon or CO_2 atmosphere.

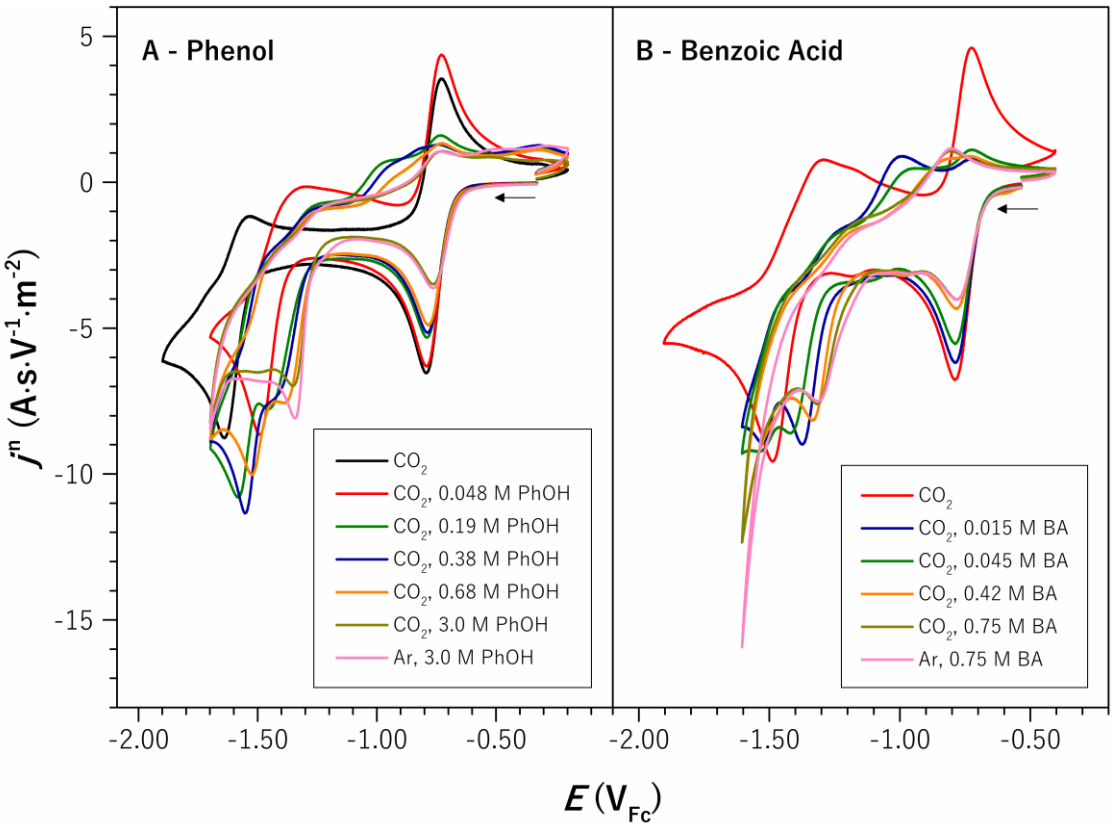

Figure C.13. CVs of Ni_s^{II} at varying concentrations of (A) PhOH and (B) BA under argon or CO_2 atmosphere.

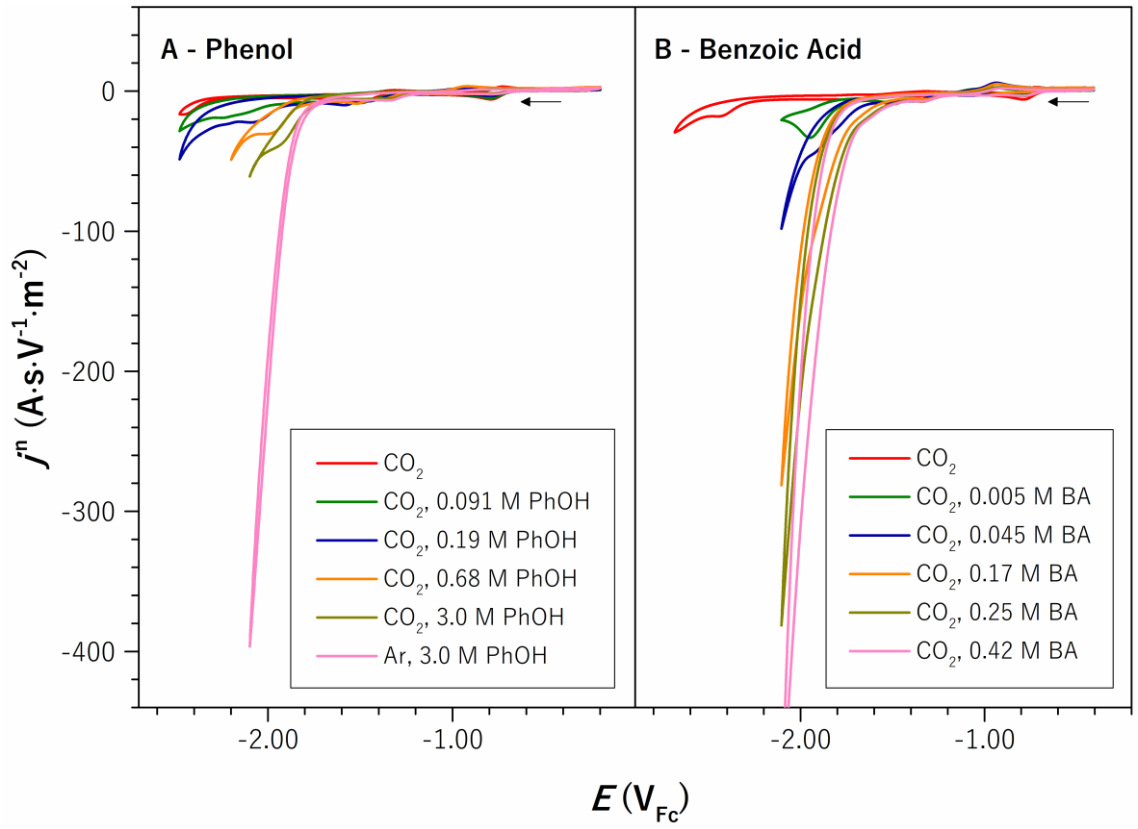

Figure C.14. Extended CVs of $\mathbf{Ni_s^{II}}$ at varying concentrations of (A) PhOH and (B) BA under argon and CO_2 atmosphere.

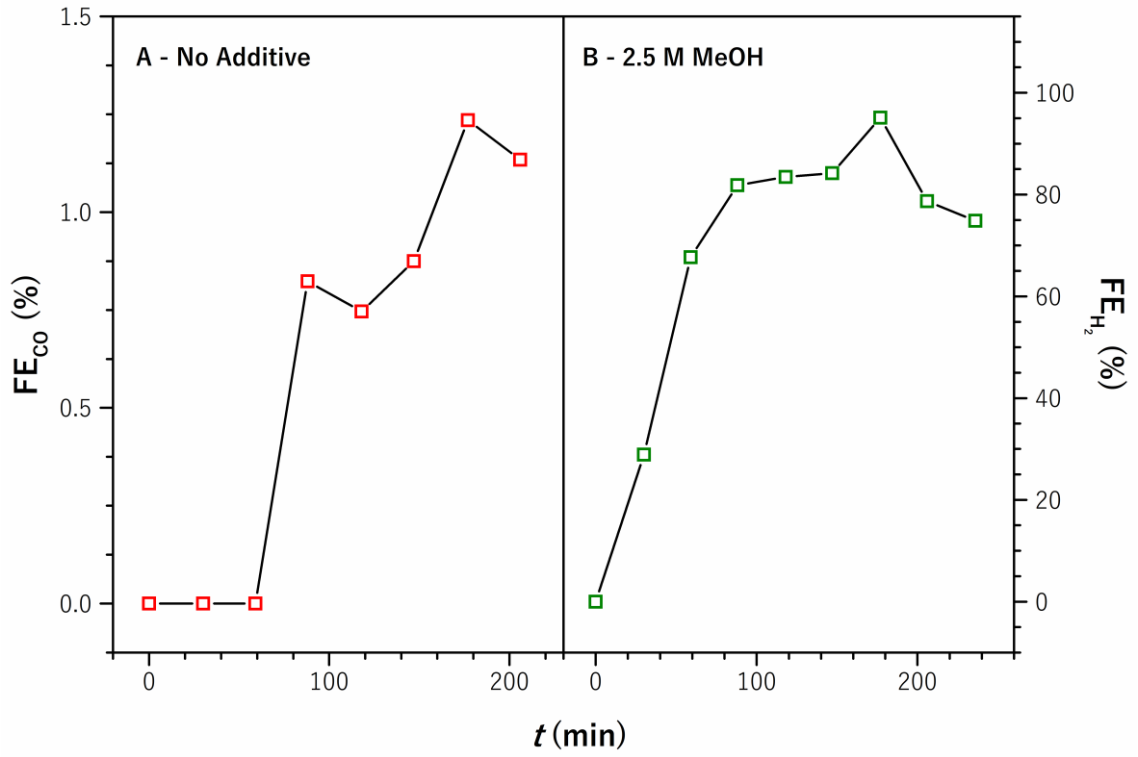

Figure C.15. FE vs. time profile for the CPE of $\mathbf{Fe_s^{II}}$ (A) without additives and (B) with 2.5 M MeOH (red: CO, green: H_2).

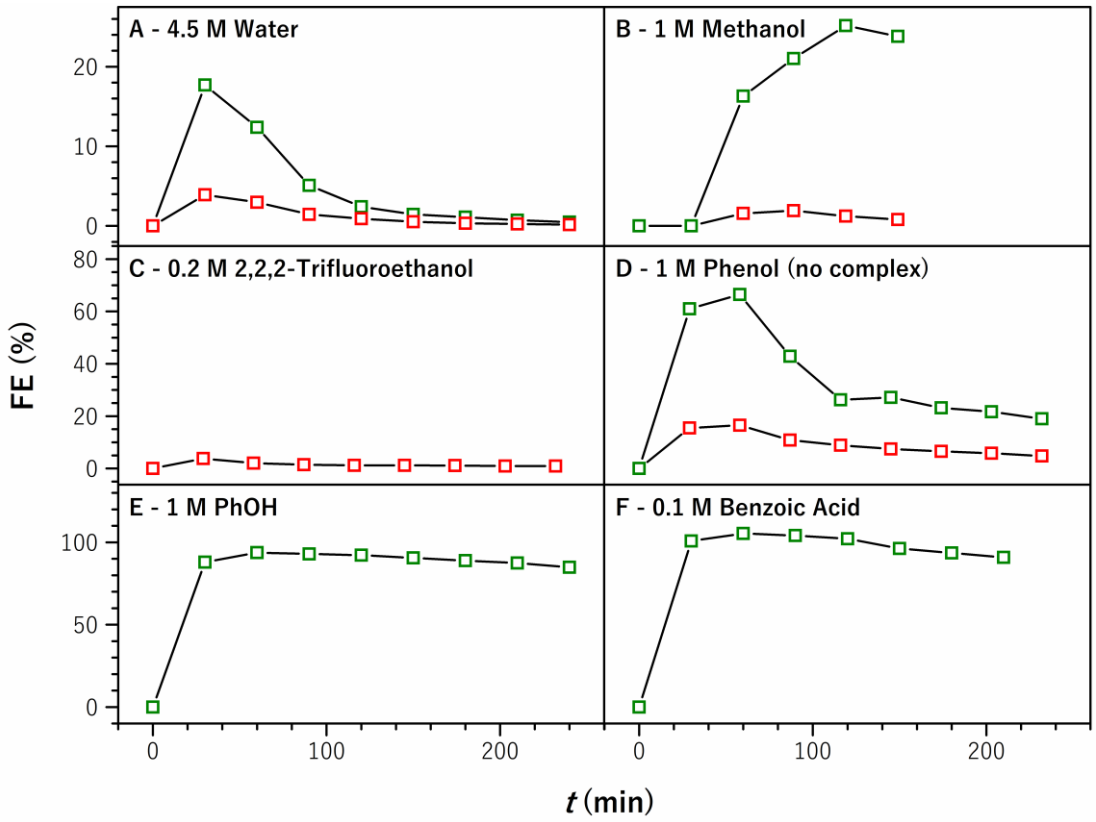

Figure C.16. FE vs. time profile for the CPE of $\mathbf{Co_s^{II}}$ with (A) 4.5 M H_2O, (B) 1 M MeOH, (C) 0.2 M TFE, (D) 1 M PhOH only, (E) 1 M PhOH as well as (F) 0.1 M BA (red: CO, green: H_2).

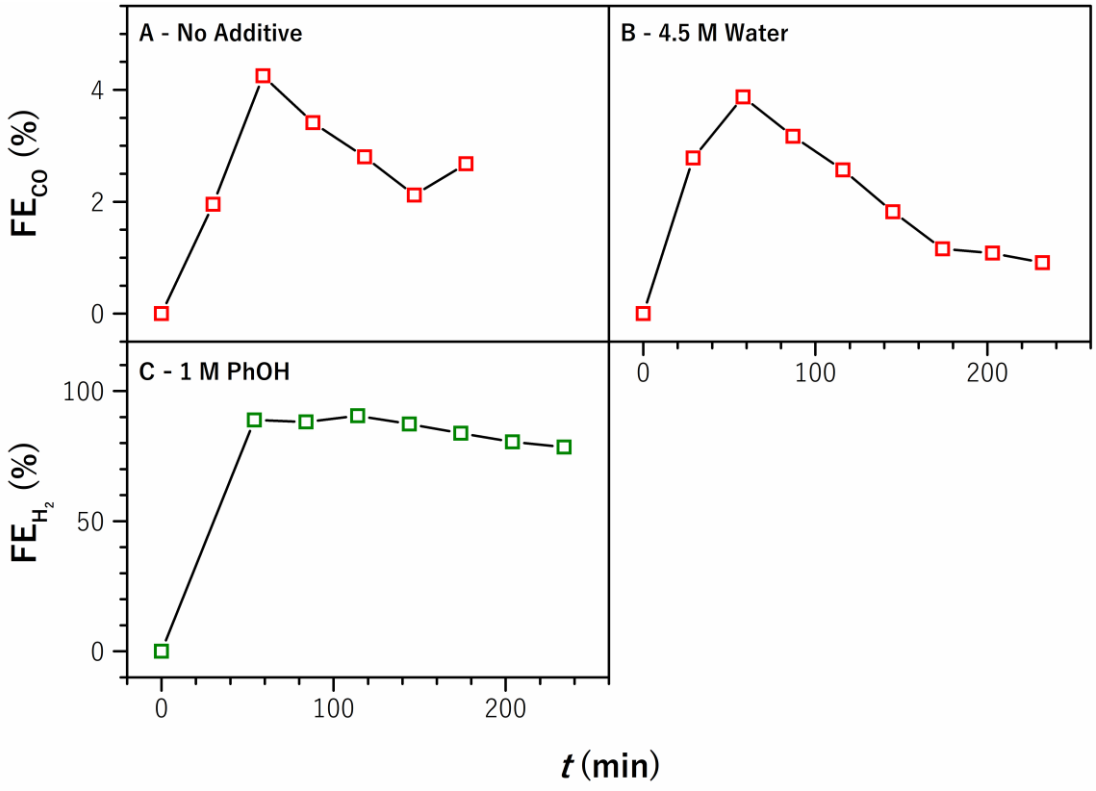

Figure C.17. FE vs. time profile for the CPE of $\mathbf{Ni_s^{II}}$ (A) without additives, (B) with 4.5 M H_2O, and (C) with 1 M PhOH (red: CO, green: H_2).

Appendix D: Electrochemical Analysis of Molecular Complexes

Cyclic Voltammetry

Cyclic voltammetry is the linear variation of an applied potential *E* while recording the resulting current *I*.[3] Although there are several instrumental requirements to consider, manifold information on the electrochemical behavior of transition metal complexes can be obtained.

a) Experimental Setup and Parameters

The electrochemical cells often consist of a three-electrode setup (Figure D.1) connected to a potentiostat, which provides the required potential, i.e., the voltage representing the driving force for a redox process, and records *I*.

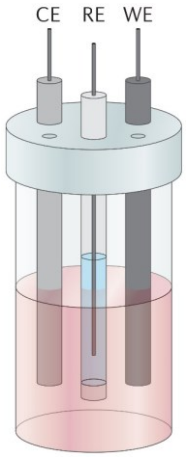

Figure D.1. Schematic representation of a three-electrode CV cell setup. Reprinted with permission from ref. [3].

The electrochemical reaction of interest occurs at the surface of the working electrode, often composed of glassy carbon, platinum, or mercury. Due to the significant involvement in the analysis process, the working electrode needs to be clean and inert in the desired potential range.[4] Analyte adsorption to the electrode surface must also be considered (*vide infra*).

A counter electrode is required to close the electric circuit and allow the complementary reaction to occur at the WE. The CE needs to exhibit a surface area higher than that of the WE to ensure that potentially slow kinetics of the counter-reaction do not affect the transformation of the analyte.

Lastly, the reaction at the reference electrode exhibits a stable equilibrium potential and serves as the reference point for determining the electric potential of the other electrodes.[4] Classic reference electrodes, such as the Normal and Reversible Hydrogen Electrode, require strict external conditions. These requirements lead to a preference for couples (e.g., Ag^+/Ag) applicable under standard laboratory conditions and the use of conversion tables to reference them to the

previously mentioned systems.[5] The potential of the electrode couple can vary between experiments, and referencing against an internal standard such as ferrocenium/ferrocene is highly recommended.[6]

Other crucial components of an electrochemical setup are the solvent and the conducting salt, also referred to as the supporting electrolyte. The former needs to combine the ability to dissolve the analyte and stability in the window of applied electrochemical potential. The supporting electrolyte must exhibit the same inertness and is introduced to enable the conductivity of the organic solutions as well as to maintain the charge balance. Tetrabutylammonium salts with non-coordinating counter-ions, such as PF_6^-, are commonly chosen in organic media to avoid interferences with the analyte during a cyclic voltammetry experiment.[4]

A general overview of basic instrumental considerations required for electrocatalysis can be found in the literature, e.g., reported by the BARAN group.[7]

b) Recording a Cyclic Voltammogram and Underlying Processes

The reversible one-electron transfer equilibrium between an oxidized catalyst species e-cat_{ox} and its reduced form e-cat_{red} [eq. (D.1), Figure 1.6] shall serve as an example to illustrate the proceedings during a cyclic voltammetry experiment.

E: $$\text{e-cat}_{ox} + e^- \rightleftarrows \text{e-cat}_{red} \quad (D.1)$$

The measurement starts from a potential E_0 (point A in Figure D.2) and is decreased with a defined scan rate v to the reverse potential E_λ at point D. The potential is led back in the reverse direction to E_0 to close the cycle (point G).[8]

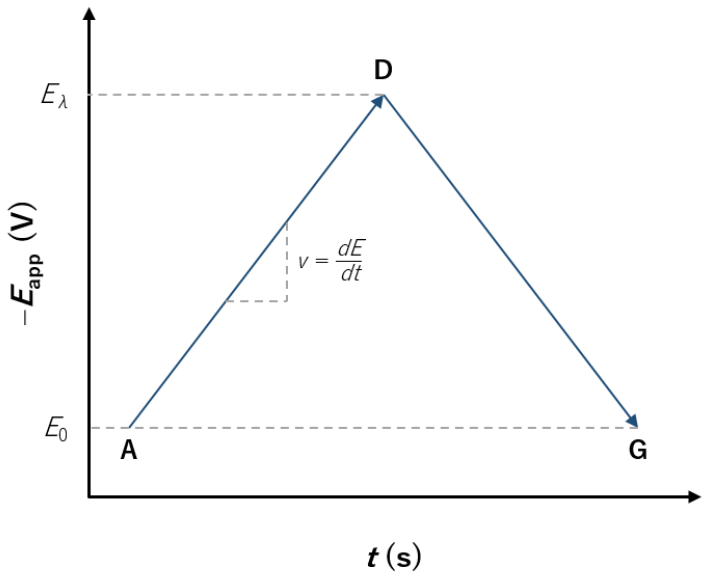

Figure D.2. Triangular potential variation during a CV experiment. Figure adapted from ref. [4].

The NERNST equation in eq. (D.2) explains the relationship between the cell potential E, the standard potential of a redox couple E^0, and the activities (often approached by more accessible concentrations) of the oxidized and the reduced species in a redox process.

$$E = E^0 + \frac{RT}{n_{e^-}F} \cdot \ln\frac{[\text{Ox}]}{[\text{Red}]} \tag{D.2}$$

with R = universal gas constant (8.314 J·mol^{-1}·K^{-1}), T = temperature, n_{e^-} = number of electrons, and F = FARADAY's constant (96485 C·mol^{-1}).

In the one-electron model reaction, the standard potential is substituted by the formal potential $E^{0'}$ [*vide infra*, eq. (D.3)].

$$E = E^{0'} + 2.3026\,\frac{RT}{n_{e^-}F} \cdot \log_{10}\frac{[\text{e-cat}_{ox}]}{[\text{e-cat}_{red}]} \tag{D.3}$$

The NERNST equation can be applied to cyclic voltammetry to predict the concentration of oxidized and reduced species with a defined standard potential $E^{0'}$ near the electrode at a specific potential E. In order to avoid perturbations by convection, the analyte solution must not be stirred during the measurement. Under this premise and complete reversibility of the electron transfer, the cyclic voltammogram will exhibit the so-called duck shape with two waves, as depicted in the center of Figure D.3.

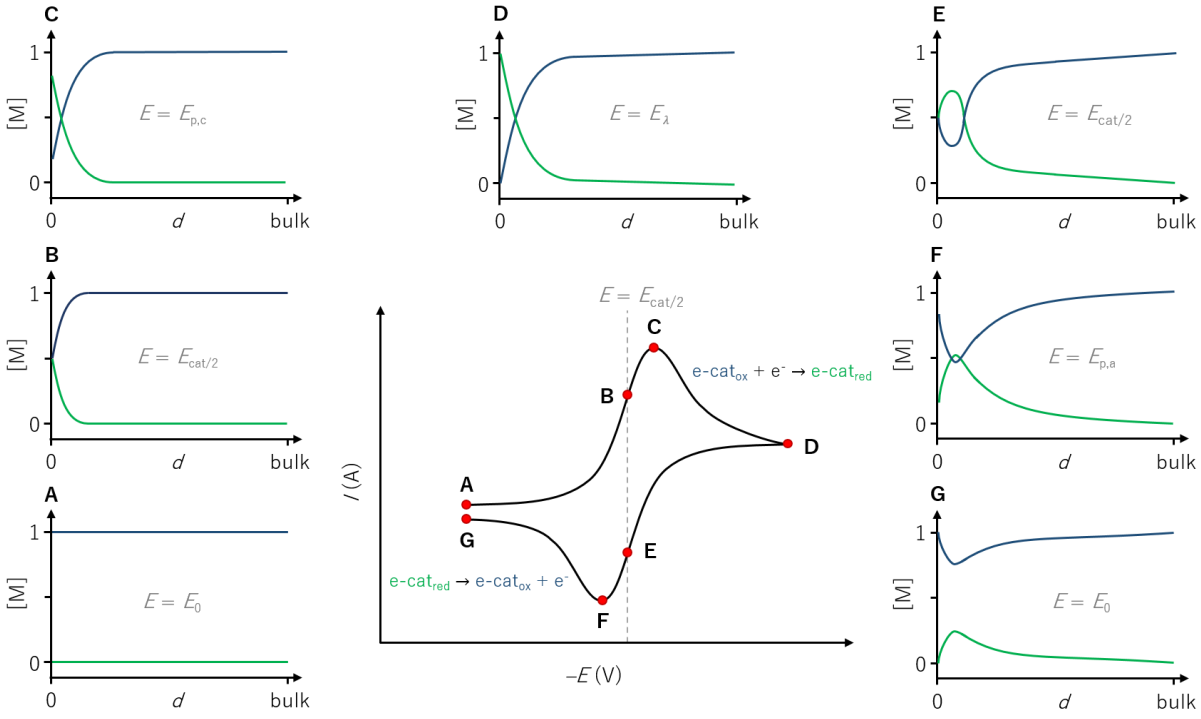

Figure D.3. A-G: Concentration profiles for e-cat$_{ox}$ (blue) and e-cat$_{red}$ (green) vs. distance from the electrode d at various points during the voltammogram (center). Figure adapted from ref. [4].

The ideal peak-to-peak separation can be found at approx. 59 mV under standard conditions, half of which will be obtained for a reversible two-electron transfer. At the starting point (A), only e-cat_{ox} is present in the system. Scanning in the negative potential direction depletes e-cat_{ox} under the simultaneous formation of e-cat_{red} and induction of an electric current at the electrode surface (B). The depletion process causes the build-up of a diffusion layer which additional analyte from the bulk solution needs to permeate to be reduced. At point C, the rate of reduction and, therefore, the electric current reaches its maximum — the cathodic peak current $i_{p,c}$. An expansion of the diffusion layer during the experiment decreases the concentration of reducible compound at the electrode surface and induces a drop in current until the reverse potential E_λ is reached (D). The same behavior can be observed for the oxidation reaction during the back scan in the positive potential direction. Point F marks the potential of anodic peak current $i_{p,a}$.

c) Obtainable Indicators in Electrochemical/-catalytic Reactions

As mentioned above, the value for $E^{0'}$ can be extracted from the voltammogram. It corresponds to $E_{cat/2}$, the potential at points B and E, located in the average between $E_{p,c}$ (C) and $E_{p,a}$ (F). Here, the concentration of oxidized and reduced species at the electrode surface is equal, simplifying the NERNST equation to $E = E^{0'}$.

Other valuable kinetic information on a reversible system can be derived with the help of the RANDLES-SEVCIK equation.

$$i_p = 0.4463 n_{e^-} F A c^0 \left(\frac{n F \nu D_0}{R T}\right)^{1/2} \tag{D.4}$$

With: A = surface area of the electrode (cm^2), D_0 = diffusion coefficient of the oxidized analyte ($cm^2 \cdot s^{-1}$), and c^0 = bulk concentration of the analyte ($mol \cdot cm^{-3}$).

The peak current of a wave in the voltammogram will increase with the scan rate due to the limited time to build up the diffusion layer. If the species diffuses freely in the reaction solution, i_p shows square root dependence on the scan rate [eq. (D.4)]. A linear dependence is observable for a surface-adsorbed species based on eq. (D.5).[9]

$$i_p = \frac{n^2 F^2}{4 R T} \nu A \Gamma^* \tag{D.5}$$

With Γ^* = surface coverage of the adsorbed species ($mol \cdot cm^{-2}$).

If a species assumed to be freely diffused does not follow the expected behavior, this can be caused by quasi-reversibility due to the electron transfer being rate-limiting. In this case, the peak-to-peak separation should increase with the scan rate.[4]

The shape of a redox wave can vary dramatically when traversing from the purely electrochemical transformation [eq. (D.1)] to a sequence of electrochemical event (**E**) and chemical transformation (**C**) or *vice versa* (**CE**).

EC mechanisms follow the sequence schematically shown in eq. (D.6) and (D.7).

E: $$A + e^- \rightleftarrows B \tag{D.6}$$

C: $$B \rightleftarrows C \tag{D.7}$$

The chemical equilibrium is described by the constant K, itself defined as the quotient of the forward (+) and backward (–) rate constant k [eq. (D.8)].

$$K = \frac{k^+}{k^-} \tag{D.8}$$

According to SAVÉANT, the CV response in an **EC** mechanism mainly depends on K and the dimensionless kinetic parameter λ representing the competition between a chemical reaction and diffusion [eq. (D.9)].[10]

$$\lambda = \frac{RT}{F}\frac{k^+ + k^-}{\nu} = \frac{RT}{F}\frac{k}{\nu} \tag{D.9}$$

The kinetic zone diagram in Figure D.4 gives an overview of the accessible regimes.

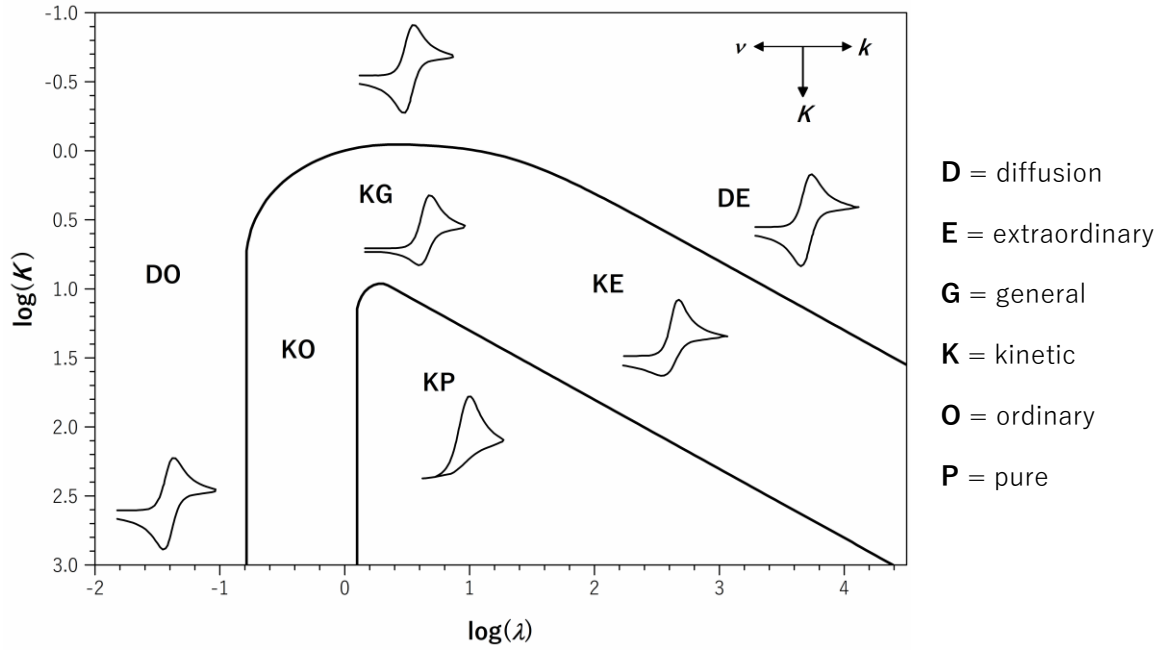

Figure D.4. Kinetic zone diagram for the **EC** mechanism adapted from ref. [10] (left) and abbreviations as proposed by the DEMPSEY group[11] (right).

The typical NERNSTIAN wave shape is retained independently from λ and k at low K values (= $k^+ + k^-$, top of Figure D.4), whereas, at high values of K (e.g., 10^3), the wave shapes are modulated as shown in Figure D.5.

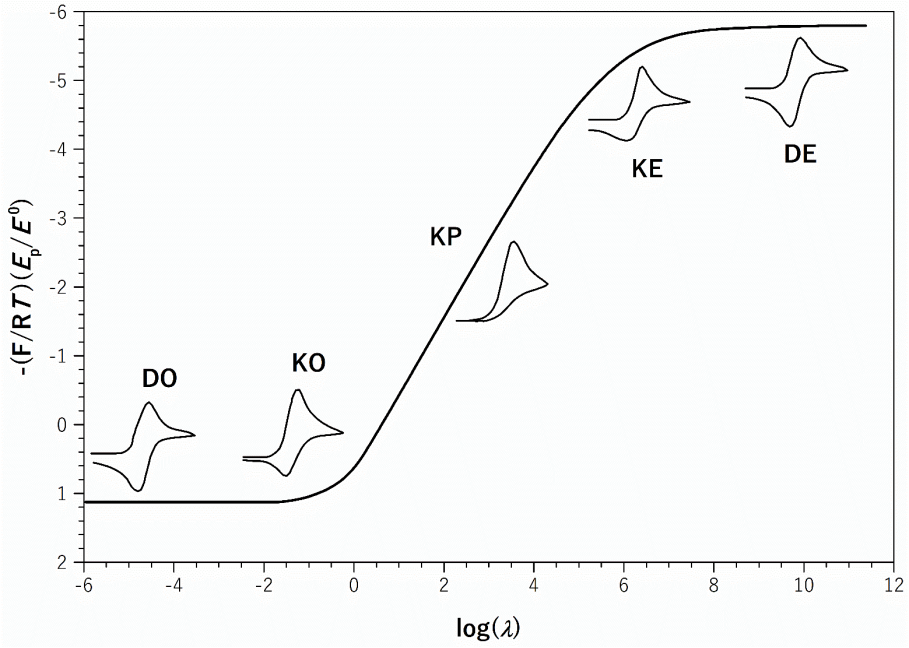

Figure D.5. CV responses in an **EC** mechanism when crossing the kinetic zone diagram (Figure D.4) at $K = 10^3$. Adapted from ref. [10].

In the KP zone (pure kinetic conditions), the forward rate constant k^+ of the chemical event relates to the voltamperometric peak potential E_p by eq. (D.10).[10]

$$E_p = E^0 - 0.78\frac{RT}{F} + \frac{RT}{2F}\ln\left(\frac{RTk^+}{Fv}\right) \qquad (D.10)$$

E_p shifts cathodically by 29.6 mV/$\log_{10}$ when increasing the scan rate or decreasing the rate constant. Noting a the intercept of the linear fit of $E_p = f[\log(v)]$, rearrangement gives equation (D.11) and allows the determination of k^+:

$$k^+ = \frac{F}{RT}\exp\left(1.56 + \frac{2F}{RT}(a - E^0)\right) \qquad (D.11)$$

The **CE** mechanism comprises the reaction sequence inverse to **EC** [eq. (D.12) and (D.13)] with the kinetic zone diagram described in Figure D.6.

C: $C \rightleftarrows A$ (D.12)

E: $A + e^- \rightleftarrows B$ (D.13)

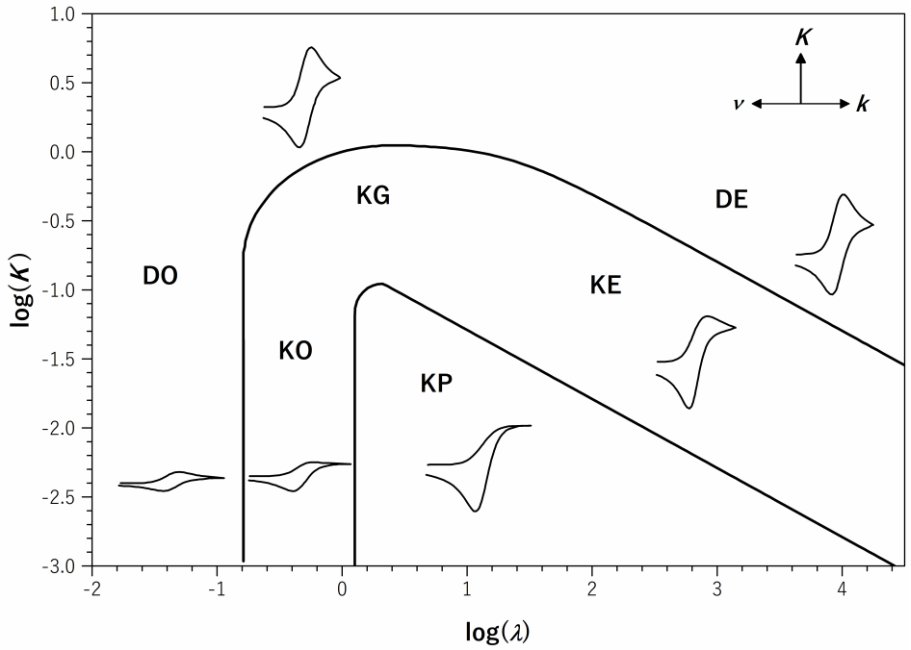

Figure D.6. Kinetic zone diagram for the **CE** mechanism adapted from ref. [10].

While a change in the kinetic regime mainly affects the potential of the wave in the **EC** mechanism, the wave shape and height are altered in the **CE** mechanism. Here, k^+ relates to the half-wave potential $E_{1/2}$ by eq. (D.14).

$$E_{1/2} = E^0_{A/B} - 0.17\frac{RT}{F} + \frac{RT}{2F}\ln\left(\frac{RTk^+}{Fv}\right) \tag{D.14}$$

The equilibrium constant K can be calculated from eq. (D.15) in the DE zone.

$$E^0 = E^0_{A/B} + \frac{RT}{F}\ln\left(\frac{K}{1+K}\right) \tag{D.15}$$

Controlled Potential Electrolysis

A potentiostat can constantly apply the catalytic potential in an electrocatalytic experiment to induce a continuous electron supply and quantitative substrate conversion. In a CPE setup, the cathodic half-cell can be separated from the anodic side by a diaphragm to avoid perturbations by unwanted byproducts generated at the counter electrode.[4] Figure D.7 schematically displays the coupling of cathodic CO_2 reduction and anodic water oxidation in such a cell.

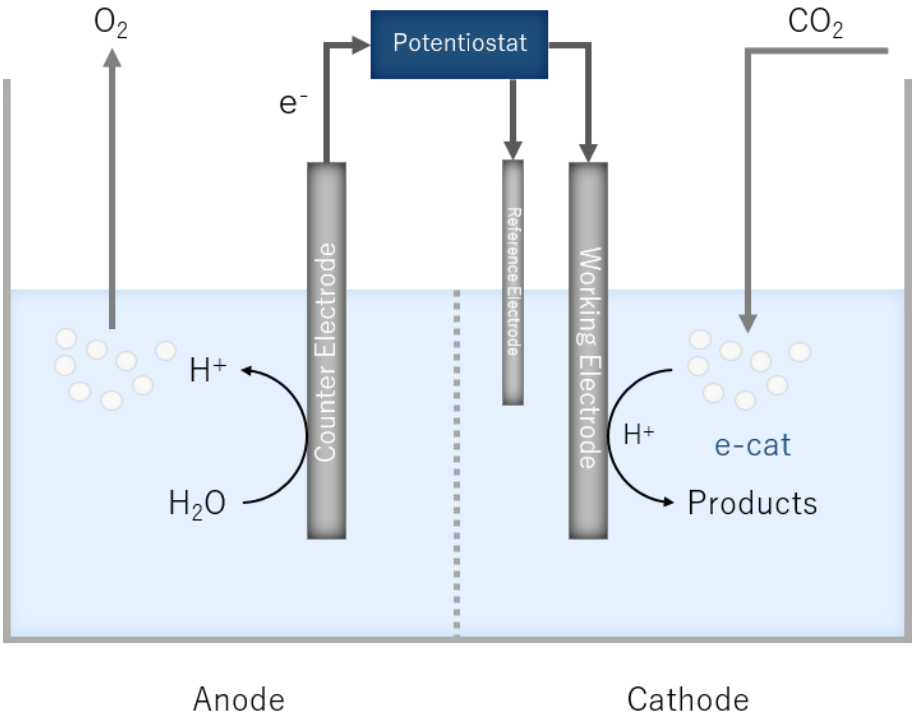

Figure D.7. Schematic representation of a divided electrochemical cell for CO_2 reduction to soluble products. Water oxidation to protons and molecular oxygen was chosen as an example of the anodic counter-reaction.

References

[1] L. Yang, D. R. Powell, R. P. Houser, *Dalton Trans.* **2007**, 955.

[2] A. W. Addison, T. N. Rao, J. Reedijk, J. van Rijn, G. C. Verschoor, *J. Chem. Soc., Dalton Trans.* **1984**, 1349.

[3] K. J. Lee, N. Elgrishi, B. Kandemir, J. L. Dempsey, *Nat. Rev. Chem.* **2017**, *1*, 0039.

[4] N. Elgrishi, K. J. Rountree, B. D. McCarthy, E. S. Rountree, T. T. Eisenhart, J. L. Dempsey, *J. Chem. Educ.* **2018**, *95*, 197.

[5] V. V. Pavlishchuk, A. W. Addison, *Inorg. Chim. Acta* **2000**, *298*, 97.

[6] a) R. R. Gagne, C. A. Koval, G. C. Lisensky, *Inorg. Chem.* **1980**, *19*, 2854; b) S. Trasatti, *Pure Appl. Chem.* **1986**, *58*, 955.

[7] C. Kingston, M. D. Palkowitz, Y. Takahira, J. C. Vantourout, B. K. Peters, Y. Kawamata, P. S. Baran, *Acc. Chem. Res.* **2020**, *53*, 72.

[8] G. A. Mabbott, *J. Chem. Educ.* **1983**, *60*, 697.

[9] A. J. Bard, L. R. Faulkner, *Electrochemical Methods*, 2nd ed., John Wiley & Sons, Inc., New York, **2001**.

[10] J.-M. Savéant, C. Costentin, *Elements of Molecular and Biomolecular Electrochemistry: An Electrochemical Approach to Electron Transfer Chemistry*, 2nd ed., John Wiley & Sons Inc., Hoboken, NJ, **2019**.

[11] D. J. Martin, B. D. McCarthy, E. S. Rountree, J. L. Dempsey, *Dalton Trans.* **2016**, *45*, 9970.